

CHARACTERIZATION OF  
AMORPHOUS AND  
CRYSTALLINE ROUGH SURFACE:  
PRINCIPLES AND APPLICATIONS

YIPING ZHAO  
GWO-CHING WANG  
TOH-MING LU

VOLUME 37  
EXPERIMENTAL METHODS IN THE PHYSICAL SCIENCES

Treatise Editors  
ROBERT CELOTTA  
THOMAS LUCATORTO



ACADEMIC PRESS

*Experimental Methods in the  
Physical Sciences*

VOLUME 37

CHARACTERIZATION OF AMORPHOUS AND CRYSTALLINE  
ROUGH SURFACE: PRINCIPLES AND APPLICATIONS

# **EXPERIMENTAL METHODS IN THE PHYSICAL SCIENCES**

Robert Celotta and Thomas Lucatorto, *Editors in Chief*

*Founding Editors*

L. MARTON  
C. MARTON

Volume 37

# Characterization of Amorphous and Crystalline Rough Surface: Principles and Applications

Yiping Zhao, Gwo-Ching Wang, and Toh-Ming Lu

*Department of Physics, Applied Physics, and Astronomy*

*Rensselaer Polytechnic Institute*

*Troy, New York*



**ACADEMIC PRESS**

A Harcourt Science and Technology Company

San Diego San Francisco New York Boston London Sydney Tokyo

This book is printed on acid-free paper. 

Copyright © 2001 by Academic Press

All rights reserved.

No part of this publication may be reproduced or transmitted in any form or by any means, electronic or mechanical, including photocopy, recording, or any information storage and retrieval system, without permission in writing from the publisher.

The appearance of the code at the bottom of the first page of a chapter in this book indicates the Publisher's consent that copies of the chapter may be made for personal or internal use of specific clients. This consent is given on the condition, however, that the copier pay the stated per copy fee through the Copyright Clearance Center, Inc. (222 Rosewood Drive, Danvers, Massachusetts 01923), for copying beyond that permitted by Sections 107 and 108 of the U.S. Copyright Law. This consent does not extend to other kinds of copying, such as copying for general distribution, for advertising or promotional purposes, for creating new collective works, or for resale. Copy fees for pre-1999 chapters are as shown on the title pages. If no fee code appears on the title page, the copy fee is the same as for current chapters. 1079-4042/00 \$35.00

Explicit permission from Academic Press is not required to reproduce a maximum of two figures or tables from an Academic Press article in another scientific or research publication provided that the material has not been credited to another source and that full credit to the Academic Press article is given.

**ACADEMIC PRESS**

*A Harcourt Science and Technology Company*  
525 B Street, Suite 1900, San Diego, CA 92101-4495, USA  
<http://www.academicpress.com>

Academic Press  
Harcourt Place, 32 Jamestown Road, London NW1 7BY, UK  
<http://www.academicpress.com>

International Standard Serial Number: 1079-4042

International Standard Book Number: 0-12-475984-X

PRINTED IN THE UNITED STATES OF AMERICA  
00 01 02 03 04 QW 9 8 7 6 5 4 3 2 1

## CONTENTS

VOLUMES IN SERIES .....	xi
PREFACE .....	xv
<b>1. Introduction</b>	
References .....	5
<b>2. Statistical Nature of Rough Surfaces</b>	
2.1 First-Order Statistics: Surface Height Distribution Function and Characteristic Function .....	7
2.2 Second-Order Statistics: Auto-Correlation Function, Height-Height Correlation Function, and Power Spectrum ..	13
2.3 Other Statistical Properties of a Random Rough Surface .....	21
2.4 Numerical Estimation of the Roughness Parameters .....	23
2.5 Summary .....	32
References .....	32
<b>3. Examples of Random Rough Surfaces</b>	
3.1 Self-Affine Surfaces .....	33
3.2 Mounded Surfaces .....	42
3.3 Anisotropic Surfaces .....	47
3.4 Dynamics of Random Rough Surface Formation .....	54
3.5 Generating Rough Surfaces .....	56
3.6 Summary .....	58
References .....	59

<b>4. Real-Space Surface Profiling Techniques</b>	
4.1 Scanning Techniques .....	63
4.2 Imaging Techniques .....	77
4.3 Summary .....	81
References .....	81
<b>5. Effects of Finite Tip and Sample Sizes</b>	
5.1 Finite Tip Size Effects in SPM Measurements .....	83
5.2 Finite Sampling Size Effect in Image Analysis .....	88
5.3 Summary .....	101
References .....	102
<b>6. Diffraction Techniques—Fundamentals</b>	
6.1 Scattering and Diffraction Concepts .....	104
6.2 Multi-Atom Diffraction .....	110
6.3 Diffraction from Rough Surfaces—General Formula .....	117
6.4 Diffraction from Rough Surfaces—Continuum Theory .....	122
6.5 Summary .....	132
References .....	132
<b>7. Diffraction from Random Rough Surfaces</b>	
7.1 General Properties of Diffraction Profiles .....	133
7.2 Diffraction from a Gaussian Rough Surface .....	135
7.3 Diffraction from Multi-Step Surfaces in 2+1 Dimensions .....	142
7.4 Summary .....	155
References .....	156

<b>8. Diffraction Techniques—Experimentation</b>	
8.1 The Diffraction Geometries .....	157
8.2 The Measured Diffraction Intensity Profile .....	165
8.3 Practical Issues in Diffraction Measurement .....	172
8.4 Summary .....	175
References .....	176
<b>9. Self-Affine Fractal Surfaces</b>	
9.1 Real-Space Characteristics .....	179
9.2 Diffraction from an Isotropic Self-Affine Gaussian Surface ..	181
9.3 An Example: The Backside of Silicon Wafers .....	189
9.4 Diffraction from Discrete Self-Affine Surfaces .....	203
9.5 Summary .....	208
References .....	209
<b>10. Mounded Surfaces</b>	
10.1 Real-Space Characteristics .....	211
10.2 Diffraction from Mounded Surfaces .....	212
10.3 Diffraction from Discrete Mounded Surfaces .....	216
10.4 Examples .....	217
10.5 Summary .....	219
References .....	221
<b>11. Anisotropic Surfaces</b>	
11.1 Real-Space Characteristics .....	223
11.2 Diffraction from Anisotropic Surfaces .....	224
11.3 An Example: The Hard-Disk Surface .....	231
11.4 Summary .....	239
References .....	239

**12. Non-Gaussian Surfaces**

12.1 Height Difference Distribution $P(z, \mathbf{r})$ and Height Difference Function $C(k_{\perp}, \mathbf{r})$ .....	241
12.2 Diffraction Structure Factors from Non-Gaussian Surfaces ..	247
12.3 Summary .....	254
References .....	254

**13. Two-Dimensional Fractal Surfaces**

13.1 A Discrete Two-Level Surface .....	255
13.2 Special Cases for Discrete Two-Level Surfaces .....	257
13.3 Continuous Two-Level Surfaces .....	266
13.4 Determination of Roughness Parameters .....	270
13.5 Summary .....	271
References .....	271

**14. Transition to Multilayer Structures**

14.1 Intensity Oscillations .....	274
14.2 Diffraction from Dynamic Roughening Fronts .....	291
14.3 Summary .....	300
References .....	300

**15. Transmission Diffraction and Fractals**

15.1 Transmission Diffraction Geometry .....	303
15.2 Three-Dimensional Fractal Structures .....	305
15.3 Diffraction Characteristics .....	306
References .....	308

**16. Effects of Surface Roughness: Examples**

16.1 Local Slope, Surface Area, and Surface Energy .....	309
--	-----

16.2 Effect of Surface/Interface Roughness on Electrical Properties of Thin Films . . . . .	311
16.3 Effect of Surface/Interface Roughness on Magnetic Properties of Thin Films . . . . .	319
16.4 Effect of Surface/Interface Roughness on Electronic Device Operations . . . . .	332
16.5 Summary . . . . .	348
References . . . . .	348
Appendix A. Growth Dynamics . . . . .	353
Appendix B. Time Evolution of the Interface Width in the Edwards-Wilkinson Equation . . . . .	381
Appendix C. Effect of Different Functional Forms of the Scaling Function on the Shape of the Diffraction Profile . . . . .	383
Appendix D. Joint Distributions of Random Processes with Non-Gaussian Height Distributions . . . . .	387
Appendix E. Height Difference Function $C(k_{\perp}, r)$ for Different Height Distributions . . . . .	391
Appendix F. A Perturbative Solution of Sine-Gorden Equation . . . . .	399
Appendix G. Speckle . . . . .	403

Appendix H. Diffraction of an Ultrafast Radiation Pulse .....	407
INDEX .....	411

# VOLUMES IN SERIES

## EXPERIMENTAL METHODS IN THE PHYSICAL SCIENCES

(formerly Methods of Experimental Physics)

*Editors-in-Chief*

*Robert Celotta and Thomas Lucatorto*

Volume 1. Classical Methods  
*Edited by Immanuel Estermann*

Volume 2. Electronic Methods, Second Edition (in two parts)  
*Edited by E. Bleuler and R. O. Haxby*

Volume 3. Molecular Physics, Second Edition (in two parts)  
*Edited by Dudley Williams*

Volume 4. Atomic and Electron Physics—Part A: Atomic Sources  
and Detectors; Part B: Free Atoms  
*Edited by Vernon W. Hughes and Howard L. Schultz*

Volume 5. Nuclear Physics (in two parts)  
*Edited by Luke C. L. Yuan and Chien-Shiung Wu*

Volume 6. Solid State Physics—Part A: Preparation, Structure, Mechanical  
and Thermal Properties; Part B: Electrical, Magnetic and Optical Properties  
*Edited by K. Lark-Horovitz and Vivian A. Johnson*

Volume 7. Atomic and Electron Physics—Atomic Interactions  
(in two parts)  
*Edited by Benjamin Bederson and Wade L. Fite*

Volume 8. Problems and Solutions for Students  
*Edited by L. Marton and W. F. Hornyak*

Volume 9. Plasma Physics (in two parts)  
*Edited by Hans R. Griem and Ralph H. Lovberg*

Volume 10. Physical Principles of Far-Infrared Radiation  
By L. C. Robinson

Volume 11. Solid State Physics  
*Edited by* R. V. Coleman

Volume 12. Astrophysics—Part A: Optical and Infrared Astronomy  
*Edited by* N. Carleton

Part B: Radio Telescopes; Part C: Radio Observations  
*Edited by* M. L. Meeks

Volume 13. Spectroscopy (in two parts)  
*Edited by* Dudley Williams

Volume 14. Vacuum Physics and Technology  
*Edited by* G. L. Weissler and R. W. Carlson

Volume 15. Quantum Electronics (in two parts)  
*Edited by* C. L. Tang

Volume 16. Polymers—Part A: Molecular Structure and Dynamics;  
Part B: Crystal Structure and Morphology; Part C: Physical Properties  
*Edited by* R. A. Fava

Volume 17. Accelerators in Atomic Physics  
*Edited by* P. Richard

Volume 18. Fluid Dynamics (in two parts)  
*Edited by* R. J. Emrich

Volume 19. Ultrasonics  
*Edited by* Peter D. Edmonds

Volume 20. Biophysics  
*Edited by* Gerald Ehrenstein and Harold Lecar

Volume 21. Solid State: Nuclear Methods  
*Edited by* J. N. Mundy, S. J. Rothman, M. J. Fluss, and L. C. Smedskjaer

Volume 22. Solid State Physics: Surfaces  
*Edited by* Robert L. Park and Max G. Lagally

Volume 23. Neutron Scattering (in three parts)  
*Edited by* K. Sköld and D. L. Price

Volume 24. Geophysics—Part A: Laboratory Measurements;  
Part B: Field Measurements  
*Edited by C. G. Sammis and T. L. Henyey*

Volume 25. Geometrical and Instrumental Optics  
*Edited by Daniel Malacara*

Volume 26. Physical Optics and Light Measurements  
*Edited by Daniel Malacara*

Volume 27. Scanning Tunneling Microscopy  
*Edited by Joseph Stroscio and William Kaiser*

Volume 28. Statistical Methods for Physical Science  
*Edited by John L. Stanford and Stephen B. Vardaman*

Volume 29. Atomic, Molecular, and Optical Physics—Part A: Charged Particles;  
Part B: Atoms and Molecules; Part C: Electromagnetic Radiation  
*Edited by F. B. Dunning and Randall G. Hulet*

Volume 30. Laser Ablation and Desorption  
*Edited by John C. Miller and Richard F. Haglund, Jr.*

Volume 31. Vacuum Ultraviolet Spectroscopy I  
*Edited by J. A. R. Samson and D. L. Ederer*

Volume 32. Vacuum Ultraviolet Spectroscopy II  
*Edited by J. A. R. Samson and D. L. Ederer*

Volume 33. Cumulative Author Index and Tables of Contents, Volumes 1–32

Volume 34. Cumulative Subject Index

Volume 35. Methods in the Physics of Porous Media  
*Edited by Po-zen Wong*

Volume 36. Magnetic Imaging and Its Applications to Materials  
*Edited by Marc De Graef and Yimei Zhu*

Volume 37. Characterization of Amorphous and Crystalline Rough Surface:  
Principles and Applications  
*By YiPing Zhao, Gwo-Ching Wang, and Toh-Ming Lu*

This Page Intentionally Left Blank

## PREFACE

The morphology of a growth front or an etch front is not only a subject of great interest from a practical point of view but also is of fundamental scientific interest. Very often surfaces are created under far-from-equilibrium conditions so that the morphology is not always smooth. A standard statistical approach to nonequilibrium processes has not been developed so far, and conventional statistical methods cannot be used to describe the complex morphology of growth or etch fronts. Starting from the early 80's, a phenomenological approach has been proposed to describe the creation of a rough growth front based on a set of continuum equations (Langevin equations). This development was complemented by extensive Monte Carlo simulations. The solutions often lead to very interesting scaling behaviors. Several books have been published to summarize this development. Recent examples are: *Fractal Concepts in Surface Growth* by A.-L. Barabási and H. E. Stanley, Cambridge University Press (1995); and *Fractals, Scaling, and Growth Far from Equilibrium* by P. Meakin, Cambridge University Press (1998).

Experimental development in the characterization of the rough morphology has generally lagged behind the theoretical progress. However, in the past decade, rapid advancement in real-space imaging and diffraction techniques has changed the situation. The improvement of the instrumentation and the fundamental understanding of the capability of scanning probe microscopy (SPM) has led to an increased use of the technique as a quantitative tool for surface roughness measurements in real space. On the diffraction techniques, since *Diffraction from Rough Surfaces and Dynamic Growth Fronts* (H.-N. Yang, G.-C Wang, and T.-M. Lu, World Scientific (1993)) was published, considerable advancement has been made both in the understanding of the diffraction characteristics of different rough surfaces and in the instrumental development which greatly improves the spatial and temporal resolutions. These advancements have allowed a wider use of diffraction techniques to characterize rough surfaces.

Scanning probe microscopy (SPM) and diffraction techniques are complementary tools for surface structural characterization. Scanning probe microscopy gives local images of the surface topography and has a tremendous visual effect. On the other hand, diffraction often can provide a statistical value of the roughness parameters from a larger sampling area in a shorter time. The extraction of the roughness parameters from diffraction requires theoretical modeling of the diffraction intensity. However, the diffraction techniques have the potential of performing real-time measurements in a hostile environment.

In addition to a detailed description of the characteristics of random rough surfaces, this book focuses on the basic principles of real-space and diffraction techniques for quantitative characterization of the rough surfaces. The book thus includes the latest developments on the characterization and measurements of a wide variety of rough surfaces. The book is not only useful for university researchers but also for industrial scientists working in the areas of thin film growth, optical coating, plasma etching, patterning, machining, polishing, tribology, etc.

After introductory remarks in Chapter 1, a detailed description of the statistical nature of the surface, including the roughness parameters such as height–height correlation, surface width, and lateral correlation length is presented in Chapter 2. The characteristics of some important examples of rough surfaces, such as the self-affine, mounded, and anisotropic surfaces are described in Chapter 3. In Chapter 4 we describe the instrumentation of various modes of scanning probe microscopy; in particular, detailed descriptions of the operation of the atomic force microscope (AFM) and scanning tunneling microscope (STM) are given. In Chapter 5, we discuss two very important effects on the use of the SPM as a quantitative tool for surface roughness characterization: the finite-size tip and the finite-sampling area. Examples are given to illustrate such effects. Fundamental concepts of diffraction are given in Chapter 6 and the derivation of the diffraction intensity for a general rough surface is given in Chapter 7. In Chapter 8, the instrumentation and various diffraction configurations that are suitable for x-ray, electron, atom, neutron, and light scattering are discussed. Chapters 9, 10, and 11 are detailed discussions of the application of the SPM and diffraction techniques in self-affine, mounded, and anisotropic rough surfaces, respectively. In each case, the comparison between the real-space images and reciprocal-space structures is fully explored. In Chapter 12, we discuss the effect of non-Gaussian height distributions on the determination of roughness parameters from diffraction. Furthermore, in Chapter 13, we present the real-space and diffraction studies of submonolayer (two-dimensional) structures. The subsequent multilevel growth and the well-known intensity oscillation phenomenon are described in Chapter 14. We compare the general diffraction characteristics from a fractal object with the diffraction from a self-affine surface in Chapter 15. We conclude this book by giving some examples of the impacts of the surface/interface roughness on electrical and magnetic properties of thin films as well as electronic device operations in Chapter 16. We discuss various dynamic growth models concisely in Appendix A. Other detailed proofs of equations and derivations of functions are in Appendices B to F. The effect of surface roughness on speckle patterns and the diffraction intensity using a pulsed incident beam are discussed in Appendices G and H, respectively.

The authors would like to take this opportunity to thank our mentors and many colleagues who have helped our careers in the areas described in this book. The list includes, but is not limited to, Dr. M. G. Lagally, M. Henzler, P. I. Cohen,

T. L. Einstein, F. Family, J. G. Amar, J. W. Evans, P. A. Thiel, E. D. Williams, S. K. Sinha, J. Krim, P. Z. Wong, K. S. Liang, P. Persans, J. F. Wendelken, R. J. Celotta, D. T. Pierce, W. Egelhoff, Jr., A. Zangwill, J. D. Gunton, G. Palasantzas, and J. E. Houston. Former graduate students H.-N. Yang, J. M. Pimbley, J.-K. Zuo, A. Chan, Q. Jiang, K. Fang, Y.-F. Liew, and Y.-L. He, and present graduate students J. B. Wedding, J. T. Drotar, and T. Karabacak have all made contributions to part of the work collected in this book. We also thank Victor Lu for typing the Appendices. Yi-Ping would like to thank his wife, Xi, and son, Troy, for their full support, encouragement, and love during the past years. The support of an NSF grant and Semiconductor Research Corporation over the years is deeply appreciated. Finally, we thank J. B. Wedding for his careful proofreading of this book.

YIPING ZHAO  
GWO-CHING WANG  
TOH-MING LU  
Troy, New York

This Page Intentionally Left Blank

## 1. INTRODUCTION

Most surfaces in nature are rough. One can encounter rough surfaces everywhere at any time. For example, every sheet of paper in this book is rough, even though we feel the sheet is smooth by our fingers' touch. In everyday life, one can find all sorts of rough surfaces – from the skin of our bodies to the surfaces of tables, from the mirrors to the walls – though they feel smooth by touching hands or look shiny by light reflection. In nature, there are also various kinds of rough surfaces. Mountains, lakes, rivers and canyons form the most beautiful, rough landscapes on the earth which impress people generation after generation. The two-dimensional ordered array of atoms on a crystalline surface give atomic scale surface height fluctuations, which exhibits the exciting beauty of the microscopic world. Rough surfaces make up one very important part in the world.

In practice, one may want to use the property of a rough surface or to eliminate the roughness. Take the deceleration zone on the sides of a highway as an example. In order to slow down the speed of a car effectively, the surfaces of the deceleration zone are intentionally made rough. But, for the car manufacturers, they always want to make the surface of a car as smooth and shining as possible in order to appeal to potential customers. In modern scientific researches as well as engineering studies, rough surfaces have attracted more and more attention in a wide range of fields including, for example, tribology, geophysics, remote sensing and acoustics.

Interface roughness is one of the key features in many important thin film technologies. The roughness of the interface directly controls many physical and chemical properties of the films. For example, the demagnetizing fields and coercivity of thin magnetic films change as the interface roughness changes [1.1, 1.2], and the electrical conductivity of thin metal films depends on roughness [1.3]. The roughness also affects surface plasmons [1.4], surface second-harmonic generation [1.5, 1.6], chemical reaction rate [1.7], contact angle of a small liquid droplet on a rough surface (increases compared to that on a smooth surface) [1.8], Brewster angle shifts [1.9, 1.10], etc.

Reduction of roughness is desirable in many thin film applications, particularly for many applications in microelectronic devices and opto-electronic devices. For example, the roughness of a silicon substrate can affect the gate oxide quality [1.11] and also the ohmic contact between a metal and a semiconductor [1.12]. Surface roughness can generate addi-

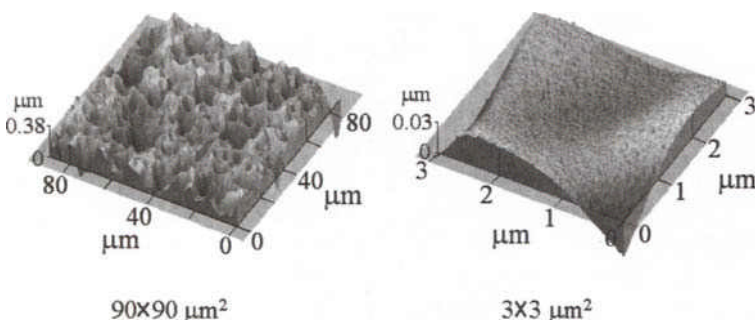


FIG. 1.1 AFM images of the backside of a Si wafer. The sampling sizes are  $90 \times 90$  and  $3 \times 3 \mu\text{m}^2$ , respectively.

tional scattering losses in optical waveguides and may modify the beating length and optical path in a grating [1.13]. However, for some applications, a rough interface can be very useful. Examples lie in catalysis and in adhesion enhancement between materials.

In addition to thin film growth technology, rough surfaces can be formed by many methods: (1) etching; (2) machining such as grinding, lapping, chemical mechanical polishing, etc.; (3) fracture of a solid; (4) solidification of a liquid; and (5) corrosion and erosion.

In order to study the issues mentioned above, one should first solve two key problems: how to describe a rough surface accurately and how to detect and measure a rough surface.

A rough surface can be defined as the surface height having a non-zero variance with respect to the mean height, which constitutes an absolutely smooth reference surface. According to this definition, one can see that any real physical surface cannot be absolutely smooth, at least with some atomic scale fluctuations. However, in practice, one does not always consider a surface down to the atomic scale. In this sense, the rough surface or smooth surface one refers to is always imposed by some constraints. There are two important constraints on the measurement of the surface which are not usually pointed out explicitly when a rough surface is defined.

One is the size (area) of the surface studied. The extent of the surface roughness depends very much on the sampling size of the surface. For example, when you look at the ground from an airplane in the air, you see mountains, lakes, canyons, basins, rivers, etc. The earth surface is seen to be very rough. When you get off the airplane and stand on the ground and look at the same hills, mountains, etc., they may look less rough compared with what you see in the air. Also, when you look at just the airfield, it is

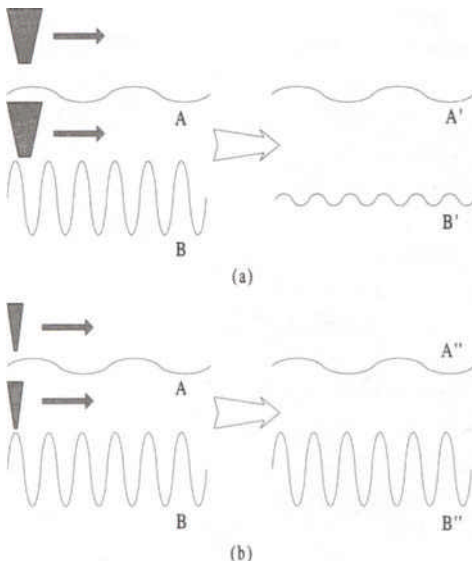


FIG. 1.2 The effect of instrument resolution. (a) A blunt tip scans across two different surfaces, A and B, resulting in A' and B'. (b) A sharp tip scans across two different surfaces, A and B, resulting in A'' and B''.

very flat! Three totally different impressions of a surface morphology would result from three different observation regimes. In the air, the observation regime may be hundreds of square kilometers. On the ground it may be several tens of square kilometers. When you focus on the airfield, it is only several square kilometers. A surface which is rough in macro-scale may be smooth in micro-scale, or vice versa. Figure 1.1 shows an example of the backside surface of a silicon wafer. These atomic force microscopy images were taken at the same sample spot with different scan sizes, i.e., the smaller scan size is the zoomed-in area of a smaller part of the sample within the large size scan. The  $90 \times 90\text{-}\mu\text{m}^2$  scan reveals a pretty rough surface, having holes and hills. As the scan size becomes smaller, there are fewer holes and hills. When the scan size becomes  $3 \times 3\text{ }\mu\text{m}^2$ , the surface is pretty smooth. Therefore, when we describe a rough surface, we should specify the region of the surface under study in order to convey accurate information.

The other constraint refers to the resolution of the instrument used in the measurements. Different instruments with different resolutions would give different knowledge of surface roughness for the same surface. This condition is illustrated in Figure 1.2, which shows that two different kinds of tips, one blunt and one sharp, are used to probe two different surfaces:

surface A has a large wavelength, which is greater than the radius of the blunt tip; and surface B has a small wavelength, which is smaller than the radius of the blunt tip, but larger than that of the sharp tip. After scanning surface A, both tips give similar results. However, for surface B, the blunt tip gives a totally different result from the real surface: the fluctuation of surface B becomes much smaller than its real surface. But the sharp tip results in a surface very similar to the real surface. Therefore, even for the same surface, different instruments with different resolutions can give totally different information of surface roughness. In fact, the resolution of an instrument specifies two limits of an observation. The vertical resolution (or height resolution, signal-to-noise ratio) determines the smallest height fluctuation in the surface that the instrument can detect, while the lateral resolution (or spatial resolution) specifies the smallest region of a surface that the instrument can reach. Hence, it is very important to specify the instrument resolution including both vertical resolution and lateral resolution.

In conclusion, the measurement of a rough surface is accurate only down to the lateral resolution and only up to the sampled size of a measuring instrument. For a particular surface area, one can define a smooth surface as one for which the height fluctuation is within the vertical resolution of the instrument used in the study.

We can classify rough surfaces in several ways. First, we can classify rough surfaces according to their statistical properties. In this sense, rough surfaces can be divided into two categories: deterministic rough surfaces and random rough surfaces. A deterministic surface is defined in the way that the surface height fluctuation can be expressed as a deterministic function of surface position. Once the form of a height function is given, the property of the whole surface is determined. For example, the surface of a reflection grating can be described as a periodic function. In the statistical point of view, surface heights between two arbitrary points on a deterministic surface are totally correlated. For a random rough surface, the surface height fluctuation cannot be expressed as a deterministic function of the surface position, and the best way to describe it is to use a random field (or process). This is the main category of surfaces we will study in this book.

Second, we can classify rough surfaces according to their continuity properties, i.e., continuous surfaces and discrete surfaces. This classification is associated with the area of the surface we study or the resolution of the instrument we use. When we focus on a surface with an area far larger than the atomic scale, or the lateral resolution of the instrument we use is far larger than the atomic scale, we can treat the surface as a continuous

surface; otherwise, we should treat the surface as a discrete surface. Surface discreteness would affect the description of a rough surface as well as its detection.

The third classification method is based on the rotational symmetry of a rough surface, and one can define an isotropic rough surface and an anisotropic rough surface. If the surface height fluctuation is independent of the surface direction, we say that the surface is isotropic. Otherwise, the surface is anisotropic. The description of an anisotropic surface is more complicated than that of an isotropic surface due to its surface directional dependence, and therefore would be more involved in its detection. In this book, although our major focus is on continuous, isotropic, random rough surfaces, we do leave some room to discuss other kinds of surfaces.

## References

- 1.1 Ernst Schlömann, "Demagnetizing fields in thin magnetic films due to surface roughness," *J. Appl. Phys.* **41**, 1617 (1970).
- 1.2 Q. Jiang, H.-N. Yang, and G.-C. Wang, "Effect of interface roughness on hysteresis loops of ultrathin Co films from 2 to 30 ML on Cu(001) surfaces," *Surf. Sci.* **373**, 181 (1997).
- 1.3 G. Palasantzas and J. Barnás, "Surface-roughness fractality effects in electrical conductivity of single metallic and semiconducting films," *Phys. Rev. B* **56**, 7726 (1997).
- 1.4 G. A. Farias and A. A. Maradudin, "Effect of surface roughness on the attenuation of surface polaritons on metal films," *Phys. Rev. B* **28**, 5675 (1983).
- 1.5 M. Leyva-Lucero, E. R. Méndez, T. A. Leskova, A. A. Maradudin, and J. Q. Lu, "Multiple-scattering effects in the second-harmonic generation of light in reflection from a randomly rough metal surface," *Opt. Lett.* **21**, 1809 (1996).
- 1.6 K. A. O'Donnell and R. Torre, "Second-harmonic generation from a strongly rough metal surface," *Opt. Commun.* **138**, 341 (1997).
- 1.7 *The Fractal Approach to Heterogeneous Chemistry: Surfaces, Colloids, Polymers*, edited by D. Avnir (Wiley, New York, 1989).
- 1.8 P. G. de Gennes, "Wetting: statistics and dynamics," *Rev. Mod. Phys.* **57**, 827 (1985).
- 1.9 M. Saillard and D. Maystre, "Scattering from metallic and dielectric rough surfaces," *J. Opt. Soc. Am. A* **7**, 982 (1990).
- 1.10 Jean-Jacques Greffet, "Theoretical model of the shift of the Brewster angle on a rough surface," *Opt. Lett.* **17**, 238 (1992).
- 1.11 R. I. Hedge, M. A. Chonko, and P. J. Tobin, "Effect of silicon substrate microroughness on gate oxide quality," *J. Vac. Sci. Technol. B* **14**, 3299 (1996).
- 1.12 T. Clausen and O. Leistikko, "The impact of the surface roughness on the electrical properties of AuGeNi/n-InP ohmic contacts," *Semicond. Sci. Technol.* **10**, 691 (1995).
- 1.13 F. Ladouceur, "Roughness, inhomogeneity, and integrated optics," *J. Lightwave Technol.* **15**, 1020 (1997).

This Page Intentionally Left Blank

## 2. STATISTICAL NATURE OF ROUGH SURFACES

A random rough surface can be described mathematically as  $h = h(\mathbf{r})$ , where  $h$  is the surface height of a rough surface with respect to a smooth reference surface defined by a mean surface height and  $\mathbf{r}$  is the position vector on the surface. The rough surface we usually encounter has the height  $h$ , which is a single-valued function of the position vector,  $\mathbf{r}$ , i.e., there are no overhangs on the surface. For this kind of random rough surface, one always assumes that the height fluctuation is a random field with respect to the position. A random field is also called a random (or stochastic) process, although the term *field* indicates that the parameter space is multidimensional. For a complete description of a random field one needs to know the  $n$ -dimensional joint distribution function  $p_n(h_1, h_2, \dots, h_n; \mathbf{r}_1, \mathbf{r}_2, \dots, \mathbf{r}_n)$ , where  $\mathbf{r}_1, \mathbf{r}_2, \dots, \mathbf{r}_n$  are a set of different positions on the surface and  $h_1, h_2, \dots, h_n$  are the corresponding random variables. A random field is called homogeneous if all the joint probability distribution functions remain the same when the set of locations  $\mathbf{r}_1, \mathbf{r}_2, \dots, \mathbf{r}_n$  is translated (but not rotated) in the parameter space. This implies that all of the probabilities depend only on the relative, not the absolute, locations of the points  $\mathbf{r}_1, \mathbf{r}_2, \dots, \mathbf{r}_n$ . For a one-dimensional random process the term *stationary* is commonly used instead of *homogeneous*. The field is isotropic if the joint probability density functions are invariant after the constellation of points  $\mathbf{r}_1, \mathbf{r}_2, \dots, \mathbf{r}_n$  is rotated in the parameter space. A random field is ergodic if all of the information about its joint distributions (and their statistics) can be obtained from a single realization of the random field, and one can use the field average instead of the ensemble average. Basically we assume that the random rough surface we study here is a homogeneous, isotropic, ergodic random field. It is necessary to give a brief review of the random field associated with the definitions of some roughness parameters of a random rough surface. We can see later that a misuse of some of the properties of a random field may lead to erroneous interpretations of the geometrical properties of rough surfaces.

### 2.1 First-Order Statistics: Surface Height Distribution Function and Characteristic Function

One of the main characteristics of a random rough surface is the height distribution function (one-dimensional distribution function),  $p(h)$ . The

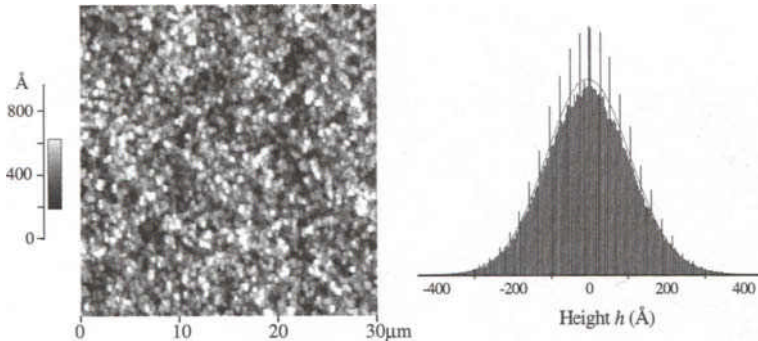


FIG. 2.1 An AFM image of an electroplated Cu surface on a silicon substrate and the corresponding surface height histogram.

meaning of  $p(h)$  is that the probability of a surface height between  $h$  and  $h + dh$  at any point on the surface is  $p(h)dh$ . The distribution  $p(h)$  is a non-negative function of  $h$  and is normalized such that

$$\int_{-\infty}^{+\infty} p(h)dh = 1. \quad (2.1)$$

The height distribution function provides a complete specification of the random variable  $h(\mathbf{r})$  at a position  $\mathbf{r}$ . Although different rough surfaces may have different height distributions, the most generally used height distribution is the Gaussian height distribution,

$$p(h) = \frac{1}{\sqrt{2\pi}w} \exp\left(-\frac{h^2}{2w^2}\right), \quad (2.2)$$

due to its mathematical simplicity and its place in the central limit theorem of the sum of large amount of random variables. Here  $w$  is the interface width, which we will define later. Figure 2.1 shows an atomic force microscopy image of an electroplated Cu surface on a silicon substrate and the corresponding surface height histogram. The solid curve is the best Gaussian fit. We can see that, for this particular rough surface, the Gaussian distribution works very well.

To describe a particular property of a random variable  $h$ , it is often much more convenient to use simpler numerical statistics determined by the distribution function. The  $n$ th-order moment of a variable  $h$ , defined

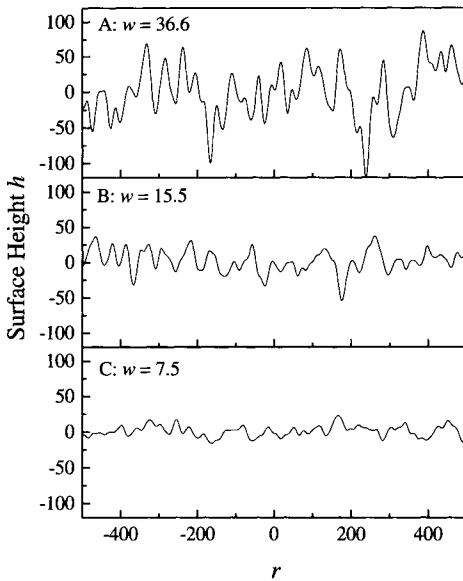


FIG. 2.2 Three different rough surfaces with different RMS roughness values.

as

$$m_n = E\{h^n\} = \int_{-\infty}^{+\infty} h^n p(h) dh, \quad (2.3)$$

s the most important numerical statistic. More generally, one can define the  $n$ th-order central moment,

$$v_n = E\{(h - \bar{h})^n\} = \int_{-\infty}^{+\infty} (h - \bar{h})^n p(h) dh, \quad (2.4)$$

where  $E\{\dots\}$  is an average operator, which takes the ensemble average of the expression inside the braces and  $\bar{h} = m_1$  is the average surface height or the 1st-order moment. For a realistic rough surface, usually we take  $i = 0$  and then  $m_n = v_n$ . In the following we only use  $m_n$  to express the  $i$ th-order (or central) moment. The assumption that  $\bar{h} = 0$  holds at any position on the surface ensures that the random field  $h(\mathbf{r})$  is homogeneous.

The 2nd-order moment of the variable  $h$  is one of the most important physical parameters people use to describe the surface roughness, and we

use  $w^2$  to represent it,

$$w^2 = m_2 = \int_{-\infty}^{+\infty} h^2 p(h) dh, \quad (2.5)$$

where  $w$  is called the root-mean-square (RMS) roughness or the interface width. Here it also equals to the standard deviation since  $\bar{h} = 0$ . The  $w$  describes the fluctuations of surface heights around an average surface height. Figure 2.2 shows three different rough surfaces with different RMS roughness values. The larger the value of  $w$ , the rougher the surface, under the condition that other roughness parameters are the same. Sometimes another parameter, the average roughness,  $w_{ave}$ , which will be discussed later, is used to describe surface roughness and is defined as the arithmetic average of height  $h$ ,

$$w_{ave} = E\{|h - \bar{h}|\} = \int_{-\infty}^{+\infty} |h - \bar{h}| p(h) dh. \quad (2.6)$$

For the same height distribution,  $w_{ave}$  is proportional to  $w$ . For example,  $w_{ave} = w\sqrt{2/\pi}$  for a Gaussian height distribution.

Usually people do not consider higher-order moments, because the 1st-order moment  $\bar{h}$  and the 2nd-order moment  $w^2$  are sufficient to characterize surface roughness for most purposes. However, higher-order moments can give more information about the surface height distribution, and sometimes one needs higher-order moments to differentiate surfaces in more detail. For example, Figure 2.3 shows two different surfaces with the same RMS roughness value  $w$ . One has a Gaussian height distribution, in which the surface height fluctuates symmetrically around the average surface height. The other one has an exponential distribution which possesses many protrusions on the surface. To describe this difference, higher-order moments would be needed. The most important higher order moments are the 3rd- and 4th-order moments. The 3rd-order moment defines the skewness of surface height,  $\gamma_3$ ,

$$\gamma_3 = \frac{m_3}{w^3} = \frac{1}{w^3} \int_{-\infty}^{+\infty} h^3 p(h) dh. \quad (2.7)$$

Note that the skewness is dimensionless in contrast to the RMS roughness which is in units of length. Skewness is a measure of the symmetry of a distribution about a mean surface level. The sign of the skewness, positive skewness or negative skewness, tells that the farther points are proportionately above or below the mean surface level, respectively. In other words, a positive skewness represents a distribution with an asymmetric tail extending out toward more positive height with respect to the mean surface

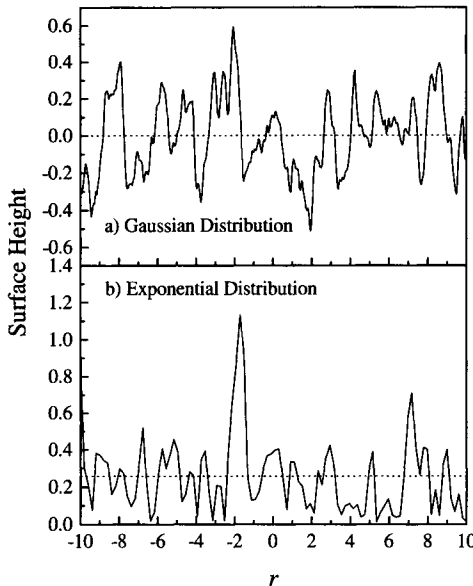


FIG. 2.3 Two different surfaces with the same RMS roughness value  $w$  but different height distributions  $h(r)$ . The dotted lines in the figure indicate the average surface height positions.

level, while a negative skewness represents a distribution whose tail extends out toward more negative height with respect to the mean surface level, as shown in Figure 2.4. For example, a distribution of bumps on a surface would have a positive skewness, while a distribution of holes will have a negative skewness. For a symmetric distribution like a Gaussian distribution, the skewness is zero. The values of the skewness for the Gaussian and exponential surfaces in Figure 2.3 are 0.13 and 1.58, respectively. (Since the two surface profiles in Figure 2.3 are sampling profiles, the calculated values of skewness are close, but not equal, to the theoretical values.) We see that an exponentially-distributed surface has a larger skewness than that of a Gaussian surface, which exactly reflects the asymmetrical protrusions.

The 4th-order moment defines the kurtosis of surface height,  $\gamma_4$ ,

$$\gamma_4 = \frac{m_4}{w^4} = \frac{1}{w^4} \int_{-\infty}^{+\infty} h^4 p(h) dh. \quad (2.8)$$

Kurtosis is also a dimensionless quantity. It is a measure of the sharpness of the height distribution function. If most of the surface features are concentrated close to the mean surface level, the kurtosis will be less than

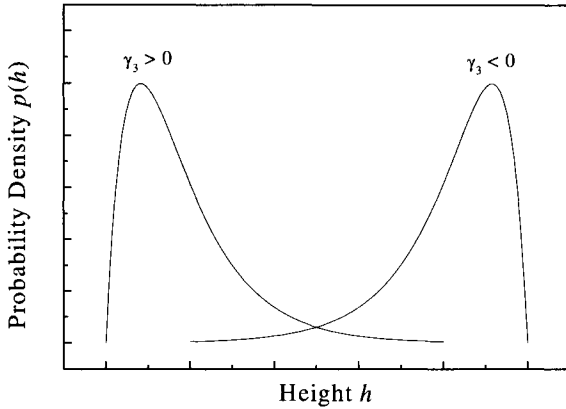


FIG. 2.4 The surface height distribution function with positive ( $\gamma_3 > 0$ ) skewness and negative ( $\gamma_3 < 0$ ) skewness.

that of the height distribution containing a larger portion of the surface features lying farther from the mean surface level. In addition, kurtosis describes the randomness of the surface profile relative to that of a perfectly random surface (Gaussian distribution) that has a kurtosis of 3.0. For  $\gamma_4 < 3$ , the distribution is platykurtic (mild peak), and for  $\gamma_4 > 3$  the distribution is leptokurtic (sharp peak). Figure 2.5 shows typical shapes of these two different distributions and a Gaussian distribution.

The equivalent function of a height distribution for the first-order statistics is the characteristic function of a height distribution,  $\varphi(k)$ , which is defined as

$$\varphi(k) = E\{\exp(-ikh)\} = \int_{-\infty}^{+\infty} p(h)e^{-ikh}dh. \quad (2.9)$$

In fact, the characteristic function  $\varphi(k)$  is the Fourier transform of the height distribution function, or the average value of the random phase  $kh$ . For example, the characteristic function for a Gaussian height distribution [Equation (2.2)] is also a Gaussian function:

$$\varphi(k) = \exp\left(-\frac{w^2 k^2}{2}\right). \quad (2.10)$$

A characteristic function has the following properties:

- (1) The characteristic function is unique and determines the height distribution function. Thus, if two random height fields have the same characteristic function, they have the same height distribution.

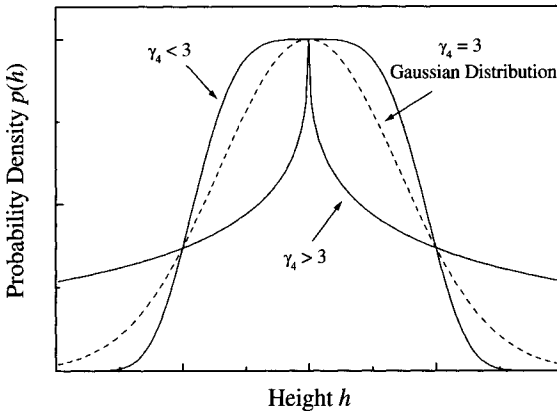


FIG. 2.5 The surface height distribution functions with different kurtosis values  $\gamma_4$ .

(2)  $\varphi(0) = 1$  and

$$m_n = \frac{1}{i^n} \left[ \frac{d^n \varphi(k)}{dk^n} \right]_{|k=0}, \quad (2.11)$$

i.e., from the characteristic function, one can get the moment directly.

Later we will see that the characteristic function plays a very important role in the theory of light scattering.

## 2.2 Second-Order Statistics: Auto-Correlation Function, Height-Height Correlation Function, and Power Spectrum

The first-order statistics or the height distribution function only describes the statistical properties of random variables of a random field at individual positions, it cannot reflect the connection between random variables at different positions. Different rough surfaces can have the same height distribution  $p(h)$  and RMS roughness  $w$  (or interface width). For example, all three sampled surface profiles shown in Figure 2.6 have the same Gaussian height distribution and the same interface width, but they look totally different because the changes in heights occur in different length scales along the surfaces. In other words, the height fluctuation frequencies are different. It is intuitive for one to think that profile C is much rougher than profile A. In order to differentiate the spatial difference, one needs to know the connection of a random field  $h(\mathbf{r})$  at two different positions  $\mathbf{r}_1$  and  $\mathbf{r}_2$ . To do that, the joint distribution probability density function

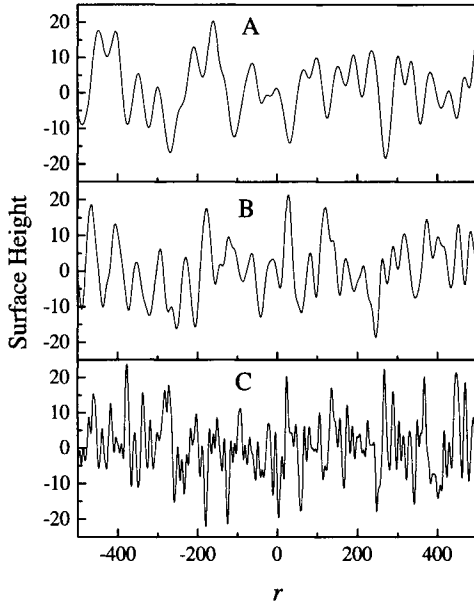


FIG. 2.6 Surface profiles with the same RMS  $w$  but different lateral correlation lengths  $\xi$ .

$p_j(h_1, h_2; \mathbf{r}_1, \mathbf{r}_2)$  of  $[h(\mathbf{r}_1), h(\mathbf{r}_2)]$  is introduced, and it satisfies

$$\int_{-\infty}^{+\infty} \int_{-\infty}^{+\infty} p_j(h_1, h_2; \mathbf{r}_1, \mathbf{r}_2) dh_1 dh_2 = 1, \quad (2.12)$$

$$\int_{-\infty}^{+\infty} p_j(h_1, h_2; \mathbf{r}_1, \mathbf{r}_2) dh_1 = p(h_2), \text{ and} \quad (2.13)$$

$$\int_{-\infty}^{+\infty} p_j(h_1, h_2; \mathbf{r}_1, \mathbf{r}_2) dh_2 = p(h_1), \quad (2.14)$$

where  $p(h_1)$  and  $p(h_2)$  are called the marginal distributions of  $p_j(h_1, h_2; \mathbf{r}_1, \mathbf{r}_2)$  and, for a homogeneous random field,  $p(h_1) = p(h_2) = p(h)$ . In general,  $p_j(h_1, h_2; \mathbf{r}_1, \mathbf{r}_2)$  is related not only to the height distribution, but also to the correlation of heights between two separated positions. In diffraction, this correlation between two positions determines the degree of interference of the scattered fields from these two points. Therefore, it plays a crucial role in the scattering density distribution. We will discuss this point later. One special case for the joint distribution function is that  $h_1$  and  $h_2$  are independent of each other. In this case,  $p_j(h_1, h_2; \mathbf{r}_1, \mathbf{r}_2)$  can be simply

expressed as

$$p_j(h_1, h_2; \mathbf{r}_1, \mathbf{r}_2) = p(h_1)p(h_2). \quad (2.15)$$

The most important statistical characteristic of a joint distribution  $p_j(h_1, h_2; \mathbf{r}_1, \mathbf{r}_2)$  is the auto-covariance function,  $G(\mathbf{r}_1, \mathbf{r}_2)$ , defined as

$$G(\mathbf{r}_1, \mathbf{r}_2) = E\{h(\mathbf{r}_1)h(\mathbf{r}_2)\} = \int_{-\infty}^{+\infty} \int_{-\infty}^{+\infty} h_1 h_2 p_j(h_1, h_2; \mathbf{r}_1, \mathbf{r}_2) dh_1 dh_2, \quad (2.16)$$

or the auto-correlation function,  $R(\mathbf{r}_1, \mathbf{r}_2)$

$$R(\mathbf{r}_1, \mathbf{r}_2) = \frac{G(\mathbf{r}_1, \mathbf{r}_2)}{w^2}. \quad (2.17)$$

Both  $G(\mathbf{r}_1, \mathbf{r}_2)$  and  $R(\mathbf{r}_1, \mathbf{r}_2)$  reflect the extension of a correlation of heights at two positions and depend on positions  $\mathbf{r}_1$  and  $\mathbf{r}_2$ . Sometimes  $R(\mathbf{r}_1, \mathbf{r}_2)$  is called the auto-correlation coefficient and is a dimensionless function. For the homogeneous, isotropic rough surfaces we consider here,  $G(\mathbf{r}_1, \mathbf{r}_2)$  and  $R(\mathbf{r}_1, \mathbf{r}_2)$  depend only on the distance between two positions  $\mathbf{r}_1$  and  $\mathbf{r}_2$ , e.g.,

$$G(\mathbf{r}_1, \mathbf{r}_2) = G(|\mathbf{r}_1 - \mathbf{r}_2|) = G(\rho), \quad (2.18)$$

and

$$R(\mathbf{r}_1, \mathbf{r}_2) = R(\rho), \quad (2.19)$$

where  $\rho = |\mathbf{r}_1 - \mathbf{r}_2|$ . The quantity  $\rho$  is the translation and sometimes is called a lag or slip. It is obvious that

$$G(0) = G(\mathbf{r}, \mathbf{r}) = E\{h(r)h(r)\} = w^2, \quad (2.20)$$

i.e., the value of an auto-covariance function  $G(\rho)$  at  $\rho = 0$  is equal to the variance of a surface height. Since  $G(\rho)$  and  $R(\rho)$  have the same property, the difference between them is only a factor  $w^2$ . In the following we only address the property of the auto-correlation function  $R(\rho)$ .

$R(\rho)$  has the following properties:

- (1)  $R(0) = 1$ .
- (2)  $R(-\rho) = R(\rho)$ , i.e.,  $R(\rho)$  is an even function.
- (3)  $|R(\rho)| \leq R(0)$ , i.e.,  $R(0)$  is a maximum of  $R(\rho)$ .
- (4) Given that  $h(\mathbf{r})$  and  $h(\mathbf{r} + \rho)$  are independent of each other for  $\rho \rightarrow \infty$ , and also  $E\{h(\mathbf{r})\} = 0$ , then  $\lim_{\rho \rightarrow \infty} R(\rho) = 0$ .

For a truly random rough surface,  $R(\rho)$  usually decays to zero with the increase of  $\rho$ . The shape of this decay depends on the type of random surfaces and the rate of decay depends on the distance over which two points become uncorrelated. The correlation length (or the lateral correlation

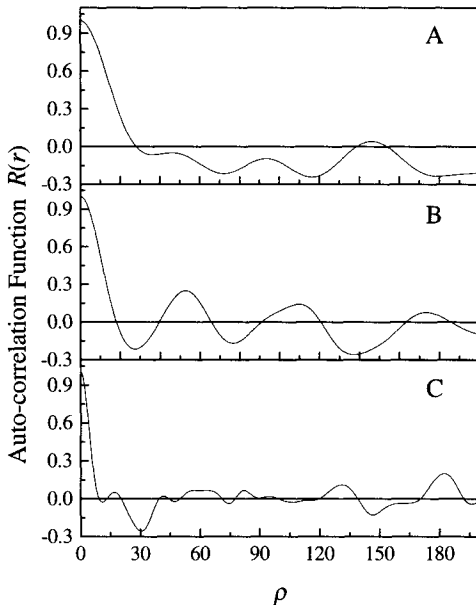


FIG. 2.7 The auto-correlation functions of the surface profiles shown in Figure 2.6.

length)  $\xi$  of an auto-correlation function is usually defined as the value of the lag length at which the auto-correlation function drops to  $1/e$  of its value at zero lag, i.e.,

$$R(\xi) = 1/e. \quad (2.21)$$

The correlation length  $\xi$  defines a representative lateral dimension of a rough surface. If the distance between two surface points is within  $\xi$ , the heights at these two points can be considered correlated. However, if the separation of two surface points is much larger than  $\xi$ , then we can say that the heights at these two points are independent of one another.

Figure 2.7 shows the auto-correlation functions for the three different surfaces in Figure 2.6. We can see that surface A has the largest correlation length while surface C has the smallest correlation length. Therefore surface C looks rougher. Some of the auto-correlation functions which appear in the literature are listed in Table 2.1 with explanations.

The auto-correlation function  $R(\rho)$  is an important function to describe the surface morphology. Different rough surfaces may have different auto-correlation functions. For example,  $R(\rho)$  for a truly random rough surface usually decreases monotonically from 1 to 0 as  $\rho$  increases from 0 to  $\infty$ , such as those functions listed in Table 2.1. However, the functional form

Table 2.1 Various auto-correlation functions for isotropic rough surfaces.

Name of Surface	Auto-Correlation Function $R(\rho)$
Gaussian	$\exp\left(-\frac{\rho^2}{\xi^2}\right)$
Exponential	$\exp\left(-\frac{ \rho }{\xi}\right)$
Seitch	$\exp\left[-\frac{ \rho }{\xi_1}(1 - e^{- \rho /\xi_2})\right]$
Lorentzian	$\frac{\xi^4}{(\xi^2 + \rho^2)^2}$
Power Law	$(1 + \frac{\rho^2}{\xi^2})^{-3/2}$
Bessel	$(1 + \frac{\rho^2}{8\xi^2}) \frac{ \rho }{\xi} K_1\left(\frac{ \rho }{\xi}\right) - \frac{\rho^2}{\xi^2} K_0\left(\frac{ \rho }{\xi}\right)$
Self-Affine	$\exp\left[-\left(\frac{ \rho }{\xi}\right)^{2\alpha}\right], 0 \leq \alpha \leq 1$

of  $R(\rho)$  for a sinusoidal surface will be a cosine function, reflecting the periodic nature of the surface. Even when the surface is a superposition of two independent fields, say a random field and a periodic field, and the amplitude of the periodic field is very small, the periodic correlation from the periodic field will dominate  $R(\rho)$  after a long lag length.

For a random rough surface, the information of the correlation functional form is very important because it represents a good description of the surface morphology. As shown in Table 2.1, most forms of  $R(\rho)$  require only one parameter, the lateral correlation length  $\xi$ , for the determination of the auto-correlation function, which then corresponds to a particular surface. Based on the discussion of roughness parameters so far, one tends to think that for surface roughness characterization, two parameters, the RMS roughness  $w$  and the lateral correlation length  $\xi$ , would be sufficient. However, real surfaces are not so simple. For example, the two sampling surface profiles shown in Figure 2.8 both have a Gaussian height distribution, the same RMS roughness  $w$ , and the lateral correlation length  $\xi$ , but the forms of  $R(\rho)$  are different: profile *A* has a Gaussian correlation and profile *B* has an exponential correlation. We can tell by a visual inspection that profile *B* is rougher than profile *A*. Therefore, the two parameters  $w$  and  $\xi$  alone are not enough to give a full description of surface roughness. One needs at least one additional parameter to describe this difference. This parameter is the roughness exponent (or Hurst exponent)  $\alpha$ , which was introduced by researchers who study the self-affine fractal geometry [2.1, 2.2]. The last row in Table 2.1 give a possible form of  $R(\rho)$  for self-affine rough surfaces.

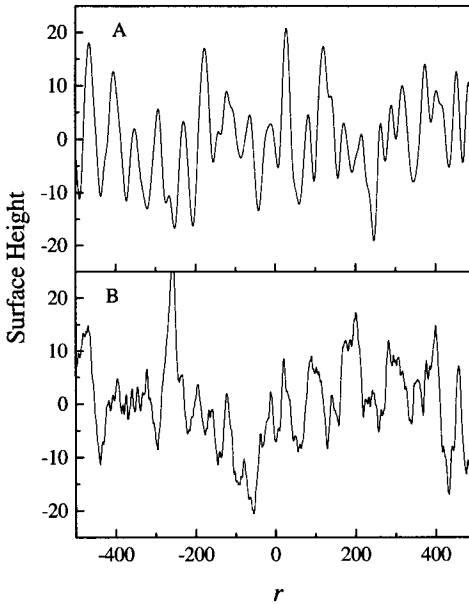


FIG. 2.8 Examples of two surfaces having the same  $w$  and  $\xi$  but which look very different.

For self-affine rough surfaces having the same  $w$  and  $\xi$ , the smaller  $\alpha$  is, the rougher the surface becomes. For example, a surface with a Gaussian correlation has  $\alpha = 1$ , while a surface with an exponential correlation has  $\alpha = 0.5$ . We shall postpone a detailed description of self-affine surfaces with different  $\alpha$  values until the next chapter.

An equivalent function to the auto-correlation function  $R(\rho)$  is the height-height correlation function (or structure function)  $H(\rho)$ , defined as

$$H(\rho) = E\{[h(\mathbf{r}) - h(\mathbf{r} + \rho)]^2\}. \quad (2.22)$$

It can be related to  $R(\rho)$  as

$$H(\rho) = 2w^2[1 - R(\rho)]. \quad (2.23)$$

For a homogeneous, isotropic random surface,  $H(\rho) = H(\rho)$ , i.e., it is also an even function with respect to  $\rho$ , and has the following properties

$$H(0) = 0, \quad H(\rho \rightarrow \infty) = 2w^2. \quad (2.24)$$

One usually uses this height-height correlation function instead of the auto-correlation function to study the properties of random surfaces. Figure 2.9

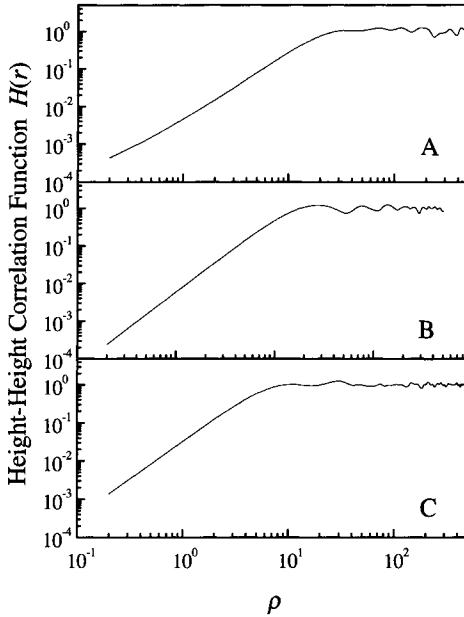


FIG. 2.9 The height-height correlation functions of surfaces shown in Figure 2.6.

shows the corresponding height-height correlation functions for the surfaces shown in Figure 2.6.

So far, we have discussed only the statistical properties of a random field in real space. It is well known that there are two equivalent expressions for a field. One is in real space, as discussed above, and the other one is in Fourier space (or reciprocal space). To consider the frequency properties of a field, an expression in reciprocal space is much more convenient. The most important statistical function in reciprocal space is the power spectrum  $P(\mathbf{k}_{||})$ , which can be simply defined as the Fourier transform of an auto-covariance function  $G(\boldsymbol{\rho})$ ,

$$P(\mathbf{k}_{||}) = \frac{1}{2\pi} \int_{-\infty}^{+\infty} G(\boldsymbol{\rho}) e^{-i\mathbf{k}_{||} \cdot \boldsymbol{\rho}} d\boldsymbol{\rho}. \quad (2.25)$$

Here  $\mathbf{k}_{||}$  is the wave vector in the Fourier space. Thus  $P(\mathbf{k}_{||})$  and  $G(\boldsymbol{\rho})$  form a Fourier transform pair,

$$G(\boldsymbol{\rho}) = \frac{1}{2\pi} \int_{-\infty}^{+\infty} P(\mathbf{k}_{||}) e^{i\mathbf{k}_{||} \cdot \boldsymbol{\rho}} d\mathbf{k}_{||}. \quad (2.26)$$

This is the famous Weiner-Khintchine relation [2.3, 2.4]. For a homogeneous, isotropic, random rough surface,  $P(\mathbf{k}_{||}) = P(k_{||})$ , i.e., the power spectrum

Table 2.2 Various power spectra for isotropic rough surfaces.

Name of Surface	Power Spectrum $P(k_{  })$
Gaussian	$\frac{w^2 \xi}{2\sqrt{\pi}} \exp\left(-\frac{k_{  }^2 \xi^2}{4}\right)$
Exponential	$\frac{w^2 \xi}{2\sqrt{\pi}} \frac{1}{1+k_{  }^2 \xi^2}$
Lorentzian	$\frac{\xi^4}{(\xi^2+k_{  }^2)^2}$
Power Law	$\frac{2w^2 \xi^2}{\pi} \exp(- k_{  }  \xi)$
Bessel	$\frac{12w^2 \xi^2}{\pi} \frac{k_{  }^4 \xi^4}{(1+k_{  }^2 \xi^2)^4}$
Self-Affine	$\frac{4\pi\alpha w^2 \xi^2}{(1+k_{  }^2 \xi^2)^{1+\alpha}}, 0 \leq \alpha \leq 1$

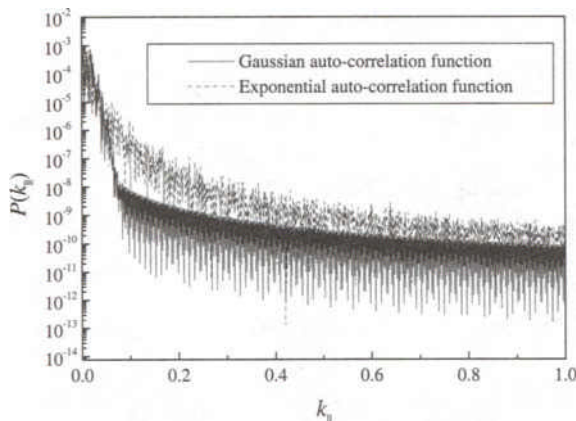


FIG. 2.10 The power spectra of the two surfaces plotted in Figure 2.8.

is also independent on the directions. It has the following properties,

- (1)  $P(\mathbf{k}_{||})$  is a real, nonnegative function.
- (2) The average power is defined as

$$\bar{P} = \int_{-\infty}^{+\infty} P(\mathbf{k}_{||}) dk_{||} = G(0) = w^2. \quad (2.27)$$

(3) If a random field has a periodic component, then  $P(\mathbf{k}_{||})$  will have impulses.

The  $P(\mathbf{k}_{||})$  is equivalent to  $G(\rho)$  when they are used in describing a random field. Table 2.2 lists some of the power spectra that have appeared

in the literature. Through a power spectrum, we can get more information about a random rough surface. For example, there is a difference between a Gaussian-correlated surface and an exponentially-correlated surface, each shown in Figure 2.8. The power spectra of these two surfaces are plotted in Figure 2.10. It is clear that the power spectrum of the exponentially-correlated surface has a longer tail in spatial frequency than that of the Gaussian-correlated surface, i.e., there are more higher spatial-frequency components in an exponentially-correlated surface. So, the surface height changes more frequently, and looks rougher.

### 2.3 Other Statistical Properties of a Random Rough Surface

Sometimes a specification of additional conditions is required to extract useful information on the physical properties of a random rough surface. In the study of the effect of surface roughness on the capacitance of a capacitor, one needs to know the actual value of surface area of the sampling rough surface. In tribology, when two surfaces are in contact with each other, one needs to know the distribution of extreme heights, the average curvature, and the distribution of curvatures. These parameters are real and would impose certain restrictions on the mathematical description of the random rough surfaces. Therefore, the surface area should exist and should have a finite value in the sampling. The extreme value, the curvature, etc., should also exist. These restrictions require that the surface is continuous, is differentiable, and has local integrals. In the following we shall give some general discussion about these properties. This discussion may help us to understand physical random rough surfaces better.

Here, we start from a one-dimensional random process. All the conclusions can be extended to a random field. Also, these results are deduced in the mean-square (MS) sense [2.3].

#### 2.3.1 Continuity

For a stationary, finite-variance, real random process,  $h(r)$  is said to be continuous in a mean-square sense at  $r_0$ , if  $\lim_{r \rightarrow r_0} E\{[h(r) - h(r_0)]^2\} = 0$ . It can be deduced that the continuity of the auto-covariance function  $G(\rho)$  at  $\rho = 0$  is a sufficient condition for the MS continuity of a process. MS continuity and finite variance guarantee that we can interchange limiting and expected value operations, for example,

$$\lim_{r \rightarrow r_0} E\{g[h(r)]\} = E\{g[h(r_0)]\}, \quad (2.28)$$

where  $g(x)$  is any ordinary, continuous function.

### 2.3.2 Differentiation

The derivative of a stationary finite-variance process  $h(r)$  is said to exist in the MS sense if there exists a random process  $h'(r)$  such that

$$\lim_{\varepsilon \rightarrow 0} E\left\{ \left[ \frac{h(r + \varepsilon) - h(r)}{\varepsilon} - h'(r) \right]^2 \right\} = 0. \quad (2.29)$$

Note that this definition does not explicitly define the derivative random process  $h'(r)$ . A sufficient condition for the existence of the MS derivative is given in the following:

A finite variance stationary real random process  $h(r)$  has a MS derivative  $h'(r)$ , if  $G(r)$  has derivatives of orders up to two at  $\rho = 0$ .

The mean and auto-covariance function of  $h'(r)$  can be obtained,

$$E\{h'(r)\} = \frac{d\bar{h}(r)}{dr} = 0 \quad (\text{stationary process}), \quad (2.30)$$

$$E\{h'(r)h'(r + \rho)\} = -\frac{d^2G(\rho)}{d\rho^2}, \quad (2.31)$$

i.e., the covariance of  $h'(r)$  is given by

$$E\{h'(r)^2\} = -\frac{d^2G(\rho)}{d\rho^2}|_{\rho=0}. \quad (2.32)$$

### 2.3.3 Integration

For a random process  $h(r)$ , the MS integral is defined as the process  $l(r)$ ,

$$l(r) = \int_{r_0}^r h(\rho)d\rho = \lim_{n \rightarrow \infty} \sum_{i=0}^{n-1} h(\rho_i)\Delta\rho_i. \quad (2.33)$$

A sufficient condition for the existence of the MS integral  $l(r)$  of a stationary finite-variance process  $h(r)$  is the existence of the integral,

$$\int_{r_0}^r \int_{r_0}^r G(\rho_1 - \rho_2)d\rho_1 d\rho_2.$$

Note that a finite variance implies that  $G(0) < \infty$  and the MS continuity implies a continuity of  $G(\rho)$  at  $\rho = 0$ , which also implies continuity for all values of  $\rho$ . These two conditions guarantee the existence of the preceding integral and the existence of the MS integral.

When a MS integral exists, we have

$$E\{l(r)\} = (r - r_0)\bar{h}, \quad (2.34)$$

$$E\{l(r_1)l(r_2)\} = \int_{r_0}^{r_1} \int_{r_0}^{r_2} G(\rho_1 - \rho_2) d\rho_1 d\rho_2. \quad (2.35)$$

The MS integral of a random process is used to define the field average (or time average, or moving average) of a random process  $h(r)$ ,

$$\langle h(r) \rangle = \lim_{L \rightarrow \infty} \frac{1}{L} \int_{r-L/2}^{r+L/2} h(\rho) d\rho, \quad (2.36)$$

or

$$\langle h(r) \rangle_L = \frac{1}{L} \int_{r-L/2}^{r+L/2} h(\rho) d\rho. \quad (2.37)$$

## 2.4 Numerical Estimation of the Roughness Parameters

In practice, various statistical parameters are obtained from a limited number of samples. This is a process of sampling and estimation. An accurate estimation is important for us to understand the surface roughness since it provides the basic information we need. Therefore, the process of accurate sampling and estimation is the first step we need to pay attention to during our measurement. In the above we have discussed that our knowledge of surface roughness is very dependent on the range of measurement and the instrumental resolution. In the following we shall combine these two points, and give the general formula to estimate the statistical parameters numerically, and the conditions imposed on the estimations.

### 2.4.1 Numerical estimation of statistical parameters

Many real-space techniques can give the surface height information directly. The information is usually digitized, which is convenient for data analysis. In the following, we use a one-dimensional surface as an example to illustrate how to estimate different statistical parameters.

A digitized one-dimensional surface can be expressed as  $h_1, h_2, \dots, h_N$ , where  $h_i$  is the surface height at the  $i$ th digitized position. We also assume that the distance between two adjacent discrete positions is  $d$ , and the total length of the surface is  $N$ . Then  $h_i$  is the surface height at the position  $id$ .

### 2.4.1.1 Average surface height

The average surface height is the arithmetic average of surface heights. Analytically it can be expressed as

$$\langle h \rangle_L = \frac{1}{L} \int_{-L/2}^{L/2} h(x) dx, \quad (2.38)$$

where  $L$  is the total length of the measured surface. For a digitized surface, the integral becomes a summation:

$$\langle h \rangle_N = \frac{1}{N} \sum_{i=1}^N h_i. \quad (2.39)$$

### 2.4.1.2 RMS roughness

In Section 2.1 we mentioned that RMS roughness is one of the most important parameters needed to characterize a rough surface. Analytically, it can be estimated as

$$\langle w \rangle_L = \left\{ \frac{1}{L} \int_{-L/2}^{L/2} [h(x) - \langle h \rangle_L]^2 dx \right\}^{1/2}, \quad (2.40)$$

or

$$\langle w \rangle_N = \left\{ \frac{1}{N} \sum_{i=1}^N [h_i - \langle h \rangle_N]^2 \right\}^{1/2}. \quad (2.41)$$

### 2.4.1.3 Skewness and Kurtosis

These two parameters represent the shape of the surface height distribution and can be estimated as

$$\langle \gamma_3 \rangle_L = \frac{1}{\langle w \rangle_L^3} \frac{1}{L} \int_{-L/2}^{L/2} [h(x) - \langle h \rangle_L]^3 dx, \text{ and} \quad (2.42)$$

$$\langle \gamma_4 \rangle_L = \frac{1}{\langle w \rangle_L^4} \frac{1}{L} \int_{-L/2}^{L/2} [h(x) - \langle h \rangle_L]^4 dx, \quad (2.43)$$

or

$$\langle \gamma_3 \rangle_N = \frac{1}{\langle w \rangle_N^3} \frac{1}{N} \sum_{i=1}^N [h_i - \langle h \rangle_N]^3, \text{ and} \quad (2.44)$$

$$\langle \gamma_4 \rangle_N = \frac{1}{\langle w \rangle_N^4} \frac{1}{N} \sum_{i=1}^N [h_i - \langle h \rangle_N]^4. \quad (2.45)$$

#### 2.4.1.4 Auto-correlation function

The auto-correlation function is given by an overlapped integral of shifted and unshifted surface height profiles. It can be estimated as

$$\langle R(r) \rangle_L = \frac{1}{\langle w \rangle_L^2} \frac{1}{L} \int_{-L/2}^{L/2} h(x)h(x+r)dx, \quad (2.46)$$

or

$$\langle R(md) \rangle_N = \frac{1}{\langle w \rangle_N^2} \frac{1}{N-m} \sum_{i=1}^{N-m} h_i h_{i+m}. \quad (2.47)$$

For a limited length sampling, we can see that when  $m$  becomes large, the data we use for an average are fewer. When  $m = N - 1$ , there is only one data point for averaging, and the accuracy of the estimation is definitely not good. Therefore, we usually neglect large  $m$  values.

#### 2.4.1.5 Height-height correlation function

Similar to the auto-correlation function, the height-height correlation function can be expressed as

$$\langle H(r) \rangle_L = \frac{1}{L} \int_{-L/2}^{L/2} [h(x+r) - h(x)]^2 dx, \quad (2.48)$$

or

$$\langle H(md) \rangle_N = \frac{1}{N-m} \sum_{i=1}^{N-m} [h_{i+m} - h_i]^2. \quad (2.49)$$

Similar to the auto-correlation function, as  $m$  increases, the number of data points becomes smaller. Therefore, for a large  $m$  value, the corresponding estimation for the height-height correlation function would not be accurate.

#### 2.4.1.6 Power spectrum

According to Section 2.2, the surface power spectrum is the Fourier transform of the auto-covariance function. Therefore, if we perform a Fourier transform for Equation (2.46) or (2.47), we can obtain the power spectrum. Furthermore, the power spectrum can also be obtained from the Fourier transform of a surface profile,

$$\langle P(k) \rangle_L = \frac{1}{L} \left| \int_{-L/2}^{L/2} h(x) e^{-ikx} dx \right|^2, \quad (2.50)$$

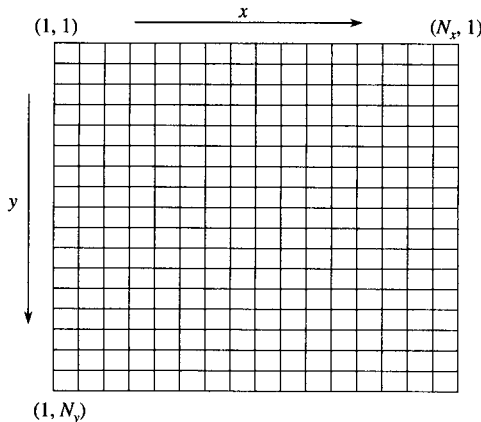


FIG. 2.11 The coordinates for the image mesh used in the text.

or

$$\langle P(k_j) \rangle_N = \frac{d}{N} \left| \sum_{m=1}^N h_m e^{-ik_j m d} \right|^2. \quad (2.51)$$

In Equation (2.51), one can make use of the fast Fourier transform (FFT) algorithm to obtain the power spectrum first, and then can perform an inverse FFT to obtain the auto-correlation function.

#### 2.4.2 Extraction of roughness parameters from surface images

In the previous section, we discussed methods to estimate numerically the roughness parameters from a one-dimensional surface profile. These methods can be extended to two-dimensional surfaces. The numerical algorithms for FFT and convolution in two dimensions can be found in the literature [2.5]. Here we concentrate on the extraction of the characteristic functions from surface images. Usually the surface images obtained by real-space profiling techniques are digitized. Assuming the image lattice is an  $N_x \times N_y$  mesh as shown in Figure 2.11, then the second-order statistical functions can be calculated.

##### 2.4.2.1 Auto-covariance function

For an isotropic surface, the auto-covariance function can be obtained along a particular direction. For example, if the fast scan is along the  $x$  direction in the SPM measurement, one could estimate the surface auto-covariance

function as

$$G(r) \approx G_s(p) = \frac{1}{N_y(N_x - p)} \sum_{l=1}^{N_y} \sum_{n=1}^{N_x - p} h(p + n, l)h(n, l). \quad (2.52)$$

A more rigorous way to estimate the auto-covariance function for an isotropic rough surface is to use the circular average,

$$\begin{aligned} G(r) &\approx G_s(\sqrt{p^2 + q^2}) \\ &= \frac{1}{(N_y - q)(N_x - p)} \sum_{l=1}^{N_y - q} \sum_{n=1}^{N_x - p} [h(p + n, l + q)h(n, l) \\ &\quad + h(N_x - p - n, l + q)h(n, l)]. \end{aligned} \quad (2.53)$$

For an anisotropic surface, since both the lateral correlation length and the roughness exponent could be direction dependent, one needs to calculate the direction-dependent characteristic functions, i.e., the two-dimensional forms of the characteristic functions. For the auto-covariance function, obviously  $G(\mathbf{r}) = G(-\mathbf{r})$  and one has

$$\begin{aligned} G(\mathbf{r}) &\approx G_s(p, q) \\ &= \frac{1}{(N_y - q)(N_x - p)} \sum_{l=1}^{N_y - q} \sum_{n=1}^{N_x - p} h(p + n, l + q)h(n, l), \text{ and} \\ G(\mathbf{r}) &\approx G_s(-p, q) = \frac{1}{(N_y - q)(N_x - p)} \times \\ &\quad \sum_{l=1}^{N_y - q} \sum_{n=1}^{N_x - p} h(N_x - p - n, l + q)h(n, l). \end{aligned} \quad (2.54)$$

#### 2.4.2.2 Height-height correlation function

The simplest way to calculate the height-height correlation function for an isotropic surface is along the fast scan direction (assumed to be the  $x$  direction):

$$H(r) \approx H_s(p) = \frac{1}{N_y(N_x - p)} \sum_{l=1}^{N_y} \sum_{n=1}^{N_x - p} [h(p + n, l) - h(n, l)]^2. \quad (2.55)$$

An alternative way is the circular average:

$$\begin{aligned} H(r) &\approx H_s(\sqrt{p^2 + q^2}) \\ &= \frac{1}{(N_y - q)(N_x - p)} \sum_{l=1}^{N_y - q} \sum_{n=1}^{N_x - p} \{[h(p + n, l + q) - h(n, l)]^2 \end{aligned}$$

$$+[h(N_x - p - n, l + q) - h(n, l)]^2\}. \quad (2.56)$$

For an anisotropic surface, the two-dimensional height-height correlation function can be calculated according to the following equations:

$$\begin{aligned} H(\mathbf{r}) &\approx H_s(p, q) \\ &= \frac{1}{(N_y - q)(N_x - p)} \sum_{l=1}^{N_y - q} \sum_{n=1}^{N_x - p} [h(p + n, l + q) - h(n, l)]^2, \text{ and} \\ H(\mathbf{r}) &\approx H_s(-p, q) \\ &= \frac{1}{(N_y - q)(N_x - p)} \times \\ &\quad \sum_{l=1}^{N_y - q} \sum_{n=1}^{N_x - p} [h(N_x - p - n, l + q) - h(n, l)]^2. \end{aligned} \quad (2.57)$$

#### 2.4.2.3 Power spectrum

The two-dimensional power spectrum can be estimated using

$$P_s(k_x, k_y) = \frac{1}{N_x N_y} \left| \sum_{m=1}^{N_x} \sum_{n=1}^{N_y} h(m, n) e^{-imk_x \Delta x - ink_y \Delta y} \right|^2. \quad (2.58)$$

For an isotropic surface, since the power spectrum is direction independent, one usually uses a circular average of the power spectrum in order to obtain better statistics,

$$P_s(k) = \frac{1}{N_k} \sum P_s(k_x, k_y) |_{k=\sqrt{k_x^2+k_y^2}}, \quad (2.59)$$

where  $N_k$  is the number of points at constant distance  $k = \sqrt{k_x^2 + k_y^2}$ , and the summation is the sum over all points having the same distance  $k$ .

#### 2.4.3 The accuracy of the estimation

In the above estimation, there are at least two factors to which one needs to pay attention. One is the total number of digitized points,  $N$ , which represents the length of the sampling surface. The other is the digitized step  $d$ , which represents the smallest lateral information one can resolve. The product of these two factors,  $L = Nd$ , is the total length of the surface. Both  $N$  and  $d$  characterize the detail of the sampling, which should be closely related to the accuracy of the estimation.

Past experiences tell us that the larger the  $N$ , the more accurate the estimation. This is based on the well-known theorem, called the law of large number (LLN) [2.6]. LLN states that for very large  $N$ , the arithmetic average  $\frac{1}{N} \sum_{m=1}^N Y_m$  for  $N$  *independent* random variables  $Y_1, Y_2, \dots, Y_N$ , is close to the expectation value. In other words, when  $N$  increases to infinity, the arithmetic average of  $N$  *independent* random variables almost becomes a constant. Note that in the above statement, we use  $N$  *independent* random variables. However, we know that most random rough surfaces are not independent; at least within the lateral correlation length  $\xi$ , the two surface heights are correlated. Under this condition, can we still apply the law of large number to our estimation? In the following, we shall consider how a limited value of the sampling length  $L$  affects the estimation and answer the above question.

Let us consider the estimation of the RMS roughness,

$$\langle w^2 \rangle_L = \frac{1}{L} \int_{-L/2}^{L/2} [h(x) - \langle h \rangle_L]^2 dx. \quad (2.60)$$

To judge whether it is a good estimation or not, we need to examine its expectation value and the convergence to the expectation value as  $L \gg \xi$ . The expectation value is given by

$$E\{\langle w^2 \rangle_L\} = \frac{1}{L} \int_{-L/2}^{L/2} E\{[h(x) - \langle h \rangle_L]^2\} dx. \quad (2.61)$$

Substituting Equation (2.38) into Equation (2.61), we obtain

$$E\{\langle w^2 \rangle_L\} = w^2 - \frac{w^2}{L^2} \int_{-L/2}^{L/2} dx \int_{-L/2}^{L/2} R(x - \rho) d\rho, \quad (2.62)$$

where  $R(\rho)$  is the auto-correlation function. If we assume that the auto-correlation function of the surface has the exponential decay form  $\exp(-|x - r|/\xi)$ , then Equation (2.62) can be calculated as

$$E\{\langle w^2 \rangle_L\} = w^2 - \frac{\xi}{L} w^2 - 2 \frac{\xi^2}{L^2} w^2 (e^{-\xi/L} - 1). \quad (2.63)$$

Obviously, the expectation value of the estimation in Equation (2.60) is not  $w^2$ ; it is biased. The bias depends on the ratio  $L/\xi$ . Figure 2.12 shows how the ratio  $L/\xi$  affects the estimation. When  $L \gg \xi$ , the estimation is close to  $w^2$ , and the bias is small. When  $L \leq \xi$ , the estimation is much smaller than  $w^2$ . In this case, even though the number of data points  $N$  is huge, the estimation still is not good.

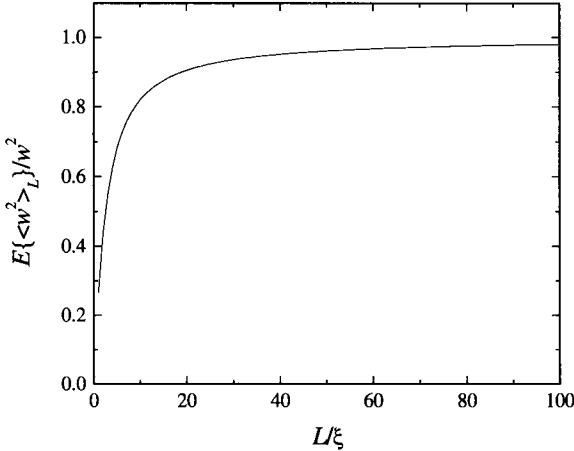


FIG. 2.12  $E\{\langle w^2 \rangle_L\}/w^2$  as a function of ratio  $L/\xi$ .

Now let us consider how the sampling step affects the estimation [2.4]. There is a famous theorem, Shannon's sampling theorem, which gives the estimation of a sampling step. It states: Given a deterministic signal  $Y(t)$  whose Fourier transform  $y(f)$  is zero beyond  $|f| > f_c$ :

$$y(f) = 0, \text{ for all } |f| > f_c,$$

then  $Y(t)$  can be completely and uniquely recovered from its sampled values at uniform intervals of  $\Delta t = 1/(2f_c)$ , and is given by

$$Y(t) = \sum_{n=-\infty}^{+\infty} Y(n\Delta t) \frac{\sin[2\pi f(t - n\Delta t)]}{2\pi f_c(t - n\Delta t)}. \quad (2.64)$$

One calls the frequency  $f_c$  as the Nyquist frequency. For a band-limited stochastic process  $Y(t)$ , for which the power spectrum satisfies

$$P(f) = 0, \text{ for all } |f| > f_c,$$

then

$$\hat{Y}(t) = \sum_{n=-\infty}^{+\infty} Y(n\Delta t) \frac{\sin[2\pi f(t - n\Delta t)]}{2\pi f_c(t - n\Delta t)} \quad (2.65)$$

is an expression for the sampling of the stochastic process in the mean-square sense:

$$E\{|Y(t) - \hat{Y}(t)|^2\} = 0. \quad (2.66)$$

Table 2.3 Summary of the statistical quantities of a random rough surface.

Terms	Definitions	Example (Gaussian Surface)
Height Distribution Function $p(h)$	The probability of surface height between $h$ and $h + dh$ at any point on the surface.	$p(h) = \frac{1}{\sqrt{2\pi}w} \exp(-\frac{h^2}{2w^2})$
Characteristic Function $\varphi(k)$	$\begin{aligned}\varphi(k) &= E\{\exp(-ikh)\} \\ &= \int_{-\infty}^{+\infty} p(h)e^{-ikh} dh\end{aligned}$	$\varphi(k) = \exp(-\frac{w^2 k^2}{2})$
Interface Width $w^2$	$w^2 = \int_{-\infty}^{+\infty} [h - \bar{h}]^2 p(h) dh$	$w^2$
Skewness $\gamma_3$	$\gamma_3 = \frac{1}{w^4} \int_{-\infty}^{+\infty} [h - \bar{h}]^3 p(h) dh$	$\gamma_3 = 0$
Kurtosis $\gamma_4$	$\gamma_4 = \frac{1}{w^4} \int_{-\infty}^{+\infty} [h - \bar{h}]^4 p(h) dh$	$\gamma_4 = 3$
Two-Point Joint Distribution $p_j(h_1, h_2; \mathbf{r}_1, \mathbf{r}_2)$	The probability of finding surface height $h_1$ at $\mathbf{r}_1$ and $h_2$ at $\mathbf{r}_2$ .	$p_j = \frac{1}{2\pi w^2 \sqrt{1-R(\mathbf{r}_1, \mathbf{r}_2)^2}} \times \exp\left\{-\frac{h_1^2 + h_2^2 - 2h_1 h_2 R(\mathbf{r}_1, \mathbf{r}_2)}{2w^2[1-R(\mathbf{r}_1, \mathbf{r}_2)^2]}\right\}$
Auto-Covariance Function $G(\mathbf{r}_1, \mathbf{r}_2)$	$G(\mathbf{r}_1, \mathbf{r}_2) = \int_{-\infty}^{+\infty} \int_{-\infty}^{+\infty} h_1 h_2 p_j(h_1, h_2; \mathbf{r}_1, \mathbf{r}_2) dh_1 dh_2$	$G(r) = w^2 \exp[-(\frac{r}{\xi})^2]$
Auto-Correlation Function $R(\mathbf{r}_1, \mathbf{r}_2)$	$R(\mathbf{r}_1, \mathbf{r}_2) = \frac{G(\mathbf{r}_1, \mathbf{r}_2)}{w^2}$	$R(r) = \exp[-(\frac{r}{\xi})^2]$
Lateral Correlation Length $\xi$	$R(\xi) = 1/e$	—
Height-Height Correlation Function $H(\mathbf{r})$	$H(\mathbf{r}) = E\{[h(\mathbf{r} + \boldsymbol{\rho}) - h(\boldsymbol{\rho})]^2\}$	$H(r) = 2w^2\{1 - \exp[-(\frac{r}{\xi})^2]\}$
Power Spectrum $P(\mathbf{k}_{  })$	$P(\mathbf{k}_{  }) = \frac{1}{2\pi} \int_{-\infty}^{+\infty} R(\boldsymbol{\rho}) e^{-i\mathbf{k}_{  } \cdot \boldsymbol{\rho}} d\boldsymbol{\rho}$	$P(k_{  }) = \frac{w^2 \xi}{2\sqrt{\pi}} \exp\left(-\frac{k_{  }^2 \xi^2}{4}\right)$

Note that for both deterministic and stochastic signals, the sampling theorem only holds for band-limited signals. The sampling theorem tells us that the signals can be recovered only when the sampling step is not larger than  $\frac{1}{2f_c}$ . If the sampling step is larger than  $\frac{1}{2f_c}$ , one cannot completely recover the signal, i.e., one loses some information about the signal.

## 2.5 Summary

In this chapter we have discussed how to characterize a rough surface. The major roughness parameters are summarized in Table 2.3.

## References

- 2.1 *Dynamics of Fractal Surfaces*, edited by F. Family and T. Vicsek (World Scientific, Singapore, 1991).
- 2.2 A.-L. Barabási and H. E. Stanley, *Fractal Concepts in Surface Growth* (Cambridge University Press, New York, 1995).
- 2.3 T. Assefi, *Stochastic Processes and Estimation: Theory with Applications* (Wiley, New York, 1979).
- 2.4 A. Papoulis, *Signal Analysis* (McGraw-Hill, New York, 1977).
- 2.5 W. H. Press, B. P. Flannery, S. A. Teukolsky, and W. T. Vetterling, *Numerical Recipes in C - The Art of Scientific Computing* (Cambridge University Press, New York, 1988).
- 2.6 H. Stark and J. W. Woods, *Probability, Random Processes, and Estimation Theory for Engineers*, 2nd Edition (Prentice Hall, Englewood Cliffs, 1994).

### 3. EXAMPLES OF RANDOM ROUGH SURFACES

In Chapter 2 we discussed how to characterize a random rough surface. We know that different rough surfaces would have different statistical parameters, especially the height distributions and the correlation functions or power spectra. In this chapter, we will discuss in detail three different surface morphologies during thin film growth/etching processes: self-affine surfaces, mounded surfaces, and anisotropic surfaces.

#### 3.1 Self-Affine Surfaces

##### 3.1.1 Definition

The fractal is a very useful concept for describing rough surfaces. The idea of fractal geometry is closely associated with the property of invariance under a change of scale. The simplest fractal object is a self-similar object, which is invariant under similarity transformations. A self-similar object looks the same (or statistically the same) when the space it occupies is stretched (dilated) uniformly by a factor  $\varepsilon$ . This property is called scale invariance. Another very useful concept for describing surface morphology is the self-affine fractal. A self-affine object looks the same after an affine transformation: If a small piece of the object is stretched with different ratios in different directions, then the enlarged object recovers (or statistically recovers) the original object. In this section we concentrate on self-affine surfaces.

A rough surface can be described by a single-valued self-affine function, which has the property [3.1]

$$h(x_1, \dots, x_n) = \varepsilon_1^{-\alpha_1} \dots \varepsilon_n^{-\alpha_n} h(\varepsilon_1 x_1, \dots, \varepsilon_n x_n), \quad (3.1)$$

where  $h$  is the surface height and  $\alpha_i$  is called the roughness exponent or Hurst exponent. Typically, there is only one characteristic roughness exponent and Equation (3.1) has a simpler form,  $h(x) = \varepsilon^{-\alpha} h(\varepsilon x)$ . For example, for a single variable  $x$ , Equation (3.1) demonstrates the fact that the function  $h$  is invariant under the following rescaling: shrink the variable  $x$  along the  $x$ -axis by a factor of  $1/\varepsilon$ ; rescale the value of the function by a different factor  $\varepsilon^{-\alpha}$ .

Therefore, a self-affine surface is a class of fractal objects that can be described by a roughness exponent, which is related to the fractal dimension

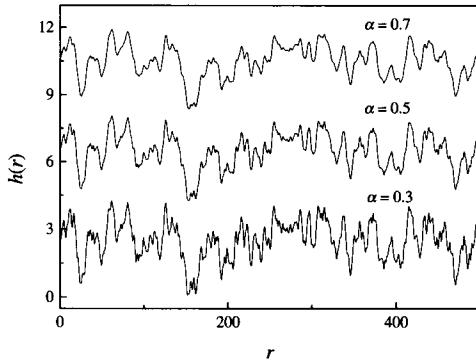


FIG. 3.1 Rough surface profiles for different values of  $\alpha$ . These three surfaces have the same values of  $w$  and  $\xi$ , but different values of the roughness exponent  $\alpha$ . The scales are in arbitrary units.

of the surface. The height-height correlation function of such a surface has the form [3.1, 3.2, 3.3, 3.4]

$$H(r) = 2w^2 f\left(\frac{r}{\xi}\right), \quad (3.2)$$

where  $f(x)$  is a scaling function, having the following properties:

$$f(x) = \begin{cases} x^{2\alpha}, & \text{for } x \ll 1; \\ 1, & \text{for } x \gg 1. \end{cases} \quad (3.3)$$

The parameter  $\alpha$  is called the roughness exponent ( $0 \leq \alpha \leq 1$ ), which describes how wiggly the surface is. The asymptotic behavior of the height-height correlation function can be written as

$$H(r) = \begin{cases} (mr)^{2\alpha}, & \text{for } r \ll \xi; \\ 2w^2, & \text{for } r \gg \xi, \end{cases} \quad (3.4)$$

where  $m = w^{1/\alpha}/\xi$  is the local slope [3.5]. It characterizes the short-range properties of the surface. Surfaces with different  $\alpha$  values are shown in Figure 3.1. One can see that a larger value of  $\alpha$  ( $= 0.7$ ) corresponds to a locally smooth surface structure while a smaller value of  $\alpha$  ( $= 0.3$ ) corresponds to a more jagged local surface morphology. The roughness exponent is directly related to the local surface fractal dimension  $D_s$  by  $d+1-D_s$ , where  $d+1$  is the dimension of the embedded space. The quantity  $\xi$  is the lateral correlation length, within which the surface heights of any two points are correlated. These three parameters,  $w$ ,  $\alpha$ , and  $\xi$ , are independent from each other and completely characterize a self-affine surface. They vary according to the process by which the surface morphology is formed.

The characteristics of a self-affine surface can also be defined through its power spectrum, which has the form

$$P(k_{||}) = w^2 g(\xi k_{||}). \quad (3.5)$$

The function  $g(y)$  has the properties,

$$g(y) = \begin{cases} 1, & \text{for } y \ll 1; \\ y^{-2\alpha-d}, & \text{for } y \gg 1. \end{cases} \quad (3.6)$$

Note that both scaling functions (3.3) and (3.6) only give the asymptotic behaviors of the characteristic functions, and the exact forms of these characteristic functions may vary. For  $0 \leq \alpha < 1$ , we can show that Equation (3.3) and Equation (3.6) are equivalent.

The relation between the power spectrum and the height-height correlation function for an isotropic 2+1-dimensional surface can be written as [3.6]

$$\begin{aligned} P(k_{||}) &= 2\pi \int_0^{+\infty} [2w^2 - H(r)] r J_0(k_{||} r) dr \\ &= 4\pi w^2 \xi^2 \int_0^{+\infty} [1 - f(x)] x J_0(k_{||} \xi x) dx, \end{aligned} \quad (3.7)$$

where  $1 - f(x) = 1 - x^{2\alpha}$  for  $x \ll 1$ , and  $1 - f(x) = 0$  for  $x \rightarrow \infty$ , and  $J_0(x)$  is the zeroth-order Bessel function. Integrating Equation (3.7) by parts, one has

$$P(k_{||}) = 4\pi w^2 k_{||}^{-2} \int_0^{+\infty} \xi k_{||} x J_1(k_{||} \xi x) f'(x) dx. \quad (3.8)$$

Here  $J_1(x)$  is the first-order Bessel function. For  $k_{||} \gg 1$ , the dominant contribution to the integral of Equation (3.8) comes from small  $x (<< 1)$ , where  $f' \approx 2\alpha x^{2\alpha-1}$ . Therefore,

$$P(k_{||}) \approx 8\pi\alpha w^2 k_{||}^{-2} \frac{2^{2\alpha} \Gamma(1+\alpha)}{\Gamma(1+\alpha)(\xi k_{||})^{2\alpha}} \propto k_{||}^{-2-2\alpha}, \text{ for } k_{||} \gg 1. \quad (3.9)$$

Thus, the definitions for a self-affine surface for Equations (3.3) and (3.6) are equivalent. This relationship is shown in Figure 3.2. However, when  $\alpha \rightarrow 1$ , the equivalence between Equations (3.3) and (3.6) is broken. One can employ numerical calculations to demonstrate this. For details, see reference [3.7].

Although the scaling forms of Equations (3.3) and (3.6) give the general characteristics of self-affine surfaces, sometimes it is more convenient to use explicit functional forms to describe the self-affine surfaces in order

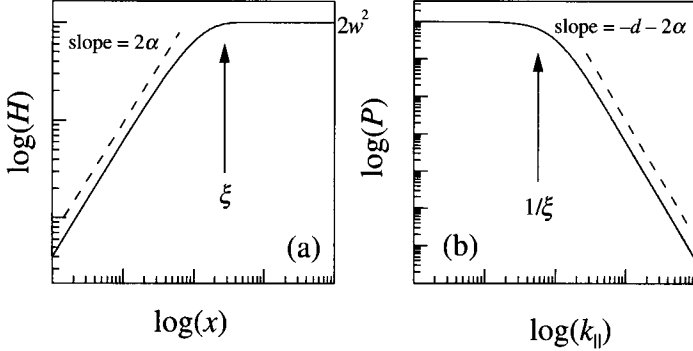


FIG. 3.2 (a) Log-log plot of the height-height correlation function of a self-affine surface. The interface width  $w$  can be determined from the plateau at large  $x$ . The roughness exponent  $\alpha$  can be extracted from the slope in the short range regime, and the lateral correlation length  $\xi$  can be determined at the crossover region. (b) Log-log plot of the corresponding power spectrum. The roughness exponent  $\alpha$  can be determined from the slope at large  $k_{||}$ , the lateral correlation length  $\xi$  is inversely proportional to the FWHM of the power spectrum, and the interface width  $w$  can be extracted from the integral of the power spectrum.

to obtain related roughness parameters. For self-affine and isotropic surfaces, Sinha et al. proposed a specific functional form for the height-height correlation function  $H(r)$  [3.8],

$$H(r) = 2w^2[1 - e^{-(\frac{r}{\xi})^{2\alpha}}]. \quad (3.10)$$

Three parameters are used to describe the morphology of a surface, i.e., the interface width  $w$ , lateral correlation length  $\xi$ , and roughness exponent  $\alpha$ . This height-height correlation function works for both 1+1 dimensions and 2+1 dimensions. From Equation (3.10), the corresponding auto-correlation function  $R(r)$  is given by

$$R(r) = e^{-(\frac{r}{\xi})^{2\alpha}}. \quad (3.11)$$

[When  $\alpha = 1$ , the 1+1-dimensional surface can be treated like a linear system with an independent Gaussian noise input  $\eta(t)$ . The system response function  $Y(t)$  is a Gaussian function with a correlation length  $\xi$ . This correlation length determines the lateral correlation length of the output. The output signal is a convolution of  $Y(t)$  and  $\eta(t)$ , i.e.,  $\int Y(t-\tau)\eta(\tau)d\tau$ .] The corresponding power spectrum takes the form ( $\alpha = 1$ )

$$P(k_{||}) = \frac{w^2\xi}{\sqrt{2}}e^{-k_{||}^2\xi^2/4}. \quad (3.12)$$

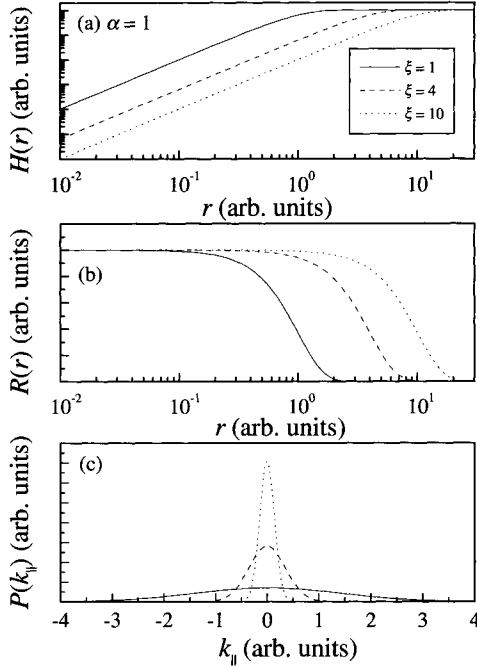


FIG. 3.3 Characteristic functions for self-affine surfaces in 2+1 dimensions: (a) height-height correlation function  $H(r)$ , (b) auto-correlation function  $R(r)$ , and (c) power spectrum  $P(k_{||})$ . Note that the height-height correlation function is plotted in a log-log scale, while the auto-correlation function and the power spectrum are plotted in linear scales from Ref. [3.9]).

In Figure 3.3 we plot three examples of these characteristic functions with  $\alpha = 1$ . It is clear that for a self-affine surface, both the height-height correlation function  $H(r)$  and auto-correlation function  $R(r)$  do not have an oscillatory behavior along the  $r$  axis. The power spectrum has only a single peak at the center, and the FWHM of the peak is inversely proportional to the lateral correlation length  $\xi$ . The local slope for this kind of surface is given by (only applied to  $\alpha = 1$  case rigorously) [3.9]

$$m^2 = \langle (\nabla h)^2 \rangle = \begin{cases} -\frac{d^2 G(r)}{dr^2}|_{r=0} = 2\frac{w^2}{\xi^2}, & \text{for 1+1 dimensions;} \\ -2\frac{\partial^2 G(r)}{\partial r^2}|_{r=0} = 4\frac{w^2}{\xi^2}, & \text{for 2+1 dimensions,} \end{cases} \quad (3.13)$$

i.e., the local slope is only determined by the interface width  $w$  and lateral correlation length  $\xi$ . (Note that the average slope  $\langle \nabla h \rangle$  is zero.)

Although Equation (3.10) is popular for describing self-affine surfaces, there is one case that Equation (3.10) cannot represent:  $\alpha = 0$ . When

$\alpha = 0$ , Equation (3.10) gives a constant height-height correlation function. In fact, as shown in Appendix A,  $\alpha = 0$  is the result of the Edwards-Wilkinson growth model, and one has a logarithmic height-height correlation function as shown in Equation (A.30) (see Appendix A). Therefore, a better phenomenological model is highly desirable.

Recently, G. Palasantzas proposed a  $K$ -correlation model [3.10], which can cover the  $\alpha = 0$  case. More conveniently this model has an analytical Fourier transform, which provides a better way to understand both the real-space and reciprocal-space behaviors of the self-affine surfaces. He suggested that the height-height correlation function can have the form,

$$H(r) = 2w^2 \left[ 1 - \frac{\alpha}{2^{\alpha-1} \Gamma(\alpha+1)} \left( \frac{r}{\xi} \right)^\alpha K_\alpha \left( \frac{r}{\xi} \right) \right], \quad (3.14)$$

where  $K_\alpha(x)$  is the  $\alpha$ -order modified Bessel function and  $\Gamma(x)$  is the Gamma function. Thus,

$$R(r) = \frac{\alpha}{2^{\alpha-1} \Gamma(\alpha+1)} \left( \frac{r}{\xi} \right)^\alpha K_\alpha \left( \frac{r}{\xi} \right). \quad (3.15)$$

The power spectrum can be written as

$$P(k_{||}) = \frac{4\pi\alpha w^2 \xi^2}{(1 + k_{||}^2 \xi^2)^{1+\alpha}}. \quad (3.16)$$

One can deduce easily from the power spectrum that the FWHM of  $P$  is inversely proportional to the lateral correlation length. This will be shown later in Chapter 9.

### 3.1.2 An example

In this section, we shall demonstrate the details of analyzing a self-affine surface. The backsides of silicon wafers exhibit self-affine structures. The left column in Figure 3.4 shows the atomic force microscopy (AFM) images of backside of silicon wafers, and the right column shows the power spectra of the corresponding surfaces calculated using Equation (2.58) [3.11]. The power spectra have rotational invariance. The cross-sections in different directions are the same, demonstrating that the backside surfaces are isotropic.

These samples are labeled as Samples #3, #5, and #10 from a list of ten samples to be discussed in detail later in Table 9.2.

Since the backside surfaces are isotropic, the height-height correlation functions for these three surfaces are calculated using Equation (2.55), and the interface width  $w$ , the lateral correlation length  $\xi$ , and the roughness

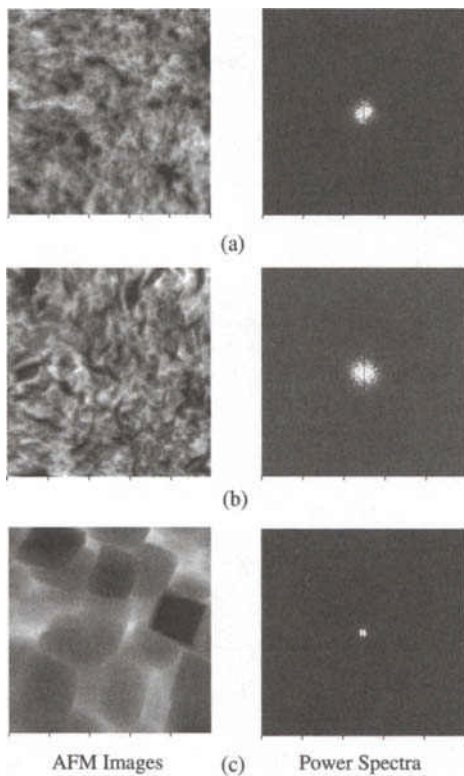


FIG. 3.4 AFM images ( $100 \mu\text{m} \times 100 \mu\text{m}$ ) and corresponding power spectra of the backsides of Si wafers: (a) Sample #3, (b) Sample #5, and (c) Sample #10 (to be discussed in Table 9.2). The gray scales of AFM images in (a), (b), and (c) are 0.8  $\mu\text{m}$ , 2.5  $\mu\text{m}$ , and 3.4  $\mu\text{m}$ , respectively. Note that all of the power spectra are circularly symmetric, except the vertical dark lines through the center, which are due to an artifact generated by the line scan (from Ref. [3.11]).

xponent  $\alpha$  can be determined as discussed in the last section. We plot the height-height correlation functions from the average of ten AFM images for Samples #3, #5, and #10 as shown in Figure 3.5. Sample #10 has the largest interface width and lateral correlation length among these three samples. However, the roughness exponents for all three samples are very close, judging from the slopes of the log-log plots at the small  $r$  region. To avoid any subjectivity for determining those roughness parameters, we use a phenomenological scaling function, Equation (3.10), to fit the height-height correlation data. For Sample #3,  $w = 169 \pm 6 \text{ nm}$ ,  $\xi = 4.2 \pm 0.02 \mu\text{m}$ ,  $\alpha = 0.93 \pm 0.02$ ; for Sample #5,  $w = 277 \pm 6 \text{ nm}$ ,  $\xi = 4.6 \pm 0.01 \mu\text{m}$ ,  $\alpha = 0.85 \pm 0.02$ ; and for Sample #10,  $w = 590 \pm 22 \text{ nm}$ ,  $\xi = 9.4 \pm 0.05 \mu\text{m}$ ,

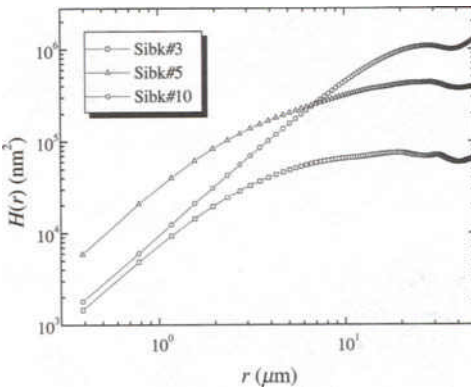


FIG. 3.5 The height-height correlation functions calculated from the AFM images obtained from Si Samples #3, #5, and #10 (from Ref. [3.11]).

$$\alpha = 0.87 \pm 0.02.$$

As we discussed in Chapter 2, one also needs to make sure that the rough surface is homogeneous and ergodic. A simple way to test the homogeneity is to scan the sample in different places and compare the statistical properties obtained from different places. If the statistical properties are within the error of the measurement, then we can say that the surface is homogeneous; otherwise the surface is not. The ergodity essentially is the run-to-run repeatability of the sample. The test of ergodity is to measure the surfaces of different samples from the same run or from different runs and compare the statistical properties. For a single sample, the homogeneity is very important. In Figure 3.6 we plot the height histogram of the three surfaces measured from different places on the samples. The scattered data points with different symbols represent the height histograms from the AFM images collected at randomly chosen positions of the same sample. The solid curves shown in Figure 3.6 are the best Gaussian fits for the height distribution. The width of the histogram is proportional to the interface width  $w$  of the surface. The height histograms of Samples #3 and #5 are very close to Gaussian distributions. The height histogram for Sample #10 deviates from a Gaussian distribution. This may be because the surface features (lateral correlation length) are large and the area scan ( $100 \mu\text{m} \times 100 \mu\text{m}$ ) is not large enough to include sufficient statistical averaging (see Section 5.2) [3.12]. Overall, the assumption of a Gaussian height distribution for those surfaces is quite good. Also, Figure 3.6 shows that for the same sample the height histograms measured at different positions are very close to each other. This means that for the same sample, statistically the height distribution does not change from place to place. The height

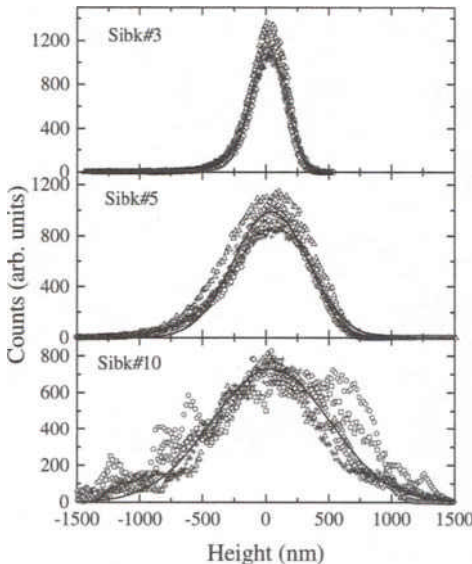


FIG. 3.6 The surface height histograms for the backside of Si Samples #3, #5, and #10 obtained by AFM. The scattered data represent the height histograms from AFM images, and different symbols denote the data taken from AFM images at randomly chosen positions of the same sample. The solid curves are the best Gaussian fits (from Ref. [3.11]).

distribution is uniform over the entire sample.

Another important test of the homogeneity of the surfaces is to check the translational invariance of statistical properties of the samples. This can be done by examining the statistical properties of the sampled surfaces at different locations on the sample. As a rough estimate, in Figure 3.7 we plot the value of height-height correlation functions from different sampled images versus the corresponding value of the average height-height correlation function for Samples #3, #5, and #10. For Samples #3 and #5, the plots of the sampling height-height correlation functions are very close to the straight line  $x = y$ , which means that, statistically, these two functions are the same. For Sample #10, the plots of the sampling height-height correlation functions deviate from the line  $x = y$  to various degrees. This could be because the scan area is not large enough to include sufficient statistical averaging [3.12]. The large deviation at large values is expected due to the finite size of the sampled image, where the height-height correlation function at large distance is estimated from a small number of sampled points. Figure 3.7 shows that the height-height correlation functions of the samples we studied are functions of only the distance between two separate

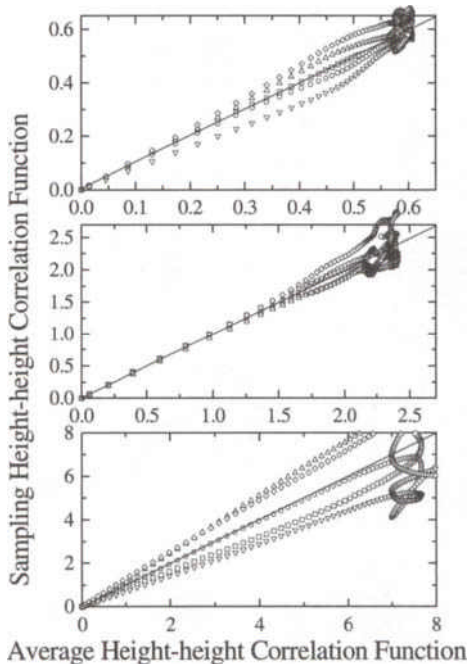


FIG. 3.7 The plots of the height-height correlation functions from different sampled images versus the average height-height correlation function for Si Samples #3, #5, and #10, respectively. Different symbols represent the data taken from the AFM images at randomly chosen positions of the same sample. The solid lines are  $x = y$  (from Ref. [3.11]).

surface points, and not functions of the surface positions, i.e., the samples are homogeneous.

In summary, we have shown in detail that the backsides of silicon wafers are isotropic, uniform, homogeneous, self-affine Gaussian surfaces.

## 3.2 Mounded Surfaces

### 3.2.1 Definition

The self-affine surfaces we discussed in the last section have no characteristic length. However, some surfaces in nature can possess regular mound structures, which exhibit a wavelength selection. This kind of surface can occur in thin film growth in the presence of a step barrier (Schwoebel barrier), which prevents adatoms from hopping down the step edge, and generates an uphill diffusion current [3.13, 3.14, 3.15, 3.16, 3.17, 3.18, 3.19]. For ex-

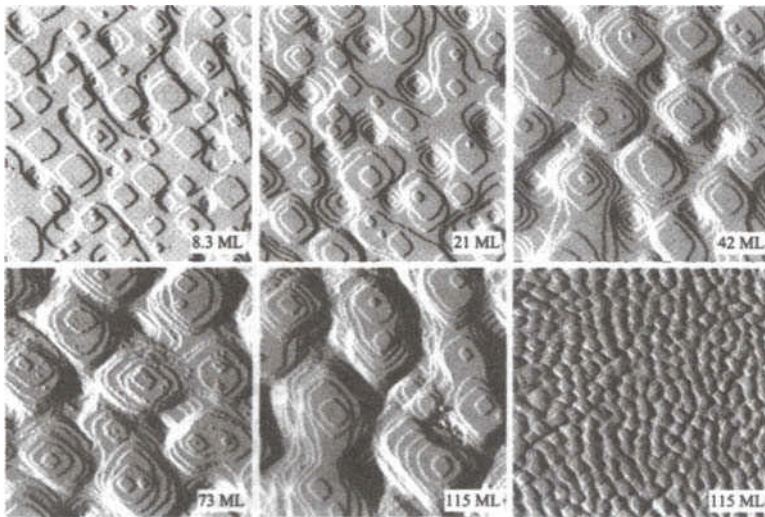


FIG. 3.8 First derivatives of STM images measured from various thickness (8.3, 21, 42, 73, 115, and 115 ML) of Cu deposited on Cu(100) at  $T \sim 299\text{K}$ . The first five images show areas of  $100\text{ nm} \times 100\text{ nm}$  while the last one is of  $500\text{ nm} \times 500\text{ nm}$  (from Ref. [3.19]).

ample, Figure 3.8 shows a STM study of homoepitaxy of Cu on Cu(100) at about 299 K [3.19]. Regular mounds are clearly present on the surface due to the step bias effect.

For a mounded surface, we propose the following form for the height-height correlation function [3.9, 3.20]:

$$H(r) = \begin{cases} 2w^2[1 - e^{-(\frac{r}{\zeta})^{2\alpha}} \cos(\frac{2\pi r}{\lambda})], & \text{for 1+1 dimensions,} \\ 2w^2[1 - e^{-(\frac{r}{\zeta})^{2\alpha}} J_0(\frac{2\pi r}{\lambda})], & \text{for 2+1 dimensions,} \end{cases} \quad (3.17)$$

where  $J_0(x)$  is the zeroth-order Bessel function. Four parameters are used to describe the surface: the interface width  $w$ , the system correlation length  $\zeta$ , the roughness exponent  $\alpha$ , and the average mound separation  $\lambda$ . For a mounded surface it is known that the local surface is quite smooth and  $\alpha = 1$  [3.11, 3.14, 3.15, 3.16, 3.17, 3.18, 3.19]. The corresponding auto-correlation functions are

$$R(r) = \begin{cases} e^{-(\frac{r}{\zeta})^{2\alpha}} \cos(\frac{2\pi r}{\lambda}), & \text{for 1+1 dimensions,} \\ e^{-(\frac{r}{\zeta})^{2\alpha}} J_0(\frac{2\pi r}{\lambda}), & \text{for 2+1 dimensions.} \end{cases} \quad (3.18)$$

According to Equation (2.21), the lateral correlation length  $\xi$  can be defined through the auto-correlation function as  $R(\xi) = 1/e$  and is a function of both  $\zeta$  and  $\lambda$ . For example, in 2+1 dimensions, if we let  $\zeta = \lambda$ , then

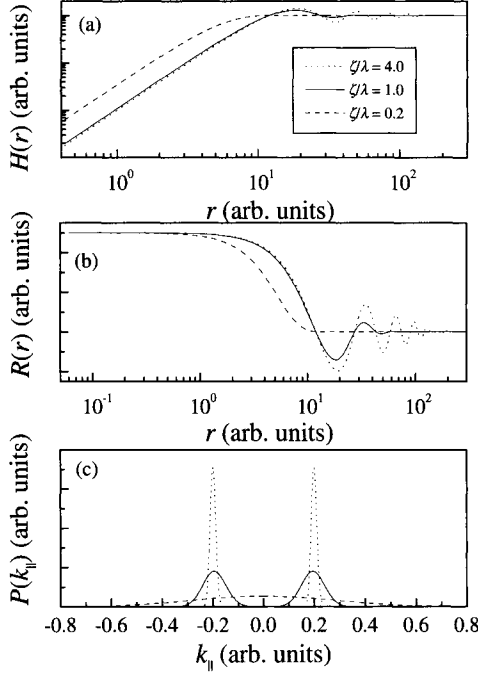


FIG. 3.9 Characteristic functions for bounded surfaces in 2+1 dimensions: (a) height-height correlation function  $H(r)$ , (b) auto-correlation function  $R(r)$ , and (c) power spectrum  $P(k_{||})$ . Note that the height-height correlation function is plotted in a log-log scale, while the auto-correlation function and the power spectrum are plotted in linear scales (from Ref. [3.9]).

$\xi = 0.27\lambda$ . [In fact, for the case of 1+1 dimensions, the surface can also be treated like a linear system with the input as a product of an independent Gaussian noise  $\eta(t)$  and a sinusoidal function  $\sin(2\pi t/\lambda)$ . The output signal is  $\int Y(t-\tau) \sin(\frac{2\pi\tau}{\lambda})\eta(\tau)d\tau$ , where the response of the system  $Y(t)$  is a Gaussian function with a system correlation length  $\zeta$ .] The system correlation length  $\zeta$  determines how randomly the mounds are distributed on the surface. Smaller  $\zeta$  means more random distribution.

The corresponding power spectra are given by, for  $\alpha = 1$ ,

$$P(k_{||}) = \begin{cases} \frac{w^2\zeta}{2\sqrt{2}}[e^{-(k_{||}-\frac{2\pi}{\lambda})^2\zeta^2/4} + e^{-(k_{||}+\frac{2\pi}{\lambda})^2\zeta^2/4}], & \text{for 1+1 dimensions,} \\ \frac{w^2\zeta^2}{2} \exp(-\frac{4\pi^2+k_{||}^2\lambda^2}{4\lambda^2}\zeta^2) I_0(\frac{\pi k_{||}\zeta^2}{\lambda}), & \text{for 2+1 dimensions,} \end{cases} \quad (3.19)$$

where  $I_0(x)$  is the zeroth-order modified Bessel function. The additional parameter, the average mound separation  $\lambda$ , makes the problem more complicated. In Figure 3.9 we plot the characteristic functions for 2+1 dimen-

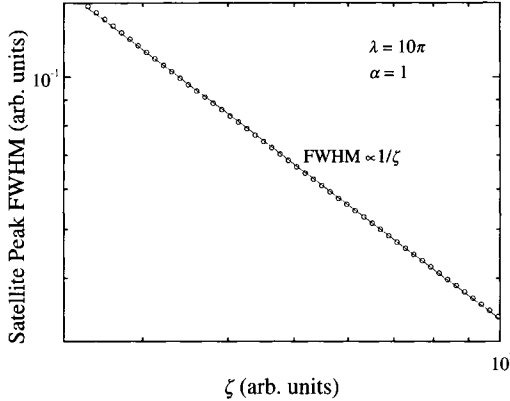


FIG. 3.10 The FWHM of the satellite peak plotted as a function of system correlation length  $\zeta$  for 2+1 dimensions (from Ref. [3.9]).

sions for various  $\zeta/\lambda$  ratios. The behavior of the characteristic functions is determined mainly by the  $\zeta/\lambda$  ratio. If  $\zeta/\lambda \geq 1$ , both the height-height correlation function  $H(r)$  and the auto-correlation function  $R(r)$  have an oscillatory behavior, and the power spectrum shows clear satellite rings. This is an essential characteristic of a mounded surface. In this case, the  $\lambda$  value determines the positions of the satellite rings,  $k_c = 2\pi/\lambda$ . The FWHM of the satellite rings decreases with increasing system correlation length  $\zeta$  for a fixed  $\lambda$ .

In fact, the FWHM of the satellite rings is inversely proportional to  $\zeta$ , as shown in Figure 3.10. When the  $\zeta/\lambda$  ratio is reduced, the oscillatory amplitude of both  $H(r)$  and  $R(r)$  decreases, and the ring position for the power spectrum also decreases even though  $\lambda$  remains unchanged. In Figure 3.11 we show the change of the ring location as a function of the  $\zeta/\lambda$  ratio. The solid curve represents  $k_c = 2\pi/\lambda$ . Although the ring position is still inversely proportional to  $\lambda$ , the exact value is very different. As the  $\zeta/\lambda$  ratio decreases further, the oscillatory behavior of both  $H(r)$  and  $R(r)$  totally disappears, and there is no longer a characteristic ring in the power spectrum.

The local slope is given by

$$m^2 = \begin{cases} 2w^2(\frac{1}{\zeta^2} + \frac{2\pi^2}{\lambda^2}), & \text{for 1+1 dimensions,} \\ 4w^2(\frac{1}{\zeta^2} + \frac{\pi^2}{\lambda^2}), & \text{for 2+1 dimensions.} \end{cases} \quad (3.20)$$

It is seen that the local slope is determined not only by the system correlation length  $\zeta$ , but also by the average mound separation  $\lambda$ . When  $\zeta/\lambda \gg 1$ ,  $m^2 \propto w^2/\lambda^2$ , i.e., the local slope is determined only by the interface width

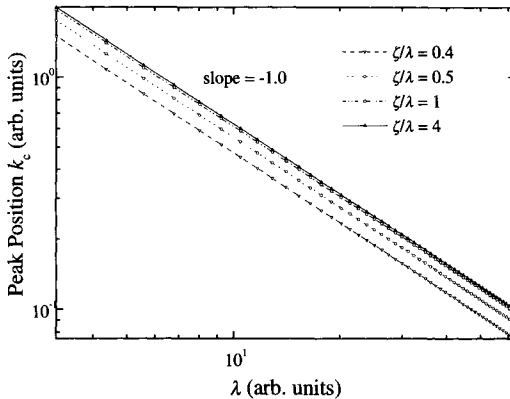


FIG. 3.11 The position of the satellite ring  $k_c$  is plotted as a function of the average mound separation  $\lambda$  for different  $\zeta/\lambda$  ratios for 2+1 dimensions. The solid curve is the plot of the relation  $k_c = 2\pi/\lambda$  (from Ref. [3.9]).

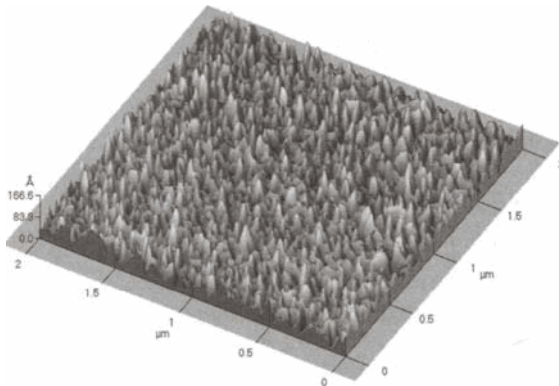


FIG. 3.12 An AFM image of an epitaxial CoGe thin film deposited on a GaAs substrate by partially ionized beam deposition (from Ref. [3.21]).

$w$  and average mound separation  $\lambda$ . However, if  $\zeta/\lambda \ll 1$ , then  $m^2 \propto w^2/\zeta^2$ .

### 3.2.2 An example

An example of a mounded surface is the epitaxial CoGe thin film deposited on GaAs substrate by partially ionized beam deposition [3.21]. Figure 3.12 shows an AFM image of the surface morphology. The surface power spectrum exhibits a ring structure as shown in Figure 3.13. Figure 3.14 plots the height-height correlation function  $H(r)$  in log-log scale calculated

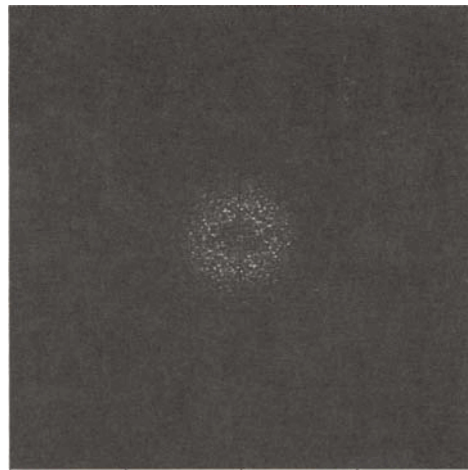


FIG. 3.13 The power spectrum of the CoGe film surface shown in Figure 3.12 (from Ref. [3.21]).

by Equation (2.55) and the circular average of the power spectrum  $P(k_{||})$  [Equation (2.59)] in linear scale. From the small- $r$  region in  $H(r)$ , we obtain  $2\alpha \approx 1.6$ , i.e.,  $\alpha \approx 0.8$ . From the plateau of  $H(r)$ , the interface width  $w$  has been extracted as 21 Å, and the cross-over region gives  $\xi \approx 0.04 \mu\text{m}$ . The ring position in the power spectrum is  $k_0 \approx 57.8 \mu\text{m}^{-1}$ , which means the average mound separation is about 0.11  $\mu\text{m}$ . The FWHM of the ring in the power spectrum is about  $62.3 \mu\text{m}^{-1}$ . Thus  $\zeta \approx 0.1 \mu\text{m}$ .

### 3.3 Anisotropic Surfaces

A major difference between one-dimensional surfaces and two-dimensional surfaces is that two-dimensional surfaces have one more degree of freedom. This freedom adds more complexity to both the description and the treatment of two-dimensional surfaces. One of the complexities is anisotropy.

A recent STM study showed that the surface morphologies of homoepitaxial GaAs films on nominally-flat GaAs(001) surfaces are highly anisotropic, with elongated multilayered features developing parallel to the [1̄10] direction [3.22, 3.23, 3.24, 3.25]. The anisotropy depends on the growth rate and substrate temperature [3.23, 3.25]. The height-height correlation functions along different directions are quite different [3.23]. Similar morphologies have also been observed in metal-organic molecular beam epitaxy (MOMBE) of InP on a nominally-flat InP(100) substrate [3.26].

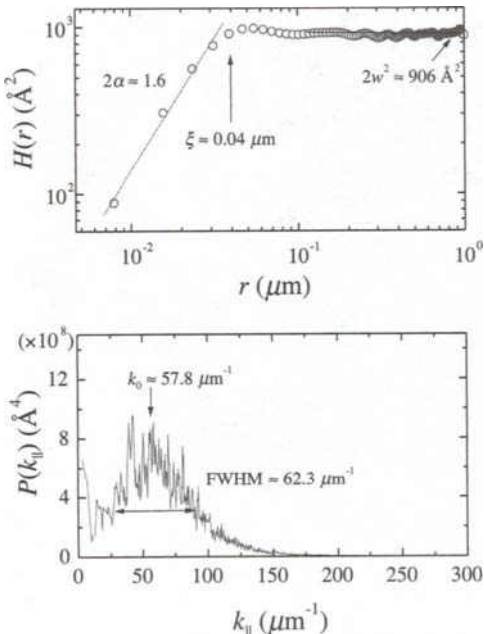


FIG. 3.14 The height-height correlation function  $H(r)$  and the circularly-averaged power spectrum  $P(k_{\parallel})$  of the CoGe film surface shown in Figure 3.12 (from Ref. [3.21]).

The surface has a pattern with elongated structures along the  $[0\bar{1}1]$  direction, and the surface anisotropy increases with time under the same growth conditions. Anisotropic surface morphologies also exist in heteroepitaxial films such as the Ge/Si system [3.27]. A recent study of InAlAs grown on InP(001) showed that the direction of the surface anisotropy can rotate during growth [3.28]. Furthermore, anisotropy appeared in the growth of materials on stepped or vicinal surfaces. For example, it was observed that for Si grown on a vicinal Si(100) substrate with a  $4^\circ$  miscut, the surface morphology showed a strong shape anisotropy along the initial  $[\bar{1}10]$  step direction [3.29].

There are at least two kinds of anisotropy for self-affine rough surfaces: correlation length anisotropy and scaling anisotropy. For correlation length anisotropy, there are different lateral correlation lengths along different directions, but the scaling properties of the surface remain the same in all directions. For scaling anisotropy, the scaling properties of the surface are direction dependent. Based on these two features, the following anisotropic random surface models are proposed. Note that, for simplicity, all the surfaces are assumed to be Gaussian.

### 3.3.1 Correlation-length anisotropy

In modeling the anisotropic seafloor morphology, Goff and Jordan introduced a form of the power spectrum  $P(\mathbf{k}_{||})$  as [3.30]

$$P(\mathbf{k}_{||}) = \frac{2\alpha\xi_x\xi_y w^2}{(1 + k_x^2\xi_x^2 + k_y^2\xi_y^2)^{1+\alpha}}, \quad (3.21)$$

where  $\xi_x$  and  $\xi_y$  are the correlation lengths in the  $x$  and  $y$  directions, respectively. Note that we can also assume other forms [3.31]. However, the asymptotic behaviors of those forms are the same. The isotropic case of Equation (3.21) was first used by Von Karman [3.32] and has been studied extensively [3.10, 3.33, 3.34]. Equation (3.21) has the following properties. 1) When  $k_x$  (or  $k_y$ )  $\rightarrow 0$  while  $k_y$  (or  $k_x$ ) remains constant,  $P(\mathbf{k}_{||}) \sim \text{constant}$ . 2) When  $k_x$  (or  $k_y$ )  $\rightarrow \infty$  while  $k_y$  (or  $k_x$ ) remains constant,  $P(\mathbf{k}_{||}) \propto k_x^{-2-2\alpha}$  (or  $P(\mathbf{k}_{||}) \propto k_y^{-2-2\alpha}$ ), i.e., the scalings in both the  $x$  and  $y$  directions are the same. 3) The FWHM of the power spectrum satisfies

$$k_{Fx}^2\xi_x^2 + k_{Fy}^2\xi_y^2 = 2^{\frac{1}{1+\alpha}} - 1, \quad (3.22)$$

where  $k_{Fx}$  and  $k_{Fy}$  are the FWHM positions of the diffraction beam along the  $k_x$  and  $k_y$  directions, respectively. Equation (3.21) describes an ellipse with the principal axes along the  $k_x$  and  $k_y$  directions. The ratio of the diameter of the short axis,  $a_x$ , and the diameter of the long axis,  $a_y$ , is

$$\frac{a_x}{a_y} = \frac{\xi_y}{\xi_x}. \quad (3.23)$$

The auto-correlation function can be written as

$$\begin{aligned} R(\mathbf{r}) &= \frac{\alpha\xi_x\xi_y}{\pi} \int \frac{e^{-i\mathbf{k}_{||}\cdot\mathbf{r}}}{(1 + k_x^2\xi_x^2 + k_y^2\xi_y^2)^{1+\alpha}} d\mathbf{k}_{||} \\ &= \frac{1}{2^{\alpha-1}\Gamma(\alpha)} \left( \frac{x^2}{\xi_x^2} + \frac{y^2}{\xi_y^2} \right)^{\alpha/2} K_\alpha \left[ \left( \frac{x^2}{\xi_x^2} + \frac{y^2}{\xi_y^2} \right)^{1/2} \right]. \end{aligned} \quad (3.24)$$

Here the function  $K_\alpha(x)$  is the modified Bessel function of the  $\alpha$ th order. The height-height correlation function  $H(\mathbf{r})$  can be expressed as

$$H(\mathbf{r}) = 2w^2 \left\{ 1 - \frac{1}{2^{\alpha-1}\Gamma(\alpha)} \left( \frac{x^2}{\xi_x^2} + \frac{y^2}{\xi_y^2} \right)^{\alpha/2} K_\alpha \left[ \left( \frac{x^2}{\xi_x^2} + \frac{y^2}{\xi_y^2} \right)^{1/2} \right] \right\}. \quad (3.25)$$

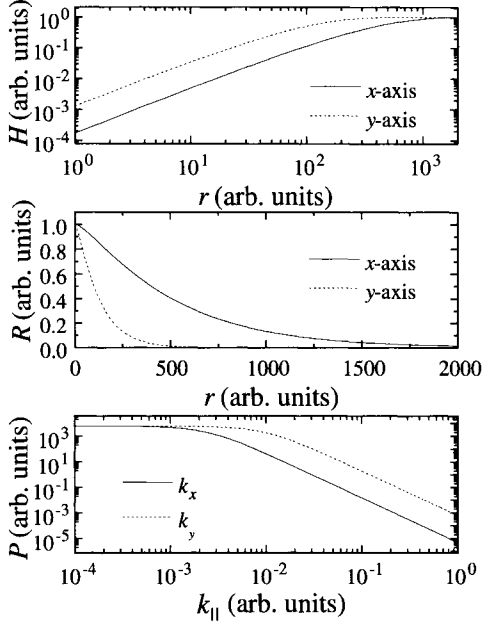


FIG. 3.15 Power spectrum  $P$ , auto-correlation function  $R$ , and height-height correlation function  $H$  of a correlation length anisotropy surface for  $\alpha = 0.75$ ,  $\xi_x = 400$ ,  $\xi_y = 100$ . Note that the power spectrum and height-height correlation function are plotted in log-log scales, while the auto-correlation function is plotted in linear scale (from Ref. [3.31]).

As  $K_\alpha(x) \approx \frac{2^{\alpha-1}\Gamma(\alpha)}{x^\alpha} + \frac{\Gamma(-\alpha)}{2^{1+\alpha}}x^\alpha$  for  $x \rightarrow 0$  and  $0 < \alpha < 1$ ;  $K_\alpha(x) \approx \sqrt{\frac{\pi}{2x}}e^{-x}$  for  $x \rightarrow \infty$ , one has

$$H(\mathbf{r}) \approx \begin{cases} \frac{\pi w^2}{2^{2\alpha-1}\alpha \sin(\alpha\pi)\Gamma^2(\alpha)} \left( \frac{x^2}{\xi_x^2} + \frac{y^2}{\xi_y^2} \right)^\alpha, & \text{for } r \rightarrow 0, \\ 2w^2, & \text{for } r \rightarrow \infty. \end{cases} \quad (3.26)$$

Figure 3.15 plots two orthogonal cross sections of the power spectrum, auto-correlation function, and height-height correlation function for  $\alpha = 0.75$ ,  $\xi_x = 400$ ,  $\xi_y = 100$ . In the log-log plot of the power spectrum, at large  $k$ , the tails of the two cross sections are parallel. Similar behavior is also observed in the log-log plot of the height-height correlation function at small  $r$ . However, the widths of the flat shoulders of the two cross sections in both the power spectra and height-height correlation functions are not the same. These are typical characteristics of a correlation-length anisotropy. We plot in Figure 3.16 the contours of the power spectrum and auto-correlation function for  $\alpha = 0.75$ ,  $\xi_x = 400$ , and  $\xi_y = 100$ . The shapes of the contours are elliptical, but the long axis in the power spectrum is

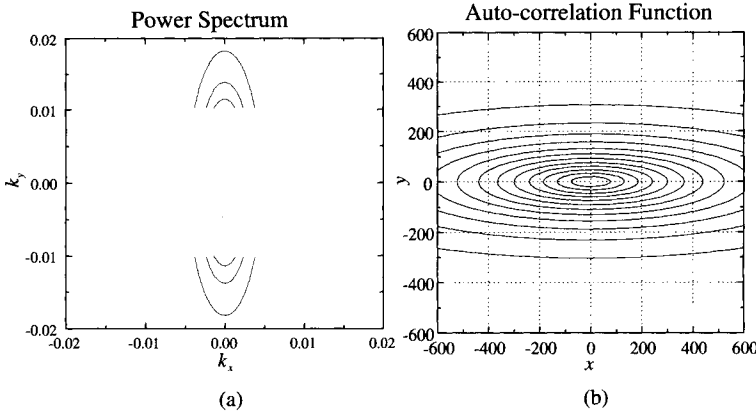


FIG. 3.16 The equal-value contours of (a) the power spectrum and (b) the auto-correlation function for  $\alpha = 0.75$ ,  $\xi_x = 400$ , and  $\xi_y = 100$ . All  $x$ ,  $y$ ,  $k_x$ , and  $k_y$  are in arbitrary units (from Ref. [3.31]).

perpendicular to the long axis in the auto-correlation function, from the properties of the Fourier transform.

### 3.3.2 Scaling anisotropy

A simple way to construct a scaling-anisotropic surface is to assume that the  $x$  and  $y$  directions have different roughness exponents. Then the power spectrum has the following form:

$$P(k_{||}) = \frac{2\xi_x\xi_y w^2 \Gamma(\frac{1}{2} + \alpha_x) \Gamma(\frac{1}{2} + \alpha_y)}{\Gamma(\alpha_x) \Gamma(\alpha_y) (1 + k_x^2 \xi_x^2)^{1/2+\alpha_x} (1 + k_y^2 \xi_y^2)^{1/2+\alpha_y}}, \quad (3.27)$$

where  $\alpha_x$  and  $\alpha_y$  are the roughness exponents in the  $x$  and  $y$  directions, respectively. Equation (3.27) has the following properties. 1) When  $k_x$  (or  $k_y$ )  $\rightarrow 0$  while  $k_y$  (or  $k_x$ ) remains constant, then  $P(\mathbf{k}_{||}) \sim \text{constant}$ . 2) When  $k_x$  (or  $k_y$ )  $\rightarrow \infty$  while  $k_y$  (or  $k_x$ ) remains constant,  $P(\mathbf{k}_{||}) \propto k_x^{-1-2\alpha_x}$  (or  $P(\mathbf{k}_{||}) \propto k_y^{-1-2\alpha_y}$ ), i.e., the scaling in both the  $x$  and  $y$  directions is not the same. 3) It is clear that the contour of the FWHM from Equation (3.27) does not have an elliptical form. However, as Equation (3.27) has a quadratic symmetry, the ratio  $\gamma$  of FWHMs for the  $k_x$  and  $k_y$  axes still reflects the surface anisotropy:

$$\gamma = \frac{\xi_y}{\xi_x} \left( \frac{2^{\frac{2}{1+2\alpha_x}} - 1}{2^{\frac{2}{1+2\alpha_y}} - 1} \right)^{1/2}. \quad (3.28)$$

Equation (3.28) shows that the ratio  $\gamma$  depends not only on the ratio of the lateral correlation lengths  $\frac{\xi_y}{\xi_x}$ , but also on the scaling exponents  $\alpha_x$  and  $\alpha_y$ ,  $\left(\frac{\frac{2}{1+2\alpha_x}-1}{\frac{2}{1+2\alpha_y}-1}\right)^{1/2}$ . One can estimate that the ratio caused by anisotropic scaling exponents ranges from 0.44 ( $\alpha_x = 1$  and  $\alpha_y = 0$ ) to 2.26 ( $\alpha_x = 0$  and  $\alpha_y = 1$ ).

The auto-correlation function can be written as

$$R(\mathbf{r}) = \frac{4 \left| \frac{\xi_x x}{2} \right|^{\alpha_x} \left| \frac{\xi_y y}{2} \right|^{\alpha_y} K_{\alpha_x} \left( \left| \frac{x}{\xi_x} \right| \right) K_{\alpha_y} \left( \left| \frac{y}{\xi_y} \right| \right)}{\Gamma(\alpha_x) \Gamma(\alpha_y) \xi_x^{2\alpha_x} \xi_y^{2\alpha_y}}, \quad (3.29)$$

and the height-height correlation function is

$$H(\mathbf{r}) = 2w^2 \left[ 1 - \frac{4 \left| \frac{\xi_x x}{2} \right|^{\alpha_x} \left| \frac{\xi_y y}{2} \right|^{\alpha_y} K_{\alpha_x} \left( \left| \frac{x}{\xi_x} \right| \right) K_{\alpha_y} \left( \left| \frac{y}{\xi_y} \right| \right)}{\Gamma(\alpha_x) \Gamma(\alpha_y) \xi_x^{2\alpha_x} \xi_y^{2\alpha_y}} \right]. \quad (3.30)$$

The asymptotic behavior of Equation (3.30) is

$$H(\mathbf{r}) \approx \begin{cases} \frac{2\pi w^2}{\sin(\alpha_x \pi) \Gamma^2(\alpha_x)} \left( \frac{x}{2\xi_x} \right)^{2\alpha_x} + \frac{2\pi w^2}{\sin(\alpha_y \pi) \Gamma^2(\alpha_y)} \left( \frac{y}{2\xi_y} \right)^{2\alpha_y}, & \text{for } r \rightarrow 0, \\ 2w^2, & \text{for } r \rightarrow \infty. \end{cases} \quad (3.31)$$

Figure 3.17 plots two orthogonal cross sections of the power spectra, auto-correlation functions and height-height correlation functions for  $\alpha_x = 0.75$ ,  $\alpha_y = 0.4$ ,  $\xi_x = 400$ , and  $\xi_y = 100$ . Unlike Figure 3.15, in the log-log plot of the power spectra, at large  $k$ , the tails of the two cross sections are not parallel. A similar behavior is also observed in the log-log plot of height-height correlation functions at small  $r$ . This is a typical characteristic of a scaling-anisotropic surface; the roughness exponents are different in different directions. The widths of the flat shoulders of these two cross sections in both the power spectra and height-height correlation functions are not the same. We plot in Figure 3.18 the contours of the power spectra and auto-correlation functions for (a)  $\alpha_x = 0.75$ ,  $\alpha_y = 0.4$ ,  $\xi_x = 400$ ,  $\xi_y = 100$ ; (b)  $\alpha_x = 0.75$ ,  $\alpha_y = 0.4$ ,  $\xi_x = 90$ ,  $\xi_y = 100$ ; and (c)  $\alpha_x = 0.75$ ,  $\alpha_y = 0.4$ ,  $\xi_x = 50$ ,  $\xi_y = 100$ . The shapes of the contours are not elliptical anymore. However, the long axis in the power spectrum is determined not only by the correlation length of the short axis in real space, but also by the roughness exponents. For example, in Figure 3.18(b),  $\xi_x < \xi_y$ , but the long axis is still in the  $k_y$  direction since  $\alpha_x > \alpha_y$ . These behaviors are also reflected in the auto-correlation plots.

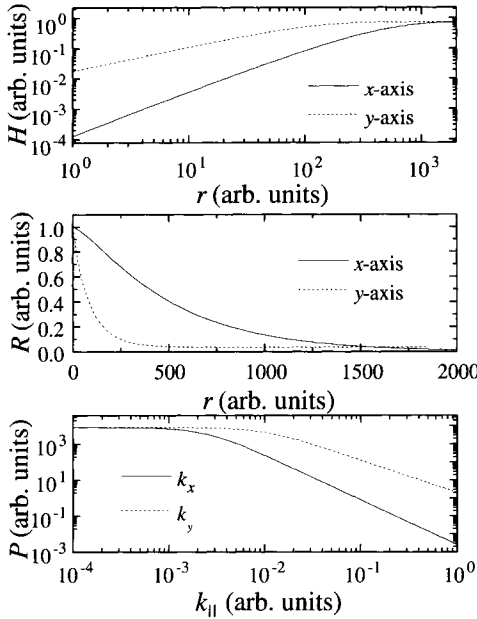


FIG. 3.17 Power spectrum  $P$ , auto-correlation function  $R$ , and height-height correlation function  $H$  for  $\alpha_x = 0.75$ ,  $\alpha_y = 0.40$ ,  $\xi_x = 400$ , and  $\xi_y = 100$ . Note that the power spectrum and height-height correlation function are plotted in log-log scales, while the auto-correlation function is plotted in a linear scale (from Ref. [3.31]).

### 3.3.3 An example

Figure 3.19 shows an AFM image of the surface of a mercury-cadmium-telluride (MCT) film grown on a stepped GaAs substrate [3.35]. It has ridges stretching from the top to bottom, and the surface morphology is anisotropic. The power spectrum is shown in Figure 3.20 and clearly shows the anisotropy. In order to obtain the direction-dependent height-height correlation function, we rotate the sample, and take AFM images at different rotation angles. In Figure 3.21 we plot the direction-dependent height-height correlation functions  $H(r)$  calculated from Equation (2.55) for rotation angles  $\phi = 0^\circ$ ,  $45^\circ$ , and  $90^\circ$ . Obviously the roughness exponents  $\alpha$  in different directions are different: for  $\phi = 0^\circ$ ,  $\alpha \approx 0.69$ ; for  $\phi = 45^\circ$ ,  $\alpha \approx 0.66$ ; and for  $\phi = 90^\circ$ , the surface exhibits multi-fractal behavior with two roughness exponents:  $\alpha \approx 0.55$  and  $\alpha \approx 0.18$ . Also, the lateral correlation lengths  $\xi$  are different in different directions. The difference in  $2w^2$  for different directions shown in the height-height correlation function plot is due to the fact that we use the one-dimensional height-height correlation function. The interface width  $w$  of the two-dimensional surface has a single

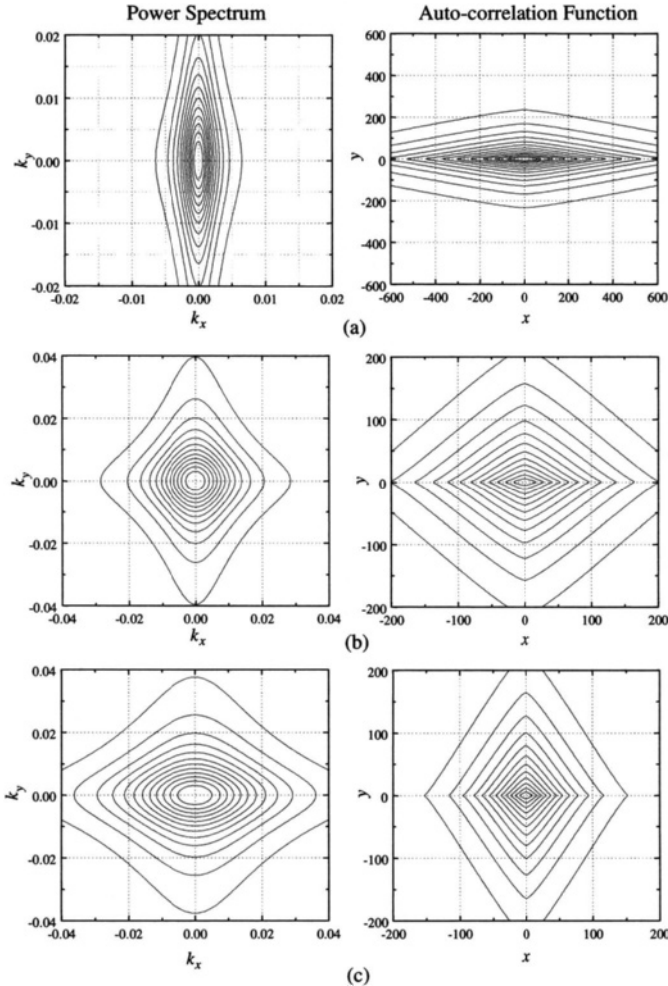


FIG. 3.18 The contour plots of the power spectra and auto-correlation functions for (a)  $\alpha_x = 0.75$ ,  $\alpha_y = 0.4$ ,  $\xi_x = 400$ ,  $\xi_y = 100$ , (b)  $\alpha_x = 0.75$ ,  $\alpha_y = 0.4$ ,  $\xi_x = 90$ ,  $\xi_y = 100$ , and (c)  $\alpha_x = 0.75$ ,  $\alpha_y = 0.4$ ,  $\xi_x = 50$ ,  $\xi_y = 100$  (from Ref. [3.31]).

value and is about 66 Å.

### 3.4 Dynamics of Random Rough Surface Formation

Very often, the phenomenon of growth/etch front roughening occurs far from equilibrium and is a subject of great interest from the fundamental point of view. During the growth/etching, three competing processes may

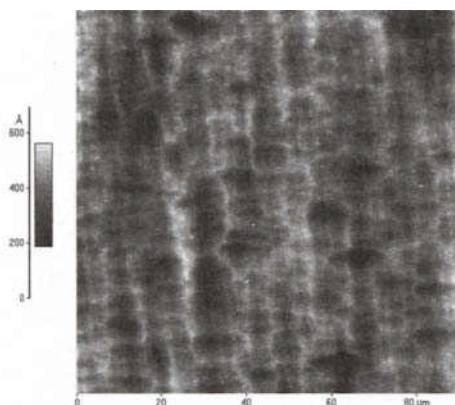


FIG. 3.19 An AFM image of a MCT film grown on a stepped GaAs substrate (from Ref. [3.35]).

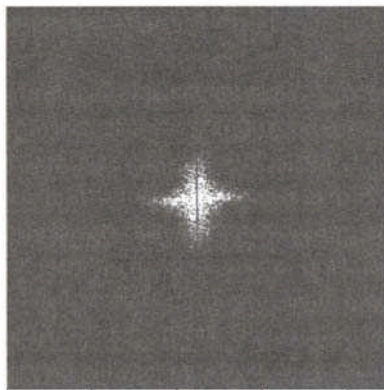


FIG. 3.20 The power spectrum of the image of the MCT film surface from Figure 3.19 (from Ref. [3.35]).

occur: random fluctuations (noises), local smoothening/roughening effects, and non-local smoothening/roughening effects. These play key roles in the evolution of surface morphology. A conventional statistical-mechanical treatment cannot be used to describe these phenomena. Recently, by employing the concept of dynamic scaling combined with analytical treatments, including the use of stochastic differential equations and simulations, considerable progress has been made in the basic understanding of the phenomena [3.1, 3.2, 3.3, 3.4]. Also, it turns out that the same theoretical framework can be used to describe a wide variety of seemingly

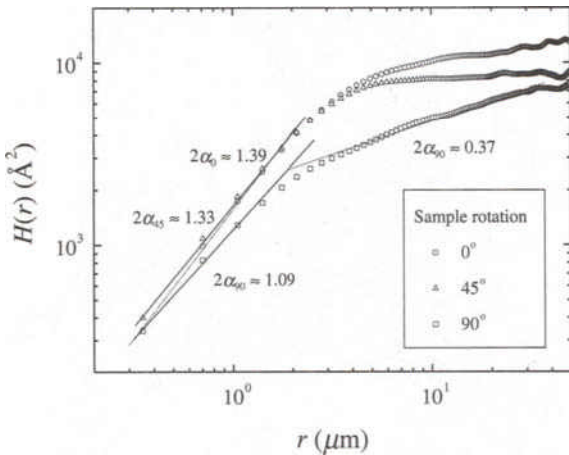


FIG. 3.21 The log-log plots of height-height correlation functions from Figure 3.19 for different sample rotation angles:  $\phi = 0^\circ, 45^\circ$ , and  $90^\circ$  (from Ref. [3.35]).

unrelated phenomena such as flux lines in superconductors [3.36], charge density waves in imperfect materials [3.37], and the gravitational field generated by the Big Bang in cosmology [3.38]. One outstanding outcome of the dynamic scaling hypothesis is the existence of universality in which the essential features of the roughness evolution depend on certain symmetries and the dimensionality of the system, but not on the detailed interactions. The classification of the universality classes of roughness evolution is one of the main focuses of many researchers.

There are two major classes of growth morphologies that are rough [3.39]: (1) Self-affine growth. In this mechanism, the average orientation of the surface is maintained, but it becomes rough; the amount of roughness grows with time, and/or the scale of observation, in a self-similar fashion. (2) Unstable growth. This occurs when the selected orientation of the substrate cannot be maintained. The instability is usually manifested by the formation of mounds or other macroscopic features on the surface. Also the morphology may not be isotropic. In Appendix A, we shall describe the dynamic equations that lead to these morphologies and the predictions of the roughness exponents and growth exponents from these equations.

### 3.5 Generating Rough Surfaces

Sometimes it is useful to generate rough surfaces numerically with different surface properties for numerical testing or model applications. In the

following we shall discuss how to generate random rough surfaces with different surface properties.

### 3.5.1 Convolution method

It is well known that when a signal  $X(t)$  passes through a system, the output signal  $Y(t)$  is the convolution of  $X(t)$  and the system response function  $G(t)$ :

$$Y(t) = \int X(t - \tau)G(\tau)d\tau. \quad (3.32)$$

If  $X(t)$  is a stochastic process, satisfying

$$\begin{cases} < X(t) > = 0, \\ < X(t)X(t') > = \delta(t - t'), \end{cases} \quad (3.33)$$

Equation (3.32) still holds, and

$$< Y(t) > = 0, \quad (3.34)$$

$$< Y(t)Y(t') > = \int G^*(t - t' - \tau)G(\tau)d\tau, \quad (3.35)$$

where  $G^*(t)$  is the complex conjugate of  $G(t)$ . That is, if  $X(t)$  is a white noise, the auto-correlation function of the output signal  $Y(t)$  is totally determined by the system response  $G(t)$ . Therefore, to generate a one-dimensional rough surface with a certain auto-correlation function  $R(t)$ , one can do the following:

- Find the power spectrum  $P(k)$  of auto-correlation function  $R(t)$ , and let the amplitude  $p(k) = \sqrt{P(k)}$ .
- Numerically generate a white noise series  $X_n$ .
- Take a discrete Fourier transform of  $X_n$  to obtain its Fourier transform  $x_n$ .
- Multiply  $x_n$  by  $p(k_n)$  to obtain the Fourier transform of the output  $y_n$ .
- Perform a inverse discrete Fourier transform of  $y_n$  to obtain  $Y_n$ .

Similar methods can also be used to generate a two-dimensional random surface. One needs only to replace all the one-dimensional quantities by the two-dimensional quantities.

### 3.5.2 Langevin equations

As discussed in Appendix A, the evolution of random rough surfaces can be described by Langevin equations. For a linear Langevin equation, one can

solve it analytically, as shown in the appendix. Then, the analytical solution provides a way to generate a random rough surface. In fact, the results are also the convolution of white noises with system responses determined by the Langevin equations as discussed in the above section. However, for the nonlinear Langevin equations, a numerical integration method may be needed.

### 3.5.3 Monte Carlo simulation

Another simple way to generate a random rough surface is to use Monte Carlo simulation following certain rules. For examples, one can look up References [3.1, 3.4] for the applications of Monte Carlo simulation in random rough surfaces. One may refer to Reference [3.40] for a detailed introduction of Monte Carlo simulation methods.

There is another method using the morphological random functions to generate all kinds of random rough surfaces [3.41]. Due to its mathematical complexity, we will not attempt to introduce it here. Interested readers can find it in Reference [3.41].

## 3.6 Summary

In this chapter, we showcased three different kinds of random rough surfaces: self-affine surfaces, mounded surfaces, and anisotropic surfaces. For a self-affine surface, one needs only three roughness parameters to characterize the surface: the interface width  $w$ , the lateral correlation length  $\xi$ , and the roughness exponent  $\alpha$ . For a mounded surface, there are four roughness parameters needed: the interface width  $w$ , the average mound separation  $\lambda$ , the system correlation length  $\zeta$ , and the roughness exponent  $\alpha$ . We considered two kinds of anisotropy: correlation length anisotropy and scaling anisotropy. For a correlation-length anisotropic surface, the scaling properties in different directions are the same, while for a scaling-anisotropic surface, the scaling properties in different directions are different. We summarize the roughness parameters for these three kinds of surfaces in Table 3.1. Finally, we also mentioned three different ways, the convolution method, the Langevin equation, and the Monte Carlo simulation, to generate a random rough surface.

Table 3.1 Summary of roughness parameters for different surfaces.

Self-Affine Surfaces	Mounded Surfaces	Anisotropic Surfaces	
Interface width $w$	Interface width $w$	Interface width $w$	
Roughness exponent $\alpha$	Roughness exponent $\alpha$	Roughness exponent $\alpha$	Direction-dependent roughness exponent $\alpha_\theta$
Lateral correlation length $\xi$	Average mound separation $\lambda$ System correlation length $\zeta$	Direction-dependent lateral correlation length $\xi_\theta$	

## References

- 3.1 *Dynamics of Fractal Surfaces*, Ed. by F. Family and T. Viscek, World Scientific, Singapore (1991).
- 3.2 T. Viscek, *Fractal Growth Phenomena* (World Scientific, Singapore, 1992).
- 3.3 A.-L. Barabási and H. E. Stanley, *Fractal Concepts in Surface Growth* (Cambridge University Press, New York, 1995).
- 3.4 P. Meakin, *Fractals, Scaling, and Growth Far from Equilibrium* (Cambridge University Press, Cambridge, 1998).
- 3.5 H.-N. Yang, G.-C. Wang, and T.-M. Lu, *Diffraction from Rough Surfaces and Dynamic Growth Fronts* (World Scientific, Singapore, 1993).
- 3.6 Y.-P. Zhao, C.-F. Cheng, G.-C. Wang, and T.-M. Lu, "Power law behavior in diffraction from fractal surfaces," *Surf. Sci. Lett.* **409**, L703 (1998).
- 3.7 H.-N. Yang and T.-M. Lu, "Inconsistency between height-height correlation and power-spectrum functions of scale-invariant surfaces for roughness exponents  $\alpha \sim 1$ ," *Phys. Rev. B* **51**, 2479 (1995).
- 3.8 S. K. Sinha, E. B. Sirota, and S. Garoff, "X-ray and neutron scattering from rough surfaces," *Phys. Rev. B* **38**, 2297 (1988).
- 3.9 Y.-P. Zhao, H.-N. Yang, G.-C. Wang, and T.-M. Lu, "Diffraction from diffusion-barrier-induced mound structures in epitaxial growth fronts," *Phys. Rev. B* **57**, 1922 (1998).
- 3.10 G. Palasantzas, "Roughness spectrum and surface width of self-affine fractal surfaces via the K-correlation model," *Phys. Rev. E* **48**, 14472 (1993).
- 3.11 Y.-P. Zhao, Irene Wu, C.-F. Cheng, Ueyn Block, G.-C. Wang, and T.-M. Lu, "Characterization of random rough surfaces by in-plane light scattering," *J. Appl. Phys.* **84**, 2571 (1998).
- 3.12 H.-N. Yang, Y.-P. Zhao, A. Chan, T.-M. Lu, and G.-C. Wang, "Sampling-induced hidden cycles in correlated random rough surfaces," *Phys. Rev. B* **56**, 4224 (1997).
- 3.13 J. Villain, "Continuum models of crystal growth from atomic beams with and without deposition," *J. Phys. I (France)* **1**, 19 (1991).
- 3.14 M. D. Johnson, C. Orme, A. W. Hunt, D. Graff, J. Sudijono, L. M. Sander, and B. G. Orr, "Stable and unstable growth in molecular beam epitaxy," *Phys. Rev. Lett.*

- 72**, 116 (1994).
- 3.15 M. Siegert and M. Plischke, "Slope selection and coarsening in molecular beam epitaxy," *Phys. Rev. Lett.* **73**, 1517 (1994).
- 3.16 P. E. Hegeman, H. J. W. Zandvliet, G. A. M. Kip, and A. van Silfhout, "Kinetic roughening of vicinal Si(001)," *Surf. Sci.* **311**, L655 (1994).
- 3.17 J. A. Stroscio, D. T. Pierce, M. D. Stiles, A. Zangwill, and L. M. Sander, "Coarsening of unstable surface features during Fe(001) homoepitaxy," *Phys. Rev. Lett.* **75**, 4246 (1995).
- 3.18 J. E. Van Nostrand, S. J. Chey, M.-A. Hasan, D. G. Cahill, and J. E. Greene, "Surface morphology during multilayer epitaxial growth of Ge(001)," *Phys. Rev. Lett.* **74**, 1127 (1995).
- 3.19 J.-K. Zuo and J. F. Wendelken, "Evolution of mound morphology in reversible homoepitaxy on Cu(100)," *Phys. Rev. Lett.* **78**, 2791 (1997).
- 3.20 J. Wallschläger, E. Z. Luo, and M. Henzler, "Diffraction characterization of rough films formed under stable and unstable growth conditions," *Phys. Rev. B* **57**, 15541 (1998).
- 3.21 K. Mello, Y.-P. Zhao, T.-M. Lu, and S. K. Murarka, unpublished results.
- 3.22 E. J. Heller and M. G. Lagally, "In situ scanning tunneling microscopy observation of surface morphology of GaAs(001) grown by molecular beam epitaxy," *Appl. Phys. Lett.* **60**, 2675 (1992).
- 3.23 R. Maboudian, V. Bressler-Hill, K. Pond, X.-S. Wang, P. M. Petroff, and W. H. Weinberg, "Effect of growth rate on the surface morphology of MBE-grown GaAs(001)-(2 × 4)," *Surf. Sci.* **302**, L269 (1994).
- 3.24 C. Orme, M. D. Johnson, J. L. Sudijono, K. T. Leung, and B. G. Orr, "Large scale surface structure formed during GaAs (001) homoepitaxy," *Appl. Phys. Lett.* **64**, 860 (1994).
- 3.25 A. J. Pidduck, G. W. Smith, A. M. Keir, and C. R. Whitehouse, "Development of anisotropic GaAs (001) surface morphology during molecular beam epitaxial growth," *Mat. Res. Soc. Symp. Proc.* **317**, 53 (1994).
- 3.26 M. A. Cotta, R. A. Hamm, T. W. Staley, S. N. G. Chu, L. R. Harriott, M. B. Panish, and H. Temkin, "Kinetic surface roughening in molecular beam epitaxy of InP," *Phys. Rev. Lett.* **70**, 4106 (1993).
- 3.27 R. L. Headrick, J.-M. Baribeau, and Y. E. Strausser, "Anisotropic roughness in Ge/Si superlattices," *Appl. Phys. Lett.* **66**, 96 (1995).
- 3.28 M. T. Sinn, J. A. del Alamo, B. R. Bennett, K. Haberman, and F. G. Celii, "Characterization of surface roughness anisotropy on mismatched InAlAs/InP heterostructures," *J. Electronic Mater.* **25**, 313 (1996).
- 3.29 N.-E. Lee, D. G. Cahill, and J. E. Greene, "Surface roughening during low-temperature Si epitaxial growth on singular vs vicinal Si(001) substrates," *Phys. Rev. B* **53**, 7876 (1996).
- 3.30 J. A. Goff and T. H. Jordan, "Stochastic modeling of seafloor morphology: inversion of sea beam data for second-order statistics," *J. Geophys. Res.* **93**, 13589 (1988).
- 3.31 Y.-P. Zhao, G.-C. Wang, and T.-M. Lu, "Diffraction from anisotropic rough surfaces," *Phys. Rev. B* **58**, 7300 (1998).
- 3.32 T. Von Karman, "Progress in the statistical theory of turbulence," *J. Mar. Res.* **7**, 252 (1948).
- 3.33 L. A. Chenov, *Wave Propagation in a Random Medium* (McGraw-Hill, New York, 1960).
- 3.34 P. A. P. Moran, "Necessary conditions for Markovian processes on a lattice," *J. Appl. Probab.* **10**, 54 (1973).
- 3.35 Y.-P. Zhao, I. Bhat, G.-C. Wang, and T.-M. Lu, unpublished results.
- 3.36 D. Ertas and M. Kardar, "Anisotropic scaling in depinning of a flux line," *Phys.*

- Rev. Lett. **73**, 1703 (1994).
- 3.37 O. Narayan and D. S. Fisher, "Dynamics of sliding charge-density waves in 4- epsilon dimensions," Phys. Rev. Lett. **68**, 3615 (1992).
  - 3.38 A. Berea and L.-Z. Fang, "Stochastic fluctuations and structure formation in the universe," Phys. Rev. Lett. **72**, 458 (1994).
  - 3.39 M. Kardar, "Dynamic scaling phenomena in growth processes," Physica B **221**, 60 (1996).
  - 3.40 K. Binder and D. W. Heermann, *Monte Carlo Simulation in Statistical Physics - An Introduction*, 3rd Edition (Springer, Berlin, 1997).
  - 3.41 D. Jeulin and P. Laurenge, "Simulation of rough surfaces by morphological random functions," J. Electronic Imaging **6**, 16 (1997).

This Page Intentionally Left Blank

## 4. REAL-SPACE SURFACE PROFILING TECHNIQUES

In the last chapter we discussed the parameters used to characterize a rough surface. The next question that one might ask is: How do we measure these parameters? In general, there are two major experimental methods used to characterize the properties of rough surfaces quantitatively. The most direct way is to measure the surface morphology using real-space imaging techniques, such as stylus profilometry (SP) and scanning probe microscopy (SPM). These techniques provide direct imaging of a surface. The other kind of technique is scattering such as light scattering, x-ray scattering, electron diffraction, neutron scattering, atom scattering, and so on. The measurement of scattered radiation from a rough surface has the advantage that it is non-destructive and can be used in a hostile environment. However, scattering techniques are indirect and require modeling to extract the roughness parameters. In this chapter and the following chapter, we shall discuss some important real-space imaging techniques, and in Chapters 6-8 we will then discuss the scattering techniques in detail.

### 4.1 Scanning Techniques

One of the most commonly employed analogies for a scanning technique is the operation of a record player, in which a stylus moves up and down with the change of topography in a rotating record to generate a signal. The scanning technique uses a probe to sense the height variations of a surface. When the probe scans across the surface, a surface morphological image is generated through the collection of sequentially measured profiles. The scanning techniques include stylus profilometry (SP), scanning tunneling microscopy (STM), atomic force microscopy (AFM), scanning optical microscopy [including confocal scanning optical microscopy (CSOM) and scanning near-field optical microscopy (SNOM)], etc.

#### 4.1.1 Stylus profilometry

The stylus instrument, through half a century of development, is one of the most widely used techniques for surface morphology measurements [4.1, 4.2]. The stylus profilometer can be used to measure surface morphology with a diamond stylus probe that touches the surface. Height variations are measured as either the stylus or the sample is being moved. The mechanical

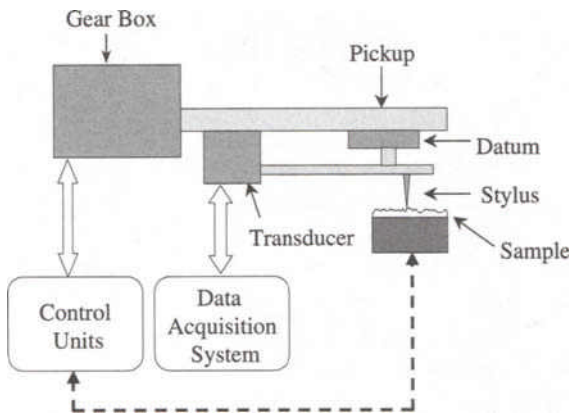


FIG. 4.1 The schematics of a stylus profilometer.

movements of the stylus are converted to electrical signals, which are then amplified to give DC output signals. Most modern stylus systems use digital data recording methods.

All of the stylus profilometry techniques have the following components: a gear box, a pickup, a datum, a stylus, a transducer, a sample holder, a control unit, and a data acquisition system, as shown in Figure 4.1. The pickup comprises the stylus, stylus holder mechanism, transducer, and any signal conditioning associated with the transducer. The pickup is driven by a gear box, which draws the stylus over a surface at a constant speed. As the system is scanned across a sample, the z-axis displacements of the stylus are sensed by the transducer (usually a linear variable differential transformer), which converts linearly the mechanical motion to the electrical signal. The signal, after being magnified by an electronic amplifier, is collected by a data acquisition system to generate the surface profile.

The lateral length of a stylus profilometer is limited by how far the pickup can traverse. Generally this length can be as large as 300 mm. The lateral resolution depends on the shape and size of the stylus tip. It also depends on the load on the stylus. Under an optimum tip and load condition, 0.05 - 0.15  $\mu\text{m}$  lateral resolution can be achieved [4.3]. The vertical range depends on the dynamic range of the transducer and can reach as much as 6 mm. The vertical resolution is limited by the noise in the linear variable differential transformer, the airborne acoustic noise, the mechanical noise, the accuracy of the traversing mechanism, and the thermal drift. For a single-profile stylus, the noise has been measured to be as small as 0.05 nm under certain conditions [4.4].

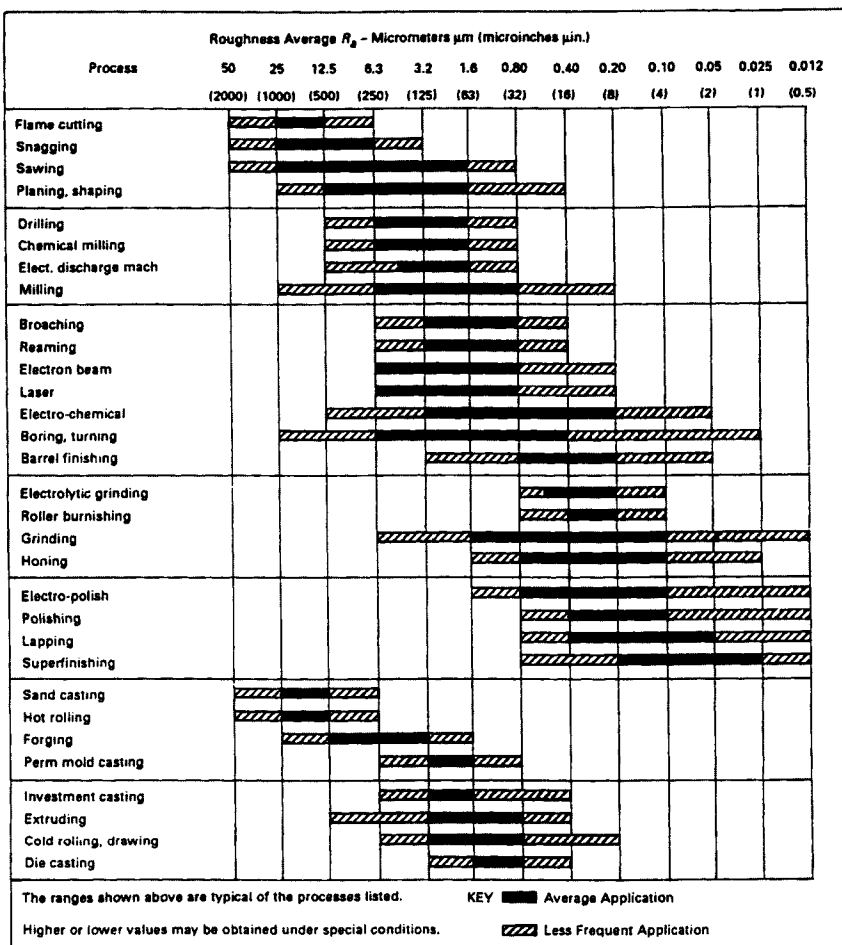


FIG. 4.2 The range of average surface roughness produced by machining (from Ref. [4.4]). Here the roughness average  $R_s$  is the average roughness *wave*.

The accuracy of a stylus profilometer is limited by the accuracies of standards used to calibrate the vertical transfer and the linearity of the transducer used. The latter is typically better than 1%, i.e., the variation in measured step heights is less than 1% over the height range of the transducer.

Stylus profilometry is usually used to characterize engineering surfaces, such as those produced by casting, forging, burnishing, machining, grinding, lapping, and honing. Figure 4.2 shows the range of average surface roughness produced by those methods [4.4].

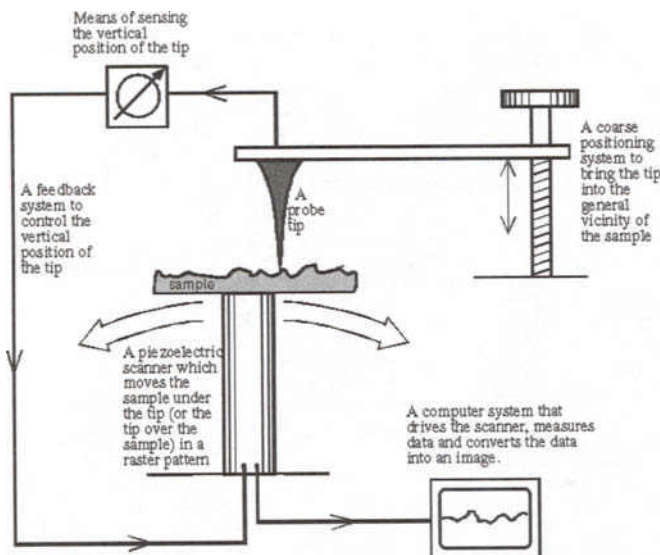


FIG. 4.3 The general principle of scanning probe microscopy (from Ref. [4.5]).

#### 4.1.2 Scanning probe microscopy (SPM)

All scanning probe microscopes contain the following components as illustrated in Figure 4.3 [4.5]: a tip and its mounting system, a tip positioning system, a sample and its holder, a piezoelectric scanner, a feedback system controlling the vertical position of the tip, and a computer system to control each unit and to acquire the data.

##### 4.1.2.1 *Scanning tunneling microscopy*

The basic principle of an STM is: A sharp conducting tip with a bias voltage applied between the tip and the sample is brought very close to the conducting sample surface ( $\sim 10 \text{ \AA}$ ) until electrons can tunnel through the vacuum barrier (Figure 4.4). The resulting tunneling current varies with the tip-to-sample spacing, and therefore is used to create an STM image. The fundamental physics of STM can be understood by studying the tunneling through a one-dimensional rectangular barrier potential in quantum mechanics.

The width of the barrier corresponds to the tip-to-sample spacing  $d$ , while the height of the barrier corresponds to the vacuum energy level  $U_0$  as shown in Figure 4.5 [4.6]. We start with the Schrödinger equation for an

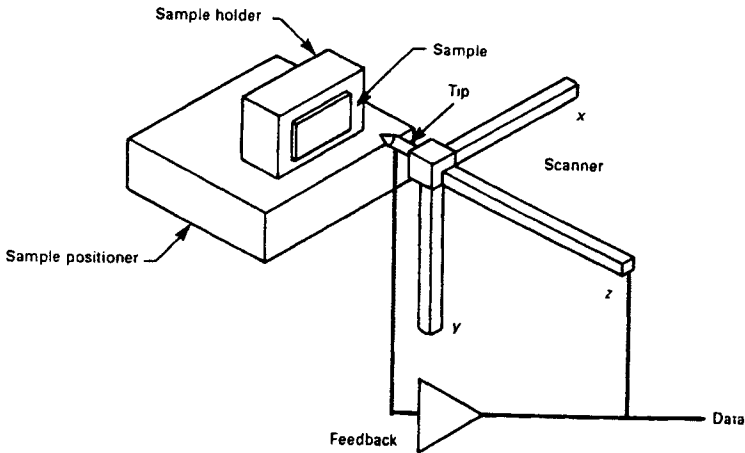


FIG. 4.4 The basic components of a scanning tunneling microscope (from Ref. [4.4]).

electron in a potential  $U(z)$  with mass  $m$ , energy  $E$ , and wave function  $\psi$ :

$$-\frac{\hbar^2}{2m} \frac{d^2}{dz^2} \psi(z) + U(z)\psi(z) = E\psi(z), \quad (4.1)$$

where  $\hbar$  is Planck's constant divided by  $2\pi$ . The potential has the height  $U_0$  in the barrier region ( $z_0 - \frac{d}{2} \leq z \leq z_0 + \frac{d}{2}$ ) with  $U_0 > E$ , and is zero everywhere else ( $z < z_0 - \frac{d}{2}$  and  $z > z_0 + \frac{d}{2}$ ). The width of the potential is  $d$ . In the classically-allowed region where  $U(z) = 0$ , Equation (4.1) has the solutions

$$\psi(z) = \psi(0) \exp(\pm ikz), \quad (4.2)$$

where  $k = \frac{\sqrt{2mE}}{\hbar}$ . In the classically-forbidden region  $U(z) = U_0$ , the solution for an electron travelling in the  $+z$  direction is

$$\psi(z) = \psi(0) \exp(-\kappa z), \quad (4.3)$$

where  $\kappa = \frac{\sqrt{2m(U_0-E)}}{\hbar}$ . Therefore, the tunneling current  $I$  across the barrier decays exponentially with the barrier width  $d$ :

$$I = |\psi(z)|^2 \propto \exp(-2\kappa d). \quad (4.4)$$

Using this simple model, we can interpret the STM signal after making the following assumptions:

- 1) For simplicity, both the tip and the sample are assumed to be an identical free-electron metal with Fermi energy level  $E_F$ .

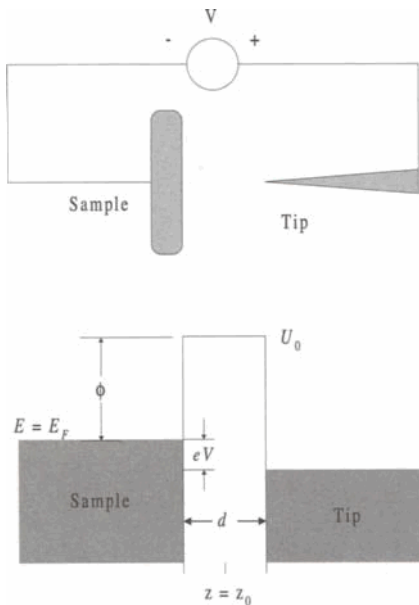


FIG. 4.5 Schematics of a one-dimensional barrier model for STM (from Ref. [4.6]).

- (2) The work function of the metal, defined as the minimum energy needed to remove an electron from the metal to the vacuum, is  $\phi = U_0 - E_F$ . For metals and semiconductors, the work function is typically 4 - 5 eV.
- (3) Since an electron can tunnel in both directions, there is no net tunneling current unless a bias voltage  $V$  is applied between the sample and the tip. If  $V$  is small such that  $eV \ll \phi$ , then the above treatment is still valid.

The value of  $\kappa$  gives an estimate of the sensitivity of an STM in the  $z$  direction. Using  $\phi = 4.8$  eV (work function for Si), we have  $\kappa = \frac{\sqrt{2m\phi}}{\hbar} \approx 1.1$  Å<sup>-1</sup>. Thus the tunneling current decays about one order of magnitude per Å. This result implies that

- (1) A sub-angstrom change in the tip-to-sample spacing can be easily detected through the measurement of the change in the tunneling current. This results in a high vertical resolution.
- (2) Small tip-to-sample spacings on the order of 1 Å are needed to detect the tunneling current.
- (3) The separation between the tip and the sample must be maintained to better than 0.1 Å in order to keep the tunneling current stable.

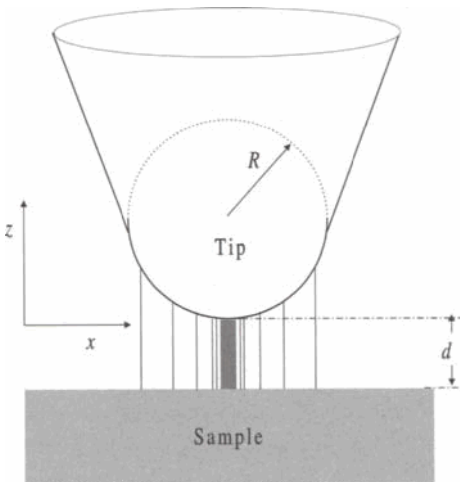


FIG. 4.6 A model used to estimate the lateral resolution of STM (from Ref. [4.6]).

- 4) The lateral resolution of an STM becomes much smaller than the tip radius due to the exponential dependence of the tunneling current on tip-to-sample separation. Quantitatively, this can be understood from the following estimation: For a spherical tip with a radius  $R$ , the height  $z$  of the tip at a lateral position  $x$  relative to the tip center (see Figure 4.6) is given by

$$z = d + \frac{x^2}{2R}. \quad (4.5)$$

Applying the one-dimensional tunneling model, the lateral current distribution is

$$I(x) = I_0 \exp\left(-2\kappa \frac{x^2}{2R}\right), \quad (4.6)$$

where  $I_0$  is the current density at the tip center ( $x = 0$ ). Therefore, the lateral current density has a Gaussian distribution with a FWHM of  $1.665\sqrt{R/\kappa}$ . For a tip radius  $R = 100 \text{ \AA}$ , the lateral resolution is  $8.3 \text{ \AA}$ .

However, the simple one-dimensional model is not really adequate for a full description of the STM measurements. The electronic structures of the tip and the surface are involved in a more complex fashion, requiring a full three-dimensional treatment. Tersoff and Hamann extended Bardeen's formalism for tunneling and gave a general expression for the tunneling

current at room temperature and small bias voltage [4.7]:

$$I = \frac{2\pi e^2 V}{\hbar} \sum_{\mu, \nu} |M_{\mu\nu}|^2 \delta(E_\nu - E_F) \delta(E_\mu - E_F), \quad (4.7)$$

where  $V$  is the applied voltage,  $M_{\mu\nu}$  is the tunneling matrix element between states  $\psi_\mu$  of the tip and  $\psi_\nu$  of the surface, and  $E_\mu$  is the energy of state  $\psi_\mu$  in the absence of tunneling. Assuming that the tip is spherical as shown in Figure 4.6, the tunneling current would have the following form:

$$I = \frac{32\pi^3}{\hbar} eV\phi^2 D_t(E_F) R^2 \kappa^{-4} e^{2\kappa R} \sum_\nu |\psi_\nu(\mathbf{r}_0)|^2 \delta(E_\nu - E_F), \quad (4.8)$$

where  $D_t$  is the density of states per unit volume of the probe tip. Thus the tunneling current is proportional to the local density of states at the Fermi energy level at the center of the tip. This means that STM can provide a direct image of electron states at the surface. In addition, since  $|\psi_\nu(\mathbf{r}_0)|^2 \propto e^{-2\kappa(R+d)}$ , the tunneling current still depends exponentially on the tip-sample separation  $d$ , which is consistent with the simple one-dimensional model.

In general there are two operational modes for an STM: constant-height mode or constant-current mode, as shown in Figure 4.7. In the constant-height mode, the tip travels in a horizontal plane above a sample and the tunneling current varies depending on the topography and the local electronic properties of the sample surface. The tunneling current measured at each location on the sample surface constitutes the data set, the topographic image.

In the constant-current mode, the STM uses a feedback loop to keep the tunneling current constant by adjusting the height of the scanner at each point of the measurement. Therefore, the motion of a scanner constitutes the data set. If the system keeps the tunneling current constant to within a few percent, then the tip-to-sample distance would be constant to within a few hundredths of an angstrom. Both modes have advantages and disadvantages. The constant-height mode is faster because the system does not need to move the tip/scanner up and down, but it provides useful information only for relatively smooth surfaces. The constant-current mode can measure irregular surfaces with high precision, but the measurement takes a longer time. For most surface morphology measurements using STM, the constant-current mode is used.

The maximum lateral length that STM can measure is determined by the actual travel length of the scanning system. Sometimes the range can be as large as 500  $\mu\text{m}$ . Atomic resolution ( $\leq 0.2 \text{ nm}$ ) is typically achievable.

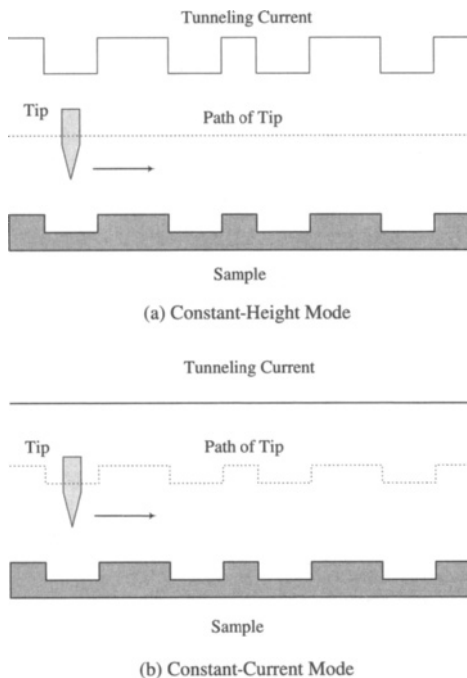


FIG. 4.7 The constant-height (a) and constant-current (b) modes for STM (from Ref. [4.5]).

The height range is limited by the travel length of the  $z$  axis of the PZT and has typical values in the order of  $2 \mu\text{m}$ . The vertical resolution is typically about  $0.1 \text{ nm}$  or less.

Since an STM measures the current between the tip and the sample, it can only measure the surfaces of metals or semiconductors.

#### 4.1.2.2 *Atomic force microscopy*

Atomic force microscopy (AFM) is one type of scanning force microscopy (SFM), which uses different kinds of intermolecular forces as the detection signal to achieve the measurement of different physical properties of a surface in nanometer scale. An AFM basically uses the van der Waals force between the tip and the sample surface. The basic measurement principle is shown in Figure 4.8. An AFM tip is mounted at the end of a cantilever. When the tip approaches a sample surface, the interaction forces between the tip and the sample cause the cantilever to deflect according to Hooke's

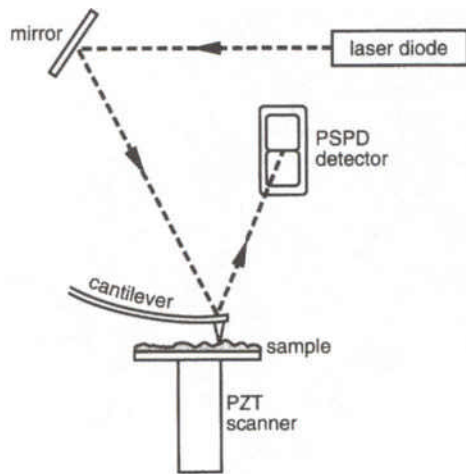


FIG. 4.8 The principle of measurement in an atomic force microscope (from Ref. [4.5]).

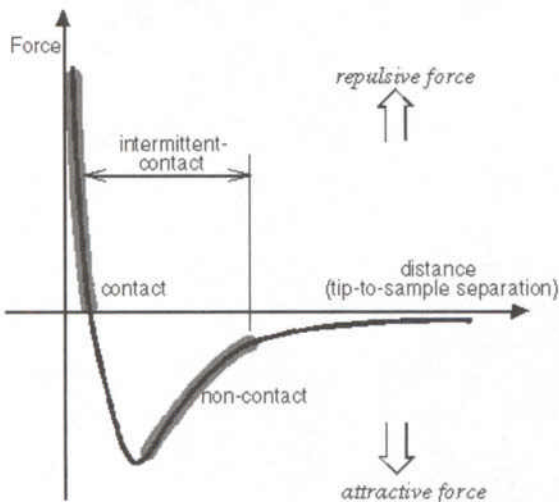


FIG. 4.9 The van der Waals force versus tip-to-sample distance (from Ref. [4.5]).

law. This deflection of a cantilever can be sensed by a position sensitive detector.

A thorough understanding of van der Waals force needs detailed quantum-mechanical treatment. Some excellent reviews on intermolecular forces can be found in References [4.8] and [4.9]. As a simple model one can use

the Lennard-Jones molecular interaction potential for the van der Waals interaction:

$$W(z) = 4\epsilon \left( \frac{\sigma^{12}}{z^{12}} - \frac{\sigma^6}{z^6} \right), \quad (4.9)$$

where  $\epsilon$  is related to the energy and  $\sigma$  is related to the distance. The force is

$$F(z) = -\frac{\partial W}{\partial z} = 24\epsilon \left( \frac{2\sigma^{12}}{z^{13}} - \frac{\sigma^6}{z^7} \right). \quad (4.10)$$

However, both Equations (4.9) and (4.10) describe the interaction between two nonpolar molecules or atoms. In a real AFM measurement, the interaction is between the tip and the sample, whereas the total force comes from the interactions between all the atoms on the tip and those on the surface. Also the shapes of the tip and the sample will affect these interactions [4.8, 4.9]. According to Sarid, the force between a spherical tip and a plane sample is [4.9]

$$F(z) = \frac{2}{3}\pi^2\epsilon n_1 n_2 R \left( \frac{1}{30} \frac{\sigma^{12}}{z^8} - \frac{\sigma^6}{z^2} \right), \quad (4.11)$$

where  $n_1$  and  $n_2$  are the atomic number densities of the tip and the sample, respectively. The radius of the tip is  $R$ . Figure 4.9 shows the van der Waals force versus tip-to-sample distance. Based on different tip-to-sample distances as shown in Figure 4.9, the AFM has three different working modes: the contact mode, the non-contact mode, and the intermittent-contact (or tapping) mode.

In the contact mode, the cantilever with a low spring constant  $k$  is held less than a few angstroms from the sample surface, and the interatomic force between the tip and the sample is repulsive. By equating the force exerted by the cantilever to the van der Waals force, we obtain

$$k(z - u) = \frac{2}{3}\pi^2\epsilon n_1 n_2 R \left( \frac{\sigma^6}{z^2} - \frac{1}{30} \frac{\sigma^{12}}{z^8} \right). \quad (4.12)$$

Therefore, by detecting the bending of the cantilever, one can measure the van der Waals force between the tip and the sample.

In contact mode, either the constant-height or constant-force detections can be used similar to those of an STM (see Figure 4.7). In the constant-height detection, the spatial variation of the cantilever deflection can be used directly to generate the topography of a surface. In the constant-force detection, a feedback is used to move the scanner up and down in order to maintain a constant force between the tip and the sample. Thus the surface morphology is generated by the scanner's trajectory.

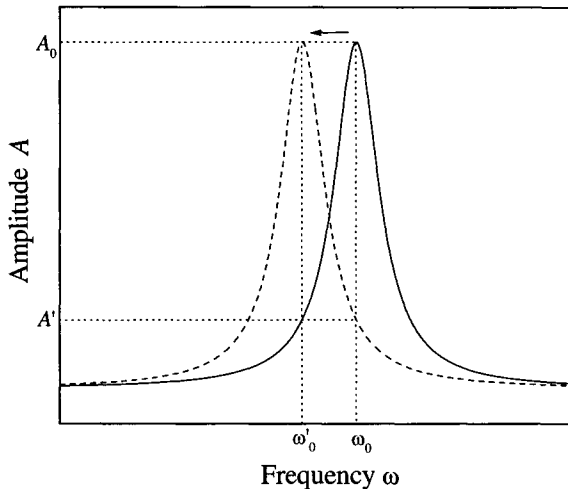


FIG. 4.10 The shift of the tip resonant frequency due to the tip-sample interaction.

In the non-contact mode, the cantilever is held in the range of tens to hundreds of angstroms from a sample surface, and the interatomic force between the tip and the sample is attractive. In this case a vibrating stiff cantilever is used for measuring the sample topography with little or no contact between the tip and the sample. At a large distance  $z$ , where the interaction between the tip and the sample can be neglected, the cantilever vibration amplitude  $A$  as a function of the frequency  $\omega$  has a Loretzian shape [4.10]:

$$A = \frac{A_0(\omega_0/\omega)}{\sqrt{1 + Q^2(\omega/\omega_0 - \omega_0/\omega)^2}}, \quad (4.13)$$

where  $\omega_0 = c\sqrt{k}$  is the resonant frequency,  $c$  is a function of the cantilever mass,  $A_0$  is the amplitude at the resonance, and  $Q$  is the quality factor ( $\gg 1$ ). As the tip approaches to the sample, the van der Waals force between the tip and the sample has to be taken into account. For a small vibrational amplitude, it causes an additional spring-type force  $f$ . Its derivative  $f'$  along the sample surface normal reduces the spring constant  $k$  and shifts the resonant frequency  $\omega_0$  to  $\omega'_0$ , given by  $\omega'_0 = c\sqrt{k - f'}$  (see Figure 4.10). If we drive the cantilever at  $\omega_0$ , we can measure the amplitude  $A'$  due to the interaction and use Equation (4.13) to calculate the new resonant frequency

$\omega_0'$ . Thus we have

$$f' = k \frac{1 - 2a^2 + \sqrt{4Q^2(a^2 - 1) + 1}}{2(Q^2 - a^2)}, \quad (4.14)$$

where  $a = A_0/A'$ . In order to derive Equation (4.14), two assumptions need to be made. First, we assume that the tip-sample interaction induces the frequency shift of the resonance, but does not induce an energy transfer that would reduce the vibrational amplitude. Second, we assume that  $f'$  does not significantly affect the vibrational mode of the lever, so that the equation  $\omega_0 = c\sqrt{k - f'}$  is valid.

Therefore, in non-contact mode, the AFM system monitors the resonant frequency or the vibrational amplitude of a cantilever and keeps it constant with the aid of a feedback system that moves the scanner up and down. By keeping the resonant frequency or the amplitude constant, the system also keeps the average tip-to-sample distance constant. Therefore, the motion of the scanner gives the topography of the surface.

For an AFM, the vertical and lateral ranges of the system are limited by the PZT transducer, which is similar to that of an STM. The height resolution is determined by the degree to which the tip-to-sample distance can be maintained constant during the scan, as well as the vibration isolation. Usually a vertical resolution  $\leq 0.1$  nm can be achieved. The lateral resolution of contact AFM is determined by the size of the tip-sample contact area. Usually lateral resolution on the order of 5 nm can be achieved.

Since AFM uses surface forces to detect the morphology, it can be applied to the surfaces of metals, semiconductors, and insulators.

#### 4.1.3 Scanning optical microscopy

The basic principle of scanning optical microscopy (SOM) is similar to that of STM and AFM. Instead of using a tunneling current or a surface force as the sensing signal, SOM uses the optical signal as a feedback to measure the surface morphology. Two most well-known SOM techniques are confocal scanning optical microscopy (CSOM) and scanning near-field optical microscopy (SNOM). In the following, we briefly discuss the principle of the CSOM technique.

##### 4.1.3.1 Confocal scanning optical microscopy

The principle of CSOM is shown in Figure 4.11 [4.11]. The illumination light, after passing through a pinhole, is focused by an objective. If the sample surface is placed exactly at the focal plane, then the light reflected

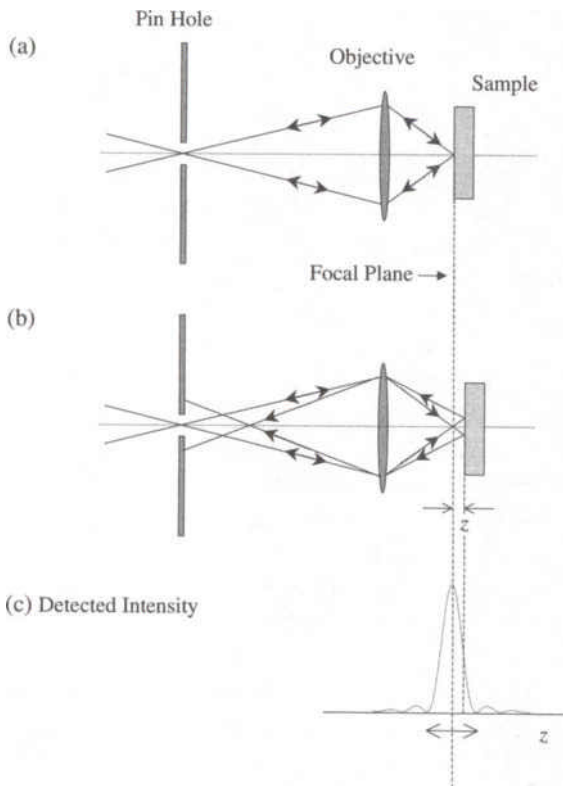


FIG. 4.11 The principle of a confocal scanning optical microscope (from Ref. [4.11]).

back from the sample surface is imaged by the objective on the pinhole as shown in Figure 4.11(a). The reflected light intensity is collected by a detector in front of the pinhole (not illustrated in Figure 4.11). If the sample moves away from the focal plane as shown in Figure 4.11(b), then the reflected light is defocused at the pinhole, and the intensity received by the detector drops dramatically. Figure 4.11(c) shows this intensity as a function of the defocusing distance  $z$ . Therefore, by using the detected intensity as a feedback signal, one can adjust the position of the PZT that holds the sample, so that the sample surface remains on the focal plane. The position variation of the PZT gives the topography of the sample surface.

The lateral resolution of the CSOM is limited by the size of the pinhole and half the optical wavelength ( $\lambda/2$ ). It can reach  $0.25 \mu\text{m}$ . The lateral scan range is limited by the translational range of the PZT and can be as large as  $0.4 \text{ mm}$ . The vertical resolution and scan range can achieve  $10 \text{ nm}$

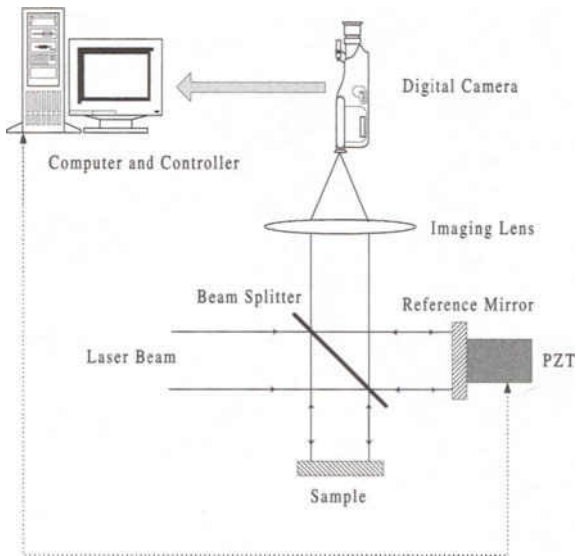


FIG. 4.12 The principle of homodyne detection for a phase-measurement technique.

and  $600 \mu\text{m}$ , respectively.

## 4.2 Imaging Techniques

In an imaging method, the radiation emitted or reflected from all points on the illuminated surface is simultaneously imaged on a video camera or an optical detector array. Therefore the topographical data from all points on the surface are accumulated nearly simultaneously.

### 4.2.1 Interferometric microscope

#### 4.2.1.1 Homodyne detection

The principle of homodyne detection for a phase-measurement technique is shown in Figure 4.12. The reflected electric field from a reference mirror can be written as

$$E_r = A_r e^{i(\omega t + \phi)}, \quad (4.15)$$

where  $A_r$  is the amplitude,  $\omega$  is the optical frequency, and  $\phi$  is the phase at the reference mirror, which can be changed by moving the PZT. The

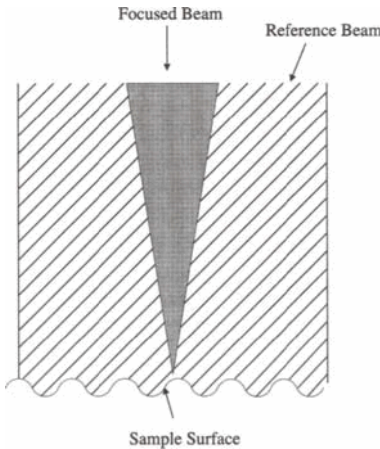


FIG. 4.13 The principle of heterodyne detection for a phase measurement technique.

electric field reflected from the sample can be expressed as

$$E_s = A_s e^{i(\omega t + \varphi)}, \quad (4.16)$$

where  $A_s$  is the amplitude,  $\varphi = \varphi_0 + kh$ ,  $\varphi_0$  is the absolute phase difference between the reference mirror and the sample,  $k = 2\pi/\lambda$  is the magnitude of the wave vector, and  $h$  is the surface height fluctuation. After the interference on a digital camera, the intensity becomes

$$I = |E_r + E_s|^2 = I_0[1 + \gamma \cos(\varphi + \phi)], \quad (4.17)$$

where  $I_0 = A_r^2 + A_s^2$  and  $\gamma = 2A_r A_s / I_0$ . Obviously there are three unknown parameters:  $I_0$ ,  $\gamma$ , and  $\varphi$ , in which  $\varphi$  contains the direct surface height information. If one changes the positions of reference mirror to three different values such as 0,  $\lambda/8$ , and  $\lambda/4$ , which correspond to  $\phi = 0$ ,  $\pi/2$ , and  $\pi$ , respectively, then one can obtain these three parameters from three equations, and therefore the surface morphology.

#### 4.2.1.2 Heterodyne detection

Another common method used in the phase detection is to introduce another laser beam with a slightly different frequency, as shown in Figure 4.13. The small, focused laser spot ( $\sim 2 \mu\text{m}$  in diameter) from a single-frequency laser with an angular frequency  $\omega_0$  is overlapped with a large, focused laser spot ( $\sim 50 \mu\text{m}$  in diameter) from the same laser but with an angular frequency offset  $\Delta\omega$  achieved by Bragg cells (or other methods

such as Zeeman splitting, etc) on the sample surface. The offset is about 1-100 MHz. The reflected laser beams from the small and the large focused spots have electric fields

$$E_{small} = A_{small} \cos[\omega_0 t + \phi_0(t) + \phi_s(t)] \quad (4.18)$$

and

$$E_{large} = A_{large} \sin[\omega_0 t + \Delta\omega t + \phi_0(t) + \overline{\phi_s(t)} + \phi_a], \quad (4.19)$$

respectively. Here  $E_{small}$  and  $E_{large}$  are the amplitudes,  $\phi_0(t)$  is the common optical phase due to the sample vibration,  $\phi_s(t)$  is the optical phase due to surface roughness,  $\overline{\phi_s(t)}$  is the averaged optical phase over the large focused spot, and  $\phi_a$  is the electronic phase associated with  $\Delta\omega$ . In the heterodyne detection, the detector output is proportional to the product of Equations (4.18) and (4.19), thus the signal received by the detector becomes

$$I = E_{small} \times E_{large} = I_{AC} + I_{DC}. \quad (4.20)$$

Here  $I_{AC}$  is the AC part of the signal,

$$I_{AC} = \frac{1}{2} A_{small} A_{large} \sin[\Delta\omega t + \overline{\phi_s(t)} - \phi_s(t) + \phi_a], \quad (4.21)$$

and  $I_{DC}$  is the DC part of the detected signal,

$$I_{DC} = \frac{1}{2} A_{small} A_{large}. \quad (4.22)$$

The ratio of the AC signal and the DC signal is

$$\frac{I_{AC}}{I_{DC}} = \sin[\Delta\omega t + \overline{\phi_s(t)} - \phi_s(t) + \phi_a]. \quad (4.23)$$

Therefore, the phase  $\phi_0(t)$  due to the sample vibration is eliminated, and the phase  $\overline{\phi_s(t)} - \phi_s(t)$  in Equation (4.23) represents the surface morphology.

The lateral scan range and resolution of phase detection techniques can be 0.2 mm and 0.4  $\mu\text{m}$ , respectively. The vertical scan range and resolution can be 150  $\mu\text{m}$  and < 1 nm, respectively.

#### 4.2.2 Nomarski differential profiling

The Nomarski differential profiler is based on the principle of Nomarski difference contrast microscopy. The basic setup is shown in Figure 4.14. The incident beam passes through a modified Wollaston prism, splitting into two closely-spaced orthogonally polarized spots. These two spots are focused onto the sample surface by an objective lens. These two beams

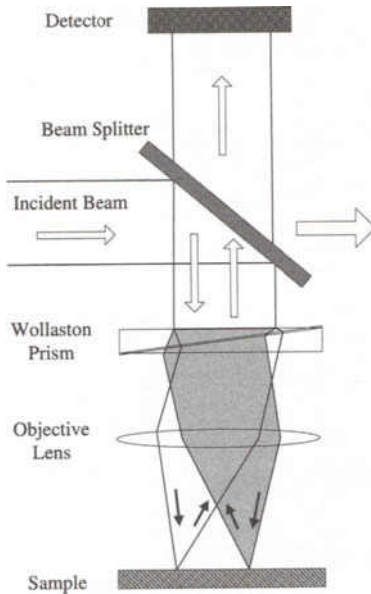


FIG. 4.14 A Nomarski differential profiler (from Ref. [4.11]).

reflecting back from the surface pass through the objective lens and the Wollaston prism, recombine, and interfere at the detector. If the two beams reflect from the flat region of a surface, then they both have the same optical path length, and there is no interference. However, if the two beams reflect from the top and the bottom surfaces of a step, then the phase difference caused by the step leads to a detected intensity either brighter or darker than the surrounding background. This is similar to the homodyne phase detection: the electric fields of these two spots reflected from the surface can be expressed as

$$E_1 = A_1 e^{i(\omega t + \phi_1)} \quad (4.24)$$

and

$$E_2 = A_2 e^{i(\omega t + \phi_{wp} + \phi_2)}, \quad (4.25)$$

where  $\phi_1$  and  $\phi_2$  are the phases of the two beams generated from the corresponding optical path lengths and  $\phi_{wp}$  is a constant phase delay that may be added to one of the polarized beams by the Wollaston prism. Typically the incident laser beam is polarized at  $45^\circ$  with respect to the optical axis of the prism, and the analyzer is oriented perpendicular to the polarization direction of the incident beam. Therefore, the intensity that the detector

receives is

$$I_{\text{det}} = \frac{1}{2}(A_1^2 + A_2^2) - A_1 A_2 \cos(\phi_{wp} + \Delta\phi), \quad (4.26)$$

where  $\Delta\phi = \phi_2 - \phi_1$ . By choosing different  $\phi_{wp}$ , one can have different imaging modes [4.11]. If  $\phi_{wp} = 0$ , one has the square-law imaging mode:

$$I_{\text{det}} = \frac{1}{2}(A_1^2 + A_2^2) - A_1 A_2 \cos(\Delta\phi). \quad (4.27)$$

This mode is used to detect large optical path length differences on a sample. If  $\phi_{wp} = \frac{\pi}{2}$ , one has the linear imaging mode:

$$I_{\text{det}} = \frac{1}{2}(A_1^2 + A_2^2) - A_1 A_2 \sin(\Delta\phi), \quad (4.28)$$

which is very sensitive to any small change in the optical path length.

In fact, the Nomarski differential profiler measures the phase shift arising from the difference in the vertical heights of two adjacent areas. Therefore, the phase shift is directly proportional to the local surface slope. By integration of the phase shift, one can obtain the surface morphology of the sample.

Typically, the lateral detection range and resolution are 100 - 200 mm and 0.8  $\mu\text{m}$ , respectively. The vertical detection range and resolution are 2  $\mu\text{m}$  and < 0.1 nm, respectively.

### 4.3 Summary

In this chapter, we briefly discussed the basic principles, the resolutions, and the measurement ranges of some popular real-space profiling techniques for rough surface characterization.

### References

- 4.1 R. E. Reason, "Progress in the appraisal of surface topography during the first half-century of instrument development," *Wear* **57**, 1 (1979).
- 4.2 T. R. Thomas, *Rough Surfaces*, 2nd Edition (Imperial College Press, London, 1999).
- 4.3 J. F. Song and T. V. Vorburger, "Stylus profiling at high resolution and low force," *Appl. Opt.* **30**, 42 (1991).
- 4.4 ASME Standards B 46.1, Surface Texture (Surface roughness, Waviness, and Lay), 1995.
- 4.5 R. Howland and L. Benatar, *A Practical Guide to Scanning Probe Microscopy* (ThermalMicroscopes, Sunnyvale, CA, 1996).

- 4.6 Anthony C.-T. Chan, "Scanning tunneling microscopy: construction and its application to study of rough surfaces," Ph.D. Thesis, Rensselaer Polytechnic Institute, 1996.
- 4.7 J. Tersoff and D. R. Hamann, "Theory of the scanning tunneling microscope," Phys. Rev. B **31**, 805 (1985).
- 4.8 J. Israelachvili, *Intermolecular and Surface Forces*, 2nd Edition (Academic Press, San Diego, 1995).
- 4.9 D. Sarid, *Scanning Force Microscopy with Applications to Electric, Magnetic and Atomic Forces*, Revised Edition (Oxford University Press, New York, 1994).
- 4.10 Y. Martin, C. C. Williams, and H. K. Wickramasinghe, "Atomic force microscope - force mapping and profiling on a sub 100-Å scale," J. Appl. Phys. **61**, 4723 (1987).
- 4.11 T. R. Corle and G. S. Kino, *Confocal Scanning Optical Microscopy and Related Imaging System* (Academic Press, San Diego, 1996).

## 5. EFFECTS OF FINITE TIP AND SAMPLE SIZES

All of the techniques discussed in the last chapter can provide information on the surface morphology. In order to obtain quantitative information, image analysis is a key step. However, before performing the image analysis, one has to make sure the image obtained is free of distortion. For example, for SPM the distortion may come from the nonlinearities of the scanner, such as intrinsic nonlinearity, hysteresis, creep, aging effect, and cross coupling. These effects can be eliminated by carefully designing the instruments, or by using software to make appropriate corrections [5.1]. Therefore a pre-analysis such as a tilt correction and a tip deconvolution is needed before further image analysis. Since SPM techniques have numerous applications in studies of microstructures and surface morphologies, it is a big concern whether or not the measured SPM image actually reflects the true surface topography. In addition, finite sample size is also a concern for reflecting the real statistics of the images. In this chapter, we shall address these two issues.

### 5.1 Finite Tip Size Effects in SPM Measurements

Sometimes the tip-sample interaction of SPM may lead to a deterioration of the sharpness of the tip by either wearing or picking up material from the sample. For example, Figure 5.1 shows four STM images of the same surface of a Si thin film epitaxially grown on Si(111) after repeated scans. The images are the 1st, 5th, 8th, and 10th scans from the top to the bottom [5.2]. During the scanning process, the STM tip becomes blunt, and the image feature size becomes bigger. The corresponding interface width, as shown in the right column in Figure 5.1, becomes smaller. In fact, the finite tip size usually causes distortions during the measurement. Figure 5.2 shows three typical ways by which the SPM tip can alter the measurement of the surface morphology [5.3]. As shown in Figure 5.2(a), if the bump at the surface of the sample is very high and sharp compared to the tip, the SPM image is an image of the tip rather than of the surface feature. If the surface feature is steep, but the aspect ratio of the tip is small, there will be some areas that the tip cannot reach as shown in Figure 5.2(b). In addition, if the surface has overhangs, the areas near the overhang cannot be measured by the tip, as shown in Figure 5.2(c). Usually one calls the distortion caused by the finite tip the tip convolution.

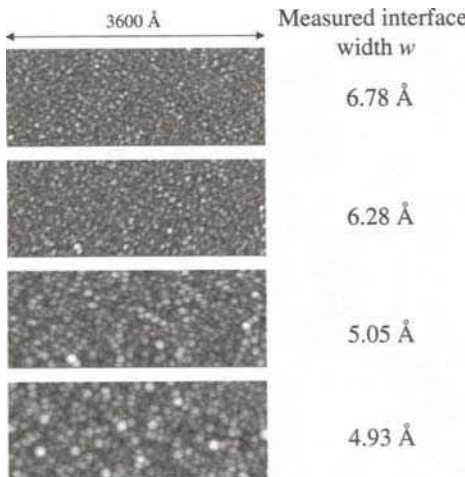


FIG. 5.1 Four STM images of the same surface area of a Si thin film epitaxially grown on Si(111) after repeated scans. The images are the 1st, 5th, 8th, and 10th scans from the top to the bottom. During the scanning process, the STM tip becomes blunt. As a result, the image feature size becomes bigger, and the corresponding interface width becomes smaller (from Ref. [5.2]).

As pointed out by Aué and De Hosson [5.3], this tip convolution is not strictly a mathematical definition. Convolution in the mathematical sense is a reversible linear process. However, as seen from Figure 5.2(b) and (c), the tip-induced distortion is usually an irreversible process, and some information about surface features may be lost due to areas unreachable by the tip. Thus, if one knows the scanned image and the exact shape of the tip, one may still not be able to reconstruct the real surface features. In order to differentiate this from convolution, Aué and De Hosson call this tip-induced distortion dilation [5.3].

In order to see how the finite tip size affects the SPM image, let us follow the discussion of Keller [5.4]. Figure 5.3 shows the detailed distortion process during a tip climbing a hill on the surface [5.4]. Here  $s(x)$  and  $i(x')$  are the true surface profile and scanned surface profile, respectively. The position of the apex of the tip is at  $x'$ , while the real contact position between the tip and the surface is at  $x$ . The tip shape  $t(\Delta x)$  is a function only of the relative position  $\Delta x = x - x'$ . At the contact point, the slope of the tip and the slope of the surface should be equal as shown in Figure 5.3, thus

$$\frac{dt(\Delta x)}{dx} = \frac{ds(x)}{dx}. \quad (5.1)$$

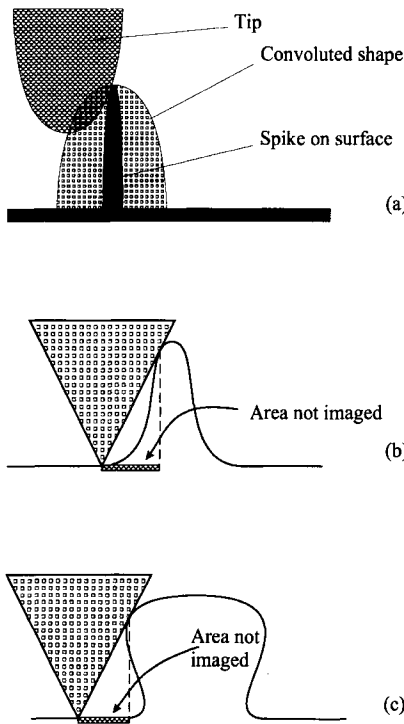


FIG. 5.2 Dilation of tip and surface (a), resulting in loss of information on single- (b) and non-single- (c) valued (overhang) surfaces (from Ref. [5.3]).

It can also be shown that the slope of the scanned surface at  $x'$  is equal to the slope of the true surface at  $x$ :

$$\frac{di(x')}{dx'} = \frac{ds(x)}{dx}. \quad (5.2)$$

In order to reconstruct the real surface, a Legendre transform can be used:

$$L[f(x)] = b(m) = f[x(m)] - mx(m), \quad (5.3)$$

where  $m = df(x)/dx$  is the slope of the function  $f(x)$ . Since the slopes of  $s(x)$  at  $x$ ,  $i(x')$  at  $x'$ , and  $t(\Delta x)$  at  $\Delta x$  are the same, then

$$L[s(x)] = L[i(x')] + L[t(\Delta x)], \quad (5.4)$$

i.e., the Legendre transform of the true surface is the sum of the Legendre transforms of the scanned surface and the tip surface. This relation is shown in Figure 5.4. Since the Legendre transform is a local nonlinear transform,

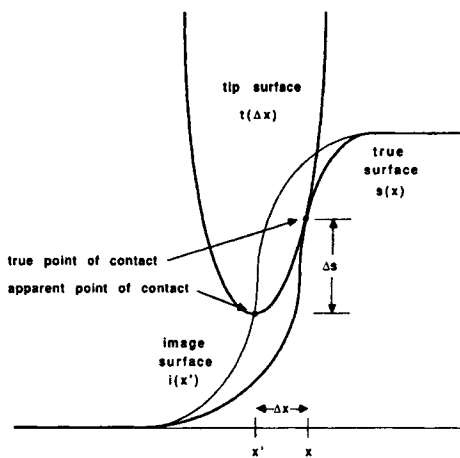


FIG. 5.3 A finite-size SPM tip in contact with a steep, high surface. The true, undisorted surface can be found if the quantities  $\Delta x$  and  $\Delta s$  can be calculated from the tip and the image surface (from Ref. [5.4]).

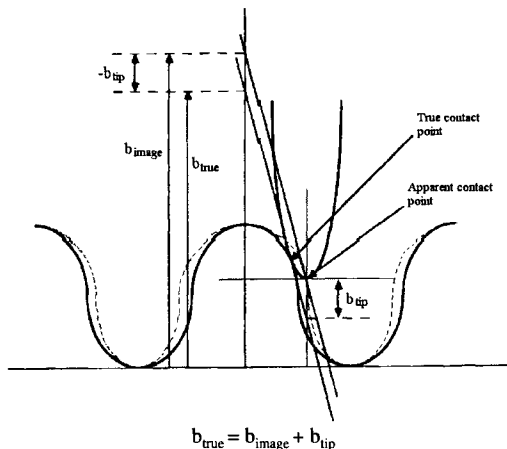


FIG. 5.4 Relationship between the Legendre transforms of the true, scanned, and tip surfaces. The Legendre transform of the tip surface is calculated with respect to the local, moving coordinate frame of the tip, which is centered on the tip end point (from Ref. [5.4]).

it is not trivial to solve Equation (5.4). Usually, numerical calculations are applied [5.3, 5.4, 5.5, 5.6].

In order to illustrate how the SPM tip affects the scaling behavior of a measured fractal surface, Aué and De Hosson did a detailed numerical

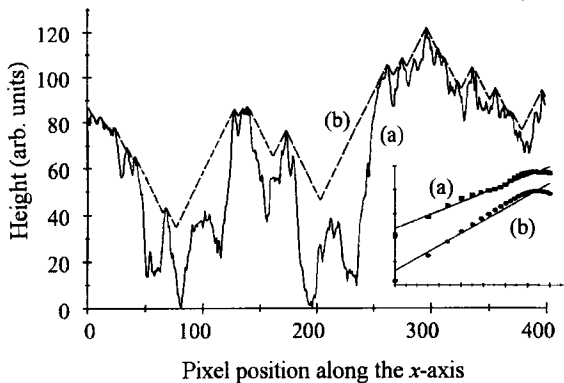


FIG. 5.5 Height profile of a fractal surface (a) before and (b) after dilation. The inset is a log-log plot of the height-height correlation function  $H(x)$  versus distance  $x$ . The results from  $H(x)$  show that (a)  $D = 1.51$  before dilation and (b)  $D = 1.34$  after dilation (from Ref. [5.3]).

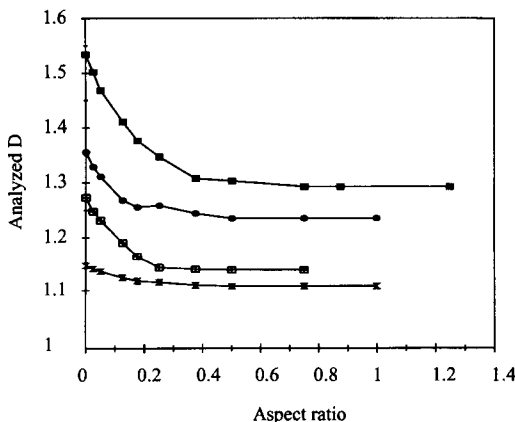


FIG. 5.6 The analyzed fractal dimension  $D$  from a simulated surface as a function of the aspect ratio of a tip. The intersections of the curves with the vertical axis give the true fractal dimensions of the surfaces (from Ref. [5.3]).

experiment [5.3]. They used a Brownian-motion-type algorithm to generate fractal surfaces with the fractal dimension  $D$  between 1.2 and 1.5. Then the scanned surfaces were generated using tips with different shapes and aspect ratios, as shown in Figure 5.5. Figures 5.6 and 5.7 show how the analyzed fractal dimension  $D$  after dilation depends on both the true fractal dimension of the surface and the aspect ratio of the tip. The dilation process would lead to an underestimation of the fractal dimension.

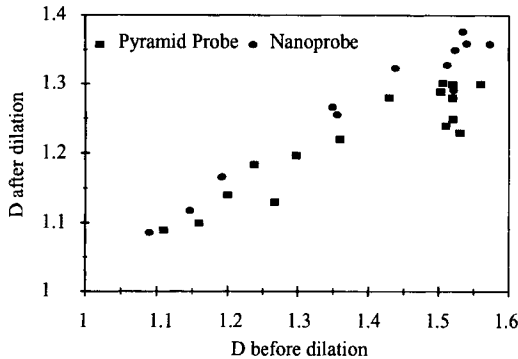


FIG. 5.7 The fractal dimension before and after dilation of tip and surface (from Ref. [5.3]).

For realistic applications, it is therefore important to quantify the relationship between the surface feature sizes (such as the lateral correlation length, interface width, and local slope) and the size and aspect ratio of the tip in order to estimate the reliability of the measurements.

## 5.2 Finite Sampling Size Effect in Image Analysis

In the imaging techniques such as AFM and STM, the image scan size,  $L_x \times L_y$ , determines the sampling size for the statistical analysis [5.7]. We assume that  $a$  is the spacing between neighboring data points along the  $x$  or  $y$  direction. For simplicity, we define all the length scale to be in units of  $a$ . Thus, we have  $L_x = N_x$  and  $L_y = N_y$ , where  $N_x$  and  $N_y$  are the number of data points along the  $x$  and  $y$  directions, respectively. In practice, for an image measured from an AFM or STM, for the statistical averaging we must consider the tip scan directions. The influence of noise on a measurement is much less significant along the fast scan direction (defined as the  $x$  direction) than that along the slow scan direction (defined as the  $y$  direction). Usually one uses Equation (2.55) to estimate the height-height correlation function  $H(r)$ . In Equation (2.55), the number of terms to be averaged is  $N_y(N_x - p)$ . Usually, we restrict ourselves in the case of  $N_x \gg p$ , which can guarantee sufficient statistics for the average. Thus, the number of terms in the average is approximately  $N_y N_x$ . With the algorithm given by Equation (2.55), we are able to analyze the height-height correlation function from the experimentally-measured surface topographies. Figure 5.8 is an AFM image of an amorphous Si film grown on a Si wafer using a thermal evaporation technique. The detailed experimentation was described in Reference

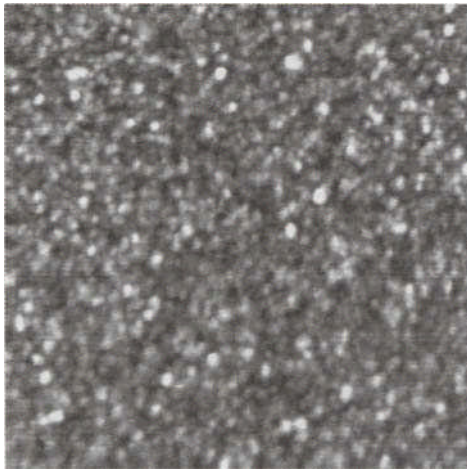


FIG. 5.8 AFM image ( $1 \mu\text{m} \times 1 \mu\text{m}$ ) of amorphous Si film deposited at room temperature for  $t = 0.25$  h using thermal evaporation technique. The deposition rate is  $\sim 1 \text{ \AA/sec}$  (from Ref. [5.7]).

[5.8]. The image has  $512 \times 512$  data points in a scale of  $1 \mu\text{m} \times 1 \mu\text{m}$ . For this amorphous Si surface, we have found that the roughness parameter  $\alpha \approx 1$  [5.8]. The sampled height-height correlation functions are plotted as thin curves in Figure 5.9. Different thin curves are calculated from different sampled images with each image being measured at a different place on the Si surface. The thick curve represents the average of over ten such thin curves. The corresponding averaged power spectrum is also plotted in Figure 5.9. From Figure 5.9, three important characteristics need to be emphasized:

- (i) Each sampled  $H_s(x)$  (corresponding to each thin curve plot) demonstrates an oscillatory behavior. These oscillations are quite random.
- (ii) The oscillation amplitude is significantly reduced after further averaging of many images, as shown in the thick curve.
- (iii) There is no split peak or shoulder structure in the power spectrum.

A similar phenomenon also occurs for a different surface morphology measured by an STM. Figure 5.10 is an STM image of a rough Si(111) surface after 500-eV  $\text{Ar}^+$  sputtering for 60 minutes. The detailed report for this experiment is described in Reference [5.9]. The image has  $256 \times 256$  data points in a scale of  $6300 \text{ \AA} \times 6300 \text{ \AA}$ . It has been determined that for this rough surface, the roughness parameter  $\alpha \approx 0.7$ . Similarly, the sampled height-height correlation function  $H_s(x)$  from an individual image shown in Figure 5.10 is plotted in Figure 5.11(a) as the thin curve. The

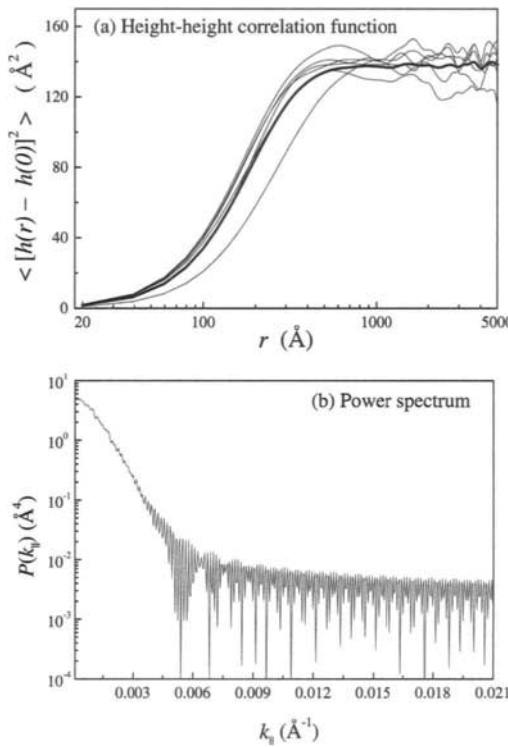


FIG. 5.9 (a) The sampled height-height correlation function calculated from the AFM images scanned from the amorphous Si film shown in Figure 5.8, where the thin curves are obtained from different sampled images and the thick curve represents the average of ten such thin curves, and (b) the corresponding power spectrum obtained from an average of ten images. No splitting in the power spectrum is observed (from Ref. [5.7]).

thick curve is the average of over ten samplings  $H_s(x)$  from different images. The averaged power spectrum is plotted in Figure 5.11(b). One can easily find that the three characteristics mentioned in (i), (ii), and (iii) are also illustrated in Figure 5.11. From the above discussion, two questions need to be addressed:

(a) The random oscillation and fluctuation in each sampled  $H_s(x)$  originating from finite data points in the finite size sampling may not represent the true statistical characteristics of the surface. The striking fact is that the number of terms to be averaged in these two cases is already very large ( $N \sim 512 \times 512$  for the AFM data and  $N \sim 256 \times 256$  for the STM data). If one used the strong law of large number to estimate the uncertainty for the sampling calculation [5.10], one could find that the relative uncertainty should be  $\sim 0.2\%$  for the AFM case and  $\sim 0.4\%$  for the STM case. How-

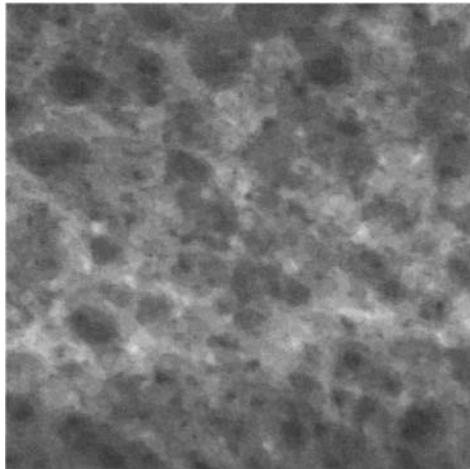


FIG. 5.10 STM image ( $6300 \text{ \AA} \times 6300 \text{ \AA}$ ) of a rough Si(111) surface after 500 eV Ar<sup>+</sup> sputtering for 60 min at 340°C. The sputtering rate is  $\sim 0.5 \text{ ML/min}$  (from Ref. [5.9]).

ever, the oscillation (or fluctuation) amplitudes shown in Figure 5.9 and Figure 5.11 are much higher than these estimates. This discrepancy results from the correlation of the system, such as the correlation among the terms averaged in Equation (2.55) and the correlation among the sampled data points measured by both AFM and STM. It is apparent that we need to establish a modified statistical law of large numbers to handle the correlated systems.

(b) From (ii) and (iii), we can conclude that both rough surfaces shown above are scale invariant. There should be no hidden cycles existing in these two systems. However, this conclusion would contradict the finding in (i). A possible explanation is that these apparent cycles shown from the thin curves (Figure 5.9 and Figure 5.11) exist because the number of sampled data points is not sufficient for the average. These oscillations would diminish for a sufficiently large number of the average, as shown in the thick curves. We shall show in the following that the correct answers to these two questions can be given from an analytical rough surface model.

Consider a continuous, non-divergent, rough surface in which the surface height  $h(\mathbf{r})$  is defined as

$$h(\mathbf{r}) = 2^{d/2} \frac{w\xi^{-d/2}}{\pi^{d/2}} \int_{-\infty}^{+\infty} \exp\left[-2\frac{(\mathbf{r}-\mathbf{u})^2}{\xi^2}\right] \eta(\mathbf{u}) d\mathbf{u}, \quad (5.5)$$

where  $w$  is the interface width and  $\xi$  is the lateral correlation length. The

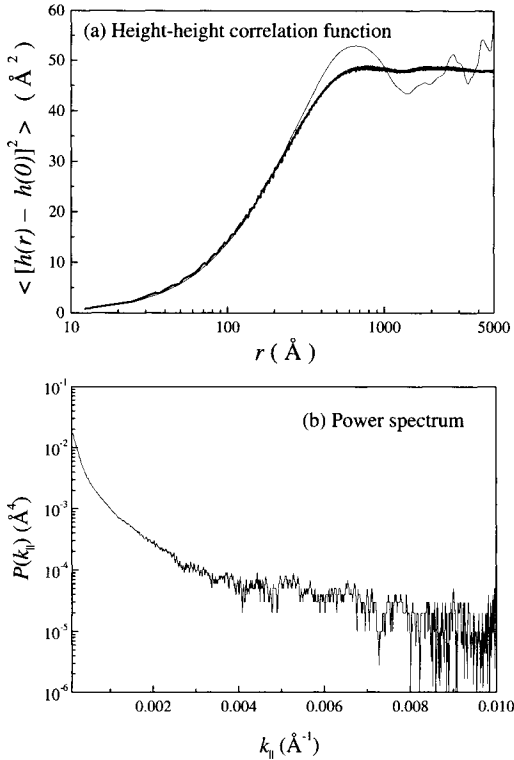


FIG. 5.11 (a) The sampled height-height correlation function (thin curve) from the STM image shown in Figure 5.10. The thick curve plot is the average of at least ten such thin curves from different images. (b) The corresponding power spectrum obtained from an average of ten images. No splitting in the power spectrum is observed (from Ref. [5.7]).

independent random Gaussian noise  $\eta(\mathbf{r})$  is defined by

$$\begin{cases} \langle \eta(\mathbf{r}) \rangle = 0, \\ \langle \eta(\mathbf{r})\eta(\mathbf{r}') \rangle = 2D\delta(\mathbf{r} - \mathbf{r}'). \end{cases} \quad (5.6)$$

In Equation (5.5), the surface height is the convolution of the Gaussian function with the independent noise function. The random noises within the region of a length scale  $\xi$  are thus correlated by the Gaussian function defining the surface morphology. We call it the random Gaussian surface model. The advantage in employing this model is that it is analytically solvable for the sampled correlation function. Furthermore, from this model, the surface morphology can be simulated by a simple numerical calculation. The properties of this model surface can be summarized as follows.

### 5.2.1 Interface width and height-height correlation function

The interface width can be calculated from Equation (5.5),

$$\langle [h(\mathbf{r}) - \langle h(\mathbf{r}) \rangle]^2 \rangle = 2^d \frac{(w\xi^{-d/2})^2}{\pi^{d/2}} \int_{-\infty}^{+\infty} \exp\left[-\frac{4(\mathbf{r}-\mathbf{u})^2}{\xi^2}\right] d\mathbf{u} = w^2, \quad (5.7)$$

which is consistent with the definition of the interface width. Here, the average surface height for the model is calculated to be  $\langle h(\mathbf{r}) \rangle = 0$ .

The auto-correlation function is calculated as

$$\langle h(\mathbf{r})h(\mathbf{r}') \rangle = w^2 \exp\left[-\frac{(\mathbf{r}-\mathbf{r}')^2}{\xi^2}\right]. \quad (5.8)$$

The height-height correlation is then given by

$$H(\mathbf{r}) = 2[w^2 - \langle h(\mathbf{r} + \mathbf{r}')h(\mathbf{r}') \rangle] = 2w^2[1 - \exp(-\frac{r^2}{\xi^2})].$$

It is shown that this model describes a scale-invariant rough surface with a roughness parameter  $\alpha = 1$ .

#### (i) The convergence of sampled average height

One can calculate the sampled average height of a continuous surface as

$$h_s = \frac{1}{L^d} \int_{-L/2}^{L/2} h(\mathbf{r}) d\mathbf{r}, \quad (5.9)$$

where  $L$  is the sampling size. In Equation (5.9), the integral notation  $\int_{-L/2}^{L/2} d\mathbf{r}$  stands for  $\int_{-L/2}^{L/2} dx$  for  $d = 1$ , but for  $d = 2$ ,  $\int_{-L/2}^{L/2} d\mathbf{r} = \int_{-L/2}^{L/2} dx \int_{-L/2}^{L/2} dy$ . In order to obtain analytical results, we can approximate the cut-off integral by the Gaussian integral,

$$\frac{1}{L^d} \int_{-L/2}^{L/2} d\mathbf{r} \Rightarrow \frac{1}{L^d} \int_{-\infty}^{+\infty} \exp\left[-\frac{\pi\mathbf{r}^2}{L^2}\right] d\mathbf{r}. \quad (5.10)$$

Such an approximation should be valid if the sampling size  $L$  is sufficiently large.

The sampled average height for a random Gaussian surface is thus calculated as

$$h_s \approx \frac{1}{L^d} \int_{-\infty}^{+\infty} \exp\left[-\frac{\pi\mathbf{r}^2}{L^2}\right] h(\mathbf{r}) d\mathbf{r}. \quad (5.11)$$

The mean square of the uncertainty for the sampled average height is then given by

$$\begin{aligned} & \langle [h_s - \langle h_s \rangle]^2 \rangle = \\ & \frac{w^2}{L^{2d}} \int_{-\infty}^{+\infty} \int_{-\infty}^{+\infty} \exp\left[-\frac{\pi \mathbf{r}^2}{L^2} - \frac{\pi \mathbf{r}'^2}{L^2}\right] \exp\left[-\frac{(\mathbf{r} - \mathbf{r}')^2}{\xi^2}\right] d\mathbf{r} d\mathbf{r}', \end{aligned} \quad (5.12)$$

where we have used the result from Equation (5.8). Further calculation gives

$$\langle [h_s - \langle h_s \rangle]^2 \rangle = \frac{\xi^d}{(\xi^2 + 2L^2/\pi)^{d/2}} w^2. \quad (5.13)$$

In the case of  $L \gg \xi$ , the standard deviation of the sampled average height is given by

$$\Delta h_s \sim \sqrt{\langle [h_s - \langle h_s \rangle]^2 \rangle} \sim w(\xi/L)^{d/2}. \quad (5.14)$$

Equation (5.14) indicates that the sampled average height converges to its mean height within an order of  $(\xi/L)^{d/2}$ .

## (ii) The convergence of the sampled interface width

The sampled interface width is defined as

$$w_s^2 = \frac{1}{L^d} \int_{-L/2}^{L/2} [h(\mathbf{r}) - h_s]^2 d\mathbf{r} \approx \frac{1}{L^d} \int_{-\infty}^{+\infty} \exp\left[-\frac{\pi \mathbf{r}^2}{L^2}\right] [h(\mathbf{r})]^2 d\mathbf{r} - h_s^2, \quad (5.15)$$

where  $h_s$  is defined from Equation (5.11). For the random Gaussian model, we have

$$\langle w_s^2 \rangle = w^2 - \frac{\xi^d}{(\xi^2 + 2L^2/\pi)^{d/2}} w^2. \quad (5.16)$$

Note that  $\langle w_s^2 \rangle$  is not exactly equal to  $w^2$ . This originates from the finite-size sampling effect. This effect leads to an offset of the average surface height by a quantity  $\langle [h_s - \langle h_s \rangle]^2 \rangle = \frac{\xi^d}{(\xi^2 + 2L^2/\pi)^{d/2}} w^2$ .

The mean square of the uncertainty for the sampled interface width is given by

$$\begin{aligned} & \langle [w_s^2 - \langle w_s^2 \rangle]^2 \rangle = \\ & \frac{2w^4}{L^{2d}} \int_{-\infty}^{+\infty} \int_{-\infty}^{+\infty} \exp\left[-\frac{\pi \mathbf{r}^2}{L^2}\right] \exp\left[-\frac{\pi \mathbf{r}'^2}{L^2}\right] \exp\left[-\frac{(\mathbf{r} - \mathbf{r}')^2}{\xi^2}\right] d\mathbf{r} d\mathbf{r}' \\ & + \langle h_s^4 \rangle - 2w^2 \langle h_s^2 \rangle - [\langle w_s^2 \rangle]^2. \end{aligned} \quad (5.17)$$

A further calculation gives

$$\langle [w_s^2 - \langle w_s^2 \rangle]^2 \rangle = 2w^4 \frac{\xi^d}{(\xi^2 + 2L^2/\pi)^{d/2}} [1 + \frac{\xi^d}{(\xi^2 + 2L^2/\pi)^{d/2}}]. \quad (5.18)$$

In the case of  $L \gg \xi$ , we have

$$\Delta w_s^2 \sim \sqrt{\langle [w_s^2 - \langle w_s^2 \rangle]^2 \rangle} \sim w^2 (\xi/L)^{d/2}. \quad (5.19)$$

Again, it is indicated that the sampled interface width would converge to its mean within an order of  $(\xi/L)^{d/2}$ .

### (iii) The convergence of the sampled height-height correlation function

For a continuous surface, the sampled height-height correlation function can be obtained by modifying Equation (2.55) as

$$H_s(r) \approx \frac{1}{L^d} \int_{-\infty}^{+\infty} \exp[-\frac{\pi \mathbf{u}^2}{L^2}] [h(\mathbf{r} + \mathbf{u}) - h(\mathbf{u})]^2 d\mathbf{u}, \quad (5.20)$$

where we have assumed that  $L \gg r$ . We have used  $\langle H_s(\mathbf{r}) \rangle = H(\mathbf{r})$ . Since we are more interested in how  $H_s(\mathbf{r})$  converges to  $H(\mathbf{r})$ , we should consider the standard deviation of  $H_s(\mathbf{r})$  given as

$$\Delta^2 H(\mathbf{r}) = \langle [H_s(\mathbf{r}) - H(\mathbf{r})]^2 \rangle = \langle [H_s(\mathbf{r})]^2 \rangle - [H(\mathbf{r})]^2. \quad (5.21)$$

For the random Gaussian model surface, the asymptotic result of  $\Delta^2 H(\mathbf{r})$  for  $L \gg r \gg \xi$  can be calculated as

$$\Delta^2 H(\mathbf{r}) = 3\pi^{d/2} 2^{2-d} w^4 (\xi/L)^d, \quad (5.22)$$

and

$$\frac{\sqrt{\Delta^2 H(\mathbf{r})}}{H(\mathbf{r})} \sim (\xi/L)^{d/2} \text{ for } L \gg r \gg \xi. \quad (5.23)$$

Equation (5.23) indicates that the sampled height-height correlation function,  $H_s(\mathbf{r})$ , would converge to  $H(\mathbf{r})$  within an order of  $(\xi/L)^{d/2}$ .

For the 1D random Gaussian model surface, the sampled height-height correlation functions are plotted in Figure 5.12. The thin dashed curve represents  $H_s(\mathbf{r})$  from an individual surface profile obtained from Monte Carlo simulations. The thin solid curve is an average of 100 such profiles (thin dashed curves). The thick curve is an average of 1000 profiles. We must emphasize that this kind of average is equivalent to the increase of the sampling size. For example, if  $M$  independent curves are averaged, the uncertainty will be reduced by a factor of  $1/\sqrt{M}$  according to the strong law of large number. Since for each surface profile (corresponding to a thin

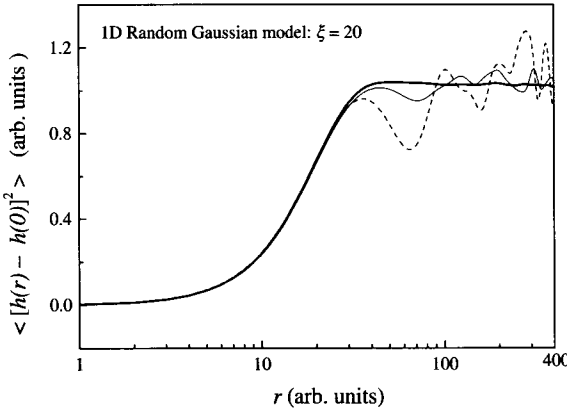


FIG. 5.12 The sampled height-height correlation function from the one-dimensional random Gaussian model calculated from Monte Carlo simulations. The sampling size is chosen to be 600 and the lateral correlation length is 20. The thin dashed curve represents  $H_S(r)$  from an individual surface profile. The thin and thick solid curves are the averages of 10 and 1000 such thin dashed curves, respectively (from Ref. [5.7]).

dashed curve), the uncertainty is  $(\xi/L)^{1/2}$ , the total uncertainty for the average is  $1/\sqrt{M}\sqrt{\xi/L} = \sqrt{\xi}/(ML)$ . This indicates that the average of  $M$  independent curves is equivalent to enlarging a single original sampling size  $L$  by a factor of  $M$ , i.e.,  $ML$ .

Figure 5.12 clearly demonstrates how the sampled correlation function  $H_s(\mathbf{r})$  converges to the true height-height correlation function  $H(\mathbf{r})$  when the sampling size increases. This is also consistent with our experimental data shown in Figure 5.9 and Figure 5.11.

### 5.2.2 Sampling-induced apparent cycle in height-height correlation function

In Figure 5.12, the sampled height-height correlation function also demonstrates the oscillatory behavior at  $r > \xi$ . These oscillations would diminish when  $(\xi/L)^{d/2} \rightarrow 0$ , as shown in both the above discussion and Figure 5.12. To find out whether or not there exist hidden cycles in these random oscillations, we can calculate the auto-correlation for the sampled function  $H_s(\mathbf{r})$ , which is defined as

$$\begin{aligned} c(\mathbf{u}, \mathbf{r}) &= < [H_s(\mathbf{u} + \mathbf{r}) - H(\mathbf{u} + \mathbf{r})][H_s(\mathbf{r}) - H(\mathbf{r})] > \\ &= < H_s(\mathbf{u} + \mathbf{r})H_s(\mathbf{r}) > - H(\mathbf{u} + \mathbf{r})H(\mathbf{r}). \end{aligned} \quad (5.24)$$

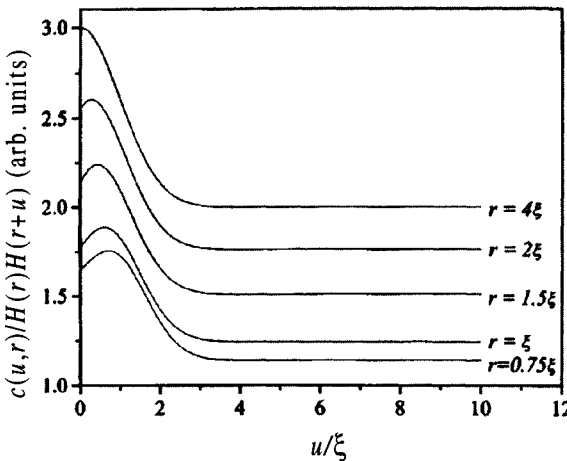


FIG. 5.13 The normalized curves,  $c(\mathbf{u}, \mathbf{r})/[H(\mathbf{u} + \mathbf{r})H(\mathbf{r})]$  against  $\mathbf{u}$ , for  $r = 0.75\xi$ ,  $\xi$ ,  $1.5\xi$ ,  $2\xi$ , and  $4\xi$ , respectively, where  $c(\mathbf{u}, \mathbf{r})$  is the autocorrelation for the sampled function  $H_S(\mathbf{r})$ , defined in Equation (5.25) (from Ref. [5.7]).

A detailed calculation of  $c(\mathbf{u}, \mathbf{r})$  for the random Gaussian model yields

$$\begin{aligned} c(\mathbf{u}, \mathbf{r}) \approx & 2^{2-d}\pi d/2w^4\left(\frac{\xi}{L}\right)^d \left\{ 2 - 2\exp\left[-\frac{\mathbf{r}^2}{2\xi^2}\right] + \exp\left[-\frac{2(\mathbf{r} + \mathbf{u}/2)^2}{\xi^2}\right] \right. \\ & \left. + \exp\left[-\frac{\mathbf{u}^2}{2\xi^2}\right] - 2\exp\left[-\frac{(\mathbf{r} + \mathbf{u})^2}{2\xi^2}\right] \right\}, \end{aligned} \quad (5.25)$$

for  $L \gg r$  and  $L \gg u > 0$ .

To show the behavior of the auto-correlation function  $c(\mathbf{u}, \mathbf{r})$ , we plot in Figure 5.13 the normalized curves,  $c(\mathbf{u}, \mathbf{r})/[H(\mathbf{u} + \mathbf{r})H(\mathbf{r})]$  against  $u$ , for  $r = 0.75\xi$ ,  $\xi$ ,  $1.5\xi$ ,  $2\xi$ , and  $4\xi$ , respectively. From Equation (5.25) and Figure 5.13, several interesting points can be addressed:

- (i) For  $u \gg x$ ,  $c(\mathbf{u}, \mathbf{r})$  decays to a constant which depends on  $r$ ,

$$c(\mathbf{u}, \mathbf{r})|_{u \gg \xi} = 2^{3-d}\pi^{d/2}w^4\left(\frac{\xi}{L}\right)^d \left\{ 1 - \exp\left[-\frac{r^2}{2\xi^2}\right] \right\}. \quad (5.26)$$

The non-zero constant means that the fluctuation in the sampled correlation function is always self-correlated no matter how large  $u$  is. This is not surprising because the sampling calculation of  $H_s(\mathbf{r})$  involves every data point in the sampled image, as indicated in Equation (2.55) and Equation (5.20). This is the main reason that  $H_s(\mathbf{r})$  has a long-range correlation.

- (ii) Figure 5.13 shows that in the vicinity of  $r = \xi$ , such as at  $r = 0.75\xi$ ,  $\xi$ , and  $1.5\xi$ , the  $c(\mathbf{u}, \mathbf{r})$  curves exhibit a profound shape, where  $c(\mathbf{u}, \mathbf{r})$

increases with  $u$  at  $0 \leq u < \xi$  and then decreases until they reach constants at large  $u$ . This suggests that the oscillation and fluctuation of the sampled correlation  $H_s(\mathbf{r})$  may have a regular cycle with a characteristic length scale  $\xi$  in the vicinity of the turning point,  $r = \xi$ . This hidden cycle can be seen clearly at near the turning point both in the modeling curve in Figure 5.12 and the experimental curves shown in Figure 5.9 and Figure 5.11. Since the oscillation amplitude diminishes as  $(\xi/L)^{d/2} \rightarrow 0$ , this hidden cycle must be a result of the sampling process in the correlated surface. We may characterize this cycle as a sampling-induced cycle.

- (iii) Away from the turning point, the plot of  $c(\mathbf{u}, \mathbf{r})$  vs.  $u$  exhibits only a monotonic decay to a constant, as shown in Figure 5.13 at  $r = 4\xi$ . It does not show a bump as it does at  $r = 0.75\xi$ ,  $\xi$ , and  $1.5\xi$ . This indicates that for  $r \gg \xi$ , the oscillations in  $H_s(\mathbf{r})$  are much more random and cannot be characterized by a single length scale. This can be directly examined from Equation (5.25), where for  $r \gg 4\xi$ , one has

$$c(\mathbf{u}, \mathbf{r})|_{r \gg \xi} \approx 2^{2-d} \pi^{d/2} w^4 \left(\frac{\xi}{L}\right)^d \left\{ 2 + \exp\left[-\frac{u^2}{2\xi^2}\right] \right\}. \quad (5.27)$$

It is shown that  $c(\mathbf{u}, \mathbf{r})$  at  $r \gg \xi$  would monotonically decay as a function of  $u$  to a constant within a range of  $\xi$ . Therefore, for  $r \gg \xi$ , what we can say is that the random oscillations in  $H_s(\mathbf{r})$  have a periodic length scale which ranges from 0 to  $\sim \xi$ .

The random Gaussian model indicates that the sampled average surface height, the sampled interface width, and the sampled height-height correlation function do not converge to their true values following the rule of  $1/\sqrt{N}$ , as in the case of the independent system. Instead, as shown in Equations (5.14), (5.19), and (5.23), respectively, they approach their means within an order of  $(\xi/L)^{d/2}$ . In this model, the system has sampled data points,  $N = L^d$ . Both  $\xi$  and  $L$  are in units of the spacing between the neighboring data points, and  $L$  is also the number of data points along a corresponding direction. The above conclusion is thus consistent with the law of large number for the correlated systems: the average of  $N$  correlated variables having a correlation length  $\xi$  would converge to their mean within an order of  $\sqrt{\xi^d/N}$ .

A very important practical issue arises from the above conclusion, which is related to the accuracy of statistical averages in a correlated system. The accuracy might not only depend on how many data points one has, but also depends more on how big the sampling size can be. In other words, it is the ratio,  $\xi/L$ , not the number of data points, that determines the accuracy.

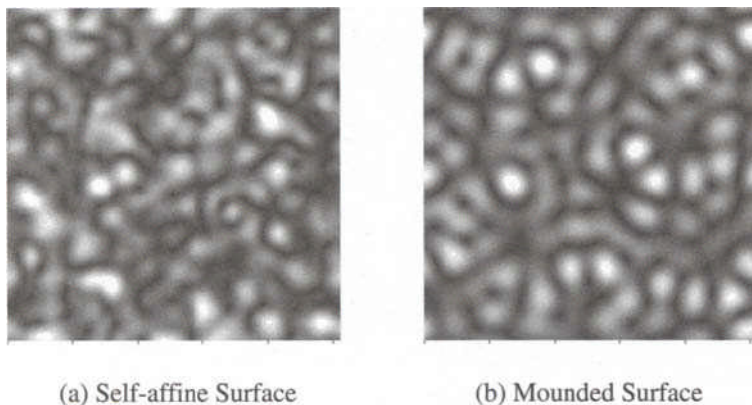


FIG. 5.14 The simulated sampling images (in arbitrary scales) of (a) a self-affine surface and (b) a bounded surface (from Ref. [5.7]).

Once the ratio  $\xi/L$  is settled, one may not be able to increase the accuracy no matter how many data points one can collect. This rule is distinctly different from the strong law of large number ( $1/\sqrt{N}$ ) for independent random variables. One must realize this important difference when dealing with correlated systems.

Another important practical issue is how to distinguish the self-affine surface from the bounded surface. The existence of sampling-induced oscillations in the height-height correlation function suggests that one should be cautious with claims of a bounded surface. A statistical average of a large number of images is required, and the condition  $\sqrt{\xi^d/N} \ll 1$  for sampling must be also imposed. To illustrate this idea, we present a numerical example. Two sampled surface images shown in Figure 5.14 were calculated from two surface models: one is a bounded surface and the other is a self-affine surface. In order to compare these two surfaces, the lateral lengths chosen are about the same ( $\sim 20$  arbitrary units). A visual inspection of Figure 5.14 reveals that a bounded surface appears to have mounds with a similar size and a regular separation, while a self-affine surface has mounds of various sizes and separations. However, judging from the sampled height-height correlation functions in Figure 5.15, one can hardly tell any difference between these two curves. Both sampled height-height correlation functions have oscillations with almost the same cycling length. If one does not have prior knowledge about these two surfaces, one may claim that they possess similar characteristics. Hence, Figures 5.14 and 5.15 demonstrate again that an examination of only one image and its height-height correlation function is not enough to distinguish between different

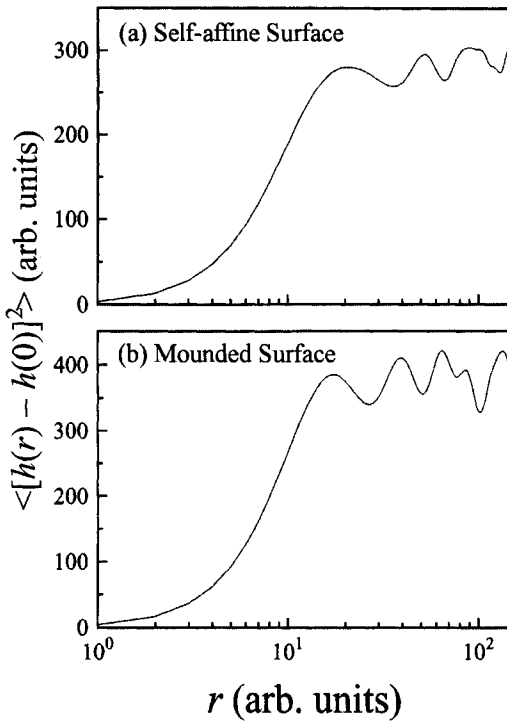


FIG. 5.15 The height-height correlation functions for (a) a self-affine surface and (b) a mounded surface from Figure 5.14 (single image sampling for each case). Note that both curves have a similar oscillatory behavior (from Ref. [5.7]).

surface morphologies. Statistics from a large number of images are needed. The thick curves in Figures 5.16(a) and 5.16(b) are the height-height correlation functions averaged over ten images for the self-affine surfaces and for the mounded surfaces, respectively. All the thin curves represent height-height correlation functions calculated from individual images. The average height-height correlation function for a mounded surface shows a profound oscillation, while the oscillation for a self-affine surface diminishes compared to individual ones. Another feature is that the oscillation for a self-affine surface is very random, but is regular for a mounded surface, especially for the first cycles, which are more or less in phase. Therefore, in order to distinguish a mound surface from a self-affine surface unambiguously, both large number statistics of images and the sampling condition  $\sqrt{\xi^d/N} \ll 1$  are required.

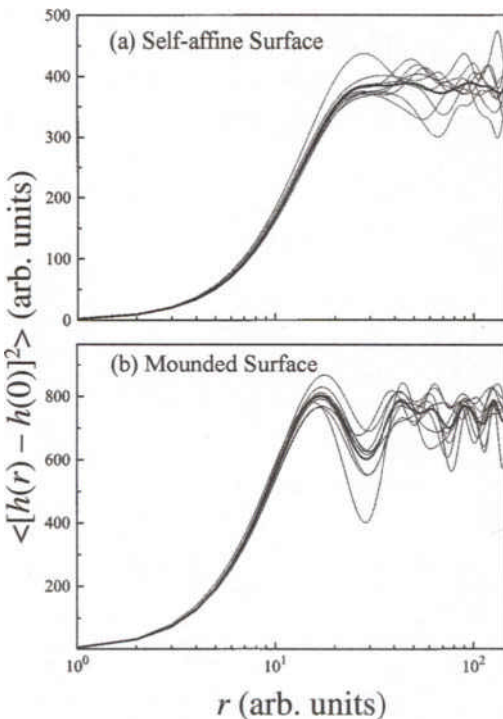


FIG. 5.16 The height-height correlation functions for (a) ten self-affine surface images and (b) ten mounded surface images. A thin curve represents the height-height correlation function for one individual image, and the thick curve is the average of ten images (from Ref. [5.7]).

### 5.3 Summary

In this chapter, we discussed the finite tip and sample size effects for SPM studies. We have shown that the aspect ratio of the tip will affect the determination of the local roughness parameters. For the sample size effect, we indicate that sampling-induced periodic cycles in height-height correlation functions are real in a scale-invariant rough surface. The oscillation amplitude approaches zero in the order of  $(\xi/L)^{d/2}$ . The existence of sampling-induced hidden cycles has a profound impact on the statistical data analysis process. It may cause problems in the search for structures in the height-height correlation functions. For a correlated system, these hidden cycles may originate from the undersampling practice, and thus might be artificial. For example, in the case of correlated rough surfaces discussed above, one may mistakenly consider these sampling-induced cycles to be ev-

idence of the existence of regular mound structures. One therefore has to be cautious when interpreting the experimental data. In order to distinguish a mounded surface from a self-affine surface, the sampling condition  $\sqrt{\xi^d/N} \ll 1$  and an average of a large number of images are required.

### References

- 5.1 S. J. Fang, S. Haplepete, W. Chen, C. R. Helms, and H. Edwards, "Analyzing atomic force microscopy images using spectral methods," *J. Appl. Phys.* **82**, 5891 (1997).
- 5.2 J. B. Wedding, T.-M. Lu, and G.-C. Wang, unpublished results.
- 5.3 J. Aué and J. Th. M. De Hosson, "Influence of atomic force microscope tip-sample interaction on the study of scaling behavior," *Appl. Phys. Lett.* **71**, 1347 (1997).
- 5.4 D. Keller, "Reconstruction of STM and AFM images distorted by finite-size tips," *Surf. Sci.* **253**, 353 (1991).
- 5.5 G. Reiss, F. Schneider, J. Vancea, and H. Hoffmann, "Scanning tunneling microscopy on rough surfaces: deconvolution of constant current images," *Appl. Phys. Lett.* **57**, 867 (1990).
- 5.6 P. Markiewicz and M. C. Goh, "Simulation of atomic force microscope tip-sample/sample-tip reconstruction," *J. Vac. Sci. Technol. B* **13**, 1115 (1995).
- 5.7 H.-N. Yang, Y.-P. Zhao, A. Chan, T.-M. Lu, and G.-C. Wang, "Sampling-induced hidden cycles in correlated random rough surfaces," *Phys. Rev. B* **56**, 4224 (1997).
- 5.8 H.-N. Yang, Y.-P. Zhao, G.-C. Wang, and T.-M. Lu, "Noise-induced roughening evolution of amorphous Si films grown by thermal evaporation," *Phys. Rev. Lett.* **76**, 3774 (1996).
- 5.9 A. Chan and G.-C. Wang, "Roughness evolution of Si(111) by low energy ion bombardment," *Surf. Sci.* **414**, 17 (1998).
- 5.10 Sheldon M. Ross, *Introduction to Probability Models*, 6th Edition (Academic Press, San Diego, 1997).

## 6. DIFFRACTION TECHNIQUES – FUNDAMENTALS

In Chapters 4 and 5 we described how to obtain surface morphology using real-space techniques and how to analyze the images. Real-space techniques can show the surface morphology directly, which is visually appealing to the human eye and gives the feeling that seeing is believing. This is the major advantage that other techniques cannot achieve. However, some disadvantages in real-space techniques may limit their applications:

1. The speed of measurements is usually slow and real-time experiments can be hard to achieve. Since most real-space measurements are performed using a probe to scan across a surface, during the measurement one normally needs to stop the processing such as deposition or etching. Therefore the information collected from a surface may not be a continuous dynamic process because of this interruption. Usually there is an assumption that goes with it: An ongoing process in a surface would freeze at the time when the process is interrupted and would not change throughout the scanning time. This approximation is valid when one deals with a system in thermal equilibrium. However, under a far-from-equilibrium condition, the relaxation process during the interruption period must be taken into consideration. This would make the interpretation of data complicated, or even impossible.

2. The statistics of data collected may not be sufficient for a limited time of data acquisition. For a real-space technique, in most cases, the product of the spatial resolution and sampling size is a constant. For a random rough surface, according to the law of large numbers, reliable statistical information about the surface can only be obtained through a large number of samplings, which requires a long time.

These two difficulties of real-space techniques limit certain applications. An alternative method to obtain surface morphology is to use diffraction (scattering) techniques to measure the reciprocal-space structure of the surface. The advantages of diffraction techniques are that they are nondestructive and noncontact and, in some cases, do not require the interruption of an experimental process. Therefore, one can achieve real-time and *in situ* measurements. The resolution of a diffraction technique is determined by the wavelength of the incident particles (Rayleigh's theory). Also, the size of the incident particle flux can be controlled freely. Combining these two conditions, we see that a diffraction technique can achieve very good statistics about the surface without sacrificing the spatial resolution. Therefore,

diffraction techniques are also widely used in surface morphology measurements. However, since diffraction deals with the reciprocal-space structure of a surface, it cannot give the surface morphology directly, and is not trivial for one to visualize. A primary goal in this book is to build a bridge connecting the real-space morphology and the diffraction pattern of a surface. In the next several chapters, we will mainly discuss how to obtain morphological information of surfaces from the diffraction.

## 6.1 Scattering and Diffraction Concepts

Diffraction is an interaction process between photons (light, x ray) or other particles (electron, neutron, atom) and matter. It is a very complicated process, which includes elastic diffraction and inelastic diffraction. In elastic diffraction the incident particles and outgoing particles have the same magnitude of momentum (energy), although the direction of outgoing momentum may differ from the direction of the incoming momentum. This process corresponds to the elastic collision in classical mechanics. If the magnitude of outgoing momentum (energy) changes, then it is an inelastic diffraction. Examples are absorption, Raman scattering, Compton scattering, and secondary particle emission. Inelastic diffraction is affected not merely by the morphology of the surface, but more importantly by the physical and chemical properties of the object and the energy of the incident particle. Therefore, inelastic diffraction is seldom used to probe surface morphology. The diffraction we refer to throughout the book will be elastic diffraction.

Diffraction has many forms. For different forms of diffraction, the physical origins are different, and the analytical methods used are also different. For example, one uses Maxwell's equations of electrodynamics to describe light scattering and Schrödinger's equation of quantum mechanics to describe matter-wave diffraction. However, if we are concerned only about surface diffraction, different forms of diffraction have many common features. The following pages describe these common features from the microscopic point of view, and establish a unified kinematic diffraction theory.

### 6.1.1 Diffraction of photons

For simplicity, we shall only consider the interaction of an electromagnetic wave with matter within the framework of classical electrodynamics. This will give us a clear physical picture and will serve our goal.

First we consider the interaction of the electromagnetic wave with a free

electron [6.1]. According to classical electrodynamics, when an electromagnetic wave with a certain frequency  $\omega$  shines on a free electron with charge  $e$  and mass  $m$ , the vibrating electric field exerts on the electron and forces the electron to vibrate with the same frequency. The vibrating electron will then radiate electromagnetic wave. Assume that the velocity of the electron under the external electromagnetic wave is far less than the speed of light, so that the length scale of the electron's movement is less than the wavelength of the incident wave. Then we can use the electric field at a fixed point as the electric field forcing the electron to move and neglect the magnetic force. Let the incident electric field be  $\mathbf{E}_0 e^{-i\omega t}$ . Then the equation of motion for the electron can be written as

$$\ddot{\mathbf{x}} = \frac{e}{m} \mathbf{E}_0 e^{-i\omega t}. \quad (6.1)$$

Here  $\mathbf{x}$  is the position of the electron, and  $\ddot{\mathbf{x}}$  is the acceleration. The solution for Equation (6.1) is

$$\mathbf{x} = -\frac{e\mathbf{E}_0}{m\omega^2} e^{-i\omega t}. \quad (6.2)$$

The radiated electric field due to the vibration of the electron is

$$\mathbf{E}_d = \frac{e}{4\pi\epsilon_0 c^2 r} \hat{\mathbf{n}} \times (\hat{\mathbf{n}} \times \ddot{\mathbf{x}}), \quad (6.3)$$

where  $\hat{\mathbf{n}}$  is the unit vector along the outgoing radiation direction,  $r$  is the distance of the observation point from the electron, and  $\epsilon_0$  is the permittivity constant. Figure 6.1 is a plot of the scattering geometry in the Cartesian coordinates. If  $\varphi$  represents the angle between  $\hat{\mathbf{n}}$  and the direction of the incident electric field, then the electric field of the scattered wave is (here we neglect the time-dependent part)

$$\mathbf{E}_d = \hat{\mathbf{n}} \frac{e^2 E_0}{4\pi\epsilon_0 mc^2 r} \sin \varphi. \quad (6.4)$$

If we consider the phase change during the wave propagation, then Equation (6.4) becomes

$$\mathbf{E}_d = \hat{\mathbf{n}} \frac{e^2 E_0}{4\pi\epsilon_0 mc^2 r} \sin \varphi e^{i\mathbf{k}_s \cdot \mathbf{r}}, \quad (6.5)$$

where  $\mathbf{k}_s$  is the scattered wave vector. Thus, the scattered electric field  $E_d$  is proportional to the incident electric field  $E_0$  and is inversely proportional to the distance  $r$  from the observation point to the electron. Note that in the above discussion, we assume that the initial position of the electron is at the origin of the coordinates.

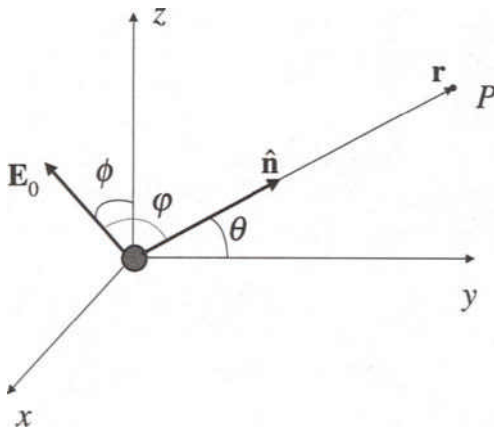


FIG. 6.1 Schematic of the scattering of electromagnetic wave from a free electron.

All complex atoms have more than one electron. If we neglect the interactions between the electrons and treat each electron as an independent electron, then the total scattered electromagnetic field  $E_d$  from a complex atom is the summation of the scattered field  $E_{dj}$  from each individual electron. Because electrons in an atom are distributed at different positions, the incident electric field acting on the  $j$ th electron will have an additional phase  $\mathbf{k}_0 \cdot \mathbf{r}_j$ , where  $\mathbf{r}_j$  is the position of the  $j$ th electron, and the electromagnetic field radiated from the  $j$ th electron also has the phase  $\mathbf{k}_s \cdot (\mathbf{r} - \mathbf{r}_j)$ . Here  $\mathbf{k}_0$  is the incident wave vector and  $\mathbf{r}$  is the vector from the center of the atom to the observation point. Usually,  $|\mathbf{r}| \gg |\mathbf{r}_j|$ , and the total scattered electromagnetic field can be expressed as

$$\mathbf{E}_d = \hat{\mathbf{n}} \frac{e^2 E_0}{4\pi\epsilon_0 mc^2 r} \sin \varphi e^{i\mathbf{k}_s \cdot \mathbf{r}} \sum_j e^{i(\mathbf{k}_0 - \mathbf{k}_s) \cdot \mathbf{r}_j}. \quad (6.6)$$

Here, the summation  $f = \sum_j e^{i(\mathbf{k}_0 - \mathbf{k}_s) \cdot \mathbf{r}_j}$  is called the atomic factor. It represents the contribution from the distribution of electrons inside the atom. Different atoms should have different  $f$  factors. If we consider that each electron spreads out into a diffuse cloud of negative charge, characterized by a charge density  $n(\mathbf{r})$  expressed in electron charge units, then the scattered electric field can be written as

$$\mathbf{E}_d = \hat{\mathbf{n}} \frac{e^2 E_0}{4\pi\epsilon_0 mc^2 r} \sin \varphi e^{i\mathbf{k}_s \cdot \mathbf{r}} \int e^{i(\mathbf{k}_0 - \mathbf{k}_s) \cdot \mathbf{r}'} n(\mathbf{r}') dV. \quad (6.7)$$

Here,  $f = \int e^{i(\mathbf{k}_0 - \mathbf{k}_s) \cdot \mathbf{r}'} n(\mathbf{r}') dV$ ,  $dV$  is the differential volume, and the integration replaces the summation. Therefore the total scattered electric

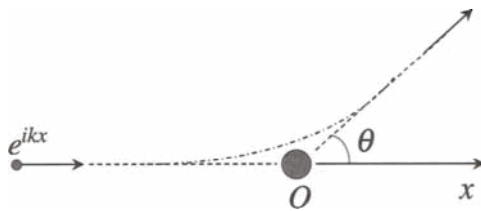


FIG. 6.2 Schematic of a particle diffracted by a short-range potential.

field  $E_d$  of an atom is proportional to the atomic factor  $f$  and has a phase change,  $\mathbf{k}_s \cdot \mathbf{r}$ , with respect to the incident field.

### 6.1.2 Diffraction of other particles

When we consider the diffraction of electrons or other particles, the classical description is not applicable. Therefore, we will use the concept of matter waves in quantum mechanics. In the framework of quantum mechanics, the diffraction process is the particle in transition from one state to another due to the interaction with the atom or nucleus within a small volume [6.2]. As shown in Figure 6.2, the incident particle comes in from the left side along the horizontal direction, and the incident wave is

$$\psi_i = e^{ikx}. \quad (6.8)$$

The wave function  $\psi$  of the diffracted particle should satisfy the steady-state Schrödinger equation:

$$-\frac{\hbar^2}{2m} \nabla^2 \psi + V(\mathbf{r})\psi = E\psi, \quad (6.9)$$

where  $E = \frac{\hbar^2 k^2}{2m}$  is the energy of the incident particle and  $V(\mathbf{r})$  is the potential energy of the particle in the target field. Let  $U(\mathbf{r}) = \frac{2mV(\mathbf{r})}{\hbar^2}$ , Equation (6.9) can be rewritten as

$$(\nabla^2 + k^2)\psi = U(\mathbf{r})\psi. \quad (6.10)$$

This equation can be solved using the method of Green's functions, and the solution is

$$\psi(\mathbf{r}) = e^{ikx} - \frac{1}{4\pi} \int \frac{e^{ik|\mathbf{r}-\mathbf{r}'|}}{|\mathbf{r}-\mathbf{r}'|} U(\mathbf{r}') \psi(\mathbf{r}') d\mathbf{r}'. \quad (6.11)$$

The second term on the right-hand side is the scattered wave function. The integration is over the volume of interaction. In fact, Equation (6.11) is the

equivalent integral equation for Equation (6.10). Assume that the energy of the incident particle is high enough that the potential  $V(\mathbf{r})$  can be treated as a perturbation, then the first-order approximation (Born approximation) of Equation (6.11) becomes

$$\psi(\mathbf{r}) \approx e^{ikx} - \frac{1}{4\pi} \int \frac{e^{ik|\mathbf{r}-\mathbf{r}'|}}{|\mathbf{r}-\mathbf{r}'|} U(\mathbf{r}') e^{ikx'} dv'. \quad (6.12)$$

Here  $U(\mathbf{r}')$  is non-zero only within a small spatial volume, therefore the integral in Equation (6.12) is confined in such a small volume. When  $r \rightarrow \infty$ , Equation (6.12) becomes

$$\psi(\mathbf{r}) = e^{ikx} - \frac{e^{ikr}}{4\pi r} \int e^{-ik\mathbf{r} \cdot \mathbf{r}'/r} U(\mathbf{r}') e^{ikx} dv'. \quad (6.13)$$

The scattered wave function can be simplified as

$$\psi_s(\mathbf{r}) = -\frac{e^{ik_s r}}{4\pi r} \int e^{-i(k_0 - k_s) \cdot \mathbf{r}'} U(\mathbf{r}') dv', \quad (6.14)$$

where  $\mathbf{k}_0 \cdot \mathbf{r}' = kx$  and  $\mathbf{k}_s = kr/r$ . If we let  $f = -\int e^{-i(k_0 - k_s) \cdot \mathbf{r}'} U(\mathbf{r}') dv'$  represent the atomic factor, then Equation (6.14) has the same form as Equation (6.7). This suggests that for both photon diffraction and matter-wave diffraction, the diffracted (or scattered) waves have the same form. Therefore, we can use this unified form to describe both of them.

### 6.1.3 General diffraction formula from a single atom

In the last two sections we have shown that microscopically both photon diffraction and matter-wave diffraction have similar forms. The only difference is their physical origins. Therefore, a unified description for both photon diffraction and matter-wave diffraction is possible. In this section, we will unify the above discussions.

The general diffraction geometry is shown in Figure 6.3 [6.3]. We consider the diffraction of a plane wave in the form of  $e^{i\mathbf{k}_0 \cdot \boldsymbol{\rho}}$  incident upon an atom. The incident wave vector  $\mathbf{k}_0$  has a magnitude of  $2\pi/\lambda$ , where  $\lambda$  is the wavelength. We define the position of the atom  $\boldsymbol{\rho} = (x, y, z)$  with respect to a reference point  $\boldsymbol{\rho} = 0$  in the surface plane. The argument  $i\mathbf{k}_0 \cdot \boldsymbol{\rho}$  describes the phase of the wave at the position of the atom. The scattered wave is received by a detector at point  $P$ , a distance  $\mathbf{R}$  away from the origin. The scattered wave has a wave vector of  $\mathbf{k}_s$ . The distance between the atom and the detector is  $\mathbf{r}$ . The scattered wave has a phase of  $ik_s r$  at the point  $P$  with reference to the atom. Therefore the total phase of the wave at the detector at point  $P$  is  $i(\mathbf{k}_0 \cdot \boldsymbol{\rho} + k_s r)$ . This phase gives a phase factor of

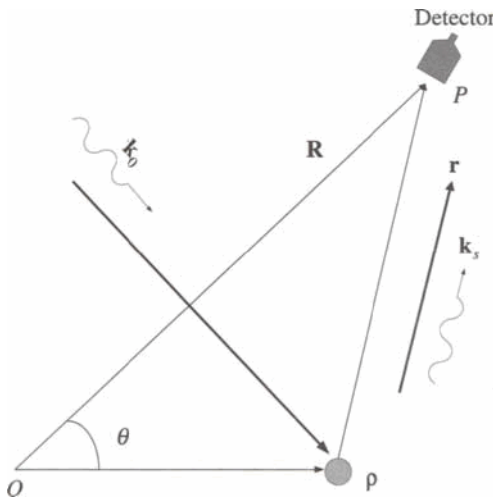


FIG. 6.3 A general schematic of the geometry for a wave diffracted by a particle (electron, atom or others) and the detection of the diffracted wave (from Ref. [6.3]).

$e^{i(\mathbf{k}_0 \cdot \rho + \mathbf{k}_s \cdot r)}$ . According to Equations (6.7) and (6.14), the total amplitude of the wave,  $A(\mathbf{k}_0, \mathbf{k}_s)$ , at point  $P$  can be written as

$$A(\mathbf{k}_0, \mathbf{k}_s) \propto \frac{f}{r} e^{i(\mathbf{k}_0 \cdot \rho + \mathbf{k}_s \cdot r)}. \quad (6.15)$$

Here,  $f$  is the atomic factor. In general,  $f$  is a slowly-varying function of the magnitude of the wave vector and the relative angle between the incident and outgoing waves. Therefore, we can treat it as a constant (this assumption may not hold for inhomogeneous surfaces).

Usually the detector is placed very far away from the scatterer, which means that  $R \gg \rho$  and  $r \approx R - \rho \cos \theta$ . The phase in Equation (6.15) can be written approximately as

$$i(\mathbf{k}_0 \cdot \rho + \mathbf{k}_s \cdot r) \approx i(\mathbf{k}_0 \cdot \rho - \mathbf{k}_s \cdot \rho \cos \theta) + ik_s R.$$

Since the direction of  $\mathbf{R}$  and  $\mathbf{r}$  look approximately the same from point  $P$  in the detector, the factor in parentheses on the right-hand side of the above equation can be written as

$$i(\mathbf{k}_0 \cdot \rho - \mathbf{k}_s \cdot \rho \cos \theta) \approx i(\mathbf{k}_0 - \mathbf{k}_s) \cdot \rho.$$

Therefore, the amplitude of the diffracted wave given by Equation (6.15)

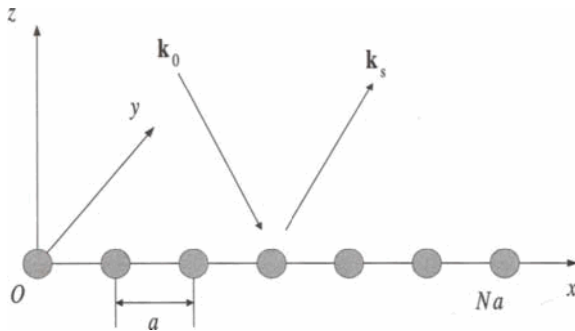


FIG. 6.4 Schematic of diffraction from a one-dimensional atomic array.

can be written in a simple form:

$$A(\mathbf{k}_0, \mathbf{k}_s) \approx \frac{f e^{i\mathbf{k}_s R}}{R} e^{i(\mathbf{k}_0 - \mathbf{k}_s) \cdot \boldsymbol{\rho}} \propto e^{i\mathbf{k} \cdot \boldsymbol{\rho}}, \quad (6.16)$$

where  $\mathbf{k} = \mathbf{k}_s - \mathbf{k}_0$  is defined as the momentum transfer in diffraction. As we shall see later the momentum transfer plays a very important role in diffraction.

## 6.2 Multi-Atom Diffraction

In Section 6.1 we discussed in detail the scattered field of an atom. However, the problem we have in general is a multi-atom problem. In this section, we use two examples to illustrate how to treat the multi-particle scattering problem. We also introduce the concept of the reciprocal-space characterization.

### 6.2.1 Diffraction from an atomic array

Let us consider the diffraction from a one-dimensional array of  $N$  atoms with a lattice constant  $a$ . The length of the array is  $Na$ . Figure 6.4 shows a schematic of the diffraction geometry. Note that although the array is one-dimensional, the diffraction itself is not restricted to one dimension. In fact, the diffraction can be three-dimensional. For simplicity, here we only consider the diffraction confined to the  $x$ - $z$  plane. That is, all the diffraction wave vectors are in the  $x$ - $z$  plane and the atoms in the array are aligned in the  $x$  direction at  $z = 0$ .

We choose the first atom in the array to be positioned at the origin  $\boldsymbol{\rho}_1 = 0$ . The  $n$ th atom is located at  $\boldsymbol{\rho}_n = (n - 1)\mathbf{a}$ . The total scattering

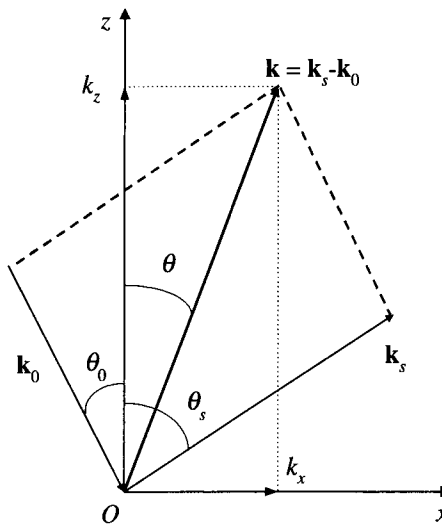


FIG. 6.5 The geometry of reciprocal space: momentum transfer and its decomposition (from Ref. [6.3]).

amplitude received by a detector at point  $P$  is the sum of the individual scattering amplitudes (Equation (6.16)) from the array of atoms:

$$A(\mathbf{k}) = e^{-i\mathbf{k} \cdot \mathbf{p}_1} + e^{-i\mathbf{k} \cdot \mathbf{p}_2} + \dots + e^{-i\mathbf{k} \cdot \mathbf{p}_N} \quad (6.17)$$

$$= \sum_{n=0}^{N-1} e^{-in\mathbf{k} \cdot \mathbf{a}} = \frac{1 - e^{-iN\mathbf{k} \cdot \mathbf{a}}}{1 - e^{-i\mathbf{k} \cdot \mathbf{a}}}. \quad (6.18)$$

The total intensity of the diffracted wave is the product of Equation (6.18) with its own complex conjugate:

$$S(\mathbf{k}) = A^*(\mathbf{k})A(\mathbf{k}) = \frac{\sin^2(N\mathbf{k} \cdot \mathbf{a}/2)}{\sin^2(\mathbf{k} \cdot \mathbf{a}/2)}. \quad (6.19)$$

There is only one important parameter in Equation (6.19), the momentum transfer  $\mathbf{k} \cdot \mathbf{a}$  along the direction of the array of atoms, i.e., the  $x$  direction shown in Figure 6.4. We can write  $\mathbf{k} \cdot \mathbf{a} = k_x a$ , where  $k_x$  is defined as the momentum transfer parallel to the  $x$  direction and is shown in Figure 6.5. In Figure 6.6 the diffraction intensity is plotted as a function of  $k_x a / \pi$  for  $N = 10$ . At  $k_x a = 2n\pi$ , where  $n$  is an integer, the diffraction intensity is maximum and equals to  $N^2$ . From the phase separation of adjacent peaks in Figure 6.6 and a known value of  $k_x$ , one can determine the lattice constant  $a$ . The full width at half-maximum (FWHM) of the individual angular profile is approximately inversely proportional to the size of the

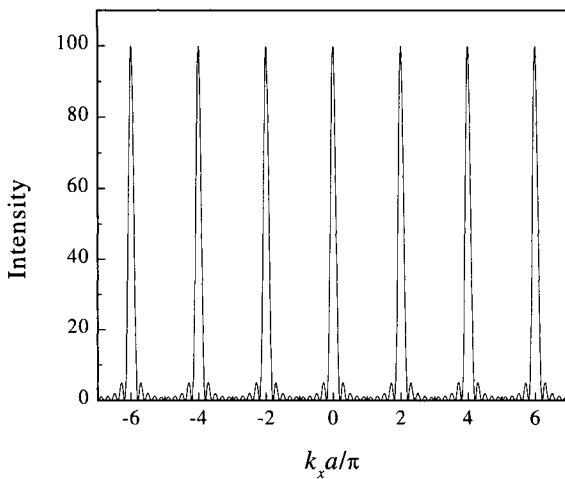


FIG. 6.6 The diffraction intensity as a function of  $k_x$  from a one-dimensional atomic array.

array  $N$  [6.3].

According to Figure 6.5, the momentum transfer  $\mathbf{k}$  can be decomposed into two components: the momentum transfer parallel to the surface in the  $x$  direction,  $k_x$ , and the momentum transfer perpendicular to the array in the  $z$  direction,  $k_z$ :

$$k_x = k_s \sin \theta_s - k_0 \sin \theta_0, \text{ and} \quad (6.20)$$

$$k_z = k_s \cos \theta_s + k_0 \cos \theta_0, \quad (6.21)$$

where  $\theta_0$  and  $\theta_s$  are the incident and scattered angles of the wave vectors with respect to the surface normal, or the  $z$  direction, respectively. The combined  $k_x$  and  $k_z$  establish the reciprocal space. For a fixed incident angle, both  $k_x$  and  $k_z$  are functions of the wavelength and the scattered angle  $\theta_s$ . However, Equation (6.19) does not contain  $k_z$ . Then, one would ask the question: What is the role of  $k_z$  in terms of determining the surface morphology?

### 6.2.2 Diffraction from one-dimensional adsorbates with double periodicity

The intensity given by Equation (6.19) is independent of  $k_z$ , the momentum transfer in the  $z$  direction. This is because the positions of atoms in the array are fixed in the  $z$  direction at  $z = 0$ . If atoms are located at positions other than  $z = 0$  along the  $z$  direction, then the intensity in

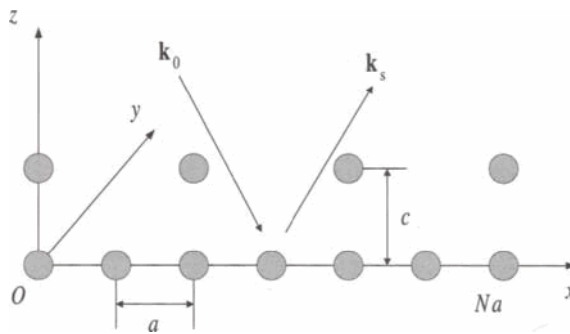


FIG. 6.7 Schematic of diffraction from a one-dimensional adsorbed atomic array.

general may depend on  $k_z$ . To demonstrate this point, let us consider the diffraction from a one-dimensional adsorbed atomic array that possesses a double periodicity as shown in Figure 6.7. The scattering amplitude can still be expressed as Equation (6.19). However, the position vectors of the surface atoms are different. For even-numbered atoms,

$$\rho_{2n} = 2n\mathbf{a},$$

and for odd-numbered atoms,

$$\rho_{2n+1} = (2n+1)\mathbf{a} + \mathbf{c}.$$

Note that  $\mathbf{c}$  is the vertical spacing along the  $z$  direction and is perpendicular to the direction of the base vector  $\mathbf{a}$ . The scattering amplitude can be written as

$$\begin{aligned} A(\mathbf{k}) &= \sum_{n=0}^{N/2-1} [e^{-2ink \cdot \mathbf{a}} + e^{-i(2n+1)\mathbf{k} \cdot \mathbf{a} - i\mathbf{k} \cdot \mathbf{c}}] \\ &= \frac{1 - e^{-iN\mathbf{k} \cdot \mathbf{a}}}{1 - e^{-2i\mathbf{k} \cdot \mathbf{a}}} [1 + e^{-i\mathbf{k} \cdot (\mathbf{a} + \mathbf{c})}]. \end{aligned} \quad (6.22)$$

The corresponding scattering intensity can be calculated as

$$S(\mathbf{k}) = \frac{4 \sin^2(Nk_x a/2)}{\sin^2(k_x a)} \cos^2\left(\frac{k_x a + k_z c}{2}\right). \quad (6.23)$$

We see that the scattering intensity depends on both  $k_x a$  and  $k_z c$ . If  $k_z c = 0$ , which means  $c = 0$  (no adsorption), or  $k_z = 0$  (totally grazing incidence), Equation (6.23) becomes Equation (6.19). However, if  $k_z c \neq 0$ , the peak intensity would be modified.

In Figure 6.8 the diffraction intensity is plotted for different  $k_z c$  values for  $N = 10$ . Notice that when  $k_z c$  increases, additional peaks at  $(2n+1)\pi$

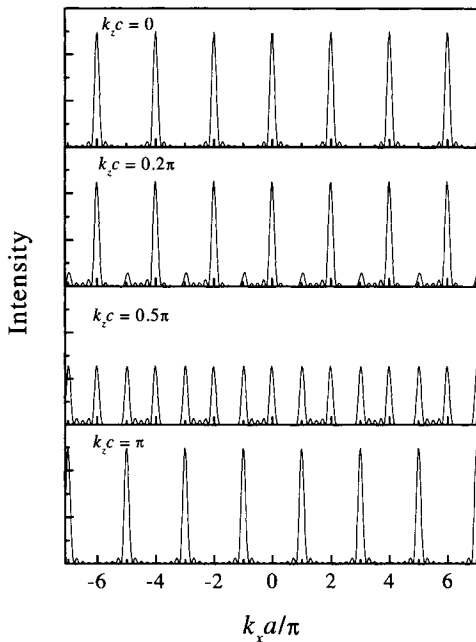


FIG. 6.8 The diffraction intensity as a function of  $k_x a$  for different  $k_z c$  values:  $k_z c = 0$ ,  $0.2\pi$ ,  $0.5\pi$ , and  $\pi$ . Notice the positions of peaks shift when  $k_z c$  increases from 0 to  $\pi$ .

appear, and their intensities become stronger. These additional peaks are due to the double periodicity of the surface caused by the adsorption, and the diffraction pattern is called the  $(2 \times 1)$  superlattice pattern. When  $k_z c = \pi$ , the original peaks at  $2n\pi$  totally disappear, and the peaks at  $(2n + 1)\pi$  become maximum. This is because the adsorbed layer provides destructive interference of waves. We also plot in Figure 6.9 the intensity change as a function of  $k_z c$  at  $k_x a = 2\pi$  and  $k_x a = \pi$ . The intensity oscillates with the change of  $k_z$ . Therefore, from the period of the oscillation, one can determine the height  $c$ .

From the above two examples, we see that  $k_x$  is inversely related to the lateral lattice constant of the array and  $k_z$  is inversely related to the vertical height difference of the arrays, just like  $a$  and  $c$  represent the characteristic lengths in real space. Therefore, the reciprocal space based on  $k_x$  and  $k_z$  completely characterizes the surface periodicity.

### 6.2.3 Superposition of diffraction waves

When we deal with a single-atom diffraction in Section 6.1.1, we first consider the diffraction from a single electron, which results in Equation (6.5).

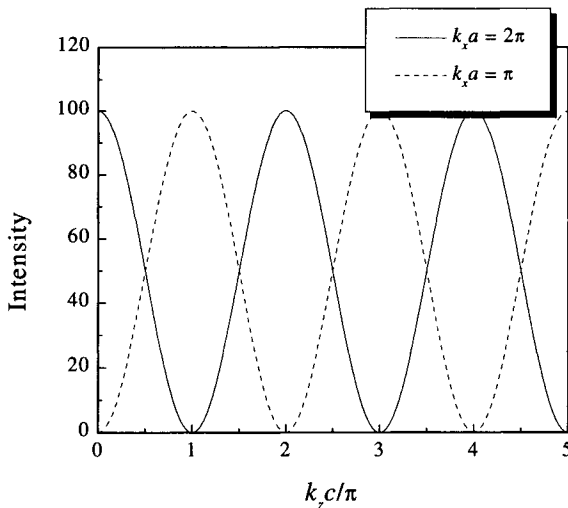


FIG. 6.9 The diffraction intensity as a function of  $k_z c$  at  $k_x a = 2\pi$  and  $k_x a = \pi$  for one-dimensional adsorbates with double periodicity.

The scattered amplitude of a complex atom with more than one electron is a superposition of the scattered fields of all the electrons in the atom. In Section 6.2.1, when we deal with the diffraction from an atomic array, we start from the single-atom diffraction formula Equation (6.16). The diffraction amplitude of the atomic array is a summation of the scattered amplitude of all of the atoms in the array. If we examine both Equations (6.5) and (6.16), they are very similar, except for a constant factor. The result for single-atom diffraction is that one can use the atomic factor,  $f$ , which represents the contribution from the distribution of electrons inside the atom, to distinguish diffraction from different atoms. The atomic factor can also be expressed as the Fourier transform of the charge density function. The above similarity in a single-atom treatment and an atomic-array treatment leads us to believe that there should be a structure factor  $F$ , similar to the atomic factor  $f$ , which uniquely reflects the surface structure, and can also be expressed by the Fourier transform of a density function  $D(\mathbf{r})$ :

$$F(\mathbf{k}) = \int D(\mathbf{r}) f e^{-i\mathbf{k} \cdot \mathbf{r}} d\mathbf{r}. \quad (6.24)$$

According to Equations (6.5) and (6.16), the diffraction amplitude can be expressed as

$$A(\mathbf{k}) = \frac{F(\mathbf{k}) e^{i\mathbf{k}_s \cdot \mathbf{R}}}{R}. \quad (6.25)$$

Using Equations (6.24) and (6.25) we can scale our diffraction problems no matter how complicated it is. For example, we can reconsider the diffraction from an atomic array according to Equations (6.24) and (6.25). If we consider here an atom having a finite mass but an infinitesimally small volume, then the density function for the atomic array can be obviously expressed as

$$D(\mathbf{r}) = \sum_{n=0}^{N-1} \delta(\mathbf{r} - n\mathbf{a}). \quad (6.26)$$

Here  $\delta(x)$  is the Dirac delta function. Therefore, the structure factor can be written as

$$\begin{aligned} F(\mathbf{k}) &= f \sum_{n=0}^{N-1} \int \delta(\mathbf{r} - n\mathbf{a}) e^{-i\mathbf{k}\cdot\mathbf{r}} d\mathbf{r} \\ &= f \sum_{n=0}^{N-1} \int \int \int \delta(x - na) \delta(y) \delta(z) e^{-i\mathbf{k}\cdot\mathbf{r}} dx dy dz \\ &= f \sum_{n=0}^{N-1} e^{-ink\cdot\mathbf{a}}. \end{aligned} \quad (6.27)$$

Equation (6.27) is identical to Equation (6.18) except for the factor  $f$ .

Now we can apply the above idea to a more complicated case: diffraction from a two-dimensional array of  $N_x \times N_y$ .  $a$  and  $b$  are the lattice constants along the  $x$  direction and the  $y$  direction, respectively. We can treat the array along the  $x$  direction as a cluster with a structure factor  $F_x$  given by Equation (6.27). Then the two-dimensional array can be treated as a one-dimensional cluster array. According to Equation (6.27), the structure factor of a cluster array can be expressed as

$$F_{2d}(\mathbf{k}) = F_x \sum_{n=0}^{N_y-1} e^{-ink\cdot\mathbf{b}} = \sum_{n=0}^{N_x-1} e^{-ink\cdot\mathbf{a}} \sum_{n=0}^{N_y-1} e^{-ink\cdot\mathbf{b}}. \quad (6.28)$$

We can also apply the same method for the scattering from a three-dimensional lattice with a lattice constant  $c$  in the  $z$  direction and a total length  $N_z c$ . If we treat the two-dimensional surface as a cluster, with the structure factor given by Equation (6.28), then again the three-dimensional lattice becomes a one-dimensional cluster array. Therefore, according to Equation

(6.27), we have

$$F_{3d}(\mathbf{k}) = F_{2d} \sum_{n=0}^{N_z-1} e^{-ink \cdot \mathbf{c}} = \sum_{n=0}^{N_x-1} e^{-ink \cdot \mathbf{a}} \sum_{n=0}^{N_y-1} e^{-ink \cdot \mathbf{b}} \sum_{n=0}^{N_z-1} e^{-ink \cdot \mathbf{c}}. \quad (6.29)$$

The corresponding scattered intensities for 2-D and 3-D lattices are, respectively,

$$S_{2d}(\mathbf{k}) = \frac{\sin^2(N_x \mathbf{k} \cdot \mathbf{a}/2) \sin^2(N_y \mathbf{k} \cdot \mathbf{b}/2)}{\sin^2(\mathbf{k} \cdot \mathbf{a}/2) \sin^2(\mathbf{k} \cdot \mathbf{b}/2)} \quad (6.30)$$

and

$$S_{3d}(\mathbf{k}) = \frac{\sin^2(N_x \mathbf{k} \cdot \mathbf{a}/2) \sin^2(N_y \mathbf{k} \cdot \mathbf{b}/2) \sin^2(N_z \mathbf{k} \cdot \mathbf{c}/2)}{\sin^2(\mathbf{k} \cdot \mathbf{a}/2) \sin^2(\mathbf{k} \cdot \mathbf{b}/2) \sin^2(\mathbf{k} \cdot \mathbf{c}/2)}. \quad (6.31)$$

From the above we see how the superposition concept is applied in diffraction. In summary, we learn that the scattered field amplitude can be calculated by multiplying the following:

- a) the scattering structure factor of an electron or nucleus,
- b) the scattering structure factor of an atom,
- c) the scattering structure factor of a unit cell or the period of a periodic structure, and
- d) the scattering structure factor of the total number of unit cells.

All the structure factors include the direction of scattering and the relative phase of the scattered waves.

### 6.3 Diffraction from Rough Surfaces – General Formula

We have discussed in the previous two sections how to obtain scattering amplitudes from a single atom and smooth surfaces with a periodic arrangement of atoms. In general, surfaces are not so regular, which we have already discussed in Chapter 2 and Chapter 3. Then one might ask, is there a general treatment of diffraction from irregular surfaces? In this section we will follow the methods of Yang et al. [6.3] but present a more general expression by considering the possibility of non-uniform surfaces that have more than one kind of atoms.

#### 6.3.1 Diffraction structure factor for a discrete surface

For a discrete rough surface, the surface height  $z$  can be expressed as a function of the position  $\rho$ , where  $z(\rho) = h(\rho)c$ ,  $\rho = m\mathbf{a} + n\mathbf{b}$ ,  $c$  is a surface

step height, and  $\mathbf{a}$  and  $\mathbf{b}$  are the basis vectors of the unit cell of a surface. Then the density for this discrete surface is

$$D(\boldsymbol{\rho}, z) = \sum_{m,n} \delta(\boldsymbol{\rho} - \boldsymbol{\rho}_{mn}) \delta[z - h(\boldsymbol{\rho})c]. \quad (6.32)$$

Let  $U(\boldsymbol{\rho}) = \sum_{m,n} \delta(\boldsymbol{\rho} - \boldsymbol{\rho}_{mn})$ , where  $U(\boldsymbol{\rho})$  is a comb function. According to Equation (6.24), the structure factor can be written as

$$\begin{aligned} F(\mathbf{k}) &= \int D(\boldsymbol{\rho}, z) f e^{-i\mathbf{k}\cdot\mathbf{r}} d\mathbf{r} \\ &= \int U(\boldsymbol{\rho}) f(\boldsymbol{\rho}) \delta(z - hc) e^{-ik_{\perp}z} e^{-i\mathbf{k}_{||}\cdot\boldsymbol{\rho}} dz d\boldsymbol{\rho} \\ &= \int U(\boldsymbol{\rho}) f(\boldsymbol{\rho}) e^{-ik_{\perp}hc} e^{-i\mathbf{k}_{||}\cdot\boldsymbol{\rho}} d\boldsymbol{\rho}. \end{aligned} \quad (6.33)$$

Equation (6.33) clearly demonstrates that there are three factors, the comb function  $U(\boldsymbol{\rho})$ , the atomic factor  $f$ , and the surface morphology  $h(\boldsymbol{\rho})$ , that would affect the structure factor of a discrete surface. The comb function  $U(\boldsymbol{\rho})$  represents the lattice positions and the symmetry of a two-dimensional lattice. According to the Fourier transform property of the comb function, the effect of a Fourier transform of the product of a comb function and another arbitrary function is to change the Fourier integral into a Fourier series with the periods determined by the comb function. The atomic factor  $f$  reflects the uniformity across the surface and would modify the amplitude of the structure factor. If the surface is uniform,  $f$  is a constant, then the structure factor is determined by both  $U(\boldsymbol{\rho})$  and  $h(\boldsymbol{\rho})$ . If the surface is non-uniform, then  $f$  is a function of surface position, and the  $f$  must be taken into account in the structure factor. The surface morphology  $h(\boldsymbol{\rho})$  causes a phase change  $e^{-ik_{\perp}h(\boldsymbol{\rho})c}$  in the structure factor. Note that this phase change is a function of  $k_{\perp}$ , the momentum transform perpendicular to the surface. Both  $f$  and  $h(\boldsymbol{\rho})$  determine the interference behavior of the scattered waves from a surface.

The scattered intensity can be written as

$$\begin{aligned} S(\mathbf{k}) &\propto F^*(\mathbf{k})F(\mathbf{k}) \\ &= \int \int U(\boldsymbol{\rho})U(\boldsymbol{\rho}')f(\boldsymbol{\rho})f(\boldsymbol{\rho}')e^{ik_{\perp}c[h(\boldsymbol{\rho}')-h(\boldsymbol{\rho})]}e^{i\mathbf{k}_{||}\cdot(\boldsymbol{\rho}'-\boldsymbol{\rho})}d\boldsymbol{\rho}d\boldsymbol{\rho}'. \end{aligned} \quad (6.34)$$

Letting  $\mathbf{r} = \boldsymbol{\rho}' - \boldsymbol{\rho}$ , then Equation (6.34) can be written as

$$S(\mathbf{k}) \propto \int \left( \int U(\boldsymbol{\rho})U(\mathbf{r} + \boldsymbol{\rho})f(\boldsymbol{\rho})f(\mathbf{r} + \boldsymbol{\rho})e^{ik_{\perp}c[h(\mathbf{r} + \boldsymbol{\rho}) - h(\boldsymbol{\rho})]} d\boldsymbol{\rho} \right) e^{i\mathbf{k}_{||} \cdot \mathbf{r}} d\mathbf{r}. \quad (6.35)$$

The integral in parentheses is a function of  $k_{\perp}$  and the lateral position vector  $\mathbf{r}$  and can be simplified as

$$\begin{aligned} & \int U(\boldsymbol{\rho})U(\mathbf{r} + \boldsymbol{\rho})f(\boldsymbol{\rho})f(\mathbf{r} + \boldsymbol{\rho})e^{ik_{\perp}c[h(\mathbf{r} + \boldsymbol{\rho}) - h(\boldsymbol{\rho})]} d\boldsymbol{\rho} \\ &= \sum_{m,n} U(\mathbf{r} + \boldsymbol{\rho}_{mn})f(\boldsymbol{\rho}_{mn})f(\mathbf{r} + \boldsymbol{\rho}_{mn})e^{ik_{\perp}c[h(\mathbf{r} + \boldsymbol{\rho}_{mn}) - h(\boldsymbol{\rho}_{mn})]} \\ &= U(\mathbf{r}) \sum_{m,n} f(\boldsymbol{\rho}_{mn})f(\mathbf{r} + \boldsymbol{\rho}_{mn})e^{ik_{\perp}c[h(\mathbf{r} + \boldsymbol{\rho}_{mn}) - h(\boldsymbol{\rho}_{mn})]}. \end{aligned} \quad (6.36)$$

Here we use the identity,  $U(\mathbf{r} + \boldsymbol{\rho}_{mn}) = U(\mathbf{r})$ . We can define a general correlation function  $G_d(k_{\perp}, \mathbf{r})$ ,

$$G_d(k_{\perp}, \mathbf{r}) = \frac{1}{N} \sum_{m,n} f(\boldsymbol{\rho}_{mn})f(\mathbf{r} + \boldsymbol{\rho}_{mn})e^{ik_{\perp}c[h(\mathbf{r} + \boldsymbol{\rho}_{mn}) - h(\boldsymbol{\rho}_{mn})]}, \quad (6.37)$$

which represents the correlation of the uniformity and morphology of a surface. Here  $N$  is the total number of scatterers on the surface. The diffraction intensity can be rewritten as

$$S(\mathbf{k}) \propto N \int U(\mathbf{r})G_d(k_{\perp}, \mathbf{r})e^{i\mathbf{k}_{||} \cdot \mathbf{r}} d\mathbf{r}. \quad (6.38)$$

Applying the following identity,

$$U(\boldsymbol{\rho}) = \sum_{m,n} \delta(\boldsymbol{\rho} - \boldsymbol{\rho}_{mn}) = \frac{1}{v} \sum_{m,n} e^{-i\mathbf{K}_{pq} \cdot \boldsymbol{\rho}}, \quad (6.39)$$

where  $v = |\mathbf{a} \times \mathbf{b}|$  is the area of a real-space unit cell and  $\mathbf{K}_{pq} = p\mathbf{k}_a + q\mathbf{k}_b$  is the reciprocal-lattice vector, where  $\mathbf{k}_a = 2\pi \frac{\mathbf{b} \times \hat{\mathbf{n}}}{\mathbf{a} \cdot (\mathbf{b} \times \hat{\mathbf{n}})}$  and  $\mathbf{k}_b = 2\pi \frac{\hat{\mathbf{n}} \times \mathbf{a}}{\mathbf{a} \cdot (\mathbf{b} \times \hat{\mathbf{n}})}$  are the reciprocal basis vectors. The diffraction intensity can finally be written as

$$S(\mathbf{k}) \propto \frac{N}{v} \sum_{p,q} \int G_d(k_{\perp}, \mathbf{r})e^{i(\mathbf{k}_{||} - \mathbf{K}_{pq}) \cdot \mathbf{r}} d\mathbf{r}. \quad (6.40)$$

This structure factor is a periodic function, with its period and symmetry determined by the basis vectors of the reciprocal lattice. The shape of the diffraction beam is determined by the Fourier integral in Equation (6.40).

If the surface is uniform, i.e., only one kind of atom exists on the surface, then  $f(\boldsymbol{\rho}) = f(\mathbf{r} + \boldsymbol{\rho}_{mn}) = f$ . We can define a height difference function

$C_d(k_\perp, \mathbf{r})$ ,

$$C_d(k_\perp, \mathbf{r}) = \frac{1}{N} \sum_{m,n} e^{ik_\perp c[h(\mathbf{r} + \boldsymbol{\rho}_{mn}) - h(\boldsymbol{\rho}_{mn})]}, \quad (6.41)$$

which represents the characteristics of a surface. In general,  $C_d(k_\perp, \mathbf{r})$  is a function of both the surface position  $\mathbf{r}$  and the momentum transfer perpendicular to the surface,  $k_\perp$ . The diffraction intensity can be expressed as

$$S(\mathbf{k}) \propto \frac{f^2}{v} \sum_{p,q} \int C_d(k_\perp, \mathbf{r}) e^{i(\mathbf{k}_{||} - \mathbf{K}_{pq}) \cdot \mathbf{r}} d\mathbf{r}. \quad (6.42)$$

If the surface is flat, but non-uniform, we can define a non-uniform correlation function  $R_d(\mathbf{r})$ ,

$$R_d(\mathbf{r}) = \frac{1}{N} \sum f(\boldsymbol{\rho}) f(\boldsymbol{\rho} + \mathbf{r}), \quad (6.43)$$

which reflects the non-uniformity of a surface. Note that, unlike the height difference function  $C_d(k_\perp, \mathbf{r})$ ,  $R_d(\mathbf{r})$  is a function of only the surface position  $\mathbf{r}$ . We see that it is this difference that allows us to differentiate the diffraction contribution of the non-uniformity from the diffraction contribution of the surface morphology. The diffraction intensity for a non-uniform and flat surface is then

$$S(\mathbf{k}) \propto \frac{1}{v} \sum_{p,q} \int R_d(\mathbf{r}) e^{i(\mathbf{k}_{||} - \mathbf{K}_{pq}) \cdot \mathbf{r}} d\mathbf{r}. \quad (6.44)$$

This intensity is a function of only  $\mathbf{k}_{||}$ .

### 6.3.2 Diffraction structure factor for a continuous surface

If we consider a non-crystalline surface, for example, an amorphous surface, which has no long-range order, then we treat the surface approximately as if it is continuous. Another case is that the wavelength of an incident beam is much longer than the lattice constant of a crystal. The wave cannot “see” individual atoms on the crystal, and then we need only to treat the surface as continuous. For a continuous surface, the surface height can be described by a function  $z = h(\boldsymbol{\rho})$ . Accordingly the density function can be written as

$$D(\boldsymbol{\rho}, z) = \delta[z - h(\boldsymbol{\rho})]. \quad (6.45)$$

The structure factor is

$$\begin{aligned} F(\mathbf{k}) &= \int D(\boldsymbol{\rho}, z) f(\boldsymbol{\rho}) e^{-i\mathbf{k}\cdot\mathbf{r}} d\mathbf{r} \\ &= \int f(\boldsymbol{\rho}) e^{-ik_{\perp} h(\boldsymbol{\rho})} e^{-i\mathbf{k}_{||}\cdot\boldsymbol{\rho}} d\boldsymbol{\rho}. \end{aligned} \quad (6.46)$$

Unlike Equation (6.33), only two factors in Equation (6.46), the atomic factor  $f$  and the surface height  $h(\boldsymbol{\rho})$ , contribute to the structure factor. As in Equation (6.33),  $f$  modifies the amplitude of the structure factor and  $h(\boldsymbol{\rho})$  causes a phase change. In fact, for a continuous surface,  $f$  should be proportional to the local atomic density. The diffraction intensity can be expressed as

$$S(\mathbf{k}) \propto F^*(\mathbf{k}) F(\mathbf{k}) = \int \int f(\boldsymbol{\rho}) f(\boldsymbol{\rho}') e^{ik_{\perp}[h(\boldsymbol{\rho}') - h(\boldsymbol{\rho})]} e^{i\mathbf{k}_{||}\cdot(\boldsymbol{\rho}' - \boldsymbol{\rho})} d\boldsymbol{\rho} d\boldsymbol{\rho}'. \quad (6.47)$$

Letting  $\mathbf{r} = \boldsymbol{\rho}' - \boldsymbol{\rho}$ , we obtain

$$S(\mathbf{k}) \propto \int \left( \int f(\boldsymbol{\rho}) f(\mathbf{r} + \boldsymbol{\rho}) e^{ik_{\perp}[h(\mathbf{r} + \boldsymbol{\rho}) - h(\boldsymbol{\rho})]} d\boldsymbol{\rho} \right) e^{i\mathbf{k}_{||}\cdot\mathbf{r}} d\mathbf{r}. \quad (6.48)$$

Equation (6.48) is similar to Equation (6.35). Accordingly, we can define a continuous version of the general correlation function,  $G_c(k_{\perp}, \mathbf{r})$ , which reflects both non-uniformity and morphology of a surface:

$$G_c(k_{\perp}, \mathbf{r}) = \frac{1}{A} \int f(\boldsymbol{\rho}) f(\mathbf{r} + \boldsymbol{\rho}) e^{ik_{\perp}[h(\mathbf{r} + \boldsymbol{\rho}) - h(\boldsymbol{\rho})]} d\boldsymbol{\rho}, \quad (6.49)$$

where  $A$  is the area of a surface. Then the scattering intensity is proportional to the Fourier transform of the function  $G_c(k_{\perp}, \mathbf{r})$ ,

$$S(\mathbf{k}) \propto A \int G_c(k_{\perp}, \mathbf{r}) e^{i\mathbf{k}_{||}\cdot\mathbf{r}} d\mathbf{r}. \quad (6.50)$$

Unlike Equation (6.40), Equation (6.50) is a non-periodic continuous function.

For a uniform surface where  $f(\boldsymbol{\rho}) = f(\mathbf{r} + \boldsymbol{\rho}) = f$ , we can also define a height difference function,  $C_c(k_{\perp}, \mathbf{r})$

$$C_c(k_{\perp}, \mathbf{r}) = \frac{1}{A} \int e^{ik_{\perp}[h(\mathbf{r} + \boldsymbol{\rho}) - h(\boldsymbol{\rho})]} d\boldsymbol{\rho}, \quad (6.51)$$

which reflects the characteristics of the surface morphology. Here,  $C_c(k_{\perp}, \mathbf{r})$  is also a function of both surface position  $\mathbf{r}$  and the momentum transfer perpendicular to the surface,  $k_{\perp}$ . Therefore,

$$S(\mathbf{k}) \propto A f^2 \int C_c(k_{\perp}, \mathbf{r}) e^{i\mathbf{k}_{||}\cdot\mathbf{r}} d\mathbf{r}. \quad (6.52)$$

That is, the diffraction intensity is proportional to the Fourier transform of the height difference function  $C_c(k_\perp, \mathbf{r})$ .

If the surface is flat, but non-uniform, we can also define a non-uniform correlation function  $R_c(\mathbf{r})$ ,

$$R_c(\mathbf{r}) = \frac{1}{A} \int f(\rho) f(\mathbf{r} + \rho) d\rho, \quad (6.53)$$

which characterizes the non-uniformity of a surface. Like  $R_d(\mathbf{r})$  in the discrete-surface case,  $R_c(\mathbf{r})$  is a function of surface position  $\mathbf{r}$  only, not a function of the momentum transfer perpendicular to the surface  $k_\perp$ .

From the above general discussion of the diffraction from a rough surface, one immediately knows that the major task in the surface diffraction is to obtain the correlation functions  $G_d(k_\perp, \mathbf{r})$ ,  $C_d(k_\perp, \mathbf{r})$ ,  $R_d(\mathbf{r})$  defined by Equations (6.37), (6.41), and (6.43), respectively, or  $G_c(k_\perp, \mathbf{r})$ ,  $C_c(k_\perp, \mathbf{r})$ ,  $R_c(\mathbf{r})$  defined by Equations (6.49), (6.51), and (6.53), respectively. The diffraction intensity is simply proportional to the Fourier transform of those correlation functions. In Chapters 7 - 12 we will show how to obtain these characteristic correlation functions for different kinds of surfaces and how they affect the diffraction patterns. From those discussions, we can predict the diffraction pattern from the known surface characteristics, or vice versa.

#### 6.4 Diffraction from Rough Surfaces – Continuum Theory

The above discussions on diffraction are based on the kinematic theory. In this theory we assume each atom scatters independently, without interrupting its neighbors or being disturbed by other atoms. In other words, each atom acts as an independent point source, and the total scattered wave is a superposition of all the scattered waves from all individual atoms. The physical picture is clear and the derivations are straightforward. However, when atoms condense to form structures like solids or liquids, each atom cannot act independently because there are strong interactions among the atoms. These collective interactions would definitely change the physical or chemical properties of the matter as well as those of the surface diffraction. Therefore, one must consider the effects of the collective behavior. There are two ways to include collective effects. One way is to start from classical physics, solving the boundary-condition problems for the Maxwell equations in electrodynamics, which is a popular way in optics. The other is to solve the boundary-value problems of the Schrödinger equation in quantum mechanics. Both cases involve solving the wave equations. One might ask: What are the relationships between Equations (6.40) and (6.50) and

those derived from Maxwell equations or the Schrödinger equation? Are Equations (6.40) and (6.50) adequate to describe all the elastic diffraction phenomena? In this section, we shall give a brief outline of the treatment from the continuous equations and show that Equations (6.40) and (6.50) in fact are quite general under certain conditions. For simplicity, only the scalar theory will be considered.

#### 6.4.1 Perturbation methods

In this method, one assumes that the fluctuation of the surface height  $h$  is very small. The scattered field caused by the fluctuation can be treated as a perturbation of the scattered field by a smooth plane. The total electric field can be written as [6.4]

$$E = E_0 + E_d, \quad (6.54)$$

where  $E_0$  is the incident field and  $E_d$  is the scattered field. As  $|h| \ll 1$ , the scattered field  $E_d$  can be expressed as

$$E_d = E_{d0} + \varepsilon E_{d1} + \varepsilon^2 E_{d2} + \dots, \quad (6.55)$$

where  $\varepsilon \sim \max(|h|)$ . The field  $E$  satisfies the wave equation (Helmholtz equation):

$$\nabla^2 E + k^2 E = 0. \quad (6.56)$$

Substituting Equations (6.54) and (6.55) into Equation (6.56), one has

$$(\nabla^2 + k^2)(E_0 + E_{d0} + \varepsilon E_{d1} + \varepsilon^2 E_{d2} + \dots) = 0. \quad (6.57)$$

In Equation (6.57), equating terms of the same order in  $\varepsilon$  gives

$$(\nabla^2 + k^2)(E_0 + E_{d0}) = 0, \text{ (zeroth-order approximation)}, \quad (6.58)$$

$$(\nabla^2 + k^2)E_{d1} = 0, \text{ (1st-order approximation)}, \quad (6.59)$$

$$(\nabla^2 + k^2)E_{d2} = 0, \text{ (2nd-order approximation)}, \quad (6.60)$$

⋮

One can see that for the order of approximation higher than the 1st-order approximation, all the perturbed fields satisfy the same wave equation. To solve these equations, one needs to know the boundary conditions.

Here we consider only Dirichlet boundary conditions:

$$E(x, y, h) = E(x, y, \varepsilon h') = 0, \quad (6.61)$$

where  $h' = h/\varepsilon$ . Equation (6.61) shows that the electric field at the surface is zero. This corresponds to a perfect conductor. The solutions for other boundary conditions, such as Neumann boundary conditions or mixed boundary conditions, can be found in Ogilvy's book [6.4].

When  $\varepsilon$  is small, one can expand Equation (6.61) into a Taylor series:

$$E(x, y, 0) + \varepsilon h' \frac{\partial E}{\partial z} \Big|_{z=0} + \varepsilon^2 h'^2 \frac{\partial^2 E}{\partial z^2} \Big|_{z=0} + \dots = 0. \quad (6.62)$$

Substituting Equations (6.54) and (6.55) into Equation (6.62) and equating terms of the same order in  $\varepsilon$ , one can obtain the following boundary conditions for the perturbation fields,

$$E_{d0}(x, y, 0) = -E_0(x, y, 0), \quad (6.63)$$

$$E_{d1}(x, y, 0) = -h' \left[ \frac{\partial E_0}{\partial z} \Big|_{z=0} + \frac{\partial E_{d0}}{\partial z} \Big|_{z=0} \right], \quad (6.64)$$

$$E_{d2}(x, y, 0) = -h'^2 \left[ \frac{\partial^2 E_0}{\partial z^2} \Big|_{z=0} + \frac{\partial^2 E_{d0}}{\partial z^2} \Big|_{z=0} \right] - h' \frac{\partial E_{d1}}{\partial z} \Big|_{z=0}, \quad (6.65)$$

⋮

Combining Equations (6.58) and (6.63), one can see that the zeroth-order approximation is the solution for the diffraction from a smooth surface. Next we consider the solutions for the higher-order perturbed terms. According to Green's theorem, the solution of the Helmholtz equation can be expressed as the following integral form

$$E_{dn}(\mathbf{r}) = \int_{\Sigma} [E_{dn}(\mathbf{r}') \frac{\partial G_g(\mathbf{r}, \mathbf{r}')}{\partial n} - G_g(\mathbf{r}, \mathbf{r}') \frac{\partial E_{dn}(\mathbf{r}')}{\partial n}] d\Sigma(\mathbf{r}'), \quad (6.66)$$

where  $\Sigma$  is the scattered surface,  $\hat{\mathbf{n}}$  is the outer normal direction of the scattered surface,  $\mathbf{r}'$  is the location of the scattered surface, and  $G_g(\mathbf{r}, \mathbf{r}')$  is Green's function satisfying the same boundary conditions. For the Dirichlet boundary problem, we can choose Green's function  $G_g(\mathbf{r}, \mathbf{r}')$ , which satisfies the following condition:

$$G_g(\mathbf{r}, \mathbf{r}') = 0, \text{ for } \mathbf{r}' \text{ on } \Sigma. \quad (6.67)$$

Then Equation (6.66) can be simplified as

$$E_{dn}(\mathbf{r}) = \int_{\Sigma} E_{dn}(\mathbf{r}') \frac{\partial G_g(\mathbf{r}, \mathbf{r}')}{\partial n} d\Sigma(\mathbf{r}'). \quad (6.68)$$

Green's function can be obtained as

$$G_g(\mathbf{r}, \mathbf{r}') = \frac{e^{ik|\mathbf{r}-\mathbf{r}'|}}{4\pi|\mathbf{r}-\mathbf{r}'|} - \frac{e^{ik|\mathbf{r}-\mathbf{r}'+2z'\hat{\mathbf{k}}|}}{4\pi|\mathbf{r}-\mathbf{r}'+2z'\hat{\mathbf{k}}|}, \quad (6.69)$$

where  $\hat{\mathbf{k}}$  is the unit vector of  $\mathbf{k}$ . The 1st-order perturbed field can be written as

$$E_{d1} = - \int_{\Sigma} h(\mathbf{r}') \left[ \frac{\partial E_0(\mathbf{r}')}{\partial z'} \Big|_{z'=0} + \frac{\partial E_{d0}(\mathbf{r}')}{\partial z'} \Big|_{z'=0} \right] \frac{\partial G_g(\mathbf{r}, \mathbf{r}')}{\partial n} d\Sigma. \quad (6.70)$$

Letting the incident field be a monochromatic plane wave,

$$E_0(\mathbf{r}) = e^{i\mathbf{k}_0 \cdot \mathbf{r}}, \quad (6.71)$$

then the zeroth-order approximation gives

$$E_{d0}(\mathbf{r}) = e^{i\mathbf{k}_0 \cdot (\mathbf{r} - 2z\hat{\mathbf{k}})}. \quad (6.72)$$

Therefore,

$$\frac{\partial E_0(\mathbf{r}')}{\partial z'} \Big|_{z'=0} + \frac{\partial E_{d0}(\mathbf{r}')}{\partial z'} \Big|_{z'=0} = 2i(\mathbf{k}_0 \cdot \hat{\mathbf{n}}) e^{i(k_{0x}x' + k_{0y}y')}. \quad (6.73)$$

For scattering in the far field where  $kr \gg 1$ ,  $r \gg r'$ , and  $|\mathbf{r}-\mathbf{r}'| \approx r - \hat{\mathbf{r}} \cdot \mathbf{r}'$ , Green's function can be approximated by

$$\begin{aligned} \frac{\partial G_g(\mathbf{r}, \mathbf{r}')}{\partial z'} &= \frac{e^{ik|\mathbf{r}-\mathbf{r}'|}}{4|\mathbf{r}-\mathbf{r}'|} \left( ik - \frac{1}{|\mathbf{r}-\mathbf{r}'|} \right) \frac{\partial |\mathbf{r}-\mathbf{r}'|}{\partial z'} \\ &\quad - \frac{e^{ik|\mathbf{r}-\mathbf{r}'+2z'\hat{\mathbf{k}}|}}{4|\mathbf{r}-\mathbf{r}'+2z'\hat{\mathbf{k}}|} \left( ik - \frac{1}{4|\mathbf{r}-\mathbf{r}'+2z'\hat{\mathbf{k}}|} \right) \frac{\partial |\mathbf{r}-\mathbf{r}'+2z'\hat{\mathbf{k}}|}{\partial z'} \\ &\approx \frac{-ie^{ikr}}{2\pi r} (\hat{\mathbf{n}}' \cdot \mathbf{k}_s) \cos(k_{sz}h) e^{-i(k_{sx}x' + k_{sy}y')}. \end{aligned} \quad (6.74)$$

When  $k_{sz}h \ll 1$ ,  $\cos(k_{sz}h) \sim 1$ , the scattering amplitude in the 1st-order approximation can be obtained as

$$E_{d1}(\mathbf{k}) \approx -\frac{e^{ikr}}{\pi r} (\hat{\mathbf{n}}' \cdot \mathbf{k}_0)(\hat{\mathbf{n}}' \cdot \mathbf{k}_s) \int h(\boldsymbol{\rho}) e^{-i\mathbf{k}_{||} \cdot \boldsymbol{\rho}} d\boldsymbol{\rho}, \quad (6.75)$$

where  $\boldsymbol{\rho} = (x', y')$ ,  $\hat{\mathbf{n}}' = \mathbf{r}'/r'$ , and  $\mathbf{k}_{||} = (k_{sx} - k_{0x}, k_{sy} - k_{0y})$ . Since  $< h > = 0$ , the 1st-order-approximated field does not contribute to the coherent field. However, it does contribute to diffuse scattering. If we use the scattering geometry shown in Figure 6.10, then the incident wave vector

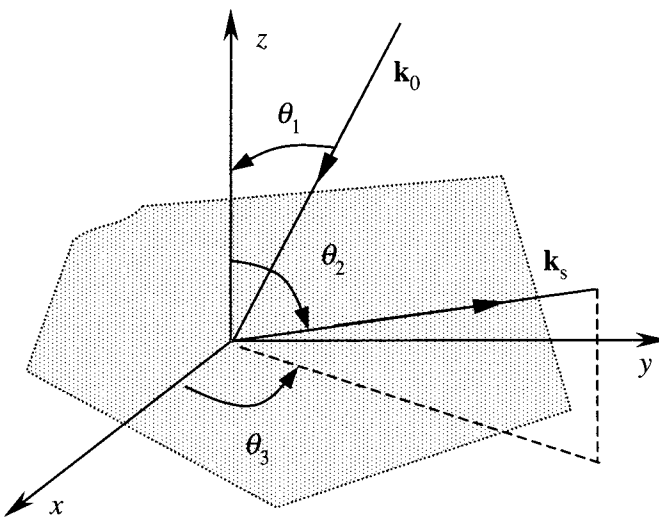


FIG. 6.10 A schematic of the scattering geometry.

$\mathbf{k}_0$  and scattering wave vector  $\mathbf{k}_s$  can be expressed as

$$\mathbf{k}_0 = k \sin \theta_1 \hat{\mathbf{i}} - k \cos \theta_1 \hat{\mathbf{k}}, \quad (6.76)$$

$$\mathbf{k}_s = k(\sin \theta_2 \cos \theta_3 \hat{\mathbf{i}} + \sin \theta_2 \sin \theta_3 \hat{\mathbf{j}} + \cos \theta_2 \hat{\mathbf{k}}), \quad (6.77)$$

and

$$\mathbf{k}_{||} = k(\sin \theta_2 \cos \theta_3 - \sin \theta_1) \hat{\mathbf{i}} + k \sin \theta_2 \sin \theta_3 \hat{\mathbf{j}}, \quad (6.78)$$

$$\hat{\mathbf{n}} \cdot \mathbf{k}_0 = k \cos \theta_1, \quad \hat{\mathbf{n}}' \cdot \mathbf{k}_s = k \cos \theta_2. \quad (6.79)$$

The average intensity caused by the 1st-order approximation is

$$\begin{aligned} < I_{d1} > &= < E_{d1} E_{d1}^* > \\ &= \frac{k^4 \cos^2 \theta_1 \cos^2 \theta_2}{(\pi r)^2} \int \int G(\rho - \rho') e^{i\mathbf{k}_{||} \cdot (\rho - \rho')} d\rho d\rho' \\ &= \frac{4k^4 \cos^2 \theta_1 \cos^2 \theta_2}{r^2} AP(\mathbf{k}_{||}). \end{aligned} \quad (6.80)$$

Here  $G(\rho - \rho')$  is the auto-covariance function of the surface defined as  $G(\rho - \rho') = < h(\rho - \mathbf{r}) h(\rho' - \mathbf{r}) >$ ,  $A$  is the area of the scattered surface, and  $P(\mathbf{k}_{||})$  is the surface power spectrum. Equation (6.80) demonstrates that the scattered field is proportional to the surface power spectrum, which is the same result as Equation (6.52) for small surface roughness, as we shall see later. The only difference is that we have an angular-dependent

amplitude. However, if we look back at Equation (6.6) for the radiation of a single electron, we can also find an angular factor,  $\sin \varphi$ , which was not included in our discussions in Sections 6.2 and 6.3. Later we will see that Equation (6.80) is equivalent to Equation (6.52) for  $k_{\perp} w \rightarrow 0$ .

One can follow exactly the same method to solve the 2nd-order or higher-order approximations. For detailed information, please refer to Reference [6.4].

#### 6.4.2 Kirchhoff approximation and Fraunhofer diffraction

It is well known that the Kirchhoff formula is the foundation of physical optics and has wide applications in optical refraction and diffraction. The physical basis for the Kirchhoff formula is the Huygens' principle, which considers the light propagation as a wave. We recall the Huygens' principle from college physics [6.5]: "All points on a wave front serve as point sources of spherical secondary wavelets. After a time  $t$ , the new position of the wave front will be the surface of tangency to these secondary wavelets." This is in fact very similar to the diffraction of an array of atoms that we considered in the previous section: every atom in the atomic array can be considered as a point source. It radiates the spherical secondary wavelets. The electrical fields detected are the coherent summation of these wavelets. Therefore, one might ask the question: Is the Kirchhoff formula, which describes the Huygens' principle for light propagation, the same as the kinematic approximation, which describes the diffraction field far from a surface?

As we try to answer this question, we will find the difference between the Kirchhoff approximation and the kinematic approximation. If we assume that the incident wave is a monochromatic plane wave, for the kinematic approximation, every atom on the surface (if the surface is uniform) radiates the same spherical wavelet, except for the phase difference, which is caused by the difference in relative surface positions and surface heights. However, in the optical case, if the surface is rough, and one stands on the surface, one can see that at different places the incident light directs onto the surface with different incident angles. According to Fresnel relations, the reflection coefficients at different places are different, except in the case of perfect reflection. The variation in surface heights and positions will also modulate the phase of the reflected wave as well. Therefore, both the amplitude and the phase of a diffracted field can be modulated by the surface morphology, and the Kirchhoff approximation should predict these two effects. In the following, we outline the Kirchhoff approximation for wave diffraction from

rough surfaces.

The formulation of problem is the same as Section 6.4.1, the total scattered field  $E$  as expressed in Equation (6.54) satisfies the wave equation [Equation (6.56)]. Applying Green's theorem, one obtains the general solution for  $E$  in an integral form [6.6]:

$$E(\mathbf{r}) = E_0(\mathbf{r}) + \int_{\Sigma'} [E_d(\mathbf{r}') \frac{\partial G_g(\mathbf{r}, \mathbf{r}')}{\partial \hat{\mathbf{n}}'} - G_g(\mathbf{r}, \mathbf{r}') \frac{\partial E_d(\mathbf{r}')}{\partial \hat{\mathbf{n}}'}] d\Sigma', \quad (6.81)$$

where  $\mathbf{r}$  is the position of the detector for measuring the diffraction field and  $\mathbf{r}'$  is the surface position. The integral is over the surface  $\Sigma'$ ,  $\hat{\mathbf{n}}'$  is the surface normal pointing toward the source, and  $G_g(\mathbf{r}, \mathbf{r}')$  is Green's function:

$$G_g(\mathbf{r}, \mathbf{r}') = \frac{e^{ik|\mathbf{r}-\mathbf{r}'|}}{4\pi|\mathbf{r}-\mathbf{r}'|}. \quad (6.82)$$

Following the treatment of Beckmann [6.6], the diffraction field can be expressed as

$$E_d(\mathbf{r}) = E(\mathbf{r}) - E_0(\mathbf{r}) = \int_{\Sigma'} [E(\mathbf{r}') \frac{\partial G_g(\mathbf{r}, \mathbf{r}')}{\partial \hat{\mathbf{n}}'} - G_g(\mathbf{r}, \mathbf{r}') \frac{\partial E(\mathbf{r}')}{\partial \hat{\mathbf{n}}'}] d\Sigma'. \quad (6.83)$$

Assuming a monochromatic incident plane wave,  $E_0(\mathbf{r}) = e^{i\mathbf{k}_0 \cdot \mathbf{r}}$ , and local reflection coefficient  $R_{ref}(\mathbf{r}')$ , then the total field near this rough surface can be approximated by

$$E(\mathbf{r}') = [1 + R_{ref}(\mathbf{r}')] e^{i\mathbf{k}_0 \cdot \mathbf{r}'}, \quad (6.84)$$

$$\frac{\partial E(\mathbf{r}')}{\partial \hat{\mathbf{n}}'} = i(\mathbf{k}_0 \cdot \hat{\mathbf{n}}') [1 - R_{ref}(\mathbf{r}')] e^{i\mathbf{k}_0 \cdot \mathbf{r}'}. \quad (6.85)$$

At far field, Green's function can be approximated using the same method as in Equation (6.74):

$$G_g(\mathbf{r}, \mathbf{r}') \approx \frac{e^{ikr}}{4\pi r} e^{-i\mathbf{k}_s \cdot \mathbf{r}'}. \quad (6.86)$$

$$\begin{aligned} \frac{\partial G_g(\mathbf{r}, \mathbf{r}')}{\partial z'} &= \frac{e^{ik|\mathbf{r}-\mathbf{r}'|}}{4|\mathbf{r}-\mathbf{r}'|} \left( ik - \frac{1}{|\mathbf{r}-\mathbf{r}'|} \right) \frac{\partial |\mathbf{r}-\mathbf{r}'|}{\partial z'} \\ &\approx \frac{-ie^{ikr}}{4\pi r} (\hat{\mathbf{n}}' \cdot \mathbf{k}_s) e^{-i\mathbf{k}_s \cdot \mathbf{r}'}. \end{aligned} \quad (6.87)$$

Substituting Equations (6.84) – (6.87) into Equation (6.83), we have

$$E_d(\mathbf{r}) = -\frac{ie^{ikr}}{4\pi r} \int_{\Sigma'} [(R_{ref}\mathbf{k} + \mathbf{k}_0 + \mathbf{k}_s) \cdot \hat{\mathbf{n}}'] e^{-i\mathbf{k} \cdot \mathbf{r}'} d\Sigma', \quad (6.88)$$

where  $\mathbf{k} = \mathbf{k}_s - \mathbf{k}_0$ , is the momentum transfer of the diffraction. If a surface is rough, then

$$\hat{\mathbf{n}}' = \frac{-\frac{\partial h}{\partial x'} \hat{\mathbf{i}} - \frac{\partial h}{\partial y'} \hat{\mathbf{j}} + \hat{\mathbf{k}}}{\sqrt{1 + (\frac{\partial h}{\partial x'})^2 + (\frac{\partial h}{\partial y'})^2}}, \quad (6.89)$$

$$d\Sigma' = \sqrt{1 + (\frac{\partial h}{\partial x'})^2 + (\frac{\partial h}{\partial y'})^2} dx' dy'. \quad (6.90)$$

Equation (6.88) can be finally written as

$$E_d(\mathbf{r}) = \frac{ie^{ikr}}{4\pi r} \int_{\Sigma'} (A \frac{\partial h}{\partial x'} + B \frac{\partial h}{\partial y'} - C) e^{-i\mathbf{k}_{||}\cdot\boldsymbol{\rho}} e^{-ik_{\perp}h(\boldsymbol{\rho})} d\boldsymbol{\rho}, \quad (6.91)$$

where for the scattering geometry shown in Figure 6.10, we have

$$\begin{aligned} A &= (1 - R_{ref}) \sin \theta_1 + (1 + R) \sin \theta_2 \cos \theta_3, \\ B &= (1 + R_{ref}) \sin \theta_2 \sin \theta_3, \\ C &= (1 + R_{ref}) \cos \theta_2 - (1 - R) \cos \theta_1 \end{aligned} \quad (6.92)$$

and  $\mathbf{k}_{||}$  is defined by Equation (6.78) and  $k_{\perp}$  is defined as  $k_{\perp} = k(\cos \theta_1 + \cos \theta_2)$ . Equation (6.91) is the general formula of Kirchhoff approximation of diffraction from a rough surface. This equation is similar to Equation (6.46) except that the atomic factor in Equation (6.46) changes into factors related to local surface slopes and the reflection coefficients. Also we should mention that the far field diffraction is usually called Fraunhofer diffraction in optics.

#### 6.4.3 Distorted-wave Born approximation (DWBA)

Essentially the objective of a scattering problem for matter wave is to solve the wave equation:

$$(\nabla^2 + k^2)\psi(\mathbf{r}) = U(\mathbf{r})\psi(\mathbf{r}), \quad (6.93)$$

under certain boundary conditions. In most cases, as explained in Section 6.1.2, one can transform the partial differential equation into an integral equation using the Green's function method, such as what was done in Sections 6.4.1 and 6.4.2. One simple way is to use the free-space Green's function and expressing Equation (6.93) as

$$\psi(\mathbf{r}) = e^{i\mathbf{k}\cdot\mathbf{r}} - \frac{1}{4\pi} \int \frac{e^{i\mathbf{k}|\mathbf{r}-\mathbf{r}'|}}{|\mathbf{r}-\mathbf{r}'|} U(\mathbf{r}') \psi(\mathbf{r}') d\mathbf{r}'. \quad (6.94)$$

If we replace the exact wave function  $\psi(\mathbf{r}')$  by a plane wave  $e^{i\mathbf{k}\cdot\mathbf{r}'}$ , then we obtain the Born approximation, as already demonstrated in Section 6.1.2. The criteria for the Born approximation are that the potential energy is much less than the kinetic energy of an incident particle (so that the potential can be treated as a perturbation) and that the scattering amplitude is correspondingly small. These criteria may not always hold. Therefore it is often possible to use a generalized form of the Born approximation, called distorted-wave Born approximation (DWBA), to treat some of the problems [6.2, 6.7]. This is usually done in the following way.

We assume that the potential  $U$  can be broken into two parts, where  $U_0$  is close to  $U$  and  $U_1$  is small compared to  $U_0$ . If the wave equation for  $U_0$  by itself is exactly solvable, then instead of using the integral equation in the form of a plane wave plus a scattered wave, as discussed in Equation (6.94), we can use an equivalent equation:

$$\psi(\mathbf{r}) = \chi(\mathbf{r}) + \frac{1}{4\pi} \int G_g(\mathbf{r}, \mathbf{r}') U_1(\mathbf{r}') \psi(\mathbf{r}') d\mathbf{r}'. \quad (6.95)$$

Here the distorted wave  $\chi(\mathbf{r})$  is the exact solution of

$$(\nabla^2 + k^2) \chi(\mathbf{r}) = U_0(\mathbf{r}) \chi(\mathbf{r}), \quad (6.96)$$

and Green's function satisfies

$$(\nabla^2 + k^2 - U_0(\mathbf{r})) G_g(\mathbf{r}, \mathbf{r}') = \delta(\mathbf{r} - \mathbf{r}'). \quad (6.97)$$

If  $U_1$  is sufficiently small, we can iterate Equation (6.95) and keep only the first term in the iteration process,

$$\psi(\mathbf{r}) \approx \chi(\mathbf{r}) + \frac{1}{4\pi} \int G_g(\mathbf{r}, \mathbf{r}') U_1(\mathbf{r}') \chi(\mathbf{r}') d\mathbf{r}'. \quad (6.98)$$

This is the result of DWBA. Now let us apply this general formalism to the scattering from a rough surface [6.8]. In this case, we have

$$U_0 = k_c^2 \theta(-z) \quad (6.99)$$

and

$$U_1 = k_c^2 \{ \theta[h(\rho) - z] \theta(z) - \theta[z - h(\rho)] \theta(-z) \}, \quad (6.100)$$

where  $k_c^2 = k^2(1 - n^2)$ ,  $n$  is the refractive index, and  $\theta(z)$  is the unit step function. We can see that the potential is decomposed into two parts: the ideal surface, which is in the  $x$ - $y$  plane, described by the potential  $U_0$ , and

the surface roughness, described by a perturbation  $U_1$ . The Fresnel theory yields the exact eigenstate for wave scattered from a planar surface:

$$\chi(\mathbf{r}) = e^{i\mathbf{k}_{0||}\cdot\boldsymbol{\rho}} \begin{cases} e^{ik_{0\perp}z} + R_{ref} e^{-ik_{0\perp}z}, & \text{if } z > 0, \\ Te^{i\tilde{\mathbf{k}}_{0\perp}z}, & \text{if } z < 0, \end{cases} \quad (6.101)$$

where  $\mathbf{k}_0 = (\mathbf{k}_{0||}, k_{0\perp})$  is the incoming plane wave vector and  $\tilde{\mathbf{k}}_0$  is the wave vector transmitted into a medium. The Fresnel reflectivity  $R_{ref}$  and transmissivity  $T$  are given by

$$R_{ref} = \frac{2k_\perp}{k_\perp + \tilde{k}_\perp}, \text{ and } T = \frac{k_\perp - \tilde{k}_\perp}{k_\perp + \tilde{k}_\perp}. \quad (6.102)$$

In the far field, Green's function can be approximated by

$$G_g(\mathbf{r}, \mathbf{r}') \approx -\frac{e^{ikr}}{4\pi r} \chi(\mathbf{r}, -\mathbf{k}_s), \text{ for } z \rightarrow \infty. \quad (6.103)$$

Then, Equation (6.98) becomes

$$\psi(\mathbf{r}) \approx \chi(\mathbf{r}) - \frac{e^{ikr}}{4\pi r} \int \chi(\mathbf{r}', -\mathbf{k}_s) U_1(\mathbf{r}') \chi(\mathbf{r}', \mathbf{k}_0) d\mathbf{r}'. \quad (6.104)$$

Since the DWBA is valid only for small roughness, and the solution  $\chi$  of the unperturbed system is continuous at  $z = 0$ , we can make the following approximations: The field above the  $x$ - $y$  plane but inside the medium is given by the transmitted part of the Fresnel solution. Therefore, we may substitute  $\chi(\mathbf{r}', -\mathbf{k}_s)$  and  $\chi(\mathbf{r}', \mathbf{k}_0)$  by  $T_s e^{-i\tilde{\mathbf{k}}_s \cdot \mathbf{r}}$  and  $T_0 e^{-i\tilde{\mathbf{k}}_0 \cdot \mathbf{r}}$ , respectively, where  $T_s$  and  $T_0$  are the Fresnel transmission coefficients for plane waves with wave vectors  $-\mathbf{k}_s$  and  $\mathbf{k}_0$ , respectively. The scattered wave can be written as

$$\psi(\mathbf{r}) \approx \chi(\mathbf{r}) - \frac{e^{ikr}}{4\pi r} T_s T_0 \int e^{-i\mathbf{k}_{0||}\cdot\boldsymbol{\rho}'} d\boldsymbol{\rho}' \int_{-\infty}^{+\infty} U_1(r') e^{-i\tilde{k}_\perp z'} dz'. \quad (6.105)$$

Substituting  $U_1$  into Equation (6.105), we finally obtain

$$\psi_s(\mathbf{r}) = \psi(\mathbf{r}) - \chi(\mathbf{r}) \approx \frac{e^{ikr}}{4i\tilde{k}_\perp \pi r} T_s T_0 \int [e^{-i\tilde{k}_\perp h(\boldsymbol{\rho}')} - 1] e^{-i\mathbf{k}_{0||}\cdot\boldsymbol{\rho}'} d\boldsymbol{\rho}'. \quad (6.106)$$

Equation (6.106) is similar to Equation (6.46) except that there is an additional constant term in Equation (6.106), which will contribute to the specular reflection. Finally, the diffuse scattering intensity can be expressed as

$$I_{diff}(k_x) \propto \frac{|k_0^2(1-n^2)|^2}{16\pi^2} |T_s|^2 |T_0|^2 S_{diff}(k_x), \quad (6.107)$$

with

$$S_{diff}(k_x) = \frac{\exp[-(k_\perp^2 + \tilde{k}_\perp^2)w^2/2]}{|k_\perp|^2} \int \int [e^{|k_\perp|^2 H(x,y)} - 1] dx dy, \quad (6.108)$$

where  $H(x, y)$  is the height-height correlation function.

In summary, under the small-roughness assumption, all the continuum theories give consistent results with the kinematic diffraction theory, except the difference in the prefactors. Therefore, in the following chapters we will concentrate on the description of various kinds of rough surfaces by the kinematic diffraction theory. Those prefactors are determined by diffraction geometry as well as by the properties of the diffracted media. In practice, the prefactors are very important for the determination of the diffraction structure factor. We will discuss in detail those factors in Chapter 9.

## 6.5 Summary

In this chapter, we discussed the general theory of diffraction from a rough surface. First we introduced the kinematic diffraction concepts by considering the diffraction of an electron or an atom. Then we unified the description and applied those concepts to multi-atom diffraction. We showed that under the kinematic diffraction theory, the diffraction from a random rough surface is a two-dimensional Fourier transform of the general characteristic function  $G_d(k_\perp, \mathbf{r})$  or  $G_c(k_\perp, \mathbf{r})$ . We also briefly introduced the continuum diffraction theories. Those theories gave consistent results with the kinematic theories.

## References

- 6.1 J. D. Jackson, *Classical Electrodynamics*, 2nd Edition (Wiley, New York, 1975).
- 6.2 L. I. Schiff, *Quantum Mechanics*, 3rd Edition (McGraw-Hill, New York, 1968).
- 6.3 H.-N. Yang, G.-C. Wang, and T.-M. Lu, *Diffraction from Rough Surfaces and Dynamic Growth Fronts* (World Scientific, Singapore, 1993).
- 6.4 J. A. Ogilvy, *Theory of Wave Scattering from Random Rough Surfaces* (Adam Hilger, Bristol, 1991).
- 6.5 D. Halliday and R. Resnick, *Fundamentals of Physics*, 3rd Edition (Wiley, New York, 1988).
- 6.6 P. Beckmann and A. Spizzichino, *The Scattering of Electromagnetic Waves from Rough Surfaces* (Pergamon Press, Oxford, 1963).
- 6.7 L. S. Rodberg and R. M. Thaler, *Introduction to the Quantum Theory of Scattering* (Academic Press, New York, 1967).
- 6.8 S. K. Sinha, E. B. Sirota, S. Garoff, and H. B. Stanley, “X-ray and neutron scattering from rough surfaces,” *Phys. Rev. B* **38**, 2297 (1988).

## 7. DIFFRACTION FROM RANDOM ROUGH SURFACES

In the last chapter, we discussed the general theory of diffraction. As mentioned in Chapter 2, most surfaces in nature or surfaces used in research are statistically rough. How does the randomness affect the behavior of the diffraction profiles, and what statistical parameters can one obtain from those profiles? We will concentrate on answering these questions in this chapter in general. The detailed diffraction characterizations of various kinds of surfaces are given in Chapters 9 to 13.

### 7.1 General Properties of Diffraction Profiles

We consider the diffraction from uniform and continuous rough (random) surfaces. As discussed in Chapter 2, we assume that the mean surface height  $\langle h \rangle = 0$  and the surface height  $h(\mathbf{r})$  is a homogeneous, ergodic random field. As a result, the height difference function can be written as

$$C(k_{\perp}, \mathbf{r}) = \langle e^{ik_{\perp}[h(\mathbf{r}+\boldsymbol{\rho})-h(\boldsymbol{\rho})]} \rangle, \quad (7.1)$$

where  $\langle \dots \rangle$  represents the ensemble average of a surface. Let  $z(\mathbf{r}) = h(\mathbf{r} + \boldsymbol{\rho}) - h(\boldsymbol{\rho})$ , then  $z(\mathbf{r})$  is a random field. Therefore, Equation (7.1) represents the characteristic function of  $z(\mathbf{r})$ , i.e., the height difference function essentially is the characteristic function of the difference of two surface heights separated by  $\mathbf{r}$ . If the distribution of  $z(\mathbf{r})$  is known as  $P(z)$ , then Equation (7.1) becomes

$$C(k_{\perp}, \mathbf{r}) = \int e^{ik_{\perp}z} P(z) dz. \quad (7.2)$$

In order to know the distribution  $P(z)$ , one needs to obtain the joint distribution  $P_j$ . This is a general way to obtain the height difference function, which we will discuss more in Chapter 11. Now let us examine the general characteristics of the height difference function  $C(k_{\perp}, \mathbf{r})$ .

- 1)  $|\mathbf{r}| \rightarrow \infty$

When  $|\mathbf{r}| \rightarrow \infty$ , the separation between two surface heights goes to infinity, the correlation coefficient between these two points is close to zero. Then we can treat the surface heights at these two points as independent

random variables. From the homogeneity and ergodicity of a surface, the surface heights at these two points have the same distribution,  $p(h)$ :

$$C(k_{\perp}, |\mathbf{r}| \rightarrow \infty) = \langle e^{ik_{\perp}h(\mathbf{r}+\boldsymbol{\rho})} \rangle \langle e^{-ik_{\perp}h(\boldsymbol{\rho})} \rangle \quad (7.3)$$

$$\begin{aligned} &= \int e^{ik_{\perp}h} p(h) dh \int e^{-ik_{\perp}h'} p(h') dh' \\ &= |\int e^{ik_{\perp}h} p(h) dh|^2 = \varphi^2(k_{\perp}), \end{aligned} \quad (7.4)$$

where  $\varphi(k_{\perp}) = \int e^{ik_{\perp}h} p(h) dh$  is the characteristic function of the height distribution  $h$ . Equation (7.3) shows that the value of  $C(k_{\perp}, |\mathbf{r}| \rightarrow \infty)$  is the square of the height characteristic function and a function of  $k_{\perp}$ .

2)  $|\mathbf{r}| \rightarrow 0$

When  $|\mathbf{r}| \rightarrow 0$ , the two points on a surface become infinitely close, so that  $[h(\mathbf{r} + \boldsymbol{\rho}) - h(\boldsymbol{\rho})]|_{|\mathbf{r}| \rightarrow 0} \rightarrow 0$ , and  $C(k_{\perp}, |\mathbf{r}| \rightarrow 0) = 1$ .

3)  $k_{\perp}w \ll 1$

If the RMS roughness  $w$  of a surface is small, or if the momentum transfer perpendicular to a surface  $k_{\perp}$  is small so that  $k_{\perp}w \ll 1$ , then  $|k_{\perp}[h(\mathbf{r} + \boldsymbol{\rho}) - h(\boldsymbol{\rho})]| \ll 1$ , and Equation (7.1) can be expanded as

$$\begin{aligned} C(k_{\perp}, \mathbf{r}) &= \langle 1 - ik_{\perp}[h(\mathbf{r} + \boldsymbol{\rho}) - h(\boldsymbol{\rho})] - \frac{1}{2}k_{\perp}^2[h(\mathbf{r} + \boldsymbol{\rho}) - h(\boldsymbol{\rho})]^2 + \dots \rangle \\ &\approx 1 - \frac{1}{2}k_{\perp}^2 \langle [h(\mathbf{r} + \boldsymbol{\rho}) - h(\boldsymbol{\rho})]^2 \rangle = 1 - \frac{1}{2}k_{\perp}^2 H(\mathbf{r}) \\ &= 1 - k_{\perp}^2 w^2 + k_{\perp}^2 w^2 R(\mathbf{r}), \end{aligned} \quad (7.5)$$

i.e.,  $C(k_{\perp}, \mathbf{r})$  directly reflects the surface correlation. Here  $H(\mathbf{r})$  and  $R(\mathbf{r})$  are the height-height correlation function and the auto-correlation function of a surface, respectively.

According to the above discussion, in general we can decompose  $C(k_{\perp}, \mathbf{r})$  into two parts

$$C(k_{\perp}, \mathbf{r}) = C(k_{\perp}, |\mathbf{r}| \rightarrow \infty) + \Delta C(k_{\perp}, \mathbf{r}), \quad (7.6)$$

and

$$\Delta C(k_{\perp}, \mathbf{r}) = C(k_{\perp}, \mathbf{r}) - C(k_{\perp}, |\mathbf{r}| \rightarrow \infty), \quad (7.7)$$

i.e.,  $C(k_{\perp}, \mathbf{r})$  can be decomposed into a surface-position-unrelated part  $C(k_{\perp}, |\mathbf{r}| \rightarrow \infty)$  and a surface-position-closely-related part  $\Delta C(k_{\perp}, \mathbf{r})$ . Then the corresponding diffraction structure factor becomes

$$S(\mathbf{k}_{||}, k_{\perp}) = S_{\delta}(\mathbf{k}_{||}, k_{\perp}) + S_{diff}(\mathbf{k}_{||}, k_{\perp}), \quad (7.8)$$

where

$$S_\delta(\mathbf{k}_{||}, k_\perp) = (2\pi)^2 \left| \int p(h) e^{ik_\perp h} dh \right|^2 \delta(\mathbf{k}_{||}), \text{ and} \quad (7.9)$$

$$S_{diff}(\mathbf{k}_{||}, k_\perp) = \int \Delta C(k_\perp, \mathbf{r}) e^{i\mathbf{k}_{||} \cdot \mathbf{r}} d\mathbf{r}. \quad (7.10)$$

The diffraction profile consists of two parts. One is a central  $\delta$ -peak intensity  $S_\delta(\mathbf{k}_{||}, k_\perp)$ , which reflects the long-range flatness of a surface. The other is a broad diffuse profile  $S_{diff}(\mathbf{k}_{||}, k_\perp)$ , which represents the short-range roughness of a surface, especially the lateral correlation and the anisotropy. In general, these two parts are different for different surface height distributions, even when the surface correlation functions are the same. However, for  $k_\perp w \ll 1$ , we have

$$\begin{aligned} S(\mathbf{k}_{||}, k_\perp) &\approx \int [1 - k_\perp^2 w^2 + k_\perp^2 w^2 R(\mathbf{r})] e^{-i\mathbf{k}_{||} \cdot \mathbf{r}} d\mathbf{r} \\ &= (2\pi)^2 (1 - k_\perp^2 w^2) \delta(\mathbf{k}_{||}) + k_\perp^2 P(\mathbf{k}_{||}), \end{aligned} \quad (7.11)$$

where  $P(\mathbf{k}_{||})$  is the surface power spectrum. Comparing Equation (7.11) to Equations (7.8)-(7.10), one has

$$S_\delta(\mathbf{k}_{||}, k_\perp) = (2\pi)^2 (1 - k_\perp^2 w^2) \delta(\mathbf{k}_{||}), \quad (7.12)$$

$$S_{diff}(\mathbf{k}_{||}, k_\perp) = k_\perp^2 P(\mathbf{k}_{||}). \quad (7.13)$$

Therefore, the  $\delta$  peak is only a function of the RMS roughness  $w$ , while the diffuse profile contains the correlation of a surface. We should emphasize that the validity of Equations (7.12) and (7.13) is only under the condition that  $k_\perp w \ll 1$ . There is no assumption about the surface height distribution. So these equations can be generally applied to any rough surface as long as the condition  $k_\perp w \ll 1$  is satisfied.

## 7.2 Diffraction from a Gaussian Rough Surface

To see more clearly how the behavior of the height difference function  $C(k_\perp, \mathbf{r})$  affects the diffraction profile, we consider in particular a Gaussian rough surface, whose surface height obeys the Gaussian distribution:

$$p(h) = \frac{1}{\sqrt{2\pi}w} e^{-h^2/2w^2}, \quad (7.14)$$

where  $w$  is the RMS roughness. It is well known that the joint distribution of two surface heights  $h_1$  and  $h_2$  at position  $\mathbf{r} + \boldsymbol{\rho}$  and  $\boldsymbol{\rho}$ , respectively, can

be written as [7.1]

$$p_j(h_1, h_2) = \frac{1}{2w\sqrt{\pi(1-R)}} \exp\left[-\frac{h_1^2 + h_2^2 - 2h_1h_2R}{2w^2(1-R)}\right], \quad (7.15)$$

where  $R$  is the correlation coefficient between these two heights, i.e., the auto-correlation function. From the joint distribution, Equation (7.15), we can obtain the distribution of  $z = h_1 - h_2 = h(\mathbf{r} + \boldsymbol{\rho}) - h(\boldsymbol{\rho})$ ,

$$P(z) = \int p_j(h_2 + z, h_2) dh_2 = \frac{1}{2w\sqrt{\pi(1-R)}} \exp\left[-\frac{z^2}{4w^2(1-R)}\right]. \quad (7.16)$$

According to Equation (2.23),  $H(\mathbf{r}) = 2w^2[1 - R(\mathbf{r})]$ , where  $H(\mathbf{r})$  is the height-height correlation function, then Equation (7.16) can be rewritten as

$$P(z) = \frac{1}{\sqrt{2\pi H(\mathbf{r})}} \exp\left[-\frac{z^2}{2H(\mathbf{r})}\right]. \quad (7.17)$$

Substituting Equation (7.17) into Equation (7.2), we finally obtain the height difference function  $C(k_\perp, \mathbf{r})$  for a Gaussian surface,

$$C(k_\perp, \mathbf{r}) = e^{-\frac{1}{2}k_\perp^2 H(\mathbf{r})}. \quad (7.18)$$

One can see that  $C(k_\perp, \mathbf{r})$  is a Gaussian decay function of  $k_\perp$  for a fixed value of  $H(\mathbf{r})$ . This particular form of the height difference function is applicable only to a Gaussian height distribution. As we shall see in Chapter 12, other forms of height distributions lead to different height difference functions and therefore different forms of diffraction profiles.

The diffraction profile for a Gaussian surface can be written in the following form [7.2, 7.3, 7.4]:

$$S(\mathbf{k}_{||}, k_\perp) = \int e^{-\frac{1}{2}k_\perp^2 H(\mathbf{r})} e^{i\mathbf{k}_{||} \cdot \mathbf{r}} d\mathbf{r}. \quad (7.19)$$

According to Equation (2.24),  $H(|\mathbf{r}| \rightarrow \infty) = 2w^2$ , we have for a Gaussian surface,

$$C(k_\perp, |\mathbf{r}| \rightarrow \infty) = e^{-k_\perp^2 w^2}, \quad (7.20)$$

$$\Delta C(k_\perp, \mathbf{r}) = e^{-k_\perp^2 w^2} [e^{k_\perp^2 w^2 R(\mathbf{r})} - 1]. \quad (7.21)$$

If we take  $R(\mathbf{r})$  as an exponential decay function,

$$R(\mathbf{r}) = e^{-r/\xi}, \quad (7.22)$$

where  $\xi$  is the lateral correlation length defined in Equation (2.21), then we can illustrate the behaviors of  $C(k_\perp, \mathbf{r})$  and  $\Delta C(k_\perp, \mathbf{r})$  in Figure 7.1. Here

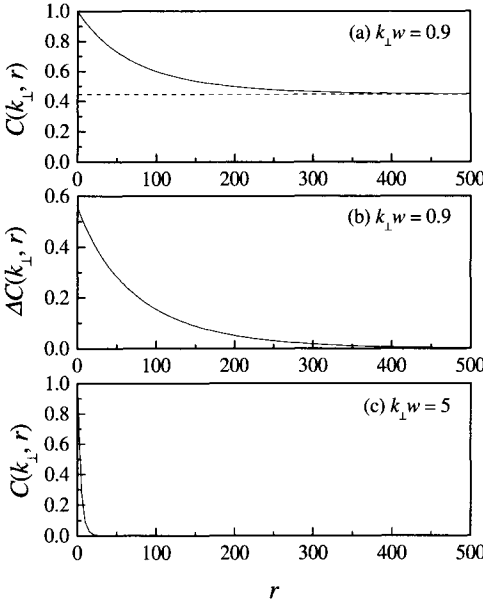


FIG. 7.1 The behaviors of height difference functions  $C(k_{\perp}, r)$ ,  $C_{\infty}(k_{\perp}, r)$ , and  $\Delta C(k_{\perp}, r)$ . (a)  $C(k_{\perp}, r)$  and  $C_{\infty}(k_{\perp}, r)$  for  $k_{\perp}w = 0.9$ . The dashed straight line represents  $C_{\infty}(k_{\perp}, r)$ . (b)  $\Delta C(k_{\perp}, r)$  for  $k_{\perp}w = 0.9$ . (c)  $C(k_{\perp}, r)$  and  $C_{\infty}(k_{\perp}, r)$  for  $k_{\perp}w = 5$ . In this case  $C_{\infty}(k_{\perp}, r) \approx 0$ . Here  $\xi = 100$  in all three cases.

we use the parameters  $k_{\perp}w = 0.9$ ,  $\xi = 100$  in Figures 7.1(a) and 7.1(b) and  $k_{\perp}w = 5$ ,  $\xi = 100$  in Figure 7.1(c). The dashed straight line parallel to the  $r$  axis,  $C_{\infty}(k_{\perp}) = C(k_{\perp}, |\mathbf{r}| \rightarrow \infty)$  is a constant background throughout the entire real-space region between  $r = 0$  and  $r \rightarrow \infty$ .  $C_{\infty}(k_{\perp})$  is thus related to the global (long-range) characteristics of the rough surface. In contrast,  $\Delta C(k_{\perp}, \mathbf{r})$  is a function equal to  $C(k_{\perp}, \mathbf{r})$  subtracted by the background  $C_{\infty}(k_{\perp})$ . As shown in Figure 7.1(b),  $\Delta C(k_{\perp}, \mathbf{r})$  quickly decays to zero at large  $r$ , and therefore is confined to the short-range regime. Figure 7.1(c) is a plot of  $C(k_{\perp}, \mathbf{r})$  with a perpendicular wave vector,  $k_{\perp}w = 5$ , larger than that of Figure 7.1(a) where  $k_{\perp}w = 0.9$ . For a large value of  $k_{\perp}w$ , since the long-range term  $C_{\infty}(k_{\perp})$  could become negligibly small, as shown in Figure 7.1(c), we have  $\Delta C(k_{\perp}, \mathbf{r}) \approx C(k_{\perp}, \mathbf{r})$ . Comparing Figure 7.1(b) with Figure 7.1(c), we notice that the extent of the short-range regime depends quite sensitively on  $k_{\perp}w$ . For a smaller  $k_{\perp}w$ , the short-range regime is larger, see Figure 7.1(b); while for a larger  $k_{\perp}w$ , as shown in Figure 7.1(c), it becomes smaller and more like a  $\delta$  function.

The diffraction profile becomes: the  $\delta$  peak,

$$S_\delta(\mathbf{k}_{||}, k_\perp) = (2\pi)^2 e^{-k_\perp^2 w^2} \delta(\mathbf{k}_{||}), \quad (7.23)$$

and the diffuse profile,

$$S_{diff}(\mathbf{k}_{||}, k_\perp) = e^{-k_\perp^2 w^2} \int [e^{k_\perp^2 w^2 R(\mathbf{r})} - 1] e^{i\mathbf{k}_{||} \cdot \mathbf{r}} d\mathbf{r}. \quad (7.24)$$

### 7.2.1 The $\delta$ peak

When a plane wave is scattered from an infinitely large and perfectly flat surface with  $w = 0$ , the diffraction profile has the shape of a sharp  $\delta$  function,

$$S_{flat}(\mathbf{k}_{||}, k_\perp) = (2\pi)^2 \delta(\mathbf{k}_{||}). \quad (7.25)$$

Compared to the  $\delta$  component in Equation (7.23) for a rough surface with the  $\delta$  function for a perfectly flat surface, the  $\delta$  component in Equation (7.23) has extra  $k_\perp$  and  $w$  dependent factors,  $C(k_\perp, |\mathbf{r}| \rightarrow \infty) = e^{-k_\perp^2 w^2}$ . The  $\delta$ -peak intensity shown above is thus proportional to a Debye-Waller-like factor, which is extremely sensitive to the global surface roughness characterized by the RMS roughness  $w$ , as well as the momentum transfer perpendicular to the surface  $k_\perp$ . The form of the  $\delta$  intensity, shown as  $(2\pi)^2 C(k_\perp, |\mathbf{r}| \rightarrow \infty) \delta(\mathbf{k}_{||})$ , implies that the existence of local defects in a rough surface cannot modify the line shape of the sharp  $\delta$  component but can significantly reduce the absolute value of the  $\delta$  intensity. One can easily verify that when  $k_\perp w \ll 1$ , the  $\delta$  peak in Equation (7.23) can be approximated by Equation (7.12).

### 7.2.2 The diffuse profile

We have shown that the diffuse profile is a measure of the short-range roughness in a rough surface. In order to show the general aspects of the diffuse profile, we rewrite Equation (7.24) as

$$S_{diff}(\mathbf{k}_{||}, k_\perp) = e^{-\Omega} \int [e^{\Omega R(\mathbf{r})} - 1] e^{i\mathbf{k}_{||} \cdot \mathbf{r}} d\mathbf{r}, \quad (7.26)$$

where  $\Omega$  is defined as  $\Omega = k_\perp^2 w^2$  and is called the Rayleigh-Strehl parameter [7.5]. In general, Equation (7.26) can be expanded as

$$S_{diff}(\mathbf{k}_{||}, k_\perp) = e^{-\Omega} \sum_{n=1}^{\infty} \frac{1}{n!} \Omega^n \int R(\mathbf{r})^n e^{i\mathbf{k}_{||} \cdot \mathbf{r}} d\mathbf{r}. \quad (7.27)$$

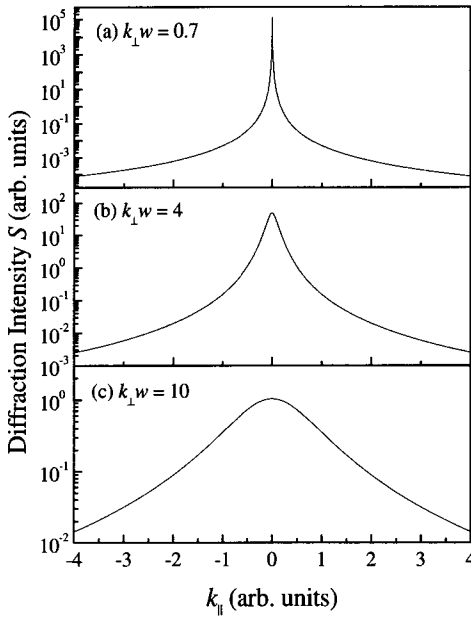


FIG. 7.2 The diffraction profiles calculated from Equation (7.19) using an exponentially-decaying correlation: (a)  $k_{\perp}w = 0.7$ , (b)  $k_{\perp}w = 4$ , and (c)  $k_{\perp}w = 10$ .

For  $\Omega \ll 1$ , Equation (7.27) reduces to

$$S_{diff}(\mathbf{k}_{||}, k_{\perp}) \approx \Omega \int R(\mathbf{r}) e^{i\mathbf{k}_{||} \cdot \mathbf{r}} d\mathbf{r} = k_{\perp}^2 P(\mathbf{k}_{||}), \quad (7.28)$$

which has the exact form of Equation (7.13). However, for  $\Omega \gg 1$ , the higher-order terms in Equation (7.27) cannot be neglected. For example, let us assume the auto-correlation function to be of exponential decay type, Equation (7.22). (Here we also assume that the surface is isotropic.) Then the diffraction profile can be directly calculated from Equation (7.19) as shown in Figure 7.2. We can see from Figure 7.2 that when  $k_{\perp}w$  is small, the diffraction profile has two parts: one is the sharp  $\delta$  peak and the other is the broad diffuse profile as shown in Figure 7.2(a). As  $k_{\perp}w$  increases, the  $\delta$  peak disappears, and the diffuse profile becomes broader as shown in Figures 7.2(b) and 7.2(c). Substituting Equation (7.22) into Equation (7.27), the diffuse profile becomes

$$S_{diff}(\mathbf{k}_{||}, k_{\perp}) = e^{-\Omega} \sum_{n=1}^{\infty} \frac{1}{n!} \Omega^n \int \exp(-n \frac{r}{\xi}) e^{i\mathbf{k}_{||} \cdot \mathbf{r}} d\mathbf{r}$$

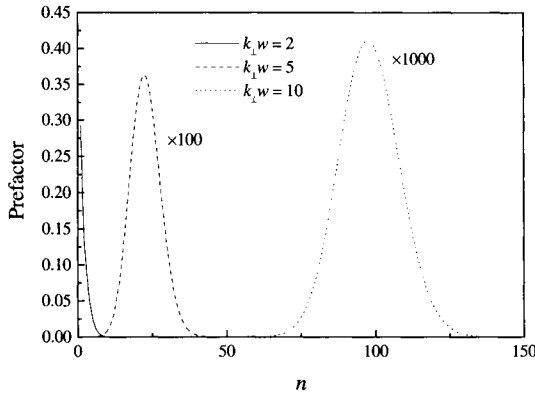


FIG. 7.3 The prefactor in each term of the summation in Equation (7.30) as a function of  $n$  for different  $k_{\perp}w$  values.

$$= 2\pi e^{-\Omega} \sum_{n=1}^{\infty} \frac{1}{n!} \Omega^n \int_0^{\infty} r \exp(-n\frac{r}{\xi}) J_0(k_{||}r) dr, \quad (7.29)$$

where  $J_0(x)$  is the zeroth-order Bessel function. Using the relation

$$\int_0^{\infty} x e^{-ax} J_0(bx) dx = \frac{a}{(a^2 + b^2)^{3/2}},$$

Equation (7.29) can be rewritten as

$$S_{diff}(\mathbf{k}_{||}, k_{\perp}) = 2\pi \xi^2 \Omega e^{-\Omega} \sum_{n=0}^{\infty} \frac{1}{n!(n+1)^3} \Omega^n Y\left(\frac{k_{||}\xi}{n+1}\right), \quad (7.30)$$

where  $Y(x) = (1+x^2)^{-3/2}$  is a two-dimensional Lorenzian function. Equation (7.30) shows that the diffuse profile for an exponentially-decaying correlation is a summation of a series of two-dimensional Lorenzian profiles, with its full width at half-maximum (FWHM) increasing as  $2\sqrt{2^{2/3} - 1} \frac{n+1}{\xi}$ . In addition, the coefficient  $\frac{1}{n!(n+1)^3} \Omega^n$  of the two-dimensional Lorenzian function  $Y(\frac{k_{||}\xi}{n+1})$  would quickly vanish as  $n > \Omega$ . Therefore, the number of the two-dimensional Lorenzian profiles,  $M$ , which contributes significantly to the diffuse profile, is finite and determined by the condition,

$$M \propto \Omega. \quad (7.31)$$

Figure 7.3 shows the prefactor  $\frac{1}{n!(n+1)^3} \Omega^{n+1} e^{-\Omega}$  as a function of  $n$  for different  $k_{\perp}w$  values. We can see that for small  $k_{\perp}w$ ,  $n = 1$  gives the maximum prefactor, and the prefactor decreases dramatically as  $n$  increases. For large  $k_{\perp}w$ , there is a value of  $N_{max}$ , at which the prefactor reaches a

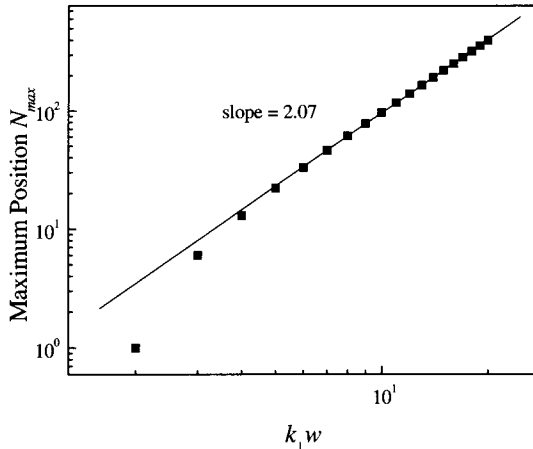


FIG. 7.4 The maximum peak position of the prefactor as a function of  $k_{\perp}w$ .

maximum. The larger the  $k_{\perp}w$  value, the greater the  $N_{max}$ . Figure 7.4 shows the maximum position  $N_{max}$  as a function of  $k_{\perp}w$ . Except for the small  $k_{\perp}w$  behavior, at large  $k_{\perp}w$ , the maximum position  $N_{max}$  is almost proportional to  $(k_{\perp}w)^2 = \Omega$ . Therefore, we can use  $N_{max}$  as a measure of  $M$ . Figure 7.5 shows the calculated diffuse profiles for  $k_{\perp}w = 10$  using the limited sum of Equation (7.30), where  $N$  is the upper cutoff of the summation. From Figure 7.4 we calculated that  $N_{max} = 97$  for  $k_{\perp}w = 10$ . Therefore, for  $N \leq N_{max}$ , the summation underestimates the diffuse profile, while for  $N > N_{max}$ , the summation gives a good estimate of the diffuse profiles. Thus, we can safely neglect all the Lorentzian terms with  $n \gg 2N_{max}$ . As  $\Omega$  becomes larger, higher-order terms should be included, and the diffuse profile becomes broader.

### 7.2.3 The integrated intensity

The total integrated intensity  $I$  can be evaluated as

$$\begin{aligned}
 I &= \int S(\mathbf{k}_{||}, k_{\perp}) d\mathbf{k}_{||} = \int \int C(k_{\perp}, \mathbf{r}) e^{i\mathbf{k}_{||} \cdot \mathbf{r}} d\mathbf{r} d\mathbf{k}_{||} \\
 &= \int C(k_{\perp}, \mathbf{r}) d\mathbf{r} \int e^{i\mathbf{k}_{||} \cdot \mathbf{r}} d\mathbf{k}_{||} = (2\pi)^2 \int C(k_{\perp}, \mathbf{r}) \delta(\mathbf{r}) d\mathbf{r} \\
 &= (2\pi)^2.
 \end{aligned} \tag{7.32}$$

The integrated  $\delta$ -peak intensity  $I_{\delta}$  is

$$I_{\delta} = \int S_{\delta}(\mathbf{k}_{||}, k_{\perp}) d\mathbf{k}_{||} = (2\pi)^2 e^{-\Omega}. \tag{7.33}$$

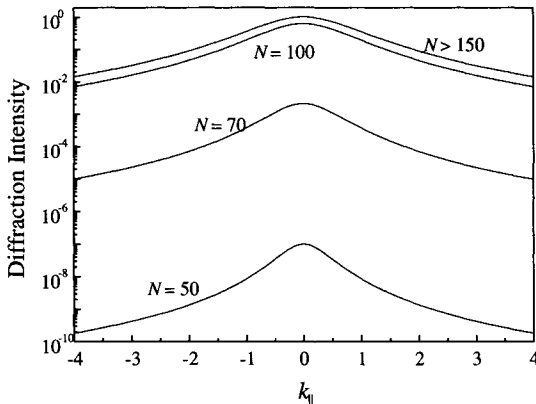


FIG. 7.5 The diffuse profiles calculated from the summation in Equation (7.30) at  $k_{\perp}w = 10$ . Here  $N$  is the upper summation limit.

Since  $S_{diff}(\mathbf{k}_{||}, k_{\perp}) = S(\mathbf{k}_{||}, k_{\perp}) - S_{\delta}(\mathbf{k}_{||}, k_{\perp})$ , the integrated diffuse intensity  $I_{diff}$  is

$$I_{diff} = (2\pi)^2(1 - e^{-\Omega}). \quad (7.34)$$

We can see that for a Gaussian surface as  $\Omega$  increases, the integrated  $\delta$ -peak intensity decreases exponentially, while the integrated diffuse intensity increases. The net result is to keep the total integrated diffraction intensity constant. The ratios of the integrated intensities,  $R_{\delta}$  and  $R_{diff}$ , can then be given by

$$R_{\delta} = \frac{I_{\delta}}{I} = e^{-\Omega} \quad (7.35)$$

and

$$R_{diff} = \frac{I_{diff}}{I} = 1 - e^{-\Omega}, \quad (7.36)$$

respectively. The exponential decay of the  $\delta$ -peak intensity ratio is the result of the characteristics of a Gaussian rough surface. A more general treatment of non-Gaussian rough surface can be found in Chapter 12.

### 7.3 Diffraction from Multi-Step Surfaces in 2+1 Dimensions

In the above discussions, we have investigated diffraction structure factors from continuous rough surfaces. A surface can be treated as a continuous surface under the condition that the wavelength of the probing wave

is much larger than the lattice constant, or if the surface under consideration is amorphous. However, when the wavelength of the incident beam is comparable to the lattice constant of a crystalline surface, or even smaller than the lattice constant, such as for x-ray scattering, electron scattering, and atom diffraction, the surface cannot be treated as a continuous surface. In this case, one must take into account the discrete nature of the surface. How does the discreteness affect the behaviors of the diffraction profiles, and what statistical parameters can one obtain from those profiles? In following sections, we will concentrate on diffraction from rough discrete surfaces. We will discuss in general how the discrete nature affects the diffraction profiles.

### 7.3.1 Height difference function of a discrete surface

For a discrete surface, the surface height can only take  $h = 0, c, 2c, 3c, \dots$ , where  $c$  is the vertical lattice constant, and the surface position  $\mathbf{r} = m\mathbf{a} + n\mathbf{b}$  where  $\mathbf{a}$  and  $\mathbf{b}$  are the basis vectors of the unit cell on the surface, and  $m, n = 0, \pm 1, \pm 2, \dots$  are integers. Because  $c$  is a constant, we can let  $d = h/c$  be a description of the surface height. In the discrete lattice case, a discrete, Gaussian height distribution does not lead to a simple form for the height difference function like Equation (7.18), but instead is given by

$$C_d(k_\perp, \mathbf{r}) = \frac{\sum_{m=-\infty}^{+\infty} e^{-\frac{1}{2}H_d(\mathbf{r})(\Phi - 2\pi m)^2}}{\sum_{m=-\infty}^{+\infty} e^{-\frac{1}{2}H_d(\mathbf{r})(2\pi m)^2}}, \quad (7.37)$$

where  $\Phi = k_\perp c$  and  $H_d(\mathbf{r}) = < [d(\mathbf{r}) - d(\mathbf{0})]^2 >$ . A more convenient height distribution that occurs more naturally in the discrete lattice case is the Poisson distribution

$$p(d = n) = \frac{e^{-\sigma}\sigma^n}{n!}, \quad (7.38)$$

which would lead to a simple form for the height difference function. Here  $\sigma$  is the average surface height and also the standard deviation of the distribution. As shown in Figure 7.6, the Poisson distribution is a skewed distribution with non-zero odd moments. As  $\sigma$  increases, the distribution becomes more symmetric and eventually would become a Gaussian distribution for a reasonably large  $\sigma$  value. Therefore the two height distribution functions give very similar results, except that the Poisson distribution can lead to a more convenient form of the height difference function. The height

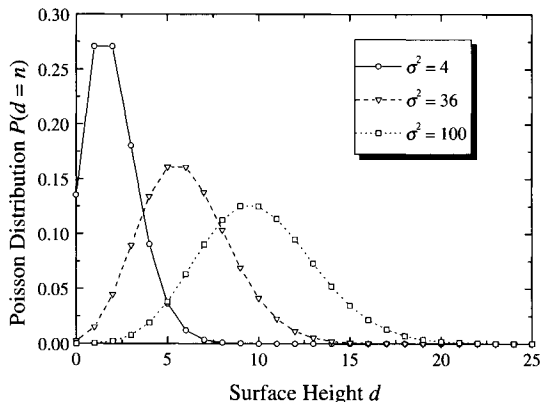


FIG. 7.6 Poisson distribution with various variances  $\sigma^2$ . Here the surface height  $d(= n)$  is in units of lattice constant (from Ref. [7.6]).

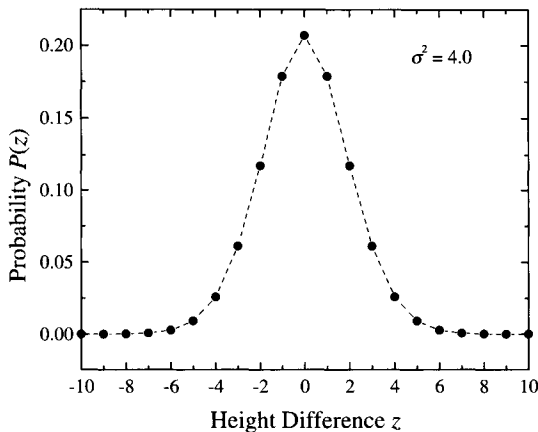


FIG. 7.7 The height difference distribution  $P(z)$  for a Poisson surface with a variance of  $\sigma^2 = 4.0$ .

difference distribution for the Poisson height distribution is

$$P(z, \mathbf{r}) = e^{-2\sigma(1-R)} I_z[2\sigma(1-R)], \quad (7.39)$$

where  $R$  is the auto-correlation function and  $I_z(x)$  is the modified Bessel function. Figure 7.7 plots the height difference distribution  $P(z)$  for a Poisson surface with a variance of 4.0. According to the discussion in Appendix E, the height difference function for a Poisson surface can be

written as [7.6]

$$C_d(k_\perp, \mathbf{r}) = e^{-H_d(\mathbf{r})(1-\cos\Phi)}. \quad (7.40)$$

Notice that  $H_d(\mathbf{r})$  has no units, but we still use  $w = \sigma$  as the RMS roughness, and the physical RMS roughness should be  $wc$ . Clearly, as shown in Equation (7.18) for the height difference function  $C_c(k_\perp, \mathbf{r})$  of a continuous surface [or other forms of  $C_c(k_\perp, \mathbf{r})$  as a result of non-Gaussian height distributions to be discussed in Chapter 12], the product  $k_\perp w$  always comes together and acts as a whole. For this case,  $C_c(k_\perp, \mathbf{r})$  is an exponentially-decaying function of  $k_\perp w$ . However, for the discrete surface, both Equation (7.37) and Equation (7.40) show that  $k_\perp$  and  $w$  act independently:  $C_d(k_\perp, \mathbf{r})$  is an exponential decay function of  $w^2$ , but is a periodic function of  $k_\perp$ . In the following, we discuss two very important aspects of the height difference function given by Equation (7.40). (Note that Equation (7.37) would exhibit quite a similar behavior [7.2, 7.3, 7.4]. For practical purposes, we can treat them as almost equivalent.)

### (i) Periodic oscillation

As an immediate result due to the periodic and discrete structure of the crystalline surface, Equation (7.40) [or Equation (7.37)] shows the reciprocal-space ( $k_\perp$ -space) periodic relations,  $C_d(k_\perp, \mathbf{r}) = C_d(k_\perp + \frac{2m\pi}{c}, \mathbf{r})$  and  $C_d(\frac{2m\pi}{c}, \mathbf{r}) = 1$ ,  $m = 0, 1, 2, \dots$  Since the relative height,  $z = [d(\mathbf{r}) - d(\mathbf{0})]$ , can only have integer values, the phase term in Equation (6.41) must have the relations,  $e^{i(\Phi+2n\pi)[d(\mathbf{r})-d(\mathbf{0})]} = e^{i\Phi[d(\mathbf{r})-d(\mathbf{0})]}$  and  $e^{i2n\pi[d(\mathbf{r})-d(\mathbf{0})]} = 1$ . Such relations do not exist in the case of a continuous surface model. To show the difference of the height difference functions between a crystalline surface and a continuous surface, we plot Equation (7.18) and Equation (7.40) as a function of  $k_\perp c/\pi$  in Figure 7.8 with a fixed parameter  $H_c(r)/c^2 = H_d(r) = 0.5$ . The continuous height difference function of Equation (7.18) monotonically decays to zero as  $k_\perp$  increases [Figure 7.8(a)]. In contrast, the discrete height difference function Equation (7.40) oscillates with a periodicity of  $2\pi/c$  [Figure 7.8(b)]. Although Figure 7.8(b) is obtained using a Poisson height distribution, the oscillatory behavior also exists for other discrete height distributions such as Gaussian distribution (for example, see Ref. [7.2, 7.3, 7.4]).

### (ii) In-phase and out-of-phase diffraction conditions

Figure 7.8(b) also shows that for a discrete surface, when  $k_\perp c = 2n\pi$ ,  $C_d(k_\perp, r)$  reaches a maximum; and when  $k_\perp c = (2n+1)\pi$ ,  $C_d(k_\perp, r)$  becomes a minimum. We call  $k_\perp c = 2n\pi$  the in-phase condition, and  $k_\perp c =$

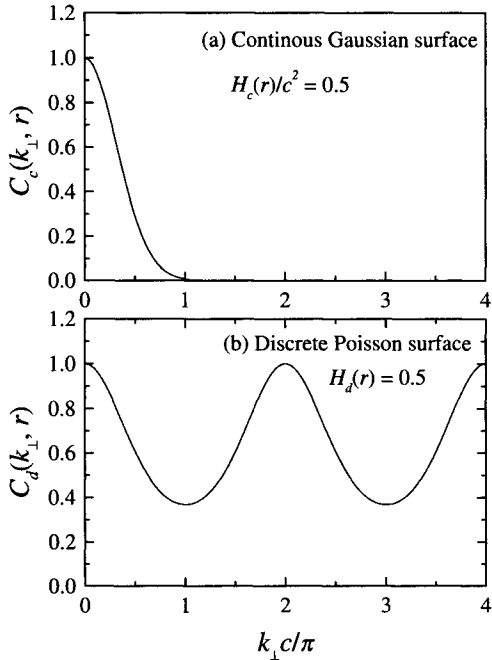


FIG. 7.8 The height difference function for (a) a continuous Gaussian surface and (b) a discrete Poisson surface.

$(2n+1)\pi$  the out-of-phase condition. If we denote  $|[\Phi]| = \min(|\Phi - 2n\pi|)$ , then  $0 \leq |[\Phi]| \leq \pi$  and  $\cos \Phi = \cos |[\Phi]|$ . At the near-in-phase condition,  $|[\Phi]|$  is small, and Equation (7.40) can be approximated by

$$C_d(k_\perp, \mathbf{r}) \approx e^{-\frac{1}{2}H_d(\mathbf{r})|[\Phi]|^2}. \quad (7.41)$$

At exactly the in-phase condition,  $|[\Phi]| = 0$  and  $C_d(k_\perp, \mathbf{r}) = 1$ . Clearly, at the in-phase condition, all the scattered waves from the surface have a phase difference of  $2n\pi, n = 0, \pm 1, \pm 2, \dots$ , and they should interfere constructively. At the near-in-phase condition, all the phase factors  $e^{i\Phi[d(\mathbf{r}) - d(0)]} = e^{i[\Phi][d(\mathbf{r}) - d(0)]}$  are close to 1; therefore the variances of the phase factors are small, which is similar to the small- $k_\perp$  condition for a continuous surface. At the near-out-of-phase condition,  $|[\Phi]| \sim \pi$ , Equation (7.40) can be approximated by

$$C_d(k_\perp, \mathbf{r}) \approx e^{-2H_d(\mathbf{r}) + \frac{1}{2}H_d(\mathbf{r})(\pi - |[\Phi]|)^2}. \quad (7.42)$$

At exactly the out-of-phase condition,  $|[\Phi]| = \pi$  and  $C_d(k_\perp, \mathbf{r}) = e^{-2H_d(\mathbf{r})}$ . In this case, the phase term,  $e^{i\Phi[d(\mathbf{r}) - d(0)]} = e^{i\pi[d(\mathbf{r}) - d(0)]}$ , can change quite dramatically between  $-1$  and  $+1$  as the result of the discrete variation of the relative height  $[d(\mathbf{r}) - d(0)]$ . In fact the scattering waves from the surface interfere destructively to the maximum extent. Clearly, for the same  $w$ , the height difference function at the in-phase condition is much larger than that at the out-of-phase condition. In fact, from Figure 7.8 we can see that  $C_d(k_\perp, \mathbf{r})$  reaches a maximum at the in-phase condition and a minimum at the out-of-phase condition.

Similar to that of the continuous-surface case, the height difference function  $C_d(k_\perp, \mathbf{r})$  can also be broken into two parts,

$$C_d(k_\perp, \mathbf{r}) = C_\infty(k_\perp) + \Delta C_d(k_\perp, \mathbf{r}), \quad (7.43)$$

with

$$C_\infty(k_\perp) = C_d(k_\perp, |\mathbf{r}| \rightarrow \infty), \text{ and} \quad (7.44)$$

$$\Delta C_d(k_\perp, r) = C_d(k_\perp, \mathbf{r}) - C_d(k_\perp, |\mathbf{r}| \rightarrow \infty). \quad (7.45)$$

Obviously, both  $C_\infty(k_\perp)$  and  $\Delta C_d(k_\perp, \mathbf{r})$  are periodic functions of  $k_\perp$ . However,  $C_\infty(k_\perp)$  and  $\Delta C_d(k_\perp, \mathbf{r})$  are exactly out of phase, as shown in Figure 7.9.

### 7.3.2 Discrete lattice effect on the diffraction from rough surfaces

The diffraction intensity for a discrete surface can be expressed as Equation (6.42). For convenience, we can rewrite it as

$$S_d(k_\perp, \mathbf{k}_\parallel) = \sum_{p,q} \int C_d(k_\perp, \mathbf{r}) e^{i(\mathbf{k}_\parallel - \mathbf{K}_{pq}) \cdot \mathbf{r}} d\mathbf{r}, \quad (7.46)$$

where  $\mathbf{K}_{pq}$  is the reciprocal-lattice vector as defined in Section 6.3. Substituting Equations (7.44) and (7.45) into Equation (7.46), the diffraction intensity can be divided into two parts: a  $\delta$  intensity

$$S_\delta(k_\perp, \mathbf{k}_\parallel) = \sum_{p,q} \int C_\infty(k_\perp) e^{i(\mathbf{k}_\parallel - \mathbf{K}_{pq}) \cdot \mathbf{r}} d\mathbf{r} \quad (7.47)$$

and a diffuse intensity

$$S_{diff}(k_\perp, \mathbf{k}_\parallel) = \sum_{p,q} \int [C_d(k_\perp, \mathbf{r}) - C_\infty(k_\perp)] e^{i(\mathbf{k}_\parallel - \mathbf{K}_{pq}) \cdot \mathbf{r}} d\mathbf{r}. \quad (7.48)$$

- (i) The  $\delta$  intensity

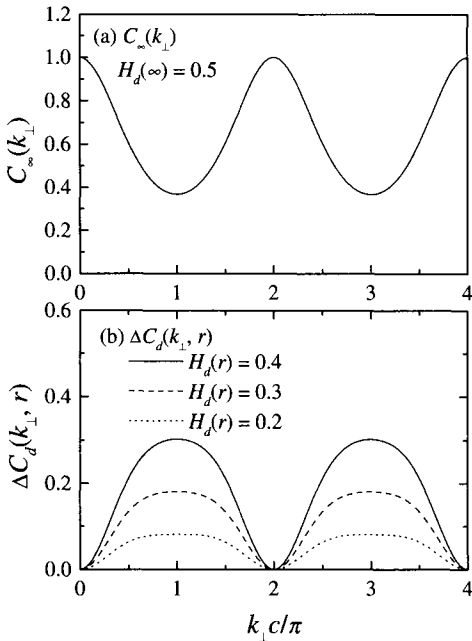


FIG. 7.9 The plot of  $C_{\infty}(k_{\perp})$  and  $\Delta C_d(k_{\perp}, r)$  as a function of the diffraction condition  $k_{\perp} c/\pi$ .

Obviously, the long-range flatness of a surface gives a summation of a series of  $\delta$  functions centered at the reciprocal-lattice positions  $\mathbf{K}_{pq}$ :

$$S_{\delta}(k_{\perp}, \mathbf{k}_{\parallel}) = (2\pi)^2 C_{\infty}(k_{\perp}) \sum_{p,q} \delta(\mathbf{K}_{pq}). \quad (7.49)$$

The amplitudes of those  $\delta$  functions are determined by  $C_{\infty}(k_{\perp})$ , which is a periodic function of  $k_{\perp}$  as discussed in the last section. In Figure 7.10 we show the  $\delta$ -peak intensity as a function of  $k_{\perp}$  for different  $w$  values. At the near in-phase condition and/or for small value of  $w$ , the  $\delta$ -peak intensity does not change very much as  $w$  increases. (This is much different from the case of the continuous surface, where for small  $k_{\perp}$  the  $\delta$ -peak intensity decays rapidly as  $w$  increases.) However, at the out-of-phase condition, for small  $w$ , the  $\delta$ -peak intensity changes dramatically when  $w$  changes. For  $w > 1$  the  $\delta$ -peak intensity at the out-of-phase condition is so weak that, even if the relative change of  $w$  is big, one can hardly tell any difference. In this case, one can see at the near-in-phase condition, the change caused by  $w$  is very obvious. Therefore, for a discrete rough surface, in order to see the  $\delta$ -peak intensity change as a result of roughness change at the small  $w$  region ( $< 1$ ), one needs to go to the out-of-phase condition. If one wants

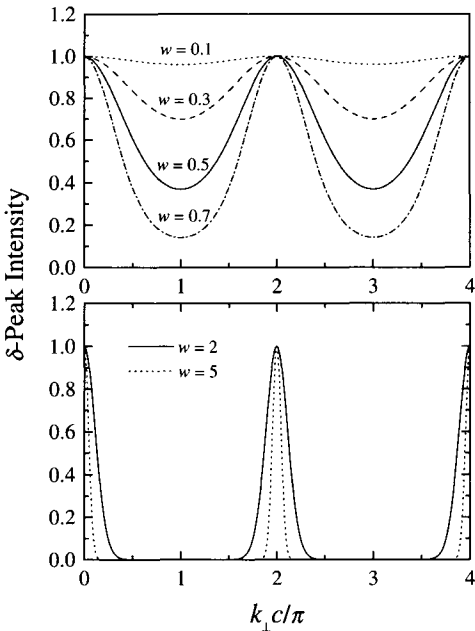


FIG. 7.10 The  $\delta$ -peak intensity as a function of  $k_{\perp} c/\pi$  for different  $w$  values.

to detect the roughness change in the large  $w$  region ( $> 1$ ), one needs to go to the near-in-phase (not exactly the in-phase) condition.

Another issue is how sensitive the intensity at the near in-phase condition is for different RMS roughness values. The sensitivity can be thought as how quickly would the intensity drop if the diffraction condition moves slightly away from the in-phase condition. This sensitivity can be expressed as

$$\frac{\Delta S_{\delta}}{S_{\delta}} \approx e^{-w^2(\Delta\Phi)^2} - 1. \quad (7.50)$$

Therefore at small  $w$  region, the  $\delta$ -peak intensity is not sensitive to a slight change away from the in-phase condition. However, for large  $w$ , the  $\delta$ -peak intensity decreases dramatically with increasing  $w$ , as seen in Figure 7.11. Therefore, for large  $w$ , experimentally it is not easy to find exactly the in-phase condition.

- ii) The diffuse intensity

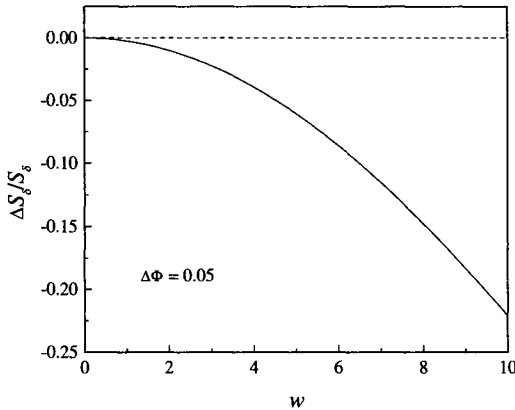


FIG. 7.11 The sensitivity of the  $\delta$ -peak intensity at the near-in-phase condition as a function of  $w$ .

The diffuse profile from a rough surface is the summation of a series of diffuse profiles centered at the reciprocal-lattice positions  $\mathbf{K}_{pq}$ :

$$S_{diff}(k_{\perp}, \mathbf{k}_{\parallel}) = \sum_{p,q} \int [e^{-H_d(\mathbf{r})(1-\cos\Phi)} - e^{-2w^2(1-\cos\Phi)}] e^{i(\mathbf{k}_{\parallel} - \mathbf{K}_{pq}) \cdot \mathbf{r}} d\mathbf{r}. \quad (7.51)$$

For small  $w$ , which satisfies  $4w^2 < 1$  (i.e., at the out-of-phase condition,  $\Phi = \pi$ ), Equation (7.51) can be reduced to

$$\begin{aligned} S_{diff}(k_{\perp}, \mathbf{k}_{\parallel}) &\approx 2w^2(1 - \cos\Phi) \sum_{p,q} \int e^{i(\mathbf{k}_{\parallel} - \mathbf{K}_{pq}) \cdot \mathbf{r}} R(\mathbf{r}) d\mathbf{r} \\ &= 8\pi^2 w^2(1 - \cos\Phi) \sum_{p,q} P(\mathbf{k}_{\parallel} - \mathbf{K}_{pq}). \end{aligned} \quad (7.52)$$

That is, if  $w$  is small, no matter what the diffraction condition is (either near the in-phase or near the out-of-phase condition), the diffuse profile is proportional to the summation of a series of surface power spectra centered at the reciprocal-lattice positions. If  $R(\mathbf{r})$  has an exponentially-decaying form as shown in Equation (7.22), then the diffuse profile becomes

$$S_{diff}(k_{\perp}, \mathbf{k}_{\parallel}) \approx 8\pi^2 w^2 \xi^2 (1 - \cos\Phi) \sum_{p,q} \frac{1}{[1 + |k_{\parallel} - K_{pq}|^2 \xi^2]^{3/2}}. \quad (7.53)$$

Figure 7.12 plots the cross section of the diffuse profiles for various  $\xi K_{BZ}$  values from a square lattice with  $w = 0.1$  and  $\Phi = \frac{\pi}{2}$ . Here  $K_{BZ} (= \frac{2\pi}{a})$  is the length of one Brillouin zone. Clearly, the lateral correlation

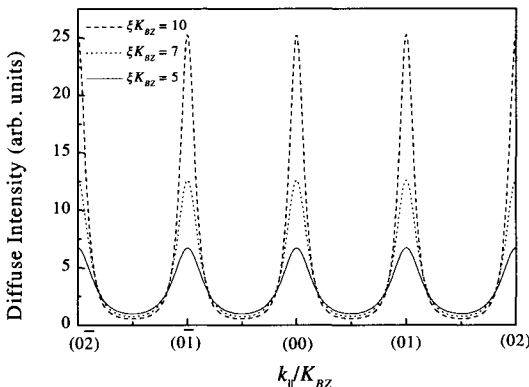


FIG. 7.12 The cross sections of the diffuse profiles for various  $\xi K_{BZ}$  values from a square lattice with  $w = 0.1$ ,  $\Phi = \frac{\pi}{2}$ .

length  $\xi$  should always be larger than the lattice constant  $a$ ; therefore, in general  $\xi K_{BZ} > 1$ . For  $\xi K_{BZ} \gg 1$  the diffuse profiles at different reciprocal-lattice positions can be separated very well, and the FWHM of a diffuse profile is determined by only the power spectrum at that lattice position. The intensity at the reciprocal-lattice position is much higher than that at the edge of the Brillouin zone. However, when  $\xi K_{BZ}$  decreases, the diffuse tails from different Brillouin zones affect each other, and the diffuse tails become much broader and higher than that of a single power spectrum. Figure 7.13 shows how the tails from different Brillouin zones affect the diffuse profile. Figure 7.13(a) is a plot of the diffuse profile from a continuous surface which can extend to several Brillouin zones. The discrete lattice effect forces the diffuse profile to extend only within one Brillouin zone. The dashed curves in Figure 7.13(b) are parts of the diffuse profile in Figure 7.13(a) within the first Brillouin zone. The contributions from the nearest-neighbor reciprocal-lattice sites are the folding of the diffuse profile in Figure 7.13(a) with respect to the straight lines  $k_{\parallel}/K_{BZ} = \pm 0.5$ , shown as the dotted curves in Figure 7.13(b). The dotted curves within the first Brillouin zone are contributions from the nearest reciprocal lattice. The contributions from the next-nearest-neighbor reciprocal-lattice sites are to fold Figure 7.13(b) with respect to  $k_{\parallel}/K_{BZ} = \pm 0.5$ . Repeating this process, and adding all the contributions in the first Brillouin zone together, one obtains the diffuse profile within a single Brillouin zone shown as the solid curve in Figure 7.13(b). In this particular model, we see that the tail of the diffuse intensity at the edge of the first Brillouin zone is much higher

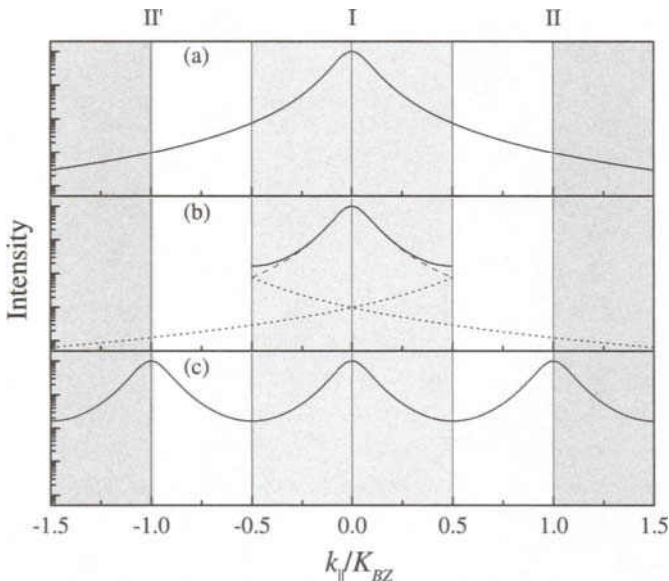


FIG. 7.13 The effect of the Brillouin zone on the tails of the diffuse profiles. The intensity in arbitrary units is plotted in a logarithmic scale.

than that of a continuous surface within one Brillouin zone, while the peak intensity is almost the same as that of the continuous surface. This is due to the fact that the near neighbors' contributions to the Brillouin zone edge are much greater than those at the center. According to the periodicity of the diffuse profile, repeating the diffuse profile in the first Brillouin zone to other Brillouin zones, one obtains the entire diffuse profile for a discrete surface, as shown in Figure 7.13(c).

Now we specifically discuss how the discrete-lattice effect at the in-phase and out-of-phase conditions affects the diffraction profiles. At the near-in-phase condition, the diffuse profile can be written as

$$S_{diff}(k_\perp, \mathbf{k}_\parallel) \approx e^{-\Omega_d} \sum_{p,q} \int [e^{\Omega_d R(\mathbf{r})} - 1] e^{i(\mathbf{k}_\parallel - \mathbf{K}_{pq}) \cdot \mathbf{r}} d\mathbf{r}. \quad (7.54)$$

Here we define  $\Omega_d = w^2 ||[\Phi]||^2$ . Except for the summation at different reciprocal-lattice sites, Equation (7.54) looks exactly the same as Equation (7.26). According to Equation (7.27), Equation (7.54) can be reduced to

$$S_{diff}(k_\perp, \mathbf{k}_\parallel) = e^{-\Omega_d} \sum_{p,q} \sum_{n=1}^{\infty} \frac{1}{n!} \Omega_d^n \int R(\mathbf{r})^n e^{i(\mathbf{k}_\parallel - \mathbf{K}_{pq}) \cdot \mathbf{r}} d\mathbf{r}. \quad (7.55)$$

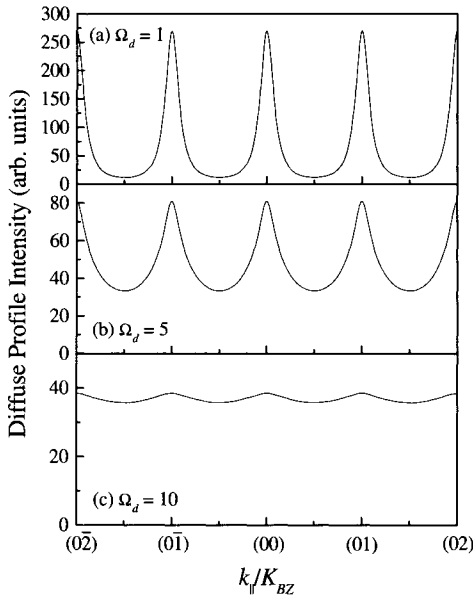


FIG. 7.14 The diffuse profiles with the increase of  $\Omega_d$  values at  $\xi K_{BZ} = 10$  and small  $\Phi$  values.

For the exponentially-decaying correlation function, Equation (7.55) becomes

$$S_{diff}(k_\perp, \mathbf{k}_\parallel) = 2\pi\Omega_d\xi^2 e^{-\Omega_d} \sum_{p,q} \sum_{n=0}^{\infty} \frac{1}{n!(n+1)^3} \Omega_d^n Y\left(\frac{|\mathbf{k}_\parallel - \mathbf{K}_{pq}| \xi}{n+1}\right). \quad (7.56)$$

As we discussed in Section 7.2, as  $w$  increases, the diffuse profile becomes broader. Figure 7.14 shows how the diffuse profile changes with the increase of  $\Omega_d$  values at  $\xi K_{BZ} = 10$  and small  $\Phi$  values. For small  $\Omega_d$ , the diffuse profiles are well separated as we discussed above. However, as  $w$  increases, the diffuse profile in each Brillouin zone becomes broader, and would extend to adjacent Brillouin zones. As a result, the diffuse profiles would become much broader than that of the continuous surface. Therefore, it is harder to distinguish the diffuse peak at the reciprocal lattice position. We can use the contrast,  $\gamma$ , to determine the degree of distinguishability

$$\gamma = \frac{I_{max} - I_{min}}{I_{max} + I_{min}}, \quad (7.57)$$

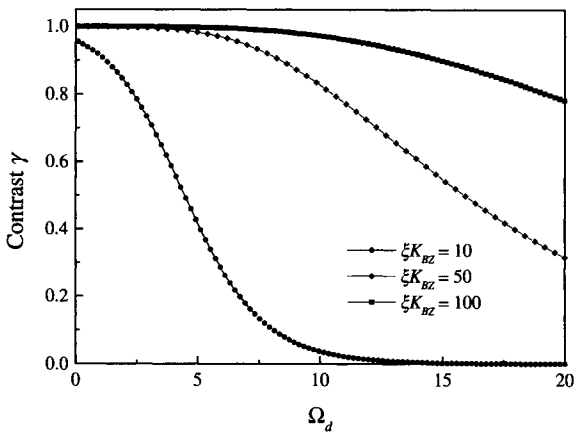


FIG. 7.15 The contrast of the diffuse profile as a function of  $\Omega_d$  for  $\xi K_{BZ} = 10, 50$ , and  $100$ .

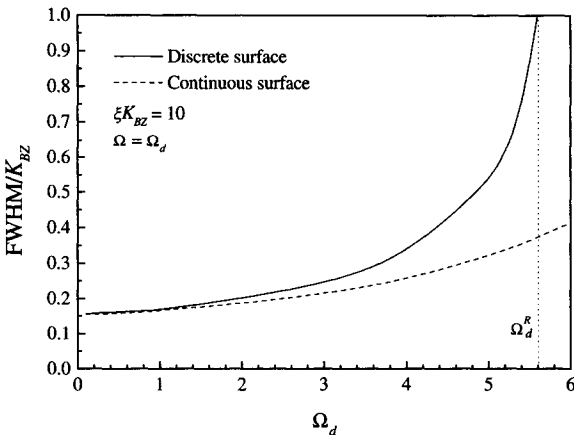


FIG. 7.16 The FWHM of a diffuse profile in one Brillouin zone as a function of  $\Omega_d$  for a discrete surface (the solid curve) and for a continuous surface (the dashed curve).

where  $I_{max}$  and  $I_{min}$  are the maximum and minimum intensities in the diffuse profile, respectively. Obviously,  $0 \leq \gamma \leq 1$ . When  $\gamma = 1$ , the contrast is maximum, and one can distinguish the diffuse profiles at the reciprocal-lattice position easily. When  $\gamma \rightarrow 0$ , and  $I_{max} \rightarrow I_{min}$ , one cannot distinguish the diffuse profiles at different reciprocal-lattice positions at all. Figure 7.15 shows the contrast of the diffuse profile as a function of  $\Omega_d$  for  $\xi K_{BZ} = 10, 50$ , and  $100$ .

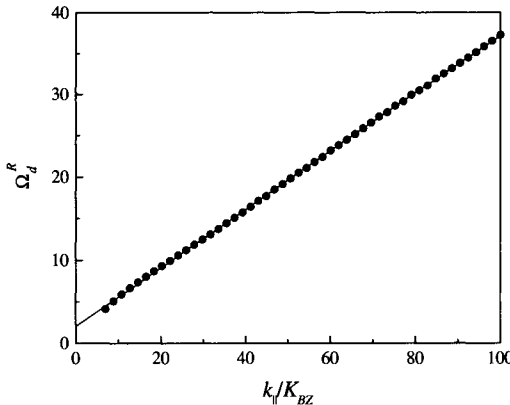


FIG. 7.17 The Rayleigh limit  $\Omega_d^R$  as a function of the lateral correlation length  $\xi K_{BZ}$ .

Figure 7.16 shows the FWHM of a diffuse profile in one Brillouin zone as a function of  $\Omega_d$  compared to that of a continuous surface. When  $\Omega_d$  increases, the FWHM of the discrete surface becomes broader than that of the continuous surface. We can see that, at certain  $\Omega_d^R(\xi)$  values, the FWHM of a discrete surface equals the size of one Brillouin zone. At this point, one almost cannot distinguish the diffraction spots at different reciprocal-lattice positions. This is a manifestation of the Rayleigh criterion. Clearly, at the near-in-phase condition, the Rayleigh criterion  $\Omega_d^R(\xi)$  is determined by both the  $\Omega_d$  value and the lateral correlation length  $\xi$ . Figure 7.17 shows that the resolution limit imposed by Rayleigh criterion  $\Omega_d^R$  is almost a linear function of the lateral correlation length  $\xi K_{BZ}$ .

At the near-out-of-phase condition, the diffuse profile becomes

$$S_{diff}(k_{\perp}, \mathbf{k}_{\parallel}) = e^{-\Pi} \sum_{p,q} \sum_{n=1}^{\infty} \frac{1}{n!} \Pi^n \int R(\mathbf{r})^n e^{i(\mathbf{k}_{\parallel} - \mathbf{K}_{pq}) \cdot \mathbf{r}} d\mathbf{r}, \quad (7.58)$$

where  $\Pi = 4w^2 - w^2(\pi - ||[\Phi]||)^2$ . Equation (7.58) is exactly the same as Equation (7.55) except that  $\Omega_d$  is changed to  $\Pi$ . Obviously, at the near-out-of-phase condition, the Rayleigh limit shifts to a lower  $w$  value.

#### 7.4 Summary

This chapter discussed the general characteristics of scattering from a random rough surface. For scattering from a continuous rough surface, the scattering profile contains two parts, the  $\delta$ -peak intensity, which reflects

the large distance roughness, and the diffuse intensity, which results from the short range roughness. The scattering profile from a discrete rough surface is periodic due to the discrete nature of the surface. The reciprocal space is divided into many Brillouin zones, and each Brillouin zone has the same scattering profile. The scattering profile within one Brillouin zone is affected by the scattering profiles from the nearest Brillouin zones.

### References

- 7.1 H. Stark and J. W. Woods, *Probability, Random Processes and Estimation Theory for Engineers*, 2nd Edition (Prentice Hall, Englewood Cliffs, 1994), p. 255.
- 7.2 H.-N. Yang, G.-C. Wang, and T.-M. Lu, *Diffraction from Rough Surfaces and Dynamic Growth Fronts* (World Scientific, Singapore, 1993).
- 7.3 H.-N. Yang, T.-M. Lu, and G.-C. Wang, "Time invariant structure factor in an epitaxial growth front," *Phys. Rev. Lett.* **68**, 2612 (1992).
- 7.4 H.-N. Yang, T.-M. Lu, and G.-C. Wang, "Diffraction from surface growth fronts," *Phys. Rev. B* **47**, 3911 (1993).
- 7.5 E. L. Church, "Fractal surface finish," *Appl. Opt.* **27**, 1518 (1988).
- 7.6 Y.-P. Zhao, G.-C. Wang, and T.-M. Lu, "Diffraction from non-Gaussian rough surfaces," *Phys. Rev. B* **55**, 13938 (1997).

## 8. DIFFRACTION TECHNIQUES – EXPERIMENTATION

In the previous chapter we discussed in detail diffraction theories from random rough surfaces. These theories are very general and can be applied to different diffraction techniques. However, because the theories are based on general kinematic diffraction treatment, different diffraction techniques have their own specifications under the kinematic assumption. Therefore, in order to apply the theories better, we need to know some details about the diffraction techniques. Since many books and reviews on different diffraction techniques already exist, we are not going to discuss each one of them in great length. References are given by light scattering [8.1], X-ray scattering [8.2, 8.3, 8.4], neutron scattering [8.2], and low-energy electron diffraction [8.5, 8.6, 8.7].

Although the detailed instrumentations for various diffraction techniques are different, the basic principles are essentially the same. In this chapter, we will discuss in detail the most common features in diffraction experiments [8.8].

### 8.1 The Diffraction Geometries

In general, there are three major components in a diffraction setup, as shown in Figure 8.1: an incident beam, which generates sources of laser beams, x rays, electrons, etc.; a sample, which diffracts the incident beam; and a detector, which collects the scattered beams.

Depending on the specifications of the beam source, one may have a multi-wavelength diffraction setup or a single-wavelength diffraction setup. For a multi-wavelength setup, the beam source can radiate multiple wavelengths, and the position of the sample and the detector can be fixed. However, one needs to put a monochromator in front of the detector in order to resolve different wavelengths. If one only collects particles scattered elastically, then when the wavelength of the incident beam is changed continuously, the corresponding momentum transfer also changes continuously. For a single-wavelength diffraction setup, different detection schemes can be used: a moving-sample scheme or a moving-detector scheme, as shown in Figure 8.2 and Figure 8.3, respectively. In the moving-sample scheme, the position of the detector is fixed, and the sample usually rotates with respect to a certain axis. As the sample rotates, the detector collects the signal associated with the rotation angle, generating angular-dependent diffraction

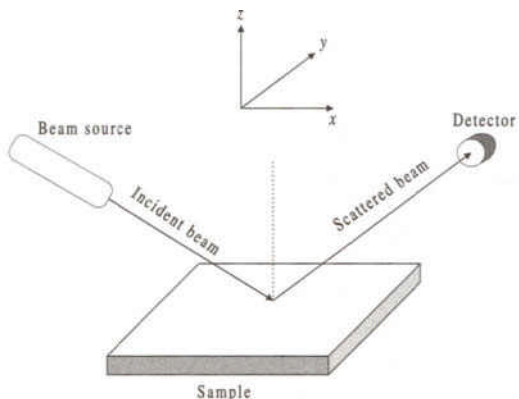


FIG. 8.1 Three major components in diffraction techniques.

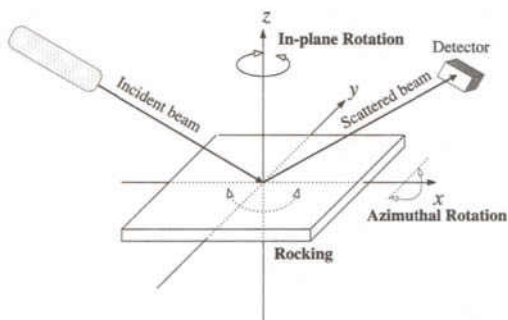
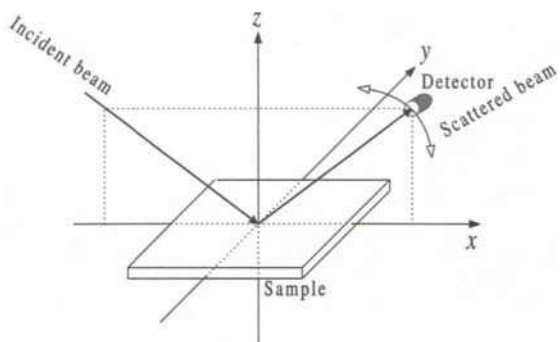
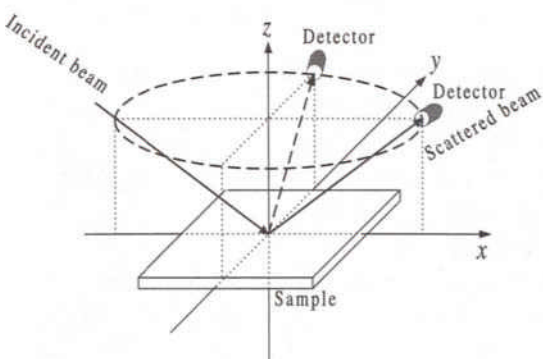


FIG. 8.2 The moving-sample scheme: rocking mode, azimuthal-rotation mode, and in-plane rotation mode.

profiles. As shown in Figure 8.2, there are three different rotation modes: the rocking mode, the azimuthal-rotation mode, and the in-plane rotation mode. As illustrated in Figure 8.2, the  $x$ - $y$  plane is the sample plane, the  $z$  direction is the sample surface normal, and the  $x$ - $z$  plane is the plane of incidence. For the rocking mode, the sample rotates in the  $x$ - $z$  incident plane with the  $y$  axis as the rotation axis. For the azimuthal-rotation mode, the rotation axis is the  $x$  axis and the sample rotates in the  $y$ - $z$  plane, the plane being perpendicular to both the sample plane and the incident plane. For in-plane rotation, the rotation axis is the  $z$  axis, i.e., the sample rotates in the sample plane. In what follows, we continue the convention of the last chapter, with "in-plane" and "out-of-plane" referring to directions relative to the *sample* plane.



a) Out-of-plane geometry



b) In-plane geometry

FIG. 8.3 The moving-detector scheme: (a) out-of-plane geometry, and (b) in-plane geometry.

In the moving-detector scheme, the position of the sample is fixed and the detector rotates with respect to a certain axis. In general, there are two different geometries for the moving detector scheme: the out-of-plane geometry and the in-plane geometry, as shown in Figures 8.3(a) and (b), respectively. For the out-of-plane geometry, the detector rotates in the incident plane, i.e., the  $x$ - $z$  plane, and the rotation axis is the  $y$  axis. For the in-plane geometry, the detector rotates in a plane parallel to the sample plane, and the rotation axis is the  $z$  axis.

In general, measurement with the moving-sample scheme is time-consuming, because very often only a point detector is used in this scheme and the sample position has to be rotated and monitored with a data acquisition system. This is similar to the scanning profiling techniques discussed in Chapter 4. In the moving-detector scheme, if only a point detector is used,

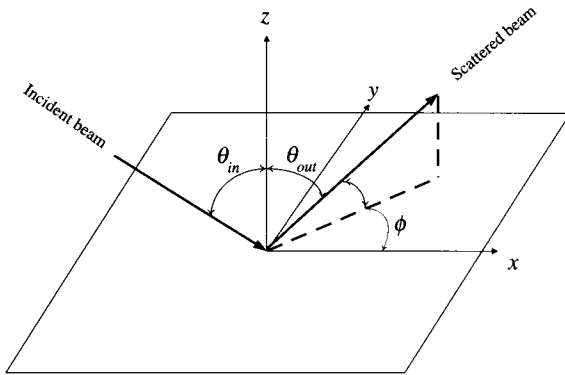


FIG. 8.4 Schematic of the diffraction coordinates.

the process is also time-consuming and real-time measurement is often difficult. However, if one uses a detector array or a charge-coupled device (CCD) camera, then one can measure the entire diffraction profile without moving either the sample or the detector. With this kind of setup, one can achieve real-time, *in situ* data collection.

As discussed in Chapter 6, for the diffraction from a random rough surface, the momentum transfer  $\mathbf{k}_s$  due to scattering can be decomposed into two parts:  $\mathbf{k}_{||}$ , the momentum transfer parallel to the sample surface, and  $\mathbf{k}_{\perp}$ , the momentum transfer perpendicular to the sample surface. In the diffraction geometry shown in Figure 8.4, one has

$$k_{\perp} = k(\cos \theta_{out} + \cos \theta_{in}), \quad (8.1)$$

$$k_x = k(\sin \theta_{out} \cos \phi - \sin \theta_{in}), \text{ and} \quad (8.2)$$

$$k_y = k \sin \theta_{out} \sin \phi, \quad (8.3)$$

where  $\theta_{in}$  is the incident angle,  $\theta_{out}$  is the polar scattering angle, and  $\phi$  is the azimuthal scattering angle. During data collections, when one rotates either the sample or the detector, the momentum transfer changes correspondingly. In the following, we discuss in detail how Equations (8.1)-(8.3) change under five different data acquisition modes.

### (1) Rocking mode

In the rocking mode, the detector is initially set in the direction of specular reflection direction, i.e.,  $\theta_{in} = \theta_{out} = \theta$  and  $\phi = 0$ . If there is no rotation, one has

$$k_{\perp} = 2k \cos \theta,$$

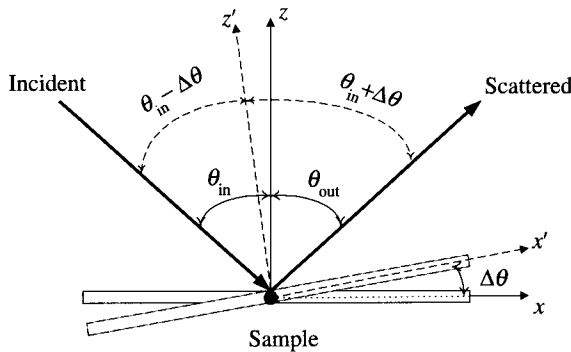


FIG. 8.5 A rocking mode.

$$\begin{aligned} k_x &= 0, \text{ and} \\ k_y &= 0. \end{aligned} \quad (8.4)$$

If the sample rotates through  $\Delta\theta$  in the  $x$ - $z$  plane, as shown in Figure 8.5, then

$$\begin{aligned} k_{\perp} &= k[\cos(\theta + \Delta\theta) + \cos(\theta - \Delta\theta)], \\ k_x &= k[\sin(\theta + \Delta\theta) - \sin(\theta - \Delta\theta)], \text{ and} \\ k_y &= 0. \end{aligned} \quad (8.5)$$

From Equation (8.5) we can see that during the rotation both  $k_{\perp}$  and  $k_x$  change with the rotation angle. In Figure 8.6 we plot the  $k_{\perp}$  and  $k_x$  as a function of the rotation angle  $\Delta\theta$  at  $\theta = 45^\circ$ . In the range of  $|\Delta\theta| \leq 10^\circ$ ,  $k_x$  changes almost linearly with the rotation angle. The perpendicular momentum transfer  $k_{\perp}$  reaches a maximum when  $\Delta\theta = 0$  and decreases when  $|\Delta\theta|$  increases. In the range of  $|\Delta\theta| \leq 10^\circ$ , the maximum change of  $k_{\perp}$  is about 22%. For the rocking mode, the maximum range of the rotation angle is from  $-(\frac{\pi}{2} - \theta)$  to  $\theta$ . Therefore the range of  $|k_x|$  is from 0 to  $\max[k|\sin(2\theta - \frac{\pi}{2}) - 1|, k|\sin 2\theta|]$ .

## (2) Azimuthal-rotation mode

For the azimuthal-rotation mode, as shown in Figure 8.7, before a rotation the detector is in the specular-reflection direction:  $\theta_{in} = \theta_{out} = \theta$  and  $\phi = 0$ , and one reproduces Equation (8.4). After rotating  $\Delta\phi$ , the momentum transfer becomes

$$\begin{aligned} k_{\perp} &= 2k \cos \theta \cos \Delta\phi, \\ k_x &= 0, \text{ and} \end{aligned}$$

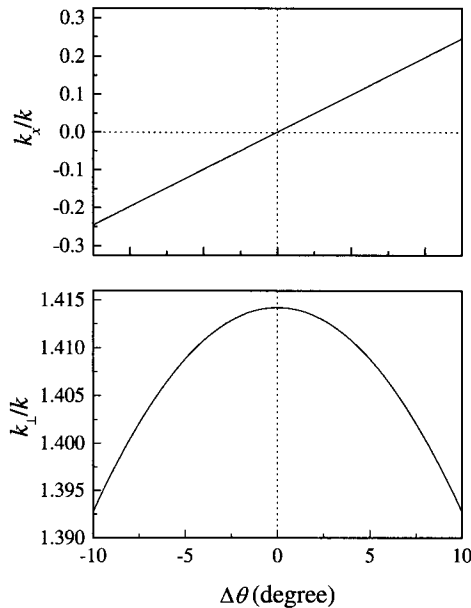


FIG. 8.6 The momentum transfer  $k_x$  and  $k_{\perp}$  as a function of rotation angle  $\Delta\theta$  for the rocking mode.

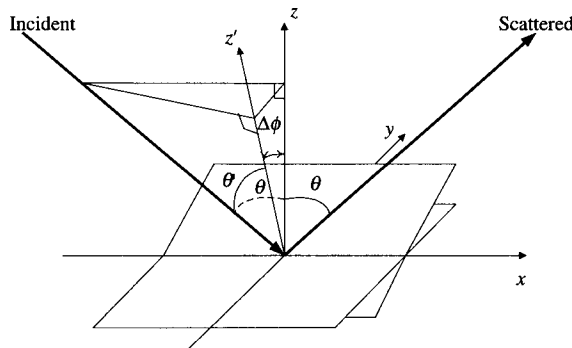


FIG. 8.7 An azimuthal-rotation mode.

$$k_y = -2k \cos \theta \sin \Delta\phi. \quad (8.6)$$

Equation (8.6) is very similar to Equation (8.5) except that in Equation (8.6)  $k_x = 0$  while in Equation (8.5)  $k_y = 0$ . In fact, if  $|\Delta\theta| \ll 180^\circ$ , the Taylor expansion in Equation (8.5) gives exactly the same result as Equation (8.6). Figure 8.8 plots  $k_{\perp}$  and  $k_x$  as a function of rotation angle

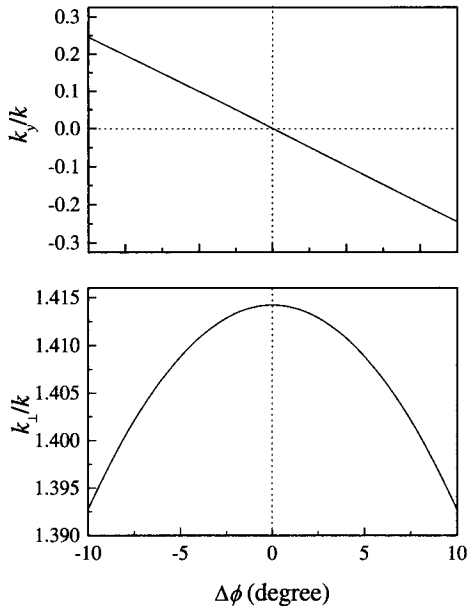


FIG. 8.8 The momentum transfer  $k_y$  and  $k_{\perp}$  as a function of the rotation angle  $\Delta\phi$  for an azimuthal-rotation mode.

$\Delta\phi$  at  $\theta = 45^\circ$  in the range of  $|\Delta\phi| \leq 10^\circ$ . The result is very similar to Figure 8.6. Therefore, for  $|\Delta\phi| \ll 180^\circ$ , both the rocking mode and the azimuthal-rotation mode should give the same diffraction structure factor. For azimuthal-rotation mode, the range of the rotation angle is from  $-90^\circ$  to  $90^\circ$ . Thus the range of  $|k_y|$  is from 0 to  $2k \cos \theta$ .

### (3) In-plane rotation mode

For the in-plane rotation mode, since the sample rotates in the sample plane,  $\theta_{in}$ ,  $\theta_{out}$ , and  $\phi$  do not change during the rotation. Therefore, before or after the rotation, Equations (8.1)-(8.3) remain the same. Strictly speaking, the in-plane rotation mode cannot provide a diffraction profile, but it can tell whether the surface is isotropic or anisotropic.

### (4) Out-of-plane geometry

For the out-of-plane geometry, the incident angle  $\theta$  is fixed, and the diffraction angle changes with the rotation of the detector in the incident plane. Usually the reflection direction acts like a reference point. Before the rotation, the momentum transfer satisfies Equation (8.4). After the

rotation, it changes into

$$\begin{aligned} k_{\perp} &= k[\cos(\theta + \Delta\theta) + \cos\theta], \\ k_x &= k[\sin(\theta + \Delta\theta) - \sin\theta], \text{ and} \\ k_y &= 0. \end{aligned} \quad (8.7)$$

Figure 8.9 plots  $k_{\perp}$  and  $k_x$  as a function of the rotation angle at  $\theta = 45^\circ$  in the range of  $|\Delta\theta| \leq 10^\circ$  for the out-of-plane geometry. Both  $k_x$  and  $k_{\perp}$  change almost linearly for small rotation angles. However, comparing Figure 8.9 with Figure 8.6 and Figure 8.8, there are two distinct differences: (1) For the same range of rotation angle, the change of  $k_x$  (or  $k_y$ ) in the out-of-plane geometry is much smaller than that in the rocking mode or the azimuthal-rotation mode, while the change of  $k_{\perp}$  is much greater. (2) As discussed in Chapter 6, usually the diffraction structure factor is symmetric with respect to  $k_{||}$ . In the case of the rocking mode or the azimuthal-rotation mode, although  $k_{\perp}$  changes with the rotation angle, the diffraction structure factor varies symmetrically. Therefore one would expect that the diffraction structure factor obtained by using these two modes should be symmetric. However, in the case of out-of-plane geometry, because  $k_{\perp}$  changes monotonically with the rotation angle, one would expect that the diffraction structure factor obtained by this mode is asymmetric.

The range of the rotation angle  $\Delta\theta$  for the out-of-plane geometry is from  $\frac{\pi}{2} - \theta$  to  $\frac{\pi}{2} + \theta$ . Therefore, the range of  $|k_x|$  is from 0 to  $\max[k(1 - \sin\theta), k|\sin(\frac{\pi}{2} + 2\theta) - \sin\theta|]$ .

### (5) In-plane geometry

For the in-plane geometry, the scattering angle is fixed at  $\theta$ . Still using the specular reflection direction as a reference point, we have

$$\begin{aligned} k_{\perp} &= 2k \cos\theta, \\ k_x &= k \sin\theta [\cos\Delta\phi - 1], \text{ and} \\ k_y &= k \sin\theta \sin\Delta\phi. \end{aligned} \quad (8.8)$$

In this case  $k_{\perp}$  is independent of the rotation angle, and only  $k_{||} = \sqrt{k_x^2 + k_y^2}$  changes with the rotation angle. From the discussion in Chapter 6, this is the ideal mode for studying the diffraction structure factor since  $k_{\perp}$  remains constant. Figure 8.10 plots  $k_{\perp}$  and  $k_{||}$  as a function of rotation angle at  $\theta = 45^\circ$  in the range of  $|\Delta\phi| \leq 10^\circ$  for the in-plane geometry. For the in-plane geometry, the range of the rotation angle is from  $-180^\circ$  to  $180^\circ$ . That is, the range of  $k_{||}$  is from 0 to  $2k \sin\theta$ , which is determined by the incident angle  $\theta$ . The range of  $k_{||}$  increases for increasing  $\theta$ .

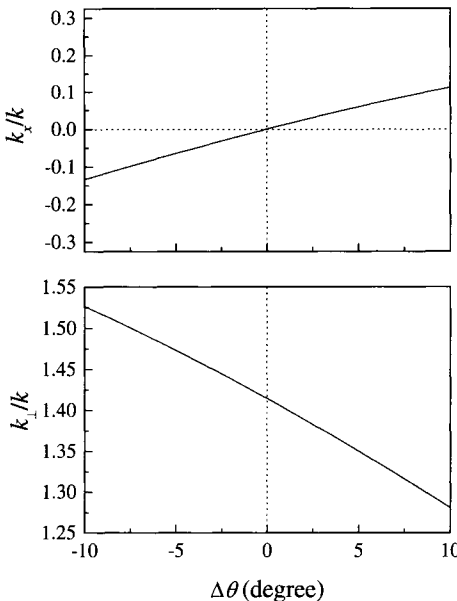


FIG. 8.9 The momentum transfer  $k_x$  and  $k_{\perp}$  as a function of rotation angle  $\Delta\theta$  for an out-of-plane geometry.

In a realistic experiment, one can combine several detection setups in order to obtain complete information of the surfaces. For example, to examine an anisotropic surface, one needs to combine the in-plane and out-of-plane geometries with the in-plane rotation mode in order to obtain the roughness parameters in different directions or one can combine a multi-wavelength diffraction setup with a moving-sample/moving-detector scheme in order to detect the surface defects or contaminations. On the other hand, a simple setup may include different modes. For example, if one uses a CCD camera instead of a point detector, one can map out a two-dimensional diffraction pattern. If one makes a cross-sectional scan of the pattern along different directions, one can obtain both the in-plane geometry profile and the out-of-plane geometry profile.

## 8.2 The Measured Diffraction Intensity Profile

In reality, the measured diffraction intensity is much more complicated. It is proportional to the diffraction structure factor, but it also contains a geometric factor. In general, the diffraction intensity  $I(\mathbf{k})$  can be written

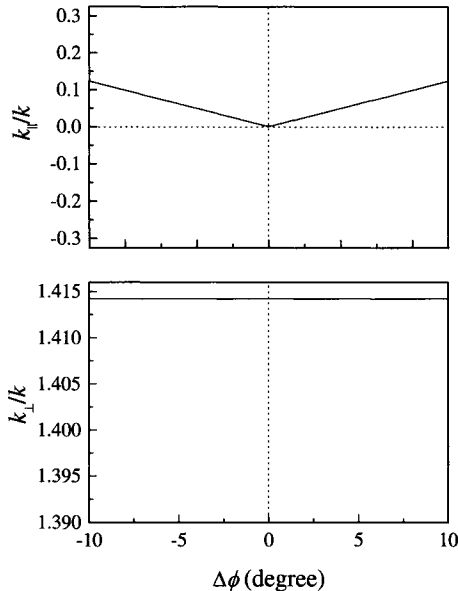


FIG. 8.10 The momentum transfer  $k_{||}$  and  $k_{\perp}$  as a function of rotation angle  $\Delta\phi$  for an in-plane geometry.

as

$$I(\mathbf{k}) = F(\theta_{in}, \theta_{out}, \phi)Y(\mathbf{k}) * S(\mathbf{k}), \quad (8.9)$$

where  $F(\theta_{in}, \theta_{out}, \phi)$  is an angular factor, which is determined by the diffraction geometry. It is also associated with the physical properties of the sample, such as the refraction index, as well as the wavelength and polarization of the incident beam. The system point spread function or the system response function is  $Y(\mathbf{k})$ . The sign “\*” represents a convolution. Therefore the system response determines the angular resolution or the reciprocal-space resolution of the system. That is to say,  $Y(\mathbf{k})$  determines the maximum sampling size. For a diffraction system where the kinematic diffraction theory is valid,  $S(\mathbf{k})$  is the diffraction structure factor, which will be discussed in the following chapters for specific examples.

All the surface morphology information is contained in the diffraction structure factor  $S(\mathbf{k})$ . In order to obtain  $S(\mathbf{k})$  from Equation (8.9), one needs to know the detailed functional form of the angular factor  $F(\theta_{in}, \theta_{out}, \phi)$  and the instrument response function  $Y(\mathbf{k})$ . For different diffraction techniques, the instrumentations are quite different. Also, parameters associated with material properties may change with the wavelength. The

responses  $Y(\mathbf{k})$  and angular factors  $F(\theta_{in}, \theta_{out}, \phi)$  differ with each diffraction technique. Even for the same diffraction technique, depending on the theory or the detailed components one uses, those two factors may also be different. In the following, we show some examples of those two factors.

### 8.2.1 The angular factor $F(\theta_{in}, \theta_{out}, \phi)$

The angular factor  $F(\theta_{in}, \theta_{out}, \phi)$  depends very much on the diffraction geometry and the diffraction theory one applies. Here we use light scattering and x-ray scattering as examples to demonstrate this point.

The problem with predicting the light scattering from a random rough surface lies in solving the Maxwell equations with the presence of a rough boundary, as discussed in Chapter 6. There are different methods to treat this problem considering different surface conditions and the nature of the incident light. For a very smooth surface ( $w \ll \lambda$ ), the perturbation method can be used and the diffraction intensity at distance  $r$  can be expressed as Equation (6.80). In this case,

$$F(\theta_{in}, \theta_{out}, \phi) \propto \frac{4Rk^4 \cos^2 \theta_{in} \cos^2 \theta_{out}}{r^2}, \quad (8.10)$$

where  $R$  is the reflectivity of a surface.

A more general treatment is to use the Kirchhoff approximation (KA) as shown in Section 6.4.2. Under the KA, the scattered amplitude can be expressed as Equation (6.91). For the surface slope  $|\nabla h| \ll 1$ , from Equation (6.91) we obtain Equation (8.10). Here

$$F(\theta_{in}, \theta_{out}, \phi) \propto \frac{1}{F_B^2}, \quad (8.11)$$

with

$$F_B = \frac{b + (ak_x + ck_y)/k_\perp}{2 \cos \theta_{in}}, \quad (8.12)$$

where

$$\begin{aligned} a &= (1 - R) \sin \theta_{in} + (1 - R) \sin \theta_{out} \cos \phi, \\ b &= (1 + R) \cos \theta_{out} - (1 - R) \cos \theta_{in}, \text{ and} \\ c &= (1 + R) \sin \theta_{out} \sin \phi. \end{aligned}$$

If we consider the polarization of the light, then [8.1]

$$F(\theta_{in}, \theta_{out}, \phi) \propto \frac{\lambda^4}{\Omega \cos^2 \theta_{out} \cos \theta_{in} Q}, \quad (8.13)$$

where  $Q$  depends on the diffraction-geometry parameters,  $Q = Q(\theta_{in}, \theta_{out}, \phi, \epsilon)$ , as well as the polarization states of the incident light and the detector. More explicitly,  $Q$  is the sum of as many as four different quantities that correspond to the four possible combinations of initial and observed polarizations. Referring the subscripts  $i$  and  $j$  to the incident and observed polarizations, respectively,  $Q$  becomes  $Q_{ij}$  for an  $i$ -polarized source and a  $j$ -sensitive receiver. If the receiver is insensitive to the polarization,  $Q = \sum_j Q_{ij}$  for a polarized source and  $Q = \frac{1}{2} \sum_i \sum_j Q_{ij}$  for an unpolarized source. Conventionally the perpendicular and parallel polarization states are labeled as  $s$  and  $p$ , respectively. The individual expressions for the  $Q_{ij}$  are [8.1]:

$$Q_{ss} = \left| \frac{(\epsilon - 1) \cos \phi_s}{(\cos \theta_i + \sqrt{\epsilon - \sin^2 \theta_i}) (\cos \theta_s + \sqrt{\epsilon - \sin^2 \theta_s})} \right|^2, \quad (8.14)$$

$$Q_{sp} = \left| \frac{(\epsilon - 1) \sqrt{\epsilon - \sin^2 \theta_s} \sin \phi_s}{(\cos \theta_i + \sqrt{\epsilon - \sin^2 \theta_i}) (\epsilon \cos \theta_s + \sqrt{\epsilon - \sin^2 \theta_s})} \right|^2, \quad (8.15)$$

$$Q_{ps} = \left| \frac{(\epsilon - 1) \sqrt{\epsilon - \sin^2 \theta_s} \sin \phi_s}{(\cos \theta_i + \sqrt{\epsilon - \sin^2 \theta_i}) (\cos \theta_s + \sqrt{\epsilon - \sin^2 \theta_s})} \right|^2, \text{ and} \quad (8.16)$$

$$Q_{pp} = \left| \frac{(\epsilon - 1) (\sqrt{\epsilon - \sin^2 \theta_s} \sqrt{\epsilon - \sin^2 \theta_i} \cos \phi_s - \epsilon \sin \theta_i \sin \theta_s)}{(\epsilon \cos \theta_i + \sqrt{\epsilon - \sin^2 \theta_i}) (\epsilon \cos \theta_s + \sqrt{\epsilon - \sin^2 \theta_s})} \right|^2. \quad (8.17)$$

The above relations can be simplified if we consider the in-plane scattering case, where  $\theta_i = \theta_s$ . That is, the parameters  $k_\perp$  (therefore  $\Omega$ ),  $\theta_i$ , and  $\theta_s$  are kept constant throughout the measurements.

For x-ray scattering, if one only considers the Born approximation, the angular factor takes a very simple form [8.9, 8.10]:

$$F(\theta_{in}, \theta_{out}, \phi) \propto 1/k_\perp^2. \quad (8.18)$$

For the DWBA, the angular factor becomes [Equations (6.107) and (6.108)] [8.9]

$$F(\theta_{in}, \theta_{out}, \phi) \propto \frac{|k^2(1 - n^2)|^2}{16\pi^2} |T_0|^2 |T_s|^2, \quad (8.19)$$

where  $T_0$  and  $T_s$  are defined by Equation (6.102).

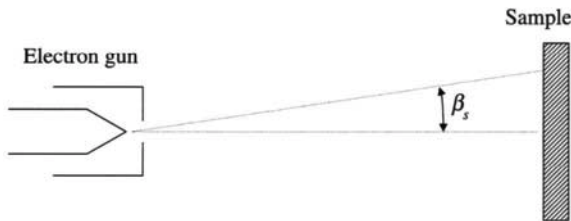


FIG. 8.11 The beam divergence in a low-energy electron diffraction (LEED) setup.

So far, we have derived the angular factor  $F(\theta_{in}, \theta_{out}, \phi)$  for the case of light scattering and x-ray scattering. Other diffraction techniques also have similar factors. For detailed discussion one can refer to the references.

In general, during an experiment, when one measures the angular diffraction profile, the angular factor  $F(\theta_{in}, \theta_{out}, \phi)$  also changes. Therefore, according to Equation (8.9), in order to obtain the diffraction structure factor, one has to remove this angular factor  $F(\theta_{in}, \theta_{out}, \phi)$  in the diffraction intensity. Only in certain special cases, for example in the light scattering, if the span angle is very small so that the angular factor is almost a constant, then one can neglect the effect caused by the angular factor.

### 8.2.2 The instrument response $Y(\mathbf{k})$

The instrument response, or the entire detection-system response, determines the ultimate reciprocal-space resolution of a diffraction system. It is caused by many factors in a non-ideal experimental environment such as finite beam size, beam divergence, energy spread, and detector width. The net result is that even if one has a perfect surface (and ideally should obtain a  $\delta$ -peak intensity), one would only observe a broadened diffraction profile with a finite width called the instrument response. In the following, we use low-energy electron diffraction as an example to demonstrate how different factors can affect the instrument response [8.11, 8.12].

#### 8.2.2.1 Energy spread and beam divergence

In the above discussions, we always assume that the incident beam is collimated and monochromatic, so that the momentum transfer is a single-valued quantity.

In reality, as the source cannot be perfect, the incident beam will have a divergence angle  $\beta_s$  as shown in Figure 8.11, and also an energy spread

$\Delta E$ . These two factors cause uncertainties in the  $k_{||}$  as well as in  $k_{\perp}$ . Since

$$E = \frac{\hbar^2 k^2}{2m}, \quad (8.20)$$

the energy spread causes an uncertainty in  $k$ ,

$$\Delta E = \frac{\hbar^2 k}{m} \Delta k, \quad (8.21)$$

i.e.,

$$\Delta k = \frac{k \Delta E}{2E}. \quad (8.22)$$

Thus, the uncertainty  $\Delta k_{||}^E$  caused by the energy spread in the  $k_{||}$  direction is

$$\Delta k_{||}^E \approx \beta_s \Delta k = \frac{k \Delta E}{2E} \beta_s. \quad (8.23)$$

The value  $\Delta k_{||}^E$  is related to the temporal coherence of the incident beam.

The uncertainty  $\Delta k_{||}^D$  caused by the beam divergence is given by

$$\Delta k_{||}^D = \beta_s k. \quad (8.24)$$

This uncertainty reflects the space coherence of the incident beam. Combining Equations (8.23) and (8.24), one has

$$\Delta k_{||}^{(1)} = \beta_s k \sqrt{1 + \left(\frac{\Delta E}{E}\right)^2}. \quad (8.25)$$

This is the instrument response width in the  $k_{||}$  direction caused by an energy spread  $\Delta E$  and a beam divergence  $\beta_s$ .

From Equation (8.25) one can define a quantity called  $l_c$ , which satisfies

$$l_c \Delta k_{||} = 2\pi; \quad (8.26)$$

i.e.,

$$l_c = \frac{\lambda}{\beta_s \sqrt{1 + \left(\frac{\Delta E}{E}\right)^2}}. \quad (8.27)$$

In the literature, some people refer to the  $l_c$  as “coherent length” instead of the energy spread and the beam divergence. Equation (8.27) connects these two different terminologies.

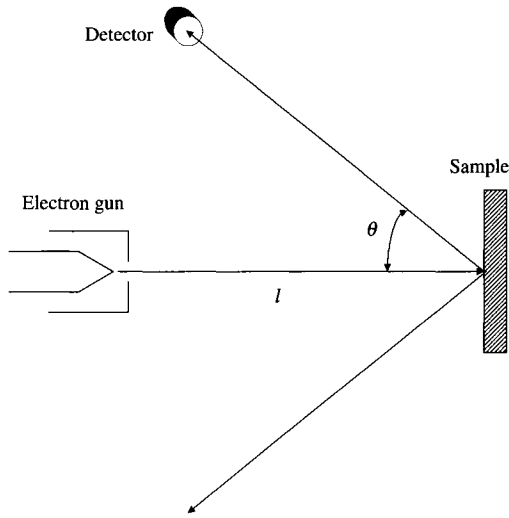


FIG. 8.12 The finite size detector in a LEED setup.

### 8.2.2.2 Detector size

If the aperture of a detector has a certain size, as shown in Figure 8.12, then the uncertainty caused by it can be written as

$$\Delta k_{||}^{(2)} = k \sin \theta_s \frac{D}{l}, \quad (8.28)$$

where  $\theta_s$  is the scattering angle,  $D$  is the diameter of the aperture, and  $l$  is the distance between the electron gun and the sample.

### 8.2.2.3 Beam size

If the incident beam has a finite size, then a similar discussion used for the finite-size detector can be applied to this case. The uncertainty becomes

$$\Delta k_{||}^{(3)} = k \sin \theta_s \frac{d}{l}, \quad (8.29)$$

where  $d$  is the diameter of the incident beam.

The above discussion shows that each instrumental component contributes a response function to the total system response. Letting each response function be  $T_i(k_{||})$  allows the total system response function to be written as

$$T(k_{||}) = T_1(k_{||}) * T_2(k_{||}) * T_3(k_{||}) * \dots, \quad (8.30)$$

where the sign “ $*$ ” denotes a convolution. Very often one can write the final system response function as a Gaussian function:

$$T(k_{||}) = \frac{1}{(2\pi)^{d/2} \Delta k_{||}} \exp\left(-\frac{k_{||}^2}{\Delta k_{||}^2}\right), \quad (8.31)$$

where  $\Delta k_{||}$  is the width of the final system response, which depends in general on all of the uncertainties in the instrumentation discussed above.

If one can measure the shapes of the functions  $I(k_{||})$  and  $T(k_{||})$  precisely, then in principle the true diffraction structure factor can be obtained precisely by either deconvolving  $I(k_{||})$  from  $T(k_{||})$  or convolving  $T(k_{||})$  with a trial function  $S(k_{||})$  iteratively until a good fit of  $I(k_{||})$  is reached. If both  $I(k_{||})$  and  $T(k_{||})$  are Gaussian functions, i.e.,

$$I(k_{||}) \propto \exp\left(-\frac{k_{||}^2}{k_{||F}^2}\right), \quad (8.32)$$

then the diffraction structure factor  $S(k_{||})$  must be a Gaussian function, with FWHM =  $\sqrt{k_{||F}^2 - \Delta k_{||}^2}$ , where  $k_{||F}$  is the measured width of the diffraction intensity profile after correcting the angular factor,  $F(\theta_{in}, \theta_{out}, \phi)$ .

### 8.3 Practical Issues in Diffraction Measurement

#### 8.3.1 Performance

The performance of a diffraction setup is determined by many factors. Using light scattering as an example, the spatial frequency window originates from three sources: the system response, the detector configuration, and the physical limit (the Rayleigh criterion). The largest rotation angle in the measurement (which determines the range of  $k_{||}$  covered in the measurement as we will show in Section 8.2) determines the upper cutoff of the spatial frequency. However, the higher frequency cutoff cannot be extended to infinity due to the Rayleigh criterion, which states that the optical resolution cannot be smaller than  $\lambda/2$ . This makes the ultimate high frequency cutoff  $4\pi/\lambda$ . For the interface width, the range in which a reliable measurement can be made is determined by the signal-to-noise ratio, the dynamic range given by the detector, and the scattering geometry. Similar analyses can be applied to other diffraction systems. Figure 8.13 summarizes the performance of some common diffraction techniques and their comparison with that of some real-space techniques.

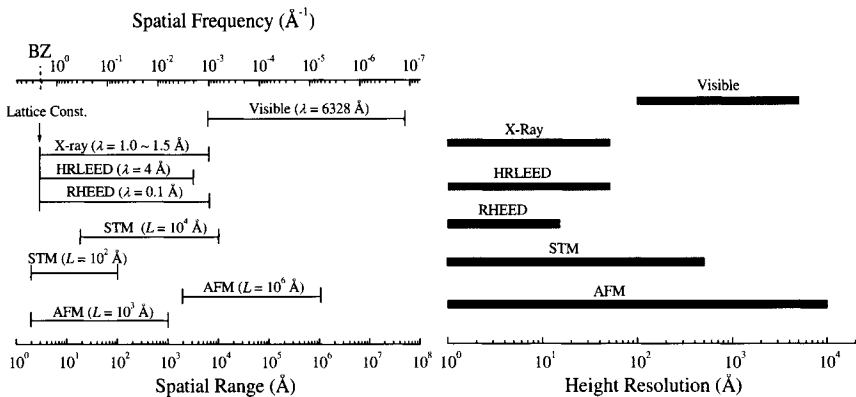


FIG. 8.13 The performance of some common diffraction techniques and some real-space profiling techniques.

### 8.3.2 Data analysis

One very important issue in any diffraction measurement is the data analysis. As we have discussed in this chapter, knowledge of the diffraction geometry is the first step toward a better understanding of the data analysis. One needs to correct for the angular factor  $F(\theta_{in}, \theta_{out}, \phi)$ . One should also measure the system response function  $Y(k_{||})$  in order to obtain the diffraction structure factor  $S(k_{||})$  accurately. To do so, one needs to perform a deconvolution, which is not trivial. Suppose that the diffraction intensity after the angular factor correction can be written as having a finite length and discrete profiles  $I(k_{||} = n)$ . Then, one has

$$I(n) = Y(n) * S(n) = \sum_{i=0}^{N-1} Y(i)S(n-i), \quad (8.33)$$

where  $N$  is the maximum length of the profile. If both  $I(n)$  and  $Y(n)$  are known, then there are basically three algorithms that can be used to obtain  $S(n)$  from Equation (8.33): (1) the matrix method, (2) the iteration method, and (3) the discrete Fourier- and inverse-Fourier-transform method. The first two methods are not trivial. The last method uses the property of the Fourier transform of a convolved pair and is simple and widely used. However, caution is also required because the indeterminate form,  $\frac{0}{0}$ , usually occurs in the process.

If the FWHM of a system response function is much smaller than the FWHM of a diffuse profile, then the effect of the system response function can be neglected. In this case, fitting the angular factor-corrected diffrac-

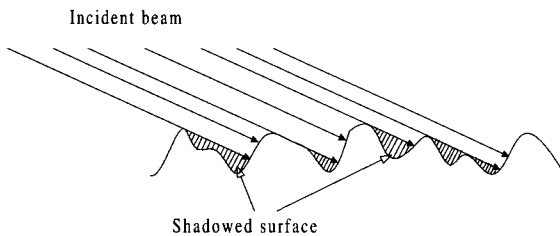


FIG. 8.14 The shadowing effect in grazing incident diffraction.

tion intensity by models can give roughness parameters. Even if the FWHM of a system response function is close to the FWHM of a diffuse profile, no deconvolution is needed if one only uses the ratio of the  $\delta$ -peak intensity to the integrated intensity to determine the interface width  $w$ .

### 8.3.3 Validity of kinematic diffraction theory

Another very important issue in diffraction data analysis is the validity of the kinematic-diffraction approximation. Since all the diffraction structure factors presented in Chapter 6-8 are based on the kinematic theory, one has to understand their limitation in realistic application. The conditions of validity of the KA for light scattering are as follows: the surface lateral correlation length is much larger than the wavelength of the incident light [8.13, 8.14], the root-mean-square slope angle of a surface is small, and all absolute values of the tangent of scattered grazing angles are greater than those of the tangent of root-mean-square slope angles [8.14]. It is shown that within the valid range of the KA, the backscattering enhancement is non-existent or very small [8.13]. There are similar restrictions imposed on other diffraction techniques. Readers can consult the references for further information.

### 8.3.4 Shadowing effect

When the incident angle of a beam with respect to the surface normal becomes very large, the shadowing effect plays an increasing role in the scattered intensity from a rough surface [8.15, 8.16]. Shadowing is the screening of parts of the rough surface by other parts, thus obscuring those parts from being measured, as shown in Figure 8.14. If the penetration depth of the beam into the surface is very short, such as in light scattering, shadowing might have an effect on the determination of the roughness parameters for the large-interface-width case under a large incident angle. Here we can fol-

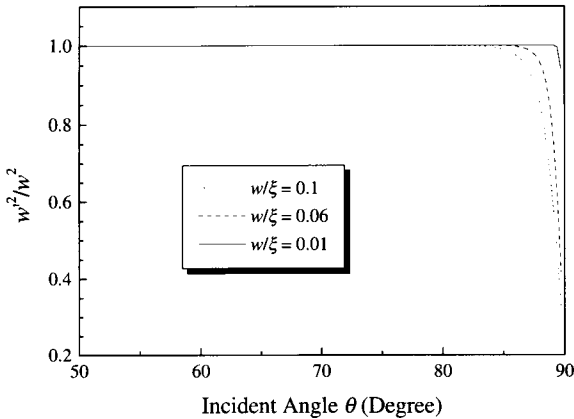


FIG. 8.15 The ratio  $w'^2/w^2$  as a function of the incident angle for  $w/\xi = 0.01, 0.06$ , and  $0.1$  (from Ref. [8.17]).

low Wagner's formula to estimate the shadowing effect [8.16]. The apparent interface width  $w'$  can be written as

$$w'^2 = \frac{w^2}{1 + z_0^2/w^2}, \quad (8.34)$$

where  $z_0$  is the solution of the following equation:

$$\frac{z_0}{\sqrt{2}w} = \frac{B}{\sqrt{\pi}} e^{z_0^2/2w^2}. \quad (8.35)$$

Here

$$B = \frac{e^{-v^2} - \sqrt{\pi} \operatorname{erfc}(v)}{4\sqrt{\pi}v}, \quad (8.36)$$

where  $\operatorname{erfc}(x)$  is the complementary error function and  $v = \xi/(2w \tan \theta)$  for the Gaussian auto-correlation function ( $\alpha = 1.0$ ). In Figure 8.15, we plot the ratio  $w'^2/w^2$  as a function of the incident angle for various  $\frac{w}{\xi}$  values. A severe shadowing effect occurs at very large incident angles, and the larger the  $\frac{w}{\xi}$  ratio, the smaller the incident angle where a severe shadowing effect occurs.

#### 8.4 Summary

This chapter presented the general aspects of the diffraction techniques. There are three important components in a diffraction setup: the source, the sample, and the detector. By varying the angles of each component,

one can achieve different diffraction geometries. We have compared in detail the effects of measurement due to these different geometries. In addition, we have shown that the measured diffraction intensity is proportional to the diffraction structure factor. In order to obtain an accurate diffraction structure factor, one needs to correct for the angular factor caused by the diffraction geometry and the property of the sample and eliminate the effect of the system response function. We also discussed some practical issues concerning diffraction data analysis.

## References

- 8.1 J. C. Stover, *Optical Scattering - Measurement and Analysis*, 2nd Edition (SPIE Optical Engineering Press, Bellinham, 1995).
- 8.2 H. Dosch, *Critical Phenomena at Surfaces and Interfaces: Evanescent X-Ray and Neutron Scattering* (Springer-Verlag, Berlin, 1992).
- 8.3 D. K. Bowen and B. K. Tanner, *High Resolution X-ray Diffractometry and Topography* (Taylor & Francis, Bristol, 1998).
- 8.4 M. Tolan, *X-Ray Scattering from Soft-Matter Thin Films* (Springer, Berlin, 1999).
- 8.5 M. A. Van Hove, W. H. Weinberg, and C.-M. Chan, *Low-Energy Electron Diffraction: Experiment, Theory and Surface Structure Determination* (Springer Verlag, London, 1986).
- 8.6 M. G. Lagally, "Diffraction techniques" in *Methods of Experimental Physics*, Vol. **22**, Edited by R. L. Park and M. G. Lagally (Academic Press, New York, 1985), pp. 237.
- 8.7 M. Henzler in *Electron Spectroscopy for Surface Analysis*, Edited by H. Ibach (Springer, Berlin, 1977).
- 8.8 Y.-P. Zhao, "In-plane light scattering from fractal surfaces – principles and experiments," Ph. D. Thesis, Rensselaer Polytechnic Institute, 1999.
- 8.9 S. K. Sinha, E. B. Sirota, S. Garoff, and H. B. Stanley, "X-ray and neutron scattering from rough surfaces," Phys. Rev. B **38**, 2297 (1988).
- 8.10 Po-zen Wong and Alan J. Bray, "Scattering by rough surfaces," Phys. Rev. B **37**, 7751 (1988).
- 8.11 R. L. Park, J. E. Houston, and D. G. Schreiner, "The LEED instrument response function," Rev. Sci. Instruments **42**, 60 (1971).
- 8.12 T.-M. Lu and M. G. Lagally, "The resolving power of a LEED diffractometer and the analysis of surface imperfections," Surf. Sci. **99**, 695 (1980).
- 8.13 A. Ishimaru and J. S. Chen, "Scattering from very rough surfaces based on the modified second-order Kirchhoff approximation with angular and propagation shadowing," J. Acoust. Soc. Am. **88**, 1877 (1990).
- 8.14 E. I. Thorsos, "The validity of the Kirchhoff approximation for rough surface scattering using a Gaussian roughness spectrum," J. Acoust. Soc. Am. **83**, 78 (1988).
- 8.15 P. Beckmann, "Shadowing of random rough surfaces," IEEE Trans. Antennas Propag. **AP-13**, 384 (1965).
- 8.16 R. J. Wagner, "Shadowing of randomly rough surfaces," J. Acoust. Soc. Am. **41**, 138 (1966).
- 8.17 Y.-P. Zhao, I. Wu, C.-F. Cheng, U. Block, G.-C. Wang, and T.-M. Lu, "Characterization of random rough surfaces by in-plane light scattering," J. Appl. Phys. **84**,

2571 (1998).

This Page Intentionally Left Blank

## 9. SELF-AFFINE FRACTAL SURFACES

So far we have discussed the characterization of random rough surfaces using real-space and diffraction techniques. Beginning with this chapter we shall present some important examples of particular kinds of rough surfaces and demonstrate the use of both real-space and diffraction techniques for the characterization and extraction of the roughness parameters. This chapter begins with a detailed analysis of the self-affine surfaces.

### 9.1 Real-Space Characteristics

As discussed in Chapter 3, for a self-affine and isotropic surface, the height-height correlation function has the scaling form

$$H(r) = 2w^2 f\left(\frac{r}{\xi}\right), \quad (9.1)$$

where

$$f(x) = \begin{cases} x^{2\alpha}, & \text{for } x \ll 1; \\ 1, & \text{for } x \gg 1, \end{cases} \quad (9.2)$$

and the auto-correlation function  $R(r)$  can be written as

$$R(r) = 1 - f\left(\frac{r}{\xi}\right).$$

One can use a phenomenological function to describe the height-height correlation function [9.1]:

$$H(r) = 2w^2 \left\{ 1 - \exp\left[-\left(\frac{r}{\xi}\right)^{2\alpha}\right] \right\}. \quad (9.3)$$

This form reflects the asymptotic behavior of the scaling function  $f(x)$  in a simple and straightforward way. However, as we discussed in Chapter 3, Equation (9.3) cannot describe the behavior when  $\alpha \rightarrow 0$  and its corresponding power spectrum does not have an analytic form. To overcome these drawbacks, we adapt the following form [9.2]:

$$H(r) = 2w^2 \left[ 1 - \frac{\alpha}{2^{\alpha-1} \Gamma(\alpha+1)} \left(\frac{r}{\xi}\right)^\alpha K_\alpha\left(\frac{r}{\xi}\right) \right], \quad (9.4)$$

and thus,

$$R(r) = \frac{\alpha}{2^{\alpha-1} \Gamma(\alpha+1)} \left(\frac{r}{\xi}\right)^\alpha K_\alpha\left(\frac{r}{\xi}\right). \quad (9.5)$$

The parameter  $\alpha$  is called the roughness exponent ( $0 \leq \alpha \leq 1$ ), which describes how wiggly the surface is. The roughness exponent is directly related to the surface fractal dimension  $D_s$  by  $\alpha = d+1 - D_s$ , where  $d+1$  is the dimension of the embedded space. The lateral correlation length  $\xi$  is the distance within which the surface heights of any two points are correlated. These three parameters,  $w$ ,  $\alpha$ , and  $\xi$ , are independent from each other and vary according to the processes by which the surface morphologies are formed. The parameters  $w$ ,  $\xi$ , and  $\alpha$  completely characterize a self-affine surface. The power spectrum can be written as

$$P(k_{||}) = \frac{4\pi\alpha w^2 \xi^2}{(1 + k_{||}^2 \xi^2)^{1+\alpha}}. \quad (9.6)$$

Since the diffraction profile is the Fourier transform of the height difference function, let us first examine the characteristics of the height difference function. The general properties of the height difference function for a Gaussian-height-distributed surface are given by Equation (7.18), and are already demonstrated in Figure 7.1. Now let us examine the FWHM of the height difference function. From Figure 7.1 we know that the FWHM of the height difference function is a function of the factor  $\Omega$ . For  $\Omega \gg 1$ , since  $\exp(-\Omega) \sim 0$ , the half-maximum position  $X$  then satisfies

$$\exp[-\frac{1}{2}k_{\perp}^2 H(X)] = 1/2. \quad (9.7)$$

Substituting Equation (9.3) into Equation (9.7), we obtain

$$X = \xi[-\ln(1 - \ln 2/\Omega)]^{1/2\alpha}. \quad (9.8)$$

Since  $\Omega \gg 1$ , Equation (9.8) can be expanded as

$$X \approx \xi(\ln 2)^{1/2\alpha} \Omega^{-1/2\alpha}. \quad (9.9)$$

Therefore, we can expect that the FWHM of the diffuse profile for  $\Omega \gg 1$  is inversely proportional to the lateral correlation length  $\xi$ , and proportional to  $\Omega^{1/2\alpha}$ . For  $\Omega \ll 1$ , we have

$$\exp[-\frac{1}{2}k_{\perp}^2 H(X)] - \exp(-\Omega) = \frac{1}{2}[1 - \exp(-\Omega)]. \quad (9.10)$$

By expanding Equation (9.10) we obtain

$$R(X) \approx \frac{1}{2}. \quad (9.11)$$

Using Equation (9.3) we can extract the half-maximum position  $X$

$$X = \xi(\ln 2)^{1/2\alpha}. \quad (9.12)$$

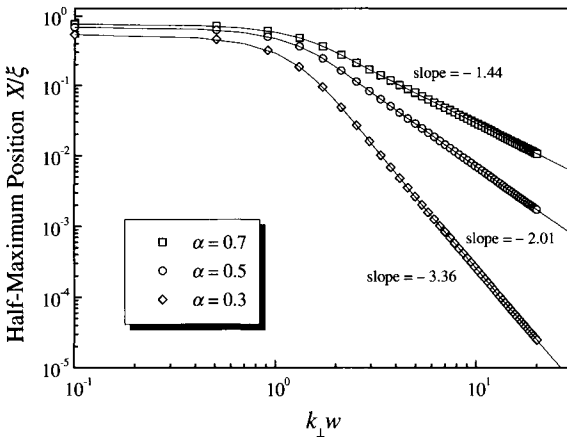


FIG. 9.1 The half-maximum position  $X$  of the height difference function  $C(k_\perp, r)$  at  $\alpha = 0.3, 0.5$ , and  $0.7$ .

In this case the half-maximum position is proportional to the lateral correlation length and has no dependence on  $\Omega$ . Therefore, we expect that the FWHM of the diffuse profile for  $\Omega \ll 1$  is inversely proportional to the lateral correlation length  $\xi$  and remains constant as long as the condition  $\Omega \ll 1$  is satisfied. A log-log plot of the half-maximum position  $X$  of the height difference function as a function of  $k_\perp w$  for different  $\alpha$  values is shown in Figure 9.1. We can see that for small  $k_\perp w$ , the half-maximum position remains almost unchanged, while for large  $k_\perp w$ , the half-maximum position decays as a power law of  $k_\perp w$ :  $X \sim (k_\perp w)^{-1/\alpha}$ , which is consistent with our asymptotic prediction in Equation (9.9).

## 9.2 Diffraction from an Isotropic Self-Affine Gaussian Surface

The  $\delta$ -peak intensity can be still expressed as Equation (7.23), and the diffuse profiles becomes

$$S_{diff}(\mathbf{k}_{||}, k_\perp) = e^{-\Omega} \sum_{n=1}^{\infty} \frac{1}{n!} \Omega^n \int r [1 - f(\frac{r}{\xi})]^n J_0(k_{||}) dr. \quad (9.13)$$

### 9.2.1 The asymptotic behavior of the diffraction structure factor

(1)  $\Omega \ll 1$

Under the conditions discussed above, the diffraction structure factor can be expressed simply as

$$S(\mathbf{k}_{||}, k_{\perp}) = (2\pi)^2 e^{-\Omega} \delta(\mathbf{k}_{||}) + \Omega e^{-\Omega} P(\mathbf{k}_{||}). \quad (9.14)$$

Substituting Equation (9.6) into Equation (9.14), we have

$$S(\mathbf{k}_{||}, k_{\perp}) = (2\pi)^2 e^{-\Omega} \delta(\mathbf{k}_{||}) + \Omega e^{-\Omega} \frac{4\pi\alpha w^2 \xi^2}{(1 + k_{||}^2 \xi^2)^{1+\alpha}}. \quad (9.15)$$

The  $\delta$ -peak intensity decays as  $e^{-\Omega}$ , and the diffuse profile is proportional to the surface power spectrum. The line shape of the diffuse profile in Equation (9.15) has a FWHM inversely proportional to the lateral correlation length,

$$\text{FWHM} = \frac{2\sqrt{2^{1/(1+\alpha)} - 1}}{\xi}. \quad (9.16)$$

The numerator varies from 2 to about 1.3 as  $\alpha$  changes from 0 to 1. This is consistent with our expectation from Equation (9.12). Equation (9.16) can be used to determine the lateral correlation length in a diffraction experiment. However, one should keep in mind that for different values of the roughness exponent  $\alpha$  the pre-factors may not be the same. Since the diffuse profile is proportional to the surface power spectrum, according to Chapter 3, the tail of the diffuse profile ( $k_{||}\xi \gg 1$ ) satisfies

$$S_{diff}(\mathbf{k}_{||}, k_{\perp}) \propto k_{||}^{-2-2\alpha}. \quad (9.17)$$

Thus, one can determine the roughness exponent  $\alpha$  from the tail of the diffraction structure factor. As long as  $\Omega \ll 1$  is satisfied, the shapes of both the  $\delta$  peak and the diffuse profile do not change; only the relative intensity changes.

On the other hand, the contribution of a diffuse factor is very small as compared to that of the  $\delta$ -peak intensity. Therefore, the total peak intensity of the diffraction structure factor is approximately proportional to the Debye-Waller-like factor,  $e^{-\Omega}$ .

## (2) $\Omega \gg 1$

Under this condition, the  $\delta$  peak is negligibly small, as  $e^{-\Omega} \rightarrow 0$ . The diffraction structure factor  $S(\mathbf{k}_{||}, k_{\perp})$  can be represented by only its diffuse profile  $S_{diff}(\mathbf{k}_{||}, k_{\perp})$ , and therefore the diffraction becomes purely “diffusive.” Figure 9.2 shows the calculated diffuse profiles for  $\alpha = 0.3, 0.5$ , and  $0.7$  at  $k_{\perp}w = 10$ . For different  $\alpha$  values the diffuse profiles have different shapes. In this case the diffraction detects only the short-range behavior

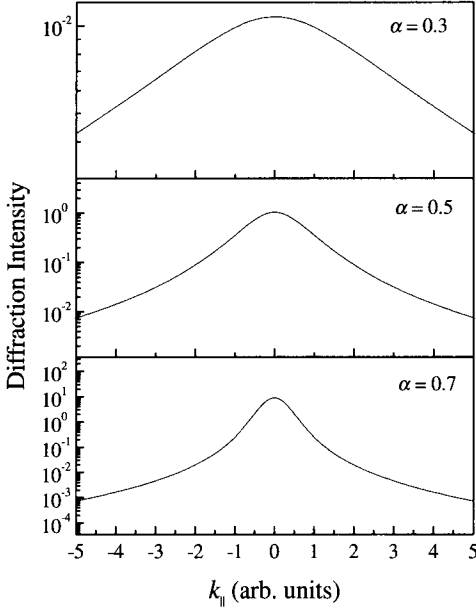


FIG. 9.2 The diffuse profiles of self-affine surfaces for  $\alpha = 0.3, 0.5$ , and  $0.7$  at  $k_{\perp}w = 10$ .

in the rough surface, and the height difference function is clearly confined to the short-range regime:

$$C(k_{\perp}, \mathbf{r}) = e^{-\frac{1}{2}k_{\perp}^2 H(\mathbf{r})} = e^{-\Omega f(\frac{r}{\xi})} \approx e^{-\Omega(\frac{r}{\xi})^{2\alpha}}. \quad (9.18)$$

Note that here we only use the asymptotic behavior of the scaling function  $f(x)$ , no special function forms of  $f(x)$  is assumed. Then the diffraction structure factor becomes

$$\begin{aligned} S(\mathbf{k}_{||}, k_{\perp}) &\approx 2\pi \int_0^{\infty} r e^{-\Omega(\frac{r}{\xi})^{2\alpha}} J_0(k_{||}r) dr \\ &= 2\pi\xi^2\Omega^{-1/\alpha} \int_0^{\infty} X e^{-X^{2\alpha}} J_0(k_{||}\xi\Omega^{-1/2\alpha}X) dX. \end{aligned} \quad (9.19)$$

Thus, the asymptotic diffraction structure factor is the Fourier transform of the height difference function in the short-range regime. Letting

$$G_{\alpha}(Y) = \int_0^{\infty} X e^{-X^{2\alpha}} J_0(YX) dX, \quad (9.20)$$

then Equation (9.19) can be rewritten as [9.3]

$$S(\mathbf{k}_{||}, k_{\perp}) \approx 2\pi\xi^2\Omega^{-1/\alpha} G_{\alpha}(k_{||}\xi\Omega^{-1/2\alpha}). \quad (9.21)$$

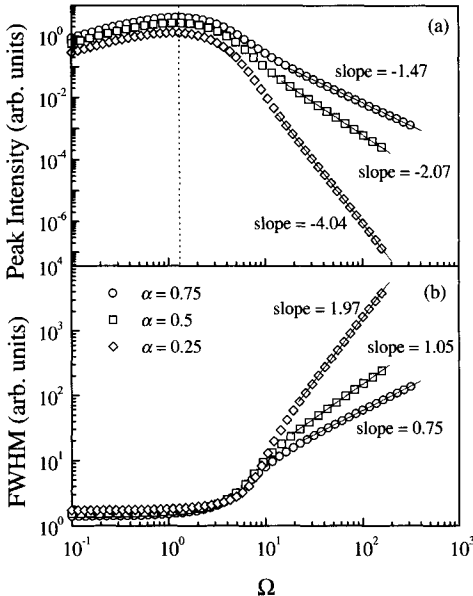


FIG. 9.3 (a) The peak intensity and (b) the FWHM of the diffuse profile as a function of  $\Omega$  for different  $\alpha$  values.

This asymptotic diffraction structure factor is the same for any form of scaling function  $f(x)$  described by Equation (3.3) for a self-affine surface. This universal form of the short-range height difference function can lead to the universal form of the diffraction structure factor characterized by  $w$ ,  $\xi$ , and  $\alpha$ . The peak intensity of the profile is

$$S(0, k_{\perp}) \propto (\xi \Omega^{-1/2\alpha})^2 = (\xi w^{-1/\alpha})^2 k_{\perp}^{-2/\alpha}, \quad (9.22)$$

and the FWHM of the profile is

$$\text{FWHM} = \frac{2Y_{\alpha}}{\xi \Omega^{-1/2\alpha}} = \frac{2Y_{\alpha}}{\xi w^{-1/\alpha}} k_{\perp}^{1/\alpha}. \quad (9.23)$$

Here  $Y_{\alpha}$  satisfies  $G_{\alpha}(Y_{\alpha}) = \frac{1}{2}G_{\alpha}(0)$ . Equation (9.22) shows that the peak intensity of the diffraction structure factor decays with  $k_{\perp}$  according to a power law, while Equation (9.23) demonstrates that the FWHM increases with  $k_{\perp}$  following a power law. However, the total scattered energy, which is approximately proportional to  $S(0, k_{\perp}) \times (\text{FWHM})^2$ , is a constant. This is the requirement of energy conservation, i.e., no matter how  $k_{\perp}$  changes, the total scattered energy should equal to the total incident energy. Figure 9.3 shows the peak intensity and the FWHM of the diffuse profile for different  $\alpha$  values. We can see that the peak intensity increases for small  $\Omega$

values and reaches a maximum at  $\Omega \approx 1$  (the dotted line). Then it decays dramatically. At large  $\Omega$ , the peak intensity decreases as a power law of  $\Omega$ . From Figure 9.3 we can estimate that  $S(0, k_{\perp}) \propto \Omega^{-1/\alpha}$ , which is consistent with Equation (9.22). The FWHM remains almost a constant for small  $\Omega$ , but increases as a power law at large  $\Omega$ . Figure 9.3(b) shows that  $\text{FWHM} \propto \Omega^{1/2\alpha}$ , which is consistent with Equation (9.23). We also should mention that in Equations (9.22) and (9.23),  $w$  and  $\xi$  are grouped together by the parameter  $\eta = \xi w^{-1/\alpha}$ . Therefore  $\eta$  is an important parameter reflecting the behavior of the short-range roughness of a surface. Obviously, Equation (9.23) is consistent with the expectation of Equation (9.9).

Now let us look at the asymptotic behavior of the tail of the diffraction structure factor. Equation (9.13) can be rewritten as

$$S_{diff}(\mathbf{k}_{||}, k_{\perp}) = e^{-\Omega} \xi^2 \sum_{n=1}^{\infty} \frac{1}{n!} \Omega^n \int_0^{\infty} x [1 - f(x)]^n J_0(k_{||} \xi x) dx. \quad (9.24)$$

For any  $\Omega$  and large  $k_{||}$  [ $\gg M^{1/\alpha} \xi^{-1}$ , where  $M$  is an upper cutoff of the summation determined by  $\Omega$  as shown in Equation (7.31)], the main contribution to the integration in Equation (9.24) is from  $x \ll 1$ ; therefore, the asymptotic behavior of the integral for large  $k_{||}$  can be written as

$$\int_0^{\infty} x [1 - f(x)]^n J_0(k_{||} \xi x) dx \approx \int_0^{\infty} x (1 - nx^{2\alpha}) J_0(k_{||} \xi x) dx. \quad (9.25)$$

Then based on the results obtained in Chapter 3 [Equations (3.7) and (3.8)], one has [9.4]

$$S_{diff}(\mathbf{k}_{||}, k_{\perp}) \approx 2\pi e^{-\Omega} \xi^{-2\alpha} A \sum_{n=1}^{\infty} \frac{1}{(n-1)!} \Omega^n k_{||}^{-2-2\alpha} = 2\pi \xi^{-2\alpha} \Omega A k_{||}^{-2-2\alpha}. \quad (9.26)$$

For any value of  $\Omega$ , the shape of a diffuse profile follows a power law for large  $k_{||}$  as shown in the asymptotic form of Equation (9.26). The general relationship for a surface embedded in  $d+1$  dimensions can be expressed as

$$S_{diff}(\mathbf{k}_{||}, k_{\perp}) \propto k_{||}^{-d-2\alpha}, \text{ for } k_{||} \gg M^{1/\alpha} \xi^{-1}. \quad (9.27)$$

As  $M \propto \Omega$ , the value of  $\Omega$  determines the onset point of the power-law tail. When  $\Omega$  increases, the onset point increases, and the power-law tail appears at larger  $k_{||}$  values. Figure 9.4 shows the log-log plot of the diffuse profiles for different  $\sqrt{\Omega}$  values and different  $\alpha$  values.

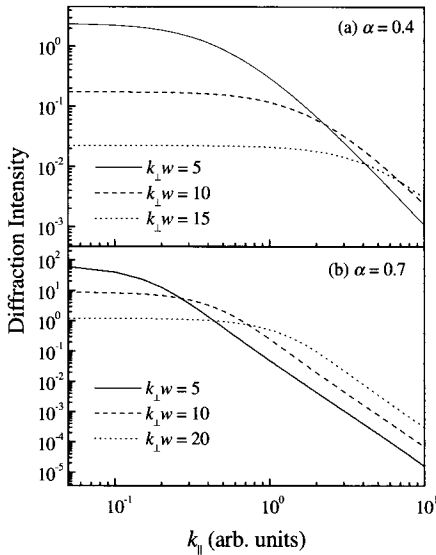


FIG. 9.4 The asymptotic behavior of the diffuse profile at large  $k_{\parallel}$  for  $k_{\perp}w > 1$ : (a)  $\alpha = 0.4$  and (b)  $\alpha = 0.7$ . Note that the tails are parallel to each other for different  $k_{\perp}w$  at large  $k_{\parallel}$ .

### 9.2.2 Determination of roughness parameters $w$ , $\xi$ , and $\alpha$ from diffraction profiles

Since the three roughness parameters,  $w$ ,  $\xi$ , and  $\alpha$ , uniquely determine the diffraction structure factor, one should also be able to retrieve these three roughness parameters uniquely from the measured diffraction profiles. In fact, this is the ultimate purpose of the diffraction measurement. Based on the above discussion, in fact, we can determine these parameters in various ways.

#### (1) RMS roughness $w$

(i) Extraction of  $w$  from the measured  $\delta$ -peak intensity  $S_{\delta}$  versus  $k_{\perp}$ . As  $S_{\delta} \propto e^{-k_{\perp}^2 w^2}$ , we can plot  $\ln(S_{\delta})$  versus  $k_{\perp}^2$ , and the slope of the plot gives  $w^2$ . This method requires changing  $k_{\perp}$  and obtaining a series of diffraction curves for different  $k_{\perp}$  values.

(ii) Extraction of  $w$  from a measured ratio,  $R_{\delta}$ , of the integrated  $\delta$ -peak intensity to the total integrated diffraction intensity. According to the relation  $R_{\delta} = \frac{I_{\delta}}{I} = e^{-\Omega}$  [Equation (7.35)], one can calculate  $w$  from a single diffraction profile.

Table 9.1 Summary of various methods for determining the roughness parameters of self-affine surfaces.

<b>Interface width <math>w</math></b>	Plot the $\delta$ intensity $S_\delta$ vs. $k_\perp^2$ , according to the relation $S_\delta \propto e^{-k_\perp^2 w^2}$ . From the $\delta$ -peak ratio, $R_\delta = e^{-k_\perp^2 w^2}$ . From the diffuse intensity ratio, $R_{diff} = 1 - e^{-k_\perp^2 w^2}$ . From the IFT of the diffraction profiles.
<b>Lateral correlation length <math>\xi</math></b>	$\text{FWHM} \propto 1/\xi$ for $k_\perp^2 w^2 \ll 1$ . From the IFT of the diffraction profiles.
<b>Roughness exponent <math>\alpha</math></b>	Plot the diffuse peak intensity $S_{diff}(0, k_\perp)$ vs. $k_\perp$ according to the relation $S_{diff}(0, k_\perp) \propto k_\perp^{-2/\alpha}$ for $k_\perp^2 w^2 \gg 1$ . Plot the FWHM vs. $k_\perp$ according to the relation $\text{FWHM} \propto k_\perp^{1/\alpha}$ for $k_\perp^2 w^2 \gg 1$ . Plot $S(k_{  }, k_\perp)$ vs. $k_{  }$ according to $S(k_{  }, k_\perp) \propto k_{  }^{-d-2\alpha}$ for $k_{  } \gg M^{1/\alpha} \xi^{-1}$ . From the IFT of the diffraction profiles.

(iii) Extraction of  $w$  from the measured ratio,  $R_{diff}$ , of the integrated diffuse intensity to the total integrated diffraction intensity. According to the relation  $R_{diff} = \frac{I_{diff}}{I} = 1 - e^{-\Omega}$  [Equation (7.36)], one can also calculate  $w$  from a single diffraction profile. In the case of  $\Omega \ll 1$ , the relationship can be simplified as  $R_{diff} \approx \Omega$ .

### (2) Lateral correlation length $\xi$

According to Equation (9.16), the FWHM of a diffuse profile at  $\Omega \ll 1$  is inversely proportional to  $\xi$ . Therefore we can determine  $\xi$  using the FWHM through a single diffraction profile. However, we should emphasize that since the proportionality factor changes for different  $\alpha$  values, unless  $\alpha$  is the same, one cannot compare the absolute  $\xi$  values measured using this relation for different surfaces.

### (3) Roughness exponent $\alpha$

(i) Extraction of  $\alpha$  from the peak intensity of a diffuse profile versus  $k_\perp$  under the condition  $\Omega \gg 1$ . According to Equation (9.22), for  $\Omega \gg 1$ ,

$S_{diff}(0, k_\perp)$  obeys a power law of  $k_\perp$ :  $S_{diff}(0, k_\perp) \propto k_\perp^{-2/\alpha}$ . Therefore, by plotting profiles versus  $k_\perp$  in a log-log scale, one should expect a straight line, and the slope of this line gives  $-2/\alpha$ . This method requires many diffraction profiles under the condition  $\Omega \gg 1$ .

(ii) Extraction of  $\alpha$  from the FWHM of a diffuse profile versus  $k_\perp$  under the condition  $\Omega \gg 1$ . According to Equation (9.23), for  $\Omega \gg 1$ , the FWHM obeys a power law of  $k_\perp$ :  $\text{FWHM} \propto k_\perp^{1/\alpha}$ . Therefore, the slope in the log-log plot is  $1/\alpha$ .

(iii) Extraction of  $\alpha$  from the tail of a diffuse profile versus large  $k_{||}$ . According to Equation (9.17), the diffuse profile has a power law behavior with large  $k_{||}$ :  $S_{diff}(\mathbf{k}_{||}, k_\perp) \propto k_{||}^{-d-2\alpha}$ , for  $k_{||} \gg M^{1/\alpha} \xi^{-1}$ . This only requires a single diffraction profile.

#### 4) Inverse Fourier transform (IFT) method

Since the diffraction profile  $S(\mathbf{k}_{||}, k_\perp)$  is the Fourier transform of the height difference function  $C(k_\perp, \mathbf{r})$ , we can perform an inverse Fourier transform to obtain  $C(k_\perp, \mathbf{r})$ . Using the simple relation  $C(k_\perp, \mathbf{r}) = e^{-\frac{1}{2}k_\perp^2 H(\mathbf{r})}$ , we can obtain the height-height correlation function  $H(\mathbf{r})$ , from which all the three roughness parameters  $w$ ,  $\xi$ , and  $\alpha$  can be determined by a single diffraction profile [9.5]. Note that, if the surface is isotropic, the inverse Fourier transform would become an inverse Hankel transform. In Table 9.1, we summarize various methods used to determine the roughness parameters.

##### 9.2.3 The reciprocal-space structure

As we have discussed in the above sections, from the diffraction profiles, we can obtain the roughness parameters. The reciprocal-space structure is determined by the surface morphology. In fact, from the above discussion, the momentum transfer perpendicular to the surface,  $k_\perp$ , is always connected with the vertical fluctuation (RMS roughness  $w$ ) of the surface, and the momentum transfer parallel to the surface,  $\mathbf{k}_{||}$ , always reflects the lateral length scale of the surface. Since  $k_\perp$  and  $\mathbf{k}_{||}$  are orthogonal in the reciprocal space, we can use a plot including both of them to characterize a rough surface. An example of this reciprocal “rod” structure for a self-affine surface with  $\alpha = 0.7$  is shown in Figure 9.5. The central dark line represents the position and strength (magnitude) of the  $\delta$ -peak intensity. The dashed curves represent the half-maximum positions of the diffuse profile where the intensity drops to half of the peak intensity of the diffuse profile. The shaded area therefore represents the region within the half-width positions

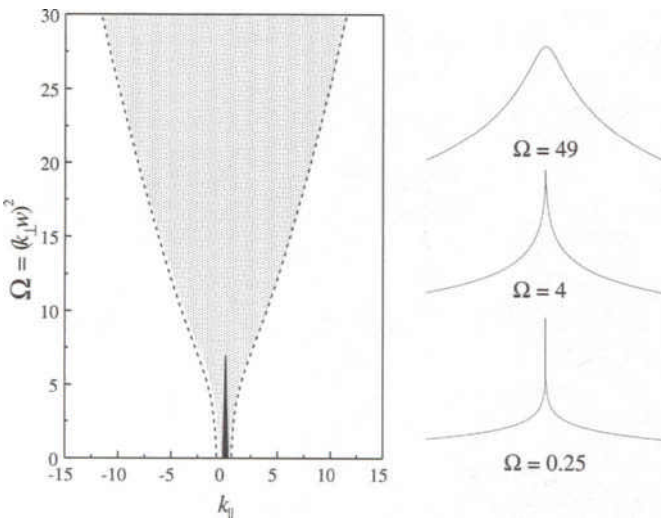


FIG. 9.5 The reciprocal-space structure of a continuous self-affine surface.

of the profile. Also the shape of the profiles at different  $\Omega$  values is shown in the right panel.

The reciprocal-rod structure captures the essence of the diffraction behavior from the self-affine surface. We can see from Figure 9.5 that the  $\delta$ -peak intensity decays as  $\Omega$  increases. Also, at the small- $\Omega$  regime, the FWHM of the diffuse profile remains almost unchanged while at large  $\Omega$  regime the FWHM increases monotonically with  $\Omega$ . These are the characteristics of the diffraction behavior of a self-affine surface as discussed in Section 9.2.1.

### 9.3 An Example: The Backside of Silicon Wafers

The validity of the above theoretical predictions of the scattering behavior from a self-affine surface has been tested in several experiments using different diffraction techniques [9.6, 9.7, 9.8, 9.9]. One such experiment was carried out by Zhao et al. [9.10], who studied the diffraction characteristics of several rough Si backside surfaces using the in-plane light scattering technique. The complete reciprocal-space structure of the self-affine rough surface was mapped out by analyzing the angular distribution of the scattered intensity. The surface roughness parameters, including the interface width, lateral correlation length, and the roughness exponent, extracted from the light scattering data were compared with those obtained by real-

Table 9.2 Summary of roughness parameters of ten Si backside samples obtained from light scattering (LS), atomic force microscopy (AFM), and stylus profilometry (SP).

No.	$w$ (nm)			$\xi$ ( $\mu\text{m}$ )		$\alpha$	
	LS	AFM	SP	LS	AFM	LS	AFM
1	$78 \pm 4$	$114 \pm 7$	$81 \pm 4$	$3.5 \pm 0.01$	$4.0 \pm 0.01$	$.80 \pm .02$	$.78 \pm 0.02$
2	$64 \pm 3$	$125 \pm 4$	$64 \pm 2$	$3.7 \pm 0.01$	$4.5 \pm 0.01$	$.89 \pm .02$	$.93 \pm 0.02$
3	$112 \pm 6$	$169 \pm 6$	$103 \pm 4$	$3.4 \pm 0.01$	$4.2 \pm 0.02$	$.89 \pm .02$	$.93 \pm 0.02$
4	$203 \pm 10$	$240 \pm 7$	$220 \pm 8$	$4.0 \pm 0.02$	$5.5 \pm 0.02$	$.94 \pm .02$	$.91 \pm 0.02$
5	$236 \pm 12$	$277 \pm 6$	$195 \pm 7$	$3.8 \pm 0.02$	$4.6 \pm 0.01$	$.91 \pm .02$	$.85 \pm 0.02$
6	$323 \pm 16$	$305 \pm 7$	$367 \pm 10$	$4.4 \pm 0.02$	$4.4 \pm 0.01$	$.97 \pm .02$	$.99 \pm 0.02$
7	$440 \pm 20$	$443 \pm 29$	$534 \pm 25$	$11.3 \pm 0.05$	$10.4 \pm 0.05$	$.88 \pm .02$	$.90 \pm 0.02$
8	$482 \pm 24$	$476 \pm 17$	$549 \pm 19$	$8.5 \pm 0.04$	$8.0 \pm 0.04$	$.87 \pm .02$	$.89 \pm .02$
9	$401 \pm 20$	$480 \pm 25$	$585 \pm 25$	$10.7 \pm 0.04$	$11.0 \pm 0.05$	$.91 \pm .02$	$.93 \pm .02$
10	$480 \pm 23$	$590 \pm 22$	$614 \pm 31$	-	$9.4 \pm 0.05$	$.89 \pm .02$	$.87 \pm .02$

space imaging techniques, including atomic force microscopy (AFM) and stylus profilometry (SP).

### 9.3.1 Experimental setup

The real-space characterizations were carried out by both AFM and SP techniques. AFM scans were measured using a Park Scientific Instruments AutoProbe CP with  $\text{Si}_3\text{N}_4$  tips. The typical radius and the tip side angle were about 10 nm and  $10^\circ$ , respectively. The SP was an alpha-step profilometer with a tip size of 5  $\mu\text{m}$ . The samples were the backsides of Si(100) wafers. The detailed real-space characterization of these surfaces was described in Section 5.1. We know that the backsides of the silicon wafers are isotropic, homogeneous, Gaussian, self-affine surfaces. The results are shown in Table 9.2. Table 9.2 also gives the interface width measured by SP. All of the measured values of the roughness exponent fall in the range 0.78 - 0.99. This suggests that the dynamics of roughness formation may be quite similar during the manufacturing of the Si wafers.

In the light scattering (LS) experiment (Figure 9.6), the incident light was a helium-neon laser with a wavelength of 632.8 nm. A spatial filter was used in order to improve the quality of the incident beam. Neutral density filters were also used to reduce the intensity of the light so that it would not saturate the photodiode array. The sample was mounted on a rotational stage to allow for a variation of incident angle  $\theta$ , measured with respect to the surface normal.

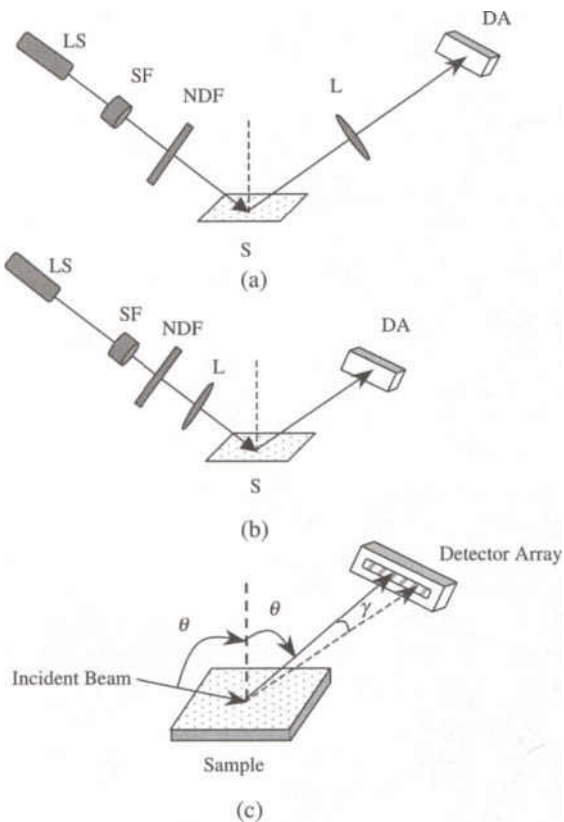


FIG. 9.6 (a) In experimental setup 1, the lens (L) is placed between the sample (S) and the detector array (DA). (b) In experimental setup 2, the lens is placed between the neutral-density filter (NDF) and the sample. (c) A schematic of the in-plane light scattering geometry for the study of surface roughness. LS represents a laser source and SF represents a spatial filter (from Ref. [9.10]).

Two configurations were used in light scattering as shown in Figures 9.6(a) and 9.6(b). The first one [Figure 9.6(a)] shows that the scattered light from the surface passed through a lens with a focal length  $f$  of 17.5 cm and that the detector was set up at the focal plane of the lens so that parallel beams entered the detector. The second setup [Figure 9.6(b)] shows that the lens was placed in front of the sample, and the detector was also located at the focal plane of the lens. That is, the sum of distances from the lens to the sample and from the sample to the detector in Figure 9.6(b) equals the distance from the lens to the detector in Figure 9.6(a). In both configurations the detector array was positioned for in-plane scattering measurement [Figure 9.6(c)]. The length  $L$  of the diode array was 2.5 cm

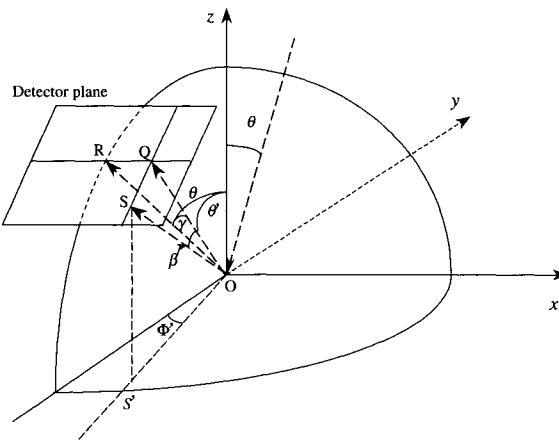


FIG. 9.7 The detailed diffraction geometry for a finite-size slit detector and the  $k$ -space coordinates,  $k_x$ ,  $k_y$ , and  $k_{\perp}$  (from Ref. [9.10]).

and contained 1024 photodiodes. The separation between two adjacent diodes was  $L/1024$ , or approximately  $25 \mu\text{m}$ . The resolution of the detector in  $k$  space was  $25 \times k_0/f \approx 1.4 \times 10^{-3} \mu\text{m}^{-1}$  for the first setup, where  $k_0 = 2\pi/\lambda$ . The resolution of the second setup depends on the distance between the sample and the detector. The advantage of the second setup is that one can change the measured  $k_{||}$  range by changing the distance between the lens and the sample. The length of each diode perpendicular to the direction of the array was 0.25 cm, which spans a  $k$ -space range of  $1.4 \times 10^{-1} \mu\text{m}^{-1}$ . Therefore each diode acts as a slit detector.

The detail of the diffraction geometry is shown in Figure 9.7. Note that in order to illustrate the scattering geometry more clearly, we rotate the original experimental setup presented in Figure 9.6 by  $180^\circ$ . The incident plane is the  $y$ - $z$  plane, and  $OR$  is a reflection direction with polar angle  $\theta$  in the  $y$ - $z$  plane. The detector plane consisting of a 1024-slit diode array is perpendicular to the  $OR$  direction. The  $OQ$  is the detector's position if the slit detector is point detector and has a polar angle  $\theta'$  ( $\neq \theta$ ). The angle  $\gamma$  between  $OQ$  and  $OR$  is the in-plane angle. The angle  $\beta$  is the polar angle from  $OQ$  to  $OS$  due to the finite size of the slit detector. The angle  $\Phi'$  is the azimuthal angle such that the projection of  $OS$  in the  $x$ - $y$  plane is in the  $-y$  direction. Using the geometry in Figure 9.7, one can write the incident wave vector as

$$\mathbf{k}_0 = (0, k_0 \sin \theta, -k_0 \cos \theta) \quad (9.28)$$

and the scattered wave vector along the  $OS$  direction as

$$\mathbf{k}_s = [k_0 \sin(\theta' + \beta) \sin \Phi', -k_0 \sin(\theta' + \beta) \cos \Phi', \cos(\theta' + \beta)]. \quad (9.29)$$

One can further determine that  $\cos \theta' = \cos \theta \cos \gamma$  and  $\tan \Phi' = \tan \gamma / \sin \theta$ . Therefore, the momentum transfers along both the  $k_x$  and  $k_y$  directions are

$$\begin{aligned} k_x &= k_0 (\tan \gamma / \sqrt{\tan^2 \gamma + \sin^2 \theta}) [\sqrt{1 - \cos^2 \theta \cos^2 \gamma} \cos \beta \\ &\quad + \cos \theta \cos \gamma \sin \beta] \\ &\approx k_0 \tan \gamma, \text{ and} \end{aligned} \quad (9.30)$$

$$\begin{aligned} k_y &= -k_0 (\sin \theta / \sqrt{\tan^2 \gamma + \sin^2 \theta}) [\sqrt{1 - \cos^2 \theta \cos^2 \gamma} \cos \beta \\ &\quad + \cos \theta \cos \gamma \sin \beta] + k_0 \sin \theta \\ &\approx -k_0 \cos \theta \sin \beta. \end{aligned} \quad (9.31)$$

The approximations can be made if both angles  $\gamma$  and  $\beta$  are small. Because of the geometry of the slit detector, the actual intensity profile measured by the detector array is the integral of  $S(k_x, k_y)$  over both the  $k_x$  and  $k_y$  directions, on the intervals  $(k_x - \Delta_x/2, k_x + \Delta_x/2)$  and  $(-\Delta_y/2, \Delta_y/2)$ :

$$S_r(k_x) = \int_{k_x - \Delta_x/2}^{k_x + \Delta_x/2} dk_x \int_{-\Delta_y/2}^{\Delta_y/2} S(k_x, k_y) dk_y. \quad (9.32)$$

From the above discussion, we know that  $\Delta_x \approx 1.4 \times 10^{-3} \mu\text{m}^{-1}$  and  $\Delta_y \approx 1.4 \times 10^{-1} \mu\text{m}^{-1}$ . Assuming  $\Delta_y \gg \text{FWHM}$  of the diffuse profile, one can extend the integration over  $k_y$  to infinity:

$$S_r(k_x) \approx \Delta_x \int_{-\infty}^{\infty} S(k_x, k_y) dk_y = \Delta_x \int e^{-k_\perp^2 H(x)/2} e^{-ik_x x} dx, \quad (9.33)$$

i.e., the scattering profile becomes the one-dimensional Fourier transform of the function  $e^{-k_\perp^2 H(x)/2}$ . Equation (9.33) is the one-dimensional analogue of Equation (7.19).

The momentum transfer parallel to the surface is  $k_{||} \approx k_x \approx k_0 \tan \gamma$ , where  $\gamma$  is the in-plane scattering angle and the  $\gamma$  is small. Also, the momentum transfer perpendicular to the surface is  $k_\perp = k_0 \cos \theta \cos \gamma + k_0 \cos \theta \approx 2k_0 \cos \theta$ , where  $\theta$  is the angle of incidence with respect to the surface normal. The range of  $k_{||}$  covered by the diode array is about  $k_0 \times L/f \approx 1.4 \mu\text{m}^{-1}$ . This range determined the size of the window in the profile measurement. The diode array could be moved along the in-plane direction to increase the range of  $k_{||}$ , thereby increasing the window size. Each scattered profile was obtained within 30 milliseconds using a diode

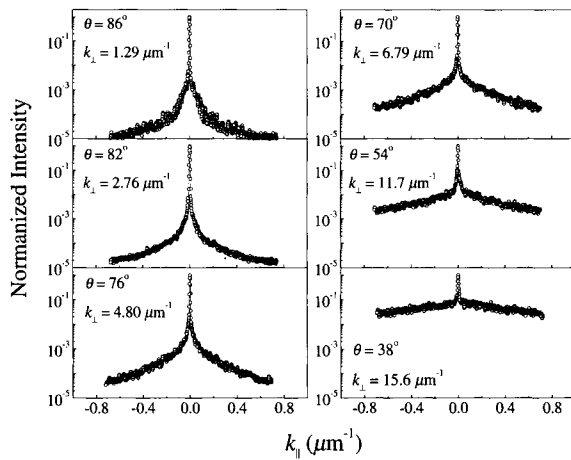


FIG. 9.8 The  $k_{\perp}$ -dependent light scattering profiles at different incident angles for Si Sample #3 (from Ref. [9.10]).

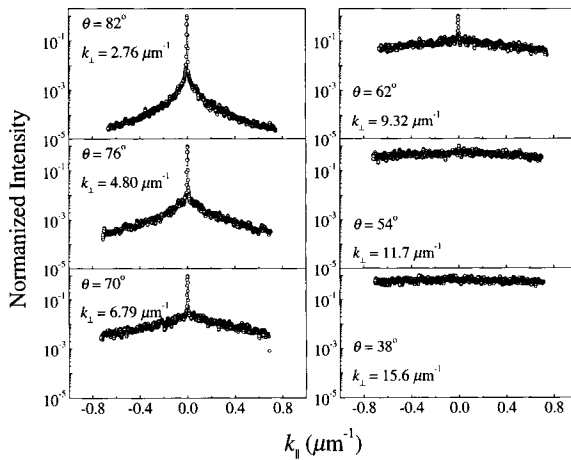


FIG. 9.9 The  $k_{\perp}$ -dependent light scattering profiles at different incident angles for Si Sample #5 (from Ref. [9.10]).

array detector. Five hundred accumulations were made for each scan of the angular profile in order to gain a high signal-to-noise ratio.

### 9.3.2 Experimental results

In Figures 9.8, 9.9, and 9.10, we plot the angular-dependent scattering profiles with different incident angles using the first setup [Figure 9.6(a)]

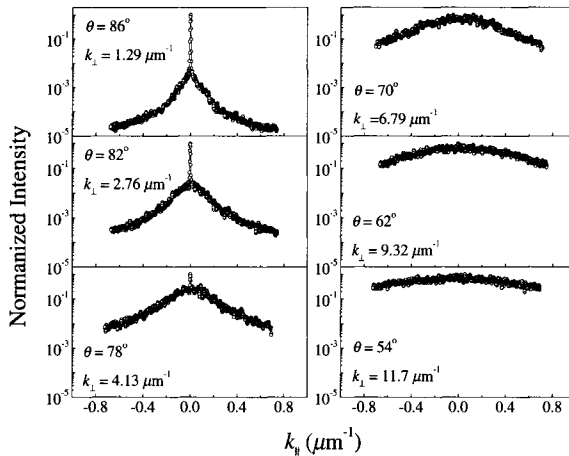


FIG. 9.10 The  $k_{\perp}$ -dependent light scattering profiles at different incident angles for Si Sample #10 (from Ref. [9.10]).

for Samples #3, #5, and #10 shown in Table 9.2, respectively. One can observe some very noticeable characteristics. 1) For very large incident angles, the scattering profile from each sample contains two parts: a sharp, central ( $\delta$ -like) peak intensity and a diffuse profile. 2) For the same sample, as the incident angle decreases, which corresponds to the increase of  $k_{\perp}$ , the central sharp intensity gradually decreases until it totally disappears. At the same time, the diffuse profile broadens. 3) The larger the interface width, the larger the incident angle at which the central peak disappears. All of these features are predicted by the diffraction theory discussed in the above sections.

One can fit the scattering profiles using a narrow Gaussian peak (which corresponds to the  $\delta$ -peak intensity convolved with the instrument broadening) and a broad diffuse intensity using Equation (7.24). The FWHM of the diffuse profile as a function of  $k_{\perp}$  can then be obtained from Equation (7.24) by assuming Equation (9.3) as the functional form of the height-height correlation function. In Figure 9.11 we plot the measured reciprocal-space structure for these three samples based on the value of the FWHM extracted from angular profiles shown in Figures 9.8, 9.9, and 9.10 as a function of  $k_{\perp}$ . The circles denote the positions of the half-maximum of the diffuse intensity. The heavy lines at  $k_{||} = 0$  represent the sharp, central peaks in the intensity profiles. These plots summarize the diffraction characteristics of the rough surfaces. These reciprocal-space structures are very similar to those predicted theoretically and shown in Figure 9.5.

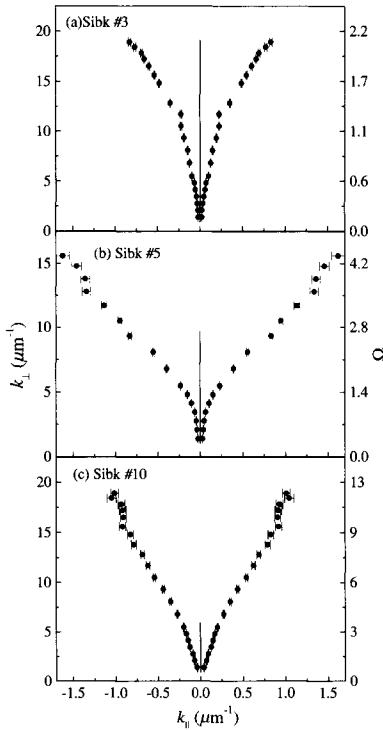


FIG. 9.11 The reciprocal-space structure for the backside of Si Samples (a) #3, (b) #5, and (c) #10 (Table 9.2). The vertical axis on the right shows the corresponding  $\Omega$  ( $= k_{\perp}^2 w^2$ ) values (from Ref. [9.10]).

### 9.3.3 Determination of the roughness parameters

#### 9.3.3.1 Interface width $w$

The interface width  $w$  can be determined through the normalized  $\delta$ -peak intensity,  $R_{\delta}$  [9.3],

$$R_{\delta} = \frac{\int S_{\delta}(k_{||}, k_{\perp}) d\mathbf{k}_{||}}{\int S(k_{||}, k_{\perp}) d\mathbf{k}_{||}} = \exp[-(k_{\perp} w)^2]. \quad (9.34)$$

In principle, one scattered intensity profile is sufficient to determine  $w$ . A more reliable value of  $w$  can be obtained by plotting  $\ln(R_{\delta})$  vs.  $k_{\perp}^2$ . The slope is equal to  $-w^2$ . In Figure 9.12 we compare the interface width  $w$  calculated from the normalized  $\delta$ -peak light scattering intensity from one profile with that measured by real-space AFM and SP techniques for ten different samples with different interface widths. The numerical values of roughness parameters are listed in Table 9.2. The dashed line represents

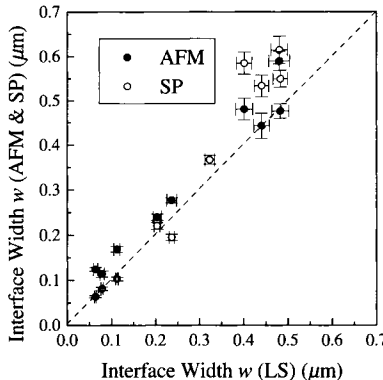


FIG. 9.12 The interface widths  $w$  measured by AFM and SP, as compared to that extracted from LS using the normalized  $\delta$ -peak method (from Ref. [9.10]).

the case where the light scattering and the real-space imaging techniques give exactly the same results. Overall, different measurement techniques are seen to give similar results. For small interface widths, the LS results and SP measurement agree very well, but AFM gives a larger value. AFM and SP give somewhat scattered values in the larger-interface-width regime.

The difference in the value of the interface width obtained from different measurements may originate from different instrumental limitations. Theoretically,  $w$  should be obtained from an infinite sampling area with an infinitely high resolution. However, as we have discussed, all measurements have certain limitations, including the instrumental resolution and the sampling size. Often, the product of the resolution and the sampling size is a constant. For our AFM measurement, the scan size is  $100 \mu\text{m}$ , and the scan pixel increment is  $0.39 \mu\text{m}$ . These values determine the spatial frequency ( $= 2\pi/l$ , where  $l$  is a real-space distance) range for AFM measurement as being from  $6.28 \times 10^{-2} \mu\text{m}^{-1}$  to  $1.6 \times 10^1 \mu\text{m}^{-1}$ . However, the tip size of the AFM is very small; the actual spatial resolution is better than  $0.39 \mu\text{m}$ . For the SP measurement, the scan size is  $500 \mu\text{m}$ , and the tip size is  $5 \mu\text{m}$ , which corresponds to a spatial frequency region from  $1.25 \times 10^{-2} \mu\text{m}^{-1}$  to  $1.25 \mu\text{m}^{-1}$ . For light scattering using a detector array, as discussed in the experimental section, the spatial frequency ranges from  $1.4 \times 10^{-3} \mu\text{m}^{-1}$  to  $1.4 \mu\text{m}^{-1}$ . Figure 9.13 illustrates these regions used in our experiments. Usually, as long as the minimum spatial frequency is far below  $2\pi/\xi$ , the error of the measured  $w$  due to the uncertainty in the lower frequency region can be neglected. This is the case for our Samples #1 - 6 ( $2\pi/\xi \leq 1.26 \mu\text{m}^{-1}$ ). Therefore, the maximum spatial frequency, i.e., the spatial resolution, determines the region where the measurement gives an

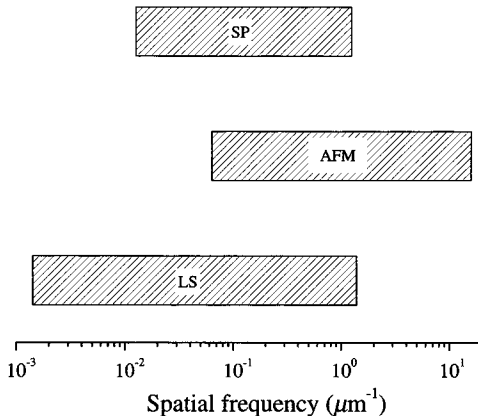


FIG. 9.13 Spatial frequency regions for LS, AFM, and SP experiments (from Ref. [9.10]).

accurate value of  $w$ . Both LS and SP have comparable maximum spatial frequencies. However, the AFM has an order of magnitude higher frequency than those two. Although the  $w$  values for LS and SP are well matched, the AFM gives a higher value. In contrast, as seen from Figure 9.12, for large interface widths (Samples #7 - 10, with  $2\pi/\xi \approx 6.28 \times 10^{-1} \mu\text{m}^{-1}$ ), SP gives higher values than those from the AFM because in this case the low spatial frequency part contributes more than the high spatial frequency does. Note that although LS has a lower minimum spatial frequency than that of SP, the measured  $w$  value is much smaller than that measured from SP. This may be due to the shadowing effect in the LS measurement.

One can also determine the roughness parameters by the inverse Fourier transform (IFT) of Equation (7.19) [9.5]. Experimentally the height-height correlation function can be determined by taking the Fourier transform of the scattered intensity profiles. Examples will be given later. In Figure 9.14 we compare the interface width determined by the IFT method with that obtained from the normalized  $\delta$ -peak intensity.

### 9.3.3.2 Lateral correlation length $\xi$

In light scattering, the lateral correlation length  $\xi$  is inversely proportional to the FWHM under the condition  $\Omega \ll 1$ . In Figure 9.15 we show the comparison of the lateral correlation length  $\xi$  determined by light scattering with that determined by the AFM technique. Again, data from ten samples were used. The  $\xi$  determined through the FWHM of LS appears to agree well with the AFM measurements, but the  $\xi$  determined by the

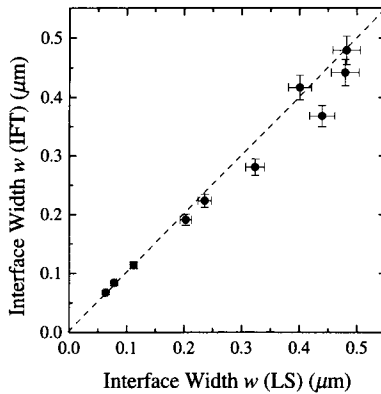


FIG. 9.14 Comparison of the interface widths  $w$  measured by light scattering using two different methods: normalized- $\delta$ -peak and inverse-Fourier-transform (IFT) techniques (from Ref. [9.10]).

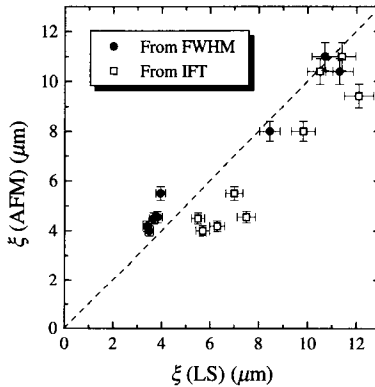


FIG. 9.15 Comparison of the lateral correlation lengths  $\xi$  measured by light scattering and AFM techniques. In the light scattering experiments, we employed two methods to extract the lateral correlation lengths: from the FWHM of the profiles obtained at small  $\Omega$  and from the IFT method (from Ref. [9.10]).

IFT technique seems to overestimate the values. The correlation length determined by SP (not shown in Figure 9.15) is considerably greater than that obtained by both AFM and LS techniques.

### 9.3.3.3 Roughness exponent $\alpha$

One way to determine  $\alpha$  from light scattering is to go to  $\Omega \gg 1$  and plot the FWHM vs.  $k_{\perp}$  in the log-log scale ( $\text{FWHM} \propto k_{\perp}^{1/\alpha}$ ) [9.3, 9.6, 9.11]. In this experiment, the largest  $k_{\perp}$  that could be reached is  $1.9 \times 10^1 \mu\text{m}^{-1}$ .

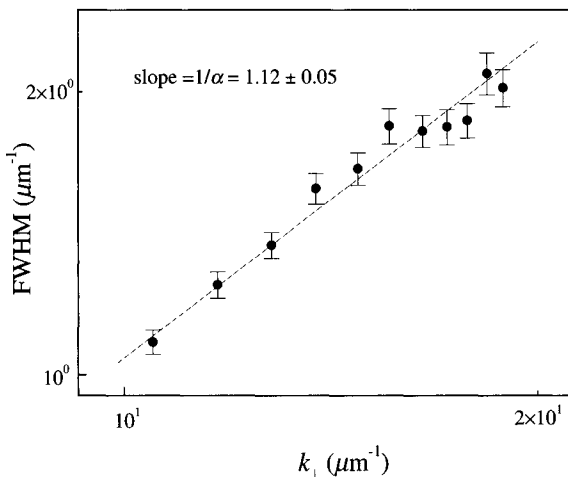


FIG. 9.16 The log-log scale plot of FWHM of the diffuse profile as a function of  $k_{\perp}$  at large  $\Omega$  for Sample #10. The slope gives  $1/\alpha$  (from Ref. [9.10]).

Therefore the condition  $\Omega \gg 1$  can be satisfied only for samples with large interface widths. In Figure 9.16 we plot the FWHM vs.  $k_{\perp}$  for Sample #10, which had a large interface width close to  $0.6 \mu m$ . The  $\alpha$  value obtained from the slope ( $= 1/\alpha$ ) of this plot is about  $0.89 \pm 0.02$ , which is consistent with that obtained by AFM,  $0.87 \pm 0.02$ .

The roughness exponent  $\alpha$  can also be determined by the IFT method without any restriction on the value of  $\Omega$  [9.5]. In Figure 9.17 we show the height-height correlation functions determined from the light scattering profiles of Samples #1 and #8. For Sample #8, the interface width is large, and both AFM and SP give higher  $w$  values compared with those obtained by IFT, but the lateral correlation lengths obtained by AFM and IFT are almost the same, and are smaller compared with the values obtained by SP. The  $\alpha$  values determined by IFT, AFM, and SP are  $0.87 \pm 0.02$ ,  $0.89 \pm 0.02$ , and  $0.91 \pm 0.02$ , respectively. The spread of  $\alpha$  is within 4%. For Sample #1, the interface width is very small. The  $w$  value determined from light scattering and SP is the same because, for large  $r$ , the height-height correlation functions overlap, but AFM gives a higher  $w$  value compared with that from LS and SP. Both AFM and light scattering give a similar correlation length, which is smaller than that of the SP measurement. The  $\alpha$  values determined by IFT, AFM, and SP are  $0.80 \pm 0.02$ ,  $0.78 \pm 0.02$ , and  $0.88 \pm 0.02$ , respectively. In Table 9.2 we summarize the roughness parameters determined by different techniques.

Another strategy to determine the value of  $\alpha$  is from the power-law

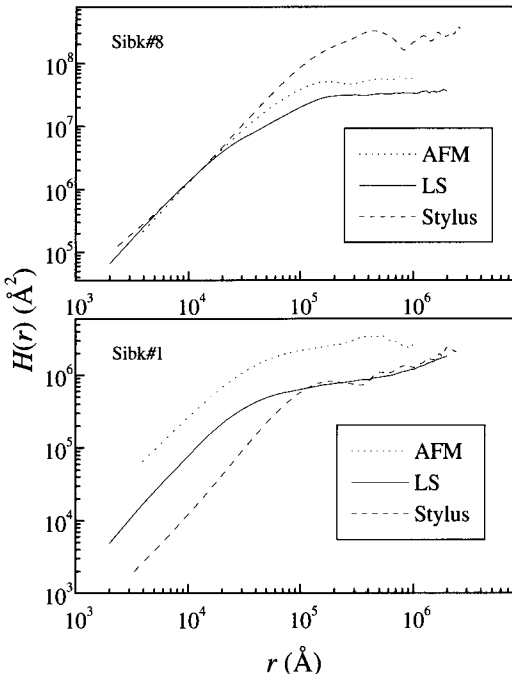


FIG. 9.17 Comparison of height-height correlation functions of Silicon backside (Sibk) Samples #1 and #8 determined by light scattering, AFM and SP (from Ref. [9.10]).

behavior at large  $k_{||}$  in the power spectrum, that is, the light scattering profiles measured under the condition  $\Omega \ll 1$  [9.3, 9.8, 9.12]. In order to obtain the higher  $k_{||}$  value, or the tail part of the scattering profiles, we used the second setup shown in Figure 9.6(b). The detector was moved along the in-plane direction by a 1-D translator with  $\pm 1 \mu\text{m}$  accuracy. In Figure 9.18 we show the measured scattering profile of Sample #5 plotted in a log-log scale. In the same graph we also plot the surface power spectrum (1-D) calculated from the AFM image for Sample #5. In order to compare the light scattering profile and AFM power spectrum, we rescaled the power spectrum to match the intensity of the scattering profile. The scattering profile and the power spectrum appear to be consistent with each other. The slope of the curves at large  $k_{||}$  gives  $-(1 + 2\alpha)$  (see later discussion). From these plots, the values of  $\alpha$  were extracted to be  $1.10 \pm 0.02$  and  $1.08 \pm 0.02$  from the power spectrum and the light scattering profile, respectively. These numbers are not quite consistent with those obtained by other methods shown above. This discrepancy is due to the inconsistency of the definition of  $\alpha$  derived from the height-height correlation and power spectrum when  $\alpha$  is close to 1 [9.13].

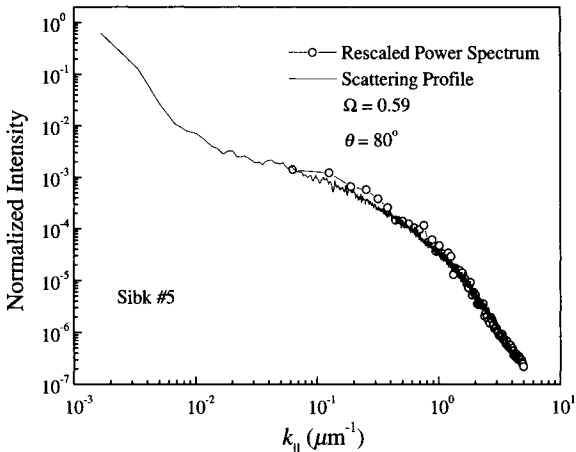


FIG. 9.18 Comparison of the surface power spectrum calculated from the AFM image and diffraction profile obtained at small  $\Omega$  for Si Sample #5 (from Ref. [9.10]).

It can also be shown that in general at large  $k_{\parallel}$  the slope of the scattering profiles is equal to  $-(d + 2\alpha)$  for any diffraction angle, or for any value of  $\Omega$  [9.4, 9.12]. Here  $d + 1$  is the dimension of the imbedded space. Figure 9.19 shows a log-log plot of the normalized light scattering intensity profiles from Sample #4 for  $\theta = 84^\circ, 80^\circ, 76^\circ, 70^\circ, 66^\circ$ , and  $60^\circ$ , which correspond to  $\Omega = 0.42, 1.38, 1.92, 2.72, 3.23$ , and  $3.97$ , respectively. Despite the differences observed in the small- $k_{\parallel}$  region, all six curves show a similar power-law behavior at large  $k_{\parallel}$ . The slopes for the tails are  $2.90, 2.91, 2.51, 2.70, 2.85$ , and  $3.00$ , respectively. The average slope extracted from the log-log plot is  $-2.81 \pm 0.07$ . Since we used a slit detector, the asymptotic power law becomes  $k_{\parallel}^{-1-2\alpha}$  instead of  $k_{\parallel}^{-2-2\alpha}$  for large  $k_{\parallel}$  [9.4, 9.10, 9.12]. From this, we determined that  $\alpha = 0.91 \pm 0.04$ , which is quite consistent with the value obtained from the AFM. Note from Figure 9.19 that as  $k_{\perp}$  increases, the power law region shifts to larger  $k_{\parallel}$ , which is also consistent with the prediction. Therefore, one can extract the value of  $\alpha$  from the tail of the profiles obtained at any scattering condition, not just in the small  $\Omega$  regime.

In this section we have explored the characteristics of the reciprocal-space structure of rough Si (backside) surfaces using light scattering for a wide range of diffraction geometries. We found that measurements using in-plane scattering geometry are particularly convenient for the mapping of the reciprocal-space characteristics. All relevant roughness parameters such as the interface width  $w$ , lateral correlation length  $\xi$ , and the roughness exponent  $\alpha$  are quantitatively extracted from these characteristics. We also

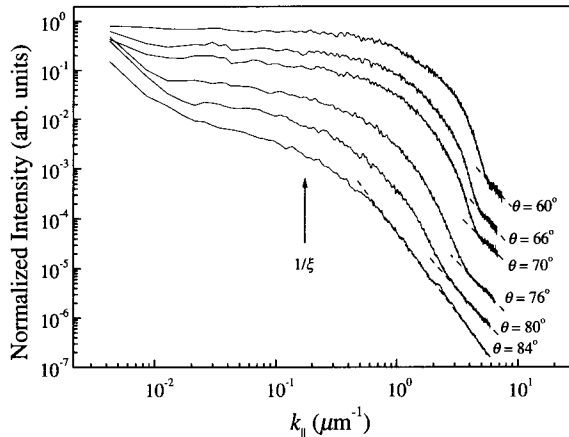


FIG. 9.19 Log-log plot of the normalized diffraction profiles from Si Sample #4 under different diffraction conditions. Note that the tails of all the profiles fall in a power law behavior (from Ref. [9.4]).

compared the results of light scattering on the determination of roughness parameters with those obtained using the real-space imaging techniques including AFM and SP.

#### 9.4 Diffraction from Discrete Self-Affine Surfaces

Now we discuss the diffuse profile from a discrete self-affine surface. For small  $w$ , where  $w$  satisfies  $4w^2 < 1$  (see Section 7.3.2), the diffuse profile can be expressed as Equation (7.51), a summation of surface power spectra at different reciprocal-lattice positions. Therefore, for a self-affine surface with the height-height correlation function given by Equation (9.4), Equation (7.51) becomes

$$S_{diff}(k_\perp, \mathbf{k}_\parallel) \approx 8\pi^2 \alpha w^2 \xi^2 (1 - \cos \Phi) \sum_{p,q} \frac{1}{[1 + |k_\parallel - K_{pq}|^2 \xi^2]^{1+\alpha}}. \quad (9.35)$$

One very important case is to investigate the tail of a diffuse profile. Figure 9.20 plots the diffuse tails in a log-log scale within one Brillouin zone for different  $\xi K_{BZ}$  values at  $\alpha = 0.4$ . For large  $\xi K_{BZ}$  values, the diffuse tail still obeys the power law. However, for small  $\xi K_{BZ}$  values, due to the overlap of diffuse tails from different Brillouin zones, the power law relation breaks down, although the FWHM of the profile does not change compared with that of a continuous surface.

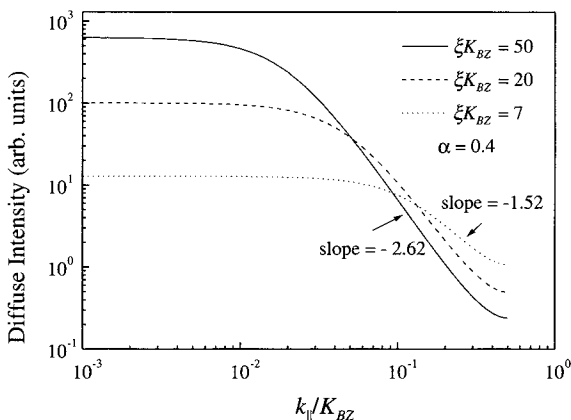


FIG. 9.20 The log-log plot of the diffuse tails within one Brillouin zone for different  $\xi K_{BZ}$  values at  $\alpha = 0.4$ .

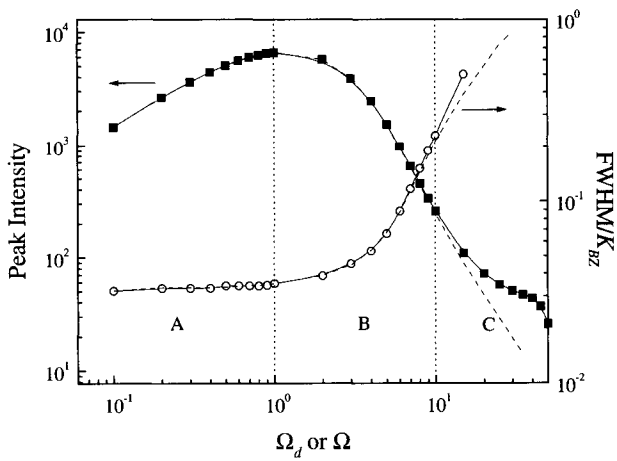


FIG. 9.21 The diffuse-peak intensity and the FWHM as a function of  $\Omega_d$  for a discrete self-affine surface with  $\alpha = 0.4$ , and  $\xi K_{BZ} = 50$  (solid curves), and those as a function of  $\Omega$  for a continuous self-affine surface with  $\alpha = 0.4$  (dashed curves).

### (i) Near-in-phase condition

At the near-in-phase condition, the diffuse diffraction profile can be expressed as Equation (7.52). It is a function of both  $\Omega_d$  and  $\mathbf{k}_{\parallel}$ . As discussed in Chapter 6, for a self-affine continuous surface, at small  $\Omega$  ( $\leq 1$ ), the diffuse peak intensity increases with  $\Omega$  while the FWHM remains almost constant. The diffuse peak intensity would peak at some moderate  $\Omega$  ( $\sim 1$ )

value while the FWHM begins to increase. For very large  $\Omega$  ( $\gg 1$ ), both the diffuse peak intensity and FWHM obey asymptotic power law behaviors [Equations (9.22) and (9.23)] with respect to  $\Omega$ . However, for a discrete surface, with the effects of other Brillouin zones, the power law asymptotic behaviors for the diffuse peak and FWHM may break down. Figure 9.21 shows the diffuse peak intensity and the FWHM as a function of  $\Omega_d$  for a discrete self-affine surface with  $\alpha = 0.4$ , and  $\xi K_{BZ} = 50$  (solid curves). For comparison, in Figure 9.21 we also plot the peak intensity and FWHM as a function of  $\Omega$  for a continuous self-affine surface with the same roughness parameters (dashed curves). For small  $\Omega_d$  ( $\leq 1$ ) values, the behavior of a discrete surface is the same as a continuous surface (region A in the figure). After reaching the intermediate  $\Omega_d$  ( $1 < \Omega_d < 10$ ) they still have similar behaviors (region B in the figure). However, at large  $\Omega_d$  ( $> 10$ ) differences appear (region C in the figure): the discrete surface has a higher diffuse peak intensity and broader profile than that of the continuous surface. At a certain  $\Omega_d$  ( $\sim 15$ ) value, the diffuse profile of a discrete surface cannot reach the half-maximum points due to the contribution from other Brillouin zones. Obviously the behaviors of the diffuse intensity and the FWHM for a discrete surface deviate from the asymptotic power law behaviors.

### (ii) Near-out-of-phase condition

The only difference between the near-out-of-phase condition and the near-in-phase condition is that  $\Omega_d = w^2 |[\Phi]|^2$  for the near-in-phase condition changes into  $\Pi = 4w^2 - w^2(\pi - |[\Phi]|)^2$  for the near-out-of-phase condition. Therefore, if we plot the peak intensity and the FWHM of a diffuse profile as a function of  $\Pi$ , they should have exactly the same behaviors as that for the near-in-phase condition, i.e., if we change  $\Omega_d$  to  $\Pi$  in Figure 9.21, then we obtain the near-out-of-phase behavior of the diffuse profile. The only difference is that for the same surface,  $\Pi \gg \Omega_d$ , i.e., at the near-out-of-phase condition, one tends to obtain the asymptotic behavior of diffuse profile more easily.

### (iii) Reciprocal-space structure

For a discrete surface, since the interface width  $w$  and the momentum transfer perpendicular to the surface  $k_\perp$  act differently due to the broken symmetry, the reciprocal-space rod structure is different for different  $w$  values. Figures 9.22 - 9.24 show the reciprocal-rod structures within one Brillouin zone for  $w = 0.1, 1$ , and  $5$ , respectively. For very small interface widths  $w$  that satisfy  $4w^2 \leq 1$ , the diffuse profile almost remains unchanged at both the near-in-phase and near-out-of-phase conditions, and

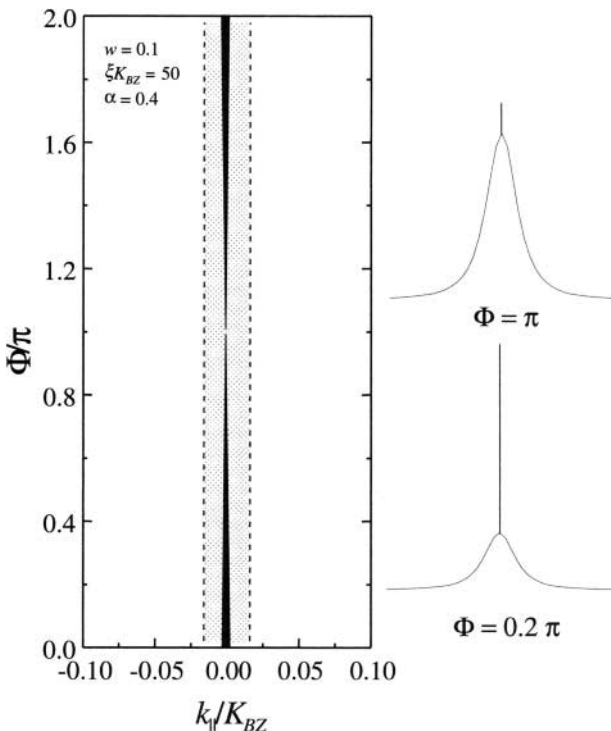


FIG. 9.22 The reciprocal-rod structures of a discrete self-affine surface within one Brillouin zone for  $w = 0.1$ . Two profiles at the out-of-phase ( $\pi$ ) and near-in-phase ( $0.2\pi$ ) conditions are shown on the right.

the contributions from other Brillouin zones are small, and the same, for the diffuse profiles along the rod. The FWHM of the diffuse profile along the rod is a constant (Figure 9.22). For an intermediate  $w$  value, at the near-in-phase condition, the FWHM does not change because the diffuse profile is proportional to the surface power spectrum. However, at the near-out-of-phase condition, as  $2w^2(1 - \cos \Phi) > 1$ , the diffuse profile becomes broader (see Figure 9.23). For a very large  $w$  value, at very near the in-phase condition, the diffuse profile is still proportional to the surface power spectrum, but as long as  $\Phi$  increases further, the diffuse profile becomes broader, and the effects of other Brillouin zones become more severe. When  $2w^2(1 - \cos \Phi) = \Omega_d^R$ , the FWHM reaches the edge of the Brillouin zone. As  $\Phi$  increases further, one cannot find the FWHM positions of the diffuse profiles within a Brillouin zone (see Figure 9.24).

As an example, we analyze the diffraction data of the rough growth front observed in the Si/Si(111) homoepitaxy experiment at the near in-

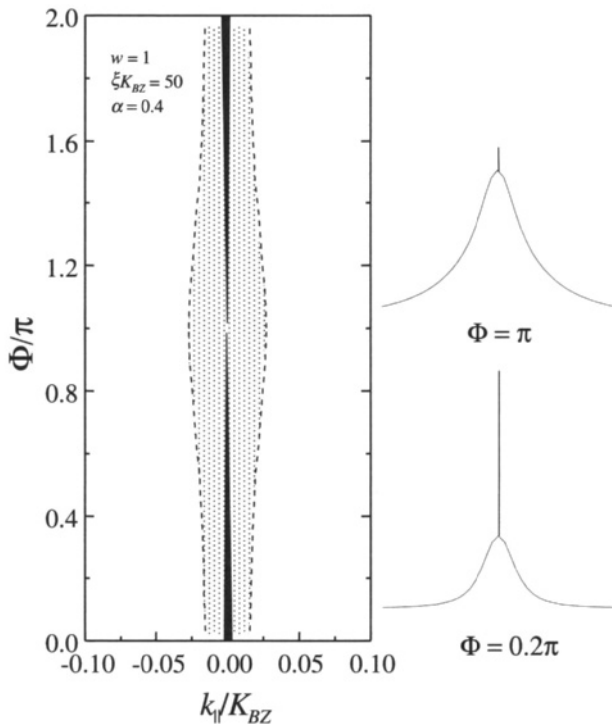


FIG. 9.23 The reciprocal-rod structures of a discrete self-affine surface within one Brillouin zone for  $w = 1$ . Two profiles at the out-of-phase ( $\pi$ ) and near-in-phase ( $0.2\pi$ ) conditions are shown on the right.

phase diffraction condition [9.14]. The growth was performed in a UHV chamber equipped with a high resolution low energy electron diffraction (HRLEED) system with an instrument resolution of  $6 \times 10^{-3} \text{ \AA}^{-1}$  (FWHM). The growth was carried out at a temperature of  $275 \pm 5^\circ\text{C}$  for 10 min, with a rate of  $8 \pm 1$  bilayer/min. The detailed experimentation can be found in References [9.11] and [9.15]. The HRLEED profiles were taken by varying the incident electron energy in order to span the reciprocal rod. Figure 9.25 shows a reciprocal-rod structure at the deposition time  $t = 10$  min. The central dotted curve indicates the peak positions of the diffuse profiles. The fluctuation is due to uncertainties in the profile measurement and the fits of the decomposed diffuse profiles. The open squares are the positions of the half-maximum of the diffuse profiles. The solid curves are fits using Equation (7.46) with Equation (9.3) as the height-height correlation function with the roughness parameters,  $w \approx 4.0 \text{ \AA}$ ,  $\alpha \approx 0.89$ , and  $\xi \approx 60 \text{ \AA}$ . This structure along the rod is similar to that shown in Figure 9.23.

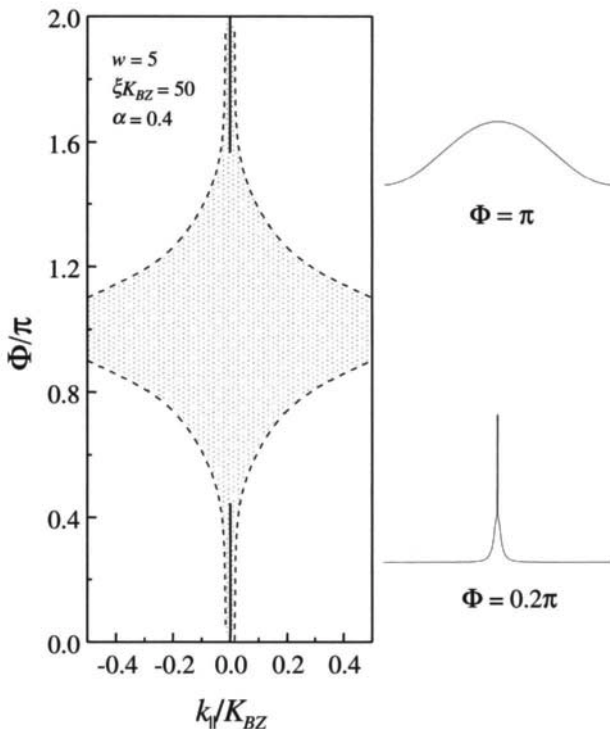


FIG. 9.24 The reciprocal-rod structures of a discrete self-affine surface within one Brillouin zone for  $w = 5$ . Two profiles at the out-of-phase ( $\pi$ ) and near-in-phase ( $0.2\pi$ ) conditions are shown on the right.

### 9.5 Summary

In this chapter, we discussed in detail the real-space and reciprocal-space structures for self-affine surfaces. In principle, all of the roughness parameters related to different kinds of surfaces can be extracted either from the measured real-space height-height correlation function or from the asymptotic behavior of the diffraction profiles. We also discussed how the discrete lattice affects the diffraction profiles. When the surface becomes discrete, some asymptotic behavior for  $\Omega > 1$  obtained from the continuous surface cannot hold. However, the asymptotic behavior at  $\Omega < 1$  is independent on the discreteness of the surface. All of the roughness parameters related to self-affine surfaces can be extracted from the asymptotic behavior of the diffraction profiles as shown in Table 9.1.

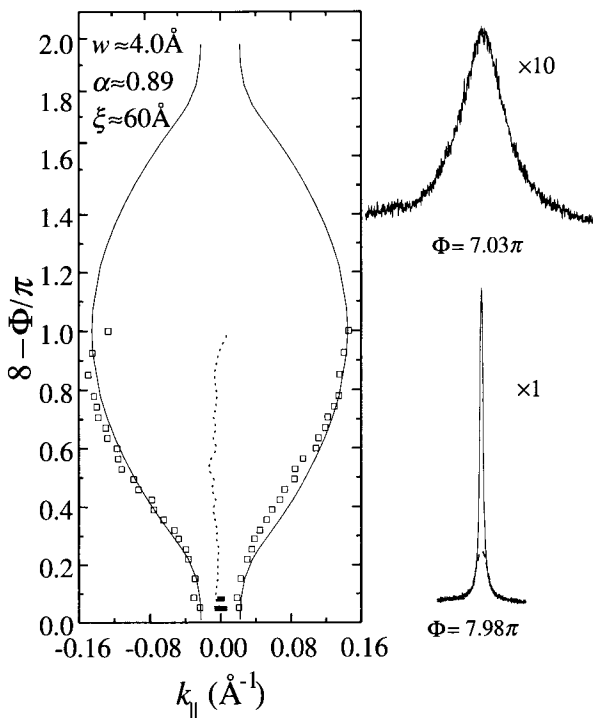


FIG. 9.25 The diffraction structure factor of the (00) beam measured from the Si/Si(111) surface grown at 275°C at the later stage of growth. The profiles on the right correspond to  $\Phi = 7.98\pi$  (near-in-phase) and  $\Phi = 7.03\pi$  (near-out-of-phase). The  $\delta$  peaks represented by the filled rectangles along the (00) rod exist at and near-in-phase conditions. The  $\delta$ -peak intensity decreases rapidly as the diffraction condition moves away from the in-phase condition. The dotted curve represents the peak positions of the diffuse profiles. The open squares represent the FWHM of the diffuse profiles. The solid curves are fits using Equation (7.46) with Equation (9.3) as the height-height correlation function with the roughness parameters,  $w \approx 4.0 \text{ \AA}$ ,  $\alpha \approx 0.89$ , and  $\xi \approx 60 \text{ \AA}$  (from Ref. [9.14]).

## References

- 9.1 S. K. Sinha, E. B. Sirota, and S. Garoff, "X-ray and neutron scattering from rough surfaces," Phys. Rev. B **38**, 2297 (1988).
- 9.2 G. Palasantzas, "Roughness spectrum and surface width of self-affine fractal surfaces via the K-correlation model," Phys. Rev. E **48**, 14472 (1993).
- 9.3 H.-N. Yang, G.-C. Wang, and T.-M. Lu, *Diffraction from Rough Surfaces and Dynamic Growth Fronts* (World Scientific, Singapore, 1993).
- 9.4 Y.-P. Zhao, C.-F. Cheng, G.-C. Wang, and T.-M. Lu, "Power law behavior in diffraction from fractal surfaces," Surf. Sci. Lett. **409**, L703 (1998).
- 9.5 Y.-P. Zhao, H.-N. Yang, G.-C. Wang, and T.-M. Lu, "Extraction of real-space correlation function of a rough surface by light scattering using diode array detectors,"

- Appl. Phys. Lett. **68**, 3063 (1996).
- 9.6 K. Fang, R. Adame, H.-N. Yang, G.-C. Wang, and T.-M. Lu, "Measurement of roughness exponent for scale-invariant rough surfaces using angle resolved light scattering," Appl. Phys. Lett. **66**, 2077 (1995).
  - 9.7 C. Teichert, J. F. MacKay, D. E. Savage, M. G. Lagally, M. Brohl, and P. Wagner, "Comparison of surface roughness of polished silicon wafers measured by light scattering topography, soft-x-ray scattering, and atomic-force microscopy," Appl. Phys. Lett. **66**, 2346 (1995).
  - 9.8 T. Salditt, T. H. Metzger, Ch. Brandt, U. Klemradt, and J. Peisl, "Determination of the static scaling exponent of self-affine interfaces by nonspecular x-ray scattering," Phys. Rev. B **51**, 5617 (1995).
  - 9.9 A. Munkholm, S. Brennan, and E. C. Carr, "A comparison of surface roughness as measured by atomic force microscopy and x-ray scattering," J. Appl. Phys. **82**, 2944 (1997).
  - 9.10 Y.-P. Zhao, Irene Wu, C.-F. Cheng, Ueyn Block, G.-C. Wang, and T.-M. Lu, "Characterization of random rough surfaces by in-plane light scattering," J. Appl. Phys. **84**, 2571 (1998).
  - 9.11 H.-N. Yang, G.-C. Wang, and T.-M. Lu, "Instability in low temperature molecular beam epitaxial growth of Si/Si(111)," Phys. Rev. Lett. **73**, 2346 (1994).
  - 9.12 E. L. Church, "Fractal surface finish," Appl. Opt. **27**, 1518 (1988).
  - 9.13 H.-N. Yang and T.-M. Lu, "Inconsistency between height-height correlation and power-spectrum functions of scale-invariant surfaces for roughness exponents  $\alpha \sim 1$ ," Phys. Rev. B **51**, 2479 (1995).
  - 9.14 Y.-P. Zhao, H.-N. Yang, G.-C. Wang, and T.-M. Lu, "Diffraction from diffusion-barrier-induced mound structures in epitaxial growth fronts," Phys. Rev. B **57**, 1922 (1998).
  - 9.15 H.-N. Yang, G.-C. Wang, and T.-M. Lu, "Real time measurements of the deterministic relaxation of an initially rough Si(111) surface," Phys. Rev. Lett. **74**, 2276 (1995).

## 10. MOUNDED SURFACES

In this chapter, we will give a detailed analysis of mounded surfaces.

### 10.1 Real-Space Characteristics

As discussed in Chapter 3, for an isotropic mounded surface, one can use a phenomenological function to describe the height-height correlation function [10.1]:

$$H(r) = 2w^2 \left\{ 1 - \exp\left[-\left(\frac{r}{\zeta}\right)^{2\alpha}\right] J_0\left(\frac{2\pi r}{\lambda}\right) \right\}. \quad (10.1)$$

Therefore, the auto-correlation function is

$$R(r) = \exp\left[-\left(\frac{r}{\zeta}\right)^{2\alpha}\right] J_0\left(\frac{2\pi r}{\lambda}\right), \quad (10.2)$$

where  $J_0(x)$  is the zeroth-order Bessel function. Four parameters are used to describe the surface, i.e., the RMS roughness  $w$ , the system correlation length  $\zeta$ , the roughness exponent  $\alpha$ , and the average mound separation  $\lambda$ . For a mounded surface it is known that the local slope is quite smooth and  $\alpha = 1$ . The overall lateral correlation length  $\xi$  can be defined through an auto-correlation function as  $R(\xi) = 1/e$  and is a function of both  $\zeta$  and  $\lambda$ . The system correlation length  $\zeta$  determines how randomly the mounds are distributed on the surface. The smaller the system correlation length  $\zeta$ , the more random the distribution. These three parameters,  $w$ ,  $\zeta$ , and  $\lambda$ , are independent from each other, and they vary according to the processes in which the surface morphologies are formed. The parameters  $w$ ,  $\zeta$ , and  $\lambda$  completely characterize a mounded surface. The corresponding power spectrum can be written as

$$P(k_{||}) = \frac{w^2 \zeta^2}{2} \exp\left(-\frac{4\pi^2 + k_{||}^2 \lambda^2}{4\lambda^2} \zeta^2\right) I_0\left(\frac{\pi k_{||} \zeta^2}{\lambda}\right), \quad (10.3)$$

where  $I_0(x)$  is the zeroth-order modified Bessel function.

Since we still assume that the surface height distribution is a Gaussian distribution, the height difference function can still be calculated using Equation (7.18). Figure 10.1 shows the height difference function for different  $k_{\perp}w$  values, 0.9 and 5.0, at  $\zeta = 1$  and  $\lambda = \pi/4$ . For small  $k_{\perp}w$ , the height difference function has oscillations, just like the auto-correlation

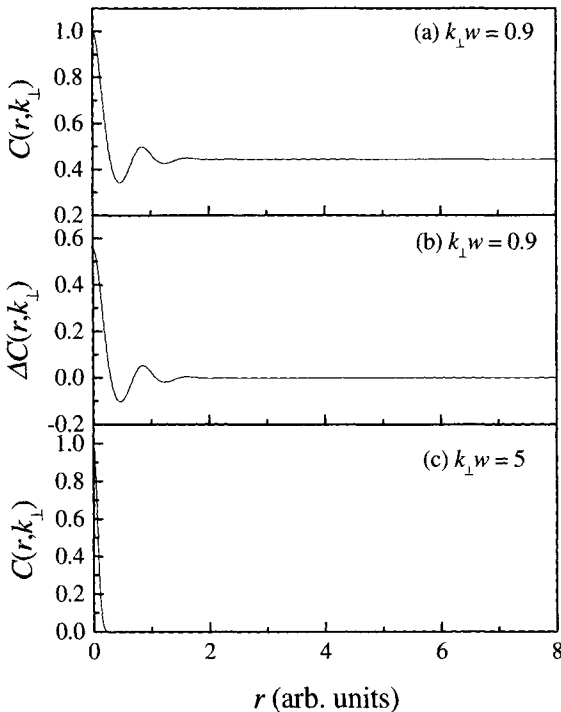


FIG. 10.1 The height difference functions  $C(k_{\perp}, r)$  and  $\Delta C(k_{\perp}, r)$  for a bounded surface. (a)  $C(k_{\perp}, r)$  at  $k_{\perp}w = 0.9$ , (b)  $\Delta C(k_{\perp}, r)$  at  $k_{\perp}w = 0.9$ , and (c)  $C(k_{\perp}, r)$  at  $k_{\perp}w = 5$ . In all cases,  $\xi = 1$  and  $\lambda = \pi/4$ .

function for the bounded surface shown in Figure 3.9. Comparing the case for a bounded surface to Figure 3.9, we expect that the diffraction profile under this condition would have a ring. However, at large  $k_{\perp}w$ , the oscillation is gone as shown in Figure 10.1(c), and the height difference function is similar to that of a self-affine surface [Figure 7.1(c)]. Therefore, we may expect that the diffuse profile has a similar behavior as the self-affine surface: only a broad profile with no ring structure will appear.

## 10.2 Diffraction from Mounded Surfaces

### 10.2.1 The asymptotic behavior of the diffraction structure factor

(1)  $\Omega \ll 1$

Under the condition  $\Omega \ll 1$ , Equation (9.14) is always correct no matter what surface morphology is being considered as long as the surface has a

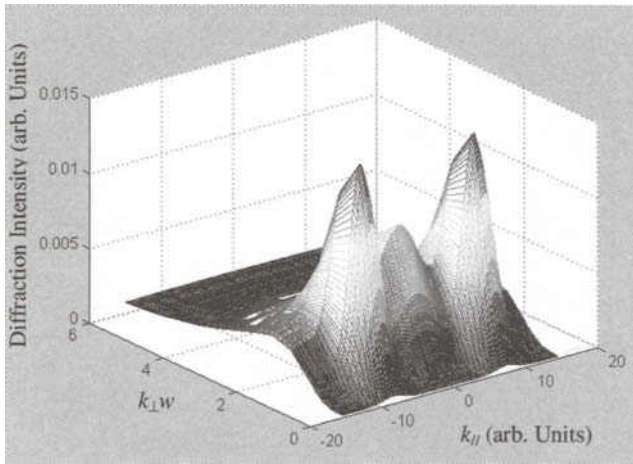


FIG. 10.2 The diffuse profiles of a bounded surface as a function of  $k_{\perp}w$  for  $\alpha = 1$ ,  $\zeta = 1$ , and  $\lambda = \pi/4$ .

Gaussian height distribution. Therefore, substituting Equation (10.3) into Equation (9.14), we have

$$S(\mathbf{k}_{||}, k_{\perp}) = (2\pi)^2 e^{-\Omega} \delta(\mathbf{k}_{||}) + \Omega e^{-\Omega} \frac{w^2 \zeta^2}{2} \exp\left(-\frac{4\pi^2 + k_{||}^2 \lambda^2}{4\lambda^2} \zeta^2\right) I_0\left(\frac{\pi k_{||} \zeta^2}{\lambda}\right). \quad (10.4)$$

The  $\delta$ -peak intensity still decays as  $e^{-\Omega}$ , and the diffuse profile is proportional to the surface power spectrum. As discussed in Section 3.2, the power spectrum has a satellite ring. The position of the ring  $k_c = \frac{2\pi}{\lambda}$  and the FWHM of the satellite ring decreases with the increasing system correlation length  $\zeta$  for a fixed  $\lambda$ , as discussed in detail in Section 3.2.

## (2) $\Omega \gg 1$

As discussed in Section 3.2, under this condition, the  $\delta$  peak is negligibly small, as  $e^{-\Omega} \rightarrow 0$ . The diffraction structure factor  $S(\mathbf{k}_{||}, k_{\perp})$  can be represented by only its diffuse profile  $S_{diff}(\mathbf{k}_{||}, k_{\perp})$ . Figure 10.2 shows the calculated diffuse profiles at  $\alpha = 1$ ,  $\zeta = 1$ , and  $\lambda = \pi/4$  for different  $k_{\perp}w$  values. Clearly at small  $k_{\perp}w$  the diffuse profiles have satellite peaks, but at large  $k_{\perp}w$  the satellite peaks disappear. In this case the diffraction detects only the short-range behavior in the bounded surface, and the short-range height difference function can be expressed as

$$C(k_{\perp}, r) \approx \exp\left[-\Omega r^2\left(\frac{1}{\zeta^2} + \frac{\pi^2}{\lambda^2}\right)\right]. \quad (10.5)$$

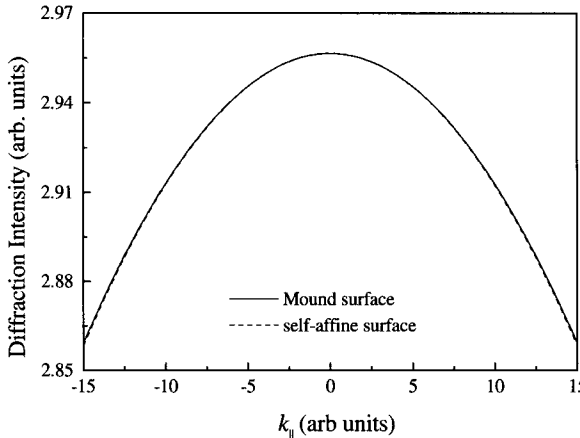


FIG. 10.3 The calculated diffuse profiles at  $k_{\perp}w = 10$  for both self-affine and mounded surfaces with the same lateral correlation length.

If we define  $\frac{1}{\xi'^2} = \frac{1}{\zeta^2} + \frac{\pi^2}{\lambda^2}$ , then the diffraction profile would have the same form as Equation (9.18) by simply substituting  $\xi$  by  $\xi'$  and letting  $\alpha = 1$  for a mounded surface. The diffraction profile becomes a simple Gaussian shape, and the characteristics of the power spectrum are totally lost. Figure 10.3 shows the calculated diffraction profiles at large  $k_{\perp}w$  ( $= 10$ ) using the height-height correlation function for the mounded surface, Equation (10.1), and the height-height correlation function for the self-affine surface, Equation (9.3), with  $\alpha = 1$ . In the calculation we assume  $\xi = \xi' = 1$ . We can see that the diffraction profiles calculated from different height-height correlation functions almost overlap. Therefore, at large  $k_{\perp}w$  one cannot tell from the diffraction profile whether the surface has mounds or not. The reason that the profile is not sensitive to the wavelength selection at large  $k_{\perp}w$  is that for a sufficiently large  $k_{\perp}w$ , the dominant contribution in Equation (7.18) is from the small  $r$  regime due to the exponential factor in the  $C(k_{\perp}, r)$ . The oscillatory behavior in the height-height correlation is in the large  $r$  regime and its contribution becomes small in the exponential factor. The FWHM has the relation

$$\text{FWHM} \propto \frac{\sqrt{\Omega}}{\xi'} \propto w \left( \frac{1}{\zeta^2} + \frac{\pi^2}{\lambda^2} \right)^{1/2} = m, \quad (10.6)$$

where  $m$  is the average local slope as defined in Equation (3.20). That is, the FWHM is also determined by the local slope.

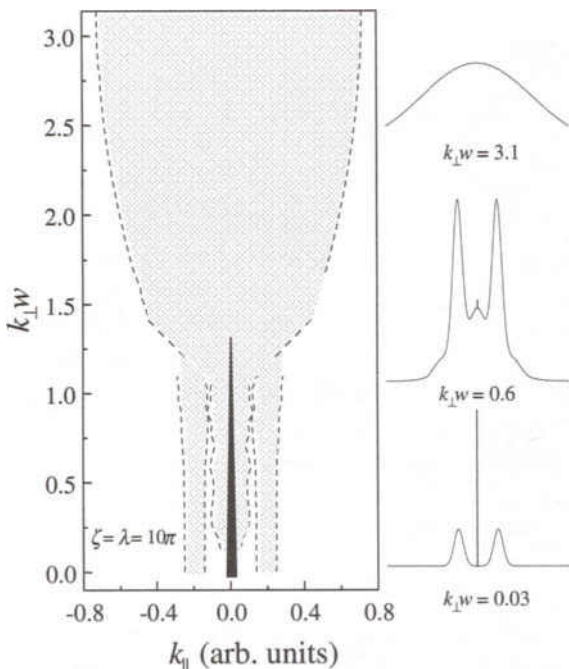


FIG. 10.4 The reciprocal-space structure of a continuous mounded surface.

### 10.2.2 The reciprocal-space structure

The reciprocal-space structure of the diffraction profile for this surface ( $\alpha = 1$ ,  $\zeta = \lambda = 10\pi$ ) is shown in Figure 10.4. At small  $k_{\perp}w$  there is a central  $\delta$  peak and a clear satellite ring around the  $\delta$  peak (see the diffraction profile at  $k_{\perp}w = 0.03$  in Figure 10.4). This profile is quite different from that of the self-affine case shown in Figure 9.5 where a broad central diffuse intensity exists in addition to the  $\delta$  peak. The satellite peak position  $k_c$  shown in Figure 10.4 is a measure of the average mound separation  $\lambda$ ,  $\lambda \approx \frac{2\pi}{k_c}$ . With the increase of  $k_{\perp}w$ , a central diffuse intensity gradually appears with increasing intensity in addition to the  $\delta$ -peak, and the FWHM of the diffuse central intensity remains almost unchanged (see the diffraction profile at  $k_{\perp}w = 0.6$  in Figure 10.4). After reaching a maximum intensity ( $k_{\perp}w \approx 0.6$ , depending on the roughness parameters,  $w$ ,  $\zeta$ , and  $\lambda$ ), the satellite peak intensity begins to decrease. The width of the central diffuse intensity continues to increase. At  $k_{\perp}w \approx 1.2$  the satellite peak is buried in the broadened central intensity. At this point virtually one cannot tell the position of the satellite peak from the profile. At large  $k_{\perp}w$ , the profile

becomes one single broad peak very similar to that obtained from a self-affine rough surface [10.1].

### 10.2.3 Determination of the roughness parameters

For a mounded surface, since  $\alpha = 1$  (usually), there are only three roughness parameters that need to be determined: the RMS roughness  $w$ , the average mound separation  $\lambda$ , and the system correlation length  $\zeta$ . The RMS roughness can be determined by the same methods as discussed in Section 9.2.2: using either the integrated  $\delta$ -peak intensity, or the integrated diffuse profile intensity, or the inverse Fourier transform method. As discussed in Section 3.2, the power spectrum directly reflects the lateral information of the mounded surface: the peak position and the FWHM of the satellite ring in the power spectrum are inversely proportional to the average mound separation  $\lambda$  and the system correlation length  $\zeta$ , respectively. Therefore, both the average mound separation  $\lambda$  and the system correlation length  $\zeta$  can be determined from the diffuse profile at small  $\Omega$  ( $< 1$ ) values since under this condition the diffuse profile is proportional to the surface power spectrum. Another way to determine these two lateral parameters is from the inverse Fourier transform. Table 10.1 summarizes the methods to determine the roughness parameters for a mounded surface.

## 10.3 Diffraction from Discrete Mounded Surfaces

The discrete lattice also affects the diffraction from a mounded surface. The diffuse profile can also be expressed by Equation (7.51), with  $H_d(r)$  being the height-height correlation function [Equation (10.1)] for an isotropic mounded surface. We can repeat the above discussion, and construct the reciprocal-rod structures for a discrete mounded surface. Figures 10.5 and 10.6 show the reciprocal-rod structures for small  $w$  and large  $w$  values. In the small interface width case ( $w = 0.23$ ), the satellite ring and the  $\delta$  peak can be seen throughout the whole rod (Figure 10.5). The FWHM of the satellite ring remains almost the same and is a reflection of the system correlation length. The intensity of satellite ring increases monotonically as  $\Phi$  increases from near 0 to  $\pi$ . For the large interface width ( $w = 3$ ), under the near-in-phase condition, there is a central  $\delta$  peak and a clear satellite ring around the  $\delta$  peak (see the diffraction profile at  $\Phi = 0.01\pi$  in Figure 10.6). The satellite peak position  $k_0$  shown in Figure 10.6 is a measure of the average mound separation  $\lambda$ . With the increase of the phase  $\Phi$ , the central diffuse intensity gradually appears with increasing intensity

Table 10.1 Summary of various methods for determining roughness parameters of mounded surfaces.

<b>Interface width <math>w</math></b>	Plot the $\delta$ intensity $S_\delta$ vs. $k_\perp$ , according to the relation $S_\delta \propto e^{-k_\perp^2 w^2}$ . From the $\delta$ -peak ratio, $R_\delta = e^{-k_\perp^2 w^2}$ . From the diffuse-intensity ratio, $R_{diff} = 1 - e^{-k_\perp^2 w^2}$ . From the IFT of diffraction profiles.
<b>Average mound separation <math>\lambda</math></b>	From the satellite peak position, $k_c = \frac{2\pi}{\lambda}$ at $k_\perp^2 w^2 < 1$ . From the IFT of diffraction profiles.
<b>System correlation length <math>\zeta</math></b>	From the FWHM of the satellite peak, $FWHM \propto 1/\zeta$ for $k_\perp^2 w^2 \ll 1$ . From the IFT of diffraction profiles.
<b>Roughness exponent <math>\alpha</math></b>	Plot $S(k_{  }, k_\perp)$ vs. $k_{  }$ according to $S(k_{  }, k_\perp) \propto k_{  }^{-d-2\alpha}$ for large $k_{  }$ . From the IFT of diffraction profiles.

in addition to the  $\delta$  peak, and the FWHM of the diffuse central intensity remains almost unchanged (see the diffraction profile at  $\Phi = 0.2\pi$ ). After reaching a maximum intensity ( $\Phi = 0.2\pi$ , depending on the roughness parameters,  $w$ ,  $\zeta$ , and  $\lambda$ ), the split satellite intensity begins to decrease. The width of the central diffuse intensity continues to broaden. At  $\Phi = 0.4\pi$  the satellite peak is buried in the broadened central intensity. At this point one virtually cannot tell the position of the satellite peak from the profile. At the out-of-phase condition, the profile becomes one single broad peak very similar to that obtained from a self-affine rough surface.

#### 10.4 Examples

Although people have studied diffusion-barrier-induced mounded surfaces for nearly ten years, a full reciprocal-space characteristics of the mounded surface has not been investigated. Most researchers have concentrated on the characteristic ring structures. For example, Zuo and Wendelken studied the dynamic roughening front of Cu/Cu(100) homoepitaxy by HRLEED and STM [10.2]. They monitored the (00) beam profiles of LEED at the out-of-phase condition during the growth process. As shown in Figure 10.7,

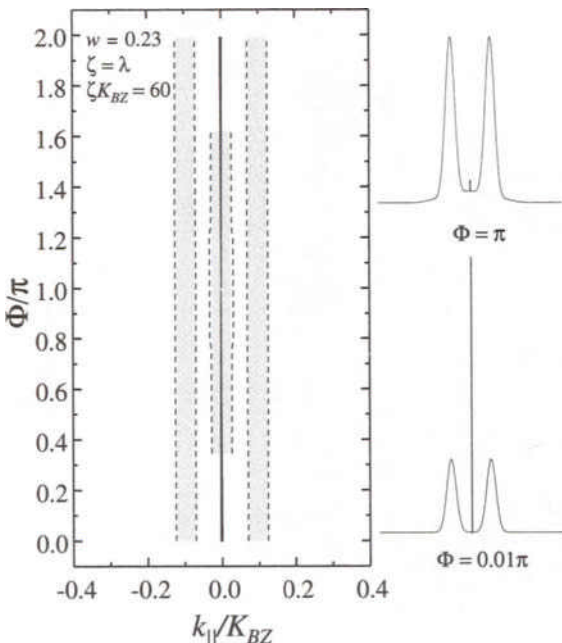


FIG. 10.5 The reciprocal-rod structures of a discrete mounded surface within one Brillouin zone for  $w = 0.23$ . Diffraction profiles at the out-of-phase ( $\pi$ ) and near-in-phase ( $0.01\pi$ ) conditions are shown in the right (from Ref. [10.1]).

the profile at  $t = 0$  only shows a sharp  $\delta$  peak. While the growth starts, a ring structure plus a sharp central peak appears. As we have already discussed above, the characteristic ring structure from the multilayer surface indicates a well-defined mounded structure there. The position of the ring characterizes the average mound separation. With the increase of the growth time, the separation between the ring becomes smaller, and the sharp central peak intensity also gradually disappears. Figure 10.8 shows a log-log plot of the position of the ring as a function of the growth time. Clearly the decay of the ring or the increase of the average mound separation obeys a power law, with  $k_0 \propto t^{-0.25 \pm 0.01}$ . This result is consistent with the STM measurement (shown in Figure 3.8) for a similar growth system.

Murty et al. performed an x-ray scattering experiment on the morphology evolution of Au(111) surface sputtered by using 500 eV  $\text{Ar}^+$  [10.3]. They also observed the satellite ring structure and showed that the position of the ring shrinks and the local slope stays constant for a longer ion bombardment time.

Although the above two experiments are fundamentally very interest-

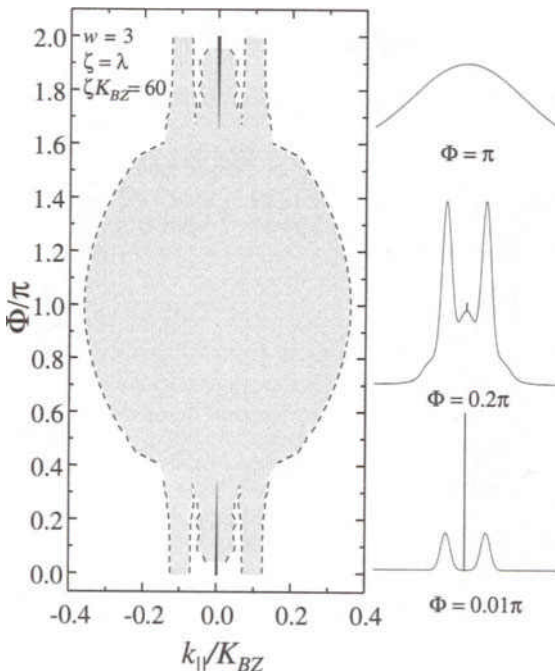


FIG. 10.6 The reciprocal-rod structures of a discrete mounded surface within one Brillouin zone for  $w = 3$  (from Ref. [10.1]). Diffraction profiles at the out-of-phase ( $\pi$ ), away from the out-of-phase ( $0.2\pi$ ), and near-in-phase ( $0.01\pi$ ) conditions are shown at the right (from Ref. [10.1]).

ing, unfortunately both of them have not considered the effect of the other lateral parameter, the system correlation length  $\zeta$ . As discussed in Chapter 3 and this chapter, the system correlation length  $\zeta$  determines the width of the satellite ring of the power spectrum, and therefore affects the ring position in both the power spectrum and diffraction profile. In addition, it also affects the determination of the local surface slope. The roughness parameters related to mounded surfaces can be extracted from the asymptotic behavior of the diffraction profiles as shown in Table 10.1.

## 10.5 Summary

In this chapter, we discussed in detail the real-space and reciprocal-space characteristics of a mounded surface. We have shown that for  $\Omega < 1$  the mounded surfaces give a ring structure in the diffraction pattern. The position of the ring reflects the average mound separation  $\lambda$ , and the FWHM

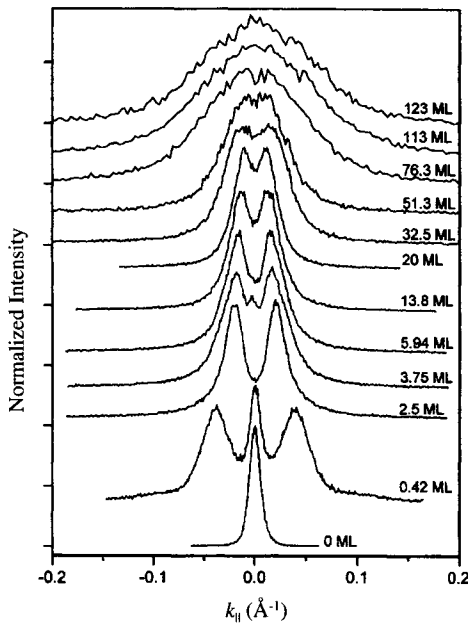


FIG. 10.7 HRLEED angular profiles of the (00) beam measured at the out-of-phase condition from Cu film deposited on Cu(100) at  $T \sim 303$  K for various thicknesses (from Ref. [10.2]).

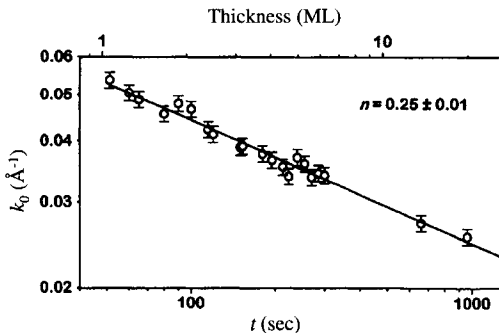


FIG. 10.8 A log-log plot of the diameter of the diffraction ring  $k_0(t)$  versus growth time  $t$  or thickness (from Ref. [10.2]).

of the ring represents the system correlation length  $\zeta$ . However, for  $\Omega > 1$  the ring structure in the diffraction pattern may disappear, leaving only a broad diffuse profile. The FWHM of the broad diffuse profile is proportional to the local slope, which is determined by both the average mound

separation  $\lambda$  and the system correlation length  $\zeta$ .

### References

- 10.1 Y.-P. Zhao, H.-N. Yang, G.-C. Wang, and T.-M. Lu, "Diffraction from diffusion-barrier-induced mound structures in epitaxial growth fronts," Phys. Rev. B **57**, 1922 (1998).
- 10.2 J.-K. Zuo and J. F. Wendelken, "Evolution of mound morphology in reversible homoepitaxy on Cu(100)," Phys. Rev. Lett. **78**, 2791 (1997).
- 10.3 M. V. Ramana Murty, T. Curcic, A. Judy, B. H. Cooper, A. R. Woll, J. D. Brock, S. Kycia, and R. L. Headrick, "X-ray scattering study of the surface morphology of Au(111) during Ar<sup>+</sup> ion irradiation," Phys. Rev. Lett. **80**, 4713 (1998).

This Page Intentionally Left Blank

## 11. ANISOTROPIC SURFACES

In this chapter, we discuss in detail the real-space and reciprocal-space characteristics of self-affine anisotropic surfaces [11.1, 11.2].

### 11.1 Real-Space Characteristics

As discussed in Chapter 3 there are two different kinds of anisotropy in surfaces: correlation-length anisotropy and scaling anisotropy. For correlation-length anisotropy the scaling properties of a surface remain the same in all directions, but the lateral correlation lengths in different directions are different. The formation of a surface with correlation-length anisotropy can be achieved simply by stretching an isotropic surface in certain directions, resulting in different lateral correlation lengths. However, for the scaling anisotropy, not only the lateral correlation lengths but also the roughness exponents could be different in different directions. As discussed in Appendix A, in dynamic growth processes, correlation-length anisotropy is the result of anisotropy of one dominant surface process, such as evaporation/condensation or surface diffusion, during the growth. In the case of anisotropic scaling, the surface is formed by at least two competing surface processes, at least one of which is anisotropic.

From the discussion in Section 3.3.1, the simplest correlation-length anisotropic surface can have the following height-height correlation function:

$$H(\mathbf{r}) = 2w^2 \left\{ 1 - \frac{1}{2^{\alpha-1} \Gamma(\alpha)} \left( \frac{x^2}{\xi_x^2} + \frac{y^2}{\xi_y^2} \right)^{\frac{\alpha}{2}} K_\alpha \left[ \left( \frac{x^2}{\xi_x^2} + \frac{y^2}{\xi_y^2} \right)^{\frac{1}{2}} \right] \right\}, \quad (11.1)$$

where  $\xi_x$  and  $\xi_y$  are the lateral correlation lengths in the  $x$  and  $y$  directions, respectively. The corresponding power spectrum can be written as

$$P(\mathbf{k}_{||}) = 2\alpha \xi_x \xi_y w^2 (1 + k_x^2 \xi_x^2 + k_y^2 \xi_y^2)^{-1-\alpha}. \quad (11.2)$$

The height-height correlation function for a scaling anisotropic surface can be expressed as

$$H(\mathbf{r}) = 2w^2 \left\{ 1 - \frac{4}{\xi_x^{2\alpha_x} \xi_y^{2\alpha_y} \Gamma(\alpha_x) \Gamma(\alpha_y)} \left| \frac{\xi_x x}{2} \right|^{\alpha_x} \left| \frac{\xi_y y}{2} \right|^{\alpha_y} K_{\alpha_x} \left( \left| \frac{x}{\xi_x} \right| \right) K_{\alpha_y} \left( \left| \frac{y}{\xi_y} \right| \right) \right\}, \quad (11.3)$$

where  $\alpha_x$  and  $\alpha_y$  are the roughness exponents in the  $x$  and  $y$  directions, respectively. The power spectrum for Equation (11.3) is

$$P(\mathbf{k}_{||}) = \frac{2\xi_x \xi_y w^2 \Gamma(\frac{1}{2} + \alpha_x) \Gamma(\frac{1}{2} + \alpha_y)}{\Gamma(\alpha_x) \Gamma(\alpha_y)} (1 + k_x^2 \xi_x^2)^{-1/2 - \alpha_x} (1 + k_y^2 \xi_y^2)^{-1/2 - \alpha_y}. \quad (11.4)$$

Since the Gaussian surface height distribution is still assumed here for the anisotropic surface, the expressions for the height difference function  $C(k_{\perp}, \mathbf{r})$ , Equation (7.18), and the diffraction profile, Equation (7.19), are still correct. Therefore, the general descriptions in Section 7.2 about the  $\delta$ -peak intensity, the diffuse profiles at different  $k_{\perp}w$  values, and the integrated intensity are true. However, since the surface is no longer isotropic, all of the characteristic functions are dependent on either vector  $\mathbf{r}$  or vector  $\mathbf{k}_{||}$ .

## 11.2 Diffraction from Anisotropic Surfaces

### 11.2.1 Diffraction beams from correlation length anisotropic surfaces

Now we consider the diffuse diffraction beam from a surface with a correlation length anisotropy. Insert Equation (11.1) into Equation (7.26) and perform the following linear transformations,

$$\begin{cases} x' &= x/\xi_x, \\ y' &= y/\xi_y, \\ r' &= \sqrt{x'^2 + y'^2}, \end{cases} \quad (11.5)$$

and

$$\begin{cases} k'_x &= k_x \xi_x, \\ k'_y &= k_y \xi_y, \\ k'_{||} &= \sqrt{k_x'^2 + k_y'^2}. \end{cases} \quad (11.6)$$

Equation (7.26) becomes

$$S_{diff}(\mathbf{k}'_{||}, k_{\perp}) = e^{-\Omega} \xi_x \xi_y \int [e^{\Omega R(\mathbf{r}')} - 1] e^{i\mathbf{k}'_{||} \cdot \mathbf{r}'} d\mathbf{r}', \quad (11.7)$$

where  $R(\mathbf{r}') = \frac{1}{2^{\alpha-1}\Gamma(\alpha)} r'^{\alpha} K_{\alpha}(r')$ . This form of auto-correlation function  $R(\mathbf{r}')$  matches the corresponding result for isotropic surfaces [Equation (9.5)]. Therefore all of the discussions in Section 9.1 can be applied to this section, except that now the momentum transfer parallel to the surface is  $\mathbf{k}'_{||}$  as defined in Equation (11.6), not  $\mathbf{k}_{||}$ . Thus, for  $\Omega \ll 1$ , the diffuse beam intensity is proportional to the surface height power spectrum, as shown in

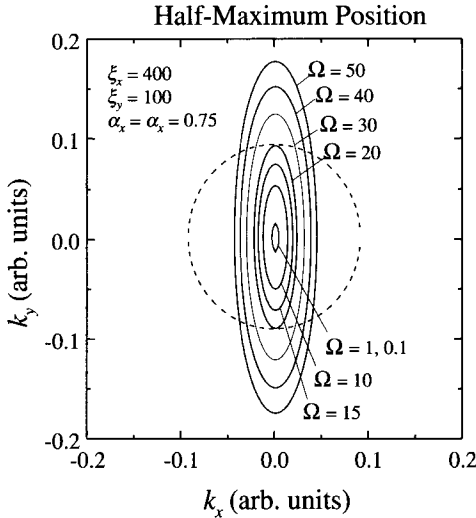


FIG. 11.1 Contours of the FWHM of a diffraction diffuse profile as a function of  $\Omega$  with  $\alpha_x = \alpha_y = 0.75$  and  $\frac{\xi_x}{\xi_y} = \frac{400}{100} = 4$ . The size of the contour increases with the  $\Omega$  value. For comparison, an isotropic surface with an isotropic scaling ( $\xi_x = \xi_y = 100$ ,  $\alpha = 0.75$ ) is also shown as the dashed curve for  $\Omega = 20$  (from Ref. [11.1]).

Equation (9.15). Under this condition, the FWHM of the diffuse beam can be written as

$$\xi_x^2 k_{Fx}^2 + \xi_y^2 k_{Fy}^2 = 2^{\frac{1}{1+\alpha}} - 1, \quad (11.8)$$

which is equivalent to Equation (3.22). Here  $k_{Fx}$  and  $k_{Fy}$  are the FWHM positions of the diffraction beam along the  $k_x$  and  $k_y$  directions, respectively. Equation (11.8) is an ellipse with the principal axes along the  $k_x$  and  $k_y$  directions. The ratio of the diameter of the short axis,  $a_x$ , and the diameter of the long axis,  $a_y$ , is

$$\frac{a_x}{a_y} = \frac{\xi_y}{\xi_x}. \quad (11.9)$$

For  $\Omega \gg 1$ , according to Equations (9.19)-(9.21), Equation (11.7) becomes

$$S_{diff}(\mathbf{k}'_{||}, k_{\perp}) \approx 2\pi \xi_x \xi_y C^{-\frac{1}{\alpha}} \Omega^{-\frac{1}{\alpha}} G_{\alpha}(C^{-\frac{1}{2\alpha}} \Omega^{-\frac{1}{2\alpha}} \mathbf{k}'_{||}), \quad (11.10)$$

where  $C = \frac{\pi}{2^{2\alpha} \alpha \Gamma^2(\alpha) \sin(\alpha\pi)}$  and  $G_{\alpha}(Y)$  is defined by Equation (9.20). The contour of the FWHM for a diffraction beam satisfies

$$\xi_x^2 k_{Fx}^2 + \xi_y^2 k_{Fy}^2 = 4Y_g^2 C^{\frac{1}{\alpha}} \Omega^{\frac{1}{\alpha}} = 4Y_g^2 C^{\frac{1}{\alpha}} (k_{\perp} w)^{\frac{2}{\alpha}}, \quad (11.11)$$

where  $Y_g$  is a constant depending only on  $\alpha$  and satisfies  $G_\alpha(Y_g) = G_\alpha(0)/2$ . Equation (11.11) for a diffraction beam under  $\Omega \gg 1$  and Equation (11.8) for a diffraction beam under  $\Omega \ll 1$  are very similar except for the diameter of the ellipse. The ratio of the diameters of the principal axes is the same. Note that the power spectrum contour is obtained for  $\Omega < 1$ . For a diffraction profile at  $\Omega \gg 1$ , the diameter of the ellipse increases as a power law of  $k_\perp$ , i.e.,  $k_\perp^{1/\alpha}$ . Figure 11.1 shows the contours of the half-maximum position of a diffuse diffraction beam projected in the  $k_x$  and  $k_y$  directions in the reciprocal space for different values of  $\Omega = (k_\perp w)^2$ . The surface is anisotropic in the lateral correlation length, with  $\xi_x = 400$ , which is different from  $\xi_y = 100$ . An isotropic scaling exists in the surface, i.e., the values of the roughness exponent  $\alpha$  along the  $x$  and  $y$  directions are the same and equal to 0.75. The two contours near the center, which correspond to small values of  $\Omega$  ( $= 0.1$  and  $1$ ), are very close in their sizes and overlap with each other. As  $\Omega$  increases the size of the contour increases. Therefore, for the correlation-length anisotropic surface model, the diffraction profile shape reflects the surface anisotropy under any diffraction condition.

For comparison, we also plotted the FWHM contour for an isotropic surface with  $\alpha = 0.75$  and  $\xi_x = \xi_y = 100$  as the dashed curve for  $\Omega = 20$  in Figure 11.1.

### 11.2.2 Diffraction beams from scaling-anisotropic surfaces

For a scaling anisotropic surface, when  $\Omega \ll 1$ , as discussed above, the diffraction beam is proportional to the surface power spectrum. For  $\Omega \gg 1$ , the diffraction profile can be written as

$$\begin{aligned} S_{diff}(\mathbf{k}_{||}, k_\perp) &= \int \exp\{-\Omega[C_x(\frac{x}{\xi_x})^{2\alpha_x} + C_y(\frac{y}{\xi_y})^{2\alpha_y}]\} e^{i\mathbf{k}_{||}\cdot\mathbf{r}} dr \\ &= \frac{\xi_x \xi_y}{\Omega^{1/\alpha_x+1/\alpha_y} C_x^{1/2\alpha_x} C_y^{1/2\alpha_y}} D_{\alpha_x}[\Omega^{-1/2\alpha_x} C_x^{-1/2\alpha_x} \xi_x k_x] \\ &\quad \times D_{\alpha_y}[\Omega^{-1/2\alpha_y} C_y^{-1/2\alpha_y} \xi_y k_y], \end{aligned} \quad (11.12)$$

where  $C_x = \frac{\pi}{2^{2\alpha_x} \alpha_x \Gamma^2(\alpha_x) \sin(\alpha_x \pi)}$ ,  $C_y = \frac{\pi}{2^{2\alpha_y} \alpha_y \Gamma^2(\alpha_y) \sin(\alpha_y \pi)}$ , and  $D_\alpha(Y) = \int_{-\infty}^{+\infty} e^{-X^{2\alpha}} e^{iXY} dX$ . When  $Y \rightarrow \infty$ , one has  $D_\alpha(Y) \propto Y^{-1-2\alpha}$ . Therefore, the ratio  $\gamma_s$  of the FWHMs for the  $k_x$  and  $k_y$  axes for the diffraction profile can be obtained as

$$\gamma_s = \frac{\xi_y Y_{\alpha_x} C_x^{1/2\alpha_x}}{\xi_x Y_{\alpha_y} C_y^{1/2\alpha_y}} (k_\perp w)^{1/\alpha_x - 1/\alpha_y} = \gamma (k_\perp w)^{1/\alpha_x - 1/\alpha_y}, \quad (11.13)$$

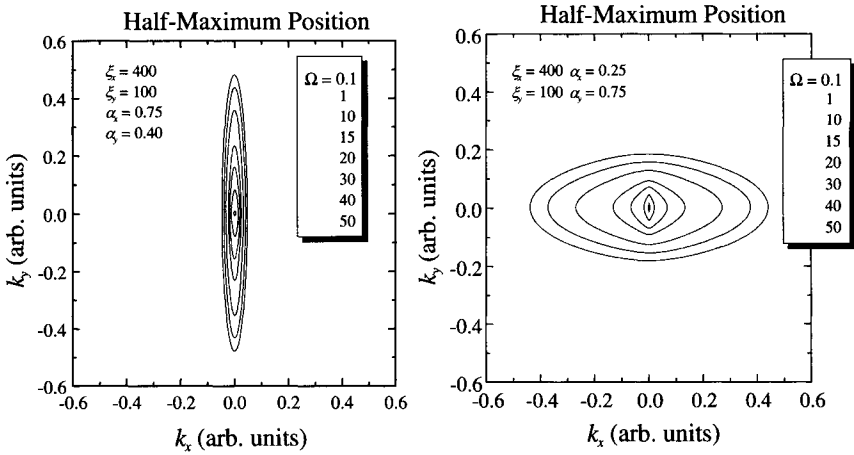


FIG. 11.2 Contours of the FWHM of a diffuse diffraction beam projected in the  $k_x$  and  $k_y$  directions of the momentum transfer in the reciprocal space for  $\xi_x = 400$ ,  $\xi_y = 100$ , and various values of  $\Omega = (k_{\perp} w)^2$ : (a)  $\alpha_x = 0.75$  and  $\alpha_y = 0.40$ , (b)  $\alpha_x = 0.25$  and  $\alpha_y = 0.75$ . The size of the contour increases with the increasing  $\Omega$  value. Note that in (b) the extreme local roughness ( $\alpha_x = 0.25$ ) in the  $x$  direction dominates the FWHM even though  $\xi_x$  is four times larger than  $\xi_y$  (from Ref. [11.1]).

where  $D_{\alpha}(Y_{\alpha}) = \frac{1}{2}D_{\alpha}(0)$ . The ratio  $\gamma_s$  is determined not only by the surface roughness parameters ( $w$ ,  $\xi$ , and  $\alpha$ ) themselves, but also depends on the diffraction condition through  $k_{\perp}$ . In Figure 11.2 we plotted several FWHM contours for different surface parameters. The contours near the center, which correspond to small values of  $\Omega$  ( $= 0.1$  and  $1$ ), again are very close in their sizes and overlap each other. As  $\Omega$  increases the size of the contour increases. The surface is anisotropic in the lateral correlation length with  $\xi_x = 400$  different from  $\xi_y = 100$ . The surface has an anisotropic scaling, i.e., the values of the roughness exponent  $\alpha$  along the  $x$  and  $y$  directions are not the same. Figure 11.2(a) shows that if  $\xi_x > \xi_y$  and  $\alpha_x (= 0.75) > \alpha_y (= 0.40)$ , the anisotropy in the shape of the diffraction beam for  $\Omega \gg 1$  is quite pronounced, especially in the  $k_y$  direction. Note that the scale in Figure 11.2(a) is increased three times as compared with that of Figure 11.1. Qualitatively the contours in Figure 11.1 and Figure 11.2(a) are similar.

However, if  $\xi_x > \xi_y$  and  $\alpha_x (= 0.25) < \alpha_y (= 0.75)$ , as shown in Figure 11.2(b), the direction of the anisotropy in the FWHM contour would rotate as the diffraction condition changes from  $\Omega \leq 1$  to  $\Omega \gg 1$  (around  $\Omega = 20$ ). This result shows that the shape of the diffraction beam depends strongly on

both the correlation-length anisotropy and the scaling anisotropy. These two anisotropies compete with each other as the diffraction condition is changed.

### 11.2.3 Line scan of the diffraction beam

Another interesting feature is the cross section of the diffraction profile from the anisotropic surface. A cross section of the diffraction beam is obtained by line scans in an experiment. For an isotropic surface, the cross section along any direction is the same, and one can obtain the interface width from the  $\delta$ -peak intensity ratio  $R_\delta$ . However, for an anisotropic surface, as the diffraction beam itself becomes anisotropic, the cross section is direction dependent. Is it still possible to obtain the interface width through a line scan of the diffraction intensity?

Without losing any generality, we can consider the cross section in the  $k_x$  direction. In a realistic detection system, the detector has a finite size. The diffraction intensity  $S_c$  (line scan) integrated over a finite  $k_y$  is

$$S_c(k_x) = \int_{-\Delta k_y}^{\Delta k_y} dk_y \int \int C(k_\perp, \mathbf{r}) e^{-i(k_x x + k_y y)} dx dy. \quad (11.14)$$

$S_c(k_x)$  can be also broken into two parts, a  $\delta$  peak,

$$S_{c\delta}(k_x) = 2\pi e^{-k_\perp^2 w^2} \delta(k_x), \quad (11.15)$$

and a diffuse profile,

$$S_{cdiff}(k_x) = \int_{-\Delta k_y}^{\Delta k_y} dk_y \int \int [C(k_\perp, \mathbf{r}) - e^{-k_\perp^2 w^2}] e^{-i(k_x x + k_y y)} dx dy. \quad (11.16)$$

For simplicity, we consider only the case of a correlation length anisotropic surface,

$$\begin{aligned} S_{cdiff}(k_x) &= \int_{-\Delta k_y}^{\Delta k_y} dk_y \int \int D(k_\perp; \frac{x}{\xi_x}, \frac{y}{\xi_y}) e^{-i(k_x x + k_y y)} dx dy \\ &= 2\pi \xi_x \int_{-\xi_y \Delta k_y}^{\xi_y \Delta k_y} dk'_y \int D(k_\perp, \mathbf{r}') e^{i\mathbf{k}'_{||} \cdot \mathbf{r}'} d\mathbf{r}', \end{aligned} \quad (11.17)$$

where  $D(k_\perp, \mathbf{r}) = C(k_\perp, \mathbf{r}) - e^{-k_\perp^2 w^2}$ . If  $\Delta k_y$  is small, Equation (11.17) can be approximated by

$$S_{cdiff}(k_x) \approx 4\pi \xi_x \xi_y \Delta k_y \int D(k_\perp, \mathbf{r}') e^{i\mathbf{k}'_{||} \cdot \mathbf{r}'} d\mathbf{r}'|_{k'_y=0}. \quad (11.18)$$

Table 11.1 Summary of various methods for determining roughness parameters of anisotropic surfaces from diffraction beams.

<b>Interface width <math>w</math></b>	Plot the $\delta$ -intensity $S_\delta$ vs. $k_\perp$ , according to the relation $S_\delta \propto e^{-k_\perp^2 w^2}$ . From the $\delta$ -peak ratio, $R_\delta = e^{-k_\perp^2 w^2}$ . From the diffuse intensity ratio, $R_{diff} = 1 - e^{-k_\perp^2 w^2}$ . From the IFT of diffraction profiles.
<b>Direction-dependent lateral correlation length <math>\xi_\theta</math></b>	$FWHM \propto 1/\xi_\theta$ for $k_\perp^2 w^2 \ll 1$ from the line scan at direction $\theta$ . From the IFT of diffraction profiles.
<b>Direction-dependent roughness exponent <math>\alpha_\theta</math></b>	Plot line scan $S_\theta(k_{  }, k_\perp)$ vs. $k_{  }$ according to $S_\theta(k_{  }, k_\perp) \propto k_{  }^{-1-2\alpha_\theta}$ for large $k_{  }$ . From the IFT of diffraction profiles.

Therefore, the integral of the diffuse profile becomes

$$\int S_{cdiff}(k_x) dk_x = 4\pi \xi_y \Delta k_y C(\Omega, \alpha), \quad (11.19)$$

where  $C(\Omega, \alpha)$  is a constant depending on both  $w$  and  $\alpha$ . Equation (11.19) shows that the integration of a diffuse profile is direction dependent. Because the  $\delta$  peak is superposed on the diffuse profile, the  $\delta$ -peak ratio (with respect to the total intensity in the line scan) also depends on the direction. If during a growth process the surface anisotropy of  $\xi$  changes, then the change in the  $\delta$ -peak ratio from a line scan reflects the changes of both  $w$  and the anisotropy. One cannot obtain the interface width from a line scan without knowing the anisotropic properties of  $\xi$  in the surface. However, if  $\Delta k_y$  is small, the line scan can be approximated by the cross section of a two-dimensional diffraction beam. One can still obtain the corresponding  $\xi$  and  $\alpha$  in a certain direction according to the discussions in previous sections. For an anisotropic scaling surface, one can obtain a similar result.

### 11.2.4 Determination of the roughness parameters

From the diffraction beam of an anisotropic surface we can determine the roughness parameters describing the surface. First, for a surface with either correlation-length anisotropy or scaling anisotropy, the RMS roughness  $w$  can be extracted from the  $\delta$ -peak intensity ratio, as discussed for both self-affine surfaces and mounded surfaces. Here we should emphasize that  $w$  cannot be obtained correctly from the line scan of a beam. However, for  $\Omega < 1$ , the diffuse beam is proportional to the power spectrum of the surface, and we can obtain the direction-dependent lateral correlation length from the FWHM of the line scan of the diffuse beam. The direction-dependent roughness exponent can also be obtained from the line scans at different directions. These methods are summarized in Table 11.1.

### 11.2.5 The reciprocal-space structure

For anisotropic surfaces, since the rotational symmetry of a surface is broken, the reciprocal-space structure becomes more complicated than that of the isotropic surfaces. A three-dimensional view is easier to visualize. Figure 11.3 shows the reciprocal-space structure for a correlation-length anisotropic surface. The central cone represents the  $\delta$ -peak intensity and the surrounding surface consists of the half-maximum positions of the diffuse profiles. In order to show the central cone, we intentionally cut out two segments of the half-maximum position surface. Figure 11.3 shows that as  $k_{\perp}w$  increases the  $\delta$ -peak intensity decreases. At small  $k_{\perp}w$  ( $< 1$ ), the shape of the half-maximum position is elliptical and the area of the ellipse remains almost unchanged, while at large  $k_{\perp}w$  ( $> 1$ ), the shape of the half-maximum position is still elliptical, but the area of the ellipse becomes increasingly large. However, the anisotropy ratios of the ellipse for both  $k_{\perp}w < 1$  and  $k_{\perp}w > 1$  are the same.

Figure 11.4 shows the reciprocal-space structure of a scaling anisotropic surface. Here we assume  $\xi_x = 4\xi_y$ ,  $\alpha_x = 0.25$ , and  $\alpha_y = 0.75$ . Figures 11.4(a) and 11.4(b) are the same plot but with different viewing angles. Again segments of the half-maximum position surface are cut off for an easy viewing near the central structures. The  $\delta$ -peak intensity shown as the central cone has the similar behavior as that of the correlation-length anisotropic surface. The shape of the half-maximum positions of the diffuse profile at  $k_{\perp}w < 1$  is elliptical, having its long axis along the  $k_y$  direction, and the area of the ellipse remaining almost unchanged. As  $k_{\perp}w$  increases, the area of the ellipse increases, and the shape also changes. At a certain  $k_{\perp}w$  value, the long axis of the ellipse switches to the  $k_x$  direction. After

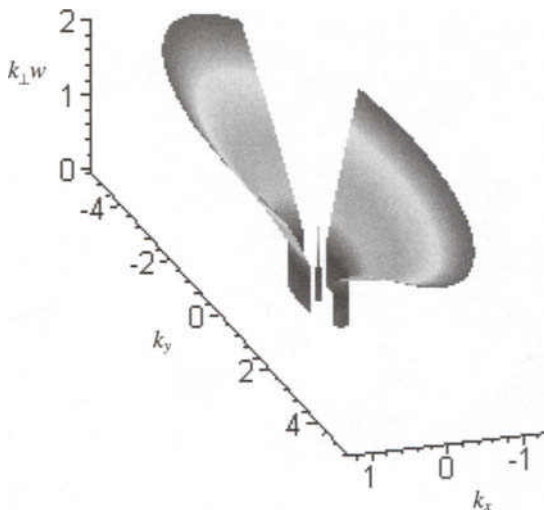


FIG. 11.3 The reciprocal-space structure of a surface with lateral anisotropy.

that, the ratio of the long axis to the short axis keeps on increasing.

### 11.3 An Example: The Hard-Disk Surface

To show the complexity in the analysis of an anisotropic surface, in this section we analyze the anisotropic hard-disk surface using AFM and light scattering techniques [11.3]. The reliability and durability of a hard disk are determined by a series of tribological factors, among which the surface roughness of the disk plays an essential role [11.4, 11.5, 11.6, 11.7]. During the read/write operation, the magnetic head initially is in contact with the hard disk. If the disk surface is too smooth, the head will stick onto the disk surface, which inhibits the start-up, and possibly causes permanent damage to the slider/disk. In order to reduce the potential damage, a surface texture is introduced, which breaks the large contact area into many small ones. Although the force per unit contact area increases after the introduction of a texture, the net starting torque is reduced. Typically a texture consists of two sets of nearly-circular lines, or grooves, on the surface [11.8]. The average separation between the grooves is comparable to the wavelength of visible light. It has been shown that the actual morphology of the texture is very important to the performance of the hard disk [11.4, 11.5, 11.6, 11.7].

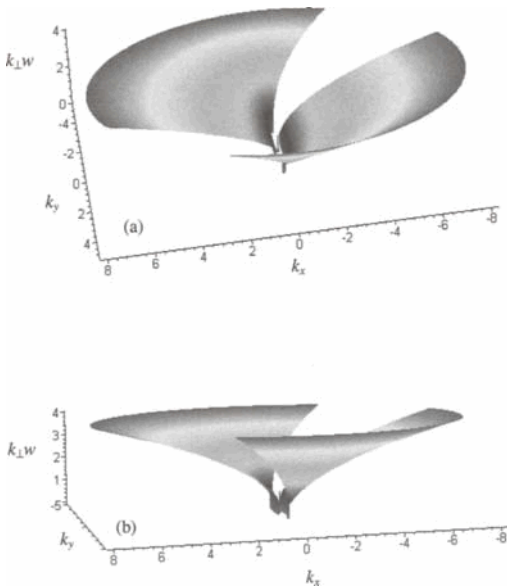


FIG. 11.4 The reciprocal-space structure of a surface with scaling anisotropy.

### 11.3.1 AFM measurements

A  $40 \mu\text{m} \times 40 \mu\text{m}$  AFM image is shown in Figure 11.5(a). AFM images display a nearly one-dimensional periodicity. The power spectrum density (PSD) can be obtained by taking the Fourier transform of the AFM images. The PSD was computed using a discrete form of the Fourier transformation. Figure 11.5(b) shows the top view of the PSD obtained from the  $40 \mu\text{m} \times 40 \mu\text{m}$  AFM image. A thin stripe lying on  $k_y = 0$  reveals the anisotropy. There is also a bow along the  $k_y$  axis near  $k_x = 0$  which is actually an artifact due to the drift of the piezosscanner during the scanning along the  $x$  direction [11.9]. This artifact causes unreliable low PSD values around that low frequency region.

Usually, to obtain a reliable PSD along only one direction out of a two-dimensional surface, one must integrate the two-dimensional PSD along the direction orthogonal to the desired direction [11.8]. This process is actually an average of all one-dimensional PSD slices, each sitting on a different frequency in the orthogonal direction, but because the PSD stripe in Figure 11.5(b) is thin enough and has high values at  $k_y = 0$ , a one-dimensional PSD function perpendicular to the groove lines ( $k_x$  axis) can be obtained simply by taking the slice of  $k_y = 0$  from the two-dimensional PSD profile shown in Figure 11.5(b). The average of the one-dimensional

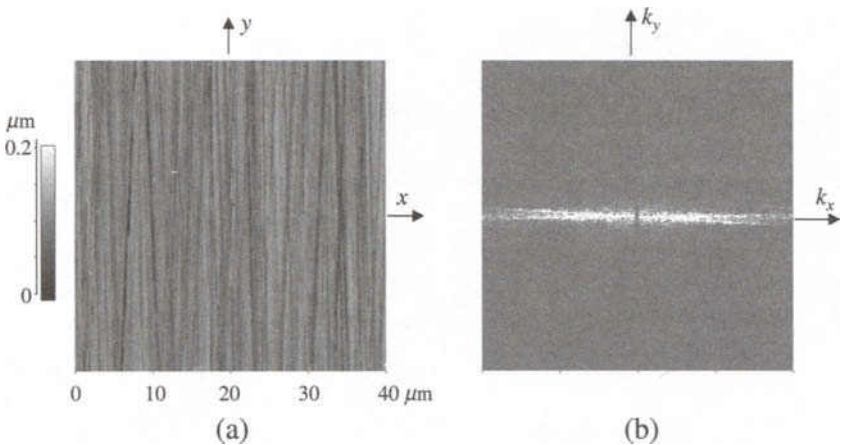


FIG. 11.5 (a) AFM image of a hard disk with  $40 \mu\text{m} \times 40 \mu\text{m}$  scan size. (b) The top view of the two-dimensional PSD obtained from the AFM image.

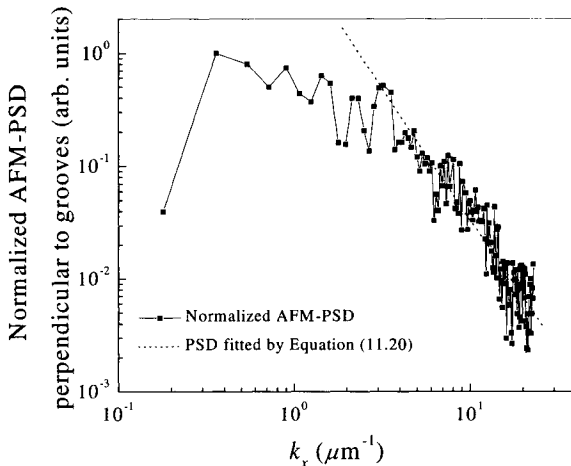


FIG. 11.6 The average AFM-PSD of 40 and 70  $\mu\text{m}$  one-dimensional PSD in the direction perpendicular to groove lines. The dotted line represents the fitting by Equation (11.20).

PSDs calculated in this way from AFM images with  $40 \mu\text{m} \times 40 \mu\text{m}$  and  $70 \mu\text{m} \times 70 \mu\text{m}$  scan sizes is shown in Figure 11.6. The average PSD obtained from these large scan sizes shows no well-isolated peak, which suggests that there is no preferred groove separation in the disk within the length scale we examined. We can calculate the lateral correlation length  $\xi_x$  using the

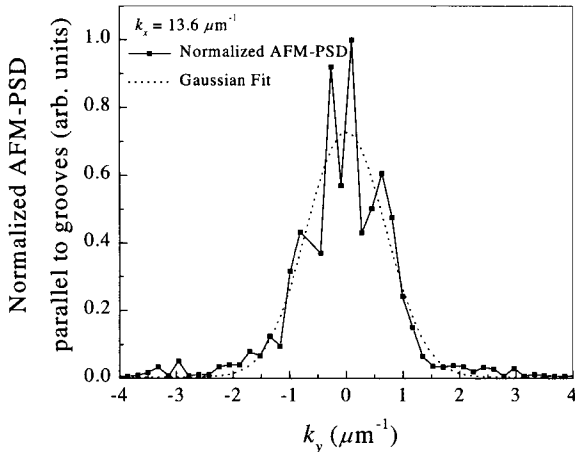


FIG. 11.7 The one-dimensional AFM-PSD along groove lines, lying at  $k_x = 13.6 \mu\text{m}^{-1}$  of Figure 11.5(b). The dotted line is a Gaussian fit to the profile.

fitting function:

$$PSD(k_{||}) = \frac{A}{(1 + k_x^2 \xi_x^2)^{1/2+\alpha_x}}, \quad (11.20)$$

where  $A$  is a free parameter and  $\xi_x$  is the lateral correlation length. We showed the fit of Equation (11.20) to the one-dimensional PSD in Figure 11.6. During the fitting process we tried not to use small-frequency data in order to avoid the artifact mentioned above. As a result, we obtained  $\xi_x = 1.18 \pm 0.22 \mu\text{m}$  and the roughness exponent  $\alpha_x = 0.57 \pm 0.05$ . The RMS roughness for the hard-disk surface can be calculated as  $w = 200 \pm 5 \text{ \AA}$ .

The finite width of the PSD stripe in Figure 11.5(b) along the  $k_y$  direction is due to the coherence length of distance in the  $y$  axis (along the groove lines) within which the grooves are coherently parallel. For instance, we first took a slice from the two-dimensional AFM-PSD at  $k_x = 13.6 \mu\text{m}^{-1}$  and plotted it in Figure 11.7. Later, we performed a Gaussian fit to this one-dimensional PSD and the correlation length  $\xi_y$  was calculated to be  $9.06 \pm 0.21 \mu\text{m}$  using the relation  $\xi_y = 4\pi/(\Delta)$ , where  $\Delta$  is the FWHM used in the Gaussian fit. We also plotted the same PSD in a log-log scale and calculated  $\alpha_y$  as  $0.99 \pm 0.15$ , from the slope of the tail part using the relation slope  $= -1 - 2\alpha$ .

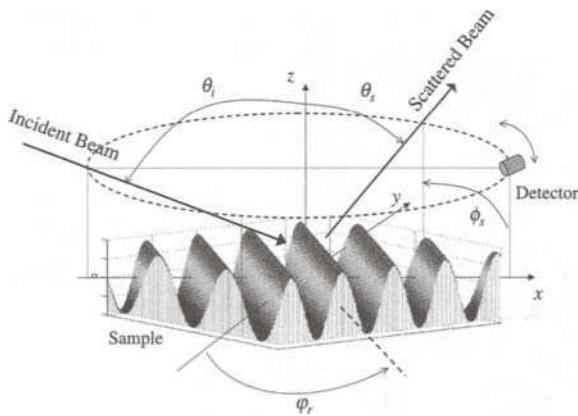


FIG. 11.8 A geometry for light scattering measurement. The sample shown is a periodic surface which can be rotated in-plane by  $\varphi_r$ . The azimuthal angle  $\phi_s$  of the detector can be rotated between  $-180^\circ$  to  $180^\circ$  in a plane parallel to the sample surface (in-plane geometry) and also the polar angle  $\theta_s$  can be rotated from  $-90^\circ$  to  $90^\circ$  in a plane perpendicular to the sample plane (out-of-plane geometry).

### 11.3.2 Light scattering

The geometry of the light scattering measurement is shown in Figure 11.8, where  $\varphi_r$  is the rotation angle of the hard-disk sample from the reference position where groove lines are perpendicular to the incident light plane. The out-of-plane measurements were carried out by setting  $\theta_i = 80^\circ$  and  $\phi_s = 0^\circ$ . Then we rotated the detector polar angle  $\theta_s$  from  $-90^\circ$  to  $90^\circ$  in a plane perpendicular to the sample plane. On the other hand, for the in-plane light scattering geometry, both the incident angle  $\theta_i$  of the He-Ne laser and the polar angle of the detector were fixed at  $47^\circ$ , but the azimuthal angle of the detector  $\phi_s$  was rotated in a plane parallel to the sample plane from  $-180^\circ$  to  $180^\circ$ . In both geometries for an RMS roughness value of  $200 \text{ \AA}$  the values of  $(k_{\perp} w)^2$  become 0.07 and 0.005 for  $\theta_i = 47^\circ$  and  $80^\circ$ , respectively. Since these values are much smaller than 1, the surface is considered to be in the small-roughness regime, and therefore, the measured light scattering intensity profiles can be converted to the PSD by Equation (6.80).

We aligned the groove lines parallel to the  $y$  axis; therefore the PSD stripe lays along the  $k_x$  direction in the reciprocal space. We performed the out-of-plane measurements with  $\phi_s = 0^\circ$  (therefore  $k_y = 0$ ). The resulting out-of-plane intensity profile was employed in Equation (6.80) to calculate the PSD perpendicular to the grooves. We showed the normalized intensity and the corresponding PSD profiles in Figure 11.9(a).

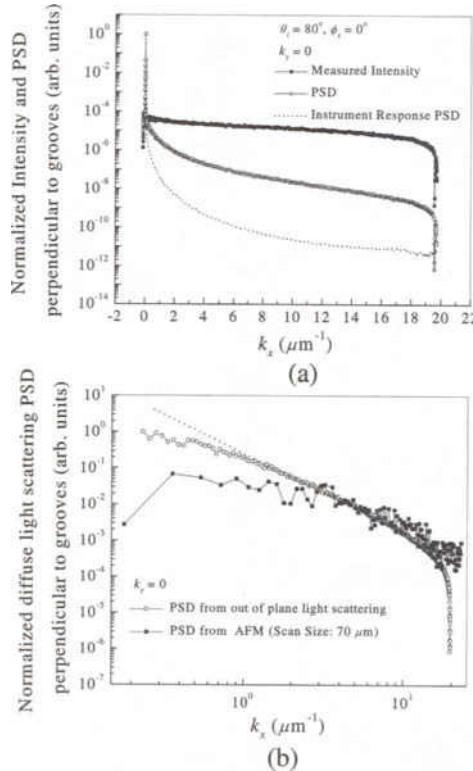


FIG. 11.9 The grooves are aligned parallel to the  $y$  axis. (a) Normalized out-of-plane intensity and PSD profiles of  $\phi_s = 0^\circ$  (at  $k_y = 0$ ). (b) One-dimensional PSD [from (a)] in the direction perpendicular to groove lines. The dotted line represents the fit by Equation (11.20).

The large drop in both the intensity and the PSD at large frequencies is due to the detector position effect, since it starts to block the incident light. In the AFM lateral-correlation-length analysis, we also plotted the one-dimensional PSD in a log-log scale [Figure 11.9(b)]. Fitting the diffuse part of the profile with Equation (11.20), we obtained the lateral correlation length  $\xi_x = 1.12 \pm 0.08 \mu\text{m}$  and the roughness exponent  $\alpha_x = 0.65 \pm 0.03$ . These values are consistent with the ones obtained from the AFM analysis. We compared the PSD profiles perpendicular to groove lines obtained from AFM (rescaled) and light scattering in Figure 11.10. A reasonable agreement between AFM and light scattering PSD exists except in the low frequency range. This is mostly due to the artifacts induced in the low frequency part of AFM-PSD profiles, as mentioned before.

In-plane light scattering measurements were also carried out. In Figure

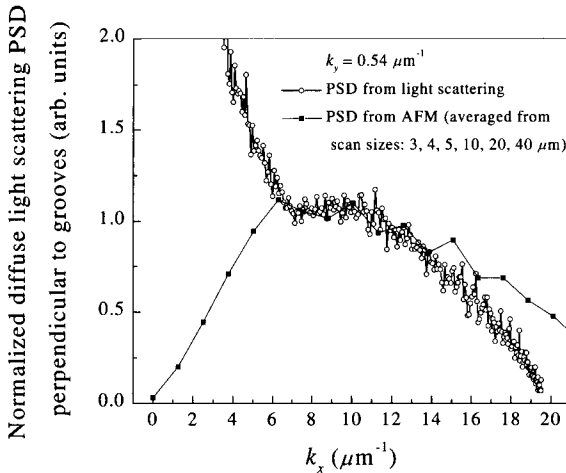


FIG. 11.10 Comparison of the PSD profiles perpendicular to groove lines obtained from AFM (Figure 11.6) and the out-of-plane light scattering [Figure 11.9(b)]. Note the present figure is in a linear scale while Figures 11.6 and 11.9(b) are in log-log scales.

11.11(a), we presented the in-plane light scattering intensity at different sample rotation angles. We see that the in-plane light scattering is very sensitive to the surface anisotropy. As expected, whenever the detector intersects with the PSD stripe in the reciprocal space, it reads a high-intensity value. We show this situation schematically in Figure 11.11(a) as an inset. For each rotation angle, the detector cuts the PSD stripe at a different  $k_x$  value, which results in a different  $\phi_s$  peak position. We can derive the change of the peak position of the in-plane light scattering profile according to the equation:

$$|\phi_{s\_peak}| = \pi - 2 |\varphi_r|. \quad (11.21)$$

Later we place the groove lines parallel to the incident beam plane (along the  $x$  axis), where the PSD wall is positioned to be at  $k_x = 0$  along the  $k_y$  axis. Then we performed a kind of “modified in-plane” measurement, where  $\theta_i$  and  $\theta_s$  were still kept constant but this time they were set to be unequal from each other. In Figure 11.11(b), we see the result of such a kind of measurement. The locations of the two peaks in the profile correspond to  $k_x = 0$ , which is consistent with the stripe-shaped picture of the two-dimensional PSD.

The observed peak widths in the tails of the light scattering profiles are due to the finite lateral correlation length in the  $y$  direction, as discussed in the AFM analysis section. In order to calculate both  $\xi_y$  and  $\alpha_y$ , we took

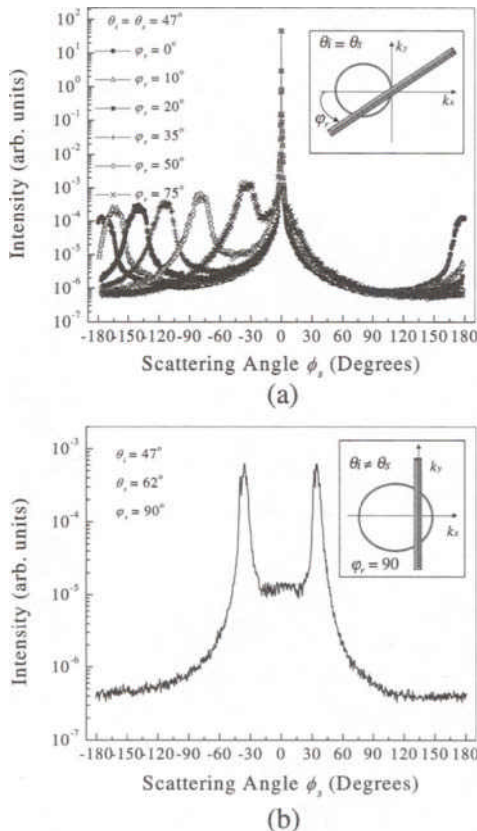


FIG. 11.11 (a) In-plane light scattering intensity at different sample rotation angles  $\varphi_r$ . The trajectory of a detector in the reciprocal space (top view) and the stripe-shaped PSD of a hard-disk surface is shown schematically in the inset. Whenever the detector intersects with the PSD stripe in the reciprocal space, it reads a high intensity value. (b) Modified in-plane light scattering intensity profile when  $\varphi_r$  is set to  $90^\circ$ . The situation in the reciprocal space is also shown as an inset.

the intensity profile for  $\varphi_r = 20^\circ$  and converted it to the corresponding PSD parallel to the  $k_y$  axis and at  $k_x = 13.6 \mu\text{m}^{-1}$  (see Figure 11.12). We performed a Gaussian fit to the light scattering PSD profile and calculated  $\xi_y$  as  $8.61 \pm 0.17 \mu\text{m}$  from the FWHM of the fit. In Figure 11.12 we also compared this in-plane light scattering PSD with the one obtained from AFM-PSD (shown in Figure 11.7) having the same  $k_x$  value. Similar to the AFM analysis we also plotted the PSD profile in a log-log scale and extracted  $\alpha_y$  to be  $1.03 \pm 0.07$  from the slope of the tail part. These values of  $\xi_y$  and  $\alpha_y$  are in good agreement with the results obtained from the PSD analysis of AFM images.

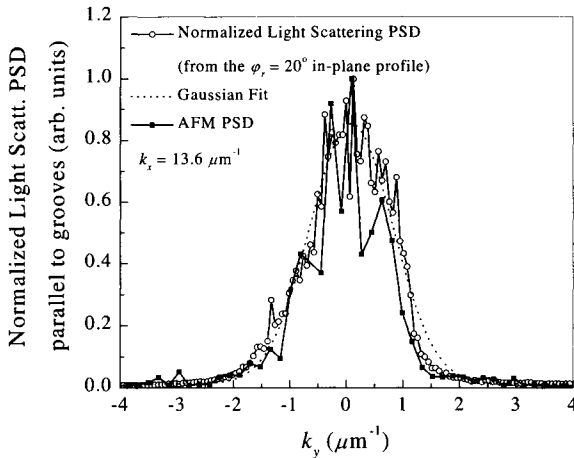


FIG. 11.12 One-dimensional PSD parallel to groove lines, lying at  $k_x = 13.6 \mu\text{m}^{-1}$  obtained from the  $\varphi_r = 20^\circ$  intensity profile of Figure 11.11(a). The width of the Gaussian fit is inversely proportional to groove lateral correlation length. The AFM-PSD shown in Figure 11.7 is also plotted for a comparison.

#### 11.4 Summary

In this chapter, we discussed in detail the characteristics of self-affine anisotropic surfaces. For the correlation-length anisotropic surface, the shape of the diffraction beam directly reflects the surface anisotropy under any diffraction condition. However, for the scaling-anisotropic surface, the anisotropic scaling exponents may alter the anisotropy in the diffraction beam shape. It can sometimes even rotate the direction of anisotropy.

#### References

- 11.1 Y.-P. Zhao, G.-C. Wang, and T.-M. Lu, "Diffraction from anisotropic random rough surfaces," *Phys. Rev. B* **58**, 7300 (1998).
- 11.2 Y.-P. Zhao, G.-C. Wang, and T.-M. Lu, "Anisotropy in growth front roughening," *Phys. Rev. B* **58**, 13909 (1998).
- 11.3 T. Karabacak, Y.-P. Zhao, T.-M. Lu, G.-C. Wang, and Y.-F Liew, "Characterization of hard-disk surface using light scattering and atomic force microscopy," *J. Appl. Phys.*, in press.
- 11.4 Finn Jorgensen, *The Complete Handbook of Magnetic Recording*, 4th Edition (McGraw-Hill, New York, 1996).
- 11.5 M. Suk, B. Bhushan, and D. B. Bogy, "Role of disk surface roughness on slider flying height and air-bearing frequency," *IEEE Trans. Magnet.* **26**, 2493 (1990).
- 11.6 M. Ito, T. Shinohara, K. Yanagi, and K. Kanaka, "Influence of surface texture of a thin-film rigid disk on frictional properties at the head-disk interface," *IEEE Trans.*

- Magnet. **26**, 2502 (1990).
- 11.7 J. K. Lee, A. Chao, J. Enguero, M. Smallen, H. J. Lee, and P. Dion, "Effect of disk cross hatch texture on tribological performance," IEEE Trans. Magnet. **28**, 2880 (1992).
  - 11.8 J. C. Stover, *Optical Scattering: Measurement and Analysis*, 2nd Edition (SPIE Optical Engineering Press, Bellingham, Washington, 1995).
  - 11.9 S. J. Fang, S. Haplepete, W. Chen, and R. Helms, "Analyzing atomic force microscopy images using spectral methods," J. Appl. Phys. **82**, 5891 (1997).

## 12. NON-GAUSSIAN SURFACES

In the last three chapters, we discussed the real-space and reciprocal-space characteristics of self-affine, mounded, and anisotropic surfaces. The basic assumption for most of these discussions is that the surface height obeys a Gaussian distribution (which is true for most rough surfaces due to the central limit theory) and that the diffraction structure factors can be obtained from a general equation, Equation (7.19). However, as discussed in Chapter 2, in some cases, the surface does not have a Gaussian height distribution, e.g., the surface in Figure 2.3(b). Then, how would the non-Gaussian height distribution affect the behavior of diffraction profiles, and what asymptotic behavior can one obtain from those profiles? We will use the isotropic self-affine surface in this chapter as an example in order to answer these questions. We will show how non-Gaussian height distributions affect the determination of the roughness parameters.

### 12.1 Height Difference Distribution $P(z, \mathbf{r})$ and Height Difference Function $C(k_{\perp}, \mathbf{r})$

Random rough surfaces are often treated as a result of stochastic processes with respect to  $\mathbf{r}$ . For a stochastic process, it is possible for different processes to have the same correlation function but different height distributions, or vice versa. Therefore, in order to determine the properties of a certain stochastic process, not only should the distribution be given, but also the correlation function, as well as higher-order correlators. Traditionally, for surface growth, more emphasis has been placed on the height-height correlation or the auto-correlation, rather than the height distribution. Theoretically, once both the mean and the correlation of the noise term  $\eta(\mathbf{r}, t)$  in a linear Langevin equation are given, the height-height correlation function can be determined. Simple examples of the linear growth models are discussed in Appendix A. Notice that there is no assumption about the height distribution.

In order to obtain diffraction structure factors from non-Gaussian surfaces, we need to know the height difference function  $C(k_{\perp}, \mathbf{r})$ . As shown in Equation (7.2), this requires the knowledge of the distribution of  $z(\mathbf{r})$ , the height difference between two surface points separated by  $\mathbf{r}$ . It turns out that we should know in advance the joint distribution of two surface heights  $h_1$  and  $h_2$  separated by  $\mathbf{r}$ . One direct method to do this is to create the

corresponding master or Fokker-Planck equation from the known Langevin equation and then obtain the height distribution and related joint distribution by solving the equation. However, solving the master or Fokker-Planck equation is not trivial due to various distributions of noise and nonlinearity (see Appendix A). It is even harder to obtain an analytical solution. A simpler way is to make assumptions about the height distributions. For simplicity, we consider only the isotropic self-affine surface. Therefore, the auto-correlation function is already known through Equation (9.5). The problem reduces to finding the joint distribution  $p_j$  given the height distribution and the correlation function. This problem has been tackled by many people since the late 1950s [12.1, 12.2, 12.3]. Beckmann summarizes those results in the following theorem [12.3]:

**Theorem 12.1** *Let  $X$  and  $Y$  be two identically-distributed random variables with given probability density  $p(x)$  and given correlation coefficient  $R(r) \geq 0$ , and let  $X$  and  $Y$  be independent for  $R = 0$ . If  $p(x)$  is proportional to the weighting function of one of the standard classical system of orthogonal polynomials  $\{Q_n\}$ , then the joint density of  $X$  and  $Y$  is*

$$p_j(x, y; R) = p(x)p(y) \sum_{n=0}^{\infty} \frac{R^n(r)}{h_n^2} Q_n(x)Q_n(y), \quad (12.1)$$

where

$$\int_a^b p(x)Q_n(x)Q_m(x)dx = h_n^2 \delta_{nm}, \text{ and} \quad (12.2)$$

$$R(r) = \frac{<xy> - <x><y>}{\sqrt{(<x^2> - <x>^2)(<y^2> - <y>^2)}}. \quad (12.3)$$

$R(r)$  is also called the auto-correlation function when  $x$  and  $y$  are random variables of the same random process.

Here we propose another method which starts from the general one-variable Langevin equation, and obtained a slightly different expression from Equation (12.1) [12.4]. Appendix E shows the detailed deduction. Then Equation (12.1) can be modified as

$$p_j(x, y; R) = p(x)p(y) \sum_{n=0}^{\infty} \frac{R(r)^{\lambda_n/\lambda_1}}{h_n^2} Q_n(x)Q_n(y), \quad (12.4)$$

where  $\lambda_n$  is the eigenvalue of  $Q_n(x)$  for the corresponding eigenequation. The only difference between Equation (12.4) and Equation (12.1) is that the power  $n$  of  $R$  in Equation (12.1) is changed to the eigenvalue of  $Q_n(x)$

for the corresponding eigenequation. However, the proof of Equation (12.4) is more general than that of Reference [12.3].

For an isotropic self-affine surface, it is clear that for  $r \rightarrow 0$ ,  $R \rightarrow 1$ , and for  $r \rightarrow \infty$ ,  $R \rightarrow 0$ ; i.e.,  $R$  satisfies the condition stated in the theorem. If we denote  $x$  as  $h(\mathbf{r} + \boldsymbol{\rho})$ ,  $y$  as  $h(\boldsymbol{\rho})$ , and  $p(x)$  as the weighting function of a system of classical polynomials  $Q_n$ , then the joint distribution  $p_j$  is given by Equation (12.4). The distribution of  $z(\mathbf{r}) (= x - y)$  (or the height difference distribution) is expressed as

$$P(z, \mathbf{r}) = \int p_j(y + z, y; R(\mathbf{r})) dy. \quad (12.5)$$

With this definition,  $C(k_\perp, \mathbf{r})$  can be written as

$$\begin{aligned} C(k_\perp, \mathbf{r}) &= \int \int p_j(x, y; R(\mathbf{r})) e^{ik_\perp(x-y)} dx dy \\ &= \sum_{n=0}^{\infty} \frac{R(\mathbf{r})^{\lambda_n/\lambda_1}}{h_n^2} |\int p(x) Q_n(x) e^{ik_\perp x} dx|^2. \end{aligned} \quad (12.6)$$

The derivations of  $P(z, \mathbf{r})$  and  $C(k_\perp, \mathbf{r})$  for various continuous and discrete distributions are given in Appendix E, and the results are summarized in Table 12.1.

Table 12.1 shows that, for a Gaussian height distribution, the height difference  $z(\mathbf{r})$  also obeys a Gaussian distribution with the variance associated with the auto-correlation coefficient  $R$ . For exponential height distribution [ $\Gamma(0, x)$ ], the height difference  $z(\mathbf{r})$  is also an exponential distribution with  $z(\mathbf{r})$  ranging from  $-\infty$  to  $+\infty$  while  $x$  ranges from 0 to  $+\infty$ . The height difference distribution for a gamma height distribution is a  $K$  distribution [see Equation (E.24) in Appendix E]. As seen from Table 12.1, all of the variances for the height difference distribution are modified by the auto-correlation coefficient  $R$ . We plot in Figure 12.1 and Figure 12.2 various height distributions and the corresponding height difference distributions with the same standard deviation and  $R = 0.5$ . The Gaussian distribution is symmetric with respect to its mean, has non-zero, even central moments, and no odd central moments. The gamma distributions are not symmetric with respect to their means, especially for the  $\kappa = 0$  case, which is the same as the exponential distribution. They are skewed distributions, with non-zero odd central moments. However, the corresponding height difference distributions are symmetric, with their means equal to zero. The greatest difference between the Gaussian distribution and the gamma distribution with respect to their height difference distributions is that  $P(z, \mathbf{r})$  for a gamma distribution has a higher probability around  $z = 0$ , a narrower dis-

Table 12.1 Summary of basic results of different height distributions (from Ref. [12.4]).

Name	Distribution Function $p(x)$	Variance $\langle [x - \langle x \rangle]^2 \rangle$	Height Difference Distribution Function $P(z, r)$	Height Difference Function $C(k_{\perp}, r)$
Gaussian	$\frac{1}{\sqrt{2\pi}w} \exp(-\frac{x^2}{2w^2})$	$w^2$	$\frac{1}{2w\sqrt{\pi(1-R)}} \exp[-\frac{z^2}{4w^2(1-R)}]$	$\exp[-\frac{1}{2}k_{\perp}^2 H(r)]$
Exponential	$\frac{1}{w} \exp(-\frac{x}{w})$	$w^2$	$\frac{1}{2w\sqrt{1-R}} \exp(-\frac{ z }{w\sqrt{1-R}})$	$\frac{1}{1+k_{\perp}^2 H(r)/2}$
Gamma	$\frac{1}{\Gamma(\kappa+1)\sigma^{\kappa+1}} x^{\kappa} e^{-x/\sigma}$	$(\kappa+1)\sigma^2$	$\frac{1}{\Gamma(\kappa+1)\sigma\sqrt{\pi(1-R)^{\kappa+1}}} (\frac{z\sqrt{1-R}}{\sigma})^{\kappa+1}$ $\times K_{\kappa+1/2}(\frac{z}{\sigma\sqrt{1-R}})$	$\frac{1}{[1+\frac{k_{\perp}^2 H(r)}{2(\kappa+1)}]^{\kappa+1}}$
Uniform	$\frac{1}{2a}$	$\frac{a^2}{3}$	$\frac{1}{4a^2} \sum_{n=0}^{\infty} (2n+1) R^{n(n+1)}$ $\times \int_{x_1}^{x_2} P_n(\frac{y+z}{a}) P_n(\frac{y}{a}) dy$	$\frac{\pi}{2k_{\perp}a} \sum_{n=0}^{\infty} (2n+1)$ $\times R^{n(n+1)} J_{n+1/2}^2(k_{\perp}a)$
Rayleigh	$\frac{x}{\sigma^2} \exp(-\frac{x^2}{2\sigma^2})$	$\frac{4-\pi}{2}\sigma^2$	$\int_0^{\infty} \frac{y(y+z)}{\sigma^4(1-R)} \exp[-\frac{y^2+(z+y)^2}{2\sigma^2(1-R)}]$ $\times I_0[\frac{y(z+y)\sqrt{R}}{\sigma^2(1-R)}] dy$	$\sum_{n=0}^{\infty} \frac{\pi k_{\perp} \sigma^2}{2} [(-\frac{1}{2})_n]^2 R^n$ $\times {}_2F_2(\frac{3}{2}, \frac{3}{2}; \frac{3}{2}, \frac{3}{2} - n; -\frac{k_{\perp}^2 \sigma^2}{2})$

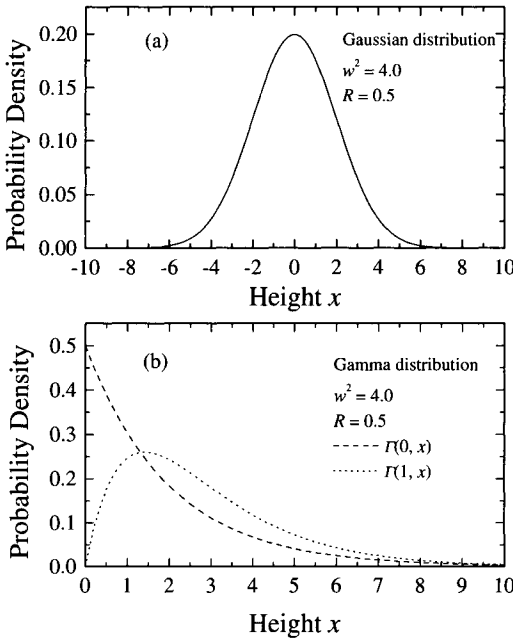


FIG. 12.1 Surface height distribution  $p(h)$  for different statistical models: Gaussian and gamma distributions (from Ref. [12.4]).

tribution width, and a longer tail than that for a Gaussian distribution. As we shall see later, this difference will have a more dramatic effect on the diffraction profiles for large  $k_{\perp}$ .

The height difference function  $C(k_{\perp}, \mathbf{r})$  also takes different forms for different height distributions as seen in Table 12.1. The plots of  $C(k_{\perp}, \mathbf{r})$  for  $\Omega \ll 1$  and  $\Omega \gg 1$  for different height distributions are shown in Figures 12.3(a) and 12.3(b). Here we assume  $\alpha = 0.75$  and  $\xi = 5.0$ . For  $\Omega \ll 1$ , the differences in  $C(k_{\perp}, \mathbf{r})$  for various distributions are very small, whereas for  $\Omega \gg 1$ , the differences are more obvious. In fact, from Table 12.1, for  $\Omega \ll 1$  all the height difference functions  $C(k_{\perp}, \mathbf{r})$  can be approximated by

$$C(k_{\perp}, \mathbf{r}) \approx 1 - \frac{1}{2} k_{\perp}^2 H(\mathbf{r}). \quad (12.7)$$

As long as  $H(\mathbf{r})$  is the same,  $C(k_{\perp}, \mathbf{r})$  will be the same no matter what the height distribution is. In fact, Equation (12.7) is exactly equal to Equation (7.5). For  $\Omega \gg 1$ , higher-order moments in Equation (12.6) will take effect. These moments depend on the height distribution as seen from Equation (12.6). For a Gaussian height distribution,  $C(k_{\perp}, \mathbf{r})$  decreases very quickly as a function of  $r$ , while for a gamma height distribution the decrease

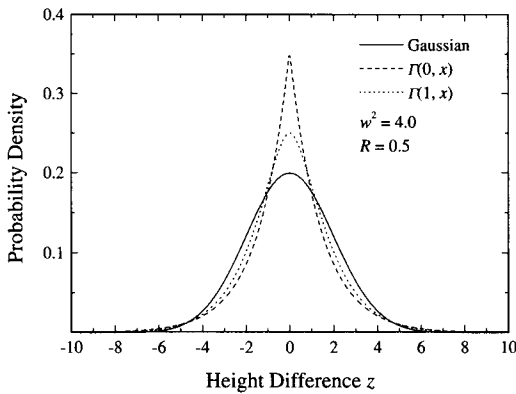


FIG. 12.2 Height difference distributions  $P(z, r)$  for different surface height distributions (from Ref. [12.4]).

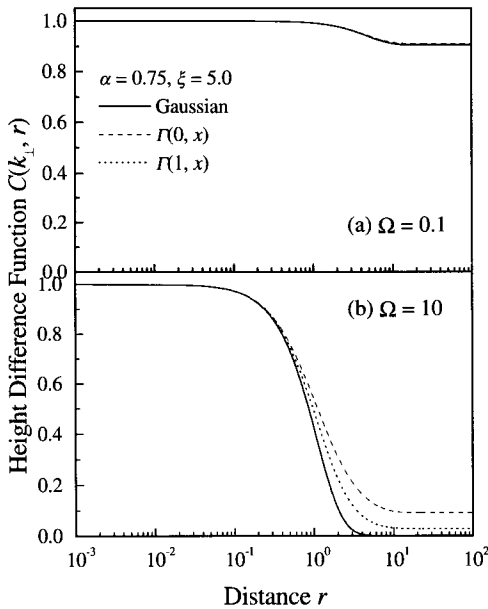


FIG. 12.3 Height difference function  $C(k_{\perp}, r)$  for different height distributions: (a)  $\Omega \ll 1$  and (b)  $\Omega \gg 1$ .

is slower, as shown in Figure 12.4. The abrupt decrease of  $C(k_{\perp}, \mathbf{r})$  for a Gaussian height distribution gives more higher-frequency terms in the Fourier transform, and the diffuse profile will be much broader than that obtained from a gamma distribution, as will be seen later in Figure 12.6

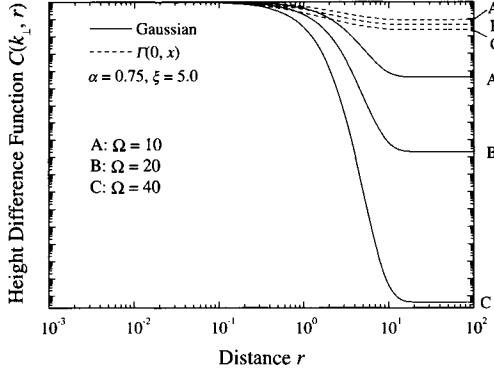


FIG. 12.4 Height difference functions  $C(k_{\perp}, r)$  for Gaussian and gamma distributions at different  $\Omega$  values (from Ref. [12.4]).

(the exponential distribution).

## 12.2 Diffraction Structure Factors from Non-Gaussian Surfaces

The height difference function  $C(k_{\perp}, \mathbf{r})$  can be broken into two parts:

$$C(k_{\perp}, \mathbf{r}) = C(k_{\perp}, \infty) + \Delta C(k_{\perp}, \mathbf{r}), \quad (12.8)$$

where  $C(k_{\perp}, \infty) = \lim_{r \rightarrow \infty} C(k_{\perp}, \mathbf{r})$ . As  $\lim_{r \rightarrow \infty} R(r) = 0$ , only the zeroth-order term in Equation (12.6) survives. For classic orthogonal polynomials,  $Q_0 = 1$ ,  $h_0^2 = 1$ , and  $\lambda_0 = 0$ , we have

$$C(k_{\perp}, \infty) = \left| \int p(h) e^{ik_{\perp} h} dh \right|^2. \quad (12.9)$$

This is the form of Equation (7.4). Therefore, the diffraction profile  $S(\mathbf{k}_{||}, k_{\perp})$  can also be written as

$$S(\mathbf{k}_{||}, k_{\perp}) = S_{\delta}(\mathbf{k}_{||}, k_{\perp}) + S_{diff}(\mathbf{k}_{||}, k_{\perp}), \quad (12.10)$$

where

$$S_{\delta}(\mathbf{k}_{||}, k_{\perp}) = (2\pi)^2 C(k_{\perp}, \infty) \delta(\mathbf{k}_{||}) = (2\pi)^2 \left| \int p(h) e^{ik_{\perp} h} dh \right|^2 \delta(\mathbf{k}_{||}), \quad (12.11)$$

and

$$S_{diff}(\mathbf{k}_{||}, k_{\perp}) = \sum_{n=1}^{\infty} \frac{1}{h_n^2} \left| \int p(h) Q_n(h) e^{ik_{\perp} h} dh \right|^2 \int R(r)^{\lambda_n / \lambda_1} e^{i\mathbf{k}_{||} \cdot \mathbf{r}} dr. \quad (12.12)$$

Table 12.2  $\delta$ -peak intensity for different height distributions (from Ref. [12.4]).

Name of Distribution	$\delta$ -Peak Intensity
Gaussian	$\exp(-k_{\perp}^2 w^2)$
Exponential	$\frac{1}{1+k_{\perp}^2 w^2}$
Gamma	$\frac{1}{(1+k_{\perp}^2 \sigma^2)^{\kappa+1}}$
Uniform	$\frac{\sin^2(k_{\perp} a)}{k_{\perp}^2 a^2}$
Rayleigh	$ {}_1 F_1(\frac{1}{2}, \frac{1}{2}; -\frac{k_{\perp}^2 \sigma^2}{2}) ^2$

From Equation (12.11) and Equation (12.12), it is clear that the  $\delta$ -peak intensity of the diffraction profile depends on the characteristic function of the surface height distribution, and the diffuse profile depends on both the surface height distribution and the correlation function. If we think of the total diffuse profile as the sum of many small diffuse profiles, then for each small diffuse profile, the surface height distribution  $p(h)$  determines the peak intensity, and the correlation function  $R(r)$  determines the shape of the diffuse profile.

### 1. The intensity of $\delta$ peak

The  $\delta$ -peak intensity is proportional to the squared modulus of the characteristic function of the height distribution  $p(h)$ . For different height distributions, the  $\delta$ -peak intensity has different relations to  $k_{\perp}$ , as seen in Table 12.2. As

$$\int p(h) e^{ik_{\perp} h} dx = \sum_{m=0}^{\infty} \frac{\nu_m}{m!} (ik_{\perp})^m, \quad (12.13)$$

where  $\nu_m$  is the  $m$ th-order moment of  $p(h)$  about the origin, we have

$$C(k_{\perp}, \infty) = \left[ \sum_{m=0}^{\infty} (-1)^m \frac{\nu_{2m}}{(2m)!} k_{\perp}^{2m} \right]^2 + \left[ \sum_{m=0}^{\infty} (-1)^m \frac{\nu_{2m+1}}{(2m+1)!} k_{\perp}^{2m+1} \right]^2. \quad (12.14)$$

For height distributions symmetric about zero, only the first term on the right-hand side of Equation (12.14) exists, but for asymmetric height distributions, the second term, i.e., the odd terms on the right-hand side, should be taken into account. If  $\langle h \rangle = 0$ , for  $\Omega < 1$ , the  $\delta$ -peak intensity can be

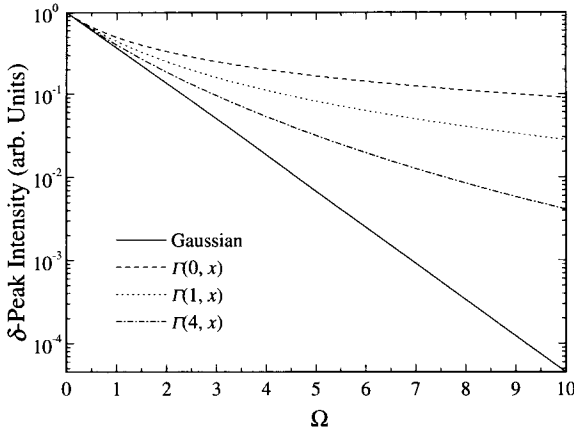


FIG. 12.5 The  $\delta$ -peak intensity versus  $\Omega$  for different height distributions (from Ref. 12.4]).

written as

$$C(k_{\perp}, \infty) \approx 1 - k_{\perp}^2 w^2 + \left(\frac{1}{4} + \frac{1}{12}\kappa_4\right)k_{\perp}^4 w^4 + \left(\frac{1}{36}\kappa_3^2 - \frac{1}{24}\kappa_4 - \frac{1}{360}\kappa_6\right)k_{\perp}^6 w^6, \quad (12.15)$$

where  $\kappa_m = \nu_m/w^m$ , for  $m > 2$ . The skewness is  $\kappa_3$ , and the kurtosis is  $\kappa_4$ . If the height distribution is more asymmetric, then there are greater contributions from the odd moments, and the distribution deviates more from the Gaussian distribution.

The total integrated intensity of a  $\delta$  peak,  $I_{\delta}$ , is

$$I_{\delta} = \int S_{\delta}(\mathbf{k}_{||}, k_{\perp}) d\mathbf{k}_{||} = (2\pi)^2 \left| \int p(h) e^{ik_{\perp} h} dh \right|^2. \quad (12.16)$$

Figure 12.5 shows the  $\delta$ -peak intensity as a function of  $\Omega$  for different height distributions. For the gamma distribution, as  $\kappa$  becomes larger, the distribution becomes more like a Gaussian distribution, and the results are closer to those obtained from the Gaussian distribution. The total integrated intensity  $I$  of the entire scattered field is

$$I = \int S(\mathbf{k}_{||}, k_{\perp}) d\mathbf{k}_{||} = (2\pi)^2. \quad (12.17)$$

Then

$$R_{\delta} = \frac{I_{\delta}}{I} = \left| \int p(h) e^{ik_{\perp} h} dh \right|^2, \quad (12.18)$$

and

$$R_{diff} = 1 - |\int p(h) e^{ik_{\perp} h} dh|^2. \quad (12.19)$$

One often uses  $R_{\delta}$  to determine the interface width  $w$  through the relation

$$R_{\delta} = e^{-k_{\perp}^2 w^2}, \quad (12.20)$$

which was derived based on the assumption of a Gaussian height distribution. In general, the relation between  $R_{\delta}$  and  $w$  also depends on the height distribution as seen from Table 12.2 and Figure 12.5. If the surface height is no longer a Gaussian distribution, Equation (12.20) should be modified according to the height characteristic function. In general, Equation (12.20) approximately holds for all kinds of distributions only when  $\Omega \ll 1$ , and  $R_{\delta}$  has the same result for different distributions.

In fact, we can extend Equations (12.18) and (12.19) to a surface with any height distribution, as demonstrated in Section 7.1. Equation (12.18) shows that  $R_{\delta}$  actually is only related to the characteristic function of the surface height distribution. Then two important results can be drawn from the discussion above:

(1) If we assume that the surface height distribution is symmetric, Equation (12.18) becomes

$$R_{\delta} = |\int p(h) \cos(k_{\perp} h) dh|^2, \quad (12.21)$$

By changing either the incident angle of the incoming beam with respect to the surface normal or the energy of the incident beam, one can change the  $k_{\perp}$  correspondingly, thereby obtaining the characteristic function of the height distribution through Equation (12.21). Then an inverse Fourier cosine transformation of the characteristic function  $R_{\delta}(k_{\perp})^{1/2}$  will give the surface height distribution. This provides a possible way to obtain the surface height distribution by diffraction.

(2) Equation (12.18) also provides us with a method to determine whether the surface height obeys a Gaussian distribution or not. Since for a surface with Gaussian distribution the characteristic function is also a Gaussian function with respect to  $k_{\perp}$  [Equation (12.20)], one can always plot  $\log[R_{\delta}(k_{\perp})]$  versus  $k_{\perp}^2$  on a linear scale. If the plot is a straight line, then the height distribution should be a Gaussian distribution; otherwise, it is a non-Gaussian distribution.

## 2. Diffuse Profile

Table 12.3 Diffuse peak intensity for different height distributions ( $\Omega \ll 1$ ) (from Ref. [12.4]).

Name of Distribution	Diffuse Peak Intensity
Gaussian	$k_\perp^2 w^2 \xi^2 \exp(-k_\perp^2 w^2)$
Exponential	$\frac{k_\perp^2 w^2 \xi^2}{(1+k_\perp^2 w^2 \xi^2)^2}$
Gamma	$(\kappa + 1) \frac{k_\perp^2 w^2 \xi^2}{(1+k_\perp^2 w^2 \xi^2)^{\kappa+2}}$
Uniform	$\frac{3\pi\xi^2}{2k_\perp a} J_{3/2}^2(k_\perp a)$
Rayleigh	$\frac{\pi}{8} k_\perp^2 \xi^2 \xi^2 {}_2F_2(\frac{3}{2}, \frac{3}{2}; \frac{3}{2}, \frac{1}{2}; -\frac{k_\perp^2 \sigma^2}{2})$

For an isotropic self-affine surface, Equation (12.12) can be written as

$$\begin{aligned} S_{diff}(k_{||}, k_\perp) &= 2\pi \sum_{n=1}^{\infty} \frac{1}{h_n^2} \left| \int p(h) Q_n(h) e^{ik_\perp h} dh \right|^2 \\ &\times \int_0^{\infty} r R(r)^{\lambda_n/\lambda_1} J_0(k_{||} r) dr. \end{aligned} \quad (12.22)$$

Two cases should be discussed:  $\Omega \ll 1$  and  $\Omega \gg 1$ .

(1)  $\Omega \ll 1$

For  $\Omega \ll 1$ , we can prove that [12.4]

$$\left| \int p(h) Q_n(h) e^{ik_\perp h} dh \right|^2 \sim O(\Omega^n). \quad (12.23)$$

Then for  $\Omega \ll 1$ , the diffuse profile

$$S_{diff}(k_{||}, k_\perp) \approx \frac{2\pi}{h_1^2} \left| \int p(h) Q_1(h) e^{ik_\perp h} dh \right|^2 \int_0^{\infty} r R(r) J_0(k_{||} r) dr. \quad (12.24)$$

The shape of a diffuse profile is determined mainly by the integral  $\int_0^{\infty} r R(r) J_0(k_{||} r) dr$ , which is proportional to the power spectrum  $P(k_{||})$  of the surface height, and has nothing to do with the surface height distribution.

However, the diffuse peak intensity depends on the specific height distributions as listed in Table 12.3. In fact, Equation (12.24) shows that the diffuse peak intensity is the squared modulus of the product of the surface height characteristic function and its first derivative.

(2)  $\Omega \gg 1$

In this case, other terms in the summation of Equation (12.12) will affect the diffuse profile. If we assume a self-affine surface and express  $R(r)$  as  $\exp[-(\frac{r}{\xi})^{2\alpha}]$ , then for both the Gaussian distribution and the gamma distribution, as  $\lambda_n = n$ , we have

$$\begin{aligned} \int_0^\infty r R(r)^n J_0(k_{||} r) dr &= \xi^2 n^{-\frac{1}{\alpha}} \int_0^\infty X \exp(-X^{2\alpha}) dX \\ &\times \sum_{m=0}^\infty \frac{(-1)^m}{(m!)^2} \left(\frac{k_{||}\xi X}{2}\right)^{2m} n^{-\frac{m}{\alpha}}, \end{aligned} \quad (12.25)$$

so

$$\begin{aligned} S_{diff}(k_{||}, k_\perp) &= 2\pi\xi^2 \sum_{m=0}^\infty \frac{(-1)^m}{(m!)^2} \int_0^\infty X \exp(-X^{2\alpha}) \left(\frac{k_{||}\xi X}{2}\right)^{2m} dX \\ &\times \left[ \sum_{n=1}^\infty \frac{n^{-\frac{m+1}{\alpha}}}{h_n^2} \times \left| \int p(h) Q_n(h) e^{ik_\perp h} dh \right|^2 \right]. \end{aligned} \quad (12.26)$$

The summation in the square brackets  $[\dots]$  has different asymptotic forms for different height distributions. For a Gaussian height distribution,

$$[\dots] = \sum_{n=1}^\infty \frac{n^{-\frac{m+1}{\alpha}}}{h_n^2} (k_\perp w)^{2n} \exp(-k_\perp^2 w^2) \approx (k_\perp^2 w^2)^{-\frac{m+1}{\alpha}} \text{ for } \Omega \gg 1. \quad (12.27)$$

Then

$$S_{diff}(k_{||}, k_\perp) \approx 2\pi\xi^2 \Omega^{-\frac{1}{\alpha}} \int_0^\infty X \exp(-X^{2\alpha}) J_0(k_{||}\xi\Omega^{-\frac{1}{2\alpha}} X) dX. \quad (12.28)$$

For an exponential height distribution,

$$[\dots] = \sum_{n=1}^\infty \frac{(k_\perp^2 w^2)^n}{(1+k_\perp^2 w^2)^{n+1}} n^{-\frac{m+1}{\alpha}} \approx \frac{1}{1+\Omega} \zeta\left(\frac{m+1}{\alpha}\right), \quad (12.29)$$

where  $\zeta(x)$  is the Riemann-Zeta function. For  $x \gg 1$ , one has [12.5]

$$\zeta(x) \approx 2^{-x} + 1, \quad (12.30)$$

which leads to

$$\begin{aligned} S_{diff}(k_{||}, k_\perp) &\approx \frac{2\pi\xi^2}{1+\Omega} \left[ \int_0^\infty X \exp(-X^{2\alpha}) J_0(k_{||}\xi X) dX \right. \\ &\quad \left. + 2^{-\frac{1}{\alpha}} \int_0^\infty X \exp(-X^{2\alpha}) J_0(2^{-\frac{1}{2\alpha}} k_{||}\xi X) dX \right]. \end{aligned} \quad (12.31)$$

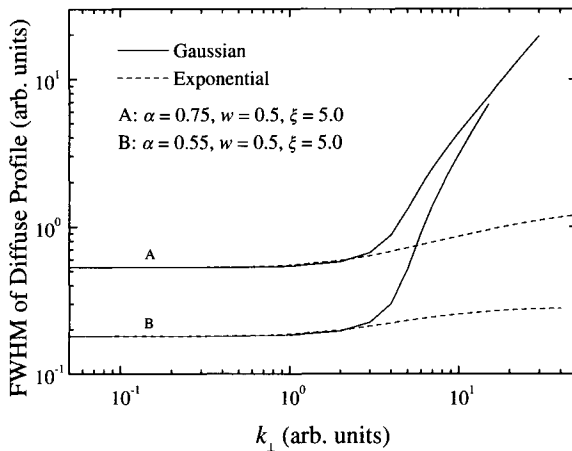


FIG. 12.6 FWHM of the diffuse profiles versus  $k_{\perp}$  for different height distributions (from Ref. [12.4]).

It is seen that different height distributions give different asymptotic results. For a Gaussian distribution, the diffuse peak intensity  $I_{diff} \propto k_{\perp}^{-2/\alpha}$ , and the  $FWHM \propto k_{\perp}^{1/\alpha}$ . Based on these two relations, one can derive the roughness exponent  $\alpha$ . However, for an exponential height distribution, there is no such relation, and one cannot obtain  $\alpha$  using the relations obtained from a Gaussian distribution. Figure 12.6 shows the FWHM of the diffuse profile as a function of  $k_{\perp}$  for different  $\alpha$  values and different height distributions. Here, we assume  $w = 0.5$  and  $\xi = 5.0$ . For  $k_{\perp} \ll 1$ , both the Gaussian height distribution and exponential distribution give the same FWHM, whereas for  $k_{\perp} \gg 1$ , they have different behaviors. For the Gaussian distribution, the FWHM diverges as  $k_{\perp}$  goes to infinity; for the exponential distribution, the FWHM will be bounded by a certain value. These results show that caution should be used when one wants to determine  $\alpha$  through the relations obtained under the assumption of a Gaussian height distribution.

One question can be raised here: How accurate does the diffraction technique need to be in order to estimate the growth kinetics without the knowledge of the surface height distribution? For  $\Omega \ll 1$ , as roughness parameters individually affect the density and shape of the diffraction profiles, one can obtain the interface width  $w$ , the lateral correlation length  $\xi$ , and the roughness exponent  $\alpha$  through the  $\delta$ -peak intensity and diffuse profile without any specific assumption about the surface height distribution. However, for  $\Omega \gg 1$ , the diffuse profile depends on both the surface height distribution and correlation function, and the relationships between

roughness parameters and diffraction profiles are much more complicated and depend very much on the surface height distribution. There is then no general method to determine the roughness parameters.

If one uses the inverse Fourier transform to determine the height-height correlation function  $H(r)$  from the diffraction profiles, the same problem also can arise since different height distributions give different forms of  $C(k_{\perp}, r)$ , as discussed above. However, for  $\Omega \ll 1$ , the approximation  $C(k_{\perp}, r) \approx 1 - \frac{1}{2}k_{\perp}^2 H(r)$  always holds without any specific assumption about the height distribution, and one can obtain the height-height correlation function directly without the knowledge of the height distribution.

### 12.3 Summary

In this chapter, we discussed in detail some characteristics of non-Gaussian height distributions and how they affect the diffraction profiles. For a self-affine surface, the asymptotic behaviors at  $\Omega \gg 1$  obtained from Gaussian surface do not hold. However, the asymptotic behavior at  $\Omega \ll 1$  is independent of the surface height distribution. So far very little experimental work has been published that illustrates the characteristics of rough surfaces with non-Gaussian height distributions, except for two-level surfaces. We are going to discuss this in the next chapter.

### References

- 12.1 J. L. Brown, "A criterion for the diagonal expansion of a second order probability distribution in orthogonal polynomials," IRE Trans. IT-4, 172 (1958).
- 12.2 E. Masry, "On the series representation of bivariate probability density functions," Proc. IEEE 57, 1771 (1969).
- 12.3 P. Beckmann, *Orthogonal Polynomials for Engineers and Physicists* (Golem, Boulder, 1973).
- 12.4 Y.-P. Zhao, G.-C. Wang, and T.-M. Lu, "Diffraction from non-Gaussian rough surfaces," Phys. Rev. B 55, 13938 (1997).
- 12.5 L. C. Andrews, *Special Functions of Mathematics for Engineers*, 2nd Edition (McGraw-Hill, New York, 1992).

## 13. TWO-DIMENSIONAL FRACTAL SURFACES

In Chapters 7 and Chapters 9-12, we covered rough surfaces that contain multiple layers of atoms. However, usually in the very initial stage of thin film formation, the growing interfaces have less than one monolayer of atoms. Obviously these surfaces do not have Gaussian height distribution functions. Also the surface can develop different morphologies. For example, Figure 13.1(a) shows the fractal-shape island formation during the initial stage of Ag deposited on the Pt(111) surface [13.1], and Figure 13.1(b) shows the compact island formation during the submonolayer deposition of Ag on Ag(100) [13.2]. Since the initial stages are very important in terms of the growth control, a detailed knowledge of the growth morphology is necessary. This chapter describes the diffraction behavior of two-level surfaces, with less than one monolayer of atoms deposited on a surface of the same material.

### 13.1 A Discrete Two-Level Surface

In some cases, such as in layer-by-layer growth in a molecular-beam epitaxy (MBE) process, the surface may have only two levels: one is the substrate and the other one is the adatom layer. In the two-level system,  $\Theta$  is the

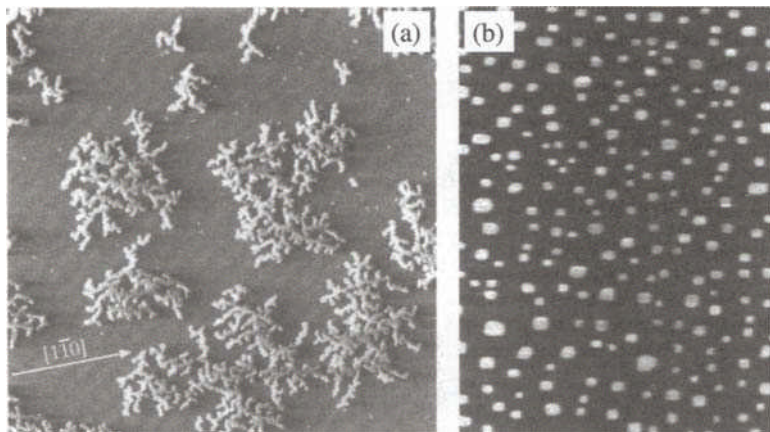


FIG. 13.1 (a) Fractal-shape island formation during the submonolayer growth of Ag on Pt at 110 K (from Ref. [13.1]). (b) Compact island formation during the submonolayer growth of Ag on Ag(100) at 295 K. The surface coverage is 0.125 ML (from Ref. [13.2]).

probability of finding an atom in the upper level, and  $1 - \Theta$  is that in the lower level. We define  $P_{mn} = P_{mn}(\mathbf{r})$  as the probability that an atom in the  $n$ th level exists at a displacement  $\mathbf{r}$  from an atom in the  $m$ th level, where 0 and 1 denote the lower and upper levels, respectively. The height difference function  $C(k_\perp, \mathbf{r})$  can be written as

$$\begin{aligned} C(k_\perp, \mathbf{r}) &= \langle \exp\{i\Phi[d(\mathbf{r}) - d(0)]\} \rangle \\ &= \Theta P_{11} + \Theta P_{10} \exp[-i\Phi] \\ &\quad + (1 - \Theta)P_{01} \exp[i\Phi] + (1 - \Theta)P_{00}. \end{aligned} \quad (13.1)$$

Since  $P_{11} + P_{10} = 1$ ,  $P_{01} + P_{00} = 1$ , and  $\Theta P_{10} = (1 - \Theta)P_{01}$ , one can obtain

$$\begin{aligned} C(k_\perp, \mathbf{r}) &= (1 - 2\Theta + 2\Theta \cos \Phi) + 2\Theta(1 - \cos \Phi)P_{11} \\ &= (1 - 4\Theta \sin^2 \frac{\Phi}{2}) + 4\Theta P_{11} \sin^2 \frac{\Phi}{2}. \end{aligned} \quad (13.2)$$

Clearly  $P_{11}(\mathbf{r})$  is the only function in  $C(k_\perp, \mathbf{r})$  related to the displacement  $\mathbf{r}$  between two surface points and should satisfy

$$P_{11}(\mathbf{r})|_{r \rightarrow 0} = 1, \quad (13.3)$$

$$P_{11}(\mathbf{r})|_{r \rightarrow \infty} = \Theta. \quad (13.4)$$

From the definition of the height difference function  $C(k_\perp, \mathbf{r})$ , Equation (13.1), the height-height correlation function,  $H(\mathbf{r})$ , can be written as

$$H(\mathbf{r}) = -\frac{\partial^2 C(k_\perp, \mathbf{r})}{\partial \Phi^2}|_{\Phi=0, |\mathbf{r}| \neq 0}. \quad (13.5)$$

Therefore,

$$H(\mathbf{r}) = 2\Theta(1 - P_{11}), |\mathbf{r}| \neq 0. \quad (13.6)$$

The diffraction intensity is

$$\begin{aligned} S_d(k_\perp, \mathbf{k}_\parallel) &= \sum_{p,q} [(2\pi)^2 (1 - 4\Theta \sin^2 \frac{\Phi}{2}) \delta(\mathbf{k}_\parallel - \mathbf{K}_{pq}) \\ &\quad + 4\Theta \sin^2 \frac{\Phi}{2} \int P_{11}(\mathbf{r}) e^{i(\mathbf{k}_\parallel - \mathbf{K}_{pq}) \cdot \mathbf{r}} d\mathbf{r}]. \end{aligned} \quad (13.7)$$

The diffraction profile from a two-level system within one Brillouin zone consists of the  $\delta$ -peak intensity and the diffuse profile, similar to the diffraction profiles from other kinds of rough surfaces discussed so far. Both the  $\delta$ -peak intensity and the diffuse intensity are functions of both  $\Theta$  and  $\Phi$ . However, for the same surface, since  $P_{11}(\mathbf{r})$  is fixed, the shape of the diffuse profile does not change even if the diffraction condition changes from the in-phase condition to the out-of-phase condition.

## 13.2 Special Cases for Discrete Two-Level Surfaces

### 13.2.1 Diffraction from random filling surfaces

The simplest two-level system that would generate an intensity oscillation based on the kinematic theory is perhaps the two-dimensional random filling of atoms on a surface [13.3, 13.4, 13.5]. This can occur if the interaction energy between adatoms is negligible (very low temperature where the adatoms hardly diffuse) or if the deposition is performed at a sufficiently high temperature that no 2-D or 3-D islanding can occur [13.6]. Each atom drops onto a surface randomly and independently. As the atom reaches the surface, it sticks on the landing site. In this case,

$$P_{11}(\mathbf{r}) = \Theta + (1 - \Theta)\delta(\mathbf{r}). \quad (13.8)$$

Therefore, the height difference function  $C(k_\perp, \mathbf{r})$  and the height-height correlation function  $H(\mathbf{r})$  can be written, respectively, as

$$C(k_\perp, \mathbf{r}) = 4\Theta(1 - \Theta) \sin^2 \frac{\Phi}{2} \delta(\mathbf{r}) + [1 - 4\Theta(1 - \Theta) \sin^2 \frac{\Phi}{2}], \text{ and} \quad (13.9)$$

$$H(\mathbf{r}) = 2\Theta(1 - \Theta), |\mathbf{r}| \neq 0. \quad (13.10)$$

The diffraction profile can be written as

$$S_d(k_\perp, \mathbf{k}_\parallel) = \sum_{p,q} \{(2\pi)^2 [1 - 4\Theta(1 - \Theta) \sin^2 \frac{\Phi}{2}] \delta(\mathbf{k}_\parallel - \mathbf{K}_{pq}) + 4\Theta(1 - \Theta) \sin^2 \frac{\Phi}{2}\}, \quad (13.11)$$

which contains a sharp  $\delta$ -peak intensity and a uniform background intensity.

In Figure 13.2 we show the cross section of the reciprocal-space structure constructed from Equation (13.11) for  $\Theta = 0.5$ . The central dark line represents the position and strength (magnitude) of the  $\delta$  intensity. As the diffuse profile is a flat background, the FWHM of the diffuse profile is infinite, which we do not show in the plot. At the out-of-phase diffraction condition where  $|\Phi| = \pi$ , both the  $\delta$ -peak intensity and the background intensity oscillate as a function of coverage. When the  $\delta$ -peak intensity is maximum, the background intensity becomes minimum, and vice versa. The oscillation originates from the constructive and destructive interferences of scattered waves from the upper and lower levels of atoms when the upper layer is not completely occupied.

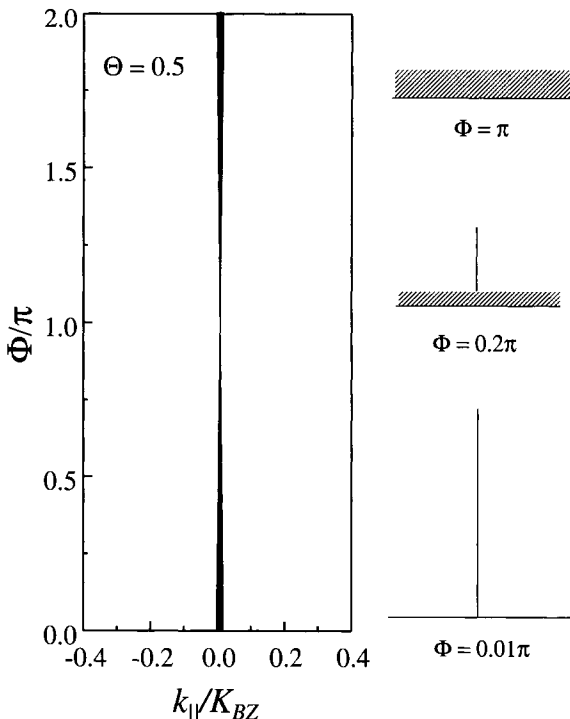


FIG. 13.2 The reciprocal-rod structures and profiles within one Brillouin zone from a random filling surface at  $\Theta = 0.5$  ML (from Ref. [13.7]).

### 13.2.2 Diffraction from random clustering surfaces

If one includes the possibility of clustering of atoms due to adatom interactions, then the situation is much more complicated even in the kinematic approximation. This is because there is an infinite number of ways that one can configure the clusters on a two-dimensional surface. The variables include the shape of the clusters, the size distribution of the clusters, and the shape and size distribution of the unoccupied regions (or the “sea”). For systems with random cluster shape and size, which would give a random two-dimensional step distribution, the pair-correlation function  $P_{11}$  can be written as

$$P_{11}(\mathbf{r}) = \Theta + (1 - \Theta)e^{-r/\xi}, \quad (13.12)$$

where  $\xi$  is the lateral correlation length, which is a measure of the average cluster size. Then the height-height correlation function  $H(\mathbf{r})$  and the

height difference function  $C(k_{\perp}, \mathbf{r})$  can be written as

$$H(\mathbf{r}) = 2\Theta(1 - \Theta)(1 - e^{-r/\xi}), |\mathbf{r}| \neq 0, \text{ and} \quad (13.13)$$

$$C(k_{\perp}, \mathbf{r}) = 4\Theta(1 - \Theta) \sin^2 \frac{\Phi}{2} e^{-r/\xi} + [1 - 4\Theta(1 - \Theta) \sin^2 \frac{\Phi}{2}]. \quad (13.14)$$

The diffraction intensity can then be calculated to give [13.8]

$$\begin{aligned} S_d(k_{\perp}, \mathbf{k}_{\parallel}) &= \sum_{p,q} \left\{ (2\pi)^2 [1 - 4\Theta(1 - \Theta) \sin^2 \frac{\Phi}{2}] \delta(\mathbf{k}_{\parallel} - \mathbf{K}_{pq}) \right. \\ &\quad \left. + \frac{8\pi\Theta(1 - \Theta) \sin^2 \frac{\Phi}{2} \xi^2}{[1 + \xi^2(\mathbf{k}_{\parallel} - \mathbf{K}_{pq})^2]^{3/2}} \right\}. \end{aligned} \quad (13.15)$$

The first term in Equation (13.15) is identical to the first term in Equation (13.11) and is the result of the scattering from the long-range order of the surface. The second term in Equation (13.15), the diffuse intensity, is a two-dimensional Lorentzian function with a FWHM of  $\frac{2\sqrt{2^{2/3}-1}}{\xi}$ . The diffuse intensity is the result of the scattering from the short-range disorder in the surface. The FWHM is inversely proportional to the lateral correlation length of the surface. In Figure 13.3 we show the cross section of the reciprocal-space structure constructed from Equation (13.15) for  $\Theta = 0.5$  ML and  $\xi = 30$ . The central dark line represents the position and strength (magnitude) of the  $\delta$  intensity. The dashed lines represent the positions of the diffuse profile at which the intensity drops to half of the peak intensity of the diffuse profile. The shaded area therefore represents the regime within the half-width positions of the profile. Also, the shapes of the profiles at different  $\Phi$  are shown on the right panel. Equation (13.15) is an extension of earlier derivations of the diffraction from the growth front with a one-dimensional random size distribution (geometric distribution) of surface steps in a two-level system [13.9, 13.10]. In the one-dimensional case, the two-dimensional Lorentzian function in the second term in Equation (13.15) is replaced by a one-dimensional Lorentzian function and the factor  $4\pi^2$  in the first term is replaced by  $2\pi$ .

A more general case involves clusters with fractal shapes, or with entire surface being fractal-like. For example, there is the submonolayer MBE growth with the presence of spontaneous “freezing” centers for the monomers, where the critical nuclear size equals zero. In this case, the pair correlation function  $P_{11}(\mathbf{r})$  can be corrected with a fractal dimension  $D$  of the surface to

$$P_{11}(\mathbf{r}) = \Theta + (1 - \Theta)e^{-(r/\xi)^D}. \quad (13.16)$$

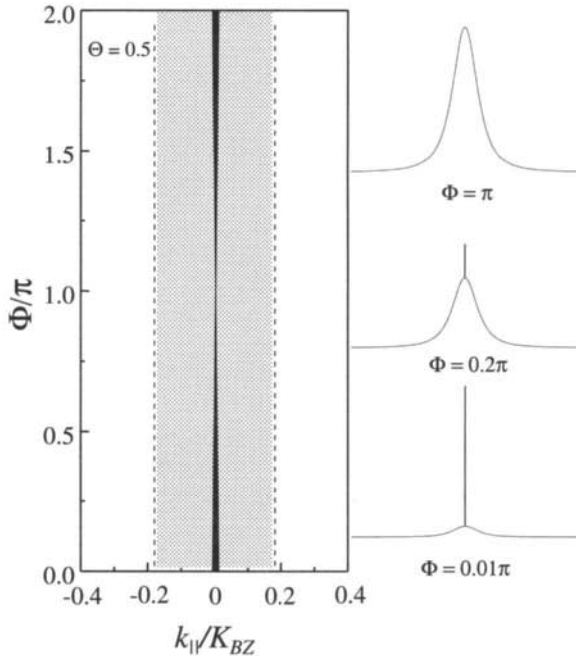


FIG. 13.3 The reciprocal-rod structures and profiles within one Brillouin zone from a random clustering surface at  $\Theta = 0.5$  ML (from Ref. [13.7]).

So the height-height correlation function  $H(\mathbf{r})$  and the height difference function  $C(k_{\perp}, \mathbf{r})$  are

$$H(\mathbf{r}) = 2\Theta(1 - \Theta)[1 - e^{-(r/\xi)^D}], |\mathbf{r}| \neq 0, \text{ and} \quad (13.17)$$

$$C(k_{\perp}, \mathbf{r}) = 4\Theta(1 - \Theta) \sin^2 \frac{\Phi}{2} e^{-(r/\xi)^D} + [1 - 4\Theta(1 - \Theta) \sin^2 \frac{\Phi}{2}]. \quad (13.18)$$

The diffraction intensity is then

$$\begin{aligned} S_d(k_{\perp}, \mathbf{k}_{\parallel}) &= \sum_{p,q} \{(2\pi)^2 [1 - 4\Theta(1 - \Theta) \sin^2 \frac{\Phi}{2}] \delta(\mathbf{k}_{\parallel} - \mathbf{K}_{pq}) \\ &\quad + 8\pi\Theta(1 - \Theta) \sin^2 \frac{\Phi}{2} G(|\mathbf{k}_{\parallel} - \mathbf{K}_{pq}|)\}, \end{aligned} \quad (13.19)$$

where  $G(k) = \int_0^{\infty} e^{-(r/\xi)^D} r J_0(kr) dr$ .

Equation (13.19) describes very well the layer-by-layer growth (epitaxy) such as Si/Si [13.11], GaAs/GaAs [13.12], and Co/Cu [13.13] at appropriate substrate temperatures where the mobility is sufficiently large. The random nature of the cluster shape and cluster distribution implies that there is no

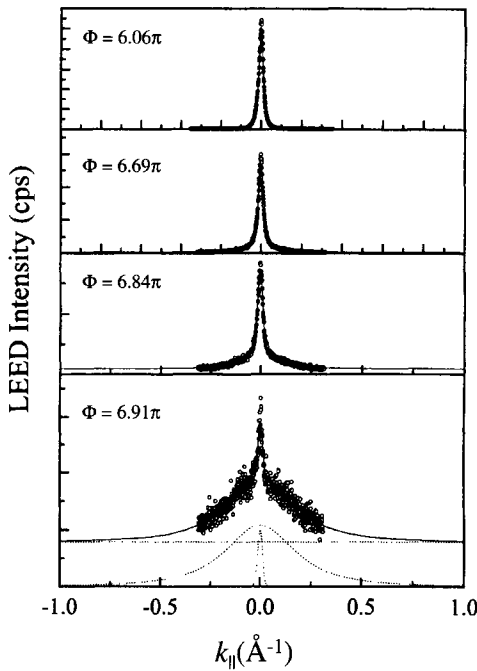


FIG. 13.4 The phase  $\Phi$  dependent LEED (00) beam profiles of epitaxial Co/Cu(100) at room temperature for 30 s. The coverage is about 0.25 ML. The solid curves are the fits using Equation (13.15). The decomposed  $\delta$  peak, 2-D Lorentzian, and background are shown in the bottom profile only. The vertical spacing  $c$  is assumed to be 1.77 Å when  $k_{\perp}$  is converted to phase  $\Phi$  (from Ref. [13.7]).

characteristic length scale (wavelength selection) in the system. Therefore the critical nuclear size would be zero and the nucleation takes place at random sites. In Figure 13.4 we plot the  $k_{\perp}$ -dependent LEED profiles of Co/Cu(100) epitaxy for 30 s [13.13]. The coverage is about 0.25 ML. The diffuse profiles are fitted using the 2-D Lorentzian function of Equation (13.19).

### 13.2.3 Two-dimensional nucleations

However, for many metals, very often the nucleation and growth lead to a well-defined 2-D island shape and a well-defined island-island separation (wavelength selection) [13.14, 13.15, 13.16, 13.17, 13.18]. This can occur when the 2-D critical nuclear size is larger than zero. Obviously Equation (13.15) is no longer valid in this case because of the change of surface structures. However, from the above discussion, we can still write  $P_{11}(\mathbf{r})$

as

$$P_{11}(\mathbf{r}) = \Theta + (1 - \Theta)R(r), \quad (13.20)$$

where  $R(r)$  satisfies

$$R(0) = 1, \quad (13.21)$$

$$R(\infty) = 0. \quad (13.22)$$

Then the diffraction profile can be written as

$$\begin{aligned} S_d(k_\perp, \mathbf{k}_\parallel) &= \sum_{p,q} \left\{ (2\pi)^2 [1 - 4\Theta(1 - \Theta) \sin^2 \frac{\Phi}{2}] \delta(\mathbf{k}_\parallel - \mathbf{K}_{pq}) \right. \\ &\quad \left. + 8\pi\Theta(1 - \Theta) \sin^2 \frac{\Phi}{2} F(|\mathbf{k}_\parallel - \mathbf{K}_{pq}|) \right\}, \end{aligned} \quad (13.23)$$

where  $F(k) = \int_0^\infty R(r)rJ_0(kr)dr$ . According to Amar et al. [13.19],  $F(k)$  has a satellite ring with the ring position  $k_0$  inversely proportional to the average cluster separation and has the following asymptotic behavior:

$$F(k) \propto k^{-D}, k \gg k_0, \quad (13.24)$$

where  $D$  is the fractal dimension of a single cluster. Here we can use a phenomenological model,

$$F(\mathbf{k}) = \frac{A}{[1 + \xi^2(\mathbf{k} - \mathbf{k}_0)^2]^{D/2}}, \quad (13.25)$$

to characterize these features. Here  $A$  is a constant, satisfying

$$\int \int \frac{A}{[1 + \xi^2(\mathbf{k} - \mathbf{k}_0)^2]^{D/2}} d\mathbf{k} = 1. \quad (13.26)$$

Therefore, the diffraction profile can be written as

$$\begin{aligned} S_d(k_\perp, \mathbf{k}_\parallel) &= \sum_{p,q} \left\{ (2\pi)^2 [1 - 4\Theta(1 - \Theta) \sin^2 \frac{\Phi}{2}] \delta(\mathbf{k}_\parallel - \mathbf{K}_{pq}) \right. \\ &\quad \left. + \frac{8\pi A \Theta(1 - \Theta) \sin^2 \frac{\Phi}{2}}{[1 + \xi^2(\mathbf{k}_\parallel - \mathbf{K}_{pq} - \mathbf{k}_0)^2]^{D/2}} \right\}. \end{aligned} \quad (13.27)$$

In Figure 13.5 we plot the reciprocal-space characteristics of the 2-D nucleation surface with  $\Theta = 0.5$  ML. The diffraction intensity has a satellite ring, like the diffuse profile of a mounded surface. However, unlike the mounded surface, this ring structure, known as the Henzler ring [13.14], would not change throughout the entire reciprocal rod. The position  $k_0$  of the split peak is a measure of the separation of clusters. The intensity

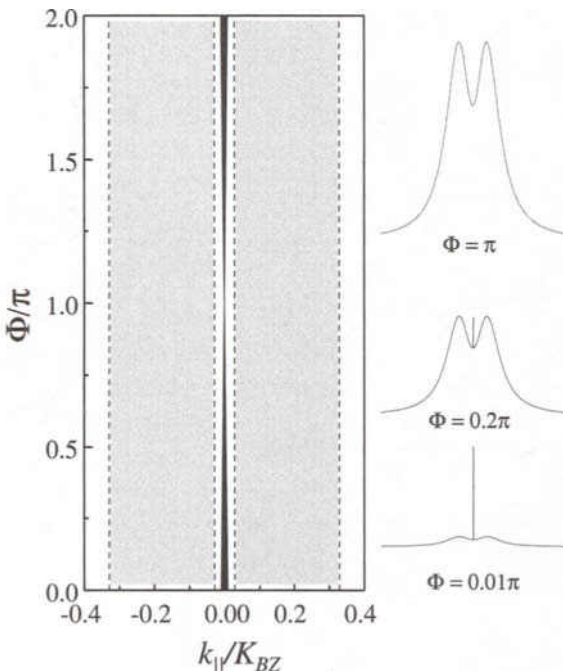


FIG. 13.5 The reciprocal-rod structures and profiles within one Brillouin zone from a two-level nucleation surface at  $\Theta = 0.5$  ML (from Ref. [13.7]).

still oscillates as a function of coverage, independent of the cluster size distribution.

The Henzler ring has been studied extensively by Henzler's group [13.11, 13.14, 13.20] and by other researchers [13.16, 13.21, 13.22]. The ring was first found in a tungsten on W(110) epitaxy experiment measured by HRLEED [13.14]. Figure 13.6 shows the LEED spots at both the in-phase and out-of-phase conditions for 0.5 ML W deposited at 400 K. One can see two clear satellite peaks for the out-of-phase condition, and the positions of the satellite peaks do not change when the electron energy is changed from the near-in-phase condition to the out-of-phase condition. Nyberg et al. studied the epitaxial films of Fe, Co, and Cu grown at 80 – 300 K on Cu(100) with HRLEED [13.16]. In all three systems rings appeared around the central  $\delta$  peaks, although the ring differed in intensity and in diameter depending on the variables of film thickness and deposition temperature. For example, Figure 13.7 shows the diffraction profiles of various thicknesses of Fe films deposited on Cu(100) at 80 K [13.16]. Satellite peaks can be clearly seen for all the thickness. However, the above exper-

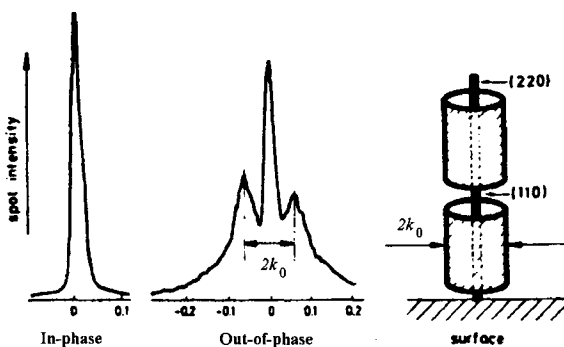


FIG. 13.6 Left and center: LEED spot profiles at the in-phase and out-of-phase conditions, respectively, for  $\theta = 0.5$  ML at  $T=430$  K substrate temperature. Right: The reciprocal-space representation of the (00) beam (from Ref. [13.14]).

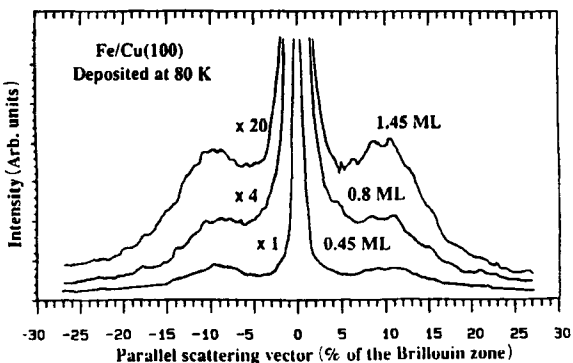


FIG. 13.7 LEED profiles of the (10) spot in the  $<010>$  azimuth for the indicated thicknesses of Fe deposited on Cu(100) at 80 K. The beam energy is 130 eV (from Ref. [13.16]).

iments lack detailed quantitative analyses. Later, Jiang et al. analyzed the HRLEED profile of a Henzler ring based on a one-dimensional surface model. In Figure 13.8 we plot the  $k_{\perp}$ -dependent angular intensity profiles of the (00) diffraction beam for the Fe/Au(100) epitaxy system at about 0.5 ML coverage [13.21]. One can clearly see the shoulder or the splitting in the diffuse profiles. The solid curves are the fits from Equation (13.23) using the gamma distribution function as the terrace width distribution. Bardotti et al. performed a detailed STM and HRLEED study of sub-monolayer growth of Ag on Ag(100) [13.22]. They measured the splitting of the satellite ring position of 0.3 ML Ag deposited at temperatures ranging between 170 and 295 K. As shown in Figure 13.9, the peak position

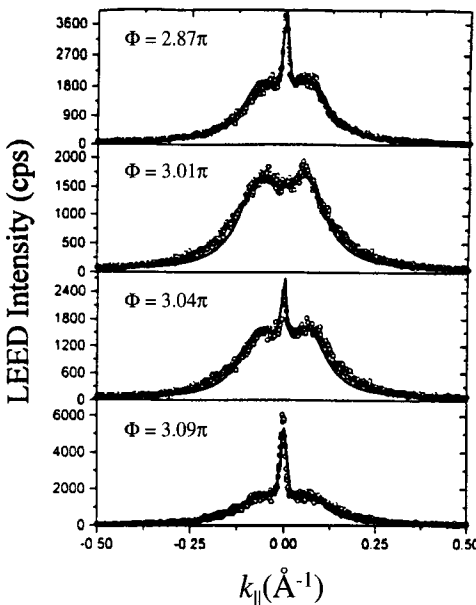


FIG. 13.8 The phase  $\Phi$  dependent angular profiles of the (00) diffraction beam for Fe/Au(001) deposition at 0.5 ML coverage. One can clearly see the shoulders or the splitting in the diffuse profiles. The solid curves are the fits from Equation (13.23) using a gamma distribution as the terrace width distribution. We use  $1.76 \text{ \AA}$  as the vertical spacing in the conversion of  $k_{\perp}$  to the phase  $\Phi$  (from Ref. [13.21]).

decreases as the temperature increases. From the Arrhenius behavior of the ring position, they can estimate the terrace diffusion barrier for Ag on Ag(100).

For the two-dimensional nucleation on surfaces, an important issue is the relationship between the island size distribution and average island separation, and the position of the diffraction ring. The relationship is not simple. Usually if the island size distribution has a maximum at a non-zero island size, we say that the surface has an island size selection. However, even if a surface has an island size selection, it does not guarantee that the surface will give a diffraction ring. An example is that of the same-sized islands randomly distributed on the surface. Also, a common interpretation of the ring position is that it is inversely proportional to the average island separation, i.e.,  $\lambda = 2\pi/k_0$ . However, in the Ag on Ag(100) experiments, Bardotti et al. found that  $\lambda = 2\pi/Ak_0$  with  $A \approx 1.6$  for 0.3 ML deposition, i.e., the value  $2\pi/k_0$  overestimates the average island separation [13.22]. So far, a full relationship between the diffraction and island size distribution or average island separation in two dimensions has not been established

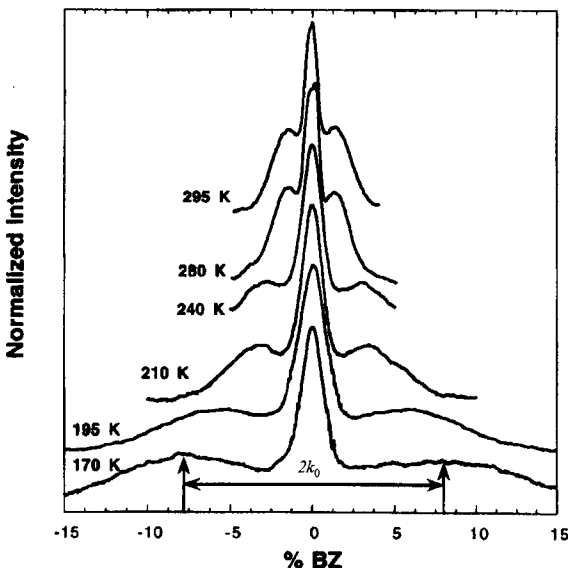


FIG. 13.9 Temperature dependence of the splitting of the (00) beam diffraction profiles for 0.3 ML of Ag on Ag(100). Shown are normalized intensities in a log scale, where normalization is relative to their maximum values (from Ref. [13.22]).

yet.

### 13.3 Continuous Two-Level Surfaces

Two-level structures can also be found in continuous surfaces. In this case, with some modifications, the diffraction formula for the discrete case can be applied to the continuous surface. In the following, we shall use the results of AFM and light scattering experiments as examples to illustrate the properties of a continuous two-level surface [13.23].

The commercial *p*-type Si(100) substrates were degreased with organic solutions in an ultrasonic bath, followed by a rinse in deionized (DI) water. About 750 nm of Al was deposited using the electron beam evaporation technique. Under an open-circuit etching condition, the sample was immersed into a 0.04-M FeCl<sub>3</sub> solution at room temperature for 200 to 480 min. Then the sample was taken out from the solution and was rinsed thoroughly in DI water. After drying, the sample was characterized by atomic force microscopy (AFM) and light scattering ex situ. All the samples we characterized gave similar results.

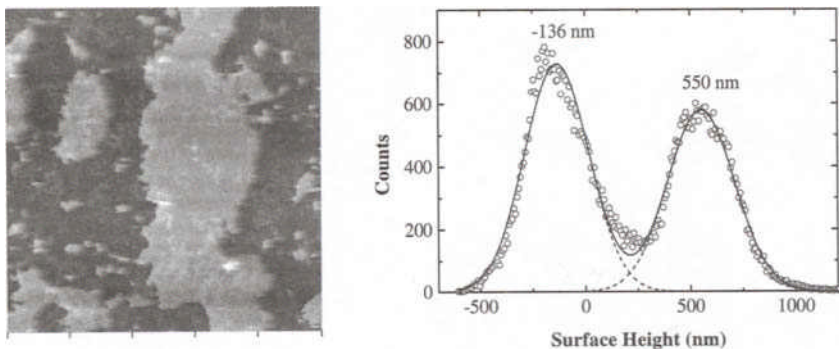


FIG. 13.10 Left: An AFM image obtained from a 250-min corroded Al film. Right: The surface height distribution of Al film on Si. Note that there are two peaks in the surface height distribution with a separation of about 690 nm. The solid curves in the height distribution are best Gaussian fits. The area under the upper level height distribution is 45% of the total area of the height distribution (from Ref. [13.23]).

### 13.3.1 Experimental results

Figure 13.10 shows one sample image and the surface height distribution obtained from AFM. Clearly the surface consists of islands, and the height distribution [Figure 13.10(b)] has two peaks. The separation between these two peaks is  $690 \pm 50$  nm, giving the height of the islands. The area of the upper level distribution is 45% of the total area of the height distribution, indicating that the fraction of the upper level area is about 0.45. The average fraction of the upper level for five AFM images is  $0.38 \pm 0.07$ . These facts lead us to believe that the pitting morphology can be described by a quasi-two-level system. (For an exact two-level surface, one would have two  $\delta$ -function peaks in the height distribution.)

In the light scattering experiments, the incident laser beam was circularly polarized. Figure 13.11 shows six representative light scattering profiles collected at various incident angles:  $12^\circ$ ,  $28^\circ$ ,  $42^\circ$ ,  $48^\circ$ ,  $54^\circ$ , and  $62^\circ$  with respect to the surface normal of a Al film after 250 min of corrosion. Two features can be immediately seen: 1) Each profile has a sharp  $\delta$ -function-like peak sitting on a diffuse broad profile, and the shapes of all the broad profiles are quite similar, 2) The peak intensity oscillates with the incident angle  $\theta$ . In Figure 13.12 we plot the peak intensity as a function of  $k_\perp$ , the momentum transfer perpendicular to the surface.

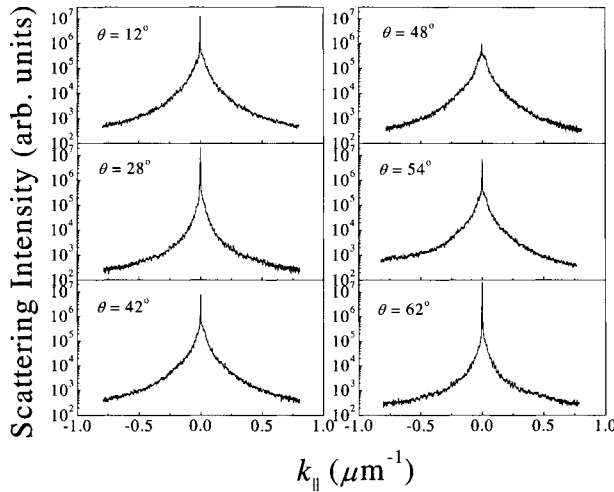


FIG. 13.11 Light scattering profiles obtained from a 250-min corroded Al film at different incident angles:  $12^\circ$ ,  $28^\circ$ ,  $42^\circ$ ,  $48^\circ$ ,  $54^\circ$ , and  $62^\circ$ . These angles correspond to  $k_\perp = 19.4$ ,  $17.5$ ,  $14.8$ ,  $13.3$ ,  $11.7$ , and  $9.3 \text{ } \mu\text{m}^{-1}$ . All the curves are shifted in order to avoid any overlapping. Note that every profile has a sharp  $\delta$ -function-like peak sitting on a diffuse broad profile, and the shapes of all of the broad profiles are quite similar. The peak intensity changes and oscillates while the incident angle  $\theta$  varies (from Ref. [13.23]).

### 13.3.2 Profile analysis

For a quasi-two-level surface, according to Equation (13.2),

$$C(k_\perp, \mathbf{r}) = [1 - 4\Theta \sin^2(\frac{k_\perp d}{2})] + 4\Theta \sin(\frac{k_\perp d}{2}) P_{11}(\mathbf{r}), \quad (13.28)$$

where  $\Theta$  is the fraction of the upper level area,  $d$  is the distance between the upper level and the lower level, or the average pit depth, and  $P_{11}(\mathbf{r})$  is the probability of an upper level at position  $\mathbf{r}$  given an upper level at position 0. In general,  $P_{11}(0) = 1$  and  $P_{11}(|\mathbf{r}| \rightarrow \infty) = \Theta$ . For an isotropic surface we assume  $P_{11}(\mathbf{r})$  has the following form:

$$P_{11}(\mathbf{r}) = \Theta + (1 - \Theta) \exp[-(\frac{r}{\xi})^{D_s}], \quad (13.29)$$

where  $\xi$  is the lateral correlation length and  $D_s$  is the surface fractal dimension [13.24]. The diffraction profile can be written as

$$\begin{aligned} S(\mathbf{k}_\parallel, k_\perp) &\propto 4\pi^2 [1 - 4\Theta(1 - \Theta) \sin^2(\frac{k_\perp d}{2})] \delta(\mathbf{k}_\parallel) \\ &+ 8\pi\Theta(1 - \Theta) \sin^2(\frac{k_\perp d}{2}) G(k_\parallel), \end{aligned} \quad (13.30)$$

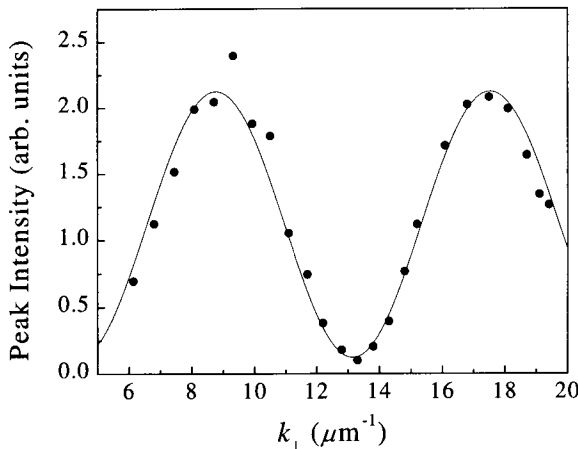


FIG. 13.12 The peak intensity plotted as a function of the momentum transfer perpendicular to the surface,  $k_{\perp}$ . The filled circles are the experimental data obtained from 250-min corroded Al film, and the solid curve is the best fit by using the function  $a \cos(k_{\perp}d) + c$  [equivalent to Equation (13.31) in the text]. The fit gives  $d = 717 \pm 3$  nm,  $a = 1.00 \pm 0.04$ ,  $c = 1.12 \pm 0.03$ . The upper level fraction  $\Theta$  is deduced to be 0.38 (from Ref. [13.23]).

where  $G(k_{||}) = \int_0^{\infty} \exp[-(\frac{r}{\xi})^{D_s}] r J_0(k_{||}r) dr$ . Therefore, the diffraction profile from a quasi-two-level surface consists of two parts: a  $\delta$  peak and a broad diffuse peak. The  $\delta$ -peak intensity oscillates as a function of  $k_{\perp}$ , the period given by the average pit depth. The diffuse profiles at any  $k_{\perp}$  condition should have the same shape. These predictions describe our experimental observations quite well as shown in Figures 13.11 and 13.12. The period of the oscillation gives the depth of the pits, which is obtained from Figure 13.12 to be  $d \approx 717 \pm 3$  nm. This is compared to the result  $d \approx 690 \pm 50$  nm obtained by the AFM technique. We must bear in mind that the sampling area in the light scattering experiment is much larger than that of the AFM.

The fraction of the pit area, i.e., the fraction of the lower level area,  $1 - \Theta$ , can be determined by two methods. First, it can be obtained through the relative  $\delta$ -peak intensity ratio,

$$R_{\delta} = 1 - 4\Theta(1 - \Theta) \sin^2\left(\frac{k_{\perp}d}{2}\right), \quad (13.31)$$

as  $d$  has already been obtained through the period of the peak intensity oscillation. The fractional pit area can also be obtained by the peak intensity oscillation. According to Equation (13.31), the ratio of the minimum peak intensity and maximum peak intensity can be written as  $(1 - \Theta)^2$ .

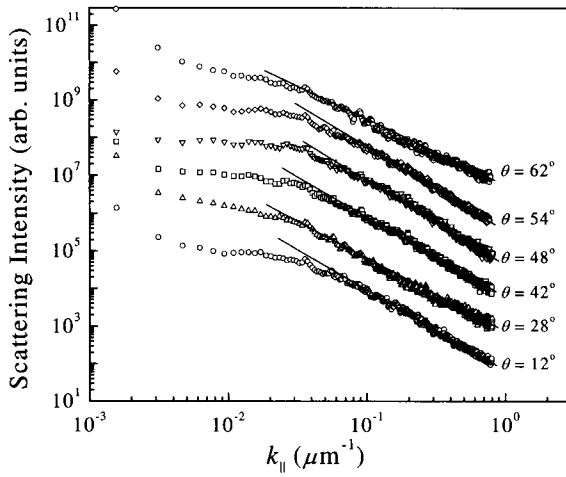


FIG. 13.13 The log-log plot of the tail part of scattering profiles at different incident angles. Note that the straight-line fits of the tails are quite parallel, giving a slope of  $-2.10 \pm 0.06$  (from Ref. [13.23]).

Therefore, according to the fit in Figure 13.12 by using Equation (13.31), we obtained  $\Theta = 0.38$ , which is consistent with the value ( $= 0.38 \pm 0.07$ ) determined by AFM.

Furthermore, according to Reference [13.25], the inverse of the FWHM of the diffuse profile is proportional to the lateral correlation length  $\xi$ , and the tail of the profile obeys a power law of  $k_{\parallel}$ ,  $S(k_{\parallel}) \propto k_{\parallel}^{-2-D_s}$ . [For our experiments, because of the use of an array of slit detectors, this relation becomes  $S(k_{\parallel}) \propto k_{\parallel}^{-1-D_s}$ .] From Figure 13.11, we obtain  $\xi = 21 \pm 3$   $\mu\text{m}$ . Figure 13.13 shows the log-log plot of the scattered angular profiles at different incident angles. From the tails of these profiles, we obtain  $D_s = 1.10 \pm 0.06$ . Therefore, the surface is slightly fractal. (For a non-fractal structure,  $D_s$  should be 1.)

### 13.4 Determination of Roughness Parameters

From the above discussion, there are four important parameters related to two-level surfaces: the coverage  $\Theta$ ; the lateral correlation length  $\xi$  for random clustering surface; the fractal dimension  $D$  for both random clustering and 2-D nucleation; and the characteristic wavevector  $k_0$  for 2-D nucleation. All of these parameters can be obtained from the diffraction profiles (here we neglect the effect of the nearest reciprocal lattice position).

(1) The coverage  $\Theta$ : The coverage can be obtained from the oscillation

of either the  $\delta$ -peak intensity or the diffuse peak intensity. For the  $\delta$ -peak intensity, at exactly the in-phase condition, it reaches a maximum of  $(2\pi)^2$ ; at exactly out-of-phase condition, it decreases to a minimum of  $(2\pi)^2(1 - 2\Theta)^2$ . Therefore, the ratio of the minimum  $\delta$ -peak intensity to the maximum  $\delta$ -peak intensity is  $\gamma = (1 - 2\Theta)^2$ . From this ratio, one can determine  $\Theta$ .

(2) The lateral correlation length  $\xi$  for random clustering surface: Since the diffuse profile is the Fourier transform of the correlation function, the shape of the diffuse profile does not change along the reciprocal rod. The lateral correlation length is inversely proportional to the FWHM of a diffuse profile.

(3) The fractal dimension  $D$  for both random clustering and 2-D nucleation: This parameter can be obtained from the tail of the diffuse profile as  $S(k_{\parallel}) \propto k_{\parallel}^{-D}$ .

(4) The characteristic wave vector  $k_0$  for 2-D nucleation: This is the position of the Henzler ring, and  $2\pi/k_0$  gives the average separation of the cluster.

### 13.5 Summary

In this chapter, we considered the real-space and reciprocal-space characteristics of two-level surfaces. For a two-level surface, the  $\delta$  peak oscillates with the change of  $k_{\perp}$ , as does the diffuse peak intensity. However, the shape of the diffuse diffraction profile remains the same with changing  $k_{\perp}$ . From the simple theory, one can easily determine the coverage  $\Theta$ , the step height  $c$  (for a discrete surface) or  $d$  (for a continuous surface), the lateral correlation length  $\xi$ , and the fractal dimension of the surface.

### References

- 13.1 H. Brune, C. Romainczyk, H. Röder, and K. Kern, "Fractal and dendritic growth patterns in two dimensions," *Nature* **369**, 469 (1994).
- 13.2 M. C. Bartelt, C. R. Stoldt, C. J. Jenks, P. A. Thiel, and J. W. Evans, "Adatom capture by arrays of two-dimensional Ag islands on Ag(100)," *Phys. Rev. B* **59**, 3125 (1999).
- 13.3 J. M. Pimbley and T.-M. Lu, "A two-dimensional random growth model in layer-by-layer epitaxy," *Surface Sci.* **139**, 360 (1984).
- 13.4 H.-N. Yang and T.-M. Lu, "Enhancement of thermal diffuse scattering by surface defects," *Phys. Rev. B* **44**, 11457 (1991).
- 13.5 H.-N. Yang, K. Fang, G.-C. Wang, and T.-M. Lu, "Vacancy-induced disordering in the Pb(100) surface," *Phys. Rev. B* **44**, 1306 (1991).

- 13.6 J. M. Pimbley and T.-M. Lu, "Exact one-dimensional pair correlation functions of a monolayer/substrate system," *J. Appl. Phys.* **57**, 1121 (1985).
- 13.7 T.-M. Lu, G.-C. Wang, and Y.-P. Zhao, "Beyond intensity oscillations," *Surf. Rev. Lett.* **5**, 899 (1998).
- 13.8 H.-N. Yang, G.-C. Wang, and T.-M. Lu, "Quantitative study of the decay of intensity oscillations in transient layer-by-layer growth," *Phys. Rev. B* **51**, 17932 (1995).
- 13.9 C. S. Lent and P. I. Cohen, "Diffraction from stepped surfaces. I. Reversible surfaces," *Surface Sci.* **139**, 121 (1984).
- 13.10 J. M. Pimbley and T.-M. Lu, "Exact one-dimensional pair correlation functions of a monolayer/substrate system," *J. Appl. Phys.* **57**, 1121 (1985).
- 13.11 K. D. Gronwald and M. Henzler, "Epitaxy of Si(111) as studied with a new high resolving LEED system," *Surface Sci.* **117**, 180 (1982).
- 13.12 C. S. Lent and P. I. Cohen, "Quantitative analysis of streaks in reflection high-energy electron diffraction: GaAs and AlAs deposited on GaAs(001)," *Phys. Rev. B* **33**, 8329 (1986).
- 13.13 Q. Jiang and G.-C. Wang, "Scaling of island size distribution and island coalescence in monolayer epitaxial growth of 1×1 films," *Surface Sci.* **324**, 357 (1995).
- 13.14 P. Hahn, J. Clabes, and M. Henzler, "LEED-investigations and work-function measurements of the first stages of epitaxy of tungsten on tungsten (110)," *J. Appl. Phys.* **51**, 2079 (1980).
- 13.15 J.-K. Zuo, J.-F. Wendelken, H. Dürr, and C.-L. Liu, "Growth and coalescence in sub-monolayer homoepitaxy on Cu(100) studied with high-resolution low-energy electron diffraction," *Phys. Rev. Lett.* **72**, 3064 (1994).
- 13.16 G. L. Nyberg, M. T. Kief, and W. F. Egelhoff, Jr., "Spot-profile-analyzing LEED study of the epitaxial growth of Fe, Co, and Cu on Cu(100)," *Phys. Rev. B* **48**, 14509 (1993).
- 13.17 J. A. Stroscio, D. T. Pierce, and R. A. Dragoset, "Homoepitaxial growth of iron and a real space view of reflection-high-energy-electron diffraction," *Phys. Rev. Lett.* **70**, 3615 (1993).
- 13.18 J. A. Stroscio and D. T. Pierce, "Scaling of diffusion-mediated island growth in iron-on-iron homoepitaxy," *Phys. Rev. B* **49**, 8522 (1994).
- 13.19 J. G. Amar, F. Family, and P.-M. Lam, "Dynamical scaling of the island-size distribution and percolation in a model of sub-monolayer molecular beam epitaxy," *Phys. Rev. B* **50**, 8781 (1994).
- 13.20 M. Henzler, "Measurement of surface defects by low-energy electron diffraction," *Appl. Phys. A* **34**, 205 (1984).
- 13.21 Q. Jiang, A. Chan, and G.-C. Wang, "Dynamic scaling of island-size distribution in submonolayer growth of 1×1 films," *Phys. Rev. B* **50**, 11116 (1994).
- 13.22 L. Bardotti, C. R. Stoldt, C. J. Jenks, M. C. Bartelt, J. W. Evans, and P. A. Thiel, "High-resolution LEED profile analysis and diffusion barrier estimation for submonolayer homoepitaxy of Ag/Ag(100)," *Phys. Rev. B* **57**, 12544 (1998).
- 13.23 Y.-P. Zhao, C.-F. Cheng, G.-C. Wang, and T.-M. Lu, "Characterization of pitting corrosion in aluminum films by light scattering," *Appl. Phys. Lett.* **73**, 2432 (1998).
- 13.24 T. Vicsek, *Fractal Growth Phenomena*, p. 23 (World Scientific, Singapore, 1989).
- 13.25 H.-N. Yang, G.-C. Wang, and T.-M. Lu, *Diffraction from Rough Surfaces and Dynamic Growth Fronts* (World Scientific, Singapore, 1993).

## 14. TRANSITION TO MULTILAYER STRUCTURES

Real-time *in situ* monitoring of the thin film growth process can tell us the fundamental physical and chemical processes during the film formation. As we discussed in Chapter 6, although real-space imaging techniques can provide direct information about the film growth, the speed and statistics of the measurement are often not adequate for real-time monitoring. On the other hand, diffraction can provide nondestructive, noncontact measurement without interrupting the growth process, and therefore is highly suitable for real-time *in situ* measurement.

In general, the growth mode in homoepitaxy is governed by the competition between the deposition and atomistic processes on the surface [14.1]. During the growth, an atom landing on the surface may either stay on the surface and wander around or evaporate back into the vapor phase. The different atomistic processes encountered by adatoms are illustrated in Figure 14.1. After deposition (a), an adatom can

- (1) diffuse across the surface (b);
- (2) evaporate back into the vapor phase (c);
- (3) meet another diffusing adatom to form a small nucleus (island) (d);

or

- (4) be captured by an existing island or a step edge (e).

Once an adatom has been captured by an island, it may

- (1) break away from the island (f); or

(2) remain bonded to the island but may diffuse along its edge until it finds a favorable site (g).

Atoms can also land on existing islands. Like an adatom on the flat surface, the atom on the island may evaporate (c), diffuse (b), or cause nucleation of another island (d). In addition, it may either hop down from the

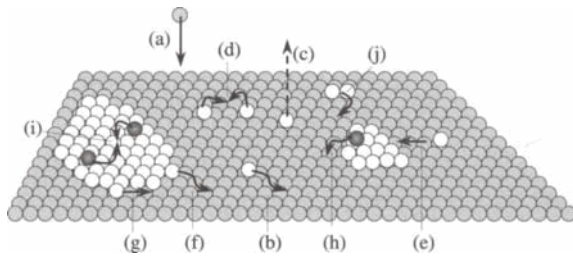


FIG. 14.1 The atomistic processes on a surface (from Ref. [14.2]).

step (h). If hopping is prevented by an additional energy barrier (Schwoebel barrier), nucleation of an island on top of an island becomes more likely (i). It is also possible that islands can migrate on the surface (j). However, depending on certain conditions, such as deposition rate and substrate temperature, only certain atomistic processes dominate the growth kinetics to determine the growth mode.

Different growth modes could exist at a defect-free surface depending on surface temperature [14.3]. At sufficiently high temperatures, the adatoms have sufficient surface mobility, and eventually all the adatoms diffuse to the step edges, leaving the surface morphology intact (step flow growth). For high deposition rates or lower temperatures, the adatoms start to nucleate on the terrace instead of totally sticking at the step edge. However, the adatoms still have large surface mobility, suppressing multilayer growth. Essentially this is the two-dimensional growth process (ideal layer-by-layer growth) discussed in the last chapter. However, at even lower temperatures, there will be some nucleation on top of the islands existing already, and multiple layers start to form, but only on a small area compared to that of the bottom layers (quasi-layer-by-layer growth). Continuing to lower deposition temperatures leads to the buildup of the multilayer structure at the very beginning of the growth, and the roughness of the film continuously increases. In this case, the growth is in the dynamic roughening regime. This chapter discusses the characteristics of these simple growth modes.

### 14.1 Intensity Oscillations

The time-dependent intensity oscillation of diffraction beams has been widely used for about two decades to monitor the rate and quality of epitaxial growth of films in real time. Although the intensity oscillation was first observed with reflection high-energy electron diffraction (RHEED) [14.4, 14.5, 14.6], the quantitative interpretation of data in order to extract the step density at the surface is not trivial and is still an ongoing research subject [14.7, 14.8]. The complication results from the multiple scattering effect. In low-energy electron diffraction (LEED), due to the near-normal-incidence diffraction geometry, it is believed that the relationship between the step density and the intensity can be effectively interpreted using the kinematic diffraction theory [14.6, 14.9, 14.10]. For atom scattering and x-ray diffraction, it is generally believed that multiple scattering is less severe and the interpretation is more straightforward. The intensity oscillation during growth is normally measured by collecting the intensity at a particular position in the reciprocal space. Although this is a convenient way to

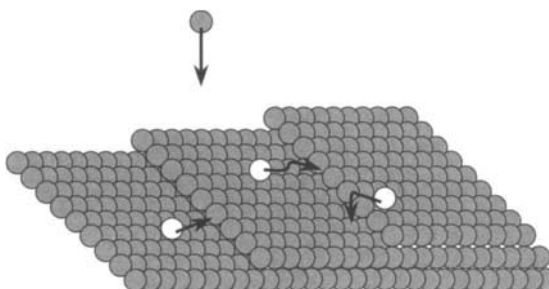


FIG. 14.2 The step flow growth mode: the deposited adatoms have a greater probability to attach to the step edges.

monitor the intensity in real time, the information obtained by this detection mode is limited. In fact, as discussed in Chapters 6 and 7, the angular diffraction profile can give more information about the lateral correlation of the surface.

#### 14.1.1 Step-flow growth

Usually there are steps on the growth substrates. Steps are the boundaries between upper terraces and lower terraces. They might occur randomly or can be created in a controlled manner by cutting the surface in an orientation close to a low-index plane. The ideal growth mode for thin film would be step growth. During the deposition, the smooth substrate morphology would remain almost the same with the growth time. At high temperatures, the growth on a stepped surface is assumed to occur by attachment of deposited atoms to steps that subsequently advance (see Figure 14.2). This growth mode is called step-flow growth and results in a smooth surface. Step-flow growth requires the deposited atoms to have high mobilities so that they diffuse and reach the existing steps before meeting other adatoms. Therefore this situation is close to thermal equilibrium. In this case the general morphology of the surface is not changed, and all the diffraction profiles should stay the same. Figure 14.3 shows the  $\delta$ -peak intensity as a function of surface coverage for both in-phase and out-of-phase conditions. The intensity is a constant.

#### 14.1.2 Layer-by-layer growth

For higher deposition rates or lower temperatures, the growth mode changes from step-flow growth to an ideal layer-by-layer growth. The adatoms still

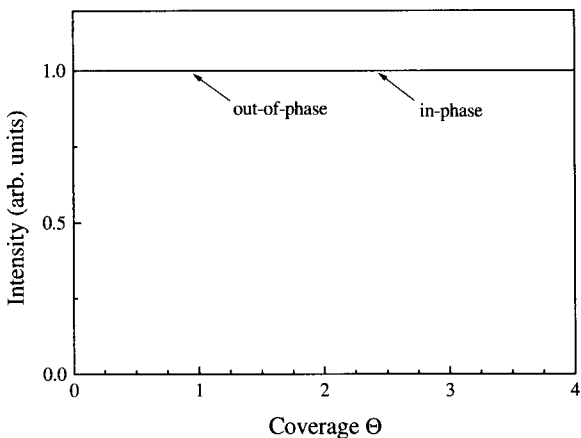


FIG. 14.3 The  $\delta$ -peak intensity as a function of surface coverage for both in-phase and out-of-phase conditions for a step-flow growth mode.

have large surface mobility. Instead of sticking only at the step edges, the adatoms diffuse on the surface until they meet each other to form dimers, which then grow into islands of monatomic height. The edges of the islands capture most of the adatoms during the deposition of one monolayer. Even for the deposited atoms landing on top of the existing island, they have a great probability to diffuse and to hop down to the bottom layer. When the available island edges become fewer due to coalescence, the formation of dimers and islands in the next layer begins. Thus, ideal layer-by-layer growth is essentially a two-dimensional growth process. The growth would complete the first layer first before it starts the second layer as shown in Figure 14.4 [14.11]. The surface roughness (step density) would oscillate with the growth time. Therefore, the fundamentals of time-dependent intensity oscillation of a diffraction beam can be understood from the two-level system considered in the last chapter.

The diffraction intensities are given by Equation (13.7) and oscillate as a function of coverage with a constant amplitude. In Figure 14.5, we plot the magnitude of the peak intensity ( $\delta$  intensity), which is the first term in Equation (13.7), as a function of coverage (or the deposition time) for  $\Phi = \pi$ , the out-of-phase diffraction condition, and  $\Phi = 0$ , the in-phase diffraction condition. Also, in Figure 14.5, we plot the diffuse intensity at a different position of the profile as a function of coverage for  $\Phi = \pi$ . The out-of-phase  $\delta$ -peak intensity and the diffuse intensity oscillate completely out of phase with the coverage: the out-of-phase  $\delta$ -peak intensity reaches a maximum while the diffuse intensity becomes a minimum, or vice versa.

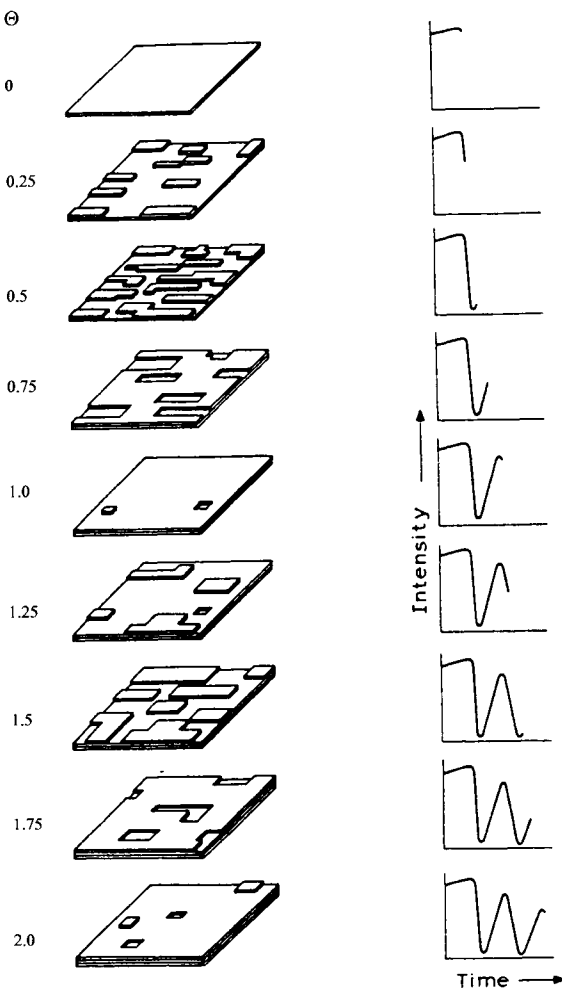


FIG. 14.4 An ideal layer-by-layer growth and diffraction intensity oscillations at the out-of-phase condition (from Ref. [14.11]).

The in-phase  $\delta$ -peak intensity still remains constant.

Since an ideal layer-by-layer growth results in a two-level surface, the shape of the diffuse profile does not change at a fixed time for different diffraction conditions, as discussed in Chapter 13. However, one would expect that the shape of the diffuse profile will change with growth time, since the morphology of the surface (2-D islands) changes in a periodic way with time. In fact, we also expect a periodic change of the FWHM of the diffuse profile as a function of time.

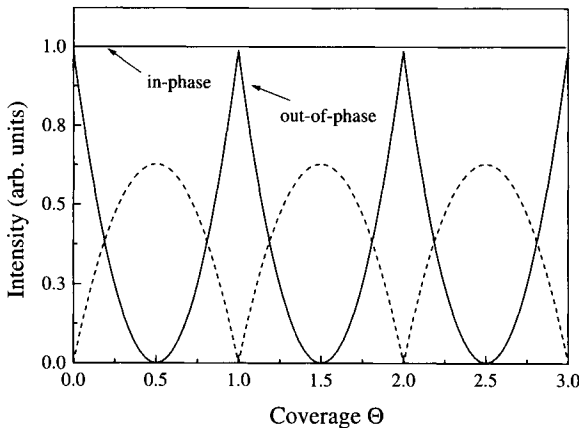


FIG. 14.5 The  $\delta$ -peak intensity as a function of surface coverage for both in-phase and out-of-phase conditions for an ideal layer-by-layer growth mode. Also shown is a diffuse intensity (dashed curve) at  $\Delta k_{||} = 0.2$ .

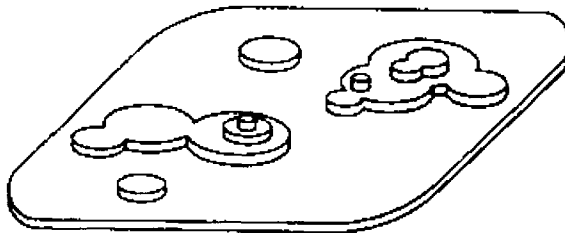


FIG. 14.6 The poly-nuclear growth (PNG) model (from Ref. [14.17]).

#### 14.1.3 Quasi-layer-by-layer growth

At higher deposition rates or lower substrate temperatures, the surface mobility of adatoms is small compared to the deposition rate. There will be some nucleation atop the already-existing islands, and multiple layers start to form, but it occupies only a small portion compared to the bottom layer (quasi-layer-by-layer growth). The interface width oscillates at an initial growth stage, but the oscillation would diminish at long time and a dynamic roughening would occur. In order to understand the growth behavior as well as the diffraction intensity, we consider two models in the following to describe this kind of growth: poly-nuclear growth (PNG) model [14.12, 14.13, 14.14] and the Sine-Gorden growth model [14.15, 14.16].

##### (i) Poly-Nuclear Growth (PNG) model

Let us consider an infinite two-dimensional flat substrate on which a film

grows through nucleation and following lateral growth, as shown in Figure 14.6 [14.14]. The disk-shaped islands nucleate at random positions and grow to form a multilayer surface. The nucleation takes place at a constant rate  $J$  per unit area per unit time, independent of time and the local surface structure. After nucleations, the radii of the islands expand laterally with a speed  $v$ , which is also assumed to be a constant independent of the size of an island. We calculate the fractional coverage in the  $n$ th layer at time  $t = j\Delta\tau$ ,  $\Theta_n(t)$  by first excluding from the total area the area not already covered by the  $(n - 1)$ th layer (to prevent overhang) and then excluding the part of the area already covered by  $(n - 1)$ th layer, which will not be covered in the  $n$ th layer at time  $t$  by the islands nucleated at all times  $\tau = i\Delta\tau$  prior to  $t$ :

$$1 - \Theta_n(t) = 1 - \Theta_{n-1}(t) + \Theta_{n-1}(t) \prod_{i=1}^j [1 - JS(j\Delta\tau, i\Delta\tau)\Theta_{n-1}(i\Delta\tau)\Delta\tau]. \quad (14.1)$$

Here  $S(j\Delta\tau, i\Delta\tau)$  is the probability that a site that is occupied in the  $n$ th layer at time  $t$  was the result of an island born at time  $\tau$ . From Equation (14.1), one can obtain the following recurrence formula [14.14]:

$$\Theta_n(t) = \Theta_{n-1}(t) \{1 - \exp[-\frac{3}{t_0^3} \int_0^t (t - \tau)^2 \Theta_{n-1}(\tau) d\tau]\}, n = 1, 2, \dots \quad (14.2)$$

with the characteristic time  $t_0 = (\frac{3}{\pi J v^2})^{1/3}$ , determined by the nucleation rate  $J$  and the island expansion rate  $v$ .  $\Theta_0(t) = 1$ , and  $\Theta_1(t) = 1 - \exp(-t^3/t_0^3)$ . Figure 14.7 shows the layer coverage  $\Theta_n$  as a function of growth time  $t$ . It takes a duration of almost  $2.5t_0$  to complete a layer totally. The exposure probability  $P_n$  of the  $n$ th layer to the vacuum, or the height distribution, can be written as  $P_n = \Theta_n - \Theta_{n+1}$ . Figure 14.8 shows the probability  $P_n$  of the exposed layer as a function of the growth time  $t/t_0$ . Both Figures 14.7 and 14.8 clearly demonstrate that a steady growth state is attained soon after the initiation of the growth (above two monolayers). Furthermore, one can calculate the average thickness  $\langle h \rangle$ , the interface width  $w$ , and the out-of-phase (anti-Bragg)  $\delta$ -peak intensity  $I_\delta$  as a function of growth time  $t/t_0$ , as shown in Figure 14.9 [14.17]. After a short transition time, the average thickness  $\langle h \rangle$  of the film increases linearly with growth time. For the interface width  $w$ , it increases dramatically during the initial transition time  $< 1$  ML, but oscillates about 0.55 with time after the transition. The out-of-phase intensity drops very quickly at the initial transition and oscillates with the growth time. From the projection in Figure 14.9 we can see that the maximum intensity always occurs

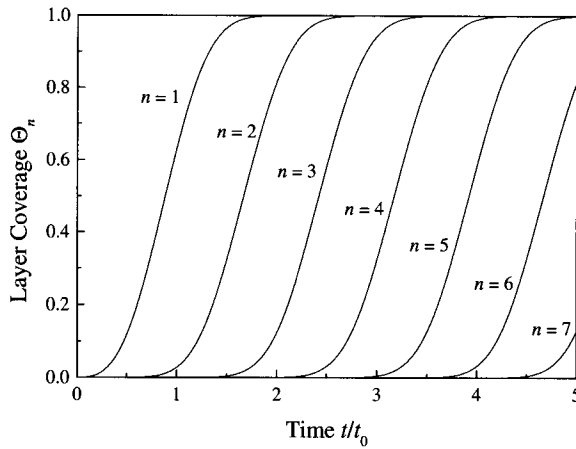


FIG. 14.7 The layer coverage  $\Theta_n$  as a function of growth time  $t/t_0$  for a one-dimensional PNG model.

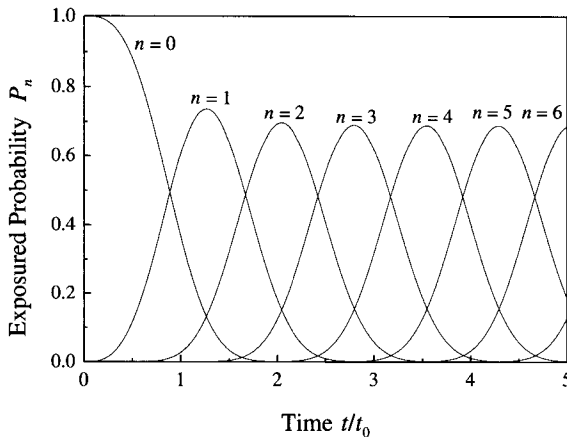


FIG. 14.8 The probability  $P_n$  of the exposed layer as a function of the growth time  $t/t_0$  for a one-dimensional PNG model.

when  $\langle h \rangle$  becomes an integer, i.e., the surface is completely covered by atoms. This is similar to the ideal layer-by-layer behavior discussed in the last section.

### (ii) Sine-Gorden equation

From Figure 14.8 we can see that in the PNG model each layer can only be exposed for about  $3t_0$ , which means that the maximum number of exposed layers is about 4. After a short transition, the PNG model eventually becomes stable, and the intensity oscillation does not diminish as

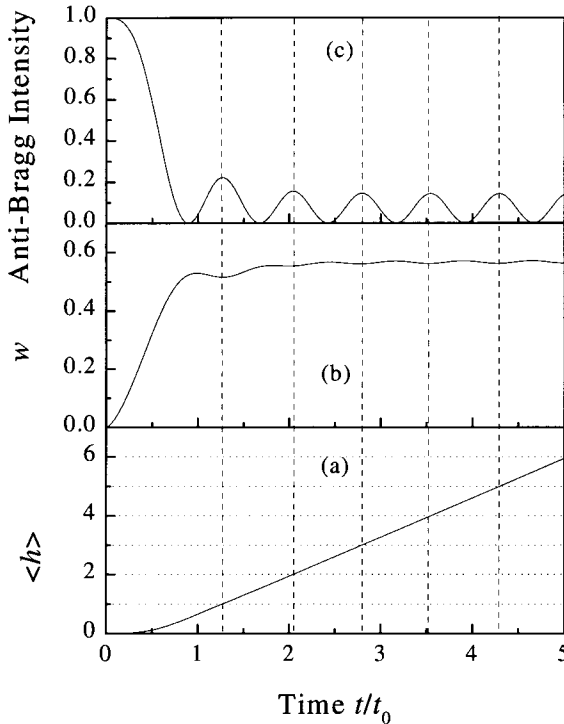


FIG. 14.9 The average thickness  $\langle h \rangle$ , the interface width  $w$ , and the out-of-phase (anti-Bragg)  $\delta$ -peak intensity  $I_\delta$  as a function of growth time  $t/t_0$  for a one-dimensional PNG model.

one expected. A more realistic growth model should be used to describe the frequently-observed damped-intensity oscillation. Recently, based on the pre-roughening phenomenon, a phenomenological Langevin equation that incorporates the processes of evaporation/condensation, surface diffusion, and 2D nucleation has been proposed as [14.15, 14.16]

$$\frac{\partial h}{\partial t} = R + v\nabla^2 h - \kappa\nabla^4 h - V \sin\left(\frac{2\pi h}{c}\right) + \eta. \quad (14.3)$$

This is the well-known stochastic Sine-Gordon equation. Here  $R$  is the growth rate and  $v\nabla^2 h$  and  $\kappa\nabla^4 h$  are the smoothening terms due to evaporation/condensation and surface diffusion, respectively. The term  $-V \sin\left(\frac{2\pi h}{c}\right)$  is the pinning force for a crystalline surface, which energetically favors integer values of surface height  $h$ , in units of lattice spacing. The amplitude of the pinning force is  $V$ . The intrinsic noise during film growth,  $\eta$ , satisfies Equation (A.8).

The physics implied in Equation (14.3) can be understood from the

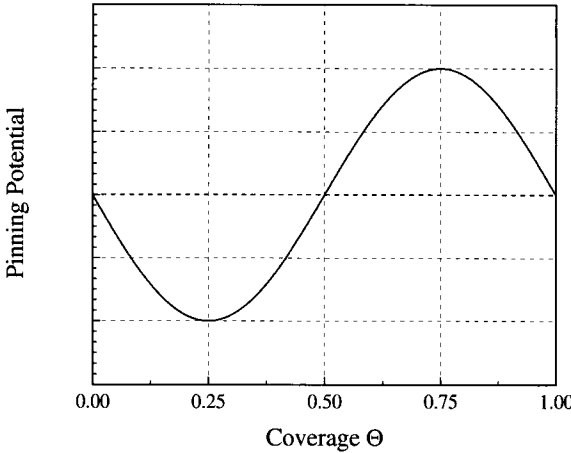


FIG. 14.10 The pinning potential as a function of coverage  $\Theta$  (from Ref. [14.16]).

following quantitative analysis [14.16]. After taking a statistical average of each term in Equation (14.3),  $\langle \nabla^2 h \rangle = 0$ , and  $\langle \kappa \nabla^4 h \rangle = 0$ , one obtains the average growth rate, satisfying

$$\frac{\partial}{\partial t} \langle h \rangle = R - V \sin\left(\frac{2\pi h}{c}\right). \quad (14.4)$$

One may notice that the term  $\frac{\partial}{\partial t} \langle h \rangle$ , representing the actual growth rate, is not equal to the impinging rate of deposition,  $R$ , because of the contribution from the pinning force,  $V_{pinning} = -V \sin\left(\frac{2\pi h}{c}\right)$ . The contribution from  $V_{pinning}$  may originate from the evaporation and condensation processes. In a quasi-layer-by-layer growth, a majority of atoms and islands are in the top few layers of the surface. The average surface height can be approximated as  $\langle h \rangle = (m + \Theta)c$ , where  $m$  is the integer part of the film thickness and  $\Theta$  is the coverage of the deposited atoms in the top few layers. In the first-order approximation, one can replace  $h$  in the pinning force by  $\langle h \rangle$ , then  $V_{pinning} \approx -V \sin\left(\frac{2\pi \langle h \rangle}{c}\right) = -V \sin(2\pi\Theta)$ . Figure 14.10 plots the pinning force as a function of coverage  $\Theta$ . The quantity  $V_{pinning}$  is negative between  $\Theta = 0$  ML and  $\Theta = 0.5$  ML and then becomes positive from  $\Theta = 0.5$  ML to  $\Theta = 1.0$  ML. A negative  $V_{pinning}$  indicates the occurrence of desorption (or evaporation) events, while a positive  $V_{pinning}$  implies the condensation.

The behavior of the pinning force mimics qualitatively the reality of the 2-D nucleation-dominated growth process. At  $\Theta \leq 0.5$ , since few atoms exist in the top layer, the probability that 2-D islands overcome the potential barrier to reach a critical island size is small. Therefore, a number

of deposited atoms, which are not stable in the crystal surface, will evaporate into the vapor phase. Thus  $V_{pinning}$  makes an increasingly negative contribution to the growth rate, as shown in Figure 14.10 between  $\Theta = 0$  ML and  $\Theta = 0.25$  ML. With increased coverage, the probability for 2-D nuclei to reach a critical island size increases. As a result, the negative pinning potential starts to decrease, as shown between  $\Theta = 0.25$  ML and  $\Theta = 0.5$  ML in Figure 14.10. When the coverage increases further, the top layer contains so many islands that the growth (i.e., an island catches a monomer) is much easier. The quantity  $V_{pinning}$  becomes increasingly positive and the condensation processes dominate for  $0.5 \leq \Theta \leq 0.75$ . Beyond  $\Theta = 0.75$  ML, since the step density on the surface decreases, the positive pinning force starts to decrease until  $\Theta = 1$  ML.

Therefore Equation (14.3) captures the essential physics in the growth processes, which involves evaporation/condensation and 2-D nucleation. However, solving Equation (14.3) is not trivial. A perturbative solution is given in Appendix F, and the power spectrum due to the evolution of surface roughness can be expressed as

$$\begin{aligned} <\Delta h(\mathbf{k}, t)^2> &= D \frac{1 - e^{-2(\kappa k^4 + \nu k^2)t}}{\kappa k^4 + \nu k^2} \\ &+ \frac{DV_0 c}{\pi R (\kappa k^4 + \nu k^2)} \sin\left(\frac{2\pi R t}{c}\right) e^{-2(\kappa k^4 + \nu k^2)t} \\ &- \frac{4DV_0 [\cos\left(\frac{2\pi R t}{c}\right) - e^{-2(\kappa k^4 + \nu k^2)t}]}{(2\pi R/c)^2 + 4(\kappa k^4 + \nu k^2)^2} \\ &- \frac{4DV_0 \pi R \sin\left(\frac{2\pi R t}{c}\right)}{c(\kappa k^4 + \nu k^2)[(2\pi R/c)^2 + 4(\kappa k^4 + \nu k^2)^2]}. \end{aligned} \quad (14.5)$$

Now let us consider the diffraction behavior from films grown by such a process. We would expect that the surface height distribution is non-Gaussian during these growth stages. Usually a general treatment of the diffraction profile is not available. However, as discussed in Chapter 7, the  $\delta$ -peak intensity can be generally expressed as

$$I_\delta = \left| \int e^{i\mathbf{k}_\perp \cdot \mathbf{h}} p(h) \right|^2. \quad (14.6)$$

For a discrete surface,

$$I_\delta = \left| \sum_d e^{i\Phi_d} p(d) \right|^2, \quad (14.7)$$

i.e., the  $\delta$ -peak intensity is proportional to the mode square of the characteristic function  $\varphi$  of the height distribution. As discussed in Chapter 7,

unless we know all the higher moments of the height distribution, we cannot completely characterize the peak intensity. However, there are two exceptions. One is at  $\Phi = 2n\pi$ , the in-phase condition, where  $I_\delta = 1$ , regardless the surface height distribution. The other one is at  $\Phi = (2n + 1)\pi$ , the out-of-phase condition (or anti-Bragg condition). Under the out-of-phase condition, the summation in Equation (14.7) can be written as

$$\varphi[(2n + 1)\pi] = \varphi(\pi) = \sum_{d=0}^{\infty} e^{i\Phi d} p(d) = \sum_{d=0}^{\infty} \cos(d\pi) p(d), \quad (14.8)$$

i.e., under the out-of-phase condition, the summation in  $\varphi(\pi)$  is real. On the other hand, since  $\sum_{d=0}^{\infty} e^{i\Phi d} p(d)$  is the characteristic function of a height distribution, it can always be expanded as [14.18]

$$\sum_{d=0}^{\infty} e^{i\Phi d} p(d) = \exp\left[\sum_{v=1}^{\infty} \frac{x_v}{v!} (i\Phi)^v\right], \quad (14.9)$$

with the coefficients  $x_v$  being called cumulants or semi-invariants, which have a close relationship with the moments:

$$\begin{aligned} x_1 &= \langle d \rangle, \\ x_2 &= w^2, \\ x_3 &= m_3, \\ x_4 &= m_4 - 3w^4, \\ x_5 &= m_5 - 10w^2m_3, \\ &\dots \end{aligned}$$

Therefore Equation (14.8) becomes

$$\varphi(\pi) = \exp\left(-\frac{\pi^2 w^2}{2} + \frac{\gamma_4 \pi^4 w^4}{24} - \dots\right) \exp\left(i\pi \langle d \rangle - i\frac{\gamma_3 \pi^3 w^3}{6} + \dots\right). \quad (14.10)$$

According to Equation (14.8), if  $\varphi(\pi)$  is real, then the imaginary part of Equation (14.10) should be zero. Thus,

$$\varphi(\pi) = \cos\left(\pi \langle d \rangle - \frac{\gamma_3 \pi^3 w^3}{6} + \dots\right) e^{-\frac{\pi^2 w^2}{2} + \frac{\gamma_4 \pi^4 w^4}{24} - \dots}. \quad (14.11)$$

The  $\delta$ -peak intensity at the out-of-phase condition becomes

$$I_\delta = \cos^2\left(\pi \langle d \rangle - \frac{\gamma_3 \pi^3 w^3}{6} + \dots\right) e^{-\pi^2 w^2 + \frac{\gamma_4 \pi^4 w^4}{12} - \dots}. \quad (14.12)$$

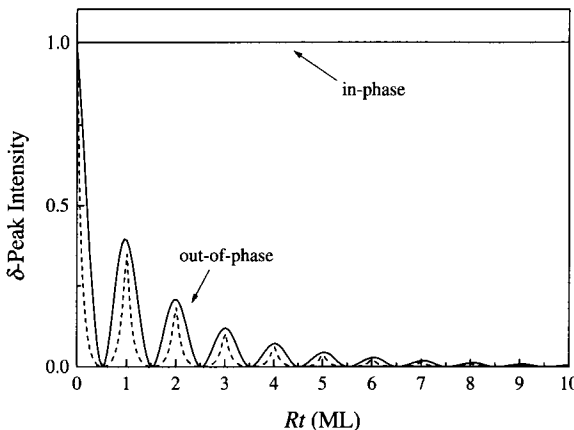


FIG. 14.11 The  $\delta$ -peak intensity as a function of surface coverage for both in-phase and out-of-phase conditions for a quasi-layer-by-layer growth mode.

This equation is a general expression obtained by Evans et al. [14.19, 14.20]. For small  $w$ , Equation (14.12) reduces to

$$I_\delta \approx \frac{1}{2}[1 + \cos(2\pi < d >)]e^{-\pi^2 w^2}, \quad (14.13)$$

which has been obtained by Yang et al. [14.16]. Substituting our solutions Equations (F.8) and (F.9) into Equation (14.13), we obtain the damped  $\delta$ -peak intensity oscillation as shown in Figure 14.11. The dashed curve is the intensity oscillation after the discrete lattice effect correction. For a comparison, we also plotted the in-phase  $\delta$ -peak intensity as a function of growth time which is a constant.

Obviously, the decay of the amplitude of the intensity oscillation is a result of a deviation from the ideal layer-by-layer growth and the roughening of the growth front where a multilevel step structure is created. The multilevel step structure can have different characteristics depending on the mechanisms of the growth front roughening. The form of the amplitude decay and the evolution of the shape of the angular profile therefore depend on the origin of the roughening. In Figure 14.12 we show the time-dependent, high-resolution low-energy electron diffraction (HRLEED) profiles of the (00) beam intensity measured *in situ* from a MBE growth of Si/Si(111) with a growth rate of 7 bilayers per minute [14.16]. The growth was performed at  $275 \pm 5^\circ\text{C}$  and the data were collected at exactly the out-of-phase diffraction condition. For growth times  $t > 0$ , the diffraction profile always consists of a  $\delta$  peak and a diffuse profile. The diffuse profile can be fitted well by a 2-D Lorentzian function as given in Equation (13.15). Figure

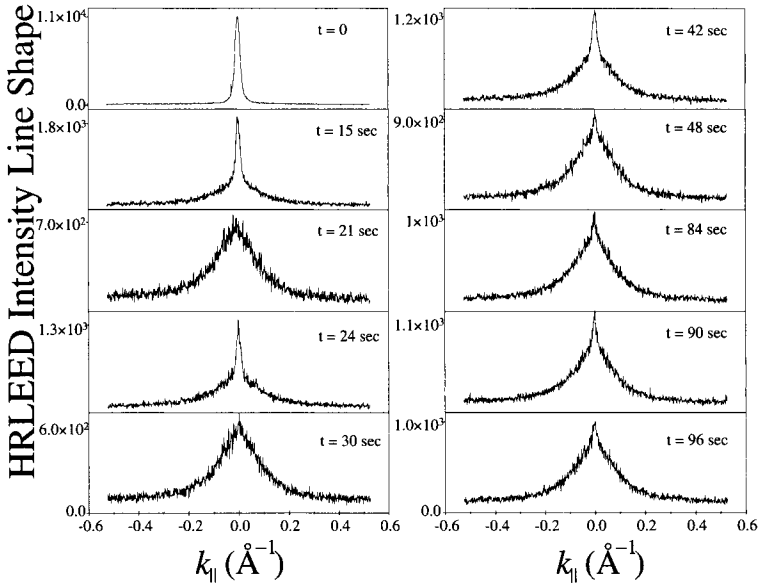


FIG. 14.12 The time-dependent HRLEED profiles of the (00) beam intensity measured from an in situ MBE growth front of Si/Si(111) at  $275 \pm 5^\circ\text{C}$ . The intensity profiles were scanned along the  $\overline{[112]}$  direction, and the data were taken at the electron beam energy  $E = 47$  eV, corresponding to an out-of-phase condition,  $\Phi \approx 7.0\pi$ . At  $t = 0$ , the line shape exhibits a sharp  $\delta$ -like profile that is identical to the HRLEED instrument response. For  $t > 0$ , the diffraction profile can be decomposed into a  $\delta$ -peak and a diffuse profile. The diffuse profile can be fit well by a 2-D Lorentzian function. Notice that the intensity of the profiles oscillates with time (from Ref. [14.16]).

14.13 plots the decomposed Bragg peak intensity as a function of time. Then the decay of the peak intensity can be fitted using  $e^{-A_1\sqrt{t}}$ , which means  $\beta = 1/4$  from Equation (14.13). The dashed curve describes the decay qualitatively.

Here we should emphasize that the intensity oscillation originates primarily from the discrete lattice effect. For a continuous surface, even when the interface width  $w$  oscillates, it would not necessarily cause a strong intensity oscillation. As an example, we consider a continuous film growth process that has an oscillatory interface width behavior as illustrated in Figure F.1(c). From the perturbation solution of the Sine-Gorden equation, the surface height fluctuation approximately obeys a Gaussian distribution. Using the diffraction formula for a Gaussian surface, we obtain the  $\delta$ -peak intensity as a function of growth time as shown in Figure 14.14. The intensity continuously decreases with only a small oscillation.

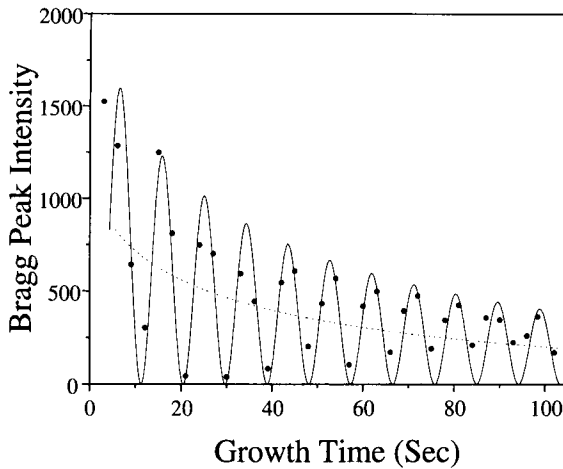


FIG. 14.13 The time-dependent Bragg peak intensity plotted as filled circles, which are extracted from the measured profiles shown in Figure 14.12. The observed damped intensity oscillation is consistent with the form  $I_0[1 + \cos(\omega t)]e^{-A_1 t^{1/2}}$ , which is plotted as the solid curve. The dashed curve represents the plot of the corresponding damping factor,  $e^{-A_1 t^{1/2}}$ . The fit shows that the growth exponent is consistent with  $\beta = 1/4$  (from Ref. [14.16]).

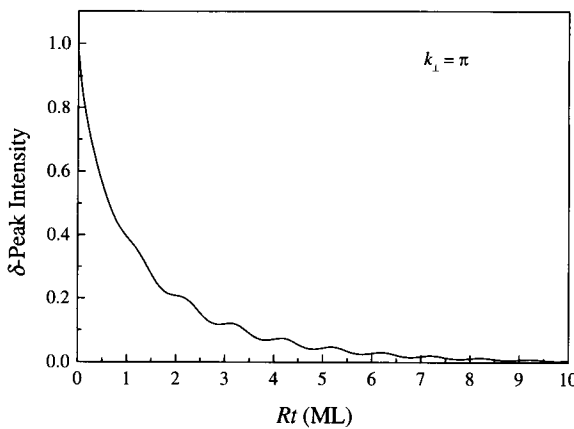


FIG. 14.14 The  $\delta$ -peak intensity as a function of film thickness from the Sine-Gorden equation.

#### 14.1.4 Reentrant layer-by-layer growth

When the growth temperature drops more, one would expect multilayer roughening, as we will discuss in the next section. One would expect that a further decrease of substrate temperature would not change the

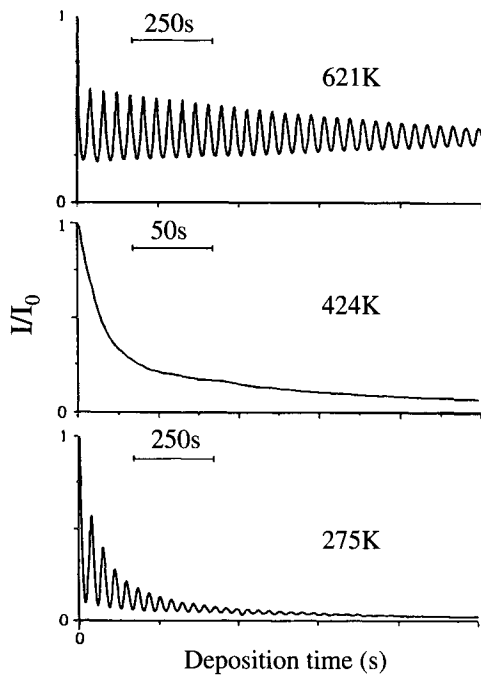


FIG. 14.15 The normalized specular He peak intensity as a function of Pt deposition time at three different temperatures (from Ref. [14.22]).

growth mode at all. However, there are exceptions. Several researchers already demonstrated experimentally that for some homoepitaxy [14.21, 14.22, 14.23] or heteroepitaxy [14.21, 14.24, 14.25] metal-on-metal growth systems, at very low temperature, the quasi-layer-by-layer growth mode will appear again. Figure 14.15 shows the He atom scattering intensity of Pt/Pt(111) as a function of growth time at different temperatures [14.22]: At a very high growth temperature (621 K), the growth is in the quasi-layer-by-layer mode. When the substrate temperature is decreased to 424 K, the growth is in the roughening growth mode, which will be discussed in the next section. However, as the temperature goes down further (275 K), the intensity oscillation appears again. This phenomenon was interpreted by the variation of the diffusion barrier height due to the island size on the surface. The decrease in temperature would reduce the length scale of the growing structure. Therefore, the hopping of adatoms from the upper layer to the lower layer becomes increasingly important and the potential barrier for surface diffusion breaks down for small irregularly-shaped islands. Therefore the possibility of Pt mass transport between different layers would be restored for these islands.

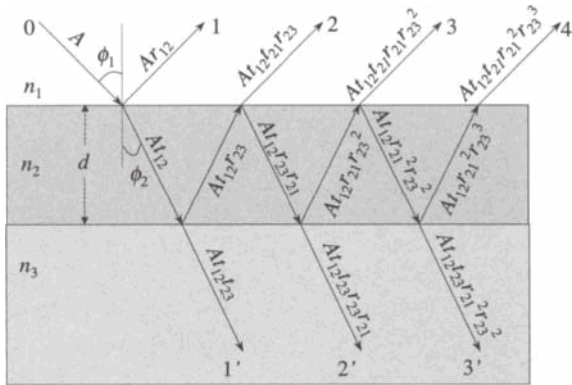


FIG. 14.16 The multiple reflection and transmission between two boundaries of a growing film.

#### 14.1.5 Other intensity oscillations

Another kind of intensity oscillations used for monitoring thin film growth from the reflection of laser beam or x-ray beam is based on the multibeam interference phenomenon between two boundaries of the growing film, as shown in Figure 14.16. When the refraction index  $n_2$  of the film is different from that of the substrate  $n_3$ , and the environment  $n_1$ , there will be multiple reflections and transmissions within the film. The total reflected amplitude is the summation of beams 1, 2, 3, .... There is a phase difference [14.26]

$$\Delta = \frac{4\pi n_2 d \cos \phi_2}{\lambda}, \quad (14.14)$$

between the adjacent reflected beams, and the total reflection from the surface is

$$\begin{aligned} R &= \frac{I_r}{I_0} = |r_{12} + t_{12}t_{21}r_{23} \frac{\cos \Delta - r_{21}r_{23}}{(1 - r_{21}r_{23} \cos \Delta)^2 + (r_{21}r_{23} \sin \Delta)^2}|^2 \\ &\quad + \left[ \frac{t_{12}t_{21}r_{23} \sin \Delta}{(1 - r_{21}r_{23} \cos \Delta)^2 + (r_{21}r_{23} \sin \Delta)^2} \right]^2, \end{aligned} \quad (14.15)$$

where  $r_{ij}$  and  $t_{ij}$  are the reflection and transmission coefficients from a medium  $i$  to a medium  $j$  ( $i, j = 1, 2, 3$ ). Here we assume medium 1 is air,  $n_1 = 1$ ; medium 2 is a dielectric film (for example, Parylene-N with  $n_2 = 2.6$ ); and medium 3 is Si, where  $n_3 \approx 3.9$  for visible light. Also, for simplicity, we assume that the  $s$ -polarized beam has a normal incidence on the sample. Then according to the well-known Snell's law and Fresnel

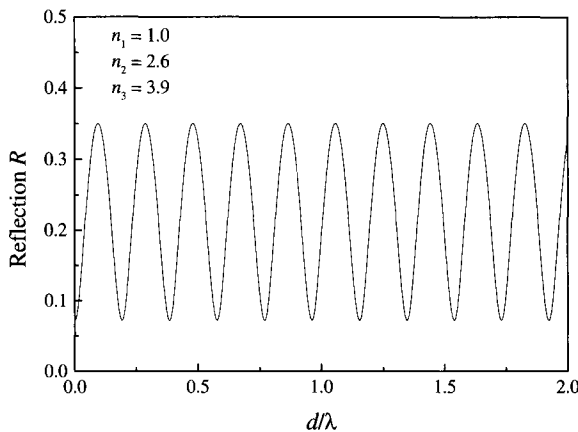


FIG. 14.17 Model calculation of the oscillation of the reflection as a function of the thickness for Parylene-N film grown on a Si substrate.

relation, one has

$$\begin{aligned} r_{12} &= -r_{21} = \frac{n_1 - n_2}{n_1 + n_2}, \\ r_{23} &= \frac{n_2 - n_3}{n_2 + n_3}, \\ t_{12} &= \frac{2n_1}{n_1 + n_2}, \text{ and} \\ t_{21} &= \frac{2n_2}{n_1 + n_2}. \end{aligned}$$

In Figure 14.17 we model the change of the reflection as a function of the thickness for Parylene-N film grown on a Si substrate. Clearly the reflection intensity oscillates with the film thickness.

The reflected intensity can also oscillate with the change of the incident angle, or the incident wavelength. One can use both Equations (14.14) and (14.15) combining with the general expression of Fresnel relationship to obtain those relations.

This kind of intensity oscillation has been widely used for real-time thickness monitoring and end point detection in many thin film processes, such as deposition, etching, annealing, and photoresist processing. For a review, see Reference [14.27]. In the x-ray community, the reflectivity oscillation as a function of incident angle or wavelength has been used to determine film thickness and interface roughness. Recently, several groups performed *in situ* real-time x-ray reflectivity experiments to monitor film thickness [14.28, 14.29, 14.30, 14.31]. For example, Figure 14.18 shows a

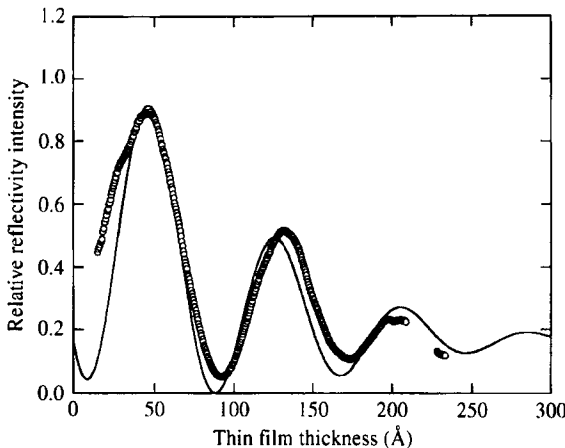


FIG. 14.18 The x-ray reflectivity as a function of Al thickness during the evaporation of Al on Si(100) substrate. The scattered data points are of the experimentally-measured reflectivity, and the solid curve is the theoretical fit assuming the surface roughness is proportional to the film thickness (from Ref. [14.28]).

recent x-ray reflectivity experiment on an Al thin film grown on Si(100) [14.28]. During the deposition, the incident angle and detector position were fixed, and the reflectivity was measured as a function of the growth time. The oscillation is similar to that in Figure 14.17, except for the decay of the reflectivity. This is due to the fact that the roughness of the Al film increases with the deposition time, while the calculation for Figure 14.17 does not take the surface roughness into account. A simple way to correct for this in Equation (14.15) is to multiply by a factor  $e^{-k_1^2 w^2}$ , where  $w$  is a function of growth time.

## 14.2 Diffraction from Dynamic Roughening Fronts

For sufficiently low substrate temperatures, the multiple layers would build up after a short transition of quasi-layer-by-layer growth or even at the very beginning of the growth. The roughness of the film increases continuously with time. In this case, the growth is in the dynamic-roughening regime discussed in Chapter 3 and Appendix A. Many discrete growth models have been proposed to study the transition to the dynamic roughening process [14.20, 14.32, 14.33, 14.34]. To capture the essence of this transition, we recently carried out a two-dimensional Monte Carlo simulation using a simplified model [14.35]: Atoms are deposited onto a one-dimensional surface with a deposition rate  $F$  and diffuse with a diffusion rate  $D$  until

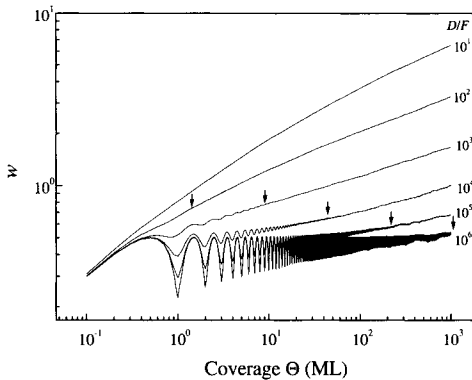


FIG. 14.19 The interface width  $w$  as a function of coverage  $\Theta$  for different values of  $D/F$ . The arrows indicate the coverage  $\Theta_t$ .

they meet other adatoms or an island of adatoms. If the encountered island consists of  $i^*$  or more atoms, the atom is incorporated into this island, and a stable, immobile island is formed. Islands of size  $i^*$  or less are allowed to decay. There are no barriers (Schwoebel barriers) for interlayer transport and no overhangs or holes. Figure 14.19 shows the interface width  $w$  as a function of growth coverage for different  $D/F$  ratios. For a given  $D/F$ , the oscillations in the interface width persist up to a certain coverage  $\Theta_t$ , which increases with  $D/F$ . Beyond  $\Theta_t$ , the crossover to kinetic roughening is observed, where  $w$  approaches a power law  $t^\beta$  with  $\beta \approx 0.2$ . Figure 14.20 shows the number of unfilled layers on the surface. After coverage  $\Theta_t$ , the number of unfilled layers increases dramatically, which exhibits the dynamic roughening process.

In the dynamic roughening regime, a multilayer structure has already been built up. The surface height fluctuation can be characterized approximately by a Poisson distribution. According to Equation (7.49), the  $\delta$ -peak intensity at the out-of-phase condition can be expressed as

$$I_\delta \propto e^{-4w^2(t)}. \quad (14.16)$$

As  $w(t) \propto t^\beta$ , the  $\delta$ -peak intensity at the out-of-phase condition decays monotonically with the growth time. Figure 14.21 shows an example for  $\beta = 1/4$ .

The  $\delta$ -peak intensity at either the in-phase condition or the out-of-phase condition is normally measured by collecting the intensity at a particular position in the reciprocal space during growth. Although this is a convenient way to monitor the intensity in real time, the information obtained by this detection mode is limited. On the other hand, in Chapters 7-12

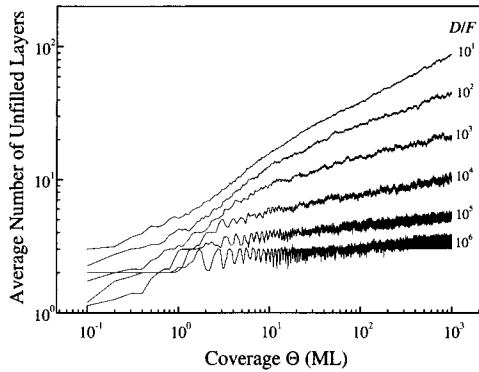


FIG. 14.20 The average number of unfilled layers as a function of coverage  $\Theta$  for different values of  $D/F$ .

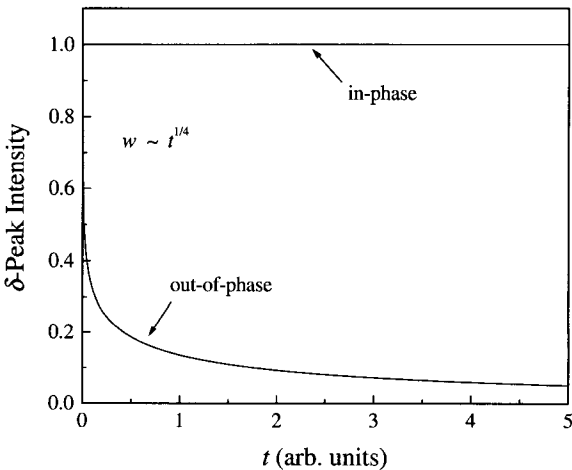


FIG. 14.21 The  $\delta$ -peak intensity as a function of growth time for both the in-phase and out-of-phase conditions for a dynamics multilayer roughening growth.

we have discussed that by measuring and analyzing the entire angular distribution of intensity (angular profile) [14.10, 14.36, 14.37], a much more complete picture of the surface morphology can be obtained. The need to measure the entire angular profile is even more obvious when a multilayer structure in the growth front is built up and the amplitude of the intensity oscillation decays as the growth proceeds. In fact, very often the amplitude may eventually diminish to the point where the intensity oscillation finally comes to an end. When the amplitude of the intensity oscillation decays to zero, one recognizes the growth front as being “rough.” Very little attention

has been paid to the nature of the roughness until recently.

As discussed in Chapters 7-12, by analyzing the entire angular distribution of the diffraction intensity, essentially one can obtain all the roughness parameters describing the morphology of the rough surface. Thus, from the dynamic behavior of the roughness parameters, one can learn the basic physical process during the film growth.

#### 14.2.1 An example of a dynamic scaling surface: Si/Si(111)

In this section we show an experimental example using the HRLEED to monitor the molecular beam epitaxial growth of Si on the Si(111) substrate [14.38]. The roughness parameters are extracted from the energy dependence of the diffraction structure factor measured near the out-of-phase condition. In the experiment, Si was evaporated into a clean  $7 \times 7$  reconstructed Si(111) substrate at  $275 \pm 5^\circ\text{C}$ . The deposition rate was about 7 bilayers/min. Each diffraction intensity profile was taken from the sample where the deposition was performed continuously to the time indicated, and the measurement was done after the sample was quenched to room temperature. Figure 14.22 shows the line shapes of the (00) HRLEED beam intensity at  $E = 47.0$  eV, the out-of-phase diffraction condition,  $\Phi \approx 7.01\pi$ , at different times during growth. For Si(111), the dimension of the Brillouin zone is  $K_{BZ} = 1.89 \text{ \AA}^{-1}$ . As shown in Figure 14.22, the line shape at  $t = 0$  is basically a  $\delta$ -like central peak, which corresponds to the HRLEED resolution. For  $t < 2$  minutes, the intensity oscillates (and decays) as shown in Figures 14.12 and 14.13 where a quasi-layer-by-layer growth is built up. For  $t > 2$  minutes, as the film grows thicker and thicker, the central spike intensity drops to zero, as shown in Figure 14.22. At the same time, the broad diffuse profile becomes stronger and stronger. This is due to the fact that the film becomes rougher and rougher, and the growth front reaches the dynamic scaling regime.

As discussed in Chapter 9, we can quantitatively estimate the interface width  $w(t)$  from the ratio  $R_\delta$  of the integrated  $\delta$ -peak intensity to the total integrated intensity. Essentially,  $-\ln(R_\delta) \propto w^2$ . In Figure 14.23, we plot  $-\ln(R_\delta)$  as a function of growth time  $t$  at  $|k_\perp c - 8\pi| = 0.349\pi$ . The plots at different time  $t$  exhibit linear relations. Therefore, the growth exponent  $\beta$  can then be extracted from the log-log plot of the slope in Figure 14.23 and is found to be  $\beta = 0.25$ . In addition, one can observe in Figure 14.22 that the diffuse profile broadens continuously with the growth time  $t$ . Figure 14.24(a) is the log-scaled plot of the FWHM of the diffuse profile as a function of  $\Phi$  at different growth times, with  $\Phi$  varying from  $7.0$  to  $7.75\pi$ . From Figure 14.24(a) one can extract the roughness exponent

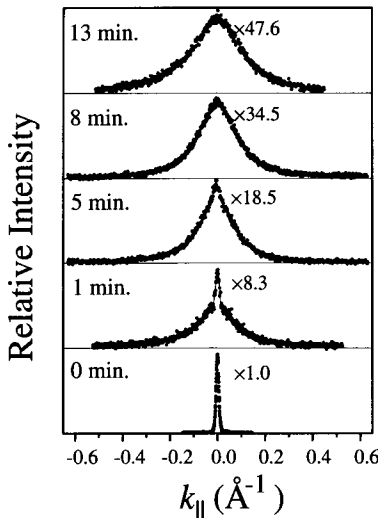


FIG. 14.22 Time-dependent angular profiles of the (00) beam scanned along the  $\bar{[1}12]$  direction at the out-of-phase condition,  $k_{\perp}c \approx 7\pi$ , for the substrate temperature of  $275 \pm 5^\circ\text{C}$ . The deposition rate was fixed at  $\sim 7$  bilayers/min. The relative intensity has been scaled up by the factor shown near the peak of each profile (from Ref. [14.38]).

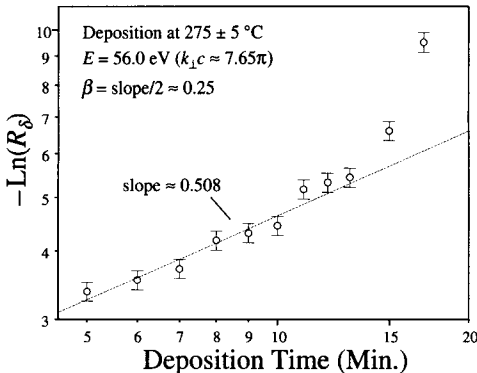


FIG. 14.23 The log-scaled relationship of  $-\ln(R_\delta)$  vs  $t$  measured at  $275 \pm 5^\circ\text{C}$  is plotted at  $|k_{\perp}c - 8\pi| = 0.349\pi$ . This plot actually shows the relationship between  $w^2$  and  $t$  (from Ref. [14.38]).

$\alpha$  for the growth as about  $1.03 \pm 0.07$ . In Figure 14.24(b) we also plot the FWHM of the diffuse profile at the out-of-phase condition  $\Phi = 7.08\pi$ . As we have shown in Chapter 9,  $\alpha$  is proportional to the local slope of the surface. Therefore, Figure 14.24(b) shows that during Si/Si(111) growth at  $275 \pm 5^\circ\text{C}$  the local slope is not stationary. In fact, it can be fit by  $\text{FWHM} \propto$

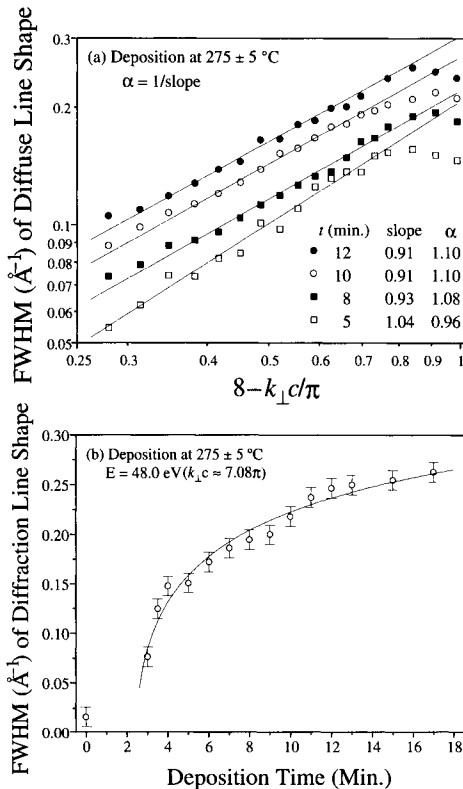


FIG. 14.24 (a) The log-scaled plots of FWHM of the diffuse profile vs.  $8 - k_{\perp}c/\pi$  at different growth times. (b) The FWHM at  $k_{\perp}c = 7.08\pi$  plotted as a function of the growth time in open circles. The solid curve results from the fit using the form  $\text{FWHM} = A\sqrt{\ln(t/\tau)}$  (from Ref. [14.38]).

$\sqrt{\ln(t)}$ . All these observations are consistent with a linear dynamic growth mechanism governed by surface diffusion discussed in Appendix A.

#### 14.2.2 An example of step bias growth: Cu/Cu (001)

Another example of the dynamic roughening front observed by HRLEED is the reversible homoepitaxy Cu/Cu(100) [14.39]. The experiments were carried out in a UHV system with a base pressure  $\sim 4.0 \times 10^{-11}$  Torr. The Cu(100) substrate was cleaned by  $\text{He}^+$  sputtering and then annealed at  $\sim 500$  °C for 5–10 min. The average terrace size on the clean Cu(100) substrate is determined by STM to be  $\sim 850$  Å. Copper was evaporated from a 99.9999% pure Cu source onto the substrate at  $T \sim 303$  K with the

deposition rate about 0.0208 ML/s. The (00) beam profiles of HRLEED at the out-of-phase condition were monitored during the growth process. As shown in Figure 10.7, the profile at  $t = 0$  shows only a sharp  $\delta$  peak. As the growth starts, a ring structure plus a sharp central peak appears. As we already discussed in Chapter 10, the characteristic ring structure in a multilayer surface indicates that a well-defined mounded structure exists on the surface. The position of the ring characterizes the average mound separation. With the increase of the growth time, the separation between the ring becomes smaller, the sharp central peak intensity also gradually disappears. Figure 10.8 shows a log-log plot of the position of the ring as a function of the growth time. Clearly the decay of the ring, or the increase of the average mound separation, obeys a power law, with  $k_0 \propto t^{-0.25 \pm 0.01}$ . This result is consistent with the STM measurement of the same growth system, Cu/Cu(001), under the same condition [14.39].

However, we notice that, for very long growth time (say 115 ML), although STM still reveals a mound structure on the surface, the ring in the LEED profile disappears (see Figure 10.7). Instead, a broad single diffraction profile appears. This is due to the fact that the interface width is so large that, at the out-of-phase condition, only the local roughness dominates the diffraction. If one moves away from the out-of-phase condition, and goes to the near-in-phase condition, one still can see the ring structure in the diffraction profile. Figure 14.25 shows the calculated diffraction profile at the near-in-phase condition ( $\Phi = 0.1\pi$ ) and the out-of-phase condition ( $\Phi = \pi$ ) using Equation (7.46) and the time-dependent interface width and mound separation data from References [14.39, 14.40]. At the out-of-phase condition, both calculated profiles and experimental data show that a satellite structure exists at the initial stages of growth. When the epitaxial layer reaches 100 ML and higher, experimental data showed that the diffraction beam became one single broad profile, and no satellite ring was observed. This is also described by our calculation [the profile at  $t = 417.5$  and  $t = 7279$  min in Figure 14.25(a)]. However, at the near-in-phase condition, although there were no experimental data, the simulated diffraction profile as a function of time always had the satellite ring, and the diameter of the ring kept shrinking, reflecting coarsening of the mounds. This is where much quantitative information could be obtained if data were available.

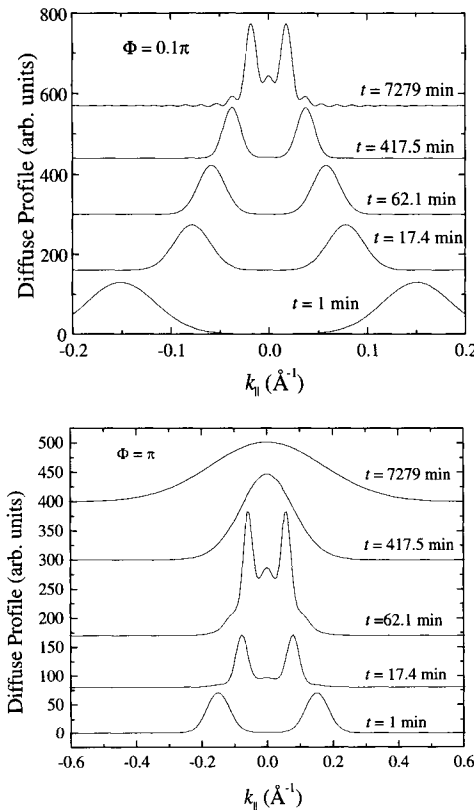


FIG. 14.25 Simulated HRLEED diffuse profiles for Cu/Cu(100) epitaxial growth: (a) out-of-phase condition ( $\Phi = \pi$ ) and (b) near-in-phase condition ( $\Phi = 0.1\pi$ ) (from Ref. [14.40]).

#### 14.2.3 Some issues of concern during measurement and analysis of the dynamic roughening by diffraction

During the measurement of the dynamic roughening by diffraction, there are several issues to which one needs to pay attention. In the following, we list some of these cases.

(1) Is the growth really in a dynamic-roughening regime? This question determines how to analyze the diffraction data. From the above discussion, for the layer-by-layer growth mode, one usually can apply a two-level surface model to describe the morphology. However, for dynamic roughening, one has to use the diffraction theory for a multilayer surface. The characteristics of the diffraction profiles are different for these two cases.

(2) Does the surface height distribution change with growth time? In

reality it is generally true that the height distribution will change with the growth time when the growth starts from a very flat substrate. One cannot always assume a Gaussian or a Poisson height distribution for all of the growth times. In this case, a discrepancy in data analysis may occur due to different height distributions. However, as long as the interface width is small such that  $k_{\perp}w \leq 1$  or  $\Pi \leq 1$ , the diffuse profile is always proportional to the surface power spectrum. Thus, no matter what the height distribution is, one can always obtain important information from the diffraction profile.

(3) How does one obtain an accurate value of the roughness exponent  $\alpha$ ? For the dynamic scaling roughening, the roughness exponent  $\alpha$  is very important for characterizing the growth mechanism. For a Gaussian surface, or a Poisson surface, if the discrete lattice effect is neglected ( $\xi^{-1} \ll K_{BZ}$ ), one can determine  $\alpha$  in several ways as shown in Table 9.1. For a non-Gaussian surface or a non-Poisson surface, there is only one way to determine  $\alpha$  correctly, i.e., from the diffuse tail under the diffraction condition  $k_{\perp}w \leq 1$  or  $\Pi \leq 1$ . For a discrete surface, if the condition  $\xi^{-1} \ll K_{BZ}$  is not satisfied, then  $\alpha$  cannot be determined from the diffraction profile unless a full numerical fit is applied.

(4) How does one obtain an accurate lateral correlation length? Under the condition that  $k_{\perp}w \leq 1$  or  $\Pi \leq 1$ , we always state that the FWHM of a diffuse profile is inversely proportional to the lateral correlation length  $\xi$  of a dynamic scaling surface. However, to determine an accurate value of  $\xi$ , one needs to know the value of  $\alpha$  as well as the shape of the height-height correlation function  $H(r)$  so that the prefactor can be determined. Usually one always assumes both the  $\alpha$  and the form of  $H(r)$  do not change with the growth time. Then the dynamic behavior of the lateral correlation length  $\xi$  can be obtained from the time-dependent FWHM of the diffuse profile. One should bear in mind that this assumption may not always be true. In this case, one may not obtain a consistent value for  $\xi(t)$ .

(5) How does one measure the long time dynamic behavior at the out-of-phase condition when the  $\delta$ -peak intensity may decay quickly to zero? As we discussed in Chapter 7, the diffraction intensity at the out-of-phase condition is very sensitive to the change of interface width. If the  $\delta$ -peak intensity decays to zero, in principle one can shift to the near-in-phase condition to continue the measurements.

(6) How does one deal with the disappearance of diffraction profile splitting due to the profile broadening at the out-of-phase condition for mound surfaces? As we discussed in the last paragraph, we need to move to the near-in-phase condition.

(7) How does one correctly measure an anisotropic surface? Two cases may happen. First, the anisotropy does not change during the growth process. However, as the interface width increases, the anisotropy of the diffraction beam at the out-of-phase condition may change during growth. Second, the morphological anisotropy also changes with growth time. In order to determine whether or not the change in diffraction beam anisotropy is due to the growth, one needs to go to  $k_{\perp}w \leq 1$  or  $\Pi \leq 1$ .

### 14.3 Summary

In this chapter, we described the dynamic aspect of the diffraction intensity for different growth mechanisms, especially with an emphasis on the out-of-phase (anti-Bragg) intensity. For the step-flow growth, the anti-Bragg intensity remains a constant during growth. For an ideal layer-by-layer growth, the anti-Bragg intensity oscillates with an increase in film coverage. For a quasi-layer-by-layer growth, since a multilayer structure gradually builds up, the anti-Bragg intensity has a damping behavior in its oscillation. For the dynamic roughening process, the anti-Bragg intensity decreases monotonically with the growth time. We also discussed several issues needed to be addressed during the measurement of dynamic growth and its data analysis.

### References

- 14.1 Zhenyu Zhang and Max G. Lagally, "Atomistic processes in the early stages of thin-film growth," *Science* **276**, 377 (1997).
- 14.2 P. Ruggerone, C. Ratch, and M. Scheffler, "Density functional theory of epitaxial growth of metals," in *The Chemical Physics of Solid Surfaces*, Vol. 8, edited by D. A. King and D. P. Woodruff (Elsevier Science, Amsterdam, 1997).
- 14.3 M. Henzler, "Growth modes in homo- and heteroepitaxial growth," *Progress in Surf. Sci.* **42**, 297 (1993).
- 14.4 J. J. Harris, B. A. Joyce, and P. J. Dobson, "Oscillations in the surface structure of Sn-doped GaAs during growth by MBE," *Surf. Sci.* **103**, L90 (1981).
- 14.5 J. N. Neave, B. A. Joyce, P. J. Dobson, and N. Norton, "Dynamics of film growth of GaAs by MBE from RHEED observations," *Appl. Phys. A* **31**, 1 (1983).
- 14.6 J. M. Van Hove, C.S. Lent, P.R. Pukite, and P.I. Cohen, "Damped oscillations in reflection high energy electron diffraction during GaAs MBE," *J. Vac. Sci. Technol. B* **1**, 741 (1983).
- 14.7 U. Korte and P. A. Maksym, "Role of the step density in reflection high-energy electron diffraction: questioning the step density model," *Phys. Rev. Lett.* **78**, 2381 (1997).
- 14.8 T. Kawamura, "Relation between surface step density and RHEED intensity," *Surf. Sci.* **298**, 331 (1993) and references therein.

- 14.9 J. M. Pimbley and T.-M. Lu, "A two-dimensional random growth model in layer-by-layer epitaxy," *Surface Sci.* **139**, 360 (1984).
- 14.10 T.-M. Lu, G.-C. Wang, and Y.-P. Zhao, "Beyond intensity oscillations," *Surf. Rev. Lett.* **5**, 899 (1998).
- 14.11 B. A. Joyce, P. J. Dobson, J. H. Neave, K. Woodbridge, J. Zhang, P. K. Larson, and B. Böger, "RHEED studies of heterojunction and quantum well formation during MBE growth-from multiple scattering to band offsets," *Surf. Sci.* **168**, 423 (1986).
- 14.12 G. H. Gilmer, "Transient in the rate of crystal growth," *J. Crystl. Growth* **49**, 465 (1980).
- 14.13 Wim van Saarloos and G. H. Gilmer, "Dynamical properties of long-wavelength interface fluctuations during nucleation-dominated crystal growth," *Phys. Rev. B* **33**, 4927 (1986).
- 14.14 Y. Ishibashi, "An analytical model of poly-nuclear growth transient," *J. Phys. Soc. Japan* **54**, 4107 (1985).
- 14.15 P. Nozières, in *Solid Far From Equilibrium*, edited by C. Godrèche (Cambridge University Press, New York, 1991), p. 135.
- 14.16 H.-N. Yang, G.-C. Wang, and T.-M. Lu, "Quantitative study of the decay of intensity oscillation in transient layer-by-layer growth," *Phys. Rev. B* **51**, 17932 (1995).
- 14.17 Y. Ishibashi, "Intensity oscillation of reflection high-energy electron diffraction (RHE ED) by a polynuclear growth model," *J. Phys. Soc. Japan* **60**, 3215 (1991).
- 14.18 Harald Cramer, *Mathematical Methods of Statistics* (Princeton University Press, Princeton, 1974).
- 14.19 M. C. Bartelt and J. W. Evans, "Transition to multilayer kinetic roughening for metal (100) homoepitaxy," *Phys. Rev. Lett.* **75**, 4250 (1995).
- 14.20 J. W. Evans and M. C. Bartelt, "Nucleation, growth, and kinetic roughening of metal(100) homoepitaxial thin films," *Langmuir* **12**, 217 (1996).
- 14.21 W. F. Egelhoff, Jr., and I. Jacob, "Reflection high-energy electron diffraction (RHEED) oscillation at 77K," *Phys. Rev. Lett.* **62**, 921 (1989).
- 14.22 R. Kunkel, B. Poelsema, L. K. Verheij, and G. Comsa, "Reentrant layer-by-layer growth during molecular-beam epitaxy of metal-on-metal substrates," *Phys. Rev. Lett.* **65**, 733 (1990).
- 14.23 B. Poelsema, R. Kunkel, N. Nagel, A. F. Becker, G. Rosenfeld, L. K. Verheij, and G. Comsa, "New phenomena in homoepitaxial growth of metals," *Appl. Phys. A* **53**, 369 (1991).
- 14.24 J. W. Evans, "Random-deposition models for thin-film epitaxial growth," *Phys. Rev. B* **39**, 5655 (1989).
- 14.25 J. W. Evans, D. E. Sanders, P. A. Thiel, and A. E. DePristo, "Low-temperature epitaxial growth of thin metal films," *Phys. Rev. B* **41**, 5410 (1990).
- 14.26 M. Born and E. Wolf, *Principles of Optics*, 6th Edition (Cambridge University Press, 1980).
- 14.27 Irving P. Herman, *Optical Diagnostics for Thin Film Processing* (Academic Press, San Diego, 1996).
- 14.28 Chih-Hao Lee and Sung-Yuh Tseng, "In situ fixed-angle x-ray reflectivity measurement of thin-film roughness and thickness during deposition," *J. Appl. Crystallography* **31**, 181 (1998).
- 14.29 Chih-Hao Lee, Hsin-Yi Lee, K. S. Liang, and Tai-Bor Wu, "In situ fixed angle x-ray reflectivity study of sputter-deposited amorphous LaNiO<sub>3</sub> thin film on Si substrate," *Physica B* **248**, 109 (1998).
- 14.30 A. Baranov, P. Kondrashov, and I. Smirnov, "In situ x-ray reflectivity for thin-film deposition monitoring and control," *Solid State Technology* May, 53 (1999)
- 14.31 A. M. Baranov and I. F. Mikhailov, "In situ x-ray investigation of thin film growth," *Thin Solid Films* **324**, 63 (1998).

- 14.32 J. G. Amar and F. Family, "Kinetics of submonolayer and multilayer epitaxial growth," *Thin Solid Films* **272**, 208 (1996).
- 14.33 B. Meng and W. H. Weinberg, "Dynamical Monte Carlo studies of molecular beam epitaxial growth models: interfacial scaling and morphology," *Surf. Sci.* **364**, 151 (1996).
- 14.34 H. Kallabis, L. Brendel, J. Krug, and D. E. Wolf, "Damping of oscillations in layer-by-layer growth," *International Journal of Modern Physics B* **11**, 3621 (1997).
- 14.35 Y.-P. Zhao, C. White, T.-M. Lu, and G.-C. Wang, to be published.
- 14.36 M. G. Lagally, D. E. Savage, and M. C. Tringides, in *Reflection High Energy Electron Diffraction and Reflection Electron Imaging from Surfaces*, eds. P. K. Larson and P. J. Dobson (Plenum, London, 1988).
- 14.37 M. Henzler, "LEED from epitaxial surfaces," *Surf. Sci.* **298**, 369 (1993).
- 14.38 H.-N. Yang, G.-C. Wang, and T.-M. Lu, "Instability in low-temperature molecular-beam epitaxy growth of Si/Si(111)," *Phys. Rev. Lett.* **73**, 2348 (1994).
- 14.39 J.-K. Zuo and J. F. Wendelken, "Evolution of mound morphology in reversible homoepitaxy on Cu(100)," *Phys. Rev. Lett.* **78**, 2791 (1997).
- 14.40 Y.-P. Zhao, H.-N. Yang, G.-C. Wang, and T.-M. Lu, "Diffraction from diffusion barrier-induced mound structures in epitaxial growth fronts," *Phys. Rev. B* **57**, 1922 (1998).

## 15. TRANSMISSION DIFFRACTION AND FRACTALS

In previous chapters, we put our main effort on the characterization of random rough surfaces and the determination of the roughness parameters associated with the statistical properties of the surfaces. One particular surface model is the self-affine rough surface, which is a fractal. From the discussions in the last few chapters, we have learned that, for the diffraction from a self-affine surface, the large- $k_{||}$  behavior of the diffuse profile obeys a power law. The power law behavior of the diffraction intensity as a function of the momentum transfer for a fractal object has been known for a long time by scientists who study small-angle diffraction (for reviews, see [15.1, 15.2]). The power law behavior of the diffraction intensity has become a standard experimental method for the measurement of the fractal dimension of an object. However, as we have discussed in Section 9.2.1, even for the same self-affine surface, if the diffraction condition (mainly  $k_{\perp}$ ) is different, then the power law behavior would appear in a different regime of  $k_{||}$ . For large  $k_{\perp}$ , the power law tail can be pushed far away from the center of the profile, which could be out of the detection limit. In this case, one may have difficulty in measuring the power law tail. Therefore, it would be interesting to compare the diffraction from a self-affine surface with the diffraction from a general fractal object, which may give us a better understanding on the power law behavior of the diffraction tail.

### 15.1 Transmission Diffraction Geometry

In general, there are two classes of diffraction modes in three-dimensional space [15.3]: one is the transmission diffraction (TD), which is applied to bulk materials, and the other is the reflection diffraction (RD), which is used to measure surfaces and interfaces. The general configuration of the TD mode is shown in Figure 15.1(a). The momentum transfer  $\mathbf{k}$  ( $k = 2|k_{in}| \sin \frac{\theta_{out}}{2}$ ) due to the diffraction (or the scattered wave vector) can be decomposed into two parts:  $k_{||}$  ( $= k_{out} \sin \theta_{out}$ ), the momentum transfer parallel to the sample surface (or momentum transfer perpendicular to incident momentum direction), and  $k_{\perp}$  ( $= k_{in} - k_{out} \cos \theta_{out}$ ), the momentum transfer perpendicular to the sample surface (or the momentum transfer parallel to incident momentum direction). If we assume that the medium consists of  $N$  particles, aggregating into aggregates, the diffraction

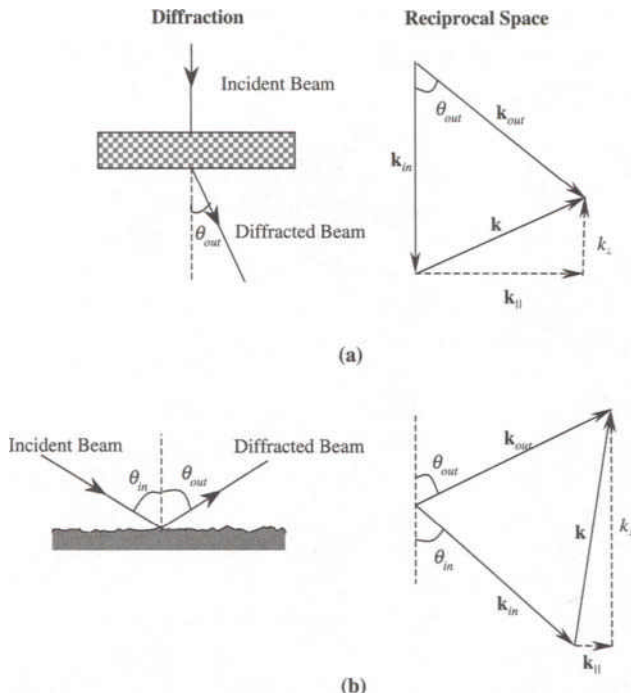


FIG. 15.1 Diffraction geometry and reciprocal-space geometry for (a) transmission diffraction and (b) reflection diffraction (from Ref. [15.3]).

intensity from this medium can be expressed as [15.1, 15.2]

$$S(k) = NS_0(ka)P(k), \quad (15.1)$$

where  $N$  is the number of identical, rigid, spherically symmetric scatterers with a diameter  $a$ . The aggregates are randomly oriented. We also assume that each particle scatters independently (no multiple scattering between or within the particles). The scattered intensity is averaged over all the orientations of aggregates. The scattered intensity distribution from one single particle is  $S_0(ka)$ . One can write

$$P(k) = 1 + 4\pi \frac{N}{V} \int_0^l r^2 g(r) \frac{\sin kr}{kr} dr, \quad (15.2)$$

which describes the effect of the particle-particle correlation in the aggregates [15.1]. Here  $N/V$  is the average density of the aggregates, and  $g(r)$  is the density-density correlation. We can see that Equation (15.1) is limited by two length scales: the size of an individual scatterer,  $a$ , and the largest

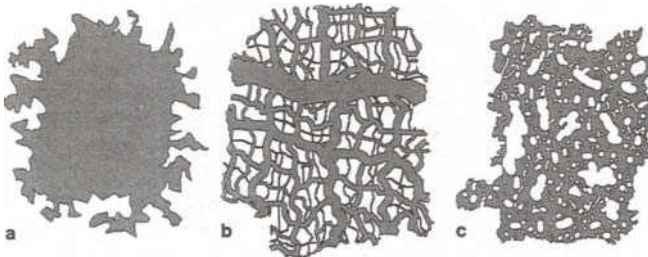


FIG. 15.2 Three different fractal objects: (a) surface fractal, (b) mass fractal, and (c) pore fractal (from Ref. [15.4]).

scale of aggregates,  $l$ . Therefore, we can obtain information within  $kl \gg 1$  and  $ka \ll 1$ .

## 15.2 Three-Dimensional Fractal Structures

Usually three classes of fractal objects shown in Figure 15.2 are being studied: surface fractal, mass fractal, and pore fractal. The surface fractal is a dense object or an aggregation of dense objects with fractal surfaces, as shown in Figure 15.2(a). The surface area of the object satisfies

$$A = A_0 r^{D_s}, \quad (15.3)$$

where  $r$  is the ruler used to measure the surface area and  $D_s$  is the fractal dimension of the surface,  $2 < D_s < 3$ . If the mass and surface of an object scale alike, then this object is called a mass fractal, as shown in Figure 15.2(b). For a mass fractal, mass  $M$  of the object scales with the measuring radius  $r$  as

$$M = M_0 r^{D_m}, \quad (15.4)$$

where  $D_m$  is the mass fractal dimension, usually  $1 < D_m < 3$ . However, if a dense object contains holes or pores as shown in Figure 15.2(c), which also has a fractal structure, it is called a pore fractal. The mass of a pore also satisfies a power law relation with  $r$ ,

$$M_p = M_{p0} r^{D_p}. \quad (15.5)$$

Here  $D_p$  is the pore fractal dimension. Clearly the mass fractal and pore fractal are very similar except the masses considered are different.

### 15.3 Diffraction Characteristics

For a mass fractal object, the density-density correlation function  $g(r)$  satisfies [15.1, 15.2],

$$g(r) = G_0 f(r/l) r^{D_m - 3}, \text{ for } r > a, \quad (15.6)$$

where  $G_0$  is a constant and  $f(r/l)$  is a cutoff function:  $f(r/l) \rightarrow 1$  for  $r/l \ll 1$  and  $f(r/l) \approx 0$  for  $r/l \gg 1$ . In the limits  $kl \gg 1$  and  $ka \ll 1$ , the diffraction intensity is governed by [15.1]

$$S(k) \approx N S_0(ka) D_m \frac{\Gamma(D_m - 1) \sin[(D_m - 1)\pi/2]}{(ka)^{D_m}}, \quad (15.7)$$

i.e., the diffraction intensity is governed by a power law. Using the Babinet principle, one can also show that for a pore fractal object, a similar power law relationship exists.

For a surface fractal object, since it is compact, it usually exhibits fractal properties in a length scale smaller than that of a mass fractal. We can treat the surface fractal object as a big particle. In this case, Equation (15.1) reduces to

$$S(k) = N S_0(ka), \quad (15.8)$$

where  $N$  is now the number of surface fractals in the medium. Another underlying assumption is that all of the surface fractals are totally randomly distributed inside the medium, and there is no correlation between them at all. In the two-phase approximation, one has

$$S_0(ka) = I_0 \int_0^a r^2 g_0(r) \frac{\sin kr}{kr} dr, \quad (15.9)$$

where  $I_0$  is a constant depending on the fraction of the volume  $\varepsilon$  occupied by one of the two phases and  $g_0(r)$  is the correlation function for the surface fractal:

$$g_0(r) \approx 1 - N_0[4\varepsilon(1 - \varepsilon)]r^{3-D_s}, \text{ for } r < a. \quad (15.10)$$

Therefore, the diffraction intensity for  $ka \gg 1$  has the form

$$S(ka) \propto k^{D_s - 6}. \quad (15.11)$$

Since  $2 < D_s < 3$ , therefore  $-4 < D_s - 6 < -3$ . For a smooth surface,  $D_s = 2$ , and one has

$$S(ka) \propto k^{-4}. \quad (15.12)$$

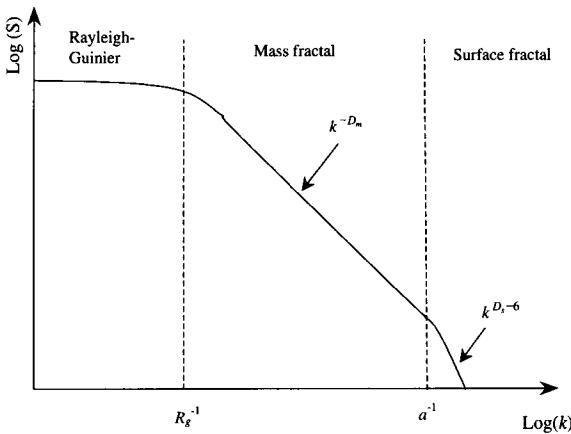


FIG. 15.3 A general diffraction profile from a fractal object.

This is the famous Porod law [15.5].

Certainly, one can treat the particle aggregates as aggregates of surface fractal particles. Then the diffraction from a mass fractal describes the correlation between the aggregated particles (in the length scale  $a < r < l$ ), and the diffraction from a surface fractal reflects local fluctuations of particle surfaces ( $r < a$ ). Therefore the diffraction intensity can be divided into three regimes as shown in Figure 15.3. At small  $k$ , the diffraction is governed by the average density of the aggregates and does not reflect the local structures of the aggregates. This is called the Rayleigh-Guinier regime. The characteristic length for this regime is the radius of gyration  $R_g$ . The second regime ( $R_g^{-1} < k < a^{-1}$ ) is due to the mass fractal, the diffraction intensity obeys the power law, Equation (15.7). The third regime ( $k > a^{-1}$ ) is the result of the surface fractal, and the diffraction intensity also obeys a power law, Equation (15.11).

Until now we have always assumed that the size of a surface fractal scatterer  $a$  is much smaller than the diameter of a probe beam. We have also assumed that the orientations of surface fractals are random so that the diffraction intensity is a statistical average of the scattered intensities from all directions. If the size of the surface fractal scatterer increases, say,  $a$  is much larger than the diameter of a probe beam, then the beam can only see part of the fractal surfaces. Then, the diffraction problems become diffraction from a random rough surface that we have discussed in great length in this book. (Here we should assume that the surface does not have overhangs.) The diffraction mode changes from TD to RD (we assume that the probe beam cannot penetrate too deeply into the surface).

The situation in RD is slightly more complicated compared to TD. The general geometry for RD is shown in Figure 15.1(b). The diffraction intensity can be rewritten as

$$S(\mathbf{k}_{||}, k_{\perp}) = \int C(k_{\perp}, \mathbf{r}) e^{i\mathbf{k}_{||} \cdot \mathbf{r}} d\mathbf{r}. \quad (15.13)$$

Here we decompose the total momentum transfer into two perpendicular components. Equation (15.13) is a two-dimensional Fourier transform, while Equation (15.1) is a three-dimensional Fourier transform. From the discussion in Section 9.2, for a self-affine surface, the tail of a diffuse profile obeys a power law,  $S(\mathbf{k}_{||}, k_{\perp}) \propto k_{||}^{-d-2\alpha}$ , which reflects the fractal dimension of a surface,  $D_s = d + 1 - \alpha$ . We also have argued that this power-law tail depends on the diffraction condition  $k_{\perp}w$ . For  $k_{\perp}w < 1$ , the power-law tail is the reflection of a surface power spectrum, and the crossover from small  $k_{||}$  to the tail (large  $k_{||}$ ) would stay the same. When  $k_{\perp}w > 1$ , the crossover would increase with the  $k_{\perp}w$  value. This would not occur in the TD mode, where the crossover is determined by either the radius of gyration  $R_g$  or the particle size  $a$ .

## References

- 5.1 P. W. Schmidt, "Use of scattering to determine the fractal dimension," in *The Fractal Approach to Heterogeneous Chemistry, Surfaces, Colloids, Polymers*, Edited by D. Avnir (Wiley, Chichester, 1989).
- 5.2 P. Pfeifer, "Small-angle scattering law for intermediates between surface, mass, and pore fractals," in *Multiple Scattering of Waves in Random Media and Random Surfaces*, Proceedings of an International Symposium, Edited by V. V. Varadan and V. K. Varadan (The Pennsylvania State University, University Park, 1987).
- 5.3 Y.-P. Zhao, C.-F. Cheng, G.-C. Wang, and T.-M. Lu, "Power law behavior in diffraction from fractal surfaces," *Surf. Sci. Lett.* **409**, L703 (1998).
- 5.4 Jean-François Gouyet, Michel Rosso, and Bernard Sapoval, "Fractal surfaces and interfaces," in *Fractals and Disordered Systems*, Edited by Armin Bunde and Shlomo Havlin, p. 229 (Springer-Verlag, Berlin, 1991).
- 5.5 A. Guinier and G. Fournet, *Small Angle Scattering of X-rays* (Wiley, New York, 1955).

## 16. EFFECTS OF SURFACE ROUGHNESS: EXAMPLES

So far, we have discussed how to characterize a rough surface using different techniques. One immediate question is: How a rough surface, as a boundary condition, affects the physical, chemical, or other properties of a material? Since this is such a broad topic in current research, here we only use some simple examples to illustrate how surface roughness affects the electrical and magnetic properties of thin films. Note that the rough surfaces we considered in this chapter are isotropic, self-affine, Gaussian surfaces.

### 16.1 Local Slope, Surface Area, and Surface Energy

Many roughness effects are closely related to the average local slope (or RMS local slope) and the surface area. In fact, these two quantities are themselves related. For an isotropic surface, the RMS surface slope is defined as

$$\rho_{rms} = \langle (\nabla h)^2 \rangle^{1/2}, \quad (16.1)$$

and the average surface area is written as

$$A_r = \langle [1 + (\nabla h)^2]^{1/2} d\mathbf{r} \rangle. \quad (16.2)$$

For small roughness,  $|\nabla h| \ll 1$ , Equation (16.2) becomes

$$A_r \approx A_0 + \frac{1}{2} \int \langle (\nabla h)^2 \rangle d\mathbf{r}, \quad (16.3)$$

where  $A_0$  is the flat surface area. For large roughness,  $|\nabla h| \gg 1$ , and Equation (16.2) becomes

$$A_r \approx \int \langle |\nabla h| \rangle d\mathbf{r} + \frac{1}{2} \int \langle |\nabla h|^{-1} \rangle d\mathbf{r}. \quad (16.4)$$

We can see that, especially in the small-roughness case,  $|\nabla h| \ll 1$ , the average surface area has a direct relationship to the RMS local slope. Since the small roughness can be treated more conveniently, in the following we will only discuss this case.

As we have discussed in Chapter 2, the definition of the RMS local slope  $\rho_{rms}$  is actually the square root of the covariance of  $\nabla h$ , the gradient of the random field  $h(\mathbf{r})$ . Rigorously speaking, in order to obtain  $\rho_{rms}$ , Equations

(2.30)-(2.32) show that the auto-covariance function  $G(r)$  of  $h(r)$  should have derivatives up to second order at  $r = 0$ . However, for a self-affine surface, since the auto-covariance function has the form  $G(r) \sim 1 - (\frac{r}{\xi})^{2\alpha}$ , for  $r/\xi \ll 1$ , and  $0 \leq \alpha \leq 1$  [in most cases  $0 \leq \alpha < 1$ ], obviously at least the second derivative of  $G(r)$  does not exist. Therefore one cannot calculate the RMS local slope using Equation (2.32). In fact, for a self-affine surface, the scaling relation only exists within a certain range of the length scale, say,  $a \leq r \leq l$ , where  $a$  is the short-length cutoff, such as the lattice constant, and  $l$  is the large-length cutoff, such as the sampling size. Beyond this range, the surface is not self-affine anymore, and the contribution to the RMS local slope can be neglected. In order to calculate the RMS local slope, one can use the property of the Fourier transform:

$$\tilde{h}(\mathbf{k}_{||}) = \frac{1}{(2\pi)^2} \int h(\mathbf{r}) e^{-i\mathbf{k}_{||}\cdot\mathbf{r}} d\mathbf{r}, \quad (16.5)$$

$$h(\mathbf{r}) = \int \tilde{h}(\mathbf{k}_{||}) e^{i\mathbf{k}_{||}\cdot\mathbf{r}} d\mathbf{k}_{||}. \quad (16.6)$$

Then

$$\nabla h = \nabla \int \tilde{h}(\mathbf{k}_{||}) e^{i\mathbf{k}_{||}\cdot\mathbf{r}} d\mathbf{k}_{||} = \int \mathbf{k}_{||} \tilde{h}(\mathbf{k}_{||}) e^{i\mathbf{k}_{||}\cdot\mathbf{r}} d\mathbf{k}_{||}, \quad (16.7)$$

and

$$\begin{aligned} & <(\nabla h)^2> = <\int \mathbf{k}_{||} \tilde{h}(\mathbf{k}_{||}) e^{i\mathbf{k}_{||}\cdot\mathbf{r}} d\mathbf{k}_{||} \cdot \int' \mathbf{k}'_{||} \tilde{h}(\mathbf{k}'_{||}) e^{i\mathbf{k}'_{||}\cdot\mathbf{r}} d\mathbf{k}'_{||}> \\ & = \int \int \mathbf{k}_{||} \cdot \mathbf{k}'_{||} e^{i(\mathbf{k}_{||} + \mathbf{k}'_{||})\cdot\mathbf{r}} <\tilde{h}(\mathbf{k}_{||}) \tilde{h}(\mathbf{k}'_{||})> d\mathbf{k}_{||} d\mathbf{k}'_{||}. \end{aligned} \quad (16.8)$$

In general, for a Gaussian surface, we have

$$<\tilde{h}(\mathbf{k}_{||}) \tilde{h}(\mathbf{k}'_{||})> = \frac{(2\pi)^4}{A_0} P(\mathbf{k}_{||}) \delta(\mathbf{k}_{||} + \mathbf{k}'_{||}). \quad (16.9)$$

Therefore,

$$<(\nabla h)^2> = \frac{(2\pi)^4}{A_0} \int_{k_l}^{k_h} k_{||}^2 P(k_{||}) d\mathbf{k}_{||}, \quad (16.10)$$

where  $A_0$  is the surface area for a flat surface and  $k_l$  and  $k_h$  are the low- and high-spatial-frequency cutoffs, respectively:  $k_l = \frac{2\pi}{l}$ , and  $k_h = \frac{2\pi}{a}$ . Clearly Equation (16.10) shows that the RMS local slope of the self-affine surface is a function only of the cutoffs. Using the power spectrum proposed in Equation (3.16), one can calculate the RMS local slope as a function of the roughness exponent  $\alpha$  as shown in Figure 16.1. One can see that, for the

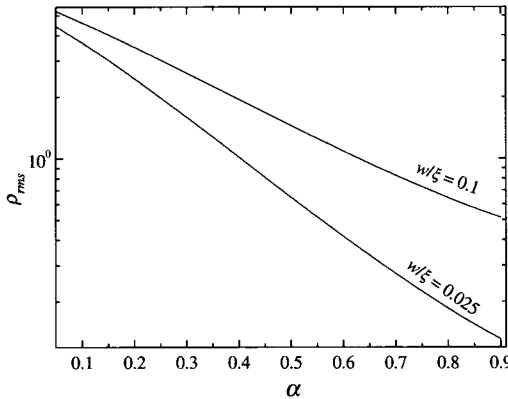


FIG. 16.1 Semilog plot of the RMS local surface slope  $\rho_{rms}$  as a function of roughness exponent  $\alpha$  for two very different roughness parameter ratios  $w/\xi$  ( $a = 0.3$  nm,  $w = 2.0$  nm, and  $\xi = 20$  and  $80$  nm).

same  $\frac{w}{\xi}$  ratio, the smaller the  $\alpha$ , the larger the RMS local slope  $\rho_{rms}$ . In fact, according to Palasantzas, the RMS local slope scales as [16.1]

$$\rho_{rms} \sim w\xi^{-\alpha}. \quad (16.11)$$

The average surface area from Equation (16.3) becomes

$$\frac{A_r}{A_0} \approx 1 + \frac{1}{2} <(\nabla h)^2> = 1 + \frac{(2\pi)^4}{2A_0} \int_{k_i}^{k_h} k_{||}^2 P(k_{||}) d\mathbf{k}_{||}. \quad (16.12)$$

Except the constant 1, the ratio of the rough surface area  $A_r$  to the flat surface area  $A_0$  has a similar behavior in  $\rho_{rms}^2$ . Obviously, the surface area of a rough surface is larger than that of the flat surface. One immediate physical property related with the surface is the surface energy  $E$ , which is proportional to the surface area [16.2]:

$$E = \gamma A, \quad (16.13)$$

where  $\gamma$  is surface/interface free energy. Thus, the increase of surface area due to roughness would increase the surface energy.

## 16.2 Effect of Surface/Interface Roughness on Electrical Properties of Thin Films

As the dimension of microelectronic devices shrinks, the effect of the finite thickness and interface of the thin film becomes more and more important. One of the most important effects is the size effect on the conductivity

of thin metallic films. As long as film thickness  $d$  becomes less than the mean free path  $\lambda_e$  of the conducting electrons, the scattering due to the film boundaries cannot be neglected, and the resistivity of the thin film will increase due to this additional boundary scattering. Based on the classical Boltzmann equation, Fuchs obtained that, in general, the electrical resistivity  $\rho_s$  of a thin metal film can be expressed as a function of the bulk resistivity  $\rho_b$ , the mean free path  $\lambda_e$ , the film thickness  $d$ , and the specularity factor  $P_0$  ( $0 \leq P_0 \leq 1$ ) [16.3]:

$$\frac{\rho_s}{\rho_b} = [1 - \frac{3\lambda_e}{2d} \int_1^\infty (\frac{1}{x^3} - \frac{1}{x^5}) \frac{1 - \exp(-dx/\lambda_e)}{1 - P_0 \exp(-dx/\lambda_e)} dx]^{-1}. \quad (16.14)$$

This general expression [Equation (16.14)] usually is not convenient for data analysis. Sondheimer obtained the asymptotic behavior of Equation (16.14) [16.4]:

$$\frac{\rho_s}{\rho_b} = 1 + \frac{3\lambda_e}{8d} (1 - P_0), \text{ for } d \gg \lambda_e, \quad (16.15)$$

$$\frac{\rho_s}{\rho_b} = \frac{4}{3} \frac{1 - P_0}{1 + P_0} \frac{\lambda_e}{d} \frac{1}{\ln(\lambda_e/d)}, \text{ for } d \ll \lambda_e. \quad (16.16)$$

According to Fuchs' theory, a fraction  $(1 - P_0)$  of the conduction electrons is scattered diffusively at the surface of the film and therefore gives rise to an extra resistivity. Thus the film is characterized by the resistivity  $\rho_b$  of the bulk metal and the mean free path  $\lambda_e$ . Surface effects are incorporated via the specularity parameter  $P_0$ . Obviously the rough boundaries of thin films would cause an additional diffuse scattering and increase the resistivity further. Fuchs did not specify the origin of  $P_0$ . Ziman considered the diffuse scattering of the electrons due to the rough boundary [16.5]. He assumed that the electron acts like a plane wave. According to the diffraction theory discussed in Chapter 7, one has a specularly-reflected part and a diffuse part, with  $e^{-k_1^2 w^2}$  being the amplitude of the reflection part. Considering the momentum and energy distribution of the electrons, one has

$$P_0 = \int \int f(k) g(\theta) e^{-4k^2 w^2 \cos^2 \theta} d\theta dk,$$

where  $f(k)$  is the energy distribution and  $g(\theta)$  is the incident angle distribution. Another simple way to incorporate surface roughness into the classic transportation theory was proposed by Namba [16.6]. He used a one-dimensional surface and assumed film thickness  $d$  to be a function of the lateral position  $x$ , and the width  $W$  of the film in the direction perpendicular to the  $x$  axis is uniform. If the distribution function of film thickness

$f(d)$  is known, then the total resistance of the film can be written as

$$R = \frac{l}{W} \int \frac{\rho(d)}{d} f(d) dd, \quad (16.17)$$

with  $l$  being the length of the film. A more detailed description of the classical size effect (CSE) can be found in the book by Tellier and Tosser [16.7].

The CSE breaks down in films with thickness  $d < \lambda_e$  and when the energy-level spectrum is discrete. In these situations, a quantum-mechanical treatment of the problem is required. Quantum-size effects (QSE) in films with perfect surfaces were studied theoretically by Sandomirskii, who solved the Boltzmann transport equation with a  $\delta$ -function potential for randomly distributed static impurities [16.8]. He obtained an oscillatory dependence of the electrical resistivity of semimetallic thin films upon thickness with an oscillation period of one-half of the Fermi wavelength  $\lambda_F$ . Generally, a new cycle of the oscillations begins when the Fermi level crosses a miniband edge. This is associated with the opening of new channels for scattering, which leads effectively to a drop in the conductivity. Using the Kubo formalism, Govindaraj and Devanathan have calculated the resistivity of thin aluminum and copper films. Their results were in good agreement with the result of Sandomirskii [16.9].

The influence of surface roughness on the conductivity of size-quantized thin metal films was studied by Leung [16.10]. He introduced the Gaussian auto-correlation function of the rough surface profiles and pointed out the importance of surface scattering in the description of the electron transport in ultrathin metal films. Using Mori's formalism, he obtained the contribution of surface roughness to the resistivity as

$$\rho_s = \frac{q\pi\hbar k_F w^2}{e^2} \tilde{R}_s, \quad (16.18)$$

with

$$\begin{aligned} \tilde{R}_s = & \frac{\tilde{\xi}^2}{t^7} \left\{ \sum_{p=1}^{p_f} p^4 a_p^2 e^{-2a_p^2 \tilde{\xi}^2} [I_0(2a_p^2 \tilde{\xi}^2) - I_1(2a_p^2 \tilde{\xi}^2)] + \right. \\ & \sum_{p=1}^{p_f} \sum_{p'=p+1}^{p_f} p^2 p'^2 e^{-(a_p^2 + a_{p'}^2) \tilde{\xi}^2} [(a_p^2 + a_{p'}^2) I_0(2a_p^2 a_{p'}^2 \tilde{\xi}^2) \\ & \left. - 2a_p^2 a_{p'}^2 I_1(2a_p^2 a_{p'}^2 \tilde{\xi}^2)] \right\}, \end{aligned} \quad (16.19)$$

where  $q = \pi n/l$ . The thickness of the film is  $l$ .  $p$  and  $p_f$  are the number

and maximum number of the nonempty energy level, respectively, and

$$\begin{aligned} a_p^2 &= \tilde{k}_F^2 - (p/t)^2, \\ \tilde{k}_F &= k_F(d)/k_F, \\ \tilde{\xi} &= k_F \xi, \text{ and} \\ t &= k_F d / \pi. \end{aligned}$$

Here  $k_F$  is the bulk Fermi wave vector given by

$$n_e = \frac{k_F^3}{3\pi^2},$$

and  $k_F(d)$  is the thickness-dependent Fermi wave vector,

$$k_F(d)/k_F = \sqrt{\frac{4t^3 + p_f(p_f + 1)(2p_f + 1)}{6p_f t^2}}.$$

The maximum number of the nonempty energy level  $p_f$  is

$$p_f = \frac{d}{\pi} k_F(d).$$

The notations  $I_0$  and  $I_1$  are the modified Bessel function of the zeroth and first order, respectively. Clearly Equation (16.18) shows that the resistivity is proportional to the interface width squared, and also increases rapidly as the lateral correlation length decreases. In order to compare his result with the CSE, Leung converted all the wave-vector sums into integrals and obtained

$$\rho_s = \frac{\tilde{\xi}^2}{2t} I(\tilde{\xi}^2), \quad (16.20)$$

with

$$\begin{aligned} I(\tilde{\xi}^2) &= \int_0^1 x \sqrt{1-x^2} dx \int_0^1 \{x' \sqrt{1-x'^2} - e^{-(x^2+x'^2)\tilde{\xi}^2} \\ &\quad \times [(x^2+x'^2)I_0(2\tilde{\xi}^2 xx') - 2xx'I_0(2\tilde{\xi}^2 xx')]\} dx'. \end{aligned}$$

Compared with Equation (16.15), he obtained

$$1 - P_0 = 4k_F^4 w^2 \xi^2 I(\tilde{\xi}^2). \quad (16.21)$$

Tešanović et al. discussed the effect of surface scattering on quantum transport in thin films with uncorrelated, atomically-rough surfaces [16.11]. Their results were applied to CoSi<sub>2</sub> to explain the enhancement of the resistivity for very thin films.

Trivedi and Ashcroft thoroughly discussed the influence of random surface roughness on the QSE [16.12]. In their work, surface roughness is incorporated as a boundary condition on the Hamiltonian, and for sufficiently small variation of the thickness the problem is handled perturbatively. Using the particle-in-box model, they found results essentially similar to Sandomirskii's, but strongly modified in the ultrathin-film range if small-scale surface roughness was included. According to their theory, the specific conductivity caused by both impurity and surface roughness is given by

$$\sigma = \frac{e^2 k_F}{\hbar \pi^2} \frac{1}{\kappa} \sum_{p=1}^{p_c} \frac{1 - p^2/\kappa^2}{\frac{2m_c+1}{k_F \lambda_i \kappa} + (\frac{w}{d})^2 \frac{s(p_c)p^2}{3\kappa}}, \quad (16.22)$$

where  $\kappa = k_F d / \pi$ ,  $p_c = \text{int}(\kappa)$ ,  $s(p_c) = (2p_c + 1)(p_c + 1)p_c / (3\kappa^3)$ ,  $\lambda_i$  is the impurity mean free path, and  $k_F$  is the Fermi wave vector. Here they assumed the surface height to be uniformly distributed. The contribution of surface roughness  $w$  is to reduce the conductivity. They also included large-scale thickness fluctuation on a scale larger than the mean free path by breaking up the film into units with slightly different thicknesses.

Fishman and Calecki studied the influence of surface roughness correlation on the conductivity of thin film using the Born approximation and found that the conductivity is closely related to the surface power spectrum [16.13]:

$$\sigma = \frac{e^2 \hbar^3}{m^2 d} \sum_{\nu=1}^N \sum_{\nu'=1}^N k_\nu^2 k_{\nu'}^2 [C^{-1}]_{\nu\nu'}, \quad (16.23)$$

where  $m$  is the electron mass,  $N$  denotes the number of occupied minibands, and  $k_\nu = [(2m/\hbar^2)(E_F - E_\nu)]^{1/2}$ , with  $E_F$  being the Fermi energy and  $E_\nu$  being the energy minimum of the  $\nu$ th miniband. The matrix  $C_{\nu\nu'}$  is determined by interminiband and intraminiband transitions due to electron scattering. For a finite confining potential,

$$C_{\nu\nu'} = \delta_{\nu\nu'} A_\nu k_\nu^2 \sum_{\mu=1}^N A_\mu (F_1)_{\mu\nu} - A_\nu A_{\nu'} k_\nu k_{\nu'} (F_2)_{\nu\nu'}, \quad (16.24)$$

with  $A_\nu = \hbar^2 \pi^2 \nu^2 / md^2$ , and

$$(F_1)_{\mu\nu} = \int_0^{2\pi} < |h(k_{\mu\nu})|^2 > d\theta, \quad (16.25)$$

$$(F_2)_{\nu\nu'} = \int_0^{2\pi} < |h(k_{\nu\nu'})|^2 > \cos \theta d\theta, \quad (16.26)$$

with

$$k_{\nu\nu'} = (k_\nu^2 + k_{\nu'}^2 - 2k_\nu k_{\nu'} \cos \theta)^{1/2}. \quad (16.27)$$

For a semiconducting film, since the number  $N$  of occupied minibands usually is 1, Equation (16.23) can be simplified as

$$\sigma = \frac{e^2}{2\pi\hbar} \left\{ \frac{4n}{\pi^2} \left[ \int_0^{2\pi} <|h(q)|^2> (1 - \cos \theta) d\theta \right]^{-1} \right\} d^6, \quad (16.28)$$

where  $q = [4\pi nd(1 - \cos \theta)]^{1/2}$ . They showed that if the lateral correlation length  $\xi$  and the electron Fermi wave vector  $k_F$  satisfy  $\xi k_F \ll 1$ , then the electrical conductivity of ultrathin films does not depend on the specific form of the roughness correlation function. Under this condition, they also found a power law behavior on the thickness-dependent conductivity,  $\sigma \propto d^s$ . For  $\xi k_F \ll 1$  the power law with  $s = 2.1 - 2.3$  describes the CoSi<sub>2</sub> thickness-dependent conductivity data well [16.14]. For a semiconducting film,  $s = 6$ , which is consistent with thickness-dependent electron mobility data of AlAs/GaAs quantum well taken by Sakaki et al. [16.15]. However, the roughness correlation function has a significant effect on the conductivity when  $\xi k_F > 1$ .

In addition to the above theoretical developments, a large amount of experimental data on the electrical resistivity of metal films has been accumulated through the work of various authors on a variety of systems [16.14, 16.16, 16.17, 16.18, 16.19, 16.20, 16.21, 16.22, 16.23, 16.24, 16.25, 16.26, 16.28, 16.29, 16.30, 16.31, 16.32]. Most of the work was interpreted by the classical transport theory, and the relationship between surface roughness and thin film resistivity has not been clearly demonstrated. A well-known example is the resistivity of CoSi<sub>2</sub> obtained by Hensel et al. as shown in Figure 16.2 [16.14]. The fitting of Fuchs' theory does not work very well. Later Tešanović et al. and Fishman et al. applied the quantum transport theory to fit the CoSi<sub>2</sub> experimental data [16.11, 16.13]. Although both groups obtained a relatively better fit, the roughness parameters they obtained are not physical. In Tešanović and Jarić's theory, the assumption of white noise as a rough surface model is essentially not physical [16.11]. In Fishman and Calecki's fit, they obtained  $w = 4$  Å and  $\xi = 2$  Å [16.13], which means that the lateral correlation length  $\xi$  of the rough surface is less than the lattice constant of CoSi<sub>2</sub>. This is equivalent to the white noise assumption by Tešanović and Jarić.

So far, only a few papers reported the QSE and related roughness with conductivity [16.24, 16.25, 16.26, 16.27, 16.28, 16.29, 16.30, 16.31, 16.32]. Fischer and Hoffmann observed the quantum size effect of Pt films de-

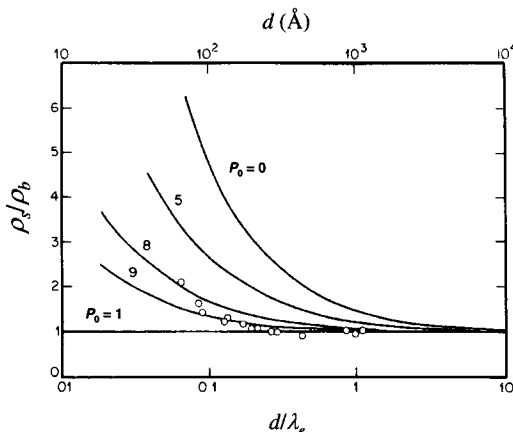


FIG. 16.2 Size effect in thin films of  $\text{CoSi}_2$ : A plot of residual resistivity (relative to the bulk resistivity  $\rho_b$ ) for 14 specimens vs. their thickness (relative to the bulk mean free path  $\lambda_e$ ). Curves representing the Fuchs theory are shown for several values of the specularity parameter  $P_0$  (from Ref. [16.14]).

posited on glass substrates [16.24, 16.25]. They prepared platinum films by electron-gun evaporation onto glass substrates under UHV conditions. During the evaporation the current through the film  $I(d)$  at constant applied voltage and its derivative  $dI/dd$  were measured using a chopper evaporation technique. The film thickness was measured during the evaporation by means of a quartz oscillator. Figure 16.3 shows three measurements of  $dI/dd$  versus thickness  $d$  for three different platinum films evaporated in a vacuum of  $10^{-8}$  mBar at 300 K with a rate of (a)  $1.0 \text{ \AA/s}$ , (b)  $2.8 \text{ \AA/s}$ , and (c)  $3.0 \text{ \AA/s}$ , respectively. The later two films clearly show the expected QSE oscillations. Later, Schumacher et al. also observed the resistivity oscillations in a variety of heterogeneous double layers:  $\text{Ag}/\text{In}$ ,  $\text{Ag}/\text{Ga}$ ,  $\text{Au}/\text{In}$ , and  $\text{Au}/\text{Ga}$ , at 6 K and 78 K, respectively [16.26, 16.27]. They found two different oscillation wavelengths. They attributed the smaller wavelength to the oscillation of surface roughness during a layer-by-layer growth, and the larger wavelength to the QSE.

Later Jalochowski et al. performed more detailed experiments by measuring the resistivity of ultrathin Pb films and Pb-In alloyed films on  $\text{Si}(111)(6 \times 6)\text{-Au}$  [16.28, 16.29, 16.30] and ultrathin Au films on  $\text{Si}(111)(7 \times 7)$  [16.31] that have the layer-by-layer growth mode. In both systems, 1-ML periodic oscillations in the resistivity vs. thickness due to the periodic change of the surface roughness were observed. The 1-ML period in resistivity is consistent with that observed in reflection high-energy electron diffraction (RHEED) intensity as a function of thickness. In the Pb and

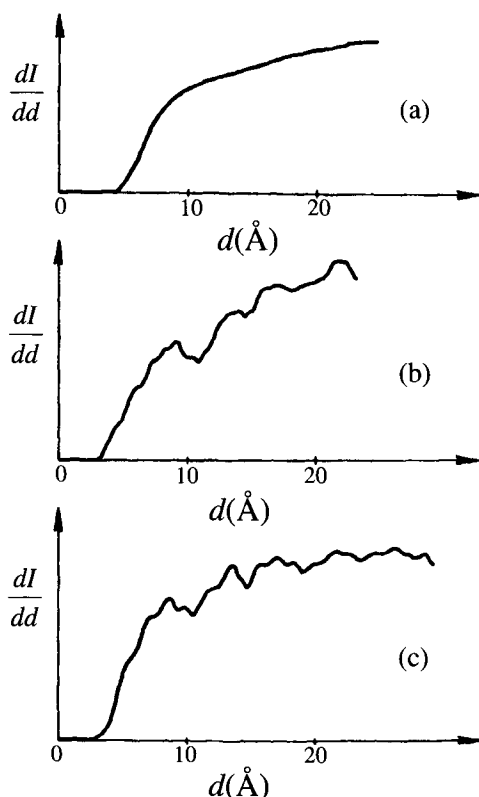


FIG. 16.3 The plots of  $\frac{dI}{dd}$  versus  $d$  during evaporation of Pt on glass with different growth rate: (a) 1.0  $\text{\AA}/\text{s}$ , (b) 2.8  $\text{\AA}/\text{s}$ , and (c) 3.0  $\text{\AA}/\text{s}$  (from Ref. [16.25]).

Pb-In systems, additional 2-ML-period oscillations due to the QSE were observed.

Luo et al. measured the increment of the resistivity of Ag thin films due to surface roughness [16.32]. Silver was deposited at a low temperature ( $\approx 130 \text{ K}$ ) onto a well-annealed, relatively thick Ag base layer ( $\approx 24 \text{ nm}$ ), which had been deposited onto a Si(111)( $7 \times 7$ ) substrate. During the deposition, the resistivity of the thin film was measured *in situ* by a van der Pauw structure, and the surface roughness was determined quantitatively afterward with HRLEED. Figures 16.4 and 16.5 show the change of the roughness parameters and resistivity as functions of the film thickness. Both resistivity and roughness increased with Ag film thickness. Since the Ag base film is much thicker than the deposited Ag film, they concluded that the increase of the resistivity is due purely to the increase of surface roughness. Using the following equation derived by Kaser and Gerlach

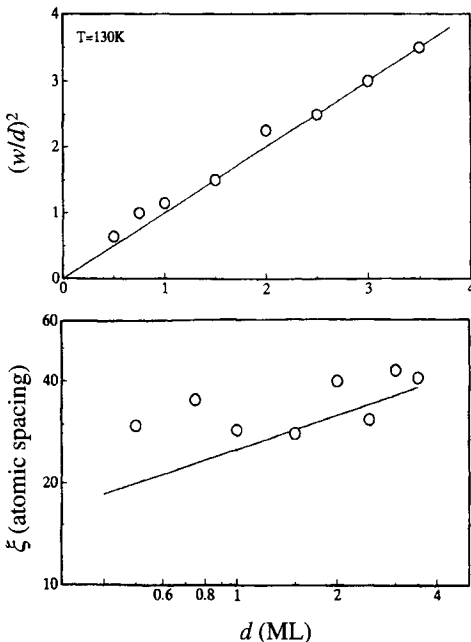


FIG. 16.4 The RMS roughness  $w$  in units of ML thickness  $d$  and the lateral correlation length  $\xi$  in units of atomic spacing of Ag films as a function of the film thickness plotted in linear and log-log scales, respectively (from Ref. [16.32]).

[16.33],

$$\rho_{sr} = \frac{9\pi\hbar w^2}{2e^2 d} F(k_F \xi), \quad (16.29)$$

where  $\rho_{sr}$  is the resistivity due to the surface roughness scattering and  $F(k_F \xi)$  is a well-defined function:

$$F(k_F \xi) \approx \begin{cases} 0.666/(k_F \xi), & \text{for } k_F \xi \gg 5, \\ \frac{4\pi}{45}(k_F \xi)^2, & \text{for } k_F \xi \ll 2. \end{cases} \quad (16.30)$$

They performed a no-free parameter fitting as shown in Figure 16.5. It can be seen that the fit agrees excellently with the measured data.

### 16.3 Effect of Surface/Interface Roughness on Magnetic Properties of Thin Films

Magnetic properties in thin films are influenced by a variety of parameters such as film thickness, crystalline structure, composition, preparation conditions, and surface/interface roughness. In the following, we summarize

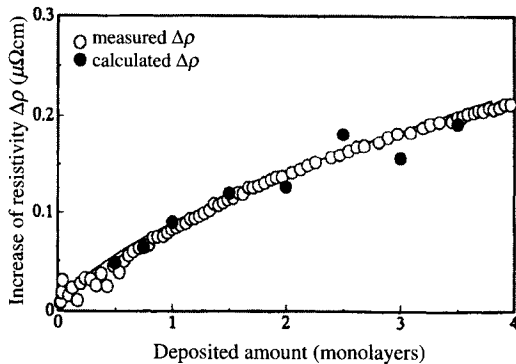


FIG. 16.5 The measured resistivity change  $\Delta\rho$  (open circles) during deposition of additional Ag at 130 K on a 116-ML well-annealed base Ag layer, and the calculated  $\Delta\rho$  (filled circles) using Equations (16.29) and (16.30), and the measured roughness parameters shown in Figure 16.4. (from Ref. [16.32]).

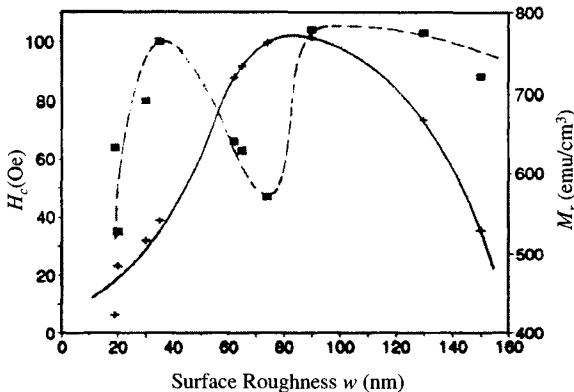


FIG. 16.6 Effect of RMS roughness  $w$  on the coercivity  $H_c$  (filled square) and the remanent magnetization  $M_r$  (+) for Ni-Co films with 11 Ni concentration (from Ref. [16.35]).

some experimental and theoretical work on the influence of surface/interface roughness on magnetic properties of thin films.

Malyutin et al. investigated the effect of surface roughness on the coercivity of chemically etched NiFeCo films (200 to 1000 Å thick) [16.34]. The coercivity of the film increases with the increase of etch time. During the etching, the thickness of the magnetic film decreases and the surface roughness increases with etch time. Vilain et al. investigated the dependence of coercivity on the surface roughness for electrodeposited NiCo alloy films [16.35]. As shown in Figure 16.6, for a 2-μm-thick film with 11%

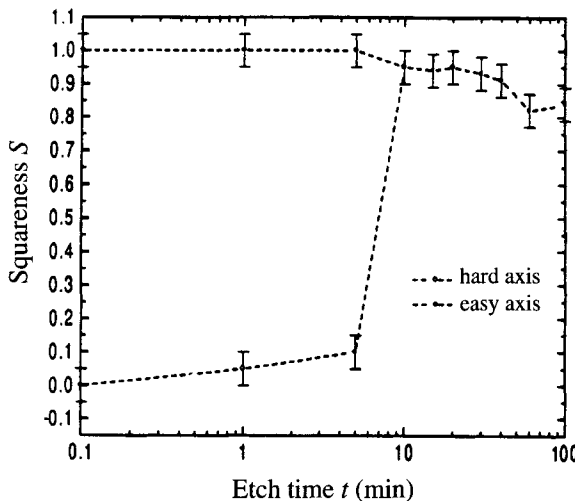


FIG. 16.7 Measured easy-axis and hard-axis squareness  $S$  of  $\sim 970\text{-}\text{\AA}$  Co films deposited on Si(100) substrates plotted as a function of plasma etch time  $t$  (from Ref.[16.37]).

Ni, the coercivity increases from 37 to 100 Oe as the RMS surface roughness increased from 200 to 350 Å. Above 350 Å, the coercivity decreases, reaching a minimum of 50 Oe around 700 Å roughness. The coercivity then increases again to about 100 Oe for roughness around 900 Å and beyond (up to 1500 Å), but the saturation magnetization and the remanent magnetization behaved differently. The remanent magnetization increases when the RMS roughness increases from 20 Å to 80 Å, and then decreases when  $w$  becomes larger than 80 Å. Kim and Shin studied the  $\text{Si}_3\text{N}_4$  underlayer roughness effect on the coercivity of the Co/Pt multilayers [16.36]. The coercivity of Co/Pt multilayers increases two-fold when the underlayer roughness increases from 2.4 to 8.8 Å.

Li et al. performed a detailed study on magnetic and morphological properties of 970-Å-thick Co films, deposited simultaneously on ten plasma-etched Si(100) substrates with different etching times [16.37, 16.38]. As the etch time  $t$  increased from 0 to 100 min, the RMS roughness  $w$  of the Co films increases almost linearly from  $\sim 5$  Å to  $\sim 1400$  Å and the lateral correlation length  $\xi$  increases from  $\sim 300$  to  $\sim 10,500$  Å. Both magneto-optic Kerr effect (MOKE) and ferromagnetic resonance (FMR) measurements gave the in-plane azimuthal angular dependence of the hysteresis loops and the ferromagnetic resonance absorption spectra. Figure 16.7 shows the squareness  $S$  of the hysteresis loop versus etch time. For  $t < 10$  min, the hard-axis squareness is close to zero and the easy-axis squareness is close to

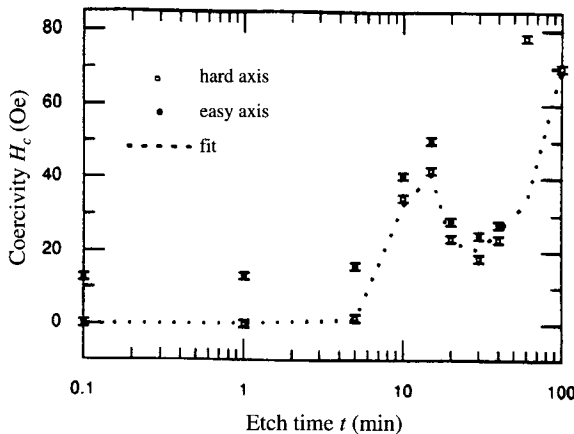


FIG. 16.8 The easy-axis and hard-axis coercivity versus etch time for  $\sim 970\text{-}\text{\AA}$ -thick Co films (from Ref. [16.38]).

one, but for  $t \geq 10$  min samples, there is no detectable difference between hard-axis and easy-axis squareness. The coercivity determined from the MOKE measurements is plotted in Figure 16.8 versus etch time  $t$  and for samples with  $t < 60$  min. Both the easy-axis and hard-axis coercivities are shown. The easy-axis coercivity was, in general, a monotonically-increasing function of the RMS roughness, except for a dip around  $t = 30$  min. Specifically, the  $H_c$  increased slightly between 13 and 15 Oe for  $t \leq 5$  min, peaked at  $\sim 50$  Oe for  $t = 15$  min, came down to  $\sim 25$  Oe for  $t = 30$  min, and then increased again to  $\sim 80$  Oe for  $t = 60$  min and  $\sim 70$  Oe for 100 min. From the MOKE and FMR measurement, the smoother films showed uniaxial magnetic anisotropy ( $t \leq 40$  min). The uniaxial anisotropy decreased with the increase of the surface roughness and disappeared for the roughest films ( $t = 60$  and 100 min). The MOKE hysteresis loop measurements suggested that, with the increasing surface roughness, the magnetization reversal changed gradually from magnetization-rotation-dominated for the smoothest films to domain-wall-motion-dominated for the roughest films.

For ultrathin films, Jiang et al. investigated the coercivity of ultrathin Co films epitaxially grown on Cu(100) substrate [16.39]. They used HRLEED to measure the surface roughness parameters of the Co films and applied surface magneto-optic Kerr effect (SMOKE) to obtain the hysteresis loop of the film. They found that the coercivity of the 6-7 ML Co film increases from  $\sim 70$  Oe for a deposition on an atomically-flat Cu substrate to  $\sim 170$  Oe for a deposition on a Cu substrate pre-roughened by  $\text{Ar}^+$  sputtering.

In ultrathin Co films deposited on rough Cu-buffered Si(111) substrates the coercivity was shown to decay with increasing film thickness  $t$  as  $t^{-0.4 \pm 0.1}$  for 12 ML to 44 ML [16.40]. On the other hand, in ultrathin Co (from 2 ML to 30 ML) deposited on smooth Cu(001) substrates, the coercivity increased up to 7-8 ML followed by a slight decrease at higher thicknesses [16.39], while a distinct coercivity behavior was revealed for films deposited on roughened Cu substrates. Nonetheless, the film growth on a flat substrate can be considered as a model system to study aspects of magnetic properties relating to an evolving microstructure. A smooth substrate avoids complications arising from substrate irregularities. Indeed, for Co films grown on smooth Cu(001) substrates, the evolving film surface appeared to be roughened at all roughness wavelengths [16.39].

The relation of the coercive field  $H_c$  for domain wall motion in thin films has been attributed to thickness fluctuations for zig-zag [16.41] and straight domain walls [16.42]. Néel [16.43] based on the same concept derived the well-known ‘4/3’-law,  $H_c \propto d^{-4/3}$ , which is valid under the assumption that the thickness fluctuation  $dd/dx$  (with  $x$  being the lateral direction along which the wall motion occurs) is a constant. However, in many cases (e.g., in NiFe films [16.42]) such a law appeared to be invalid in agreement with the fact that the assumption that  $dd/dx$  is constant cannot always be employed. On the other hand, Soohoo [16.41] fit a rather wide variety of coercivity data for thicknesses larger than 20 nm under the constraint that  $dd/dx$  was increasing with film thickness on the order close to 1. Such an increment of the thickness fluctuations [16.41] was attributed to the roughness changes occurring at short roughness wavelengths.

In the following we explore the relationship between the surface roughness and the coercivity, especially how the properties of magnetic domains change with surface roughness. First we will examine the effect of roughness on the demagnetizing factor of thin magnetic films [16.44]. Then we use the relationship between the demagnetizing factor and domain property as well as the coercivity force, applying the simple argument from energy minimization, and show the relationships among roughness, domain properties, and the coercive force. This treatment is straightforward and may not give a quantitative result, but can show the qualitative trend.

### 16.3.1 Demagnetizing factor

The basic assumptions made here are that the film is uniform and is a single domain with a homogeneous magnetization  $\mathbf{M}_0$  throughout the film. We assume the general case, for which the two interfaces of the magnetic

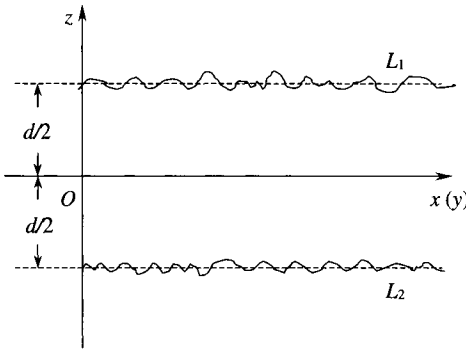


FIG. 16.9 A cross section of a rough film lying in the  $x$ - $y$  plane. The growth front is in the  $z$  direction. The film thickness is  $d$ , with the boundaries  $L_1: \frac{d}{2} + h_1(\mathbf{r})$  and  $L_2: -\frac{d}{2} + h_2(\mathbf{r})$  (from Ref. [16.44]).

film as shown in Figure 16.9 are rough. These interfaces are described by the boundaries  $\frac{d}{2} + h_1(\mathbf{r})$  and  $-\frac{d}{2} + h_2(\mathbf{r})$ , respectively, with  $h_i(\mathbf{r})(i = 1, 2)$  being single-valued surface height fluctuations. Here  $d$  is the average film thickness. The magnetization in a film can be written as

$$\mathbf{M}(\mathbf{r}, z) = \mathbf{M}_0[u(z + \frac{d}{2} - h_2(\mathbf{r})) - u(z - \frac{d}{2} - h_1(\mathbf{r}))], \quad (16.31)$$

with a step function  $u(z)$ . According to Jackson [16.45], for a uniform magnetization, the magnetic scalar potential can be written as

$$\begin{aligned} \Phi_M(\mathbf{r}, z) &= \oint \frac{\hat{n}' \cdot \mathbf{M}(\mathbf{r}, z)}{\sqrt{(\mathbf{r} - \mathbf{r}')^2 + (z - z')^2}} da' \\ &= \int \frac{\frac{\partial h_1}{\partial x'} M_{0x} + \frac{\partial h_1}{\partial y'} M_{0y} - M_{0z}}{\sqrt{(\mathbf{r} - \mathbf{r}')^2 + [z - \frac{d}{2} - h_1(\mathbf{r}')]^2}} d\mathbf{r}' \\ &\quad - \int \frac{\frac{\partial h_2}{\partial x'} M_{0x} + \frac{\partial h_2}{\partial y'} M_{0y} - M_{0z}}{\sqrt{(\mathbf{r} - \mathbf{r}')^2 + [z + \frac{d}{2} - h_2(\mathbf{r}')]^2}} d\mathbf{r}'. \end{aligned} \quad (16.32)$$

Note that  $\hat{n}'$  is the surface normal pointing away from the surface, and  $da'$  is the differential surface area. According to Schlömann [16.46], the self-energy can be written as

$$W = -\frac{1}{2} \int \int \mathbf{H} \cdot \mathbf{M} dr dz, \quad (16.33)$$

with the magnetic field strength  $\mathbf{H} = \nabla \Phi_M$ . Substituting Equation (16.33) into (16.32), one can obtain the final expressions for the demagnetizing

factors  $N_{xx}$ ,  $N_{yy}$ , and  $N_{zz}$  in real space:

$$\begin{aligned}
 N_{xx} &= \frac{1}{4\pi dA_0} \int \int \left\{ \frac{\frac{\partial h_1}{\partial x'} \frac{\partial h_1}{\partial x}}{\sqrt{(\mathbf{r} - \mathbf{r}')^2 + [h_1(\mathbf{r}) - h_1(\mathbf{r}')]^2}} \right. \\
 &\quad - \frac{\frac{\partial h_2}{\partial x'} \frac{\partial h_1}{\partial x}}{\sqrt{(\mathbf{r} - \mathbf{r}')^2 + [d + h_1(\mathbf{r}) - h_2(\mathbf{r}')]^2}} \\
 &\quad - \frac{\frac{\partial h_1}{\partial x'} \frac{\partial h_2}{\partial x}}{\sqrt{(\mathbf{r} - \mathbf{r}')^2 + [h_2(\mathbf{r}) - h_1(\mathbf{r}') + d]^2}} \\
 &\quad \left. + \frac{\frac{\partial h_2}{\partial x'} \frac{\partial h_2}{\partial x}}{\sqrt{(\mathbf{r} - \mathbf{r}')^2 + [h_2(\mathbf{r}) - h_2(\mathbf{r}')]^2}} \right\} d\mathbf{r} d\mathbf{r}', \quad (16.34) \\
 N_{yy} &= \frac{1}{4\pi dA_0} \int \int \left\{ \frac{\frac{\partial h_1}{\partial y'} \frac{\partial h_1}{\partial y}}{\sqrt{(\mathbf{r} - \mathbf{r}')^2 + [h_1(\mathbf{r}) - h_1(\mathbf{r}')]^2}} \right. \\
 &\quad - \frac{\frac{\partial h_2}{\partial y'} \frac{\partial h_1}{\partial y}}{\sqrt{(\mathbf{r} - \mathbf{r}')^2 + [d + h_1(\mathbf{r}) - h_2(\mathbf{r}')]^2}} \\
 &\quad - \frac{\frac{\partial h_1}{\partial y'} \frac{\partial h_2}{\partial y}}{\sqrt{(\mathbf{r} - \mathbf{r}')^2 + [h_2(\mathbf{r}) - h_1(\mathbf{r}') + d]^2}} \\
 &\quad \left. + \frac{\frac{\partial h_2}{\partial y'} \frac{\partial h_2}{\partial y}}{\sqrt{(\mathbf{r} - \mathbf{r}')^2 + [h_2(\mathbf{r}) - h_2(\mathbf{r}')]^2}} \right\} d\mathbf{r} d\mathbf{r}', \\
 N_{zz} &= \frac{1}{4\pi dA_0} \int \int \left\{ \frac{1}{\sqrt{(\mathbf{r} - \mathbf{r}')^2 + [h_1(\mathbf{r}) - h_1(\mathbf{r}')]^2}} \right. \\
 &\quad - \frac{1}{\sqrt{(\mathbf{r} - \mathbf{r}')^2 + [d + h_1(\mathbf{r}) - h_2(\mathbf{r}')]^2}} \\
 &\quad - \frac{1}{\sqrt{(\mathbf{r} - \mathbf{r}')^2 + [h_2(\mathbf{r}) - h_1(\mathbf{r}') + d]^2}} \\
 &\quad \left. + \frac{1}{\sqrt{(\mathbf{r} - \mathbf{r}')^2 + [h_2(\mathbf{r}) - h_2(\mathbf{r}')]^2}} \right\} d\mathbf{r} d\mathbf{r}'.
 \end{aligned}$$

Here  $N_{xx}$ ,  $N_{yy}$ , and  $N_{zz}$  are the diagonal components of the demagnetizing tensor  $\overrightarrow{\mathbf{N}}$ . A similar calculation can be applied to the non-diagonal components  $N_{xy}$ ,  $N_{yz}$ , and  $N_{zx}$ . If we assume that the surface roughness  $w$  is much smaller than the film thickness  $d$  ( $w \ll d$ ), then the roughness can be treated as a small perturbation. In this limit the in-plane demagnetizing factor  $N_{xx}$  can be approximated as

$$N_{xx} \approx \frac{1}{4\pi dA_0} \int \int \left\{ \frac{\frac{\partial h_1}{\partial x'} \frac{\partial h_1}{\partial x} + \frac{\partial h_2}{\partial x'} \frac{\partial h_2}{\partial x}}{|\mathbf{r} - \mathbf{r}'|} - \frac{2 \frac{\partial h_2}{\partial x'} \frac{\partial h_1}{\partial x}}{\sqrt{(\mathbf{r} - \mathbf{r}')^2 + d^2}} \right\} d\mathbf{r} d\mathbf{r}'.$$

Using the Fourier transform treatment, we obtain the ensemble average, which finally yields

$$N_{xx} \approx \frac{(2\pi)^4}{2dA_0} \int \frac{q_x}{q} [P_1(\mathbf{q}) + P_2(\mathbf{q}) - 2e^{-qd} \langle h_1(\mathbf{q})h_2(\mathbf{q}) \rangle] d\mathbf{q}. \quad (16.36)$$

A similar expression for  $N_{yy}$  can be obtained. The element  $N_{zz}$  can be calculated from the orthogonality condition [16.46]

$$N_{zz} = 1 - N_{xx} - N_{yy}. \quad (16.37)$$

For a magnetic thin film grown from a smooth surface,  $h_2 = 0$ , Equation (16.36) can be simplified as

$$N_{xx} \approx \frac{(2\pi)^4}{2dA_0} \int \frac{q_x}{q} P_1(\mathbf{q}) d\mathbf{q}, \quad (16.38)$$

which is actually the formula obtained by Schlömann [16.46]. For an isotropic self-affine surface, due to the isotropy,  $N_{xx} = N_{yy}$ . Substituting Equation (3.16) into Equation (16.38) we can obtain  $N_{xx}$  as

$$\begin{aligned} N_{xx} &= \frac{\alpha w^2}{2d\xi} \{ 2^{-\alpha-\frac{1}{2}} \sqrt{\pi} \Gamma(1-\alpha) (\xi q_h)^{\frac{1}{2}-\alpha} [\mathbf{H}_{\frac{1}{2}-\alpha}(\frac{\alpha}{\xi q_h}) - Y_{\frac{1}{2}-\alpha}(\frac{\alpha}{\xi q_h})] \\ &\quad - 2^{-\alpha+\frac{1}{2}} \sqrt{\pi} \Gamma(-\alpha) (\xi q_h)^{-\frac{1}{2}-\alpha} [\mathbf{H}_{-\frac{1}{2}-\alpha}(\frac{\alpha+1}{\xi q_h}) - Y_{-\frac{1}{2}-\alpha}(\frac{\alpha+1}{\xi q_h})] \}, \end{aligned} \quad (16.39)$$

where  $\mathbf{H}_v(x)$  is the Struve function,  $Y_v(x)$  is the Neumann function, and  $q_h$  is the upper spatial frequency boundary. Note that we assume that the statistics are sufficient to cover the entire scaling region. Obviously for any self-affine surface, the in-plane demagnetizing factor to its leading order scales as  $N_{xx(yy)} \propto \frac{w^2}{d\xi}$  from Equation (16.39). Figure 16.10 shows how the roughness exponent  $\alpha$  affects the demagnetizing factor. As  $\alpha$  increases from 0.001 to 1, the in-plane demagnetizing factor decreases almost three orders of magnitude. The dependence of the demagnetizing factor on the roughness exponent  $\alpha$  can be understood in the following: The roughness exponent  $\alpha$  essentially represents how many high-spatial-frequency surface components are included in the surface. As  $\alpha$  goes from 1 to 0 (from smooth facet to more wiggly local slope variation), more and more high-frequency components are included in the power spectrum, which means that the surface has more small features with local variations. This will generate more “magnetic poles” on the surface parallel to the film plane and will give rise to a stronger in-plane demagnetizing field. Therefore, as  $\alpha$  decreases,  $N_{xx}$  should increase.

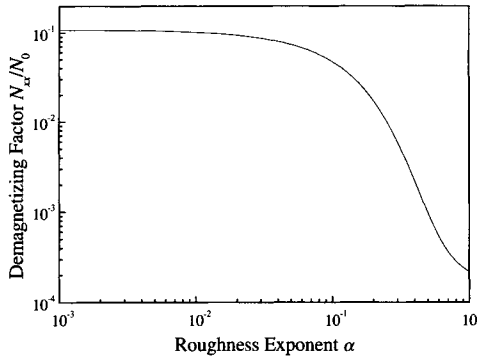


FIG. 16.10 Log-log plot of the in-plane demagnetizing factor  $N_{xx}/N_0$  as a function of the roughness exponent  $\alpha$  for an isotropic self-affine surface. Here  $N_0 = \frac{w^2}{d\xi}$  (from Ref. [16.44]).

### 16.3.2 Domain wall thickness

The surface energy  $\sigma_w$  for the domain wall can be written as [16.47, 16.48, 16.49]

$$\sigma_w = \sigma_{ex} + \sigma_{an} + \sigma_{mag}, \quad (16.40)$$

where  $\sigma_{ex}$  is the exchange energy,  $\sigma_{an}$  is the anisotropy energy, and  $\sigma_{mag}$  is the magnetostatic energy. In general, for a  $180^\circ$  domain, the exchange energy  $\sigma_{ex}$  can be expressed as

$$\sigma_{ex} = \frac{A\pi^2}{D}, \quad (16.41)$$

where  $A$  is the exchange constant defined as  $A = JS^2/a$ ,  $J$  is the exchange integral,  $S$  is the spin,  $a$  is the atomic length scale, and  $D$  is the thickness of the domain wall.

The anisotropy energy  $\sigma_{an}$  can be written as

$$\sigma_{an} = \frac{K_1 D}{2}, \quad (16.42)$$

where the in-plane anisotropy constant  $K_1 = K_v + 2K_s/d$ ,  $K_v$  is the in-plane volume anisotropy constant,  $K_s$  is the surface anisotropy constant, and  $d$  is the film thickness.

The magnetostatic energy  $\sigma_{mag}$  is

$$\sigma_{mag} = \pi N D M_s^2, \quad (16.43)$$

where  $N$  is the demagnetizing factor and  $M_s$  is the saturation magnetization.

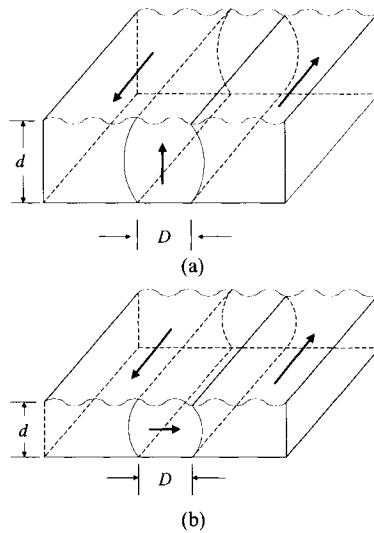


FIG. 16.11 (a) Bloch wall bounded by a rough surface and (b) Néel wall bounded by a rough surface.

Therefore

$$\sigma_w = \frac{A\pi^2}{D} + \frac{K_1 D}{2} + \pi N D M_s^2. \quad (16.44)$$

The minimizing surface energy for the domain wall requires that

$$\frac{K_1}{2} + \pi N M_s^2 + \pi D M_s^2 \frac{\partial N}{\partial D} - \frac{A\pi^2}{D} = 0. \quad (16.45)$$

For both Bloch walls and Néel walls,  $\sigma_{ex}$  and  $\sigma_{an}$  are the same. However, the magnetostatic energy  $\sigma_{mag}$  is different due to the difference in the demagnetizing factor  $N$ . For a perfect flat surface,

$$N_{Bloch}^0 = \frac{D}{d+D}, \quad (16.46)$$

for a Bloch wall, and

$$N_{Néel}^0 = \frac{d}{d+D}, \quad (16.47)$$

for a Néel wall. These are well-known results [16.47, 16.48, 16.49]. Now we consider that the surface of the magnetic film is rough. For a Bloch wall, as shown in Figure 16.11(a), the surface roughness would decrease the demagnetizing factor perpendicular to the film surface. According to

Equation (16.37),

$$N_{Bloch} \approx N_{Bloch}^0(1 - 2n_{xx}). \quad (16.48)$$

Here  $n_{xx}$  is the ratio  $N_{xx}/N_{zz}^0$  caused by a rough surface. However, for a Néel wall as shown in Figure 16.11(b), the surface roughness would enhance the demagnetizing factor parallel to the film surface:

$$N_{Néel} \approx N_{Néel}^0(1 + n_{xx}). \quad (16.49)$$

Now if we assume that  $n_{xx}$  is not a function of  $D$  (which means  $D \gg \xi$ ,  $\xi$  is the lateral correlation length of the rough surface), we can estimate the effect of roughness on the domain wall thickness  $D$ . For a Bloch wall, at the bulk limit where  $d \gg D$ , the magnetostatic energy term  $\sigma_{mag}$  can be neglected [16.48, 16.49]:

$$D \approx \sqrt{2\pi}(A/K_1)^{1/2}, \quad (16.50)$$

i.e., the domain wall thickness almost remains unchanged with surface roughness. However, if  $K_1 \ll 2\pi M_s^2$ , the anisotropy energy  $\sigma_{an}$  can be neglected, and

$$D \approx \pi \left[ \frac{A}{\pi(1 - 2n_{xx})M_s^2} \right]^{1/2}, \quad (16.51)$$

i.e., the domain wall thickness would increase. The surface energy of the domain wall becomes

$$\sigma_w = \pi M_s \sqrt{4\pi A(1 - 2n_{xx})}, \quad (16.52)$$

i.e., the surface energy of the domain wall would decrease.

For a Néel wall, if  $d \gg D$ , Equation (16.45) gives

$$D \approx \pi \left[ \frac{A}{\pi(1 + n_{xx})M_s^2} \right]^{1/2} \quad (16.53)$$

and

$$\sigma_w = \pi M_s \sqrt{4\pi A(1 + n_{xx})}. \quad (16.54)$$

Thus the Néel wall thickness decreases with the roughness but the wall energy increases. We must notice that in this case  $D$  cannot always decrease according to Equation (16.53) because as  $D$  is close to  $\xi$ ,  $n_{xx}$  also becomes  $D$  dependent.

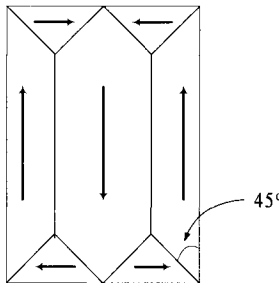


FIG. 16.12 Closure domains.

### 16.3.3 Domain width

Now let us consider the effect of surface roughness on the domain width. Here we consider the closure domain as shown in Figure 16.12. The domain energy can be written as [16.38, 16.49]

$$E_d = E_w + E_{an} + E_{mag} = \frac{\sigma_w[d + (\sqrt{8} - 1)L]}{L} + \frac{K_1 L}{2} + \pi NLM_s^2, \quad (16.55)$$

where  $L$  is the domain width. Usually,  $L \gg \xi$ ,  $N$  is independent of  $L$ . Thus the energy-minimizing process gives the size of the domain wall:

$$L = \left( \frac{2\sigma_w d}{K_1 + \pi NM_s^2} \right)^{1/2}. \quad (16.56)$$

If we assume the effect of roughness on the surface energy  $\sigma_w$  of domain wall to be small, then  $\sigma_w$  is almost a constant. Therefore, for a Bloch wall, we have

$$L_{Bloch} = \left[ \frac{2\sigma_w d}{K_1 + \pi(1 - 2n_{xx})M_s^2} \right]^{1/2}, \quad (16.57)$$

i.e., for a Bloch wall, the increase of surface roughness will increase the size of the domain. However, for the Néel wall,

$$L_{Néel} = \left( \frac{2\sigma_w d}{K_1 + \pi n_{xx} M_s^2} \right)^{1/2}, \quad (16.58)$$

i.e., the increase of surface roughness will decrease the size of the Néel wall.

### 16.3.4 Coercivity from wall movement

The coercivity caused by domain wall movement can be written as [16.42]

$$H_c = \frac{1}{2M_s} \left[ \frac{\partial \sigma_w}{\partial d} \frac{dh}{dx} + \frac{\sigma_w}{d} \frac{dh}{dx} + \frac{\sigma_w}{l} \frac{dl}{dx} \right]. \quad (16.59)$$

The contribution due to domain length  $l$  is usually small, so that

$$H_c^{mov} = \frac{1}{2M_s} \left[ \frac{\partial \sigma_w}{\partial d} + \frac{\sigma_w}{d} \right] \frac{dh}{dx}. \quad (16.60)$$

From the statistical point of view, for a rough surface, we use RMS local slope  $\rho_{rms}$  instead of  $\frac{dh}{dx}$ . Thus Equation (16.60) becomes

$$H_c^{mov} = \frac{1}{2M_s} \left[ \frac{\partial \sigma_w}{\partial d} + \frac{\sigma_w}{d} \right] \rho_{rms}. \quad (16.61)$$

Therefore we learn that the coercivity is closely related to the surface roughness. Substituting Equation (16.52) or Equation (16.54) into Equation (16.61), we have

$$H_c^{mov} = \frac{\pi \sqrt{\pi A(1 \pm n_{xx})}}{M_s} \left[ \frac{\partial M_s}{\partial d} + \frac{M_s}{d} \right] \rho_{rms}. \quad (16.62)$$

Here the plus sign corresponds to the Néel wall, and the minus sign corresponds to the Bloch wall. In general, for ultrathin film, the saturation magnetization  $M_s$  depends on the film thickness. According to Glass and Klein [16.50], for a face-centered cubic film,

$$\frac{M_s(d)}{M_s^0} = 1 - \frac{1}{16\pi S^2 G_3} \frac{kT}{J} \sum_{k_3=0}^{G_3} (1 + \cos k_3)^{-1} [\ln(1 - e^{-B}) - \ln(1 - e^{-A})], \quad (16.63)$$

where  $G_i$  is the number of cubic cells in the  $i$ th direction of the crystal [ $G$  is a large number ( $\sim 10^7$  or more)], and

$$\begin{aligned} A &= \frac{16JS}{kT} [(1 + \pi^2/4G^2) - (1 - \pi^2/4G^2) \cos k_3], \\ B &= \frac{16JS}{kT} [(1 + \pi/4) - (1 - \pi/4) \cos k_3], \text{ and} \\ k_3 &= \frac{2\pi\lambda_3}{G_3}. \end{aligned}$$

In fact,  $G_3 = d/c$ , where  $c$  is the lattice constant. Therefore, the coercivity has a complicated relationship with the film thickness  $d$ .

### 16.3.5 Coercivity from wall rotation

If a magnetic field is applied to the film, which causes the domain to rotate coherently, the energy of a domain can be expressed as [16.42, 16.48, 16.49]

$$\begin{aligned} E &= E_{an} + E_H + E_w + E_{mag} \\ &= LK_1 \sin^2 \varphi - LH M \cos \phi - \frac{1}{2} LN_e M^2 \cos^2 \varphi - \frac{1}{2} LN_h M^2 \sin^2 \varphi \end{aligned}$$

$$+ \sigma_w [1 - \cos \varphi]^2, \quad (16.64)$$

where  $\varphi$  is the angle between the magnetization  $M$  and the easy axis and  $H_e$  ( $H_h$ ) and  $N_e$  ( $N_h$ ) are the magnetic field and demagnetizing factor in the easy (hard) direction. The angle  $\phi$  between the magnetic field  $H$  and the magnetization  $M$  is  $\phi = \theta - \varphi$ , where  $\theta$  is the angle between the magnetic field and the easy axis. For equilibrium  $\frac{\partial E}{\partial \varphi} = 0$ , therefore

$$(K_1 + \frac{1}{2}N_e M^2 - \frac{1}{2}N_h M^2) \sin 2\varphi - 2HM \sin(\theta - \varphi) + \frac{\sigma_w}{L}(2 \sin \varphi - \sin 2\varphi) = 0. \quad (16.65)$$

Then  $\frac{\partial^2 E}{\partial \varphi^2} = 0$  implies

$$(K_1 + N_e M^2 - N_h M^2) \cos 2\varphi + HM \cos(\varphi - \theta) + \frac{\sigma_w}{L}(\cos \varphi - \cos 2\varphi) = 0. \quad (16.66)$$

Let  $\theta = 0$ , we obtain the coercive force in the easy axis as

$$H_c^{rot} = \frac{K_1}{M} + (N_e - N_h)M. \quad (16.67)$$

For the Néel wall, since  $N_e = N_h$ ,  $H_c^{rot}$  is independent on surface roughness. However, for the Bloch wall, since  $N_e = N_{zz} = 1 - 2N_{xx}$  and  $N_h = N_{xx}$ , we have

$$H_c^{rot} = \frac{K_1}{M} + (1 - 2N_{xx})M. \quad (16.68)$$

Clearly, as roughness increases, the rotational coercive force for the Bloch wall decreases.

## 16.4 Effect of Surface/Interface Roughness on Electronic Device Operations

As the dimension of the microelectronic devices shrinks, the effect of surface and interface properties of a material used in the fabrication will play a more important role. For example, for the thin film deposition case, if the dynamic roughening exists during the deposition, the ratio of the surface roughness to the film thickness would be proportional to  $d^{\beta-1}$ , where  $0 \leq \beta \leq 1$  is the growth exponent and  $d$  is the film thickness. Thus for a thinner film, the variation of thickness is much larger than that for a thicker film. Therefore, the effect of roughness will become more pronounced.

Ke Chen et al. demonstrated that the roughness of the polyimide substrate has a strong influence on the electrical properties and yields of thin  $TaO_x$  capacitors [16.51]. In their experiments, five different types of Kapton sheets (100E, 100V, 100HA, 200HA, and 2 mil PI) were used as the

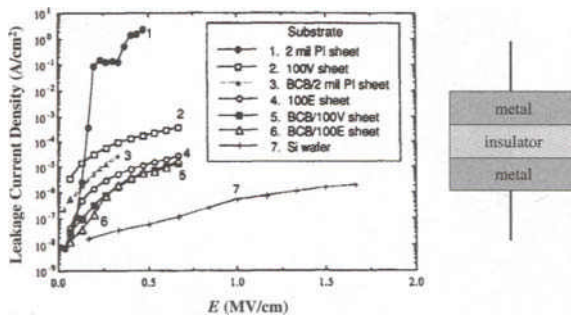


FIG. 16.13 Leakage current density versus applied field strength for the  $\text{TaO}_x$  thin film capacitors fabricated on different substrates (from Ref. [16.51]).

substrates. The test structures for all the substrates were the same metal-insulator-metal (MIM) structures as shown in Figure 16.13. The electrical measurements, such as current-voltage (I-V) and capacitance-voltage (C-V) characteristics, and the surface morphology of the substrates measured by AFM, SEM, and stylus profilometry, were analyzed. The typical leakage-current density versus applied field strength characteristics are given in Figure 16.13 for the different substrates used. Orders of magnitude difference in the leakage-current density were observed for  $\text{TaO}_x$  capacitors on different substrates. The capacitors fabricated on Si show the best performance with a 97% yield, the lowest leakage-current density ( $5 \times 10^{-8} \text{ A/cm}^2$  at 0.33 MV/cm), and excellent dielectric strength. The capacitors on the 2 mil PI sheet showed electrical properties with a wide spread in values and a 30% yield. Compared with capacitors on Si substrate, the leakage-current density was five orders of magnitude higher, and the dielectric breakdown occurred at a much lower applied field strength. Yields between 40% – 70% were obtained for capacitors fabricated on the other substrates, and the leakage-current densities were several orders of magnitude higher than those of the Si substrates. Both SEM and AFM studies showed different surface finishes on these substrates. There were many cone-like surface spikes on the 2 mil PI sheet. The largest structure had a height  $\sim 0.5 \mu\text{m}$  (which is larger than the thickness of  $\text{TaO}_x$  film) and a diameter  $\sim 27 \mu\text{m}$ . The 100V type sheet shows many straight ridges and grooves at the surface. The height of these surfaces is about 100 nm. The surface of the 100E type sheet looks very smooth, with a few surface protrusions having a height of 200 nm. Figure 16.14 shows the measured average roughness and protrusion peak-to-valley distance of these substrates by stylus profilometry. These results are consistent with the results obtained from AFM. The above analysis shows that the polyimide substrates have different surface finishes,

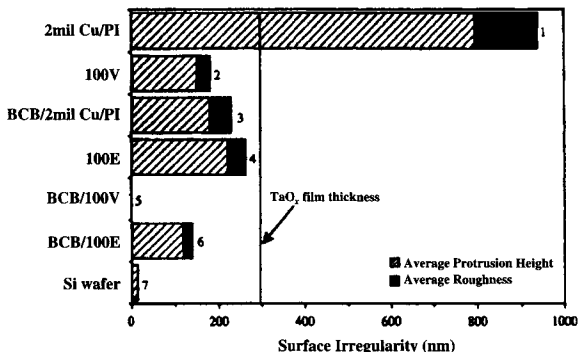


FIG. 16.14 The surface irregularities of the polyimide sheets studied using profilometry (from Ref. [16.51]).

and the surface irregularities or roughness may be a very important factor affecting the electrical properties of the  $\text{TaO}_x$  capacitors. In order to confirm this, BCB, a low-dielectric-constant organic material with a high degree of planarization, was used in an attempt to overcome the surface roughness associated with the sheets. Figure 16.14 also gives the resulting surface condition after BCB coating and curing measured by stylus profilometry. The surface roughness was reduced by more than 4 times for the 2 mil PI sheet and about 2 times for the 100E sheet after BCB coating. As seen from Figure 16.13, the  $\text{TaO}_x$  capacitors fabricated on the BCB-coated polyimide sheets show much improved capacitance properties as compared to their nonplanarized counterparts: more than two orders of magnitude reduction in leakage-current density, an increase in the breakdown field strength, and a large capacitor yield ( $\sim 90\%$ ). In order to illustrate clearly the effect of planarization, the leakage-current density measured at a field strength of 0.3 MV/cm for each substrate is correlated to the protrusion height measured by profilometry in Figure 16.15. Obviously, the reduction of leakage-current density is closely related to the decrease of the surface roughness.

Hegde et al. studied the effect of silicon substrate microroughness on the quality of the gate oxide [16.52]. They fabricated MOS capacitors with an area of  $62,500 \mu\text{m}^2$  on 125 mm, *n*-type silicon (100) wafers. After removing the sacrificial oxide in 10:1 buffered oxide etch (BOE), the Si wafers had an RMS roughness  $w < 0.2 \text{ nm}$ . These Si wafers were then wet-etched for various times in a 750:1  $\text{HNO}_3:\text{HF}$  solution at room temperature to intentionally roughen the substrates. Gate oxides of 15 nm thickness were grown at  $900^\circ\text{C}$  in  $\text{O}_2$  with 3 HCl. Figure 16.16 is the plot of the RMS roughness of both the Si substrate and the gate oxide surface as a function of Si etch

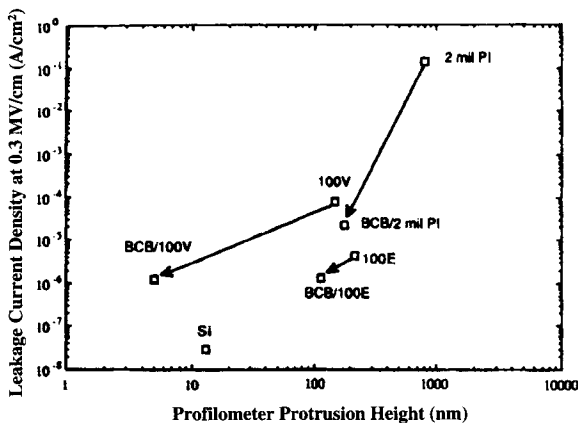


FIG. 16.15 Leakage current densities of capacitors fabricated on various polyimide sheets correlated to substrate protrusion height as measured by profilometry. The arrows indicate the improvement of electrical-testing results and surface-defect heights upon substrate surface planarization using BCB (from Ref. [16.51]).

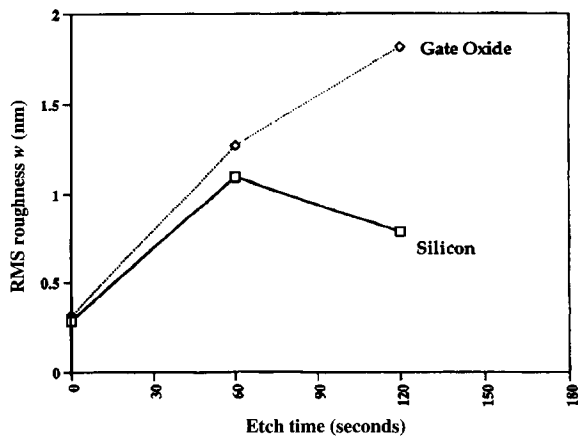


FIG. 16.16 The RMS roughness of the Si substrate and the top gate oxide film as a function of Si etch time (from Ref. [16.52]).

time. The extended etch (120 s) leaves the gate oxide surface rough. Figure 16.17 shows the average electric field required to maintain a fixed current density of  $1.5 \times 10^{-5} \text{ A/cm}^2$  as a function of gate oxide roughness. For the case of electron injection from the polysilicon, the average electrical field is found to decrease with an increase of the gate oxide surface roughness. The substrate injection field strength is stable for  $w$  values below 0.70 nm. They attributed the enhanced tunneling with increased microroughness to more

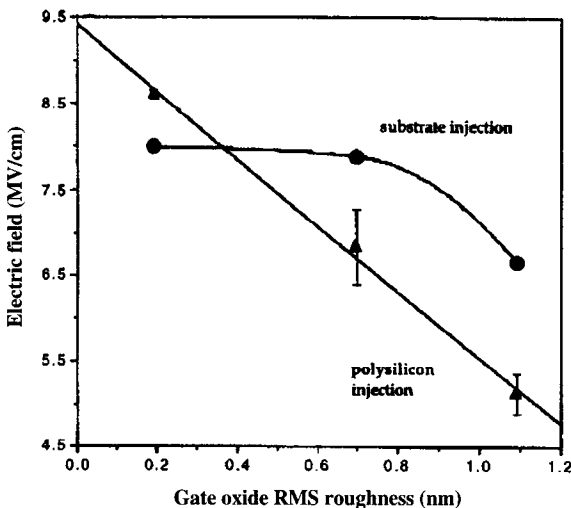


FIG. 16.17 The relationship between the surface roughness and the Fowler - Nordheim average field strength (from Ref. [16.52]).

efficient injection at the tips of the asperities due to local field enhancement. Chin et al. studied the effect of native oxide on the quality of gate oxide [16.53]. They used HF-vapor passivation in conjunction with an H<sub>2</sub> bake to reduce the formation of native oxide and lower the thermal budget. They showed that RMS roughness of the 2.7-nm gate oxide with HF-vapor treatment and in situ H<sub>2</sub> bake is 0.01 nm, whereas for a control sample the RMS roughness is 0.29 nm. The electrical properties of the thin gate oxide also improved. Figure 16.18 shows the measured I-V characteristics of the MOS diodes with a 2.7-nm oxide. A reduced leakage-current density at low voltages (< 0.5 V) was observed for the sample with HF-vapor treatment and in situ H<sub>2</sub> bake.

In the following we will present a quantitative study of metal/dielectric interface roughness effects on the electric field, capacitance, and leakage current within a thin film capacitor [16.54].

#### 16.4.1 Electric potential and electric field of a capacitor with a single rough boundary

Consider a parallel-plate capacitor with one rough electrode surface at potential  $V$  and one smooth electrode surface (substrate) at zero potential, as shown in Figure 16.19. Here  $\epsilon$  is the dielectric constant of the filling material,  $d$  is the average thickness, and  $h(x, y)$  is the surface height fluctuation. In order to calculate the electrostatic potential, one needs to solve

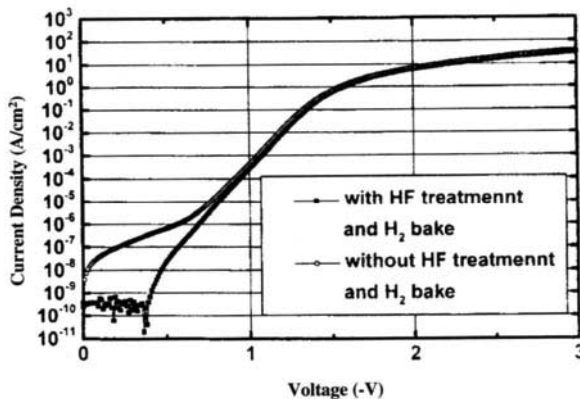


FIG. 16.18 I-V characteristics of the 27 Å oxide (a) with and (b) without the HF-vapor treatment and H<sub>2</sub> bake (from Ref. [16.53]).

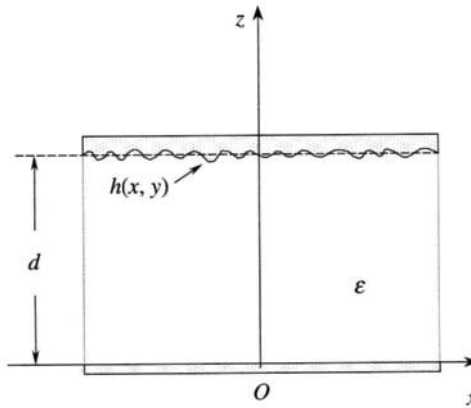


FIG. 16.19 Schematic of a parallel plate capacitor with a rough boundary. The  $\epsilon$  is the dielectric constant of the filling material,  $d$  is the average thickness of the dielectric, and  $h(x, y)$  is the fluctuation of the thickness (from Ref. [16.54]).

the Laplace equation between the capacitor planes

$$\nabla^2 \Phi(x, y, z) = 0, \quad (16.69)$$

that obeys the boundary conditions

$$\Phi(x, y, z = 0) = 0, \quad (16.70)$$

and

$$\Phi(x, y, z = f(x, y)) = V. \quad (16.71)$$

Here  $\Phi$  is the electrostatic potential and  $z = f(x, y)$  is the rough electrode surface. If we assume that  $f(x, y) = d + \epsilon h(x, y)$ , where  $\epsilon \ll 1$ , then we can apply a perturbation method for the potential on the rough boundary to solve the Laplace equation, Equation (16.69). Thus, the boundary condition Equation (16.71) can be expanded as a Taylor series in the form:

$$\Phi(x, y, d) + \Phi_z(x, y, d)\epsilon h(x, y) + \frac{1}{2!}\Phi_{zz}(x, y, d)\epsilon^2 h^2(x, y) + \dots = V, \quad (16.72)$$

where  $\Phi_z = \frac{\partial \Phi}{\partial z}$ ,  $\Phi_{zz} = \frac{\partial^2 \Phi}{\partial z^2}$ , and so on. We also assume that the potential takes a similar perturbing form

$$\Phi(x, y, z) = \Phi^{(0)}(x, y, z) + \epsilon \Phi^{(1)}(x, y, z) + \epsilon^2 \Phi^{(2)}(x, y, z) + \dots \quad (16.73)$$

Substituting Equation (16.73) into Equation (16.69), we find that, for any order of perturbation,  $\Phi^{(n)}(x, y, z)$  satisfies the Laplace equation

$$\nabla^2 \Phi^{(n)}(x, y, z) = 0. \quad (16.74)$$

Furthermore, the boundary conditions for various orders of perturbation are:

*Zeroth order:*

$$\begin{aligned} \Phi^{(0)}(x, y, z=0) &= 0; \\ \Phi^{(0)}(x, y, z=d) &= V, \end{aligned} \quad (16.75)$$

which yields the solution

$$\Phi^{(0)}(x, y, z) = \frac{Vz}{d}. \quad (16.76)$$

*First order:*

$$\begin{aligned} \Phi^{(1)}(x, y, z=0) &= 0; \\ \Phi^{(1)}(x, y, z=d) &= -h(x, y)\Phi_z^{(0)}(x, y, d). \end{aligned} \quad (16.77)$$

*Second order:*

$$\begin{aligned} \Phi^{(2)}(x, y, z=0) &= 0; \\ \Phi^{(2)}(x, y, z=d) &= -h(x, y)\Phi_z^{(1)}(x, y, d) - \frac{1}{2}h^2(x, y)\Phi_{zz}^{(0)}(x, y, d). \end{aligned} \quad (16.78)$$

For a perturbation higher than the first order, we can employ the Fourier transform technique to solve the Laplace equation with boundary conditions similar to Equations (16.77) and (16.78).

$$\nabla^2 \Phi^{(n)}(x, y, z) = \frac{\partial^2}{\partial z^2} \Phi^{(n)}(x, y, z) + \nabla_r^2 \Phi^{(n)}(x, y, z) = 0, \quad (16.79)$$

where  $\mathbf{r} = (x, y)$  represents the position vector in the  $x$ - $y$  plane. Performing a Fourier transform in the  $x$ - $y$  plane according to the following equations, we obtain

$$\tilde{\Phi}^{(n)}(\mathbf{q}, z) = \frac{1}{(2\pi)^2} \int \Phi^{(n)}(\mathbf{r}, z) e^{i\mathbf{q}\cdot\mathbf{r}} d\mathbf{r}, \text{ and} \quad (16.80)$$

$$\Phi^{(n)}(\mathbf{r}, z) = \int \tilde{\Phi}^{(n)}(\mathbf{q}, z) e^{-i\mathbf{q}\cdot\mathbf{r}} d\mathbf{q}. \quad (16.81)$$

Then the Laplacian equation takes the form:

$$\frac{\partial^2 \tilde{\Phi}^{(n)}(\mathbf{q}, z)}{\partial z^2} - k^2 \tilde{\Phi}^{(n)}(\mathbf{q}, z) = 0. \quad (16.82)$$

The general solution of Equation (16.82) can be put in the form

$$\tilde{\Phi}^{(n)}(\mathbf{q}, z) = A^{(n)}(\mathbf{q}) e^{qz} + B^{(n)}(\mathbf{q}) e^{-qz}. \quad (16.83)$$

Applying the boundary condition at  $z = 0$ , one has

$$A^{(n)}(\mathbf{q}) = -A^{(n)}(\mathbf{q}), \quad (16.84)$$

which alternatively implies that

$$\tilde{\Phi}^{(n)}(\mathbf{q}, z) = 2A^{(n)}(\mathbf{q}) \sinh(qz). \quad (16.85)$$

The  $A^{(n)}(\mathbf{q})$  can be determined by the boundary condition at  $z = h_0$ . For the first-order perturbation we find the potentials in Fourier and real spaces, respectively, to be

$$\tilde{\Phi}^{(1)}(\mathbf{q}, z) = -\frac{V}{d} \frac{\sinh(qz)}{\sinh(qd)} \tilde{h}(\mathbf{q}), \text{ and} \quad (16.86)$$

$$\Phi^{(1)}(\mathbf{r}, z) = -\frac{V}{d} \int \frac{\sinh(qz)}{\sinh(qd)} \tilde{h}(\mathbf{q}) e^{-i\mathbf{q}\cdot\mathbf{r}} d\mathbf{q}. \quad (16.87)$$

Similarly, by using the property of convolution of the Fourier transform for the second-order perturbation, we obtain

$$\tilde{\Phi}^{(2)}(\mathbf{q}, z) = \frac{V}{d} \int \frac{\cosh(q'd) \sinh(qz)}{\sinh(q'd) \sinh(qd)} q' \tilde{h}(\mathbf{q}') \tilde{h}(\mathbf{q} - \mathbf{q}') d\mathbf{q}', \text{ and} \quad (16.88)$$

$$\begin{aligned} \Phi^{(2)}(\mathbf{r}, z) &= \frac{V}{d} \int \left[ \int \frac{\cosh(qd) \sinh(qz)}{\sinh(q'd) \sinh(qd)} q' \tilde{h}(\mathbf{q}') \tilde{h}(\mathbf{q} - \mathbf{q}') d\mathbf{q}' \right] \\ &\quad \times e^{-i\mathbf{q}\cdot\mathbf{r}} d\mathbf{q}. \end{aligned} \quad (16.89)$$

If we set  $\epsilon = 1$ , then the average electrostatic potential between two plates (electrodes) can be approximated by

$$\langle \Phi \rangle \approx \langle \Phi^{(0)}(\mathbf{r}, z) \rangle + \langle \Phi^{(1)}(\mathbf{r}, z) \rangle + \langle \Phi^{(2)}(\mathbf{r}, z) \rangle. \quad (16.90)$$

According to Equations (16.87), (16.89), and (16.9), Equation (16.90) can be simplified as

$$\langle \Phi \rangle \approx \Phi^{(0)} + \langle \Phi^{(2)} \rangle, \quad (16.91)$$

where

$$\Phi^{(0)} = \frac{Vz}{d}, \text{ and } \langle \Phi^{(2)} \rangle = \frac{(2\pi)^4 Vz}{A_0 d^2} \int_{q_l}^{q_h} \frac{\cosh(q'd)}{\sinh(q'd)} q' P(q') dq'. \quad (16.92)$$

Equation (16.91) shows that surface roughness causes an additional potential  $\langle \Phi^{(2)} \rangle$  across the film, and this additional potential is still proportional to the distance  $z$  from the bottom plate. Therefore, the effect of roughness increases the effective potential  $\langle \Phi \rangle$  between the two plates. As a result, the average electric field increases (where the average transverse fields are zero):

$$\langle \mathbf{E}(\mathbf{r}, z) \rangle = -\langle \nabla \Phi \rangle \approx \mathbf{E}^{(0)} + \langle \mathbf{E}^{(2)} \rangle, \quad (16.93)$$

where

$$\mathbf{E}^{(0)} = -\hat{e}_3 \frac{V}{d}, \text{ and } \langle \mathbf{E}^{(2)} \rangle = \hat{e}_3 \frac{(2\pi)^4 V}{Ad^2} \int_{q_l}^{q_h} \frac{\cosh(q'd)}{\sinh(q'd)} q' P(q') d\mathbf{q}', \quad (16.94)$$

with  $\hat{e}_3$  being the unit vector in the  $z$  direction. Thus, surface roughness increases the average electric field inside the insulating film or, in other words, the effective thickness of the insulating film decreases. Substituting Equation (3.16) into Equation (16.94), and normalizing  $w$ ,  $\xi$ , and  $q'$  by  $d$  as  $\Delta = w/d$ ,  $L = \xi/d$ , and  $q = q'd$ , respectively, Equation (16.93) becomes

$$\frac{\langle E \rangle}{E^{(0)}} = 1 + \Delta^2 L^2 \int \frac{q^2 \coth(q)}{(1 + \alpha L^2 q^2)^{1+\alpha}} dq. \quad (16.95)$$

Equation (16.95) clearly shows that roughness increases the average electric field in the film. The increased field is proportional to the square of interface width  $w$  and also has a complicated relationship with both the lateral correlation length  $\xi$  and the roughness exponent  $\alpha$ . Figure 16.20 shows the dependence of the electric field ratio  $\langle E \rangle / E^{(0)}$  on the normalized lateral correlation length  $L$  for various roughness exponents  $\alpha$  at a fixed  $\Delta = 0.01$ . For a fixed roughness exponent  $\alpha$ , as  $L$  increases, the electric field ratio  $\langle E \rangle / E^{(0)}$  decreases, but remains larger than 1. At very large  $L$ , the

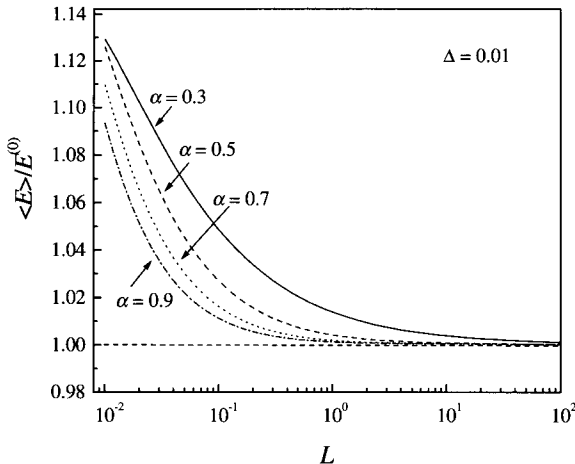


FIG. 16.20 Semilog plot of the ratio of electrostatic fields  $\langle E \rangle / E^{(0)}$  as a function of the normalized lateral correlation length  $L (= \xi/d)$  for  $\Delta (= w/d) = 0.01$ , and  $\alpha = 0.3, 0.5, 0.7$ , and  $0.9$  (from Ref. [16.54]).

surface essentially becomes very smooth, and the roughness has no effect on the electric field. For a fixed  $L$ , as  $\alpha$  decreases, the electric field ratio increases. For  $L \ll 1$  and  $\alpha = 0.3$ , the electric field  $\langle E \rangle$  can increase to about 15% of  $E^{(0)}$ . This seems insignificant. Notice that the RMS roughness  $w$  is only 1% of the thickness for this case. The change of electric field will be more significant for ultrathin dielectric films where  $\Delta$  is much larger than 0.01 for the same value of  $w$ .

#### 16.4.2 Roughness effects on capacitance with one rough electrode

The surface charge density  $\sigma$  on a rough capacitor plate is given by  $\sigma = \epsilon \mathbf{E} \cdot \hat{n}$  with  $\hat{n} = (\nabla h - \hat{e}_3)/[1 + (\nabla h)^2]^{1/2}$  being the unit vector normal to a rough surface plate at  $z = d + h(\mathbf{r})$ . Within the second-order perturbation expansion and an ensemble average over possible roughness configurations, the average capacitance,

$$\langle C \rangle = \langle Q \rangle / V = \frac{1}{V} \int \langle \sigma \rangle ds, \quad (16.96)$$

is given by

$$\begin{aligned} \langle C \rangle &= \frac{A_0 \epsilon}{d} \left\{ 1 + \frac{1}{A_0} \int [\langle h \nabla^2 h \rangle + \langle (\nabla h)^2 \rangle] d\mathbf{r} \right. \\ &\quad \left. + \frac{(2\pi)^4}{A_0 d} \int \coth(q'd) q' P(q') d\mathbf{q}' \right\}. \end{aligned} \quad (16.97)$$

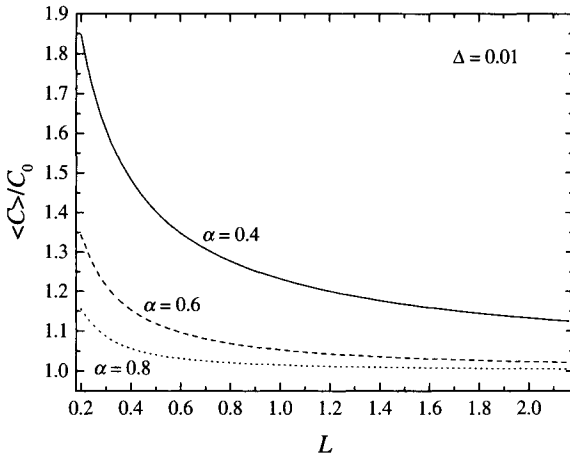


FIG. 16.21 Capacitance ratio  $\langle C \rangle / C_0$  as a function of the normalized lateral correlation length  $L$  ( $= \xi/d$ ) for  $\Delta (= w/d) = 0.01$ , and  $\alpha = 0.4, 0.6$ , and  $0.8$  (from Ref. [16.54]).

Substituting the following Fourier transform,

$$\int \langle (\nabla h)^2 \rangle d\mathbf{r} = \int \langle h \nabla^2 h \rangle d\mathbf{r} = \frac{(2\pi)^4}{A_0} \int_{q_l}^{q_h} q'^2 P(q') d\mathbf{q}', \quad (16.98)$$

into Equation (16.97) gives

$$\frac{\langle C \rangle}{C_0} = 1 + \frac{2(2\pi)^4}{A_0^2} \int_{q_l}^{q_h} q'^2 P(q') d\mathbf{q}' + \frac{(2\pi)^4}{A_0 d} \int \coth(q'd) q' P(q') d\mathbf{q}', \quad (16.99)$$

where  $C_0$  is the capacitance for a smooth plate. To calculate morphology effects on  $\langle C \rangle$  using Equation (16.99), one needs knowledge of the roughness spectrum. The excess capacitance due to surface roughness depends on the RMS roughness  $w$  as  $\langle C \rangle - C_0 \sim w^2$  because  $\langle P(q') \rangle \sim w^2$ .

Figure 16.21 shows the calculated capacitance ratio  $\langle C \rangle / C_0$  as a function of the normalized lateral correlation length  $L$  for various roughness exponents  $\alpha$ . As the roughness exponent decreases (rougher surface at short wavelengths or  $< \xi >$ ) the roughness contributions drastically increase the capacitance by more than 30% for small roughness exponents  $\alpha < 0.5$  and a moderate roughness parameter ratio  $w/\xi \sim 0.01$  close to the weak-roughness limit. In fact, as the roughness exponent  $\alpha$  decreases or the ratio  $w/\xi$  increases, the area of the rough capacitor plate increases. This leads effectively to a larger charge storage. Therefore, nanoscale surface roughness can drastically increase capacitance characteristics, altering microelectronic device operations and characteristics.

### 16.4.3 Roughness effects on leakage currents in a capacitor with one rough electrode

Since the surface roughness can alter the average electrostatic field, it can also alter the leakage current of an insulating film. Independent of the mechanism that causes the leakage current, the leakage-current density typically has an exponential relationship with the electric field. Therefore, the higher the field is, the higher the leakage-current density is. For a rough electrode, due to the fluctuation of the surface height, the local electric field will vary from place to place as we have derived in Equation (16.93). At the peak of a rough surface, the electric field is larger than the valley, and we expect the leakage-current density at the peak to be higher than that at the valley. If the leakage-current density was proportional only to the electric field, then the average leakage current would show very little effect due to surface roughness. However, as the leakage-current density changes exponentially with the electric field, the leakage current at the peak will gain more than that lost at the valley. Therefore, the net effect of surface roughness is to increase the leakage-current density, even though other conditions are kept the same. In the following we take two conduction mechanisms, Schottky emission and the Poole-Frenkel effect, as examples to show how the surface roughness affects the leakage-current density. Other conduction mechanisms follow a similar method.

- (1) Schottky emission: This type of conduction over the potential barrier of a metal/insulator interface is analogous to the thermionic emission except the difference that the applied electric field lowers the barrier height of the interface. The emission current density is given by [16.55, 16.56, 16.57, 16.58]

$$J_{sc} = A_s T^2 e^{-\Phi_s/k_B T} e^{\beta_s \sqrt{E}/k_B T}, \quad (16.100)$$

with  $A_s (= 120 \text{ A}/\text{deg}\cdot\text{cm}^2)$  being the Dushman-Richardson constant,  $T$  is the absolute temperature,  $\Phi_B$  is the Schottky potential barrier (depending on, e.g., metal work function, surface states, image forces, etc.) at the interface,  $k_B$  is the Boltzmann constant,  $\beta_s = e^{3/2}/\sqrt{4\pi\varepsilon\varepsilon_0}$ , and  $\varepsilon_0$  is the permittivity of the vacuum [16.56, 16.57, 16.58].

- (2) Poole-Frenkel effect: This effect is characterized by a mechanism similar to that of the Schottky effect, except that a field is applied to excite the thermal electrons from traps into the conduction band of an insulator [16.55, 16.56, 16.57, 16.58]. The resulting current density has the form

$$J_{pf} = \mu E e^{-\Phi_s/2k_B T} e^{2\beta_s \sqrt{E}/k_B T}, \quad (16.101)$$

where  $\mu$  is the conductivity, and the barrier lowered by an applied field is twice of that observed in Schottky emission. This is due to the immobility of positive charges associated with the traps.

In both cases, the main roughness contribution to a leakage current arises from the exponential dependence of the current, where the  $z$  component of the electric field (altered by roughness) yields the dominant effect. Thus, by making an expansion of the electric field  $E$  in Equations (16.100) and (16.101), we obtain the final leakage-current formulas that incorporate roughness effects to the second-order perturbation theory:

For Schottky emission assuming  $\langle E^{(2)} \rangle / E^{(0)} \ll 1$ , we obtain

$$\frac{\langle J_{sc} \rangle}{J_{sc}^0} = \exp\left(\frac{\beta_s \sqrt{E^{(0)}}}{2k_B T} \frac{\langle E^{(2)} \rangle}{E^{(0)}}\right), \quad (16.102)$$

where  $J_{sc}^0 = A_s T^2 e^{-\Phi_s/k_B T} e^{\beta_s \sqrt{E^{(0)}}/k_B T}$ , is the unperturbed leakage-current density for a smooth metal/insulator interface, and the ratio  $\langle E^{(2)} \rangle / E^{(0)}$  can be obtained from Equation (16.94).

For the Poole-Frenkel effect we obtain

$$\frac{\langle J_{pf} \rangle}{J_{pf}^0} = \left(1 + \frac{\langle E^{(2)} \rangle}{E^{(0)}}\right) \exp\left(\frac{\beta_s \sqrt{E^{(0)}}}{k_B T} \frac{\langle E^{(2)} \rangle}{E^{(0)}}\right), \quad (16.103)$$

with  $J_{pf}^0 = \mu E^{(0)} e^{-\Phi_s/2k_B T} e^{2\beta_s \sqrt{E^{(0)}}/k_B T}$  being the unperturbed leakage-current density for a smooth metal/insulator interface.

Equations (16.102) and (16.103) are very similar. From the discussion of the electric field, we learn that  $\langle E^{(2)} \rangle \propto w^2$ . Therefore, we expect that the leakage current density increases exponentially with  $w^2$ . Also since  $\langle E^{(2)} \rangle$  decreases monotonically with increasing normalized lateral correlation length  $L$  and increasing roughness exponent  $\alpha$ , we would expect a similar behavior in the leakage current density. Figure 16.22 shows the dependence of the Schottky and Poole-Frenkel leakage-current densities on the normalized lateral correlation length  $L$  for various values of  $\alpha$  at  $\Delta = 0.01$ . In both cases our calculations were performed for an insulating film with relatively low permittivity  $\epsilon = 3.9$  (which corresponds to  $\text{SiO}_2$ ) and a field strength  $E^{(0)} = 10^8 \text{ V/m}$  at room temperature  $T = 300 \text{ K}$ . We see that Figure 16.22 has a similar behavior as Figure 16.20, as expected. The only difference between the Schottky emission and the Poole-Frenkel effect is that for the same rough surface the leakage-current density in the Poole-Frenkel effect is higher than that in the Schottky emission. We plot in Figure 16.23 the leakage-current density ratio as a function of the normalized interface width  $\Delta$  for (a)  $L = 10$  and (b)  $L = 1$  at different

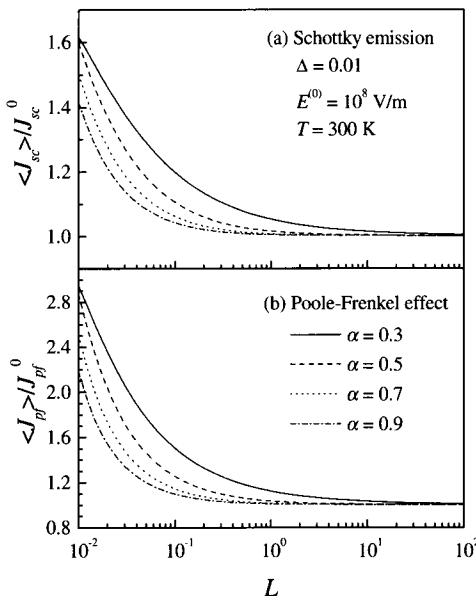


FIG. 16.22 Semilog plot of the leakage-current density ratio for (a) Schottky emission and (b) the Poole-Frenkel effect as a function of the normalized lateral correlation length  $L (= \xi/d)$  for  $\Delta (= w/d) = 0.01$ ,  $E^{(0)} = 10^8$  V/m,  $T = 300$  K, and roughness exponent  $\alpha = 0.3, 0.5, 0.7$ , and  $0.9$  (from Ref. [16.54]).

roughness exponent  $\alpha$  values. The field strength  $E^{(0)} = 10^8$  V/m. Clearly the leakage current increases drastically with the increase of the normalized interface width  $\Delta$ . For a relatively smooth surface  $L = 10$ , the leakage-current density can be almost 30 times greater at  $\Delta > 0.1$  and  $\alpha = 0.3$  [see Figure 16.23(a)]. However, as  $L$  decreases, the effect of interface width  $w$  becomes even more significant as shown in Figure 16.23(b). It is also interesting to notice that even for the same rough surface, the change of the applied field strength  $E^{(0)}$  will also change the degree of the roughness effect. Figure 16.24 shows the leakage-current density ratio as a function of the applied field strength  $E^{(0)}$  for (a)  $L = 10$  and (b)  $L = 1$  at  $\Delta = 0.01$ . The ratio increases as  $E^{(0)}$  increases, but the effect is not so significant under the condition  $\Delta = 0.01$  that we considered in Figure 16.24.

The above treatments for both the capacitance and the leakage current are based on a mean-field point of view. There are still some open questions. For the capacitance, in practice the size of the electrode cannot be infinite. In this case one needs to consider the edge effect of the capacitance. In general the edge effect will contribute a geometric factor, which tends to increase the capacitance. If the size of the electrode is much larger than

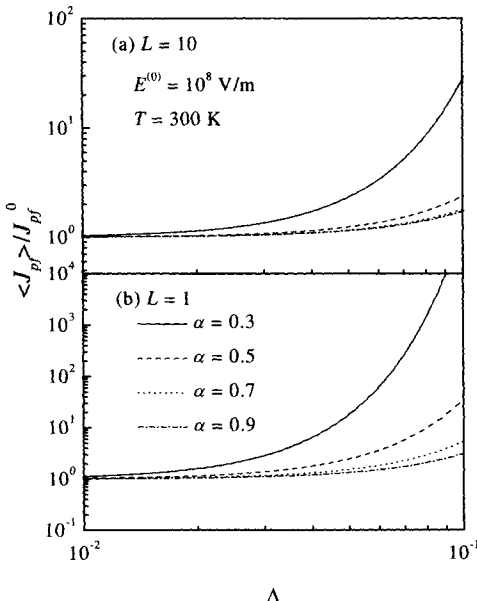


FIG. 16.23 The leakage-current density ratio  $<J_{pf}>/J_{pf}^0$  for the Poole-Frenkel effect as a function of the normalized RMS roughness  $\Delta$  for (a)  $L = 10$  and (b)  $L = 1$  in log-log scale at  $E^{(0)} = 10^8$  V/m,  $T = 300$  K, and roughness exponent  $\alpha = 0.3, 0.5, 0.7$ , and  $0.9$ . Here  $L = \xi/d$  and  $\Delta = w/d$  (from Ref. [16.54]).

the lateral correlation of the rough electrode, we would expect a similar behavior of capacitance as in the infinite-electrode case. However, if the electrode size is smaller than the lateral correlation length of the rough electrode, since only limited spatial frequencies from the roughness will contribute to the capacitance, then the total contribution from the rough surface will decrease. This is only a simple extrapolation from our above discussion. Detailed behavior can be obtained by considering a finite size capacitor bounded by one rough electrode [16.59].

Another issue is the critical breakdown field strength  $E_c$  under the presence of surface roughness. We have shown that surface roughness will increase the field  $E^{(0)}$  to the effective electric field by  $E^{(0)} + < E^{(2)} >$  inside the insulating film. If we assume that the critical field for an insulating film is fixed, then the presence of surface roughness will reduce the breakdown field by a value of  $< E^{(2)} >$ . This intuitive discussion may work fine for a thermal breakdown, because in order to induce the breakdown, the heat generated by the electric field cannot be localized. However, for a pure electrical breakdown, a localized breakdown may happen first, especially at the peak of a rough surface. This localized breakdown requires only a much

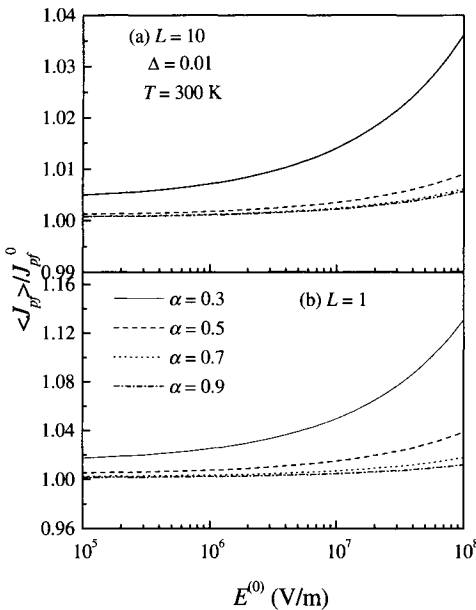


FIG. 16.24 Semilog plot of the leakage-current density ratio  $\langle J_{pf} \rangle / J_{pf}^0$  for Poole-Frenkel effect as a function of the apparent field strength  $E^{(0)}$  for (a)  $L = 10$  and (b)  $L = 1$  at  $\Delta = 0.01$ ,  $T = 300$  K, and roughness exponent  $\alpha = 0.3, 0.5, 0.7$ , and  $0.9$ . Here  $L = \xi/d$  and  $\Delta = w/d$  (from Ref. [16.54]).

smaller electric field,  $E^{(0)}$ , and opens conducting channels from the upper electrode to the lower electrode. As the field increases, those channels become wider and wider. These opened channels will definitely enhance the electric fields in the vicinities of the peaks, and therefore at a certain field strength they cause a global breakdown. Detailed investigation of such a behavior is still not available.

We have to point out that in actual experimental situations the conduction mechanism may have a more complex behavior. It has been observed that in crystalline and amorphous films (deposited on  $\text{SiO}_2/n\text{-Si}$  substrates) with a relatively high dielectric constant  $\epsilon \approx 31$ , under a moderate field ( $10^7$  V/m –  $3.5 \times 10^7$  V/m), the conduction processes are electrode-limited (Schottky emission), while under higher fields ( $> 3.5 \times 10^7$  V/m) conduction processes are bulk-limited (Poole-Frenkel emission) [16.60, 16.61, 16.62]. As shown in Figure 16.22, one would expect that the roughness would have different impacts on the leakage currents.

## 16.5 Summary

In this chapter, we discussed some examples of the effects of surface/interface roughness on the magnetic and electric properties of thin solid films. There are other effects on different physical phenomena with the presence of rough surfaces, such as wetting [16.63, 16.64, 16.65, 16.66], mechanical contact and tribology [16.67, 16.68], tunneling [16.69, 16.70, 16.71], and so on, that we did not cover.

## References

- 16.1 G. Palasantzas, "Static and dynamic aspects of the rms local slope of growing random surfaces," *Phys. Rev. E* **56**, 1254 (1997).
- 16.2 G. Palasantzas, "Roughness effects on the thermal stability of thin films," *J. Appl. Phys.* **81**, 246 (1997).
- 16.3 K. Fuchs, "The conductivity of thin metallic films according to the electron theory of metals," *Proc. Cambridge Philos. Soc.* **34**, 100 (1938).
- 16.4 E. H. Sondheimer, "The mean free path of electrons in metals," *Adv. Phys.* **1**, 1 (1952).
- 16.5 J. M. Ziman, *Electrons and Phonons – The Theory of Transport Phenomena in Solids* (Oxford, London, 1960).
- 16.6 Y. Namba, "Resistivity and temperature coefficient of thin metal films with rough surface," *Jpn. J. Appl. Phys.* **9**, 1326 (1970).
- 16.7 C. R. Tellier and A. J. Tosser, *Size Effects in Thin Film* (Elsevier, Amsterdam, 1982).
- 16.8 V. B. Sandomirskii, "Quantum size effect in a semimetal film," *Soviet Physics JETP* **25**, 101 (1967).
- 16.9 G. Govindaraj and V. Devanathan, "Quantum size effect in thin metal films," *Phys. Rev. B* **34**, 5904 (1986).
- 16.10 K. M. Leung, "Electrical resistivity of metallic thin films with rough surfaces," *Phys. Rev. B* **30**, 647 (1984).
- 16.11 Z. Tešanović, M. V. Jarić, and S. Maekawa, "Quantum transport and surface scattering," *Phys. Rev. Lett.* **57**, 2760 (1986).
- 16.12 N. Trivedi and N. W. Ashcroft, "Quantum size effects in transport properties of metallic films," *Phys. Rev. B* **38**, 12298 (1988).
- 16.13 G. Fishman and D. Calecki, "Surface-induced resistivity of ultrathin metallic films: a limited law," *Phys. Rev. Lett.* **62**, 1302 (1989).
- 16.14 J. C. Hensel, R. T. Tung, J. M. Poate, and F. C. Unterwald, "Specular boundary scattering and electrical transport in single-crystal thin films of CoSi<sub>2</sub>," *Phys. Rev. Lett.* **54**, 1840 (1985).
- 16.15 H. Sakaki, T. Noda, K. Hirakawa, M. Tanaka, and T. Matsusue, "Interface roughness scattering in GaAs/AlAs quantum wells," *Appl. Phys. Lett.* **51**, 1934 (1987).
- 16.16 M. S. P. Lucas, "Surface scattering of conduction electrons in gold films," *Appl. Phys. Lett.* **4**, 73 (1963).
- 16.17 M. S. P. Lucas, "Size effects in double-layer metallic films," *Thin Solid Films* **170**, 435 (1971).
- 16.18 K. L. Chopra, L. C. Bobb, and M. H. Frnancome, "Electrical resistivity of thin single-crystal gold films," *J. Appl. Phys.* **34**, 1699 (1963).

- 16.19 K. L. Chopra, "Electrical resistivity of silver films at low temperatures," *Phys. Lett.* **15**, 73 (1965).
- 16.20 D. C. Larsen and B. T. Boiko, "Electrical resistivity of thin epitaxially grown silver films," *Appl. Phys. Lett.* **5**, 155 (1964).
- 16.21 B. Fischer and G. von Minnigerode, "A direct indication for specular reflection of conduction electrons at the vacuum boundary of metal films," *Z. Phys. B* **42**, 349 (1981).
- 16.22 J. W. C. Devries, "Temperature and thickness dependence of the resistivity of thin polycrystalline aluminium, cobalt, nickel, palladium, silver and gold films," *Thin Solid Films* **167**, 25 (1988).
- 16.23 A. V. Danilov, S. E. Kubatkin, I. L. Landau, I. A. Parshin, and L. Rinderer, "Insulating modifications in cold deposited films of metals," *Chinese J. Phys.* **36**, 428 (1998).
- 16.24 H. Hoffmann and G. Fischer, "Electrical conductivity in thin and very thin platinum films," *Thin Solid Films* **58**, 25 (1979).
- 16.25 G. Fischer and H. Hoffmann, "Oscillations of the electrical conductivity with film thickness in very thin platinum films," *Solid State Commun.* **35**, 793 (1980).
- 16.26 D. Schumacher and D. Stark, "Electrical conduction in superimposed metal films," *Surf. Sci.* **123**, 384 (1982).
- 16.27 D. Schumacher, *Surface Scattering Experiments with Conduction Electrons* (Springer-Verlag, Heidelberg, 1993).
- 16.28 M. Jalochowski and E. Bauer, "Quantum size and surface effects in the electrical resistivity and high-energy electron reflectivity of ultrathin lead films," *Phys. Rev. B* **38**, 5272 (1988).
- 16.29 M. Jalochowski, E. Bauer, H. Knoppe, and G. Lilienkamp, "Experimental evidence for quantum-size-effect fine structures in the resistivity of ultrathin Pb and Pb-In films," *Phys. Rev. B* **45**, 13607 (1992).
- 16.30 M. Jalochowski, M. Hoffmann, and E. Bauer, "Quantized Hall effect in ultrathin metallic films," *Phys. Rev. Lett.* **76**, 4227 (1996).
- 16.31 M. Jalochowski and E. Bauer, "Resistance oscillations and cross-over in ultrathin gold films," *Phys. Rev. B* **37**, 8622 (1988).
- 16.32 E. Z. Luo, S. Heun, M. Kennedy, J. Wollschläger, and M. Henzler, "Surface roughness and conductivity of thin Ag films," *Phys. Rev. B* **49**, 4858 (1994).
- 16.33 A. Kaser and E. Gerlach, "Scattering of conduction electrons by surface roughness in thin metal films," *Z. Phys. B* **97**, 139 (1995).
- 16.34 V. I. Malyutin, V. E. Osukhovskii, Yu. D. Vorobiev, A. G. Shishkov, and V. V. Yudin, "Structure and magnetic properties of etched NiFeCo films," *Physica Status Solidi A* **65**, 45 (1981).
- 16.35 S. Vilain, J. Ebothe, and M. Troyon, "Surface roughness and composition effects on the magnetic properties of electrodeposited Ni-Co alloys," *J. Magn. Magn. Mater.* **157**, 274 (1996).
- 16.36 J.-H. Kim and S.-C. Shin, "High coercivity in Co/Pt multilayers," *Jpn. J. Appl. Phys. Part 1* **35**, 342 (1996).
- 16.37 M. Li, G.-C. Wang, and H.-G. Min, "Effect of surface roughness on magnetic properties of Co films on plasma-etched Si(100) substrates," *J. Appl. Phys.* **83**, 5313 (1998).
- 16.38 M. Li, Y.-P. Zhao, G.-C. Wang, and H.-G. Min, "Effect of surface roughness on magnetization reversal of Co films on plasma-etched Si(100) substrates," *J. Appl. Phys.* **83**, 6287 (1998).
- 16.39 Q. Jiang, H.-N. Yang, and G.-C. Wang, "Effect of interface roughness on hysteresis loops of ultrathin Co film from 2 to 30 ML on Cu(001) surfaces," *Surf. Sci.* **373**, 181 (1997).

- 16.40 H.-G. Min, S.-H. Kim, M. Li, J.B. Wedding, and G.-C. Wang, "Thickness dependent coercivity of ultrathin Co films on rough substrates: Cu-buffered Si(111)," *Surf. Sci.* **400**, 19 (1998).
- 16.41 R. F. Soohoo, "Influence of particle interaction on coercivity and squareness of thin film recording media," *J. Appl. Phys.* **52**, 2461 (1981).
- 16.42 S. Middelhoeck, *Ferromagnetic Domains in Thin Ni-Fe Films* (Drukerij Wed. G. Van Soest N. V., Amsterdam, 1961).
- 16.43 L. Néel, "Énergie des parois de Bloch dans les couches minces," *Comptes Rendus Acad. Sci. (Paris)* **241**, 533 (1955).
- 16.44 Y.-P. Zhao, G. Palasantzas, G.-C. Wang, T.-M. Lu, and J. Th. M. De Hosson, "Surface/interface roughness induced demagnetizing effect in thin magnetic films," *Phys. Rev. B* **60**, 1216 (1999).
- 16.45 J. D. Jackson, *Classical Electrodynamics*, 2nd Edition, p.194 (Wiley, New York, 1975).
- 16.46 E. Schlömann, "Demagnetizing fields in thin magnetic films due to surface roughness," *J. Appl. Phys.* **41**, 1617 (1970).
- 16.47 C. Kittel, "Physical theory of ferromagnetic domains," *Rev. Mod. Phys.* **21**, 541 (1949).
- 16.48 R. F. Soohoo, *Magnetic Thin Films* (Harper and Row, New York, 1965).
- 16.49 M. Prutton, *Thin Ferromagnetic Films* (Butterworths, Washington, 1964).
- 16.50 S. J. Glass and M. J. Klein, "Thin ferromagnetic films," *Phys. Rev.* **109**, 288 (1958).
- 16.51 Ke Chen, Matt Nielsen, S. Soss, Eugene J. Rymaszewski, Toh-Ming Lu, and C. T. Wan, "Study of Tantalum oxide thin film capacitors on metallized polymer sheets for advanced packaging applications," *IEEE Transactions on Components, Packaging, and Manufacturing Technology B* **20**, 117 (1997).
- 16.52 Rama I. Hegde, Mark A. Chonko, and Philip J. Tobin, "Effect of silicon substrate microroughness on gate oxide quality," *J. Vac. Sci. Technol. B* **14**, 3299 (1996).
- 16.53 Albert Chin, B. C. Lin, W. J. Chen, Y. B. Lin, and C. Tsai, "The effect of native oxide on thin gate oxide integrity," *IEEE Electron Device Letters* **19**, 426 (1998).
- 16.54 Y.-P. Zhao, G.-C. Wang, T.-M. Lu, G. Palasantzas, and J. Th. M. De Hosson, "Surface roughness effect on capacitance and leakage current of an insulating film," *Phys. Rev. B* **60**, 9157 (1999).
- 16.55 S. M. Sze, *Semiconductor Devices: Physics and Technology* (John Wiley & Sons, NY, 1985).
- 16.56 D. R. Lamb, *Electrical Conduction Mechanisms in Thin Insulating Films* (Spottiswoode, Ballatyne & Co Ltd., 1967).
- 16.57 J. J. O'Dwyer, *The Theory of Electrical Conduction and Breakdown in Solid Dielectrics* (Oxford University Press, 1973).
- 16.58 K. D. Leaver and B. N. Chapman, *Thin Films* (Wykeham Publications LTD, London and Winchester, 1971).
- 16.59 G. T. Carlson and B. L. Illman, "The circular disk parallel plate capacitor," *Am. J. Phys.* **62**, 1099 (1994).
- 16.60 E. Ezhilvalavan and T.-Y. Tseug, "Conduction mechanisms in amorphous and crystalline Ta<sub>2</sub>O<sub>5</sub> thin films," *J. Appl. Phys.* **83**, 4797 (1998).
- 16.61 F.-C. Chiu, J.-J. Wang, J. Y.-M. Lee, and S.-C. Wu, "Leakage currents in amorphous Ta<sub>2</sub>O<sub>5</sub> thin films," *J. Appl. Phys.* **81**, 6911 (1997).
- 16.62 J. G. Simmons, "Transition from electrode-limited to bulk-limited conduction processes in metal-insulator-metal systems," *Phys. Rev.* **166**, 912 (1968).
- 16.63 P. G. de Gennes, "Wetting: statics and dynamics," *Rev. Modern Phys.* **57**, 827 (1985).
- 16.64 Jaroslaw Drelich and Jan D. Miller, "The effect of solid surface heterogeneity and roughness on the contact angle/drop (bubble) size relationship," *J. Colloid and In-*

- terface Sci. **164**, 252 (1994).
- 16.65 G. Palasantzas, "Wetting on rough self-affine surfaces," Phys. Rev. B **51**, 14612 (1995).
  - 16.66 Roland R. Netz and David Andelman, "Roughness-induced wetting," Phys. Rev. E **55**, 687 (1997).
  - 16.67 Tom R. Thomas, *Rough Surfaces*, 2nd Edition (Imperial College Press, London, 1999).
  - 16.68 *Handbook of Micro/Nano Tribology*, Edited by Bharat Bhushan (CRC Press, Boca Raton, 1995).
  - 16.69 H. C. Liu and D. D. Coon, "Interface-roughness and island effects on tunneling in quantum wells," J. Appl. Phys. **64**, 6785 (1988).
  - 16.70 Peter Johansson, "Effects of interface-roughness scattering on resonant tunneling," Phys. Rev. B **46**, 12865 (1992).
  - 16.71 D. Z.-Y. Ting and T. C. McGill, "Interface roughness effects on transport in tunnel structures," J. Vac. Sci. Technol. B **14**, 2790 (1996).

This Page Intentionally Left Blank

## Appendix A GROWTH DYNAMICS

In this appendix, we shall discuss three different surface morphologies during the kinetic roughening processes: self-affine surfaces, mounded surfaces, and anisotropic surfaces. Our main purpose is to show how different morphologies can be formed under different physical conditions. More detailed kinetic roughening theory can be found in recent excellent books and review articles [A.1, A.2, A.3, A.4].

### A.1 Self-Affine Growth

#### A.1.1 The dynamic scaling concept

The self-affine growth mechanism is usually referred to as noise-induced roughening. As an example, Figure A.1 shows an experimental result of noise-induced roughening in amorphous silicon grown by thermal evaporation [A.5]. In this mechanism, the roughening is the result of the competition between the inherent thermal noise (roughening) in the growth system and the surface smoothening effect. In this case, the dynamic scaling hypothesis is essential in understanding the growth behavior.

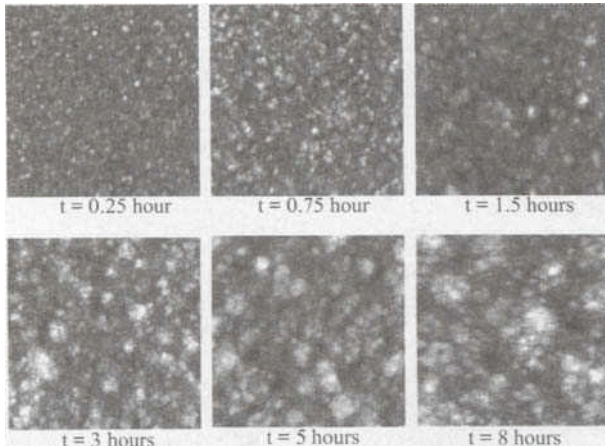


FIG. A.1 AFM images ( $1 \mu\text{m} \times 1 \mu\text{m}$ ) of amorphous silicon deposited at room temperature for different growth time  $t = 0.25, 0.75, 1.5, 3, 5$ , and  $8 \text{ hrs}$  (from Ref. [A.5]).

It is assumed that in dynamic scaling the time-dependent height-height correlation function satisfies the relation

$$H(r, t) = 2[w(t)]^2 f\left[\frac{r}{\xi(t)}\right], \quad (\text{A.1})$$

where  $f(x)$  is the scaling function satisfying Equation (3.3), and both the interface width and lateral correlation length change as power laws of the growth time,

$$w(t) \propto t^\beta, \quad (\text{A.2})$$

and

$$\xi(t) \propto t^{1/z}. \quad (\text{A.3})$$

Here the exponent  $\beta$  is called the growth exponent. It describes how the vertical width of the surface scales with time. The exponent  $z$  is called the dynamic exponent, it describes how the lateral length of the surface scales with time. Equations (A.2) and (A.3) represent the time scale-invariant aspect of the growth front. According to Equation (3.3) the time-dependent height-height correlation function has the following asymptotic behavior

$$H(r, t) \propto \begin{cases} r^{2\alpha} t^{2\beta - 2\alpha/z}, & \text{for } r \ll \xi(t), \\ t^{2\beta}, & \text{for } r \gg \xi(t). \end{cases} \quad (\text{A.4})$$

Dynamic scaling requires that

$$z = \frac{\alpha}{\beta}. \quad (\text{A.5})$$

Under this condition, the short-range behavior of the height-height correlation function is time independent:

$$H(r, t) \propto \begin{cases} r^{2\alpha}, & \text{for } r \ll \xi(t), \\ t^{2\beta}, & \text{for } r \gg \xi(t). \end{cases} \quad (\text{A.6})$$

An example of a height-height correlation function obeying Equation (A.5) is shown in Figure A.2(a). From Equation (A.4) one can see that it is also possible that the dynamic scaling hypothesis Equation (A.5) may break down. In this case the short-range behavior of the height-height correlation function can also be a function of growth time. An example is shown in Figure A.2(b). The growth behavior obeying the dynamic scaling hypothesis is called the stationary growth, and the dynamic scaling breakdown case is the non-stationary growth.

In the following we give some simple models that form self-affine rough surfaces.

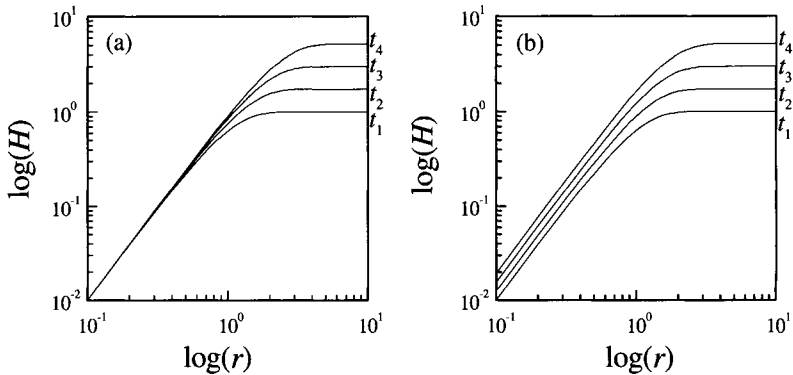


FIG. A.2 (a) The time-dependent height-height correlation function  $H(r, t)$  for stationary growth, which shows the essential characteristics of the dynamic scaling hypothesis. Note that for different times the short-range behaviors of  $H(r, t)$  are invariant with time and overlapped. (b) The time-dependent height-height correlation function  $H(r, t)$  for non-stationary growth. In this case the short-range behaviors of  $H(r, t)$  are functions of growth time. In the figures, we assume that  $t_4 > t_3 > t_2 > t_1$  (from Ref. [A.6]).

### A.1.2 A linear growth model

In this model, the roughening is caused by a competition between the inherent thermal noise in the growth system and the smoothing effect of condensation/evaporation on the surface [A.7]. Sometimes the capillary effect, i.e., Mullins diffusion [A.8], is also included. A simple linear Langevin equation including all of these effects is given by

$$\frac{\partial h(\mathbf{r}, t)}{\partial t} = \nu \nabla^2 h - \kappa \nabla^4 h + \eta(\mathbf{r}, t). \quad (\text{A.7})$$

The first term,  $\nu \nabla^2 h$ , on the right hand side is the result of the Gibbs-Thompson relation describing the thermal equilibrium interface between the vapor and solid/liquid. The term  $\nabla^2 h$  is the small slope expansion of the surface curvature, and the prefactor  $\nu$  is proportional to the surface tension coefficient, and we will refer to it as the surface tension term. The second term,  $-\kappa \nabla^4 h$ , is the result of surface diffusion due to the curvature-induced chemical potential gradient. The prefactor  $\kappa$  is proportional to the surface diffusion coefficient and it is referred to as the surface diffusion term. The term  $\eta(\mathbf{r}, t)$  is a Gaussian white noise arising from the deposition, satisfying

$$\begin{cases} \langle \eta(\mathbf{r}, t) \rangle = 0, \\ \langle \eta(\mathbf{r}, t) \eta(\mathbf{r}', t') \rangle = 2D\delta(\mathbf{r} - \mathbf{r}')\delta(t - t'). \end{cases} \quad (\text{A.8})$$

The solution of Equation (A.7) is simple and straightforward through a spatial Fourier transformation, given by [A.9]

$$h(\mathbf{r}, t) = \left(\frac{1}{2\pi}\right)^{d/2} \int e^{i\mathbf{k}_{||} \cdot \mathbf{r}} d\mathbf{k}_{||} \int \Theta(\mathbf{k}_{||}, \tau) e^{-(\kappa k_{||}^4 + \nu k_{||}^2)(t-\tau)} d\tau, \quad (\text{A.9})$$

where  $\Theta(\mathbf{k}_{||}, \tau)$  is the spatial Fourier transformation of  $\eta(\mathbf{r}, t)$ ,

$$\Theta(\mathbf{k}_{||}, \tau) = \left(\frac{1}{2\pi}\right)^{d/2} \int \eta(\mathbf{r}, t) e^{-i\mathbf{k}_{||} \cdot \mathbf{r}} dr, \quad (\text{A.10})$$

and

$$\begin{cases} <\Theta(\mathbf{k}_{||}, t)> = 0, \\ <\Theta(\mathbf{k}_{||}, t)\Theta(\mathbf{k}'_{||}, t')> = 2D\delta(\mathbf{k}_{||} + \mathbf{k}'_{||})\delta(t - t'). \end{cases} \quad (\text{A.11})$$

Clearly the time integration in Equation (A.9) is the convolution of a white noise and a response function. Therefore, one can view the growth process as a linear system. The white Gaussian noise is the input signal. The growth mechanism is the response of the system, and the output is the convolution of these two. The power spectrum is given by

$$P(\mathbf{k}_{||}) = 4D \frac{1 - e^{-2(\kappa k_{||}^4 + \nu k_{||}^2)t}}{\kappa k_{||}^4 + \nu k_{||}^2}. \quad (\text{A.12})$$

A plot of the power spectrum with different  $\kappa/\nu$  ratios and growth time  $t$  is shown in Figure A.3. We can see that the self-affine roughening is a result of a Gaussian white noise passing through a low-pass filter. The FWHM of the power spectrum is determined by both the  $\kappa/\nu$  ratio and deposition time  $t$  and is a reflection of the lateral correlation length  $\xi$ . The interface width  $w$  can be calculated from the power spectrum according to the following relation:

$$w^2 = \int P(\mathbf{k}_{||}) d\mathbf{k}_{||}. \quad (\text{A.13})$$

The numerical integration of  $w^2$  for different  $\kappa/\nu$  ratios is shown in Figure A.4 for 1+1 and 2+1 dimensions. We can see that the growth exponents are dependent on the  $\kappa/\nu$  ratios as well as the dimension of the embedded space.

The height-height correlation function  $H(\mathbf{r}, t)$  can also be obtained from Equation (A.9) and is given by

$$H(\mathbf{r}, t) = 4D \left(\frac{1}{2\pi}\right)^d \int [1 - \cos(\mathbf{k}_{||} \cdot \mathbf{r})] \frac{1 - e^{-2(\kappa k_{||}^4 + \nu k_{||}^2)t}}{\kappa k_{||}^4 + \nu k_{||}^2} d\mathbf{k}_{||}. \quad (\text{A.14})$$

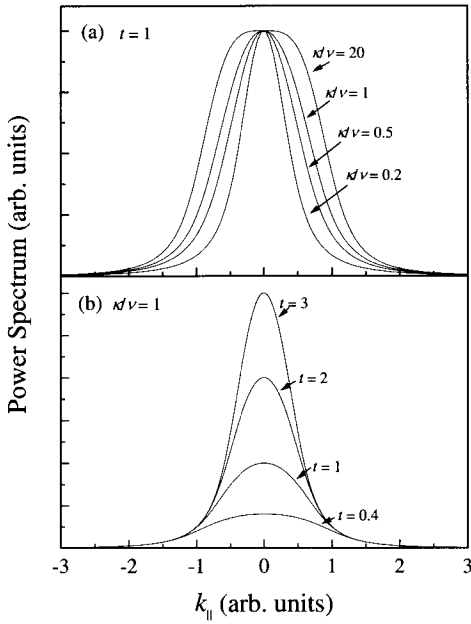


FIG. A.3 The power spectra of noise-induced roughening fronts determined by Equation (A.12). (a) The  $\kappa/\nu$  ratio dependence for  $t = 1$ . As  $\kappa/\nu$  ratio increases the FWHM of the power spectrum increases. (b) The time dependence for  $\kappa/\nu = 1$ . The FWHM of the power spectrum decreases with increasing growth time (from Ref. [A.9]).

There is no analytical form for the height-height correlation function.

Now let us consider two simple cases using the scale invariance property of self-affine growth. The first case is  $\kappa = 0$ , i.e., the growth is dominated by the evaporation/condensation processes. Then Equation (A.7) becomes the well-known Edwards-Wilkinson (EW) equation [A.7]:

$$\frac{\partial h(\mathbf{r}, t)}{\partial t} = \nu \nabla^2 h + \eta(\mathbf{r}, t). \quad (\text{A.15})$$

One can rescale the interface both horizontally and vertically

$$\mathbf{r} \rightarrow \varepsilon \mathbf{r}, \text{ and} \quad (\text{A.16})$$

$$h \rightarrow \varepsilon^\alpha h, \quad (\text{A.17})$$

and simultaneously rescale the time,

$$t \rightarrow \varepsilon^z t. \quad (\text{A.18})$$

The scaling behavior of the noise is obtained by first rescaling Equation

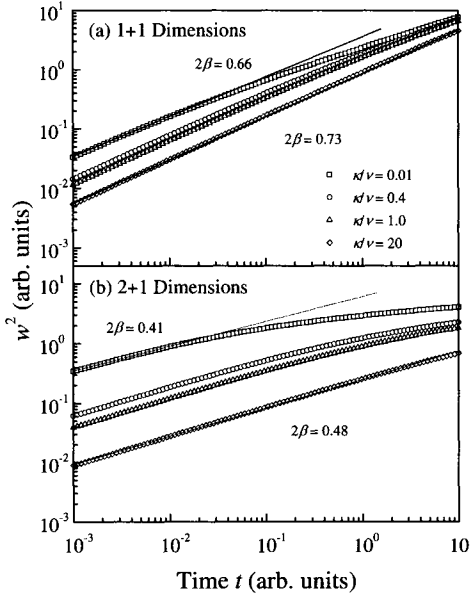


FIG. A.4 Time evolution of the interface width  $w^2$  of the noise-induced growth fronts. (a) 1+1 dimensions, (b) 2+1 dimensions (from Ref. [A.9]).

(A.8):

$$\langle \eta(\varepsilon\mathbf{r}, \varepsilon^z t)\eta(\varepsilon\mathbf{r}', \varepsilon^z t') \rangle = 2D\delta(\varepsilon\mathbf{r} - \varepsilon\mathbf{r}')\delta(\varepsilon^z t - \varepsilon^z t'). \quad (\text{A.19})$$

We note that

$$\delta(c\mathbf{r}) = c^{-d}\delta(\mathbf{r}). \quad (\text{A.20})$$

Therefore Equation (A.19) can be rewritten as

$$\langle \eta(\varepsilon\mathbf{r}, \varepsilon^z t)\eta(\varepsilon\mathbf{r}', \varepsilon^z t') \rangle = 2D\varepsilon^{-d-z}\delta(\mathbf{r} - \mathbf{r}')\delta(t - t'). \quad (\text{A.21})$$

Then the noise scales as

$$\eta(\mathbf{r}, t) \rightarrow \varepsilon^{-d/2-z/2}\eta(\mathbf{r}, t). \quad (\text{A.22})$$

After rescaling, Equation (A.15) becomes

$$\frac{\partial h(\mathbf{r}, t)}{\partial t} = \varepsilon^{z-2}\nu\nabla^2 h + \varepsilon^{-d/2+z/2-\alpha}\eta(\mathbf{r}, t). \quad (\text{A.23})$$

Here, we multiply both sides by  $\varepsilon^{z-\alpha}$ . After rescaling, one should obtain an interface that is statistically indistinguishable from the original one,

i.e., the rescaled Langevin equation Equation (A.23) should be identical to Equation (A.15). This requires that

$$\varepsilon^{z-2} = 1 \quad (\text{A.24})$$

and

$$\varepsilon^{-d/2+z/2-\alpha} = 1. \quad (\text{A.25})$$

Finally, we see that

$$z = 2, \alpha = \frac{2-d}{2}, \text{ and } \beta = \frac{2-d}{4}. \quad (\text{A.26})$$

Equation (A.26) shows that the exponents are closely related to the dimensionality. One particular case is  $d = 2$ , where we have  $\alpha = 0$  and  $\beta = 0$ . Does this mean the surface stops growing rougher? Let us go back to the analytical solution Equation (A.9).

The interface width  $w$  obeys the relation

$$w^2(t) \propto \int_0^{1/a} \frac{1 - e^{-2\nu k_{||}^2 t}}{k_{||}} dk_{||} = \int_0^{1/a} \frac{1 - e^{-\xi^2 k_{||}^2}}{k_{||}} dk_{||}, \quad (\text{A.27})$$

where  $a$  is the short length-scale cutoff and  $\xi = \sqrt{2\nu t}$  is the lateral correlation length. The integral in Equation (A.27) can be calculated analytically as shown in Appendix B,

$$w^2(t) \propto \ln[1 + \frac{t}{\tau_c}], \quad (\text{A.28})$$

where  $\tau_c = a^2/2\nu$  is a time constant. Equation (A.28) demonstrates that at the very initial growth stage,  $t \ll \tau_c$ , we have  $w^2(t) \propto \frac{t}{\tau_c}$ , i.e.,  $\beta = 0.5$ . This is the regime where only random deposition takes place. However, at later time,  $t \gg \tau_c$ , we have  $w^2(t) \propto \ln(\frac{t}{\tau_c})$ , and this is the dynamic scaling regime. We see that  $w^2$  obeys a logarithmic behavior (not power law) with respect to growth time  $t$  when  $\beta = 0$ . Now let us investigate the height-height correlation function. In this case the height-height correlation function can be written as

$$H(\mathbf{r}, t) \propto \int [1 - J_0(k_{||} r)] \frac{1 - e^{-2\nu k_{||}^2 t}}{k_{||}} dk_{||}. \quad (\text{A.29})$$

A detailed calculation gives the asymptotic behavior of  $H(\mathbf{r}, t)$ :

$$H(\mathbf{r}, t) \propto \begin{cases} \ln(r), & \text{for } a \ll r \ll \xi, \\ 2w^2, & \text{for } r \gg \xi. \end{cases} \quad (\text{A.30})$$

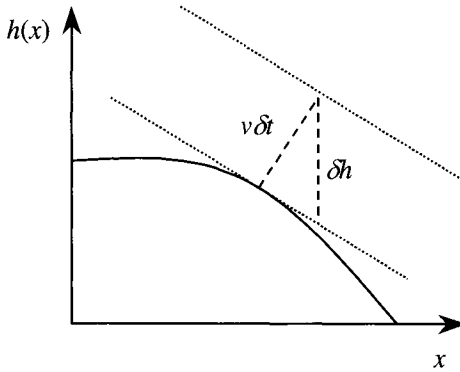


FIG. A.5 The growth normal to the local surface giving rise to the nonlinear term in the KPZ equation (from Ref. [A.3]).

Equation (A.30) shows that, for  $\alpha = 0$ , the short-range behavior of the height-height correlation function is not a power law anymore. Instead, it is logarithmic.

The other simple case is  $\nu = 0$ , where the growth is dominated by surface diffusion. Equation (A.7) becomes the Mullins diffusion equation [A.8]:

$$\frac{\partial h(\mathbf{r}, t)}{\partial t} = -\kappa \nabla^4 h + \eta(\mathbf{r}, t). \quad (\text{A.31})$$

One can use a similar scaling argument to show that

$$z = 4, \alpha = \frac{4-d}{2}, \text{ and } \beta = \frac{4-d}{8}. \quad (\text{A.32})$$

We can see that the general linear Langevin equation is a combination of the EW Equation (A.15) and Mullins diffusion Equation (A.31). The scaling argument cannot be applied to Equation (A.7) because there is a crossover from EW to Mullins diffusion. Therefore the  $\beta$  value for Equation (A.7) ( $\frac{2-d}{4} \leq \beta \leq \frac{4-d}{8}$ ) is between the Edwards-Wilkinson model,  $\frac{2-d}{4}$ , and the Mullins diffusion model,  $\frac{4-d}{8}$ .

### A.1.3 Other self-affine growth models

There are other growth models that can result in self-affine surface morphologies. One such model is the Kardar-Parisi-Zhang (KPZ) model [A.10]. In this model, the growth direction is along the local surface normal as shown in Figure A.5. The height increment  $\delta h$  along the  $z$  axis is given by

$$\delta h = \sqrt{(v\delta t)^2 + (v\delta t \nabla h)^2} = v\delta t \sqrt{1 + (\nabla h)^2}. \quad (\text{A.33})$$

Table A.1 Summary of some important 2+1-dimensional noise-induced roughening models.

Model Name	$\frac{\partial h}{\partial t} =$	Roughness Exponent $\alpha$	Growth Exponent $\beta$
Random Deposition	$\eta$	-	0.5
Edwards-Wilkinson Model	$\nu \nabla^2 h + \eta$	0	0
Mullins Diffusion Model	$-\kappa \nabla^4 h + \eta$	1	0.25
Kardar-Parisi-Zhang Model	$\nu \nabla^2 h + \frac{\lambda}{2} (\nabla h)^2 + \eta$	.38	0.24

If the slope of the surface is small ( $|\nabla h| \ll 1$ ), one can expand Equation (A.33)

$$\frac{\partial h}{\partial t} = v + \frac{v}{2} (\nabla^2 h) + \dots \quad (\text{A.34})$$

This suggests that a nonlinear term  $(\nabla h)^2$  should be present in the growth equation. Adding this nonlinear term to the EW equation, one obtains the famous KPZ equation:

$$\frac{\partial h}{\partial t} = \nu \nabla^2 h + \frac{\lambda}{2} (\nabla^2 h) + \eta(\mathbf{r}, t). \quad (\text{A.35})$$

The KPZ equation is nonlinear, and there is no analytical solution. To solve the KPZ equation one needs to use a numerical method or a renormalization method, which is beyond the scope of this book. Interested readers can find these methods in Reference [A.3]. In Table A.1 we summarize the general properties of some useful self-affine growth models.

## A.2 Mounded Growth

In some cases the roughening is due not only to noise present in the system, but also other roughening mechanisms due to the atomic dynamical processes on the surface or from transport properties away from the surface. In this case, if there is no smoothening effect, the growth will become unsta-

ble and the interface width will grow exponentially with increasing growth time. This kind of process seldom happens. Instead, there are always certain smoothening effects competing with the roughening mechanisms. The result of the competition may lead to a selected spatial frequency by which the system prefers to grow, i.e., the surface will have a characteristic length. This type of growth is referred as mounded growth.

### A.2.1 Step-bias-induced instability

In this growth model, the step barrier (Schwoebel barrier) prevents adatoms from hopping down the step edge, which generates an uphill diffusion current [A.11, A.12, A.13, A.14, A.15, A.16, A.17, A.18]. There are two important features in this kind of growth: (i) The surface consists of regular mound structures, having a wavelength selection. During growth, mounds coarsen, and the average mound separation  $\lambda$  grows as a power law  $\lambda \propto t^\Delta$ , with  $\Delta$  ranging from 0.16 to 0.26 [A.14, A.15, A.16, A.17, A.18]. (ii) The slope of mounds remains essentially constant after an initial transient regime. This is known as the slope selection. The selected slope is usually very small (less than 1.0) [A.11, A.12, A.13, A.14, A.15, A.16, A.17, A.18]. Figure 3.4 shows an STM study of homoepitaxy of Cu on Cu(100) at about 299 K [A.18]. Regular mounds are clearly present on the surface due to the step bias effect. This growth mechanism can be described by a nonlinear Langevin equation proposed by Johnson et al. [A.12]:

$$\frac{\partial h}{\partial t} = -\nu \nabla \frac{\nabla h}{1 + (\nabla h)^2} - \kappa \nabla^4 h + \eta(r, t), \quad (\text{A.36})$$

where both  $\nu$  and  $\kappa$  are positive. The first term on the right-hand side represents the up-hill growth due to the Schwoebel barrier effect, and the second term is due to surface diffusion (capillary effect). The up/down ( $h \leftrightarrow -h$ ) symmetry is still preserved by this equation, although it is nonlinear. During the initial stage,  $|\nabla h|$  is small, and Equation (A.36) can be expanded as

$$\frac{\partial h}{\partial t} = -\nu \nabla^2 h - \kappa \nabla^4 h + \eta(r, t), \quad (\text{A.37})$$

Equation (A.37) looks very similar to Equation (A.7) for the noise-induced rough surface except that the first term on the right-hand side has a negative coefficient. This implies that the solution for Equation (A.37) is unstable. The coefficient  $\nu$  refers to the adatom diffusion process (the Schwoebel barrier effect), whereas the same coefficient in Equation (A.7) stands for the effect of surface tension, or the evaporation/condensation

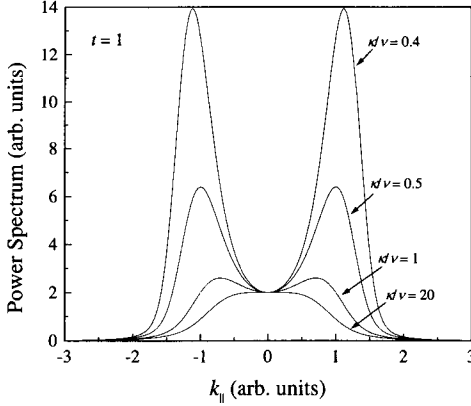


FIG. A.6 The  $\kappa/\nu$  ratio-dependent power spectra of the zeroth-order solution for the growth-front roughening caused by step bias. In this case,  $t = 1$  (from Ref. [A.9]).

process. Despite the different physical origins of Equation (A.7) and Equation (A.37), the solutions for the power spectra are similar, except for the negative sign in front of  $\nu$ :

$$P(\mathbf{k}_{||}) = 4D \frac{1 - e^{-2(\kappa k_{||}^4 - \nu k_{||}^2)t}}{\kappa k_{||}^4 - \nu k_{||}^2}. \quad (\text{A.38})$$

Equation (A.38) always has a maximum at  $k_c = \sqrt{\frac{\nu}{2\kappa}}$  (characteristic wave-vector), which implies that the power spectrum  $P(\mathbf{k}_{||})$  has a ring structure (in 2+1 dimensions), and the peak position of the ring,  $k_c$ , reflects the wavelength selection (average mound separation),  $\lambda = \frac{2\pi}{k_c}$ , of the growth mechanism as shown in Figure A.6 (here we let  $t = 1$ ). This ring structure is the main difference between the two mechanisms, the step-bias-induced instability and the noise-induced roughening, as discussed above.

It is interesting to note that the selected wavelength is determined only by the coefficients  $\kappa$  and  $\nu$ , which correspond to the relative strength of surface diffusion and Schwoebel barrier. The ratio  $\kappa/\nu$  plays a very important role for this growth mechanism. If  $\kappa/\nu \gg 1$ , which suggests that either the Schwoebel barrier is small or surface diffusion is fast, the selected wavelength will be too long to be detected for a given technique (both real-space imaging and diffraction techniques). In this case, the dominant roughening mechanism would still be noise-induced dynamic roughening. In fact, as shown in Figure A.6, as the  $\kappa/\nu$  ratio increases, the satellite ring intensity decreases and the ring radius shrinks. For sufficiently large  $\kappa/\nu$  (the curve for  $\kappa/\nu = 20$  as shown in Figure A.6), one can hardly tell whether there exists a satellite ring or not. In this case, the capillary effect dominates,

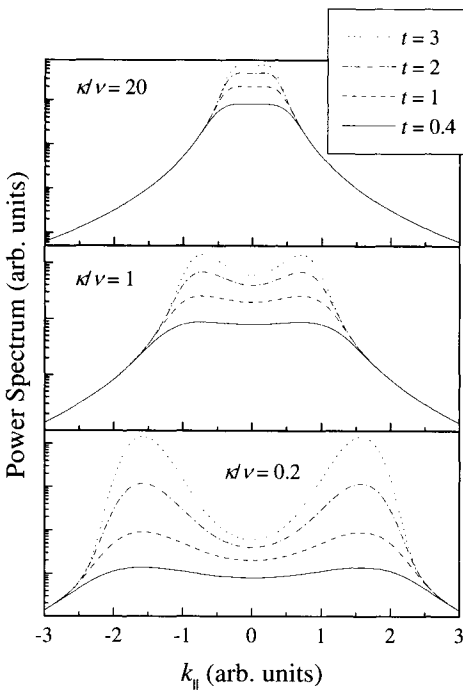


FIG. A.7 The time-dependent power spectra for the initial stage of mound growth for  $\kappa/\nu = 20, 1$ , and  $0.2$  (from Ref. [A.9]).

and the growth is governed by Mullins diffusion, which gives  $\beta = 0.25$ .

Figure A.7 shows a semilog plot of the time evolution of the power spectrum for selected  $\kappa/\nu$  ratios. For a large  $\kappa/\nu$  ratio ( $= 20$ ), and after a long time deposition ( $t = 3$ ), only a tiny ring appeared in the power spectrum, which may not be able to be detected in an experiment. However, for a medium  $\kappa/\nu$  ratio ( $= 1$ , which is in the crossover region), at the very beginning, the ring structure is still not observable, but after a sufficiently long time, a clear satellite ring would appear. For a small  $\kappa/\nu$  ratio, which means that the Schwoebel barrier dominates, the ring structure is obvious in the power spectrum even at the initial stage. Another interesting point is that the FWHM of the satellite ring (or the power spectrum for large  $\kappa/\nu$  ratio) is a function of both time  $t$  and ratio  $\kappa/\nu$ . As the growth time becomes longer, the satellite ring becomes more obvious and sharper, which means that the local surface height fluctuations are more correlated (i.e., the correlation length increases). Only when the local height fluctuations have a correlation length compatible to, or larger than, the average mound separation can mounds dominate the morphology of the surface. This sug-

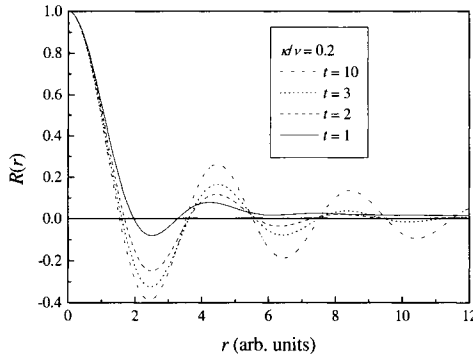


FIG. A.8 The auto-correlation function for  $\kappa/\nu = 0.2$  at different growth times. Note that the first zero crossing positions are different for different times (from [A.9]).

gests that in order to describe a mounded surface, one needs at least two independent lateral lengths: one for describing the wavelength selection and the other for describing the local roughness correlation. The relative weight of these two lateral length scales determines the final morphology of the surface.

Another point worth mentioning is that the location of the first zero crossing in the auto-correlation function is usually used as a measure of the average mound separation [A.18, A.19, A.20, A.21, A.22]. This is not entirely accurate. Figure A.8 shows the auto-correlation function for  $\kappa/\nu = 0.2$  at different growth times. From the discussion above, the average mound separation  $\lambda$  is determined entirely by the  $\kappa/\nu$  ratio, and different times should give the same mound separation value. As shown in Figure A.8, the auto-correlation function has different zero crossing positions at different times, i.e., the shorter the growth time, the longer the first zero crossing position. This is due to the effect of the competition between the two lateral lengths. Therefore, for a realistic growth system, both lateral lengths could change with growth time, and the use of the first zero crossing position in the auto-correlation function as a sole measure of the average mound separation may be misleading.

For surfaces in both 1+1 and 2+1 dimensions, at the initial stage of growth the interface width  $w$  grows as a power law in time  $t$ ,  $w \propto t^\beta$ , with  $\beta > \frac{3}{8}$  for 1+1 dimensions, and with  $\beta > \frac{1}{4}$  for 2+1 dimensions (Figure A.9). For a longer time,  $w$  increases exponentially with  $t$ , and the unstable Laplacian term dominates the growth [which may not satisfy the small slope approximation assumed for Equation (A.37), and the nonlinearity of Equation (A.36) should be included].

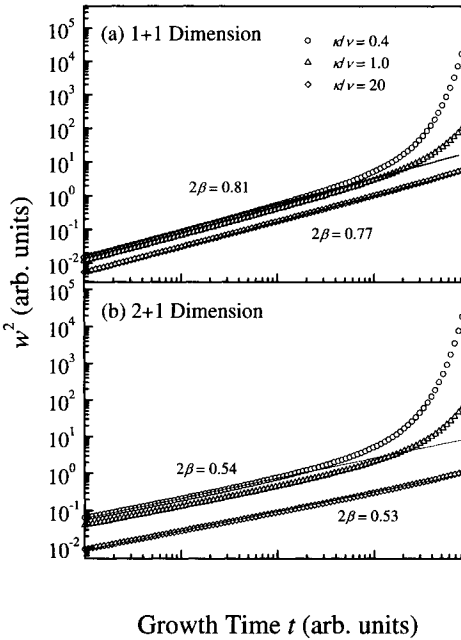


FIG. A.9 Time evolution of the interface width  $w^2$  for initial growth of mound growth fronts: (a) 1+1 dimensions and (b) 2+1 dimensions (from Ref. [A.9]).

### A.2.2 Other mound growth models

There are other mound-formation models besides the step bias mechanism. One of these models includes the shadowing effect, which has been used to describe sputtering growth. During growth, the atoms arrive at the growth front either from a fixed angle or from random angles. For random incidence, the crests of the surface would receive more deposited atoms than the valleys of the same surface because the receiving solid angle at the crests is larger than that in the valleys. Therefore the growth rate at the crests is higher than that at the valleys, which causes a growth instability. In this case the growth equation can be written as [A.23]

$$\frac{\partial h}{\partial t} = \nu \nabla^2 h + F \Omega(\mathbf{r}, h) + \eta(\mathbf{r}, t), \quad (\text{A.39})$$

where  $F$  is the deposition rate and  $\Omega(\mathbf{r}, h)$  is the exposure angle. A numerical calculation of Equation (A.39) indicates that after a short transient, the interface width grows linearly with time ( $\beta = 1$ ). There is also a characteristic wavevector  $k_c$  that decays as  $k_c \propto t^{-p}$ , with  $p = 0.33 \pm 0.02$  [A.24, A.25].

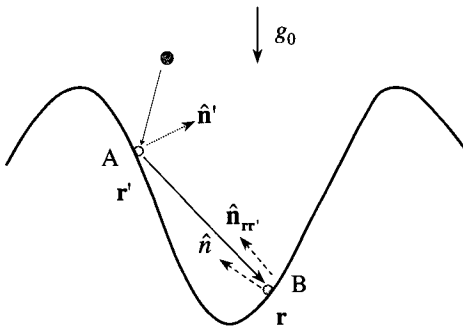


FIG. A.10 A schematic showing the re-emission model (from Ref. [A.26]).

Zhao et al. found that plasma-etched Si(100) surfaces also have a regular mound (hole) structure. The interface width grows linearly with etching time and the roughness exponent  $\alpha = 0.96 \pm 0.06$ . The characteristic wave vector also obeys a power law with growth time, with  $p \approx 1.3 \pm 0.3$ . They proposed a surface re-emission model to explain this unusual behavior [A.26]. Since the pressure in the typical plasma-etching system is of the order of 100 mTorr or less, the Knudsen number (the ratio of the mean free path of any gas particles to the characteristic length of the surface features) is large. Hence, collisions between particles within the surface features can be neglected. Therefore, the etching particle can travel in a straight line until it hits the surface at another point. They assumed that the film evolves slowly compared to the redistribution of flux due to the surface features. As shown in Figure A.10, in this model, particles are incident on a surface, and this flux either etches the surface (or deposits on the surface if the process is deposition) at the point of incidence or redistributes itself according to certain re-emission modes and surface features. The probability of an incoming particle sticking to the surface is  $s_0$  ( $0 \leq s_0 \leq 1$ ), where  $s_0$  is called the zeroth-order sticking coefficient. Incoming particles are called zeroth-order particles, while an  $n$ th-order particle that has been re-emitted is called an  $(n+1)$ th-order particle. The probability of an  $n$ th-order particle sticking is  $s_n$  ( $0 \leq s_n \leq 1$ ), and there is a probability of  $(1 - s_n)$  that this particle would not stick, but would, instead, go somewhere else (in other words, the flux is redistributed). We denote the overall flux of  $n$ th-order particles at in-plane position  $\mathbf{r}$  at time  $t$  by  $F_n(\mathbf{r}, t)$ . The surface evolution can be described by the continuum equation [A.27]

$$\frac{\partial h}{\partial t} = \nu \nabla^2 h - \kappa \nabla^4 h \mp \sqrt{1 + (\nabla h)^2} [s_0 F_0(\mathbf{r}, t) + \dots + s_n F_n(\mathbf{r}, t) + \dots] + \eta. \quad (\text{A.40})$$

The minus sign in front of the third term in Equation (A.40) indicates an etching process and the plus sign indicates a deposition process. This model also takes into account of the growth or etching which takes place in the direction normal to the surface. The fluxes  $F_n$  satisfy, for diffuse re-emission [A.27],

$$F_{n+1}(\mathbf{r}, t) = (1 - s_n) \int Z(\mathbf{r}, \mathbf{r}', t) F_n(\mathbf{r}', t) \frac{(\hat{\mathbf{n}}_{\mathbf{rr}'} \cdot \hat{\mathbf{n}}) P(\hat{\mathbf{n}}_{\mathbf{r}'\mathbf{r}}, \hat{\mathbf{n}}')}{(\mathbf{r} - \mathbf{r}')^2 + (h - h')^2} dA', \quad (\text{A.41})$$

where  $\hat{\mathbf{n}}$  is the unit normal pointing out of the surface at position  $\mathbf{r}$ ,  $\hat{\mathbf{n}}'$  is the unit normal at position  $\mathbf{r}'$ ,  $\hat{\mathbf{n}}_{\mathbf{rr}'}$  is the unit vector pointing from  $\mathbf{r}$  to  $\mathbf{r}'$ , and  $\hat{\mathbf{n}}_{\mathbf{r}'\mathbf{r}}$  is the unit vector pointing from  $\mathbf{r}'$  to  $\mathbf{r}$ . The term  $P(\hat{\mathbf{n}}_{\mathbf{r}'\mathbf{r}}, \hat{\mathbf{n}}')$  is the probability distribution of the re-emitted flux (the probability per solid angle that the particle will be re-emitted in the given direction) and, for thermal re-emission (as we will see later), it is equal to  $(\hat{\mathbf{n}}_{\mathbf{rr}'} \cdot \hat{\mathbf{n}})/\pi$ . The term  $Z(\mathbf{r}, \mathbf{r}', t)$  is equal to one except when there is no line of sight between the surface elements at  $\mathbf{r}$  and  $\mathbf{r}'$  or  $(\hat{\mathbf{n}}_{\mathbf{rr}'} \cdot \hat{\mathbf{n}})$  is negative, in which case  $Z$  is zero. Both numerical calculations and Monte Carlo simulations showed that the etching of surfaces by first-order flux belongs to a new universality class with scaling exponents  $\alpha \approx \beta \approx z \approx 1$ , and the surface has a hole morphology, which gives the wavelength selection.

### A.3 Anisotropic Growth

An important origin of morphological anisotropy is surface transport anisotropy. Several dynamic processes may be involved. The most important processes that affect the morphology are surface tension, surface diffusion, step barrier (Schwoebel barrier), and stress or strain in the surface. During thin film growth, processes such as surface tension and surface diffusion tend to smoothen the surface. For a vicinal surface, the surface tension depends on orientation [A.28]. An anisotropic surface diffusion was also observed in the Si(100) substrate. Diffusion along surface dimer rows is 1000 times faster than the diffusion across the dimer rows [A.29, A.30, A.31, A.32]. Recent calculations of the step diffusion barrier of Si(100) surface also showed an anisotropy [A.33]. Surface strain or stress due to lattice mismatch or defects can induce surface diffusion. Therefore, the anisotropic properties of surface stress or strain can cause surface anisotropy [A.34, A.35, A.36, A.37].

In general, a substrate anisotropy does not always lead to anisotropic growth unless it induces an anisotropic atomic transport. As an example, we consider the isotropic Edwards-Wilkinson growth Equation (A.15) with

an anisotropic substrate morphology as the initial condition. The solution for the power spectrum is

$$P(\mathbf{k}_{||}, t) = 2D \frac{1 - e^{-2\nu k_{||}^2 t}}{\nu k_{||}^2} + P_0(\mathbf{k}_{||}) e^{-2\nu k_{||}^2 t}, \quad (\text{A.42})$$

where  $P_0(\mathbf{k}_{||})$  is the power spectrum of the anisotropic substrate. As time  $t$  increases, the effect of the substrate anisotropy becomes less important. For  $t \rightarrow \infty$  the surface becomes isotropic because the contribution of the second term diminishes. Therefore, if there is no surface transport anisotropy, a growth front started from an anisotropic substrate will eventually become isotropic after a long time.

The simplest anisotropic growth equation is an anisotropic form of Equation (A.7), which can be written as [A.38]

$$\frac{\partial h}{\partial t} = \nu_1 \frac{\partial^2 h}{\partial x^2} + \nu_2 \frac{\partial^2 h}{\partial y^2} - \kappa_1 \frac{\partial^4 h}{\partial x^4} - \kappa_2 \frac{\partial^4 h}{\partial y^4} - \kappa_3 \frac{\partial^4 h}{\partial x^2 \partial y^2} + \eta(\mathbf{r}, t), \quad (\text{A.43})$$

where  $\nu_1$  is a surface tension term along the  $x$  axis,  $\nu_2$  is a surface tension term along the  $y$  axis,  $\kappa_1$  and  $\kappa_2$  are surface diffusion terms along the  $x$  axis and the  $y$  axis, respectively, and  $\kappa_3$  is the cross diffusion term between the  $x$  and  $y$  axes. Equation (A.43) can also be solved using a Fourier transform method. The solution for the power spectrum at time  $t$  is

$$P(\mathbf{k}_{||}, t) = 4D \frac{1 - \exp[-2(\nu_1 k_x^2 + \nu_2 k_y^2 + \kappa_1 k_x^4 + \kappa_2 k_y^4 + \kappa_3 k_x^2 k_y^2)t]}{\nu_1 k_x^2 + \nu_2 k_y^2 + \kappa_1 k_x^4 + \kappa_2 k_y^4 + \kappa_3 k_x^2 k_y^2}. \quad (\text{A.44})$$

In the following, we consider three possible combinations of anisotropic surface tension and anisotropic surface diffusion in Equation (A.44).

(i) Surface tension only:  $\kappa_i = 0$ ,  $\nu_i \neq 0$

If the surface diffusion is negligible, Equation (A.44) reduces to an anisotropic Edwards-Wilkinson equation with the power spectrum

$$P(\mathbf{k}_{||}, t) = 4D \frac{1 - \exp[-2(\nu_1 k_x^2 + \nu_2 k_y^2)t]}{\nu_1 k_x^2 + \nu_2 k_y^2}. \quad (\text{A.45})$$

Letting  $Q_x = k_x t^{1/2}$  and  $Q_y = k_y t^{1/2}$ , Equation (A.45) then becomes

$$P(\mathbf{Q}, t)/t = 4D \frac{1 - \exp[-2(\nu_1 Q_x^2 + \nu_2 Q_y^2)]}{\nu_1 Q_x^2 + \nu_2 Q_y^2}. \quad (\text{A.46})$$

Figure A.11 plots the cross sections of the scaled power spectra  $P(\mathbf{Q}, t)/t$  in both the  $Q_x$  and  $Q_y$  directions and the contours of the scaled power

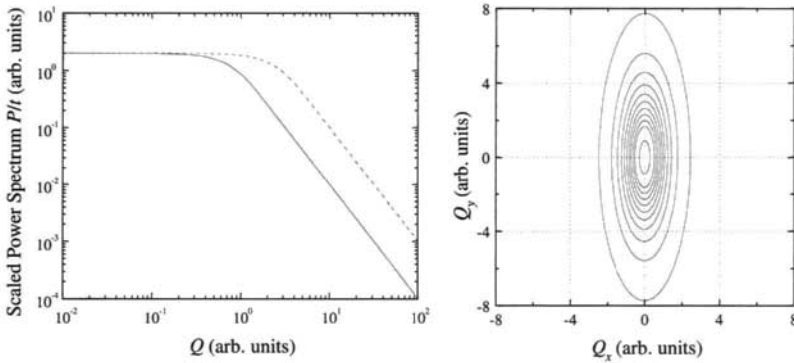


FIG. A.11 Left: Log-log plots of the scaled power spectrum along the  $Q_x$  (solid curve) and  $Q_y$  (dashed curve) directions for  $\nu_1 = 1.0$ ,  $\nu_2 = 0.1$ ,  $\kappa_1 = 0.0$ ,  $\kappa_2 = 0.0$ , and  $\kappa_3 = 0.0$ . Right: Contour plots of the scaled power spectrum (from Ref. [A.38]).

spectra for  $\nu_1 = 1.0$ ,  $\nu_2 = 0.1$ . For large  $k_{||}$  values, the cross sections of the power spectra in both the  $Q_x$  and  $Q_y$  directions obey the same power law with the value of the exponent equal to  $-2$ . This means that the roughness exponent  $\alpha = 0$  through the relationship between  $\alpha$  and the slope: slope  $= -d - 2\alpha$ , where  $d$  is the dimension of the embedded space. Therefore  $\alpha$  is not direction-dependent. However, the flat shoulder extends to different  $Q$  values in the  $Q_x$  and  $Q_y$  directions. The curve in the  $Q_y$  direction has its shoulder extending a factor of  $\sqrt{10}$  farther in  $Q$  values than that of the curve in the  $Q_x$  direction. This difference shows that the lateral length scales  $\xi$  in these two directions are different, i.e.,  $\xi_x \cong \sqrt{10}\xi_y$ . The lateral correlation lengths in the  $x$  and  $y$  directions equal  $\sqrt{2\nu_1 t}$  and  $\sqrt{2\nu_2 t}$ , respectively, and their ratio is  $\sqrt{\frac{\nu_1}{\nu_2}}$ . In fact if we do a linear transformation:  $\sqrt{\frac{\nu_1}{\nu_2}}k_y \rightarrow k'_y$ ,  $\sqrt{k_x^2 + k_y'^2} \rightarrow k'_{||}$ , then Equation (A.45) becomes isotropic,

$$P(k'_{||}, t) = 4D \frac{1 - e^{-2\nu_1 k'_{||}^2 t}}{\nu k'^2_{||}}. \quad (\text{A.47})$$

Therefore, except for the existence of an anisotropy in the lateral correlation length, the anisotropic EW equation has similar dynamic properties compared to those of the isotropic EW equation, i.e.,  $\beta = 0$ ,  $\alpha = 0$ , and  $z = 2$ .

(ii) Surface diffusion only:  $\kappa_i \neq 0$ ,  $\nu_i \approx 0$

If the surface tension contribution is negligible, then Equation (A.43) reduces to an anisotropic Mullins-diffusion equation. The corresponding

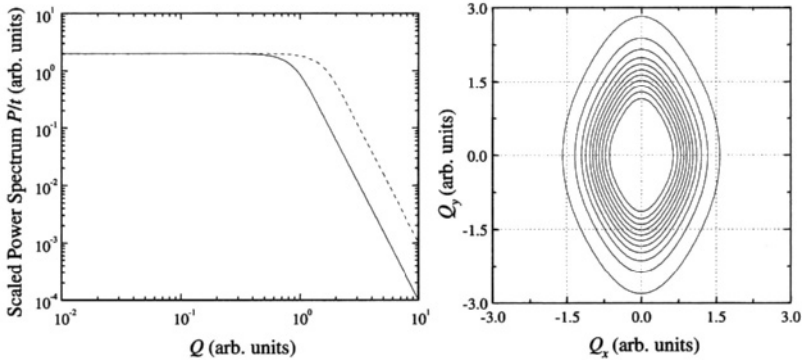


FIG. A.12 Left: Log-log plots of scaled power spectrum along the  $Q_x$  (solid curve) and  $Q_y$  (dashed curve) directions for  $\nu_1 = 0.0$ ,  $\nu_2 = 0.0$ ,  $\kappa_1 = 1.0$ ,  $\kappa_2 = 0.1$ , and  $\kappa_3 = 1.1$ . Right: Contour plots of the scaled power spectrum (from Ref. [A.38]).

power spectrum is

$$P(\mathbf{k}_{||}, t) = 4D \frac{1 - \exp[-2(\kappa_1 k_x^4 + \kappa_2 k_y^4 + \kappa_3 k_x^2 k_y^2)t]}{\kappa_1 k_x^4 + \kappa_2 k_y^4 + \kappa_3 k_x^2 k_y^2}. \quad (\text{A.48})$$

Letting  $Q_x = k_x t^{1/4}$  and  $Q_y = k_y t^{1/4}$ , Equation (A.48) then becomes

$$P(\mathbf{Q}, t)/t = 4D \frac{1 - \exp[-2(\kappa_1 Q_x^4 + \kappa_2 Q_y^4 + \kappa_3 Q_x^2 Q_y^2)]}{\kappa_1 Q_x^4 + \kappa_2 Q_y^4 + \kappa_3 Q_x^2 Q_y^2}. \quad (\text{A.49})$$

The cross sections of the scaled power spectra  $P(\mathbf{Q}, t)/t$  in the  $Q_x$  and  $Q_y$  directions shown in Figure A.12 have a similar behavior compared to case A shown in Figure A.11, except that the value of the power is  $-4$ , which leads to the same roughness exponent  $\alpha = 1$  in the  $Q_x$  and  $Q_y$  directions. The shoulders extend to different values of  $Q$  due to the anisotropic diffusions in the  $x$  and  $y$  directions, which results in different values of  $\xi$  in the  $x$  and  $y$  directions. One can also perform a linear transformation by using  $\sqrt{\frac{\kappa_2}{\kappa_1}} k_y \rightarrow k'_y$ ,  $\sqrt{k_x^2 + k_y'^2} \rightarrow k'_{||}$  in Equation (A.48) to make the power spectrum isotropic. Therefore, the dynamic behavior of the anisotropic Mullins-diffusion equation is similar to that of the isotropic Mullins-diffusion equation, which gives  $\beta = 0.25$ ,  $\alpha = 1$ , and  $z = 4$ .

Note that, for either case A or case B, the power law behavior in the large- $k_{||}$  regime is the same for both the  $k_x$  and  $k_y$  directions, i.e., the scaling is isotropic. However, the lateral correlation length scale  $\xi$  is anisotropic. For equal values of  $\frac{\nu_1}{\nu_2}$  in case A and  $\frac{\kappa_1}{\kappa_2}$  in case B the anisotropy in case A is more obvious than that in case B, as seen from the larger difference in the shoulder separation in case A.

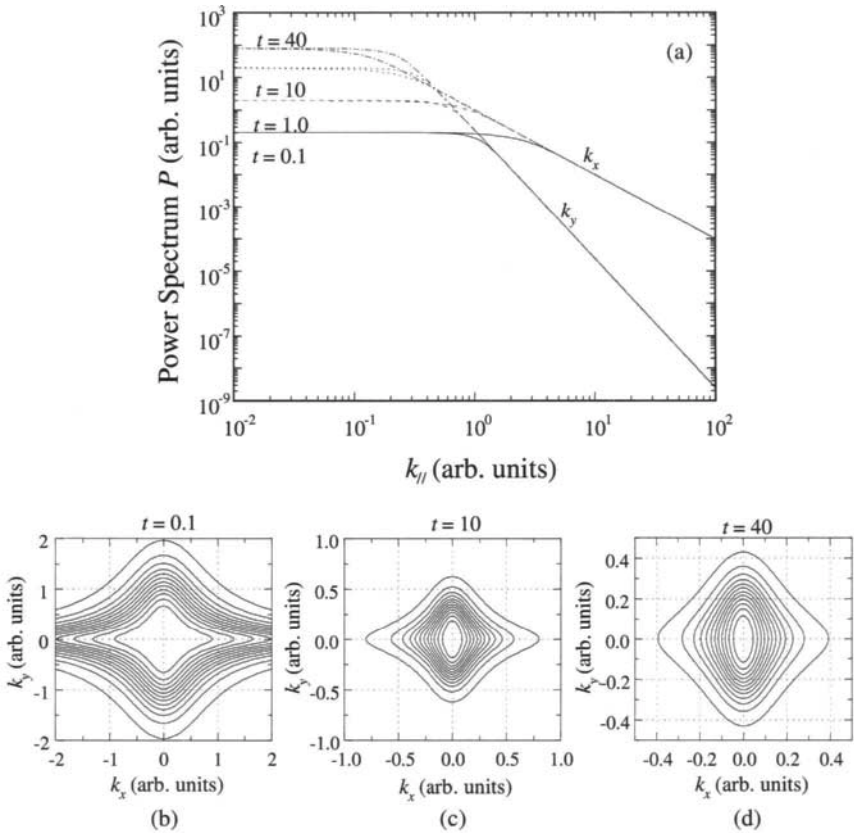


FIG. A.13 (a) Log-log plots of power spectra along the  $k_x$  and  $k_y$  directions for  $\nu_1 = 1.0$ ,  $\nu_2 = 0.1$ ,  $\kappa_1 = 0.0$ ,  $\kappa_2 = 4.0$ , and  $\kappa_3 = 40$  at different growth times,  $t = 0.1, 1.0, 10$ , and  $40$ . Contour plots of the power spectra at (b)  $t = 0.1$ , (c)  $t = 10$ , and (d)  $t = 40$  (from Ref. [A.38]).

### (iii) General case: $\kappa_i \neq 0$ , $\nu_i \neq 0$

One very interesting case involves the possibility that different physical processes dominate in different directions. For example, we consider what happens if surface tension dominates in the  $x$  direction ( $\nu_1 \gg \kappa_1$ ) while surface diffusion dominates in the  $y$  direction ( $\nu_2 \ll \kappa_2$ ). In this case, the scaling forms [Equations (A.46) and (A.49)] do not exist. Figure A.13 plots cross sections of the power spectra in both the  $k_x$  and  $k_y$  directions, and the contours of the power spectra for  $\nu_1 = 1.0$ ,  $\nu_2 = 0.1$ ,  $\kappa_1 = 0.0$ ,  $\kappa_2 = 4.0$ , and  $\kappa_3 = 40$  at different growth times. (Note that in Figure A.13 all the tails overlap for both  $k_x$  and  $k_y$  directions.) There are two notable features

in Figure A.13. The power spectra along the  $k_x$  and  $k_y$  directions scale differently at large  $k$ , giving different values of  $\alpha$ . The anisotropy in the lateral correlation length still exists since the extension of the flat shoulders in the  $k_x$  and  $k_y$  directions are different. Initially the flat shoulder in the  $k_x$  direction is longer than the shoulder in the  $k_y$  direction. With increasing growth time  $t$ , the extension of the flat shoulders in the  $k_x$  and  $k_y$  directions becomes closer and closer. Then at a certain time ( $t > 10$ ) the flat shoulder in the  $k_x$  direction becomes shorter than that of the  $k_y$  direction and we can see that the anisotropy of power spectra contours rotates 90 degrees.

It is clear that, in this case, the growth in the  $x$  direction is dominated by the surface tension term and therefore the lateral correlation length  $\xi_x$  changes as  $\xi_x = (2\nu_1 t)^{1/2}$ . The growth in the  $y$  direction is governed by the surface diffusion term and  $\xi_y = (2\kappa_2 t)^{1/4}$ . The anisotropy ratio is  $\chi = \frac{\xi_x}{\xi_y} = (\frac{2\nu_1^2}{\kappa_2})^{1/4} t^{1/4}$ . For  $t < 1$ ,  $\chi < 1$ . At time  $t_c = \frac{\kappa_2}{2\nu_1^2}$ ,  $\chi = 1$ . For  $t > \frac{\kappa_2}{2\nu_1^2}$ ,  $\chi > 1$ , and the anisotropy rotates. This behavior can be used to explain, qualitatively, the rotation of anisotropy in InAlAs growth on InP(001) observed by Sinn et al. [A.39]. For longer times, the anisotropy ratio increases as a power law of time,  $\chi \propto t^{1/4}$ , and the surface becomes more and more anisotropic. Under the condition  $\kappa_2 < 2\nu_1^2$ ,  $t_c < 1$ , one may not be able to observe the anisotropy rotation during the growth because the transition time is very short. The surface morphology still has a scaling anisotropy, but the anisotropy does not rotate within the time scale considered.

The dynamic properties in this case would also change because different growth mechanisms govern the growth in different directions. Let us consider a special case where  $\nu_1 \neq 0$ ,  $\nu_2 = 0$ ,  $\kappa_1 = 0$ ,  $\kappa_2 \neq 0$ , and  $\kappa_3 = 0$ . Equation (A.43) becomes

$$\frac{\partial h}{\partial t} = \nu_1 \frac{\partial^2 h}{\partial x^2} - \kappa_2 \frac{\partial^4 h}{\partial y^4} + \eta(\mathbf{r}, t). \quad (\text{A.50})$$

Equation (A.50) states that the surface growth process is governed by surface tension in the  $x$  direction and by surface diffusion in the  $y$  direction. Use the scaling approach of Section A.1,

$$\left\{ \begin{array}{lcl} t \rightarrow t' & = & \epsilon t, \\ h \rightarrow h' & = & \epsilon^\beta h, \\ x \rightarrow x' & = & \epsilon^{1/z_x} x, \text{ and} \\ y \rightarrow y' & = & \epsilon^{1/z_y} y, \end{array} \right. \quad (\text{A.51})$$

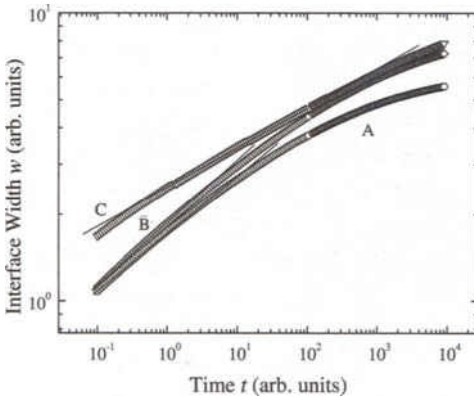


FIG. A.14 Interface width  $w$  as a function of growth time  $t$  for A:  $\nu_1 = 1.0$ ,  $\nu_2 = 0.1$ ,  $\kappa_1 = 0.0$ ,  $\kappa_2 = 4.0$ , and  $\kappa_3 = 40$ , B: for  $\nu_1 = 4.0$ ,  $\nu_2 = 0.1$ ,  $\kappa_1 = 0.0$ ,  $\kappa_2 = 1.0$ , and  $\kappa_3 = 40$ , and C:  $\nu_1 = 1.0$ ,  $\nu_2 = 0$ ,  $\kappa_1 = 0$ ,  $\kappa_2 = 4.0$ , and  $\kappa_3 = 0$  (from Ref. [A.38]).

Equation (A.50) becomes

$$\frac{\partial h}{\partial t} = \varepsilon^{1-2/z_x} \nu_1 \frac{\partial^2 h}{\partial x^2} - \varepsilon^{1-4/z_y} \kappa_2 \frac{\partial^4 h}{\partial y^4} + \varepsilon^{\frac{1}{2}-\beta-\frac{1}{2z_x}-\frac{1}{2z_y}} \eta(\mathbf{r}, t). \quad (\text{A.52})$$

Therefore, we obtain  $\beta = 1/8$ ,  $z_x = 2$ ,  $z_y = 4$ , and  $\alpha_x = \beta z_x = 1/4$ ,  $\alpha_y = \beta z_y = 1/2$ . Note that the direction-dependent  $\alpha$  values are quite different from those of both the EW model and the Mullins-diffusion model.

In Figure A.14 we plot the interface width  $w$  as a function of growth time  $t$  from a numerical integration of Equation (A.44) for specific cases of the three conditions discussed above:  $\nu_1 = 1.0$ ,  $\nu_2 = 0.1$ ,  $\kappa_1 = 0.0$ ,  $\kappa_2 = 4.0$ ,  $\kappa_3 = 40$ ;  $\nu_1 = 4.0$ ,  $\nu_2 = 0.1$ ,  $\kappa_1 = 0.0$ ,  $\kappa_2 = 1.0$ , and  $\kappa_3 = 40$  and  $\nu_1 = 1.0$ ,  $\nu_2 = 0$ ,  $\kappa_1 = 0$ ,  $\kappa_2 = 4.0$ , and  $\kappa_3 = 0$ . The values of the growth exponent  $\beta$  under these three conditions are about 0.20, 0.19, and 0.13, respectively. These  $\beta$  values lie between 0 (isotropic EW model) and 0.25 (isotropic Mullins-diffusion model). Here we should emphasize that, for each condition, there is only one  $\beta$  value for the growth even though the surface is anisotropic. However, the dynamic exponent  $z = \frac{\alpha}{\beta}$  is direction-dependent for the anisotropic scaling case.

It is clear from the slopes of the tails of the power spectra that a scaling anisotropic surface can be formed only when two (or more) different anisotropic physical mechanisms (e.g., condensation/evaporation and surface diffusion) are involved in the smoothening of the growth front. In different directions, different mechanisms dominate. Under the dynamic scaling hypothesis, the lateral correlation length scales differently with time in different directions,  $\xi_i \propto t^{1/z_i}$ , and the height-height correlation function

scales differently in different directions with different roughness exponents.

#### A.4 Surface Height Distribution during Thin-Film Roughening

If we want to know the time evolution of the distribution of  $h(\mathbf{r}, t)$ , a more detailed assumption about the statistical characteristics of the noise  $\eta(\mathbf{r}, t)$  should be made. As the  $n$ th-order correlation of the noise term  $\eta(\mathbf{r}, t)$  is defined, the solution of the Langevin equation would satisfy a certain master equation. A very simple case is to assume that  $\eta(\mathbf{r}, t)$  is a Gaussian-Markov process, i.e.,  $\eta(\mathbf{r}, t)$  not only satisfies Equation (A.8), but also meets the following conditions:

For odd  $n$ ,

$$\langle \eta(\mathbf{r}_1, t_1)\eta(\mathbf{r}_2, t_2)\dots\eta(\mathbf{r}_n, t_n) \rangle = 0. \quad (\text{A.53})$$

For even  $n$ ,

$$\begin{aligned} & \langle \eta(\mathbf{r}_1, t_1)\eta(\mathbf{r}_2, t_2)\dots\eta(\mathbf{r}_n, t_n) \rangle = \\ & a_1\delta(\mathbf{r}_1 - \mathbf{r}_2)\delta(\mathbf{r}_3 - \mathbf{r}_4)\dots\delta(\mathbf{r}_{n-1} - \mathbf{r}_n) \\ & \times\delta(t_1 - t_2)\delta(t_3 - t_4)\dots\delta(t_{n-1} - t_n) \\ & +a_2\delta(\mathbf{r}_1 - \mathbf{r}_3)\delta(\mathbf{r}_2 - \mathbf{r}_4)\dots\delta(t_1 - t_3)\delta(t_2 - t_4)\dots, \end{aligned} \quad (\text{A.54})$$

i.e., the ensemble average of the  $n (= 2m)$ th product of  $\eta(\mathbf{r}_i, t_i)$  is expressed as all the possible linear combinations of  $2m$  delta functions. For a Gaussian-Markov process, the corresponding master equation can be reduced to a Fokker-Planck equation. If we denote by  $P[h(\mathbf{r}), t]$  the distribution functional of the surface position function  $h(\mathbf{r})$ , for example, the corresponding Fokker-Planck equation for Equation (A.15) is [A.40]

$$\frac{\partial P[h, t]}{\partial t} = -\nu \int \frac{\delta}{\delta h}[P\nabla^2 h]d\mathbf{r} + D \int \frac{\delta^2 P}{\delta h^2}d\mathbf{r}. \quad (\text{A.55})$$

It has been proved that the solution for Equation (A.55) is Gaussian. However, if other statistical properties are satisfied [instead of just Equations (A.53) and (A.54)], then the Fokker-Planck equation will not take the form of Equation (A.55) and the distribution will not be a Gaussian distribution.

For a non-linear Langevin equation, even if  $\eta(\mathbf{r}, t)$  is a Gaussian-Markov process, the height distribution may not possess the Gaussian form. A famous example is the KPZ model Equation (A.35) [A.10]. The appearance of the nonlinear term  $(\nabla h)^2$  breaks the up/down symmetry, the symmetry of the interface fluctuations with respect to the mean interface height, and

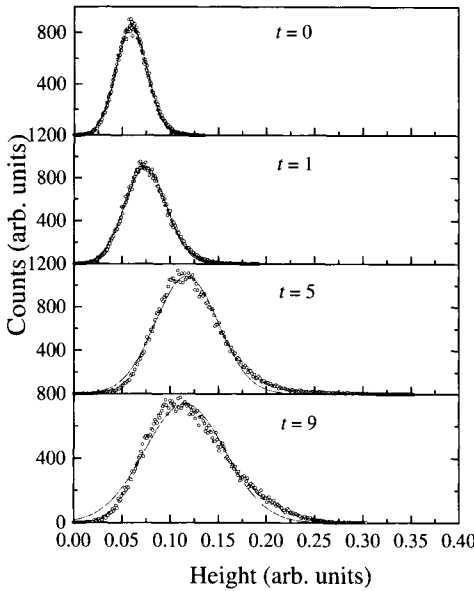


FIG. A.15 Evolution of surface height distribution with the number of iterations  $t$  for the KPZ model in 2+1 dimensions: numerical results (from Ref. [A.41]).

the height distribution becomes asymmetric. The Fokker-Planck equation for Equation (A.35) is

$$\frac{\partial P[h, t]}{\partial t} = - \int \frac{\delta}{\delta h} \{ [\nu \nabla^2 h + \frac{\lambda}{2} (\nabla h)^2] P \} d\mathbf{r} + D \int \frac{\delta^2 P}{\delta h^2} d\mathbf{r}. \quad (\text{A.56})$$

The solution for Equation (A.56) in 1+1 dimensions can be written as [A.40]

$$\begin{aligned} P(\Delta h) &\approx \exp[-\frac{(\Delta h)^2}{L}], \text{ for } t \gg L^z, \\ P(\Delta h) &\approx \exp[-(\frac{|\Delta h|}{t^{1/3}})^v], \text{ for } t \ll L^z. \end{aligned} \quad (\text{A.57})$$

Here  $\Delta h = h - \langle h \rangle$ ; for  $\Delta h > 0$ ,  $v = 3/2$  and for  $\Delta h < 0$ ,  $v \approx 2.5$ . For evolution over a long time, the surface height reaches the steady-state Gaussian distribution, while over a short time, it is a skewed distribution.

To make it clear, in Figures A.15 and A.16 we plot our results obtained from the numerical integration of the KPZ equation in 2+1 dimensions with a system size of  $256 \times 256$  at the initial stage. The noise term  $\eta(\mathbf{r}, t)$  is simulated by a random noise generator with Gaussian distribution. Figure A.15 shows how the surface height distribution evolved with the number of iterations  $t$ . The solid curve represents the best Gaussian fit. Figure A.16 shows the skewness and kurtosis [defined in Equations (2.7) and (2.8)] versus the number of iterations. For a Gaussian distribution, skewness =

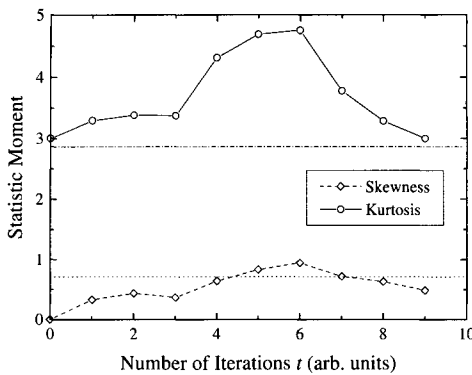


FIG. A.16 The higher-order moment coefficients skewness and kurtosis versus the number of iterations  $t$  in the KPZ model in 2+1 dimensions (from Ref. [A.41]).

0.0, and kurtosis = 3.0, as seen for  $t = 0$ . However, for  $t > 0$ , skewness is greater than 0.0, which shows the asymmetric distribution of surface height. (For 2+1 dimensions, the height distribution does not approach a steady-state Gaussian distribution.)

## References

- A.1 *Dynamics of Fractal Surfaces*, edited by F. Family and T. Vicsek (World Scientific, Singapore, 1991).
- A.2 T. Vicsek, *Fractal Growth Phenomena* (World Scientific, Singapore, 1992).
- A.3 A.-L. Barabási and H. E. Stanley, *Fractal Concepts in Surface Growth* (Cambridge University Press, New York, 1995).
- A.4 P. Meakin, *Fractals, Scaling, and Growth Far from Equilibrium* (Cambridge University Press, Cambridge, 1998).
- A.5 H.-N. Yang, Y.-P. Zhao, G.-C. Wang, and T.-M. Lu, "Noise-induced roughening evolution of amorphous Si films grown by thermal evaporation," *Phys. Rev. Lett.* **76**, 3774 (1996).
- A.6 T.-M. Lu, H.-N. Yang, and G.-C. Wang, "When interface gets rough...," in *Fractal Aspects of Materials*, Mat. Res. Soc. Symp. Proc. Vol **367**, edited by F. Family, P. Meakin, B. Sapoval, and R. Wool, p. 283 (Material Research Society, Pittsburgh, 1995).
- A.7 S. F. Edwards and D. R. Wilkinson, "The surface statistics of a granular aggregate," *Proceedings of the Royal Society (London) A* **381**, 17 (1982).
- A.8 W. W. Mullins, "Theory of thermal grooving," *J. Appl. Phys.* **33**, 77 (1957).
- A.9 Y.-P. Zhao, H.-N. Yang, G.-C. Wang, and T.-M. Lu, "Diffraction from diffusion-barrier-induced mound structures in epitaxial growth fronts," *Phys. Rev. B* **57**, 1922 (1998).
- A.10 M. Kardar, G. Parisi, and Y.-C. Zhang, "Dynamical scaling of growing interfaces," *Phys. Rev. Lett.* **56**, 899 (1986).
- A.11 J. Villain, "Continuum models of crystal growth from atomic beams with and without deposition," *J. Phys. I (France)* **1**, 19 (1991).

- A.12 M. D. Johnson, C. Orme, A. W. Hunt, D. Graff, J. Sudijono, L. M. Sander, and B. G. Orr, "Stable and unstable growth in molecular beam epitaxy," *Phys. Rev. Lett.* **72**, 116 (1994).
- A.13 M. Siegert and M. Plischke, "Slope selection and coarsening in molecular beam epitaxy," *Phys. Rev. Lett.* **73**, 1517 (1994).
- A.14 P. E. Hegeman, H. J.W. Zandvliet, G. A. M. Kip, and A. van Silfhout, "Kinetic roughening of vicinal Si(001)," *Surf. Sci.* **311**, L655 (1994).
- A.15 J. A. Stroscio, D. T. Pierce, M. D. Stiles, A. Zangwill, and L. M. Sander, "Coarsening of unstable surface features during Fe(001) homoepitaxy," *Phys. Rev. Lett.* **75**, 4246 (1995).
- A.16 J. E. Van Nostrand, S. J. Chey, M.-A. Hasan, D. G. Cahill, and J. E. Greene, "Surface morphology during multilayer epitaxial growth of Ge(001)," *Phys. Rev. Lett.* **74**, 1127 (1995).
- A.17 F. Tsui, J. Wellman, C. Uher, and R. Clarke, "Morphology transition and layer-by-layer growth of Rh(111)," *Phys. Rev. Lett.* **76**, 3164 (1996).
- A.18 J.-K. Zuo and J. F. Wendelken, "Evolution of mound morphology in reversible homoepitaxy on Cu(100)," *Phys. Rev. Lett.* **78**, 2791 (1997).
- A.19 J. G. Amar and F. Family, "Characterization of surface morphology in epitaxial growth," *Surf. Sci.* **365**, 177 (1996).
- A.20 P. Smilauer and D. D. Vvedensky, "Coarsening and slope evolution during unstable epitaxial growth," *Phys. Rev. B* **52**, 14263 (1995).
- A.21 M. Siegert and M. Plischke, "Formation of pyramids and mounds in molecular beam epitaxy," *Phys. Rev. E* **53**, 307 (1996).
- A.22 M. Rost and J. Krug, "Damping of growth oscillations in molecular beam epitaxy: a renormalization group approach," *Journal de Physique I* **7**, 1627 (1997).
- A.23 R. P. U. Karunasiri, R. Bruinsma, and J. Rudnick, "Thin-film growth and the shadowing instability," *Phys. Rev. Lett.* **62**, 788 (1989).
- A.24 J. H. Yao and H. Guo, "Shadowing instability in three dimensions," *Phys. Rev. E* **47**, 1007 (1993).
- A.25 J. H. Yao and H. Guo, "Interfacial dynamics with long-range screening," *Phys. Rev. E* **47**, 3903 (1993).
- A.26 Y.-P. Zhao, J. Drotar, G.-C. Wang, and T.-M. Lu, "Roughening in plasma etch fronts of Si(100)," *Phys. Rev. Lett.* **82**, 4882 (1999).
- A.27 J. T. Drotar, Y.-P. Zhao, T.-M. Lu, and G.-C. Wang, "Mechanisms for plasma and reactive ion etch-front roughening," *Phys. Rev. B* **61**, 3012 (2000).
- A.28 J. B. Hudson, *Surface Science – An Introduction* (Butterworth-Heinemann, Boston, 1992).
- A.29 Y.-W. Mo, B. S. Swartzentruber, R. Kariotis, M. B. Webb, and M. G. Lagally, "Growth and equilibrium structures in the epitaxy of Si on Si(001)," *Phys. Rev. Lett.* **63**, 2393 (1989).
- A.30 Y. W. Mo, J. Kleiner, M. B. Webb, and M. G. Lagally, "Activation energy for surface diffusion of Si on Si(001): a scanning-tunneling-microscopy study," *Phys. Rev. Lett.* **66**, 1998 (1991).
- A.31 R. J. Hamers, U. K. Kohler, and J. E. Demuth, "Epitaxial growth of silicon on Si(001) by scanning tunneling microscopy," *J. Vac. Sci. Technol. A* **8**, 195 (1990).
- A.32 B. Voigtlander, T. Weber, P. Smilauer, and D. E. Wolf, "Transition from island growth to step-flow growth for Si/Si(100) epitaxy," *Phys. Rev. Lett.* **78**, 2164 (1997).
- A.33 S. Kodiyalam, K. E. Khor, and S. Das Sarma, "Calculated Schwoebel barriers on Si(111) steps using an empirical potential," *Phys. Rev. B* **53**, 9913 (1996).
- A.34 D. J. Srolovitz, "On the stability of surfaces of stressed solids," *Acta Metall.* **37**, 621 (1989).

- A.35 F. Jonsdottir and L. B. Freund, "Evolution of surface roughness of a strained epitaxial film due to interface misfit dislocations," in *Mechanisms of Thin Film Evolution*, Mat. Res. Soc. Symp. Proc. Vol. **633**, p. 309, edited by S. M. Yalisove, C. V. Thompson, and D. J. Eaglesham (Materials Research Society, Pittsburgh, 1993).
- A.36 C. Roland and G. H. Gilmer, "Epitaxy on surfaces vicinal to Si(001). I. Diffusion of silicon adatoms over the terraces," Phys. Rev. B **46**, 13428 (1992).
- A.37 C. Roland and G. H. Gilmer, "Epitaxy on surfaces vicinal to Si(001). II. Growth properties of Si(001) steps," Phys. Rev. B **46**, 13437 (1992).
- A.38 Y.-P. Zhao, G.-C. Wang, and T.-M. Lu, "Anisotropy in growth front roughening," Phys. Rev. B **58**, 13909 (1998).
- A.39 M. T. Sinn, J. A. del Alamo, B. R. Bennett, K. Haberman, and F. G. Celii, "Characterization of surface roughness anisotropy on mismatched InAlAs/InP heterostructures," J. Electronic Mater. **25**, 313 (1996).
- A.40 T. Halpin-Healy and Y.-C. Zhang, "Surface growth, directed polymers, and all that," Phys. Rep. **254**, 215 (1995).
- A.41 Y.-P. Zhao, G.-C. Wang, and T.-M. Lu, "Diffraction from non-Gaussian rough surfaces," Phys. Rev. B **55**, 13938 (1997).

This Page Intentionally Left Blank

## Appendix B TIME EVOLUTION OF THE INTERFACE WIDTH IN THE EDWARDS-WILKINSON EQUATION

In order to evaluate the behavior of the interface width  $w$  versus growth time  $t$  of the Edwards-Wilkinson equation, we follow the general treatment of Yang et al. [B.1] for Equation (A.27).

The general form of Equation (A.27) can be expressed as

$$\int_0^{1/b_c} \frac{1 - \exp[-(\xi q)^\gamma]}{q^{\gamma-\delta}} dq, \quad (\text{B.1})$$

where  $\gamma > 0$  and  $\delta > -1$ . The effect of the short-wavelength cutoff  $1/b_c$  in the integral can be approximated by a Gaussian cutoff,  $\exp[-(b_c q)^\gamma]$ , i.e.,

$$\int_0^{1/b_c} \frac{1 - \exp[-(\xi q)^\gamma]}{q^{\gamma-\delta}} dq \approx \int_0^\infty \frac{1 - \exp[-(\xi q)^\gamma]}{q^{\gamma-\delta}} \exp[-(b_c q)^\gamma] dq. \quad (\text{B.2})$$

Equation (B.2) becomes

$$\int_0^\infty \frac{\exp[-aq^\gamma] - \exp[-sq^\gamma]}{q^{\gamma-\delta}} dq = g(\gamma, \delta, s). \quad (\text{B.3})$$

In order to calculate  $g(\gamma, \delta, s)$ , we first differentiate  $g(\gamma, \delta, s)$  with respect to  $s$ :

$$\frac{\partial g(\gamma, \delta, s)}{\partial s} = \int_0^\infty q^\delta e^{-sq^\gamma} dq = Cs^{-(\delta+1)/\gamma}, \quad (\text{B.4})$$

where  $C$  is a constant and equals  $\int_0^\infty x^\delta e^{-x^\gamma} dx = \gamma^{-1} \Gamma(\frac{\delta+1}{\gamma})$ . We can obtain  $g(\gamma, \delta, s)$  by reintegrating Equation (B.4), which gives

$$\begin{aligned} g(\gamma, \delta, s) &= C \int_a^s s^{-(\delta+1)/\gamma} ds \\ &\propto \begin{cases} \ln(s/a), & \text{for } (\delta+1)/\gamma = 1, \\ s^{1-(\delta+1)/\gamma} - a^{1-(\delta+1)/\gamma}, & \text{for } (\delta+1)/\gamma \neq 1. \end{cases} \end{aligned} \quad (\text{B.5})$$

Inserting  $a = b_c^\gamma$  and  $s = \xi^\gamma + b_c^\gamma$  into Equation (B.5), we obtain an analytical result:

$$\int_0^{1/b_c} \frac{1 - \exp[-(\xi q)^\gamma]}{q^{\gamma-\delta}} dq \sim \begin{cases} \ln[1 + (\xi/b_c)^\gamma], & \text{for } (\delta+1)/\gamma = 1, \\ [1 + (\xi/b_c)^\gamma]^{1-(\delta+1)/\gamma} - 1, & \text{for } (\delta+1)/\gamma \neq 1. \end{cases} \quad (\text{B.6})$$

Therefore, for  $\gamma = 2$  and  $\delta = 1$ , i.e.,  $(\delta+1)/\gamma = 1$ , we obtain the  $w(t)$  behavior for the Edwards-Wilkinson equation. For  $\gamma = 4$  and  $\delta = 3$ , we can obtain the  $w(t)$  behavior for the Mullins diffusion equation.

### Reference

3.1 H.-N. Yang, G.-C. Wang, and T-M. Lu, unpublished.

## Appendix C EFFECT OF DIFFERENT FUNCTIONAL FORMS OF THE SCALING FUNCTION ON THE SHAPE OF THE DIFFRACTION PROFILE

In Section 9.2.1 we discussed the general asymptotic behaviors of diffraction profiles based on the asymptotic scaling function  $f(x)$ . We also used a special functional form Equation (9.3) to illustrate the behaviors of the scattering profiles. In order to calculate the diffraction profiles, one does need a functional form for a scaling function. Here we will discuss how sensitively the functional form of a scaling function affects the diffraction profile.

For examples, as discussed in Chapter 3, the real-space structure factor can have other forms. Among all the proposed forms, the following forms differ the most [C.1]:

$$H(r) = 2w^2 \exp[-\alpha(\frac{r}{\xi})][2 \cosh(\frac{r}{\xi}) - 2]^\alpha, \text{ and} \quad (\text{C.1})$$

$$H(r) = 2w^2 \{1 - \exp[-(\frac{r}{\xi})^2]\}^\alpha. \quad (\text{C.2})$$

Figure C.1 plots the height-height correlation functions Equations (C.1) and (C.2) for  $\alpha = 0.7$ . We can see that both Equations (C.1) and (C.2) have the same asymptotic behaviors for small  $r$  and large  $r$ , satisfying the scaling form  $f(x)$  shown in Equation (3.3). However, the crossover from small  $r$  to large  $r$  is quite different as shown in Figure C.1. Equation (C.2) has a more abrupt crossover than that of Equation (C.1). This dif-

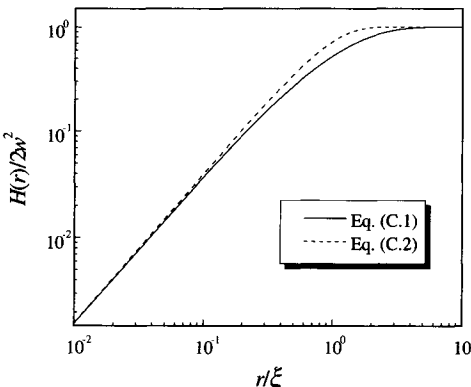


FIG. C.1 The plot of different forms of height-height correlation function for a self-affine surface with  $\alpha = 0.7$ .

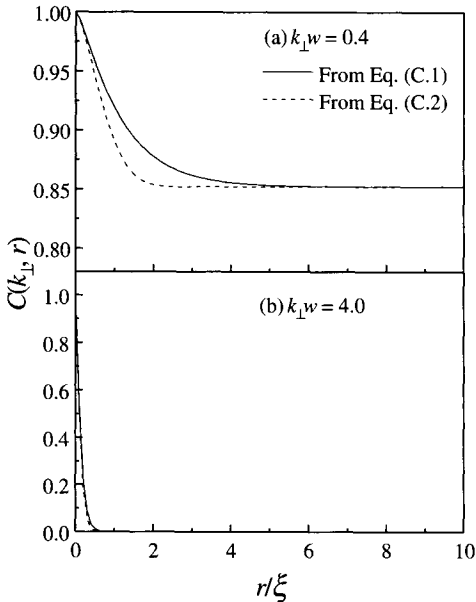


FIG. C.2 The height difference function resulting from different forms of the height-height correlation function for (a)  $k_{\perp}w = 0.4$  and (b)  $k_{\perp}w = 4.0$ .

ference in the crossover behavior would cause a difference in the height difference function  $C(k_{\perp}, r)$ . Figure C.2 shows the height difference functions calculated from both Equations (C.1) and (C.2) for  $k_{\perp}w = 0.4$  and 4.0 at  $\alpha = 0.7$ . For small  $k_{\perp}w$  the height difference function  $C(k_{\perp}, r)$  is very different for different forms of the height-height correlation function, but for large  $k_{\perp}w$  the height difference function  $C(k_{\perp}, r)$  is quite similar for different forms of the height-height correlation function. Therefore, we would expect the diffraction profiles at small  $k_{\perp}w$  are quite different while at large  $k_{\perp}w$  the profiles are similar for different functional forms of the height-height correlation function. In fact, as discussed in Section 9.2.1, at small  $k_{\perp}w$ , the diffuse profile is proportional to the power spectrum. If the crossover of the height-height correlation function is different, then the crossover in the power spectrum should also be different. However, at large  $k_{\perp}w$ , as discussed in Equations (9.18) and (9.19), the diffuse profile is only determined by the asymptotic behavior in the small  $r$  regime. Since both Equations (C.1) and (C.2) have the same asymptotic behavior at small  $r$ , they would give the same diffuse profile. Substituting Equations (C.1) and (C.2) into Equation (7.26) and performing the numerical integration, we can obtain the diffraction profiles from different height-height correlation

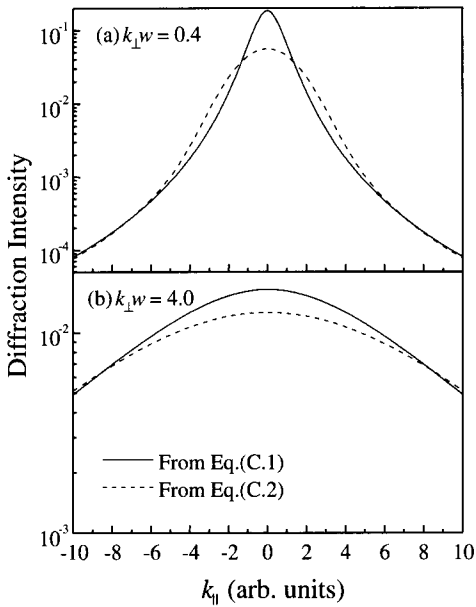


FIG. C.3 The diffuse profiles calculated from different forms of the height-height correlation function for the same roughness parameters:  $w = 1.0$ ,  $\xi = 1.0$ , and  $\alpha = 0.7$ .

functional forms as shown in Figure C.3 for  $k_{\perp}w = 0.4$  and  $4.0$ . We can see that the diffuse profiles at small  $k_{\perp}w$  are very different for different forms of the height-height correlation function, but as  $k_{\perp}w$  increases, the difference between the diffuse profiles of these two forms of height-height correlation function becomes less obvious. In Figure C.4, we plot the peak intensity and FWHM of the diffuse profile as a function of  $\Omega$  for these two forms of the height-height correlation function. As we can see, at small  $\Omega$ , both the peak intensity and the FWHM are different for different forms of height-height correlation function. This is mainly due to the fact that at small  $\Omega$ , the diffuse profile is proportional to the surface power spectrum, and they are very different for these two different height-height correlation functions. However, the asymptotic behavior of the FWHM still remains the same, i.e., the FWHM almost remains unchanged at small  $\Omega$ . As  $\Omega$  increases, the difference in both the peak intensity and the FWHM become smaller. At large  $\Omega$ , there is almost no difference in the peak intensity and the FWHM of the diffuse profile, and both the peak intensity and the FWHM obey the same asymptotic behavior as we have shown in Equations (9.22) and (9.23).

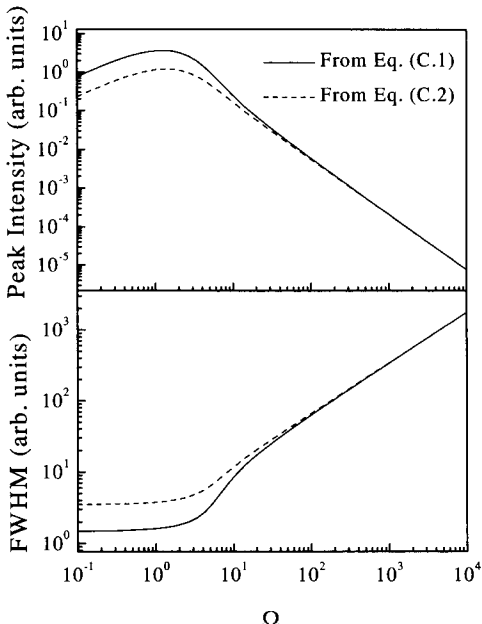


FIG. C.4 The peak intensity and the FWHM of the diffuse profiles calculated from different forms of the height-height correlation function for the same roughness parameters:  $w = 1.0$ ,  $\xi = 1.0$ , and  $\alpha = 0.7$ .

#### Reference

- C.1 G. Palasantzas and J. Krim, "Effect of the form of the height-height correlation function on diffuse X-ray scattering from a self-affine surface," Phys. Rev. B **48**, 2873 (1993).

## Appendix D JOINT DISTRIBUTIONS OF RANDOM PROCESSES WITH NON-GAUSSIAN HEIGHT DISTRIBUTIONS

A general single-variable Langevin equation takes the form [D.1, D.2],

$$\frac{dx}{dr} = h(x, r) + g(x, r)\eta(r), \quad (\text{D.1})$$

where  $\eta(r)$  is a Gaussian-Markov process, satisfying

$$\begin{cases} <\eta(r)> = 0, \\ <\eta(r)\eta(r')> = 2\delta(r - r'). \end{cases} \quad (\text{D.2})$$

Here we adopt the Stratonovich interpretation of Equation (D.1). The corresponding Fokker-Planck equation for Equation (D.1) is

$$\frac{\partial p(x|x_0; r)}{\partial r} = -\frac{\partial}{\partial x} [A(x, r)p(x|x_0; r)] + \frac{\partial^2}{\partial x^2} [B(x, r)p(x|x_0; r)], \quad (\text{D.3})$$

where

$$A(x, r) = h(x, r) + g(x, r)\frac{\partial g(x, r)}{\partial x}, \quad (\text{D.4})$$

$$B(x, r) = g^2(x, r), \quad (\text{D.5})$$

and  $p(x|x_0; r)$  is the conditional probability density, and  $x$  and  $x_0$  are separated by distance  $r$ . We now consider the solution of Equation (D.3) corresponding to an initial value,

$$p(x|x_0; r = 0) = \delta(x - x_0), \quad (\text{D.6})$$

and the reflecting barriers' boundary conditions,

$$\frac{\partial}{\partial x} [B(x, r)p] - A(x, r)p = 0, \text{ at } x = x_1, x_2. \quad (\text{D.7})$$

A further assumption can be made concerning the coefficient  $A(x, r)$  and  $B(x, r)$ :

$$\begin{cases} A(x, r) = A(x)F(r), \\ B(x, r) = B(x)F(r). \end{cases} \quad (\text{D.8})$$

Then Equation (D.3) can be solved by separation of variables. Letting

$$p(x|x_0; r) = X(x)T(r), \quad (\text{D.9})$$

we have

$$\frac{dT}{dr} = -\lambda F(r)T(r), \text{ and} \quad (\text{D.10})$$

$$\frac{d^2}{dx^2} [B(x)X(x)] - \frac{d}{dx} [A(x)X(x)] + \lambda X(x) = 0. \quad (\text{D.11})$$

The solution for Equation (D.10) is obvious:

$$T(r) = T(0) \exp[-\lambda \int_0^r F(r)dr]. \quad (\text{D.12})$$

The solution for Equation (D.11) is an eigenvalue problem of a second-order ordinary differential equation. We can give some special form of  $A(x)$  and  $B(x)$ , and Equation (D.11) can be changed to a Sturm-Liouville equation. Letting

$$B(x) = \beta(cx^2 + dx + e), \quad (\text{D.13})$$

$$A(x) = \frac{dB(x)}{dx} + \beta(ax + b), \quad (\text{D.14})$$

and

$$\frac{dW(x)}{dx} = \frac{ax + b}{cx^2 + dx + e} W(x). \quad (\text{D.15})$$

Equation (D.11) becomes a standard Sturm-Liouville equation,

$$\frac{d}{dx} \left[ B(x)W(x) \frac{dX}{dx} \right] + \lambda W(x)X = 0, \quad (\text{D.16})$$

with the boundary condition

$$B(x)W(x) \frac{dX}{dx} = 0, \quad x = x_1, x_2. \quad (\text{D.17})$$

Therefore, the general solution for Equation (D.3) is

$$p(x|x_0; t) = W(x) \sum_n e^{-\lambda_n \int_0^t F(t)dt} Q_n(x)Q_n(x_0), \quad (\text{D.18})$$

where  $Q_n(x)$  is the eigenfunction of Equations (D.16) and (D.17), and  $\lambda_n$  is the corresponding eigenvalue. The  $Q_n$  satisfy the following ortho-normalization relation:

$$\int_{x_1}^{x_2} W(x) Q_n(x) Q_m(x) dx = \delta_{nm}. \quad (\text{D.19})$$

In fact,  $Q_n(x)$  are the classic orthogonal polynomials. If the probability density for  $x_0$  is given as  $W(x_0)$ , then the joint distribution for  $x$  and  $x_0$  is

$$p(x, x_0; r) = W(x) W(x_0) \sum_n \bar{R}^{\lambda_n} Q_n(x) Q_n(x_0), \quad (\text{D.20})$$

where

$$\bar{R}(r) = \exp \left[ - \int_0^r F(r) dr \right]. \quad (\text{D.21})$$

The correlation function  $R(r)$  is given as

$$R(r) = \bar{R}(r)^{\lambda_1}. \quad (\text{D.22})$$

## References

- D.1 H. Risken, *The Fokker-Planck Equations: Methods of Solution and Applications* (Springer-Verlag, New York, 1984).
- D.2 J. Honerkamp, *Stochastic Dynamical System: Concepts, Numerical Methods, Data Analysis*, translated by K. Lindenberg (VCH, New York, 1994).

This Page Intentionally Left Blank

## Appendix E HEIGHT DIFFERENCE FUNCTION $C(k_{\perp}, r)$ FOR DIFFERENT HEIGHT DISTRIBUTIONS

The individual height distributions are discussed below.

### E.1 Continuous Surface

#### A. Gaussian distribution

If the surface height obeys the Gaussian distribution,

$$p(x) = \frac{1}{\sqrt{2\pi}w} \exp\left(-\frac{x^2}{2w^2}\right). \quad (\text{E.1})$$

Equation (E.1) is the weighting function of Hermite polynomials  $H_n(x)$ :

$$\int_{-\infty}^{\infty} \frac{1}{\sqrt{2\pi}w} \exp\left(-\frac{x^2}{2w^2}\right) H_n\left(\frac{x}{\sqrt{2w}}\right) H_m\left(\frac{x}{\sqrt{2w}}\right) dx = 2^n n! \delta_{nm}, \quad (\text{E.2})$$

i.e.,

$$h_n^2 = 2^n n!. \quad (\text{E.3})$$

The eigenvalue is  $\lambda_n = n$ . Therefore,

$$p_j(x, y; R) = \frac{1}{2\pi w^2} \exp\left(-\frac{x^2 + y^2}{2w^2}\right) \sum_{n=0}^{\infty} \frac{R^n}{2^n n!} H_n\left(\frac{x}{\sqrt{2w}}\right) H_n\left(\frac{y}{\sqrt{2w}}\right). \quad (\text{E.4})$$

As

$$\sum_{n=0}^{\infty} \frac{t^n}{2^n n!} H_n(x) H_n(y) = (1 - t^2)^{-1/2} \exp\left[\frac{2xyt - (x^2 + y^2)t^2}{1 - t^2}\right], \quad (\text{E.5})$$

the joint distribution for the Gaussian height distribution is

$$p_j(x, y; R) = \frac{1}{2\pi w^2 \sqrt{1 - R^2}} \exp\left[-\frac{x^2 + y^2 - 2xyR}{2w^2(1 - R^2)}\right]. \quad (\text{E.6})$$

This is the well-known joint distribution function for a Gaussian process. According to Equation (12.5), the height difference distribution is

$$P(z, r) = \frac{1}{2w\sqrt{\pi(1 - R)}} \exp\left[-\frac{z^2}{4w^2(1 - R)}\right]. \quad (\text{E.7})$$

Equation (E.7) indicates that the height difference  $z$  also obeys the Gaussian distribution. From the definition of the height-height correlation function  $H(r)$ ,

$$H(r) = \langle [h(r) - h(0)]^2 \rangle = 2w^2(1 - R), \quad (\text{E.8})$$

one has

$$P(z, r) = \frac{1}{\sqrt{2\pi H(r)}} \exp\left[-\frac{z^2}{2H(r)}\right], \quad (\text{E.9})$$

and the height difference function is

$$C(k_\perp, r) = \exp\left[-\frac{1}{2}k_\perp^2 H(r)\right]. \quad (\text{E.10})$$

### B. Exponential distribution

$$p(x) = \frac{1}{w} \exp\left(-\frac{x}{w}\right), \quad x \geq 0. \quad (\text{E.11})$$

This is an asymmetric distribution, and its corresponding orthogonal polynomials are Laguerre polynomials  $L_n(x)$ :

$$h_n^2 = \int_0^\infty \frac{1}{w} \exp\left(-\frac{x}{w}\right) L_n\left(\frac{x}{w}\right) L_n\left(\frac{x}{w}\right) dx = 1. \quad (\text{E.12})$$

The corresponding eigenvalue  $\lambda_n = n$ . Therefore,

$$p_j(x, y; R) = \frac{1}{w^2} \exp\left(-\frac{x+y}{w}\right) \sum_{n=0}^{\infty} R^n L_n\left(\frac{x}{w}\right) L_n\left(\frac{y}{w}\right). \quad (\text{E.13})$$

As

$$\sum_{n=0}^{\infty} L_n(x) L_n(y) t^n = \frac{1}{1-t} \exp\left(-t \frac{x+y}{1-t}\right) I_0\left(\frac{2\sqrt{xyt}}{1-t}\right), \quad (\text{E.14})$$

where  $I_0(x)$  is the zeroth-order modified Bessel function. Then

$$p_j(x, y; R) = \frac{1}{w^2(1-R)} \exp\left[-\frac{x+y}{w(1-R)}\right] I_0\left[\frac{2\sqrt{xyR}}{w(1-R)}\right]. \quad (\text{E.15})$$

Therefore,

$$\begin{aligned} P(z, r) &= \int_0^\infty \frac{1}{w^2(1-R)} \exp\left[-\frac{z+2y}{w(1-R)}\right] I_0\left[\frac{2\sqrt{(y+z)yR}}{w(1-R)}\right] dy \\ &= \frac{1}{2w\sqrt{1-R}} \exp\left(-\frac{|z|}{w\sqrt{1-R}}\right), \end{aligned} \quad (\text{E.16})$$

i.e.,

$$P(z, r) = \frac{1}{2w\sqrt{1-R}} \exp\left(-\frac{|z|}{w\sqrt{1-R}}\right), \quad -\infty \leq z \leq \infty. \quad (\text{E.17})$$

This means that the height difference distribution is still exponential but it becomes symmetric. In this case,

$$C(k_{\perp}, r) = \frac{1}{1 + \frac{1}{2}k_{\perp}^2 H(r)}. \quad (\text{E.18})$$

This is different from that of the Gaussian distribution.

### C. Gamma distribution

$$p(x) = \frac{1}{\Gamma(\kappa+1)\sigma^{\kappa+1}} x^{\kappa} e^{-x/\sigma}, \quad x \geq 0. \quad (\text{E.19})$$

This is the weighting function of associated Laguerre polynomials:

$$\begin{aligned} h_n^2 &= \int_0^{\infty} \frac{1}{\Gamma(\kappa+1)\sigma^{\kappa+1}} x^{\kappa} \exp\left(-\frac{x}{\sigma}\right) L_n^{(\kappa)}\left(\frac{x}{\sigma}\right) L_n^{(\kappa)}\left(\frac{x}{\sigma}\right) dx \\ &= \frac{\Gamma(n+\kappa+1)}{\Gamma(\kappa+1)\Gamma(n+1)}. \end{aligned} \quad (\text{E.20})$$

The corresponding eigenvalue  $\lambda_n = n$ . The joint distribution is

$$\begin{aligned} p_j(x, y; R) &= \frac{1}{\Gamma(\kappa+1)\sigma^{2\kappa+2}} (xy)^{\kappa} \exp\left(-\frac{x+y}{\sigma}\right) \sum_{n=0}^{\infty} \frac{\Gamma(n+1)}{\Gamma(n+\kappa+1)} \\ &\quad \times R^n L_n^{(\kappa)}\left(\frac{x}{\sigma}\right) L_n^{(\kappa)}\left(\frac{y}{\sigma}\right), \end{aligned} \quad (\text{E.21})$$

and

$$\begin{aligned} &\sum_{n=0}^{\infty} \frac{\Gamma(n+1)R^n}{\Gamma(n+\kappa+1)} L_n^{(\kappa)}(x) L_n^{(\kappa)}(y) = \\ &\frac{1}{(xyR)^{\kappa/2}(1-R)} \exp\left(-R\frac{x+y}{1-R}\right) I_{\kappa}\left(\frac{2\sqrt{xyR}}{1-R}\right), \end{aligned} \quad (\text{E.22})$$

where  $I_{\kappa}(x)$  is the  $\kappa$ th-order modified Bessel function. Then

$$\begin{aligned} p_j(x, y; R) &= \frac{1}{\Gamma(\kappa+1)\sigma^{\kappa+2}(1-R)R^{\kappa/2}} (xy)^{\kappa/2} \\ &\quad \times \exp\left[\frac{x+y}{\sigma(1-R)}\right] I_{\kappa}\left[\frac{2\sqrt{xyR}}{\sigma(1-R)}\right]. \end{aligned} \quad (\text{E.23})$$

The height difference distribution is calculated as

$$\begin{aligned} P(z, r) = & \frac{1}{\Gamma(\kappa + 1)\sigma\sqrt{\pi}(1 - R)^{\kappa+1}} \left( \frac{z\sqrt{1 - R}}{2\sigma} \right)^{\kappa+1/2} \\ & \times K_{\kappa+1/2} \left( \frac{z}{\sigma\sqrt{1 - R}} \right), \end{aligned} \quad (\text{E.24})$$

where  $K_\nu$  is a modified Bessel function. The height difference function is then

$$C(k_\perp, r) = \frac{1}{[1 + k_\perp^2 \sigma^2 (1 - R)]^{\kappa+1}}. \quad (\text{E.25})$$

Note that for this distribution, the interface width  $w$  is expressed as

$$w^2 = (\kappa + 1)\sigma^2. \quad (\text{E.26})$$

Therefore,

$$C(k_\perp, r) = \frac{1}{[1 + \frac{k_\perp^2 H(r)}{2(\kappa+1)}]^{\kappa+1}}. \quad (\text{E.27})$$

The exponential distribution is a special case when  $\kappa = 0$ .

#### D. Rayleigh distribution

$$p(x) = \frac{x}{w^2} \exp\left(-\frac{x^2}{2w^2}\right), x \geq 0. \quad (\text{E.28})$$

This is also an asymmetric distribution. The corresponding orthogonal polynomials are Laguerre polynomials  $L_n(x)$ :

$$h_n^2 = \int_0^\infty \frac{x}{w^2} \exp\left(-\frac{x^2}{2w^2}\right) L_n\left(\frac{x^2}{2w^2}\right) L_n\left(\frac{x^2}{2w^2}\right) dx = 1. \quad (\text{E.29})$$

The joint distribution is

$$p_j(x, y; R) = \frac{xy}{\sigma^4} \exp\left(-\frac{x^2 + y^2}{2\sigma^2}\right) \sum_{n=0}^{\infty} R^n L_n\left(\frac{x^2}{2\sigma^2}\right) L_n\left(\frac{y^2}{2\sigma^2}\right). \quad (\text{E.30})$$

Using Equation (E.14), Equation (E.30) becomes

$$p_j(x, y; R) = \frac{xy}{w^4(1 - R)} \exp\left[-\frac{x^2 + y^2}{w^2(1 - R)}\right] I_0\left[\frac{2xy\sqrt{R}}{w^2(1 - R)}\right]. \quad (\text{E.31})$$

Therefore,

$$P(z, r) = \int_0^\infty \frac{y(y+z)}{w^4(1-R)} \exp\left[-\frac{y^2 + (z+y)^2}{2w^2(1-R)}\right] I_0\left[\frac{y(y+z)\sqrt{R}}{w^2(1-R)}\right] dy \quad (\text{E.32})$$

and

$$C(k_\perp, r) = \sum_{n=0}^{\infty} \frac{\pi k_\perp w^2}{2} [(-\frac{1}{2})_n]^2 R^n {}_2F_2(\frac{3}{2}, \frac{3}{2}; \frac{3}{2}, \frac{3}{2} - n; -\frac{k_\perp^2 w^2}{2}), \quad (\text{E.33})$$

where  ${}_2F_2(\alpha, \beta; \gamma, \eta; z)$  is a hyper-geometric function.

### E. Uniform distribution

$$p(x) = \frac{1}{2a}, \quad -a \leq x \leq a. \quad (\text{E.34})$$

The corresponding polynomials are Legendre polynomials  $P_n(x)$ :

$$h_n^2 = \int_{-a}^a \frac{1}{2a} P_n(\frac{x}{a}) P_n(\frac{x}{a}) dx = \frac{1}{2a}. \quad (\text{E.35})$$

The corresponding eigenvalue is  $\lambda_n = n(n+1)$ . The joint distribution is

$$p_j(x, y; R) = \frac{1}{4a^2} \sum_{n=0}^{\infty} (2n+1) R^{n(n+1)/2} P_n(\frac{x}{a}) P_n(\frac{y}{a}). \quad (\text{E.36})$$

The height difference distribution is

$$P(z, r) = \frac{1}{4a^2} \sum_{n=0}^{\infty} (2n+1) R^{n(n+1)/2} \int_{x_1}^{x_2} P_n(\frac{y+z}{a}) P_n(\frac{y}{a}) dy, \quad (\text{E.37})$$

where  $x_1$  and  $x_2$  are the integration boundary,  $x_1 = \max[-a-z, -a]$ , and  $x_2 = \min[a-z, a]$ . The range of  $z$  is from  $-2a$  to  $2a$ . The height difference function is therefore

$$C(k_\perp, r) = \frac{\pi}{2k_\perp a} \sum_{n=0}^{\infty} (2n+1) R^{n(n+1)/2} J_{n+1/2}^2(k_\perp a). \quad (\text{E.38})$$

## E.2 Discrete Surfaces

We consider the Poisson distribution:

$$p(x) = \frac{e^{-a} a^x}{x!}, \quad x = 0, 1, 2, \dots, \quad a > 0. \quad (\text{E.39})$$

The corresponding orthogonal polynomials are Charlier polynomials, defined as [E.1]

$$C_n(x, a) = a^{-n} L_n^{(x-n)}(a), \quad (\text{E.40})$$

where  $L_n^{(x-n)}(a)$  is the associated Laguerre polynomial. The orthogonality relation is given by

$$\sum_{x=0}^{\infty} p(x) C_n(x, a) C_m(x, a) = \frac{a^{-n}}{n!} \delta_{nm}. \quad (\text{E.41})$$

Therefore,

$$h_n^2 = \frac{a^{-n}}{n!}. \quad (\text{E.42})$$

The joint distribution function is

$$p_j(x, y; R) = \frac{e^{-2a} a^{x+y}}{x! y!} \sum_{n=0}^{\infty} \left(\frac{R}{a}\right)^n n! n! L_n^{(x-n)}(a) L_n^{(y-n)}(a), \quad (\text{E.43})$$

and

$$\begin{aligned} & \sum_{k=0}^{\infty} k! t^k L_k^{(a-k)}(x) L_k^{(\beta-k)}(y) = \\ & \beta! t^{\beta} (1-ty)^{a-\beta} e^{txy} L_{\beta}^{(a-\beta)} \left[ -\frac{(1-tx)(1-ty)}{t} \right]. \end{aligned} \quad (\text{E.44})$$

Therefore,

$$p_j(x, y; R) = \frac{e^{-2a} a^x}{x!} R^y (1-R)^{x-y} e^{aR} L_y^{(x-y)} \left[ -\frac{a(1-R)^2}{R} \right]. \quad (\text{E.45})$$

The height difference distribution  $P(z, r)$  can be written as

$$\begin{aligned} P(z, r) &= \sum_{y=0}^{\infty} p(z+y, y; R) = \frac{e^{-2a+aR}(1-R)^2 a^z}{z!} \\ &\times \sum_{y=0}^{\infty} \frac{(aR)^y}{(z+1)_y} L_y^z \left[ -\frac{a(1-R)^2}{R} \right]. \end{aligned} \quad (\text{E.46})$$

Since

$$\sum_{k=0}^{\infty} \frac{t^k}{(\alpha+1)_k} L_k^{\alpha}(x) = \Gamma(\alpha+1)(tx)^{-\frac{\alpha}{2}} e^t J_{\alpha}(2\sqrt{tx}), \quad (\text{E.47})$$

then

$$P(z, r) = (-1)^{-\frac{z}{2}} e^{-2a(1-R)} J_z[2(1-R)i] = e^{-2a(1-R)} I_z[2a(1-R)], \quad (\text{E.48})$$

where  $I_z(x)$  is modified Bessel function. Therefore,

$$C(k_{\perp}, r) = \sum_{z=-\infty}^{\infty} e^{-2a(1-R)} I_z[2a(1-R)] e^{ik_{\perp}cz}, \quad (\text{E.49})$$

where  $c$  is the lattice constant along the  $z$  axis. Let  $\Phi = k_{\perp}c$ , then

$$\begin{aligned} C(k_{\perp}, r) &= e^{-2a(1-R)} I_0[2a(1-R)] \\ &+ 2e^{-2a(1-R)} \sum_{n=1}^{\infty} I_n[2a(1-R)] \cos(n\Phi), \end{aligned} \quad (\text{E.50})$$

i.e.,

$$C(k_{\perp}, r) = e^{-2a(1-R)(1-\cos\Phi)}. \quad (\text{E.51})$$

The height-height correlation function is

$$H(r) = \sum_{z=-\infty}^{\infty} z^2 e^{-2a(1-R)} I_z[2a(1-R)] = 2a(1-R). \quad (\text{E.52})$$

Therefore,

$$C(k_{\perp}, r) = e^{-H(r)(1-\cos\Phi)}. \quad (\text{E.53})$$

### Reference

- E.1 G. Szego, *Orthogonal Polynomials*, American Mathematical Society Colloquium Vol. XXIII (American Mathematical Society, Providence, RI, 1959).

This Page Intentionally Left Blank

## Appendix F A PERTURBATIVE SOLUTION OF SINE-GORDEN EQUATION

In this appendix, we give a perturbation solution of Equation (14.3) for a small pinning force. Letting  $V = \varepsilon V_0$ , where  $\varepsilon$  is small and  $h = h_0 + \varepsilon h_1 + \varepsilon^2 h_2 + \dots$ , Equation (14.3) can be written as

$$\frac{\partial h_0}{\partial t} = R + v\nabla^2 h_0 - \kappa\nabla^4 h_0 + \eta, \quad (\text{F.1})$$

$$\frac{\partial h_1}{\partial t} = v\nabla^2 h_1 - \kappa\nabla^4 h_1 - V_0 \sin\left(\frac{2\pi h_0}{c}\right). \quad (\text{F.2})$$

Letting  $h_0(\mathbf{r}, t) = h_{0,0}(t) + h_{0,1}(\mathbf{r}, t)$ , we have

$$h_{0,0}(t) = Rt, \quad (\text{F.3})$$

$$\tilde{h}_{0,1}(\mathbf{k}, t) = \int_0^t \Theta(\mathbf{k}, \tau) e^{-(\kappa k^4 + \nu k^2)(t-\tau)} d\tau, \quad (\text{F.4})$$

where  $\Theta(\mathbf{k}, t)$  and  $\tilde{h}_{0,1}(\mathbf{k}, t)$  are the spatial Fourier transform of  $\eta(\mathbf{r}, t)$  and  $h_{0,1}(\mathbf{r}, t)$ , respectively, as defined in Equations (A.9) and (A.10). Clearly  $h_{0,0}$  is the average height (or thickness) of the zeroth-order perturbation, and  $h_{0,1}$  is the height fluctuation of the zeroth-order perturbation. Usually,  $h_{0,0} \gg \sqrt{\langle h_{0,1}^2 \rangle}$ , therefore Equation (F.2) can be further approximated by

$$\frac{\partial h_1}{\partial t} = v\nabla^2 h_1 - \kappa\nabla^4 h_1 - V_0 \sin\left(\frac{2\pi Rt}{c}\right) - \frac{2\pi V_0}{c} h_{0,1} \cos\left(\frac{2\pi Rt}{c}\right). \quad (\text{F.5})$$

Similarly, letting  $h_1(\mathbf{r}, t) = h_{1,0}(t) + h_{1,1}(\mathbf{r}, t)$ , we obtain

$$h_{1,0}(t) = \frac{V_0 c}{2\pi R} [\cos\left(\frac{2\pi R t}{c}\right) - 1], \quad (\text{F.6})$$

$$\tilde{h}_{1,1}(\mathbf{k}, t) = -\frac{2\pi V_0}{c} \int_0^t \cos\left(\frac{2\pi R \tau}{c}\right) \tilde{h}_{0,1}(\mathbf{k}, \tau) e^{-(\kappa k^4 + \nu k^2)(t-\tau)} d\tau. \quad (\text{F.7})$$

Therefore, the average thickness of a film grows as

$$\langle h \rangle \approx Rt + \frac{V_0 c}{2\pi R} [\cos\left(\frac{2\pi R t}{c}\right) - 1], \quad (\text{F.8})$$

and the power spectrum due to surface roughness evolves as

$$\langle \Delta h(\mathbf{k}, t)^2 \rangle = D \frac{1 - e^{-2(\kappa k^4 + \nu k^2)t}}{\kappa k^4 + \nu k^2}$$

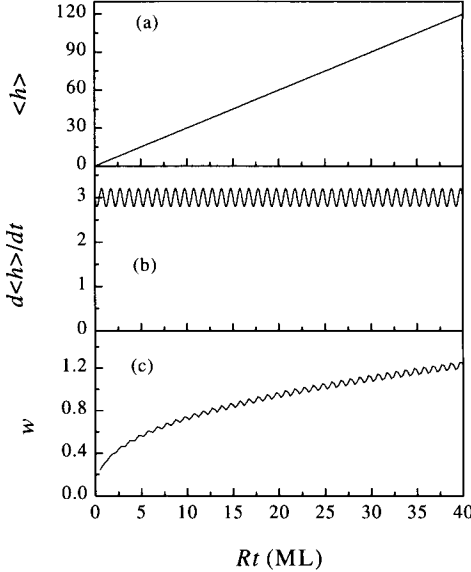


FIG. F.1 The average thickness  $\langle h \rangle$ , the growth rate  $\frac{d\langle h \rangle}{dt}$ , and the interface width  $w$  as a function of growth time at a fixed rate  $R$  for  $\nu = 0$ ,  $\kappa = 2$ ,  $D = 0.5$ ,  $R = 3$ ,  $c = 3$ , and  $V_0 = 0.2$ .

$$\begin{aligned}
 &+ \frac{DV_0c}{\pi R(\kappa k^4 + \nu k^2)} \sin\left(\frac{2\pi Rt}{c}\right) e^{-2(\kappa k^4 + \nu k^2)t} \\
 &- \frac{4DV_0[\cos\left(\frac{2\pi Rt}{c}\right) - e^{-2(\kappa k^4 + \nu k^2)t}]}{(2\pi R/c)^2 + 4(\kappa k^4 + \nu k^2)^2} \\
 &- \frac{4DV_0\pi R \sin\left(\frac{2\pi Rt}{c}\right)}{c(\kappa k^4 + \nu k^2)[(2\pi R/c)^2 + 4(\kappa k^4 + \nu k^2)^2]}. \quad (\text{F.9})
 \end{aligned}$$

Figure F.1 shows the change of the average thickness  $\langle h \rangle$ , the growth rate  $\frac{d\langle h \rangle}{dt}$ , and the interface width  $w$  as a function of growth time for  $\nu = 0$ ,  $\kappa = 2$ ,  $D = 0.5$ ,  $R = 3$ ,  $c = 3$ , and  $V_0 = 0.2$ . As  $V_0 \ll R$ , the average thickness increases almost linearly with time, but the actual growth rate oscillates with a small amplitude depending on the pinning force  $V_0$ . The interface width increases and the oscillation amplitude becomes larger and larger as the time increases. The above treatment does not account for the discrete nature of the lattice, especially at the very initial stages. For example, when  $\Theta = 0.5$ , the interface width  $w$  should not be less than 0.5. However, from Figure F.1 we can see that the calculated  $w$  is less than 0.4. This inconsistency arises when we neglect the discrete lattice effect in the Langevin equation, Equation (14.3). As long as the  $\Theta$  is not an integer, no matter what smoothening mechanism dominates the growth,

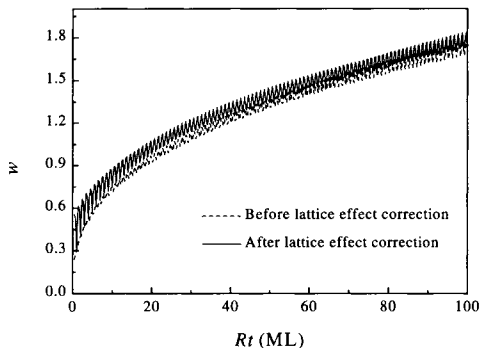


FIG. F.2 The interface width  $w$  as a function of growth time  $t$  before and after the discrete lattice effect correction.

the crystalline surface has to be rough. This is the intrinsic nature of a crystalline surface. A continuous equation washes out this nature. In order to incorporate the discrete lattice effect, we make the following simple assumption: if the surface is not totally covered by adatoms, i.e.,  $Rt/c$  is not an integer, we assume that the surface has two basic growth modes: one is the 2-D growth and the other one is dynamic roughening. Those two modes are independent of each other. Therefore, the total interface width should be  $w_t = \sqrt{w^2 + \Theta(1 - \Theta)}$ . Figure F.2 shows the interface width  $w$  as a function of growth time  $t$  before and after the discrete lattice effect correction. At the very initial growth stage, the discrete lattice effect contributes quite a lot to the  $w$  value, while for long times the Langevin equation dominates the roughening.

This Page Intentionally Left Blank

## Appendix G SPECKLE

One very interesting question for diffraction from a rough surface is the behavior of the diffraction pattern when  $\Omega \rightarrow \infty$ , where  $\Omega = k_{\perp}^2 w^2$ . In Chapter 7 we discussed the asymptotic cases for both  $\Omega \ll 1$  and  $\Omega \gg 1$  and showed that different roughness parameters can be extracted from the diffraction profile. However, in the limit  $\Omega \rightarrow \infty$ , the  $\delta$ -peak intensity  $I_{\delta} \approx 0$ , and the FWHM of the diffuse profile will become infinite since the height difference function  $C(k_{\perp}, r) \rightarrow \delta(r)$ . In fact, in this case, one cannot observe a diffraction profile. All one can observe is the scattering intensity fluctuation in the space as shown in Figure G.1. The phenomenon is called speckle and has been studied for almost a century [G.1, G.2, G.3]. The main areas of study are the statistical properties of the speckle pattern caused by a random phase screen (including those by rough surfaces) and corresponding applications [G.1, G.2, G.3]. Here we will concentrate on how the speckle pattern relates to the surface roughness.

The fluctuation of the scattered intensity  $\Delta I(\mathbf{k})$  can be expressed as

$$\Delta I(\mathbf{k}) = I(\mathbf{k}) - \langle I(\mathbf{k}) \rangle, \quad (\text{G.1})$$

where  $I(\mathbf{k})$  is the measured intensity and  $\langle I(\mathbf{k}) \rangle$  is the average intensity. We define the mean square speckle contrast as

$$\gamma^2(\mathbf{k}) = \frac{\langle \Delta I(\mathbf{k})^2 \rangle}{\langle I(\mathbf{k}) \rangle^2}, \quad (\text{G.2})$$

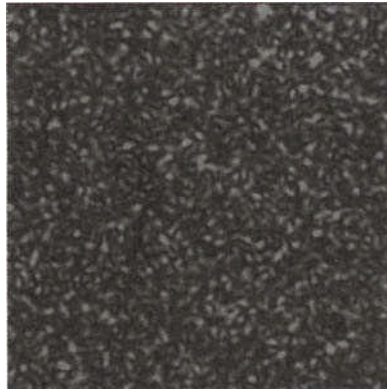


FIG. G.1 A speckle pattern generated by a random phase screen. Image is provided by Prof. C.-F. Cheng.

where  $\langle \Delta I(\mathbf{k})^2 \rangle$  is the mean square intensity fluctuation. The speckle correlation  $\sigma(\mathbf{k}_1, \mathbf{k}_2)$  can be defined as

$$\sigma(\mathbf{k}_1, \mathbf{k}_2) = \frac{\langle \Delta I(\mathbf{k}_1) \Delta I(\mathbf{k}_2) \rangle}{\langle I(\mathbf{k}_1) \rangle \langle I(\mathbf{k}_2) \rangle}, \quad (\text{G.3})$$

where  $\mathbf{k}_1$  and  $\mathbf{k}_2$  are momentum transfers. In the following, we concentrate on how to calculate the speckle correlation  $\sigma(\mathbf{k}_1, \mathbf{k}_2)$  from a self-affine Gaussian rough surface.

In general, the diffraction amplitude can be expressed as Equation (6.46). If we assume the atomic factor  $f$  in Equation (6.46) is a constant, and if we also consider the finite-aperture effect, then the diffraction amplitude  $F(\mathbf{k})$  can be written as

$$F(\mathbf{k}) = \int_{-\infty}^{+\infty} t(\boldsymbol{\rho}) e^{-ik_{\perp} h} e^{-i\mathbf{k}_{||} \cdot \boldsymbol{\rho}} d\boldsymbol{\rho}. \quad (\text{G.4})$$

Here  $t(\boldsymbol{\rho})$  is an aperture function resulting from the finite beam size and the instrumentation of the experimental setup. The diffraction intensity  $I(\mathbf{k})$  is

$$\begin{aligned} I(\mathbf{k}) &= F(\mathbf{k}) F(\mathbf{k})^* \\ &= \int_{-\infty}^{+\infty} \int_{-\infty}^{+\infty} t(\boldsymbol{\rho}) t(\boldsymbol{\rho}')^* e^{-ik_{\perp} [h(\boldsymbol{\rho}) - h(\boldsymbol{\rho}')] } e^{-i\mathbf{k}_{||} \cdot (\boldsymbol{\rho} - \boldsymbol{\rho}')} d\boldsymbol{\rho} d\boldsymbol{\rho}'. \end{aligned} \quad (\text{G.5})$$

Therefore the mean intensity is

$$\begin{aligned} \langle I(\mathbf{k}) \rangle &= \int_{-\infty}^{+\infty} \int_{-\infty}^{+\infty} t(\boldsymbol{\rho}) t(\boldsymbol{\rho}')^* \langle e^{-ik_{\perp} [h(\boldsymbol{\rho}) - h(\boldsymbol{\rho}')] } \times e^{-i\mathbf{k}_{||} \cdot (\boldsymbol{\rho} - \boldsymbol{\rho}')} d\boldsymbol{\rho} d\boldsymbol{\rho}' \\ &= \frac{1}{(2\pi)^2} \int_{-\infty}^{+\infty} S(\mathbf{q}_{||}, k_{\perp}) |T(\mathbf{q}_{||} - \mathbf{k}_{||})|^2 d\mathbf{q}_{||}, \end{aligned} \quad (\text{G.6})$$

where  $S(\mathbf{q}_{||}, k_{\perp})$  is the diffraction structure factor defined in Equation (7.19) and  $T(\mathbf{k}_{||}) = \int_{-\infty}^{+\infty} t(\boldsymbol{\rho}) e^{-i\mathbf{k}_{||} \cdot \boldsymbol{\rho}} d\boldsymbol{\rho}$ . As  $\Omega \rightarrow \infty$ ,  $S(\mathbf{q}_{||}, k_{\perp})$  varies very slowly compared with  $T(\mathbf{k}_{||})$ , i.e., the profile  $T(\mathbf{k}_{||})$  is much narrower than  $S(\mathbf{q}_{||}, k_{\perp})$ . Therefore,

$$\langle I(\mathbf{k}) \rangle \approx A S(\mathbf{q}_{||}, k_{\perp}), \quad (\text{G.7})$$

where  $A = \frac{1}{(2\pi)^2} \int_{-\infty}^{+\infty} |T(\mathbf{q}_{||})|^2 d\mathbf{q}_{||}$ .

Then,

$$\Delta I(\mathbf{k}) = F(\mathbf{k}) F(\mathbf{k})^* - \langle F(\mathbf{k}) F(\mathbf{k})^* \rangle \quad (\text{G.8})$$

and

$$\begin{aligned}
 <\Delta I(\mathbf{k}_1)\Delta I(\mathbf{k}_2)> &= <[F(\mathbf{k}_1)F(\mathbf{k}_1)^*-< F(\mathbf{k}_1)F(\mathbf{k}_1)^*>] \\
 &\quad \times [F(\mathbf{k}_2)F(\mathbf{k}_2)^*-< F(\mathbf{k}_2)F(\mathbf{k}_2)^*>]> \\
 &= <F(\mathbf{k}_1)F(\mathbf{k}_1)^*F(\mathbf{k}_2)F(\mathbf{k}_2)^*> \\
 &\quad - <F(\mathbf{k}_1)F(\mathbf{k}_1)^*>< F(\mathbf{k}_2)F(\mathbf{k}_2)^*> \\
 &= <F(\mathbf{k}_1)F(\mathbf{k}_1)^*F(\mathbf{k}_2)F(\mathbf{k}_2)^*> \\
 &\quad - <I(\mathbf{k}_1)>< I(\mathbf{k}_2)>. \tag{G.9}
 \end{aligned}$$

When  $\Omega \rightarrow \infty$ , the scattered field  $F(\mathbf{k})$  can be treated as a circular complex Gaussian field [G.4, G.5], and the above equation becomes

$$<\Delta I(\mathbf{k}_1)\Delta I(\mathbf{k}_2)> = |< F(\mathbf{k}_1)F(\mathbf{k}_2)^*>|^2. \tag{G.10}$$

Substituting Equation (G.4) into Equation (G.10), we have

$$\begin{aligned}
 < F(\mathbf{k}_1)F(\mathbf{k}_2)^*> &= \frac{1}{(2\pi)^2} e^{-\frac{1}{2}(k_{\perp 2}-k_{\perp 1})^2 w^2} \int_{-\infty}^{+\infty} S(\mathbf{q}_{||}, \sqrt{k_{\perp 1}k_{\perp 2}}) \\
 &\quad \times T^*(\mathbf{q}_{||} - \mathbf{k}_{||2})T(\mathbf{q}_{||} - \mathbf{k}_{||1})d\mathbf{q}_{||}. \tag{G.11}
 \end{aligned}$$

Also under the assumption  $\Omega \rightarrow \infty$ , we can treat  $S(\mathbf{q}_{||}, k_{\perp})$  as a constant, thus Equation (G.11) can be simplified as

$$< F(\mathbf{k}_1)F(\mathbf{k}_2)^*> \approx [< I(\mathbf{k}_1)>< I(\mathbf{k}_2)>]^{1/2} \chi(\mathbf{k}_1 - \mathbf{k}_2), \tag{G.12}$$

where

$$\chi(\mathbf{k}_1 - \mathbf{k}_2) = e^{-\frac{1}{2}(k_{\perp 2}-k_{\perp 1})^2 w^2} \frac{\int_{-\infty}^{+\infty} T^*(\mathbf{q}_{||})T(\mathbf{q}_{||} - \mathbf{k}_{||1} + \mathbf{k}_{||2})d\mathbf{q}_{||}}{\int_{-\infty}^{+\infty} |T(\mathbf{q}_{||})|^2 d\mathbf{q}_{||}}. \tag{G.13}$$

Combining Equations (G.3), (G.10), and (G.12), we obtain

$$\sigma(\mathbf{k}_1, \mathbf{k}_2) = \chi^2(\mathbf{k}_1 - \mathbf{k}_2). \tag{G.14}$$

Equation (G.14) gives the relation between the speckle correlation and the RMS roughness through the function  $\chi$ . Note that neither the lateral correlation length  $\xi$  nor the roughness exponent  $\alpha$  enters into Equation (G.14) because of the assumption of circular-complex Gaussian statistics. Also, the contrast will be a function only of the aperture function. Other more complicated treatments can be found in the literature [G.1, G.2, G.3]. We should emphasize that using the speckle (of light) method, such as the contrast versus aperture size, or the multi-angle or multi-wavelength speckle correlation, one can measure RMS roughnesses up to 20  $\mu\text{m}$ .

### References

- G.1 *Laser Speckle and Related Phenomena*, Edited by J. C. Dainty, 2nd Edition (Springer-Verlag, Berlin, 1984).
- G.2 *Speckle Metrology*, Edited by Rajpal S. Sirohi (Marcel Dekker, New York, 1993).
- G.3 *Selected Papers on Speckle Metrology*, Edited by Rajpal S. Sirohi (SPIE Optical Engineering Press, Bellingham, 1991).
- G.4 H. M. Pedersen, "Second-order statistics of light diffracted from Gaussian, rough surfaces with application to roughness dependence of speckles," *Optica Acta* **22**, 523 (1975).
- G.5 H. M. Pedersen, "Theory of speckle dependence on surface roughness," *J. Opt. Soc. Am.* **66**, 1204 (1976).

## Appendix H DIFFRACTION OF AN ULTRAFAST RADIATION PULSE

Until now all the diffraction formulas we considered are diffraction from a continuous monochromatic beam. How about when the incident beam becomes non-continuous, say, a pulse? In this appendix, we discuss how the rough surface affects an electromagnetic pulse.

The electromagnetic pulse can be written as

$$E(t) = e^{-i\omega_0 t} f(t), \quad (\text{H.1})$$

where  $\omega_0$  is the central frequency of the pulse and  $f(t)$  is the shape of the pulse, which can be expressed in the frequency domain as

$$f(t) = \frac{1}{\sqrt{2\pi}} \int_{-\infty}^{\infty} F(\omega) e^{-i\omega t} d\omega. \quad (\text{H.2})$$

Therefore the expression for the electrical field becomes

$$E(t) = \frac{1}{\sqrt{2\pi}} \int_{-\infty}^{\infty} F(\omega) e^{-i(\omega+\omega_0)t} d\omega. \quad (\text{H.3})$$

For a wave propagating in a vacuum, there is no dispersion, so

$$\omega = ck, \quad (\text{H.4})$$

where  $c$  is the speed of light and  $k$  is the wave number. Thus Equation (H.3) can be re-written as

$$E(t) = \frac{c}{\sqrt{2\pi}} \int_{-\infty}^{\infty} F(k) e^{-i(k+k_0)ct} dk, \quad (\text{H.5})$$

i.e.,

$$F(k) \propto \tilde{F}[E(t)]. \quad (\text{H.6})$$

Here the symbol  $\tilde{F}$  means Fourier transform. From Chapter 6, we know that the scattering amplitude for a parallel monochromatic plane wave scattered from a rough surface can be written as

$$A(\mathbf{k}) = \int e^{i\mathbf{k}_\perp \cdot \mathbf{h}(\boldsymbol{\rho})} e^{-i\mathbf{k}_{||} \cdot \boldsymbol{\rho}} E_0(\mathbf{k}) d\boldsymbol{\rho}, \quad (\text{H.7})$$

where  $E_0(\mathbf{k})$  is the amplitude of incident plane wave. Combining Equations (H.7) and (H.5), the electrical field  $E_{st}(t)$  for the pulse after it scattered

from a rough surface becomes

$$E_{st}(t) = \frac{c}{\sqrt{2\pi}} \int_{-\infty}^{\infty} F(k) e^{-i(k+k_0)ct} dk \int e^{ik_{\perp}h(\rho)} e^{-i\mathbf{k}_{||}\cdot\rho} d\rho. \quad (\text{H.8})$$

If the detection direction is fixed at the specular-reflection direction,  $\mathbf{k}_{||} = 0$ , then

$$\begin{aligned} E_{st}(t) &= \frac{c}{\sqrt{2\pi}} \int_{-\infty}^{\infty} F(k) e^{-i(k+k_0)ct} dk \int e^{ik_{\perp}h(\rho)} d\rho \\ &= \frac{c}{\sqrt{2\pi}} \int_{-\infty}^{\infty} F(k) e^{-i(k+k_0)ct} \varphi(k_{\perp}) dk, \end{aligned} \quad (\text{H.9})$$

where  $\varphi(k_{\perp}) = \langle e^{ik_{\perp}h(\rho)} \rangle$  is the characteristic function of the surface height distribution. As  $k_{\perp} = 2(k + k_0) \cos \theta$ , Equation (H.9) can be written as

$$E_{st}(t) = \frac{c}{\sqrt{2\pi}} \int_{-\infty}^{\infty} F(k) \varphi(k + k_0) e^{-i(k+k_0)ct} dk, \quad (\text{H.10})$$

i.e.,

$$F(k) \varphi(k + k_0) = \frac{1}{c} \tilde{F}[E_{st}(t)]. \quad (\text{H.11})$$

That is, the characteristic function of the surface height distribution can be obtained from the specularly reflected pulse. For example, if we assume the incident pulse has a Gaussian shape with a width  $\tau_0$ ,

$$f(t) = \exp\left(-\frac{t^2}{2\tau_0^2}\right), \quad (\text{H.12})$$

then

$$F(k) = \exp\left(-\frac{k^2 c^2 \tau_0^2}{2}\right). \quad (\text{H.13})$$

If the rough surface also has a Gaussian height distribution,

$$p(h) = \exp\left(-\frac{h^2}{2w^2}\right), \quad (\text{H.14})$$

then

$$\varphi(k + k_0) = \exp\left[-\frac{(k + k_0)^2 w^2 \cos^2 \theta}{2}\right]. \quad (\text{H.15})$$

Therefore the specularly reflected pulse becomes

$$E_{st}(t) \propto e^{-k_0^2 w^2 \cos^2 \theta} \tilde{F}\left\{\exp\left[-\frac{(c^2 \tau_0^2 + w^2 \cos^2 \theta)(k + \frac{k_0 w^2 \cos^2 \theta}{c^2 \tau_0^2 + w^2 \cos^2 \theta})^2}{2}\right]\right\}. \quad (\text{H.16})$$

From Equation (H.16) we can see that a rough surface has at least three effects on the specularly reflected pulse: (1) the amplitude of the pulse will decrease according to  $\exp[-k_0^2 w^2 \cos^2 \theta + \frac{1}{2}(\frac{k_0 w^2 \cos^2 \theta}{c^2 \tau_0^2 + w^2 \cos^2 \theta})^2]$ ; (2) the pulse will broaden according to surface roughness, and the FWHM becomes  $\sqrt{\tau_0^2 + \frac{w^2 \cos^2 \theta}{c^2}}$ ; and (3) there is a time delay in the scattered pulse.

This Page Intentionally Left Blank

# INDEX

## A

- Adatoms, atomistic processes, 273–274  
AFM, *see* Atomic force microscopy  
Anisotropic surfaces, 47–48  
    correlation-length anisotropy, 49–51  
    diffraction from, 223–224  
        beams from correlation length anisotropic surfaces, 224–226  
        beams from scaling-anisotropic surfaces, 226–228  
        line scan of diffraction beam, 228–230  
    growth dynamics, 368–375  
    hard-disk surface as example, 231  
        AFM measurements, 232–235  
        light scattering, 235–238  
    mercury-cadmium-telluride film on stepped GaGa substrate as example, 53–54  
real-space characteristics, 223–224  
roughness parameters, determination, 230  
    reciprocal-space structure, 230–231  
scaling anisotropy, 51–53  
Atomic force microscopy, 71–75  
    continuous two-level fractal surfaces, 267  
    hard-disk surface, 232–235  
    scanning probe microscopy, 71–75  
    Si wafer backside, 38–39  
Auto-correlation function, 15–18  
    for anisotropic surfaces, 49–51  
    for mounded surfaces, 43  
    for self-affine surfaces, 38  
    numerical estimation, 24  
Auto-covariance function, 15  
    extraction from surface images, 26–27  
Average surface height, numerical estimation, 24

## B

- Born approximation, 108, 132

## C

- Confocal scanning optical microscopy, 75–77  
CSOM, *see* Confocal scanning optical microscopy

## D

- $\delta$  peak  
    Gaussian rough surfaces, 138  
    mounded surfaces, 213  
    non-Gaussian surfaces, 248–250  
Diffraction  
    from anisotropic surfaces, 224–239  
        beams from correlation length anisotropic surfaces, 224–226  
        beams from scaling-anisotropic surfaces, 226–228  
        line scan of diffraction beam, 228–230  
    from continuous two-level surface, 266  
        examples, 267–270  
    from discrete mounded surfaces, 216–217  
        examples, 217–219  
    from discrete self-affine surfaces, 203  
        near-in-phase condition, 204–205  
        near-out-of-phase condition, 205  
        reciprocal-space structure, 205–207  
    from discrete two-level surface, 256  
        from random clustering surfaces, 258–261  
        from random filling surfaces, 257–258  
        from two-dimensional nucleations, 261–266  
    from dynamic roughening fronts, 291–294  
    from Gaussian rough surfaces, 135–138  
         $\delta$  peak, 138  
        diffuse profile, 138–141  
        integrated intensity, 141–142  
    from isotropic self-affine Gaussian surface, 181  
        diffraction structure factor, asymptotic behavior of, 181–186  
        reciprocal-space structure, 188–189  
        roughness parameters, determination from diffraction profiles, 181–186  
        inverse Fourier transform method, 188  
        lateral correlation length  $\xi$ , 187  
        RMS roughness  $w$ , 186–187  
        roughness exponent  $\alpha$ , 187–188  
    from mounded surfaces, 212–219  
        asymptotic behavior of the diffraction structure factor, 212–215

- Diffraction, from mounded surfaces (*continued*)  
 reciprocal-space structure, 215–216  
 from multi-step surfaces in 2+1 dimensions,  
 142–143  
 discrete lattice effect, 147  
 $\delta$  intensity, 147–149  
 diffuse intensity, 149–155  
 height difference function of discrete  
 surface, 143–145  
 in-phase/out-of-phase diffraction  
 conditions, 145–147  
 periodic oscillation, 145  
 from non-Gaussian surfaces, 247–248  
 diffuse profile, 250–254  
 $\delta$ -peak intensity, 248–250  
 from rough surfaces  
 continuum theory, 122–123  
 distorted-wave Born approximation,  
 129–132  
 Fraunhofer diffraction, 129  
 Kirchhoff approximation, 127–129  
 perturbation methods, 123–127  
 general formula, 117  
 diffraction structure factor for  
 continuous surfaces, 120–122  
 diffraction structure factor for discrete  
 surfaces, 117–120  
 from single atom, general formula, 108–110  
 general concepts, 104  
 geometries of, 157–160  
 azimuthal-rotation mode, 161–163  
 in-plane, 164–165  
 in-plane-rotation mode, 163  
 out-of-plane, 163–164  
 rocking mode, 160–161  
 measured intensity profile, 165–167  
 angular factor, 167–169  
 instrument response, 169  
 beam size, 171–172  
 detector size, 171  
 energy spread and beam divergence,  
 169–170  
 measurement  
 data analysis, 173–174  
 kinematic diffraction theory, validity of,  
 174  
 setup performance, 172–173  
 shadowing effect, 174–175  
 modes, in three-dimensional space, 303  
 multi-atom  
 from atomic array, 110–112  
 one-dimensional adsorbates with double  
 periodicity, 112–114  
 superposition of diffraction waves,  
 114–117  
 of atomic particles, 107–108  
 of photons, 104–107  
 of ultrafast radiation pulse, 407–409  
 Diffraction profiles  
 determination of roughness parameters from,  
 181–186  
 inverse Fourier transform method, 188  
 lateral correlation length  $\xi$ , 187  
 RMS roughness  $w$ , 186–187  
 roughness exponent  $\alpha$ , 187–188  
 effects of functional forms of scaling  
 function, 383–386  
 general properties, 133–135  
 Distorted-wave Born approximation, 129–132  
 Dynamic roughening fronts, diffraction from,  
 291–294  
 Cu/Cu(001), as example of step-bias growth,  
 294–296  
 measurement and analysis, issues, 298–300  
 Si/Si(111), as example of dynamic scaling  
 surface, 294–296
- E**
- Edwards–Wilkinson equation, time evolution of  
 interface width in, 381  
 Electromagnetic pulse, rough surface effects,  
 407–409  
 Electronic devices, operations, surface/interface  
 roughness effects, 332–336  
 on capacitance with one rough electrode,  
 341–342  
 on electrical potential and electric field of  
 capacitor with single rough boundary,  
 336–341  
 on leakage currents in capacitor with one  
 rough electrode, 343–347
- F**
- Films, *see* Thin films  
 Fokker–Planck equation, 242  
 Fractal structures  
 diffraction characteristics, 306–308  
 three-dimensional, 305

- Fractal surfaces, *see also specific types*  
 continuous two-level surfaces, 266  
   AFM and light scattering results, 267  
   profile analysis, 268–270  
   roughness parameters, determination,  
     268–270  
 two-dimensional, discrete, 255–257  
   diffraction  
     from random clustering surfaces,  
       258–261  
     from random filling surfaces, 257  
   two-dimensional nucleations, 261–266
- Fraunhofer diffraction, 129
- G**
- Geometries, diffraction, 157–160  
 azimuthal-rotation mode, 161–163  
 in-plane, 164–165  
 in-plane-rotation mode, 163  
 out-of-plane, 163–164  
 rocking mode, 160–161
- Growth, films, intensity oscillations  
 layer-by-layer growth, 275–277  
 quasi-layer-by-layer growth, 278  
   poly-nuclear growth model, 278–280  
   Sine–Gorden equation, 280–286  
 reentrant layer-by-layer growth, 287–288  
 step-flow growth, 275
- Growth dynamics  
 anisotropic surfaces, 368–375  
 mounded surfaces, 361–362  
   other growth models, 366–368  
   step-bias-induced instability, 362–365  
 self-affine surfaces  
   dynamic scaling concept, 353–355  
   Kardar–Parisi–Zhang model, 360–361  
   linear growth model, 355–360
- Growth exponent,  $\beta$ , 354
- H**
- Hard-disk surface, as example of anisotropic surface, 231
- AFM measurements, 232–235  
 light scattering, 235–238
- Height difference function  
 continuous surface  
   exponential distribution, 392–393
- gamma distribution, 393–394  
 Gaussian distribution, 391–392  
 Rayleigh distribution, 394–395  
 uniform distribution, 395
- discrete surface, 395–397
- Height distribution  
 characteristic function, 12–13  
 Gaussian, 8, 10  
 non-Gaussian, 241–247  
   joint distributions of random processes  
     with, 387–389
- Height distribution function, 7–13
- Height-height correlation function, 18–19  
 extraction from surface images, 27–28
- finite sampling size effect  
 interface width, 93–96  
 sampling-induced apparent cycle, 96–101
- for anisotropic surfaces, 49–52  
 for mounded surfaces, 43  
 for self-affine surfaces, 34–38  
 for two-level surfaces, 256  
 numerical estimation, 25
- Henzler ring, 262–264
- I**
- Imaging techniques, 77  
 finite sampling size effect, 88–92  
   and height-height correlation function  
     interface width, 93–96  
     sampling-induced apparent cycle,  
       96–101
- interferometric microscope  
 heterodyne detection, 78–79  
 homodyne detection, 77–78  
 Nomarski differential profiling, 79–81
- Interface width, *see* RMS roughness
- Interferometric microscope  
 heterodyne detection, 78–79  
 homodyne detection, 77–78
- Isotropic self-affine Gaussian surface  
 diffraction from  
   diffraction structure factor, asymptotic  
     behavior of, 181–186  
   roughness parameters, determination from  
     diffraction profiles, 186  
   interface width  $w$ , 196–198  
   inverse Fourier transform method, 188  
   lateral correlation length  $\xi$ , 187, 198–199  
   RMS roughness  $w$ , 186–187

- Isotropic self-affine Gaussian surface, roughness parameters, determination from diffraction profiles (*continued*)
   
    roughness exponent  $\alpha$ , 187–188, 199–202
   
surface roughness effects
   
    local slope and surface area, 309–311
   
    on electronic device operations, 332–336
   
        electrical potential and electric field of capacitor with single rough boundary, 336–341
   
        on capacitance with one rough electrode, 341–342
   
    on leakage currents in capacitor with one rough electrode, 343–347
   
Isotropic self-affine Gaussian surfaces, surface roughness effects
   
    on thin film electrical properties, 311–319
   
    on thin film magnetic properties, 319–323
   
        coercivity from wall movement, 330–331
   
        coercivity from wall rotation, 331–332
   
    demagnetizing factor, 323–326
   
    domain wall thickness, 327–329
   
    domain width, 330
   
    surface energy, 311
- J**
- Joint distribution probability density function, 13–15
- K**
- Kirchhoff approximation, 127–129
- Kurtosis, of surface height, 11–12
   
    numerical estimation, 24
- L**
- Langevin equations, in generation of rough surfaces, 57–58
- Lateral correlation length  $\xi$ , 16
   
    determination for
   
        anisotropic surface, 229–230
   
        isotropic self-affine Gaussian surface, 187
   
        mounded surface, 43
   
Light scattering
- continuous two-level fractal surfaces, 267
   
hard-disk surface, 235–238
- M**
- Maxwell's equation, 104, 122–123
- Monte Carlo simulation, in generation of rough surfaces, 58
- Mounded surfaces
   
    CoGe thin film on GaAs substrate as example, 46–47
   
    definition, 42–46
   
diffraction from
   
    asymptotic behavior of the diffraction structure factor, 212–215
   
    reciprocal-space structure, 215–216
   
    roughness parameters, determination, 216
   
discrete, diffraction from, 216–217
   
    examples, 217–219
   
growth dynamics, 361–362
   
    other growth models, 366–368
   
    step-bias-induced instability, 362–365
   
    real-space characteristics, 211–212
- Multilayer structures
   
    Cu/Cu(001), as example of step-bias growth, 294–296
   
dynamic roughening fronts, diffraction from, 291–294
   
intensity oscillations, 274–275
   
    and incident angle/wavelength changes, 290–291
   
    and multibeam interference, 289–290
   
layer-by-layer growth, 275–277
   
quasi-layer-by-layer growth, 278
   
    poly-nuclear growth model, 278–280
   
    Sine–Gorden equation, 280–286
   
reentrant layer-by-layer growth, 287–288
   
step-flow growth, 275
   
Si/Si(111), as example of dynamic scaling surface, 294–296
- N**
- Nomarski differential profiling, 79–81
- Non-Gaussian surfaces
   
    diffraction structure factors from, 247–248
   
    diffuse profile, 250–254
   
     $\delta$ -peak intensity, 248–250

- height difference distribution and height difference function, 241–247
- Nyquist frequency, 30
- P**
- Photons, diffraction of, 104–107
- Porod law, 306–307
- Power spectrum, 19–21
- anisotropic surface, 49–51
  - extraction from surface images, 28
  - mounded surface, 44
  - numerical estimation, 25–26
  - self-affine surface, 35–38
- R**
- Rayleigh–Guinier regime, 307
- Real-space surface profiling techniques, 63; *see also* Imaging techniques; Scanning techniques
- disadvantages and limitations, 103–104
- Reflection diffraction, 303, 307–308
- RMS (root-mean-square) roughness  $w$ , 10
- isotropic self-affine Gaussian surface, 186–187
  - numerical estimation, 24
  - accuracy of, 29
- Rough surfaces, *see also specific types*
- classification of, 4–5
  - definition, 2
  - diffraction from
    - continuum theory, 122–123
    - general formula, 117
    - diffraction structure factor for continuous surfaces, 120–122
    - diffraction structure factor for discrete surfaces, 117–120  - diffraction profiles, general properties, 133–135
  - first order statistics: surface height distribution and characteristic function, 7–13
  - formation dynamics, 54–56
  - Gaussian, diffraction from, 135–138
    - $\delta$  peak, 138
    - diffuse profile, 138–141
    - integrated intensity, 141–142  - generation of, 56–57
- convolution method, 57
- Langevin equations, 57–58
- Monte Carlo simulation, 58
- measurement, constraints on, 2–3
- multi-step, in 2+1 dimensions, diffraction from, 142–143
- discrete lattice effect, 147
- $\delta$  intensity, 147–149
  - diffuse intensity, 149–155
- height difference function of discrete surface, 143–145
- in-phase/out-of-phase diffraction conditions, 145–147
- periodic oscillation, 145
- other statistical properties, 21
- continuity, 21–22
  - differentiation, 22
  - integration, 22–23
- roughness parameters, extraction from surface images, 26
- accuracy of, 28–32
  - auto-covariance function, 26–27
  - height–height correlation function, 27–28
  - power spectrum, 28
- statistical parameters, numerical estimation, 23
- auto-correlation function, 25
  - average surface height, 24
  - height–height correlation function, 25
  - power spectrum, 25–26
  - RMS roughness, 24
  - skewness and kurtosis, 24
- Roughness exponent  $\alpha$ , isotropic self-affine Gaussian surface, 187–188, 199–202
- Roughness parameters
- anisotropic surfaces, determination, 230
  - reciprocal-space structure, 230–231
  - continuous two-level fractal surfaces, determination, 270–271
- isotropic self-affine Gaussian surface determination, 186
- interface width  $w$ , 196–198
  - inverse Fourier transform method, 188
  - lateral correlation length  $\xi$ , 187, 198–199
  - RMS roughness  $w$ , 186–187
  - roughness exponent  $\alpha$ , 187–188, 199–202
- determination from diffraction profiles, 181–186
- inverse Fourier transform method, 188
  - lateral correlation length  $\xi$ , 187

- Roughness parameters, isotropic self-affine Gaussian surface (*continued*)
  - RMS roughness  $w$ , 186–187
  - roughness exponent  $\alpha$ , 187–188
 mounded surfaces, determination, 216
 rough surfaces, extraction from surface
  - images, 26
  - accuracy of, 28–32
  - auto-covariance function, 26–27
  - height–height correlation function, 27–28
  - power spectrum, 28
 silicon wafer backside, determination, 196–198
 interface width  $w$ , 196–198
 lateral correlation length  $\xi$ , 198–199
 roughness exponent  $\alpha$ , 199–202
- S**
- Scanning probe microscopy, 66–71
 atomic force microscopy, 71–75
 finite tip effects in, 83–88
 scanning tunneling microscopy, 66–71
- Scanning techniques, 63
 scanning optical microscopy, 75
 confocal scanning optical microscopy, 75–77
 scanning probe microscopy, 66–71
 atomic force microscopy, 71–75
 scanning tunneling microscopy, 66–71
 stylus profilometry, 63–65
- Scanning tunneling microscopy, 66–71
- Scattering, general concepts, 104–107
- Schrödinger's equation, 104, 122–123
- Self-affine surfaces, *see also* Isotropic self-affine Gaussian surface
 definition, 33–38
 discrete, diffraction from, 203
  - near-in-phase condition, 204–205
  - near-out-of-phase condition, 205
  - reciprocal-space structure, 205–207
 growth dynamics
  - dynamic scaling concept, 353–355
  - Kardar–Parisi–Zhang model, 360–361
  - linear growth model, 355–360
 real-space characteristics, 179–181
 Si wafer backside as example, 38–42
- Silicon
 Si/Si(111), as example of dynamic scaling surface, 294–296
- wafer backside, as example of self-affine surface, 38–42
- roughness parameters, determination, 196–198
 interface width  $w$ , 196–198
 lateral correlation length  $\xi$ , 198–199
 roughness exponent  $\alpha$ , 199–202
- testing validity of scattering behavior
 predictions, 189–190
 experimental results, 194–195
 experimental setup, 190–194
- Sine–Gorden equation, 280–286
 perturbative solution of, 399–401
- Skewness, of surface height, 10–11
 numerical estimation, 24
- SP, *see* Stylus profilometry
- Speckle, 403–405
- STM, *see* Scanning tunneling microscopy
- Stylus profilometry, 63–65
- Surface height distribution, during thin film
 roughening, 375–377
- Surface roughness effects
 and speckle pattern, 403–405
 local slope and surface area, 309–311
 on electromagnetic pulse, 407–409
 on electronic device operations, 332–336
 electrical potential and electric field of capacitor with single rough boundary, 336–341
 on capacitance with one rough electrode, 341–342
 on leakage currents in capacitor with one rough electrode, 343–347
- on thin film electrical properties, 311–319
- on thin film magnetic properties, 319–323
 coercivity from wall movement, 330–331
 coercivity from wall rotation, 331–332
 demagnetizing factor, 323–326
 domain wall thickness, 327–329
 domain width, 330
- T**
- Thin films
 CoGe, on GaAs substrate, as example of
 mounded surface, 46–47
 growth modes, 273–274
 roughening, surface height distribution
 during, 375–377

- surface/interface roughness effects on  
electrical properties, 311–319  
magnetic properties, 319–323  
    coercivity from wall movement,  
        330–331  
    demagnetizing factor, 323–326  
    domain wall thickness, 327–329  
    domain width, 330
- Transmission diffraction geometry, 303–304
- Two-level surfaces, 255–272  
    continuous two-level surfaces, 264–270  
        example, 264–270  
    discrete two-level surfaces, 255–264  
        diffraction intensity, 256  
        height difference function, 256  
        height–height correlation function, 256
- random clustering surface, 258–261  
random filling surface, 257–258  
two-dimensional nucleation, 261–266  
    Henzler ring, 262–264
- roughness parameter determination,  
    270–271
- U**
- Ultrafast radiation pulse, diffraction of, 407–409
- W**
- Weiner–Khinchine relation, 19

This Page Intentionally Left Blank